Proceeding of the 12th International Conference in Electrical Impedance Tomography (EIT 2011).

The Department of Electronic and Electrical Engineering, **University of Bath**, Bath, UK, **4-6 May 2011**.

- Dr. Manuchehr Soleimani (chair)
- Prof. Eung-je Woo (co-chair)

EIT Conference 4-6 May 2011

Programme of events

Day	Time	Event	Room
Wednesday 4 May	09:00-11:00	EIDORS Master class by Prof Andy Adler and Prof Bill Lionheart (Attendance optional)	4 East 2.32
	11:00-13:30	**Registration**	2 East Foyer (level 2)
	12:30-13:30	**Buffet lunch**	Wessex Restaurant
	13:30-14:00	**Welcome to the Conference** 1. Opening of the conference by Prof K Edge, Pro-VC of the University of Bath 2.Introduction by the chairman of the conference Dr Manuch Soleimani 3. Announcement of the physic. Meas. special issue: Prof R Bayford (Editor in Chief of IOP Physi. Meas.)	2 East 3.1
	14:00- 16:00	**Session 1** **Track 1- Application brain 1- experimental recordings** **Chair: Prof B Brown** 1. David Holder, Andrea Romsauerova' , Joshua Luis, Jonathan Cornell, Brett Packham, Emma Smith, Karolina Wloch, Darius Parvin, Sujin Ahn and Sung Chan Jun, *A method for recording Electrical Impedance Tomography images in human acute stroke subjects.* 2. Feng Fu , Chaoshuang Chen, Feng Xiao, Xuetao Shi, Ruigang Liu, Fusheng You, Xiuzhen Dong, Detection of *Brain Electrical Impedance Change after Ionization Injury: Preliminary Results* 3. P. Manwaring, R. Halter, K. Moodie, S. Kane, A. Hartov, *An animal model configuration for combined EIT imaging and ICP monitoring of intracranial trauma*	2 East 3.1

1		4. H McCann, S T Ahsan, J L Davidson, R L Robinson, P Wright, A Bryan, B J Pollard, T Quraishi and C J D Pomfrett, *Preliminary observations with fEITER data under auditory stimulation* 5. Xuetao Shi, Fusheng You, Liang Wang, Feng Fu, Ruigang Liu, Canhua Xu, Xiuzhen Dong, *Monitoring of Intraventricular Hemorrhage Changes in-vivo in a Piglet Model by Electrical impedance tomography* 6. Maureen Clerc, Laurent Koessler, Jean-Michel Badier, Martine Gavaret, *In vivo scalp-to-skull conductivity ratio calibration: an EIT study* -- **Track 2- Algorithm inverse 1** **Chair: Prof WRB Lionheart** 1. Bart Truyen, Luca Dimiccoli, Jan Cornelis, *A residual minimizing solver for the inverse problem of EIT* 2. D. G¨ursoy, Y. Mamatjanyand H. Scharfetter, *Augmenting information content through multimodal impedance imaging* 3. Lesparre N., Adler A., Gibert D., Nicollin F., *Electrical Impedance Tomography in geophysics, application of EIDORS* 4. Hongbin Wang, Guizhi Xu, Guoya Dong, Ying Li, Shuai Zhang, Weili Yan, *A Newton Iterative Method with Initial Conductivity Estimation from Dynamic Algorithm* 5. E A Attardo , A Borsic, R Halter, *Jacobian Optimization for 3D Electric Impedance Tomography via GPU acceleration* 6. Alistair Boyle, Andy Adler, Andrea Borsic, *Scaling the EIT Problem*	--------- 4 East 3.10
	16:00-16:30	Tea & coffee break	2 East 3.4

.1	16:30-18:00	**Session 2:** **Track 1- Application brain 2- technical consideration** **Chair: Prof D Holder** 1. Tugba Doru, Brett Packham, Hwan Koo and David Holder*, Is the 16 channel Spiral16 or 32 channel EEG31 electrode protocol better for stroke MF imaging in the head shaped tank?* 2. *P. YOUNG, F. HERMANS, R.M. HEETHAAR, A. DATTA and M. BIKSON, FE modelling and meshing of patient-specific anatomical models* 3. Sujin Ahn, Tong In Oh, Sung Chan Jun1k, Jin Keun Seo and Eung Je Woo, *Validation of weighted frequency-di_erence EIT using a hemisphere model and phantom* 4. B. Packham, H. Koo, S. Ahn, S. C. Jun and D. S. Holder, *Evaluation of the UCH Mk2.5 Multi-Frequency EIT system for imaging stroke in liquid filled anatomically realistic tanks.* -- **Track 2- Algorithm inverse 2** **Chair: Dr A Borsic** 1. Eun Jung Lee, Jin Keun Seo, Munkh Erdene, Tong In Oh and Eung Je Woo, *Breast EIT using a new projected image reconstruction method with multifrequency measurements* 2. Maureen Clerc, Jean-Michel Badier, Emmanuel Olivi, Alexandre Gramfort, Theodore Papadopoulo, *OpenMEEG for calibrating the conductivity of nested compartment models* 3. Peyman Rahmati, Manuchehr Soleimani, and Andy Adler, L*evel set based reconstruction algorithm for EIT lung images* 4. M. P. Ramirez T., R. A. Hernandez-Becerril, C. M. Robles G*., On a numerical interpolation technique for obtaining piecewise separable-variables conductivity functions*	2 East 3.1 --------- 4E3.10

Thursday 5 May	09:00-10:30	**Session 3:** **Invited talks Clinical Thoracic** **Chair: Prof. I Frerichs** 1. **Brian Brown, Invited Speaker** 2. **Stephan Böhm, Invited Speaker** 3. **Marc Bodenstein, Invited Speaker**	2 East 3.1
	10:30-11:00	Tea & coffee break	2 East 3.4
	11:00-13:00	**Session 4:** **Track 1- Clinical Thoracic 2** **Chair: Dr Stephan Böhm** 1. Zhanqi Zhao, Rainald Fischer, Ullrich Müller-Lisse, Knut Möller, *Ventilation inhomogeneity in cystic fibrosis patients as measured by means of electric impedance tomography* 2. Satoru Nebuya , Naoaki Itakura , Junko Kataoka, Brian H. Brown, Makoto Noshiro, *Measurement of lung air volume during digital sport shooting using EIT*	2 East 3.1

3. G. Hahn, A. Just, J. Dittmar, M. Quintel, *An integrated lung function reference laboratory for test and calibration of EIT devices*

4. Damien Ferrario, Andy Adler, Josesp Solà, Stephan Böhm and Marc Bodenstein, *Unsupervised localization of heart and lung regions in EIT images: a validation study*

5. Sven Pulletz, Ute Achtzehn, Andreas Pechmann, Michael Quintel, Norbert Weiler, Inéz Frerichs, *Effects of high-frequency oscillatory ventilation determined by EIT in patients with chronic airway obstruction*

6. Gunnar Elke, Matthew K. Fuld, Ahmed F. Halaweish, Norbert Weiler, Eric A. Hoffman and Inéz Frerichs, *Regional ventilation distribution in sub-lobar acute lung injury – An experimental validation study on electrical impedance tomography*

4E3.10

Track 2- Instrumentation 1
Chairs: Dr Tong In Oh

1. Iasonas F. Triantis, Loucas Constantinou, Panagiotis Kassanos, Andreas Demosthenous and Richard Bayford, *Towards the development of a fully integrated circuit for multi-frequency impedance measurements*

2. Nan Li, W Zhang, W Wang, N Huber and H Xu, *Bio-impedance Measurement Method Based on Digital Auto Balancing Bridge*

3. Pascal O. Gaggero, Andy Adler, Josef X. Brunner, Stephan Böhm, Peter Seitz, *Active Electrode Based Electrical Impedance Tomography System*

4. Pil Joong Yoo, Hun Wi, Tong In Oh and Eung Je Woo, *Parallel multi-frequency EIT system with self-calibration: KHU Mark2.5*

		5. Hun Wi, Pil Joong Yoo, Tong In Oh and Eung Je Woo, *Cascaded multi-channel EIT system with fast data acquisition by frequency-division and space-division multiplexing* 6. H Koo, B Packham and D Holder, *Optimization of calibration method to enable imaging acute stroke using the portable serial UCH Mk2.5 Multi-frequency Electrical Impedance Tomography (MFEIT) system*	
	13:00-14:00	Buffet lunch	Wessex Restaurant
	14:00- 16:00	**Session 5:** **Track 1- Applications-thoracic 2 and general** **Chair: Prof R Patterson** 1. T F Yamaguchi , L Q Wang, M Katashima, K Maki and S Kuriki, *Practical human abdominal fat estimation utilising electrical impedance tomography* 2. J Nasehi Tehrani, A Thiagalingam, C Jin, A van Schaik, W Chik, M.A. Barry, and A McEwan, *Feasibility of using internal electrodes to improve the accuracy Cardiac Electrical impedance tomography* 3. Robert P, Patterson, Jie Zhang, Fei Yang, and Andy Adler, *Evaluation of Reconstructed Images of Regional Lung Changes Using a Model* 4. Hyunji Kim, Tae Eui Kim, Tong In Oh and Eung Je Woo , *Integration of EIT with ECG and respiration monitoring* 5. V Trokhanova, M B Okhapkin, L A Musaeva and A V Korjenevsky, *Using of electrical impedance mammography for monitoring of the efficiency of dyshormonal breast diseases treatment*	2 East 3.1

		6. N Béqo, B Lingham, C Lobstein-Adams, G Sze and W Wang, *Dual scans with Combined Ultrasound and Electrical Impedance Mammography* -- **Track 2- Algorithm and forward modelling 1** **Chair: Prof A Adler** 1. Bart lomiej Grychtol, William R B Lionheart, Gerhard K Wolf, Marc Bodenstein, and Andy Adler, *The importance of shape: thorax models for GREIT* 2. J.L. Davidson, R.A. Little, P. Wright, J. Naish, R. Kikinis, G.J.M. Parker and H. McCann, *Co-registration and fusion of EIT images with MRI scan data* 3. Just, J. Dittmar, M. Quintel, G. Hahn, *Constructing resistive mesh phantoms by an equivalent 2D resistance distribution of a 3D cylindrical object* 4. Maimaitijiang Yasheng and Andy Adler, *Electrode positions and current patterns for 3D EIT* 5. J. Forsyth, A. Borsic, R. Halter, A. Hartov, K.D. Paulsen, *Optical Shape Capture and Meshing of the Breast* 6. Y. Mamatjan, D. Gursoy and A. Adler, *Electrode positions and current patterns for 3D EIT*	--------- 4E3.10
	16:00-16:30	Tea & coffee break	2 East 3.4

	16:30-18:00		
3.1		# Session 6: **Track 1- Clinical bioimpedance** **Chair: Prof A Korjenevsky** 1. Yuqing Wan, Ryan Halter, Andrea Borsic and Alex Hartov, *Preliminary clinical study on prostate cancer detection using transrectal EIT* 2. Fusehng You, Hua Cai, Xuetao Shi, Canhua Xu, Feng Fu, Ruigang Liu, Xiuzhen Dong, *Measurement the resistivity-temperature properties of liver tissue and applying EIT to monitor hyperthermia treatment based on phantom* 3. Naimul Islam, Adrian Wilson, *Preliminary results on using electrical impedance to determine tissue composition in support of non-invasive temperature measurement.* 4. Martina F. Callaghan, Torben Lund, Ivan M. Roitt, Richard H. Bayford, *Characterisation of the morphological and growth patterns of colorectal tumour cell lines via electrical impedance spectroscopy* -- **Track 2- Algorithm and forward modelling 2** **Chair: Dr A McEwan** 1.P.D. Ledger, *Electrical Impedance Tomography Inverse Solutions using High Order Finite Elements and LSQR* 2. P. Kantartzis, A. Kunoth, R. Pabel, P. Liatsis, *Multi-scale interior potential approximation for EIT* 3.P. Kantartzis, A. Kunoth, R. Pabel2, P. Liatsis, *Single-scale interior potential approximation for EIT* 4.Gang HU, Min-you CHEN, Wei HE, Jin-qian ZHAI, *A Novel Forward Problem Solver Based on Meshfree Method for Electrical Impedance Tomography*	2 East 3.1 ---------- 4E3.10

		5.Borsic, H. Syed, R. J. Halter, A. Hartov, *Using Ultrasound Information in EIT Reconstruction of the Electrical Properties of the Prostate* 6.N Béqo, N Huber, R Bilal, W Zhang, G Qiao, and Wei Wang, *Fast method for artefact detection and breast boundary definition*	
	19:30-21:00	**Conference dinner**	Assembly Rooms, City of Bath
Friday 6 May	8:30-10:30	**Session 7:** **Track 1- MIT/MREIT** **Prof EJ Woo** 1. Hyung Joong Kim, Young Tae Kim, Atul S. Minhas, Zijun Meng, and Eung Je Woo*, Breast MREIT Phantom Experiments Using Less Than 1 mA Injection Currents* 2. Hyung Joong Kim, Young Tae Kim, Atul S. Minhas, Zijun Meng, and Eung Je Woo, *Feasibility of high-resolution MREIT with less than 1 mm pixel size* 3. K Wei, M Soleimani, *An FPGA Based Magnetic Induction Tomography System for prospective biomedical applications* 4. Ruigang Liu, Ye Li, Wenlei Liu, Feng Fu, Xuetao Shi, Fusheng You, Xiuzhen Dong, *Magnetic induction tomography based on brain physical phantom* 5. Axel Cordes and Steffen Leonhardt, *Development of the new Multichannel Simultaneous Magnetic Induction Measurement System (MUSIMITOS 2+)*	2 East 3.1

		--- **Track 2- Instrumentation 2** **Chair: Prof A Wilson** 1. R. Pikkemaat, B. Venema, H. Luepschen and S. Leonhardt, *High speed multi-frequency EIT device* 2. J. Cuan-Lee, R. Martinez-Alonso, R. G. Moreno-Alvarado, J. J. Gutierrez C.4, M. P. Ramirez T, *On a new electronic design for data acquisition and conditioning for Electrical Impedance Tomography measurements* 3. B Tunstall and N Huber*, Standardised Phantom for Electrical Impedance Tomography: A Proposal* 4. C Lobstein-Adams, N Béqo and W Wang, *Electrical Impedance assisted Ultrasound guided Focused Ultrasound Surgery: A comprehensive out-patient procedure?* 5. G Sze, W Wang, D C Barber and N Huber, *Preliminary study of the sensitivity of the Sussex Mk4 Electrical Impedance Mammography planar electrode system* 6. Guizhi Xu, Shuai Zhang, Ying Li, Jianjun Zhang, Guoya Dong, *Review of the Research and Development in EIT*	---------- 4E3.10
	10:30-11:00	Tea & coffee break	2 East 3.4
	11:00-13:00	**Session 8:** **Track 1 - Micro EIT and instrumentation** **Chair: Prof R Bayford** 1. Tuykin T.S., Cherepenin V.A., Gulyaev Yu.V., Korjenevsky A.V. and Sapetsky S.A., *Development of an EIT system with a tiny electrode matrix*	2 East 3.1

| | | **2.** Tong In Oh, Eunjung Lee, Jin Keun Seo , Eung Je Woo and Tingting Zhang, *Conductivity image reconstruction method for a new microscopic electrical impedance tomography (micro-EIT) system*

3. Qin Liu, Tong In Oh, Eun Jung Lee, Eung Je Woo and Jin Keun Seo, *Microscopic electrical impedance tomography system with hexagonal sample container: experimental feasibility study*

4. Eun Jung Lee, Jin Keun Seo , Munkh Erdene, Tong In Oh and Eung Je Woo, *Imaging of regional conductivity change using a planar array of voltage-sensing electrodes and two pairs of currentinjection electrodes*

Track 2 – Modelling
Chair: Prof A Adler

1. P. Hashemzadeh, A. Adler and R. Bayford, *The Statistics of Normalized Data in Electrical Impedance Tomography.*

2. M. P. Ramirez T., J. J. Gutierrez C. *On the electrical current trajectories when the conductivity is a polynomial function*

3. Weida Zhang, N Huber and W Wang, *Modelling the Stainless Steel Electrode for EIT System of Saline Tank*

4. Rebecca J Yerworth, Richard Bayford, *Robustness of GREIT reconstruction algorithm with respect to reciprocity errors in the data.* | ---------
4E3.10 |
| | 13:00-14:00 | Buffet lunch | Wessex Restaurant |

An animal model configuration for combined EIT imaging and ICP monitoring of intracranial trauma

P. Manwaring[1], R. Halter[1], K. Moodie[2], S. Kane[2], A. Hartov[1]

[1]Thayer School of Engineering, Dartmouth College, Hanover, NH, USA
[2]Department of Surgery, Dartmouth Medical School, Hanover, NH, USA

Introduction

Electrical impedance tomography of the brain is a challenging proposition in part due to the thick and highly-resistive cranium found in most mammals. Much research has gone into overcoming these challenges by exploring optimal electrode placements, optimal current excitation patterns, highly-sensitive instruments, and new algorithms (1-4). We have previously described the use of a centrally-located electrode, which increases sensitivity significantly (5). We hypothesize that a mixed-instrument device incorporating an intracranial pressure (ICP) sensor and a centrally-located electrode would resolve the cranial insulative impediment. Since placement of an ICP sensor as an external ventricular drain is a routinized procedure in management of traumatic brain injury, cross adaptation as a central EIT electrode could facilitate more effective monitoring of the evolving pathology, including cerebral edema and hemorrhage.

We have constructed such a device and incorporated it with a portable EIT system designed for use in an operating room or ICU environment with a commercially available physiological monitor. The completed multi-modal system is used to record the effects of manipulations to cerebral blood flow, traumatic brain injury, and intracerebral hematoma. Physiological effects and impedance data are recorded in synchrony for post-processing analysis. Herein we briefly describe the use of a central electrode and pressure sensor combination, the recording system, and IACUC-approved animal model for exploring the use of EIT in head trauma.

A Central Electrode

The international standard of care for traumatic brain injured individuals with a Glasgow Coma Scale score of 8 or below is to surgically insert an intracranial pressure (ICP) transducer (6) commonly configured as an external ventricular drain or parenchymal pressure sensor. Through such monitoring the clinician can detect increasing ICP, delayed intracerebral hemorrhage and anticipate need for further imaging by CT or need for surgical intervention. The devices come in many configurations from semi-rigid to very flexible. We adapted a commonly employed commercially available ICP sensor based on strain gauge technology for purposes of simplicity, expense, and in anticipation of eventual human trials (Codman ICP Express, Codman & Shurtleff, Inc., Raynham, MA, USA). The central electrode and ICP sensor assembly can be seen in Fig. 1a. This assembly connects to a custom built female Luer-to-1/4 inch Universal Pipe Thread (UPT) cranial bolt adapter, which can be tightened into the cranium via a burr-hole (see Fig. 1b). This allows the tip of the

electrode and ICP sensor assembly to sit 1.5 cm centrally into the brain of the animal analogous to typical positioning in a human patient (see Fig. 1c).

<table>
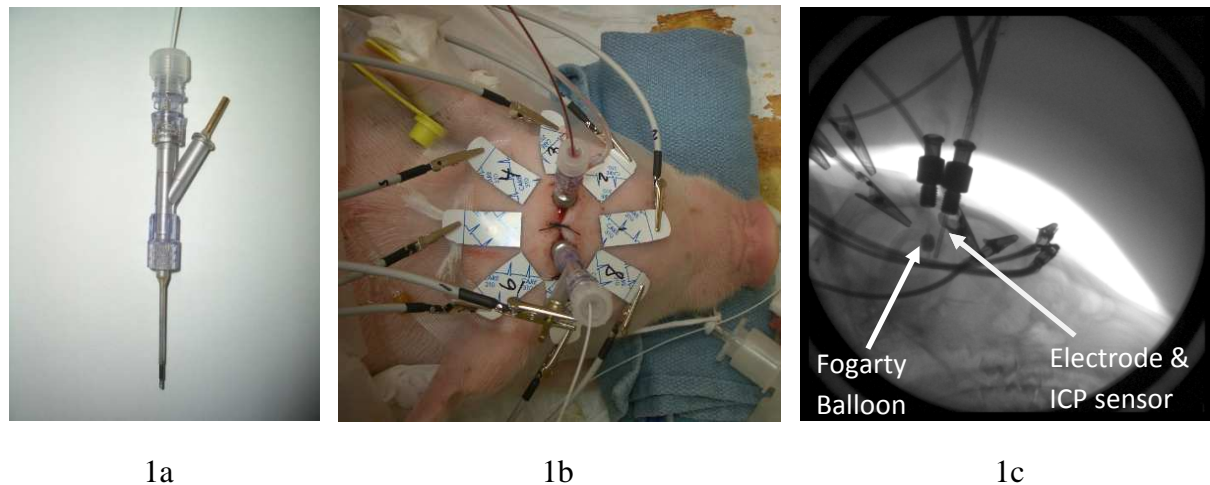<tr><td>1a</td><td>1b</td><td>1c</td></tr>
</table>

Figure 1 – (a) Shows the central electrode and ICP sensor assembly. (b) Shows the animal model setup with 8 peripheral and 1 central electrodes. The second cranial bolt has a Tuohy-Borst adapter and Fogarty catheter attached. (c) Shows the inflated Fogarty balloon and central electrode in a right-lateral fluoroscope image.

The Animal Model

As piglet brains have similar blood flow to human children, this animal is considered a practical investigational model (7). Further, piglets also have thinner cranium comparable to human proportions. Finally, their brains are sufficiently large to explore TBI injury patterns. The typical piglet will weigh 7-11kg at 3-4 weeks and have a skull thickness of 3-4mm, sufficient to anchor the cranial bolt for the central electrode.

The piglet is anesthetized with midazolam and ventilated throughout the procedure with isoflurane. Following induction, a femoral arterial pressure sensor is placed for continuous arterial blood pressure (ABP) monitoring. Then left and right ¼-inch diameter cranial burr-holes are drilled into the skull approximately 1 cm lateral to the midline (saggital suture) and 1 cm anterior to the coronal suture. A cruciate puncture is carefully placed in the Dura and the cranial bolts are tightened into place. Through one bolt is placed the central electrode and ICP sensor assembly. Through the other is placed an intraparenchymal central-lumen Fogarty catheter (Model 12TLW403F, Edwards Life Sciences, LLC, Irvine, CA, USA), which is sealed with a Tuohy-Borst adapter. Following the placement of the bolts and ensuring a hydraulic seal, 8 peripheral one-time use 1x2cm Ag/AgCl adhesive ECG electrodes (Kendall Care 310, Tyco Healthcare, Mansfield, MA, USA) are placed circumferentially about the crown of the head. These will be used as EIT electrodes. At this point the EIT system is connected to the electrodes and all raw data is recorded through the duration of the procedure. The excitation frequency is 50kHz with a frame rate of 100Hz.

Various manipulations known to affect blood flow are performed sequentially. Hyperventilation to 30 mmHg pCO_2 is commenced to decrease blood volume and flow in the brain. Next, pCO_2 is raised to 50-55 mmHg by hypoventilation or rebreathing to induce hyperemia and increased ICP. Normalization of pCO_2 to 40 mm Hg is then achieved. Each manipulation starts with a 10 minute stabilization period, followed by 10 minutes of

manipulation and stabilization back to normal parameters (10-10-10 protocol). Focal mass effect is then induced with a Fogarty balloon in the frontal lobe white matter inflated with 150 uL of iohexol to create a local, asymmetric hemispheric disturbance in blood flow (see fig. 1c). Balloon inflation is visualized in real-time with a fluoroscope. Following the same 10-10-10 protocol post deflation, freshly drawn arterial blood is injected through the central lumen of the catheter to create an intraparenchymal and sometimes partial intraventricular hematoma. This induces rapid, abnormal elevation of ICP. An IV push of mannitol (osmotic diuretic agent) is employed to diminish ICP followed by a 30 minute observation period. Finally, an injection of adenosine is given to create a transient heart block and decrease in blood pressure. The animal is euthanized with Euthasol (a pentobarbital sodium mixture). EIT and physiological data are recorded for an additional 5 minutes post-mortem.

To date 12 piglets have been studied.

Observations

EIT baseline conductivity data have been seen to drift substantially over the duration of these experiments. Each experiment typically lasts 4-5 hours. Therefore, data of interest are analyzed during each manipulation's 10-10-10 window using difference imaging techniques and we do not compare the start of the experiment to the end.

Manipulation of pCO_2 greatly affects ICP and EIT as expected. When comparing conductivity data before and during hyperventilation, we see a decrease in ICP and an increase in conductivity. During hypoventilation we see an overall increase in ICP and conductivity. The Fogarty balloon inflation is readily seen in the EIT reconstruction as the expected region of low conductivity (see Fig. 2a). We see a corresponding increase in ICP. The injection of blood routinely shows an increase in conductivity (see Fig. 2b). The effect of mannitol on the brain at this point of physiologic manipulations is modest. ICP is seen to decrease slightly (1-3 mmHg) after 30 minutes, but EIT data show an increase in conductivity, which may be an effect of the molecule itself, continued swelling, or unrelated baseline drift. The effects of adenosine (transient heart block and corresponding decrease in blood pressure) are readily seen in the physiological data as a decrease in ICP and blood pressure and as a global decrease in conductivity. All parameters, including conductivity, return toward their previous state within 5 minutes. Euthanizing of the animal likewise shows a global, but non-returning decrease in ICP, ABP, and conductivity.

Conclusion

In this paper we present a unique EIT electrode configuration for use in an animal model exploring the effects of brain injury. The animal model is designed to provide EIT insight into blood-flow and volume effects through various manipulations. These data are synchronously recorded with physiological data such as ICP, ABP, and ECG for post-processing analysis. While a complete analysis is yet to be performed, the preliminary results discussed in this paper suggest that our model is producing the expected outcomes.
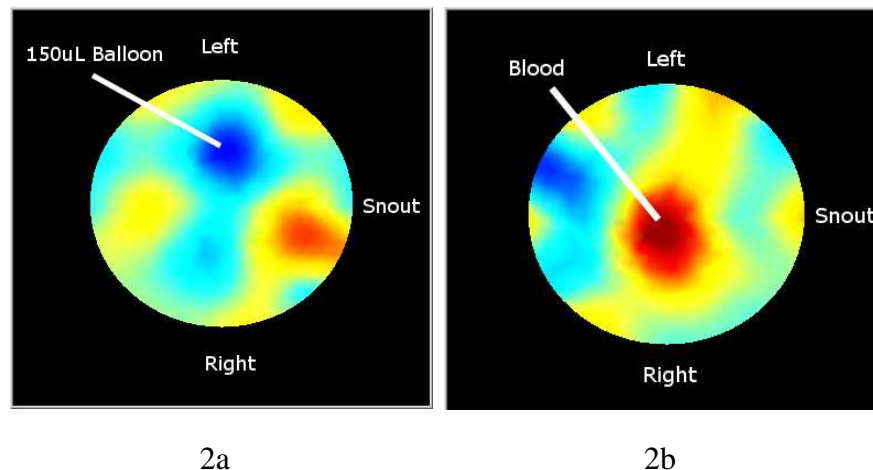
2a   2b

Figure 2 – (a) Shows the conductivity reconstruction of the inflated 150uL Fogarty balloon. (b) Shows the effect of blood injected through the central lumen of the Fogarty catheter. The blood is seen to have migrated from the injection site.

References

1. Tidswell T, Gibson A, Bayford RH, Holder DS. Three-dimensional electrical impedance tomography of human brain activity. NeuroImage. 2001 ;13(2):283–294

2. Gilad O, Ghosh A, Oh D, Holder DS. A method for recording resistance changes non-invasively during neuronal depolarization with a view to imaging brain activity with electrical impedance tomography. J. of neurosc. methods. 2009 May 30;180(1):87-96

3. Tidswell AT, Bagshaw AP, Holder DS. Yerworth RJ, Eadie L, Murray S, et al. A comparison of headnet electrode arrays for electrical impedance tomography of the human head. Phys. Meas.. 2003; 24(2):527

4. Zhang Y, Passmore PJ, Yerworth RJ, Bayford RH. Statistical analysis for brain EIT images using SPM. In: Third Int. Conf. on Med. Information Visualisation-- BioMedical Visualisation. London, England: IEEE Computer Society; 2005. p. 60-67

5. Manwaring PK, Halter RJ, Borsic A, Hartov A. A modified electrode configuration for brain EIT. J. of Physics: Conference Series. 2010 Apr 1

6. Smith M. Monitoring intracranial pressure in traumatic brain injury. Anesthesia and analgesia. 2008 Jan ;106(1):240-8.

7. Duhaime AC. Large animal models of traumatic injury to the immature brain. Dev. Neurosc.. 2006; 28(4-5):380–387

Practical human abdominal fat estimation utilising electrical impedance tomography

T F Yamaguchi[1,2] , L Q Wang[3], M Katashima[1], K Maki[4] and S Kuriki[2,3]

[1]Health Care Foods Research Laboratories, Kao Corporation, Sumida, Tokyo 131-8501, Japan
[2]Graduate School of Advanced Science and Technology, Tokyo Denki University, Chiyoda, Tokyo 101-8457, Japan
[3]Research Center for Advance Technologies, Tokyo Denki University, Inzai, Chiba 270-1382, Japan
[4]Clinic Saint Louis, Yamashina, Kyoto 607-8011, Japan
*E-mail: yamaguchi.tohru@kao.co.jp

Abstract. The aim of the present study was the development of low-cost device for estimating visceral fat using electrical impedance tomography to image cross sections of the human abdomen. The device has a mechanism to attach 64 electrodes with double-ring configuration. Alternating current of 1.0 mArms with a frequency of 500 kHz was applied to the human umbilical level, after which the potential difference between every pair of adjoining electrodes and the abdominal outline was measured. The conductivity image was then derived by means of iteration of the finite element method and non-linear optimisation. From the derived image, we estimated the ratio of the abdominal fat by assuming mixture model of the conductivity in image. This study reports on the entire process from impedance measurement to conductivity imaging and abdominal fat estimation. By modifying the electrode arrangement and circuit design, the impedance measurement and the derived images were improved, allowing us to achieve stable imaging and abdominal fat quantification.

Key words: electrical impedance tomography, abdominal fat, visceral fat, metabolic syndrome

1. Introduction

Metabolic syndrome is a disease state related to dietary habits and lack of exercise, and it is becoming a significant health problem worldwide. A fundamental cause of metabolic syndrome is thought to be abdominal obesity [1]. Recent epidemiological research [2] suggests that the risk of metabolic syndrome is strongly related to the accumulation of visceral fat rather than abdominal subcutaneous fat.

Visceral fat can be assessed by X-ray computed tomography (CT) by measuring the fat area in the cross section of the abdomen at the umbilical level [3]. The threshold level of visceral fat identified as carrying a risk is 100 cm^2 in the Japanese guidelines for metabolic syndrome [4]. However, CT is difficult to apply for preventive diagnosis, because of its expense and non-negligible dose of radiation.

To overcome such disadvantages, we attempted to image the abdominal fat by utilising electrical impedance tomography (EIT), a radiation-free and inexpensive measuring method. We have partially succeeded in imaging a cross section of abdominal fat with a proto-type device [5]. In the present study, we significantly modified the device design and the image reconstruction software. Furthermore we tried to quantify the abdominal fat from the EIT image.

2. Method
2.1. Device

The developed device (Fig. 1) was based on the proto-type device which has the semi-automatic electrode attaching mechanism of the stainless-steel electrodes [5], we redesigned the electrode arrangement and the electronic circuit. The new device has 64 electrodes comprising of two layers in a ring, separated vertically, with 32 electrodes that surrounds the abdomen, whereas the previous version has only 32 electrodes with a mono-layer

arrangement. An alternating current of 1.0 mArms with a frequency of 500 kHz was applied to the subject's abdomen through the selected pair of electrodes at every other position. Then, the difference in the electric potential in the 32 pairs of adjacent electrodes were measured for the entire loop, *i.e.*, 32 potential differences, for the 32 current patterns, and a total of 1024 data points were measured. We acquired only the real part of the complex potential differences using a lock-in amplifier. The outline-shape data were also measured using position sensors on 32 electrode stations.

The push-pull type of constant-current circuit was allocated close to the 32 electrode stations to achieve the good frequency characteristics. For the potential measurements, high input-impedance pre-amplifiers were also allocated very close to the 64 electrodes to achieve stable measurements. The control software for the measurement was programmed in the C language using LabWindows/CVI (Version 2009, National Instruments Corp., Austin, TX, USA).

2.2 Data pre-processing and image reconstruction software

Using new device, potential differences of the entire loop were measured with the four-terminal method. We made pre-processing of the potential differences to remove the offsets of operational amplifiers, applying Kirchhoff's voltage law in which summing up of the voltage in a closed loop should be zero if the signs are considered. In addition, a data modification using reciprocal relations and a data smoothing with a polynomial regression described in the previous study [5] were applied.

The algorithm of the image reconstruction software is described below.
1) The cross-sectional shape was constructed using the outline-shape data, and then, triangular mesh was spread out on the two-dimensional shape. The mesh size was small in the outer portion and large in the inner portion.
2) A three-dimensional model was built up with several two-dimensional shapes with the same mesh arrangement, assuming homogeneity in the lengthwise direction. At that time, the triangles became triangular prisms.
3) The Laplace equation for the electric potential was solved for each node of the mesh using the finite element method (*i.e.*, solving the forward problem).
4) The conductivities of each triangular prism were updated using the Marquardt method [6] of nonlinear optimisation method (*i.e.*, solving the inverse problem).
5) Iterations were made between the above processes of 3) and 4) until convergence was obtained.
6) A spatial filter was applied on the cross-sectional image of the model. The filter's constant was conditional to the mesh size.

Although, the software was mainly programmed with FORTRAN77, it was packed in an extension package of R statistical analysis software [7]. As a result, the usability of the software was improved without the loss of execution speed.

2.3. Estimation of abdominal fat

Although several organs can be found in a cross section of the human abdomen, such as the large intestine, the small intestine, skeletal muscle, visceral fat, subcutaneous fat and the spine, each of these items could be classified as muscle or fat, except for the spine. Therefore, the

conductivity would be distributed in the range between that of muscle and fat. Taking this fact into consideration, we proposed a method focused on the estimation of the fat ratio from an EIT image.

The brightness of a pixel in the black and white EIT image corresponds to the logarithmic transformed conductivity, and distributes within the lower and upper limits of $[a,b]$. This distribution may be a truncated mixture distribution, which has two peaks for muscle and fat. The probability density function, $f_\theta(z)$ would be as follows:

$$f_\theta(z) = \frac{(1-\lambda)g_1(z)}{G_1(b)-G_1(a)} + \frac{\lambda g_2(z)}{G_2(b)-G_2(a)}$$

where, g_1 and g_2 are the probability density functions of muscle and fat, respectively, and G_1 and G_2 are cumulative distribution functions of muscle and fat, respectively. λ is the ratio of fat which is the parameter of interest. In the present study, we assumed a normal distribution for g_1 and g_2. The unknown parameters λ and θ, which are the mean and the variance of the normal distributions, were estimated using the maximum likelihood method.

3. Results

The subjects were the authors: two in their 40s and one in his 60s. The measurement took approximately 20 minutes, and the image reconstruction took approximately four minutes with a PC equipped with a 2.4 GHz processor. The derived EIT images, the MRI images, and the histograms of the brightness of pixels in the EIT images are shown in Fig. 2, where fitted probability density functions are superimposed. The estimated quantified values are presented in Table 1. The estimated total fat area from the EIT and MRI images were consistent. The visceral fat area was not estimated because the visceral cavity could not be identified clearly in the EIT image.

4. Discussion

Although we applied dry stainless steel electrodes and a semi-automatic attaching mechanism to make the process practical, the data collection was stable because of the modification of the electric circuits. Although the normal distributions were fitted to our logarithmic transformed conductivity data, more research is needed to identify the specific distribution with the best fit.

One of the limitations of the system is that it takes a long time to perform a measurement. If the time required for a measurement can be reduced, new extensions of the study, such as multi-frequency measurement can be expected.

5. Conclusion

In the present study, we reported the entire procedure from impedance measurement to quantification of abdominal fat. Although the number of subjects was limited, we achieved good image reconstruction and quantification of abdominal fat because of redesign to the electrode arrangement and circuit design of the previous preliminary device.

References
[1] J. P. Despr´es, I. Lemieux: Abdominal obesity and metabolic syndrome. Nature. 444(7121): 881–887, 2006.
[2] Y. Matsushita, T. Nakagawa, S. Yamamoto, Y. Takahashi, T. Yokoyama, M. Noda, T. Mizoue:

Associations of visceral and subcutaneous fat areas with the prevalence of metabolic risk factor clustering in 6292 Japanese individuals: the Hitachi health study. Diabetes Care. 33: 2117-2119, 2010.

[3] T. Yoshizumi, T. Nakamura, M. Yamane, A. H. Islam, M. Menju, K. Yamasaki, T. Arai, K. Kotani, T. Funahashi, S. Yamashita, Y. Matsuzawa: Abdominal fat: standardized technique for measurement at ct. Radiology. 211(1): 283–286, 1999.

[4] Y. Matsuzawa: Metabolic syndrome– definition and diagnostic criteria in japan. J Atheroscler Thromb. 12(6): 301–301, 2005.

[5] T. Yamaguchi, K. Maki, M. Katashima: Practical human abdominal fat imaging utilizing electrical impedance tomography. Physiol Meas. 31(7): 963–978, 2010.

[6] D. Marquardt: An algorithm for least-squares estimation of nonlinear parameters. J. Soc. Ind. Appl. Math. 11(2): 431-441, 1963.

[7] R. Ihaka, R. Gentleman: R: A language for data analysis and graphics. J Comput Graph Stat. 5(3): 299–314, 1996.

Table 1 Estimated abdominal fats from EIT and MRI images (cm^2)

Subject	EIT image		MRI image *	
	Visceral fat area	Total fat area	Visceral fat area	Total fat area
A	-	92	42	142
B	-	235	155	261
C	-	114	139	235

* Estimations using FatVizCalc (Lisit, Co., Ltd., Tokyo, Japan)
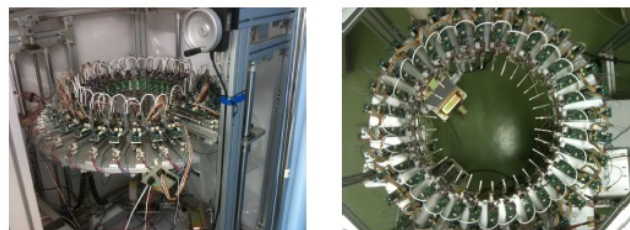
Fig. 1. Photographs of the developed device: side view (left) and top view (right).
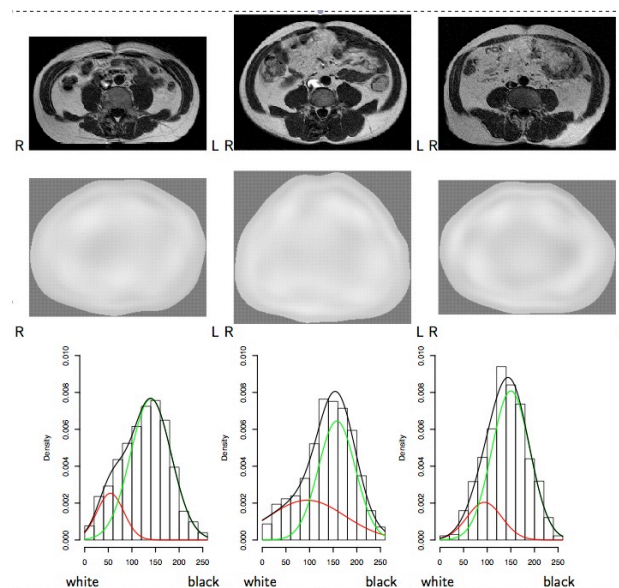
Fig. 2. MRI image (upper), EIT image (middle) and fitted distributions (lower) for three subjects. Red, green and black lines represent fat component, muscle component and mixture of those, respectively.

Preliminary results on using electrical impedance to determine tissue composition in support of non-invasive temperature measurement.

Naimul Islam[1,2], Adrian Wilson[1,3]

[1] Department of Physics, University of Warwick, CV4 7AL, Gibbet Hill Road, Coventry, UK.

[2] Department of Physics, University of Dhaka, Dhaka-1000, Bangladesh.

[3] Department of Clinical Physics and Bioengineering, University Hospital, Coventry, UK.

1. Introduction

Electrical impedance measurements are one of the techniques proposed for determining the temperature during hyperthermia treatments for cancer although the commonly reported temperature resolutions of 10°C are much larger than the 1°C required clinically (Esrick and McRae, 1994). Hyperthermia is used in the treatment of cancers to either ablate tissue or as a sensitising agent which can be used in conjunction with radiotherapy or chemotherapy. One of the major limitations in the use of hyperthermia, in particular mild hyperthermia which is used as a sensitising agent, is the lack of a non-invasive measurement technique to give the spatial temperature distribution to guide therapy (Lagendijk, 2000). Gersing (1999) suggested that extra-cellular volume changes resulting from vasodilatation was the primary effect with tissue heating and this occurred immediately on heating in normal tissue but was delayed in cancerous tissue. The propagation velocity of ultrasound changes with temperature and techniques based on this have been widely investigated because of high intensity focussed ultrasound (HIFU) ablation techniques (ter Haar, 1999). A change in propagation velocity of 0.4%/°C is commonly quoted. However, this is only applicable to liver over a limited temperature range (35-50°C). Other tissues have different changes in propagation velocity with temperature with some, including fat, having negative temperature coefficients (Duck, 1990). In this paper we examine the potential of electrical impedance measurements to quantify the amount of fat in localised tissue volumes within the body as part of a novel technique for non-invasively measuring temperature deep within the body.

2. Method:

Our aim was to take simultaneous multi-frequency EIT and ultrasound propagation velocity measurements of tissue samples in a test cell. However in this paper we only report the results of electrical impedance measurements.

Test cell: A cylindrical Perspex test cell was constructed having an internal diameter of 40mm diameter and a height of 24 mm which allowed simultaneous ultrasound and multi-frequency EIT measurements (figure 1). The
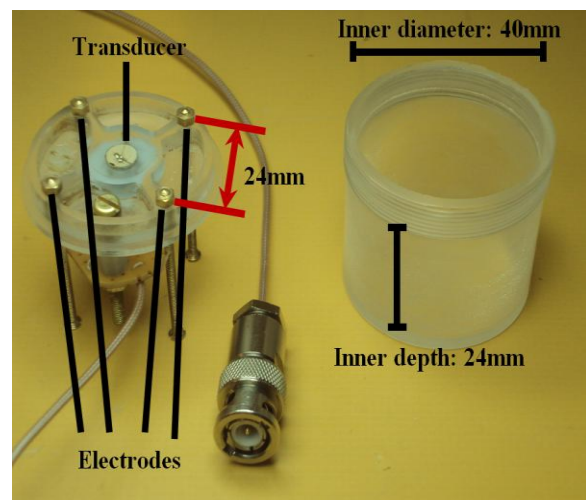

Figure 1: The Perspex test cell showing the positions of the electrodes and PZT element.

vertical walls of the chamber and its base were 2mm thick. A 7mm diameter 1MHz PZT transducer was located at the centre of the lid of the cell and four brass/stainless steel electrodes positioned at the corner of a hypothetical square centred on the PZT element with a 24mm spacing between the electrodes. To ensure similarity between the spatial sensitivity of the two measurements, the diameter of the PZT element and the electrode spacing were selected so that the position of the last axial maximum in the ultrasound field was at the same depth as the peak in the average sensitivity for the tetrapolar electrical impedance measurements (Brown et. al., 2000a; Islam et. al., 2010) – approximately 8mm.

Sample preparation: For this preliminary study we selected liver and fat: the former because it is a target for HIFU and much work has been done on its temperature characteristics; and the latter because it is found in liver and it has a negative temperature coefficient. The results reported in this paper are for fresh lambs liver and fat samples obtained from domestic butchers. We needed to have a way of varying the fat content of the samples. To do this we sliced the liver and fat so that the slices were approximately 6mm thick. Using different combinations of liver and fat slices the composition of the tissue in the test cell could be varied. The density of the fat and liver tissue was measured. From this, and the weight of the individual slices, the percentage composition of the tissue being measured by mass and by volume was determined.

Temperature change: Having filled the test cell with the tissue slices required for a particular experiment, two K-type thermocouples were inserted into the tissue through the lid. These were positioned away from the centre line through the tissue to avoid interference with the measurements. The test cell was then placed in a water bath heated by a thermostatically controlled hot plate fitted with a magnetic stirrer (Fisher Scientific, FB65314). The tissue sample was increased from room temperature to 45°C in 5°C increments. Temperature measurements were made using the two K-type thermocouples connected to a digital thermometer (Digitron Ltd, model 2098).

Data acquisition: For the multi-frequency electrical impedance measurements we use a pair of electrodes on one side of the hypothetical square as the drive electrodes and the pair on the other side of the square as the receive electrodes. The instrumentation was essentially a single channel version of the Sheffield Mk3.5a system (Wilson et al, 2001). Measurements were made at 11 frequencies simultaneously (1, 2, 4, 8, 16, 32, 64, 128, 256, 512, 1024 kHz) with an injected constant current of 200µA p-p at each frequency which gave a total current of 1.2mA p-p. The amplified receive signal from the impedance measurement was fed to one channel of a two channel high speed digitiser (National Instruments, USB-5133) sampling at 100MHz. The magnitude and phase components for each frequency in the injected current signal were calculated from the FFT of the digitised receive signal. In this paper we only report magnitude values.

3. Results

Figure 2 shows the impedance spectrum results for 100% fat sample; a 38% fat, 62% liver sample and a 100% liver sample. Impedance values have been normalised to the impedance value obtained at 1kHz for each measurement. The results for the 100% fat sample showed that below 512kHz there was only a small change in the transfer impedance as a function of frequency and that there was only a small change in impedance with temperature. For the 100% liver sample there was a single dispersion frequency which varied with temperature. At high frequencies there was a much larger change in impedance with temperature than for

the fat but below the dispersion frequency the results converged towards becoming independent of temperature as the frequency decreased.
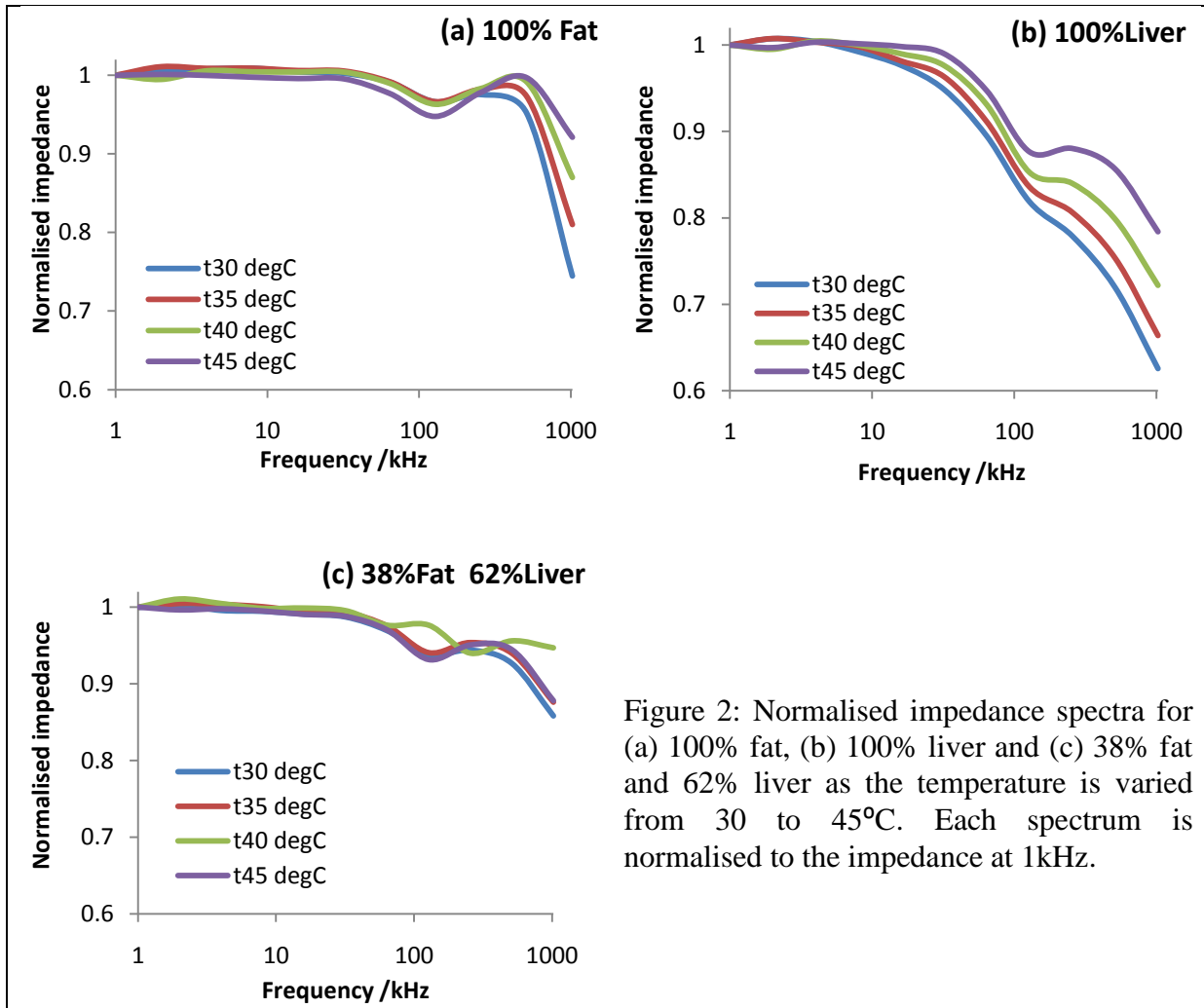

Figure 2: Normalised impedance spectra for (a) 100% fat, (b) 100% liver and (c) 38% fat and 62% liver as the temperature is varied from 30 to 45°C. Each spectrum is normalised to the impedance at 1kHz.

Figure 2 also shows the result for a sample with 38% fat. The dispersion frequency is almost independent of temperature and the changes in impedance with temperature are much less than those for the 100% liver sample. Measurements with a lower percentage of fat showed a similar pattern. Since a clear difference between the 100% fat sample and the 100% liver sample is the dispersion in the liver sample, the ratio between the impedance at the lowest frequency and the higher frequency values was investigated to determine its potential to characterise the percentage of fat in the sample. The results for the ratio of
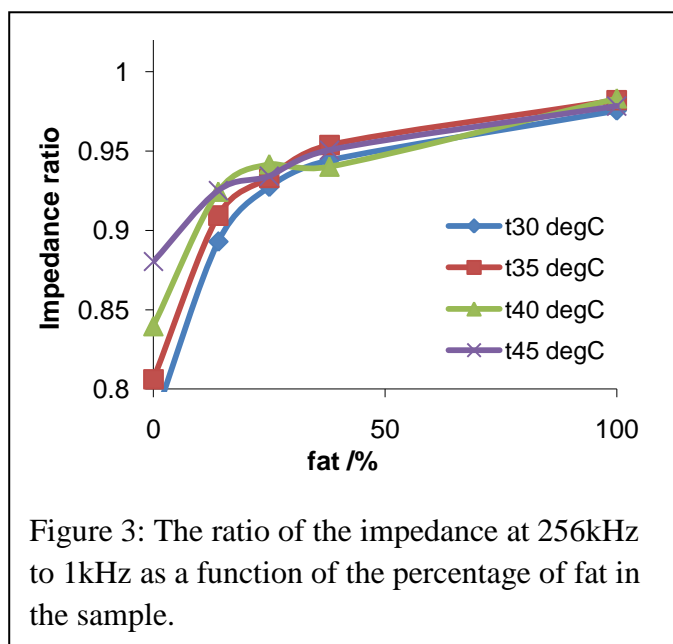
Figure 3: The ratio of the impedance at 256kHz to 1kHz as a function of the percentage of fat in the sample.

1kHz to 256kHz are shown in figure 3. This figure shows that there is little change in the ratio with temperature for tissue containing more than 10% fat. Above 10% fat there was an approximately linear change: a 1% change in the ratio for every 10% change in the amount of fat in the sample.

4. Discussion

The characteristics of the impedance measurements for the 100% fat and 100% liver sample were as expected. The lack of a cellular structure with a conducting intracellular fluid in the fat gives rise to the observed transfer impedance values below 512kHz which are independent of frequency. Above 512kHz we believe the lipid within fat cells forms the dielectric giving rise to the change in impedance at 1MHz. Clearly further measurements are needed to confirm that this is the case, but preliminary modelling work gives results which are consistent with these experimental measurements. The dispersion at around 64kHz in the 100% liver sample reflects the cellular nature of the tissue and a Cole-Cole model could be fitted to these data (Brown et. al., 2000b). The rapid disappearance of a well defined dispersion frequency in samples with even small percentages of fat was unexpected. Both 3D FEM and lumped parameter modelling do not predict this behaviour. One possibility was that low conductivity saline pools between layers of fat and liver which does not occur when tissues are of similar type are adjacent. However, when thin layers of 1ms cm^{-1} saline were introduced into the 3D models, these failed to predict the observed behaviour. The origin of this finding is currently unclear and required further investigation.

Our analysis of the experimental data to date has been based on simple factors. Modelling may provide a better method of relating the results to tissue composition and potentially to the non-invasive determination of temperature. The tissue we used was non-living and therefore some of the changes which are reported to result in impedance changes with temperature (e.g. changes in membrane conductivity, Gersing, 1999) may not be reflective of those that would be observed in living tissue. Similarly, to create liver tissue with a known fat composition we have used layers of tissue and this in itself may not be reflective of the structure of natural living tissue. Thus caution is needed in interpreting the results reported. However, the results do provide evidence that electrical impedance measurement when used in conjunction with other techniques may improve the non-invasive temperature estimation.

5. References

Brown BH, Wilson AJ, Bertemes-Filho P. (2000a). Bipolar and tetrapolar transfer impedance measurements from a volume conductor. *Electronic Letters,* 36:2060-2062.

Brown BH, Tidy JA, Boston K, Blackett AD, Smallwood RH, Sharp F. (2000b). Relation between tissue structure and imposed electrical current flow in cervical neoplasia. *Lancet,* 355 (9207):892-895.

Duck F. (1990) Physical properties of tissue. Pub. Academic Press Ltd., London.

Gersing E. (1999). Monitoring temperature-induced changes in tissue during hyperthermia by impedance impedance methods. *Annals New York Academy Sciences,* 873:13-20.

Islam N, Rabbani KS-e, Wilson A. (2010). The sensitivity of focussed electrical impedance measurements. *Physiol. Meas.,* 31:S97-S109.

Lagendijk, JJW. (2000). Hyperthermia treatment planning. *Phys. Med. Biol.,* 45:R61–R76.

McRae DA, Esrick MA. (1993). Changes in electrical impedance of skeletal muscle measured during hyperthermia. *Int. J. Hyperthermia*, 9:247-261.

ter Haar GR. (1999). Therapeutic Ultrasound. *Eur. J. Ultrasound,* 9:3-9.

Wilson AJ, Milnes P, Waterworth AR, Smallwood RH, Brown BH. (2001). Mk3.5: A modular, multi-frequency successor to the Mk3a EIT/EIS System. *Physiol. Meas,* 22:49-54.

Feasibility of using internal electrodes to improve the accuracy Cardiac Electrical impedance Tomography

J Nasehi Tehrani[1], A Thiagalingam[2], C Jin[1], A van Schaik[1], W Chik[2], M.A. Barry[2], and A McEwan[1]

[1]School of Electrical and Information Engineering, CARLAB
The University of Sydney, Australia, NSW 2006
[2] Department of Echocardiography, Westmead Hospital, Westmead, NSW 2145

joubin@ee.usyd.edu.au

Abstract. We are developing a method to monitor cardiac function in intensive care units with critically ill patients. The current gold standard is a gated heart pool scan, which provides a good assessment of global heart function, but with low resolution, long lead time, and radiation risks. Less accurate alternatives include trans-esophageal echocardiography, where the ultrasonic probe is inserted into the esophagus behind and close to the heart, and trans-thoracic echocardiography, where the probe observes the heart through the intercostal spaces. These echo modalities often do not provide satisfactory results in these patients due to lung and rib artifact, and the sizes of probe currently used for the trans-esophagus echocardiogram is large, inconvenient for patients, and unable to be left indwelling. EIT is a safe, inexpensive and potentially fast method for global cardiac output imaging but the spatial resolution is presently low. The previous methods for imaging and measurements of cardiac function were completely noninvasive[1]. Here we study internal electrode movement artefacts and report on a pilot experiment where an internal catheters based electrode were located in the superiour vena cava (SVC) and esophagus behind heart. Reliable impedance changes were recorded over 5 ECG cycles demonstrating that internal electrode movement was low and that the electrode returns to the same position each cyle. This gives us confidence to use a static internal electrode position in our EIT mesh and to continue with EIT imaging experiements.

1. Introduction

There is a need in critical care unit for continuous cardiopulmonary monitoring techniques. One of the methods to measure stroke volume is electrical impedance tomography. ECG-gated electrical impedance tomography (EIT) is able to localize the impedance variations occurring during the cardiac cycle [2]. EIT constructs cross sectional images of the electrical impedance changes during the cardiac cycle. The aim of the present study is to investigate the feasibility of internal electrodes in improving the application of EIT to cardiology. All of the previous EIT studies were performed with the electrodes spaced around the thorax. Internal electrodes can improve the quality of EIT images[3]. In critical care units specialist can insert internal catheters inside the esophagus and heart. Gathering the information from esophagus right behind the left ventricle [4]and also extra electrodes inside the heart give us more observation details in cardiac function imaging. In this research we evaluate internal electrode movement artefacts and placement to determine the feasibility of using internal electrodes in EIT.

2. Motion artifacts

One of the main artifacts in data acquisition from internal electrodes is catheter movements. This could happen because of blood flow inside the heart during contraction or thorax movements due to respiration. For simulation and measurement of motion artifacts we used an instrument that is prepared for ablation research in Westmead Hospital. The ablation probe was located in a saline bath to simulate the impedance of blood. This ablation probe is actuated by a motor in the transverse plane inside the saline with timing automatically synchronized to a simulated QRS ECG. We measured the four terminal transimpedance between ablation probe and a fixed stainless steel electrode located inside saline. The saline inside the bath is continuously pumped to an external vessel to simulate circulation similar to normal blood flow inside the heart. The movement of the probe is adjustable with microcontroller addressed via a serial cable to a computer. For measuring impedance a precision impedance analyzer (Agilent 4294A) used in this experiment[5]. This impedance analyzer has an external trigger used as a synchronizer within 10ms of the R peak of the QRS pulse. Figure 1 shows the ablation probe with 4 electrodes and the result of impedance changes at 50 kHz from 0 mm in the first trace (top) to 9 mm in the last trace (bottom).
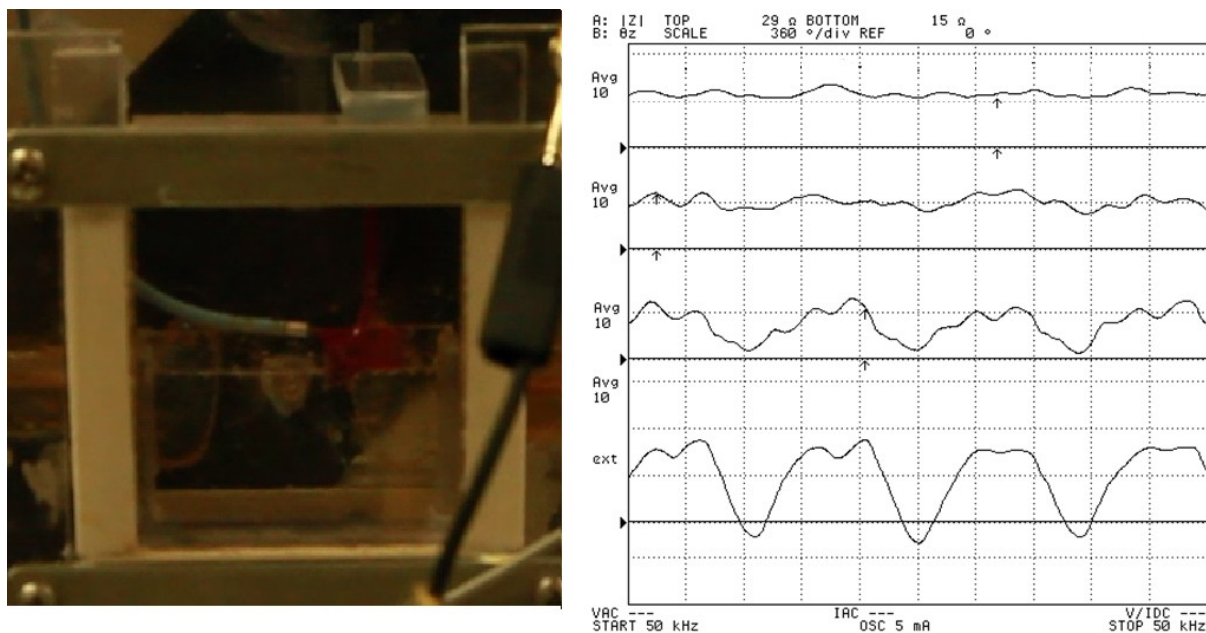
Fig.1. The Ablation probe with 4 electrodes on the tip and the result of impedance measurement with source current 5 mA, 50 kHz. The graph (scale 1.4ohms per divsion) from top to bottom show the changes of impedance related to 0mm, 2mm, 4mm, and 9mm probe movement. The signal is averaged 10 times to decrease the noise level.

The first trace shows impedance changes related to the water pump when there was no movement of the probe. As the probe movement is increased the pulse synchronised impedance changes become clearly visible at 4mm. Overall the results show that motion less than 2mm produces an impedance change of less than 0.5ohm.

3. Material and Methods

For evaluating ablation probes for EIT measurement, we measured four terminal transimpedance in a sheep model in a situation very similar to the patient in critical care units.

Ventilation and anesthesia are controlled. 4 surface electrodes were connected to the left side between rib 4 and 5 (L1-L4) and 4 surface electrodes connected to the right side between rib 4 and 5 (R1-R4) (figure 2a). R4 and L4 as shown in figure 2b are closest to the sternum. We chose not to use any electrode on sternum because of the high impedance in this area. L1 and R1 are the most lateral surface electrodes. A Quadra-polar catheter was inserted from left internal jugular vein through superior vena cava (SVC). The SVC is easily accessible via an internal jugular venous puncture, or a central venous line which is quite common in the Intensive Care Unit setting. We hypothesise that advantages of using the SVC could be first a low impedance path to the right ventricular blood pool; second the SVC electrode creates an appropriate vector with the electrode in the esophagus and the external chest connections. There is motion artifact in the SVC predominantly due to diaphragmatic artifacts; however this is relatively minor compared to the volume we are measuring. In addition a deca-polar electrode catheter was inserted into the esophagus right behind left ventricle (LV). All of the electrodes were connected together to provide a low contact impedance electrode with high current density. The location of the internal electrodes was adjusted with fluoroscopy. Figure 2 shows the locations of the electrodes.
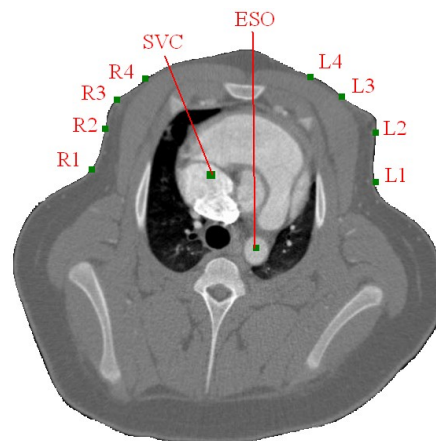
Fig.2. The left picture shows the location of the electrodes on the left side of the sheep. The right hand side shows the location of all electrodes on the CT scan.

For decreasing the noise level the impedance measurement was synchronised to within 10ms of the R peak of an ECG recorded with additional electrodes. For each channel the number of average screening set to 5. The ventilator was controlled to halt ventilation for 10 seconds for each impedance measurement to eliminate the noise of lungs movement. I+ (current injection positive line) inserted into esophagus. And the V- (voltage measurement negative line) inserted into the SVC. I-(current injection negative line) was manually switched around the body from L1 to R1 and for each injection voltage of other electrodes measured related to the V- electrode inside the SVC.

4. Results
Figure 3 shows the result of measurements. We have done 56 measurements base on the injection protocol explained in section 3. The title of each image in the figure 3 shows the method of injection and measurement. For example L1R1 means that I- connects to electrode L1 and voltage measured between electrode R1 and the SVC. In each row there are 7 different voltage measurements based on the same protocol of injection and in each column we use 8 different protocol of injection. The average range of impedance between SVC and electrodes was near 830Ω and these were subtracted from each pulse. The changes vary from 0.4-0.1 ohms which comparable to the lowest movement artifact measured above.
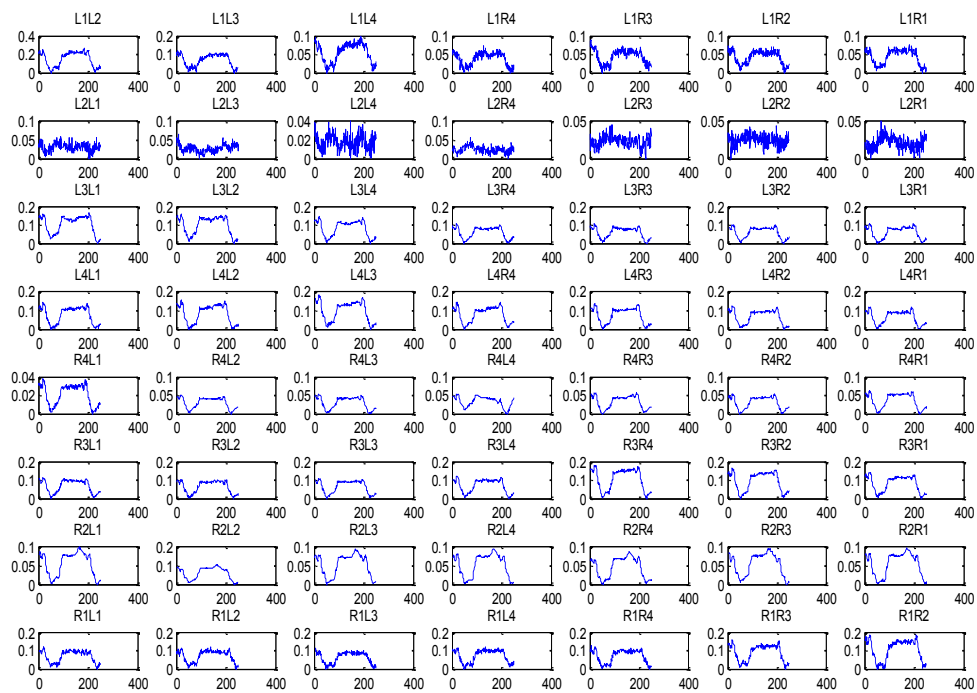
Fig.3. Four terminal transimpedance measurement changes based on different protocol of injection using internal and external electrode. An average baseline of 830ohms was subtracted from each.

5. Conclusion

In this research we used ablation catheters as internal electrodes for electrical impedance tomography. The results (except the faulty electrode L2) show that the signals are robust, consistant for 5 ECG cycles and can be used for EIT as additional data for improving the quality of the cardiac function imaging. In the next step in our research we are going to use these ablation catheters in EIT imaging of cardiac output function with the view of application in critical care units.

References

[1]   Noordegraaf, A.V., Improvement of cardiac imaging in electrical impedance tomography by means of a new electrode configuration. Physiol. Meas., 1996. **17**: pp. 179-188.

[2]   Brown B H, L.A.D., Blood flow imaging using electrical impedance tomography. Clin. Phys. Physiol. Meas., 1992. **A 13**: pp. 175-179.

[3]   Tehrani, J.N., 3D EIT for cardiac function imaging using internal electrodes: preliminary simulation and pilot results. International workshop on MR-based impedance imaging, Seoul, December 8-10, 2010.

[4]   R.P.PATTERSON, possible technique to measure ventricular volume using electrical impedance measurements with an esophagus electrode. Med. & Biol. Eng. & comput., 1987. **26**: pp. 677-679.

[5]   W.R.Fan, Maximum entropy regularization method for electrical impedance tomography combined with a normalized sensitivity map. Elsevier, Flow Measurement and Instrumentation 2010. **21**: pp. 277-283.

Monitoring of Intraventricular Hemorrhage Changes *in-vivo* in a Piglet Model by Electrical impedance tomography

Xuetao Shi[1], Fusheng You[1], Liang Wang[2], Feng Fu[1], Ruigang Liu[1], Canhua Xu[1], Xiuzhen Dong[1]*

[1] E-Department of Medical Electronic Engineering, School of Biomedical Engineering, Fourth Military Medical University, Xi'an, 710032, P. R. China.
[2] Department of Neurosurgery, Tangdu Hospital, Fourth Military Medical University, Xi'an 710038, People's Republic of China.
* *Correspondence author:* dongyang@fmmu.edu.cn

Abstract: Intraventricular hemorrhage (IVH) is an independent predictor of poor outcome. Early detection or diagnosis would significantly reduce the rate of disability and mortality, and improve the prognosis of the patients. In order to verifies the feasibility of monitoring of IVH by electrical impedance tomography (EIT) method, blood was infused into lateral ventricular of anaesthetized piglets and impedance information were measured by 16 stainless needle electrodes that placed in a circle on the scalp. The images were reconstructed using a back projection algorithm. Most significant reconstruction value as well as average reconstruction value were calculated and associated with the injection of blood. The results show that EIT can successfully detect IVH, and may be used to evaluate the IVH volume in this animal model.

Keywords: EIT; intraventricular hemorrhage; Imaging monitoring

1. Introduction

Intraventricular hemorrhage (IVH) is bleeding inside or around the ventricles, the spaces in the brain containing the cerebral spinal fluid. IVH is often been found in very low birth weight (VLBW) newborns, people with moderate to severe traumatic brain injuries, and people with intracerebral hemorrhage related to high blood pressure. Up to now, this type of hemorrhage is an independent predictor of poor outcome [1]. Prognosis is dismal as it is a major cause of severe cognitive and motor development impairment. Several studies have demonstrated a direct relation between IVH volume and poor outcome or mortality [2]. It may be important to intervene in treating IVHs in it early stages. Although current medical imaging modalities, such as CT and ultrasonography, have certain sensitivity, IVHs are not easily found and are often misdiagnosed as migraine or tension headaches during the early stages, until critical amounts of bleeding result in significant symptoms. Therefore, developing a non-invasive facility capable of detecting and monitoring the onset of IVH in real time are greatly required.

Developed in the early 1980s by Barber and Brown, electrical impedance tomography (EIT) produces images of the distribution of resistivity (or conductivity) in the target area. As a rapid imaging, non-invasive, radiation-free, functional imaging technique, EIT offers the possibility for many medical applications, including head, chest, heart and abdominal imaging.

During past 20 years, our team has intensively studied the possibility of continuous monitoring of brain pathological process include ischemic and hemorrhagic stroke based on numerical simulation, physical phantom and animal mode l[3,4]. The present study was designed to determine whether EIT could detect IVH and its volume in vivo.

2. Materials and methods

2.1 Experimental animal model

The animal protocol for this study was approved by the Institutional Animal Care and Use Committees of the Fourth Military Medical University.

6 piglets (weight, 15 to 16 kg) were obtained from a local farm. They were deprived of food and water overnight before the experimental procedure. All surgical procedures were performed with the use of aseptic techniques. Piglets were initially anesthetized with ketamine (25 to 30 mg/kg) IM. After sedation, pentobarbital (35 mg/kg) was administered through an ear vein to achieve a deep surgical level of anesthesia. After placement of the femoral vein catheter, pentobarbital was infused at a rate of 10 mg/kg per hour throughout the remainder of the experiment. Core temperature was measured with a rectal thermistor probe and was maintained at $38.5 \pm 0.5°C$ with the use of a warm water blanket.

Before blood infusion, the animal's head was shaved and disinfected, and full aseptic techniques were used. Thereafter, 16 sterile stainless needle electrodes were placed annularly on the surface of the scalp. A cranial hole (1.5 mm) was then drilled 10 mm to the right of the sagittal and 2 mm anterior to the coronal suture. A 7.5- scalp acupuncture was then inserted vertically (guided by the piglet brain atlas of Yoshikawa, 1961) into the center of the right lateral ventricular and cemented in place. 2 ml of anticoagulant blood was infused into the ventricular manually using a 5 ml syringe within 3 minutes. The position of electrodes and scalp acupuncture were given in figure 1.
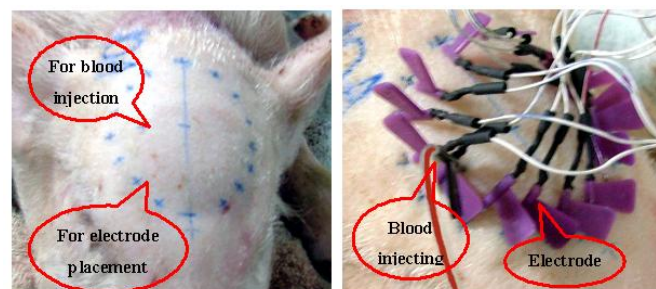
Figure 1. The location (left) and placement (right) of the electrodes and the blood injecting tube.

2.2 EIT monitoring and data analysis

The EIT system was developed by our group [5]. The system can acquire the entire boundary voltages needed in imaging reconstruction in one second. Current was injected through opposing scalp electrodes in a "polar drive" pattern and the corresponding outputting signals were obtained by the others adjacent electrodes. The measurements were made with 50 kHz and 1.25 mA drive current. Before the blood infusing, we collected the data as reference for at least 30 minutes. After the blood infusion was finished, we continuously collected the data for 30 minutes.

The imaging algorithm we chosen is a back-projection algorithm, which can reconstruct the relative impedance changes inside the imaging area. The relative impedance changes of the target area were deputed to the color spectrum. Besides the imaging, we also choose the

most significant reconstruction value (MSRV) and the average reconstruction value (ARV) that calculated from imaging results to describe the tendency and the degree of the impedance various.

2.3 Validation of the IVH model

After whole experiment was finished, we had an X-ray CT (GE Company) scan on 2 piglets to validate the model. Then, all of the piglets were sacrificed with pentobarbital overdose, and the skull of the piglets was immediately removed and the entire brain tissue was taken out via surgery to observe the injected blood distribution directly.

3. Results

The EIT boundary voltages were successfully collected in 6 piglets. During the process of data collection, each piglet remained still and alive.

3.1 Anatomy results

As shown in figure 2, volume expending change was found in the right lateral ventricular for 2 subjects by CT scan, and a breakage was also found in the ventricular at each piglet by autopsy methods. These results show that the IVH model was successful.
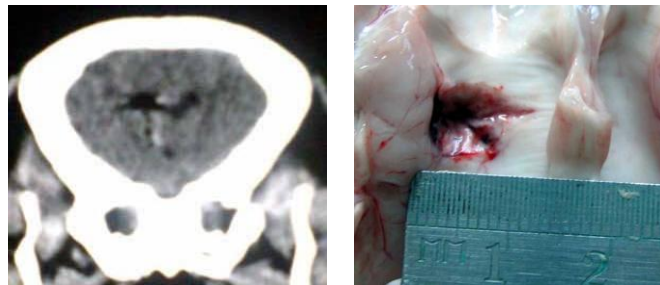
Figure 2. X-ray CT imaging (left) and autopsy (Right) results of IVH on piglets.
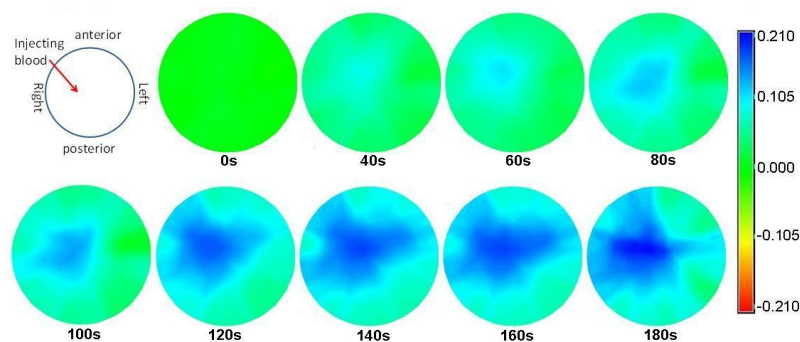
Figure 3. A series of EIT images from one of the subjects demonstrating resistivity changes within the entire course of blood injection

3.2 EIT imaging results

The EIT images obtained during the process show that during the 30 minutes before blood injection, there were no significant resistivity changes in EIT images. Than, as the blood injection begins, an increase in resistivity was seen in all subjects. As the amount of blood increased, the amplitude of resistivity changes became significant, and the area became large. After the injection of 2ml blood, the changes reached their maximum. The typical EIT images reconstructed during the injection of blood were shown in figure 3. Here, the first picture shows the mapping between an EIT image and actual orientation of the subjects, and the picture labeled 0s is the image taken before the injection of blood. The picture labeled 180s is the image taken after the injection of blood.

Figure 4 shows MSRV and ARV of images along the time axis. The MRV and AVR represent the maximal and the average resistivity variation respectively in EIT image. From these plots, we can see that both parameters increased almost monotonically as blood injection continue.
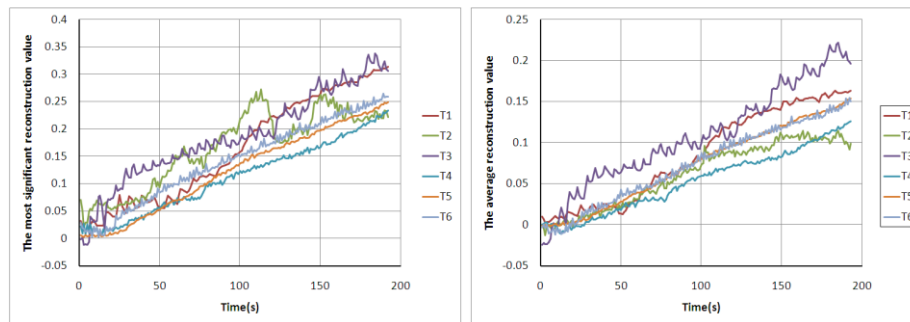

Figure 4. Plots of MSRV (left) and ARV (right) in EIT images against time for the subjects.

4. Discussion and conclusions

IVH is a dangerous disease with pool prognosis. In this study, we injected 2ml of blood into 6 living piglets to build the IVH animal model, and performed EIT imaging experiment on them. The final imaging results show that the resistivity in corresponding area inside the animal's brain increased during the injection of blood. Both of the MSRV and ARV of the images have a significantly positive correlation-ship with the volume of blood that injected to the animals lateral ventricular. The resistivity increase in this study may caused by the fact that the resistivity of blood is higher than that of cerebrospinal fluid (CSF). When blood was injected, some of the CSF that assembled in ventricular originally will be replaced by the blood, and cause an increase in resistivity in these place. Therefore, the results suggest the feasibility of detect and monitor the onset of IVH by EIT method. The relationship between MSRV or ARV and the volume of blood injected may also imply that they may be useful parameters to estimate the IVH volume.

References
[1]. Hallevi H, Albright K, Aronowski J, et al. Intraventricular hemorrhage: Anatomic relationships and clinical implications. *Neurology.* 2008; 70: 848–852.
[2]. Young WB, Lee KP, Pessin MS, et al. Prognostic significance of ventricular blood in supratentorial hemorrhage: A volumetric study. *Neurology.* 1990;40:616–619.
[3]. Shuai W J et al Image monitoring of an intraperitoneal bleeding model of pigs using electrical impedance tomography Physiol. Meas. 2008; 29: 217–25.
[4]. Meng Dai, Liang Wang, Canhua Xu, Lianfeng Li, Guodong Gao and Xiuzhen Dong. Real-time imaging of subarachnoid hemorrhage in piglets with electrical impedance tomography. Physiol. Meas. 2010; 31: 1229–1239.
[5]. Xuetao Shi, Fusheng You, Feng Fu, Ruigang Liu, Yu You, Meng Dai, Xiuzhen Dong。 Preliminary Research on Monitoring of Cerebral Ischemia Using Electrical Impedance Tomography Technique. Proc. IEEE/EMBS 29th Ann. Int. Conf., 2008, 1188-1191.

Validation of weighted frequency-difference EIT using a hemisphere model and phantom

Sujin Ahn[1], Tong In Oh[2], Sung Chan Jun[1]‖, Jin Keun Seo[3] and Eung Je Woo[2]

[1]School of Information and Communications, Gwangju Institute of Science and Technology, Gwangju, Korea
[2]Department of Biomedical Engineering, Kyung Hee University, Gyeonggi-do, Korea
[3]Department of Computational Science and Engineering, Yonsei University, Seoul, Korea

Abstract. Frequency-difference electrical impedance tomography (EIT) using a weighted voltage difference has been recently proposed for imaging haemorrhagic stroke, abdominal bleeding and tumor. Adopting hemispherical models and phantoms whose admittivity distributions change with frequency, we investigated the performance of the weighted frequency difference EIT to detect an anomaly. We found that the simple frequency-difference method fails to detect the anomaly whereas reconstructed images using the weighted frequency-difference method clearly visualize the anomaly. The weighted frequency-difference method is robust against modeling errors of boundary shape deformations and displaced electrode positions. We also found that the method is capable of detecting an anomaly surrounded by a shell-shaped obstacle simulating the skull.

Keywords: EIT, Frequency-difference EIT, Weighted frequency-difference EIT

1. Introduction

Though time-difference EIT has been successfully applied to lung imaging, it is not adequate for imaging tumor or stroke since a time-referenced data without any anomaly is not available. Noting that biological tissues show frequency-dependent admittivity spectra, frequency-difference EIT has been proposed (Griffiths *et al* 1987, McEwan *et al* 2006). Seo *et al* (2008) suggested a weighted frequency-difference EIT (WFD) algorithm to annihilate a global change of the admittivity inside an imaging object with respect to frequency. Since this enhances the local frequency-dependent contrast of the anomaly, the WFD method outperforms the simple frequency-difference (FD) method. To validate its performance in a three-dimensional case, we carried out numerical simulations and phantom experiments. We will describe simulation results of the WFD method using hemisphere models including modeling errors, which will be followed by experimental results using hemisphere phantoms in similar settings.

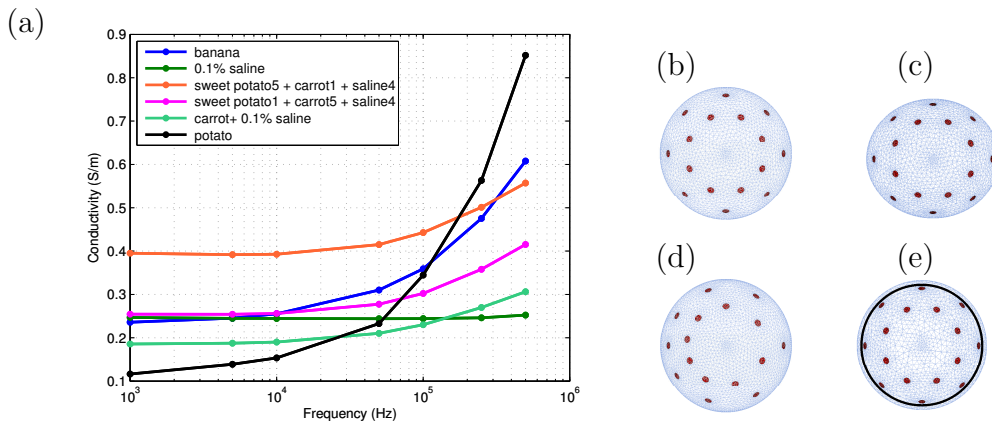‖ To whom correspondence should be addressed (scjun@gist.ac.kr)

(a)

Figure 1: (a) Conductivity spectra. The mixture "sweet potato5+carrot1+saline" consisted of sweet potato pieces, carrot pieces and saline with the ratio of 5:1:4. The composition of "sweet potato1+carrot5+saline" was 1:5:4. (b) Hemisphere Ω_1, (c) deformed hemisphere Ω_2, (d) hemisphere with non-uniformly positioned electrodes Ω_3 and (e) hemisphere with an inner shell Ω_4.

2. Methods

2.1. Settings for simulations and phantom experiments

In numerical simulations, we used the conductivity spectra in figure 1(a) to produce synthetic data. We considered the following five cases.

- Case 1. $\Omega_1 = \{(x, y, z)|x^2 + y^2 + z^2 \leq 9^2, z \leq 0\}$ (figure 1(b)).
- Case 2. $\Omega_2 = \{(x, y, z)|(x/1.1)^2 + (y/0.9)^2 + z^2 \leq 9^2, z \leq 0\}$ (figure 1(c)).
- Case 3. $\Omega_3 = \Omega_1$ with non-uniformly positioned electrodes (figure 1(d)).
- Case 4. Ω_4 is same as Ω_1 but has a shell $\{(x, y, z)|8.4^2 \leq x^2+y^2+z^2 \leq 8.7^2, z \leq 0\}$ with a low conductivity value (figure 1(e)).
- Case 5. Ω_5 is same as Ω_1 but decomposed by two compartments. We let D_1 and D_2 be the upper and lower parts such that $D_1 = \{(x, y, z) \in \Omega_1|y \geq 0\}$ and $D_2 = \{(x, y, z) \in \Omega_1|y < 0\}$. We assigned different admittivity values to D_1 and D_2.

We put an anomaly with 3 cm diameter. We tried two different materials for the background including 0.1% saline and mixture of saline, carrot pieces and potato pieces. The anomaly was a piece of either carrot or potato. For Ω_5, we tried different background materials by altering the compositions of saline, carrot pieces and potato pieces. We computed boundary voltages at 1, 100, 250 and 500 kHz for each case and added Gaussian noise of 20 dB SNR. In phantom experiments using a KHU Mark1 EIT system (Oh *et al* 2007), we tried to duplicate the settings of the simulation studies as much as possible. We computed a sensitivity matrix using a separate mesh of the basic hemisphere Ω_1 with a homogeneous conductivity. We used the same sensitivity matrix for all five cases to investigate effects of modeling errors. We used the singular value decomposition (SVD) with the Tikhonov regularization for image reconstructions. In each reconstructed image, we identified the anomaly as the biggest blob over the half-maximum conductivity change.
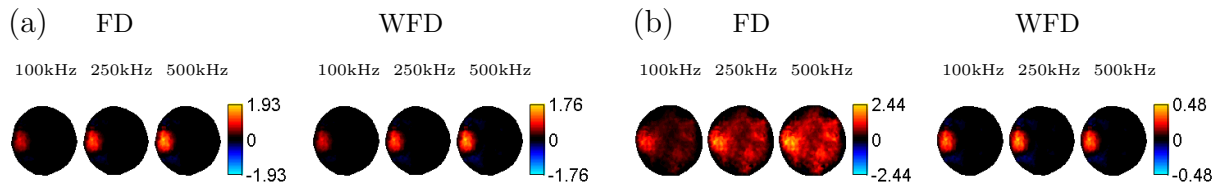
Figure 2: Simulation results of the hemisphere Ω_1. (a) Banana anomaly in the saline. (b) Potato anomaly in the mixture of carrot pieces and saline. Data at 1 kHz was used as a reference.
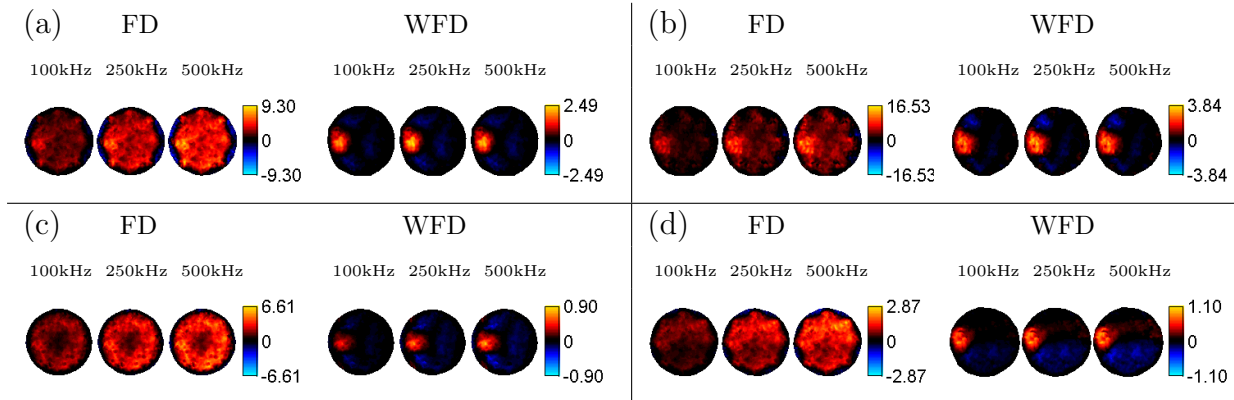

Figure 3: Simulation results of the potato anomaly in the mixture of carrot pieces and saline: (a) shape deformation (Ω_2), (b) non-uniformly placed electrodes (Ω_3), (c) shell-shaped obstacle (Ω_4) and (d) inhomogeneous admittivity distribution (Ω_5). Data at 1 kHz was used as a reference.

3. Results

When the background was the saline, there was no difference between the FD and WFD methods (figure 2(a)). For the background material of the mixture of carrot pieces in the saline, however, the FD method produced severe artifacts (figure 2(b)). All FD images in figure 3 indicate that the artifacts due to the global change of the frequency-dependent background conductivity are dominating. Figure 3(a) shows the effects of the boundary shape error. The WFD images clearly show the anomaly with a localization error of about 2% of the diameter of Ω_1. The conductivity contrast of the anomaly region in the WFD images slowly decreased along z direction and this resulted in slight blurring of the anomaly. When there were more electrodes near the anomaly, it appeared in the WFD images with a higher conductivity contrast (figure 3(b)). From figure 3(c), we found that the WFD method effectively removed the influence of the shell-shaped obstacle and successfully visualized the anomaly. The WFD images on figure 3(d) successfully visualized the anomaly in the inhomogeneous background. We found that the WFD method is always superior to the FD method.

4. Discussion and Conclusions

We demonstrated that the WFD method performs well in three-dimensional settings including modeling errors. We found that it detects an anomaly enclosed by a shell-
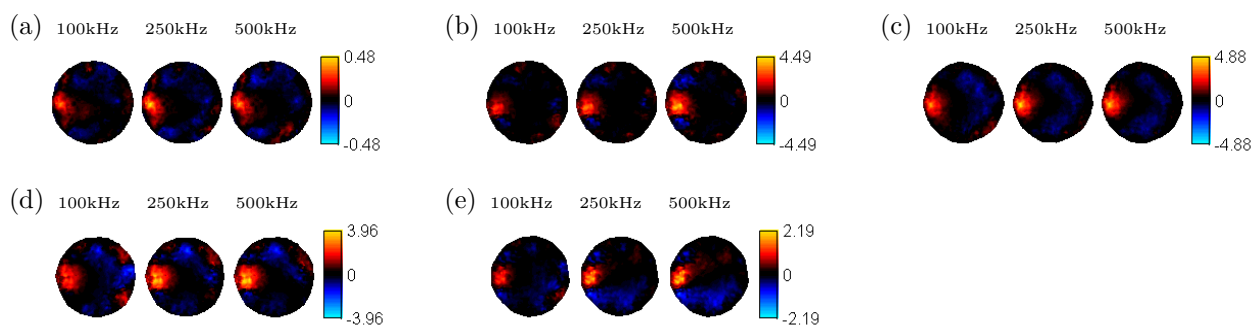
Figure 4: Experimental results. (a) Hemisphere, (b) deformed hemisphere, (c) non-uniformly placed electrodes, (d) shell-shaped obstacle and (e) inhomogeneous background. For (a) to (d), we used a potato anomaly in the background of the mixture of carrot pieces and saline. For (e), we used a banana anomaly and the two background regions were filled with 1:5:4 and 5:1:4 mixtures of sweet potato pieces, carrot pieces and saline. Data at 1 kHz was used as a reference.

shaped obstacle. Though we demonstrated that the WFD method can deal with a relatively simple inhomogeneous background, it is not clear if it will detect an anomaly located in a more general inhomogeneous background with a complicated frequency-dependent admittivity distribution. The capability to detect an anomaly using the WFD method depends upon the admittivity contrast of the anomaly with respect to the background at different frequencies. As long as the anomaly shows a distinct admittivity contrast at two different frequencies at least, the detectability will be high.

Acknowledgments

References

Griffiths H and Ahmed A 1987 A dual-frequency applied potential tomography technique: computer simulations *Clin. Phys. Physiol. Meas.* **8** 103-7

Jun S C, Kuen J, Lee J, Woo E J, Holder D and Seo J K 2009 Frequency-difference EIT (fdEIT) using weighted difference and equivalent homogeneous admittivity: validation by simulation and tank experiment *Physiol. Meas.* **3**0 1087-99

McEwan A, Romsauerova A, Yerworth R, Horesh L, Bayford R and Holder D 2006 Design and calibration of a compact multi-frequency EIT system for acute stroke imaging *Physiol. Meas.* **27** S199-210

Oh T I, Woo E J and Holder D 2007 Multi-frequency EIT system with radially symmetric architecture: KHU Mark1 *Physiol. Meas.* **28** S183-96

Seo J K, Lee J, Kim S W, Zribi H and Woo E J 2008 Frequency-difference electrical impedance tomography (fdEIT): algorithm development and feasibility study *Physiol. Meas.* **29** 929-44

High speed multi-frequency EIT device and

R. Pikkemaat[1], B. Venema[1], H. Luepschen[2] and S. Leonhardt[1]

[1] Philips Chair for Medical Information Technology, RWTH Aachen University,
Pauwelsstraße 20, 52074 Aachen, Germany

[2] Department of Anesthesiology and Intensive Car Medicine, University of Bonn, Germany
Sigmund-Freud-Str. 25, 53105 Bonn, Germany

pikkemaat@hia.rwth-aachen.de

Abstract

In this work we propose a EIT device being capable to use frequencies between 1 kHz and 350 kHz. Besides the modes of operation *difference in time* and *difference in frequency* the device is able to perform a special multi frequency mode. This mode is called *frequency sweep mode* (DSM) and may be used for a combined (visual and parametric) monitoring to identify intra thoracic changes of fluid content and thus helps to diagnose edema and arising pneumonias very early.

1. Introduction and Motivation

Since first devices have been developed [Brown 1987] to assess the regional distribution of electrical impedance several aspects of improvement have been proposed. Besides technical properties like signal to noise ratio (SNR) and parasitic effects the speed of acquiring data is a frequently considered aspect. Using a 16 electrode based EIT-system, 104 linearly independent surficial voltage measurements are required to calculate one image. Current commercial EIT devices (e.g. the Draeger EIT Evaluation Kit 2, EEK2) provide a frame rate up to 40 frames per second (fps). This frame rate is in general high enough to show even fast dynamics, e.g. like perfusion related signals [Deibele 2008]. Although this frame rate may be sufficient, an increase of speed is still useful. If the data acquisition lasts only a fourth of the usual acquisition time, the same frame rate could be provided, but each frame may be computed from a mean of four measurements and thus, the signal to noise ratio is halved. Because of this reason we propose a new EIT device, *"Aachen Mark 1.7"*, being capable to capture as many simultaneous voltage measurements as possible and provides an FPGA based quadrature demodulation to keep the time for data processing very low.

Conventional EIT devices only measure a certain determined frequency, e.g. 80 kHz. Because absolute EIT imaging requires exact knowledge about spatial conditions (the shape of a patient's thorax and the electrodes' positions) and the transient properties of the measurement chain most EIT devices use relative voltages to calculate a relative change in regional impedance. The

difference in time (DIT) imaging in which a reference can be defined as the dataset with the smallest summed up voltages (i.e. the smallest summed up impedance). Thus the EIT shows the current difference of regional impedance compared to the reference. If the EIT is not applied to volumes in which rather strong changes of regional impedance occur frequently, like in thoracic EIT, the DIT-EIT is not suitable to deliver robust imaging data. Hence, s potential monitoring of the stomach or other organs is not possible. Considering variation of specific complex impedance of different kinds of tissue at a certain frequency [Trokhanova 2008], the idea of using *difference in frequency* (DIF) imaging is straight forward to visualize different tissues. Similar to the KHU Mark 1 [Oh 2007] the *Aachen Mark 1.7* provides either a DIT or a DIF mode of operation. Furthermore the device is capable to drive a special multi frequency mode, called *frequency sweep mode* (FSM). The FSM is a special mode, which is not optimized for fast image acquisition. In this mode the injected current sweeps through the whole range of frequency at one position of current-injection (similar to BIS measurements). Because of this procedure the device is able to find the most suitable combination of four point measurements to detect lung edema or even to differentiate the location of an arising pneumonia.

2. Methods

2.1. Data acquisition

The Aachen Mark 1.7 is designed as a serial parallel EIT system. The current injection is designed serially. We used a modified Howland current source. As in most EIT devices the current injection is performed using all 16 adjacent pairs of electrodes. In contrast to other device all voltage measurements are performed in parallel. Thus, the whole data set of 208 voltages (104 linearly independent) can be a recorded in 16 cycles, whereas one cycle is defined as one multiplexer setting as shown in figure 1.
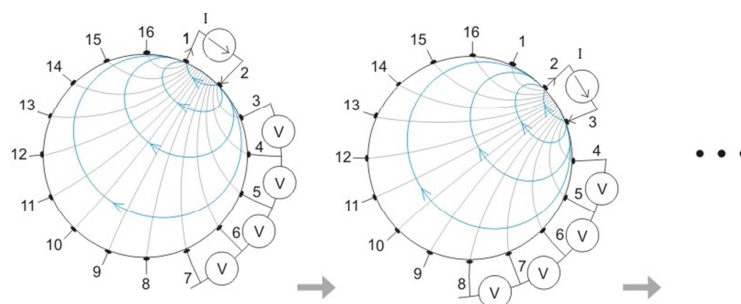

Figure-Fehler! Kein Text mit angegebener Formatvorlage im Dokument.**-1 Measurement procedure of the Aachen Mark 1.7: completely parallel voltage acquisition enables the system to collect all necessary data in a minimum of time**

For fast data processing a FPGA is used to perform fast quadrature demodulation. The combination being frequently used in fast EIT systems provides a very high performance and robust data processing.

2.2. Multi frequency modes of operation

The Aachen Mark 1.7 can be used in difference in time (DIF) and difference in frequency operation mode. Although there are different possibilities to deal with multi-frequency EIT measurements [Jun 2009], we decided to first use a simple "difference of two frequencies" imaging. In this short presentation we will not focus on this method, because there are a couple of scientific papers dealing with this topic.

We decided to implement the *frequency sweep mode*, FSM, to combine the potential of DIF and DIT imaging with scalar (non-imaging) analysis concerning the thoracic bio impedance. Therefore we use a sweep of frequencies from 1 kHz to 350 kHz as known from bio impedance spectroscopy (BIS) at each position of current injection, as shown in figure 2:
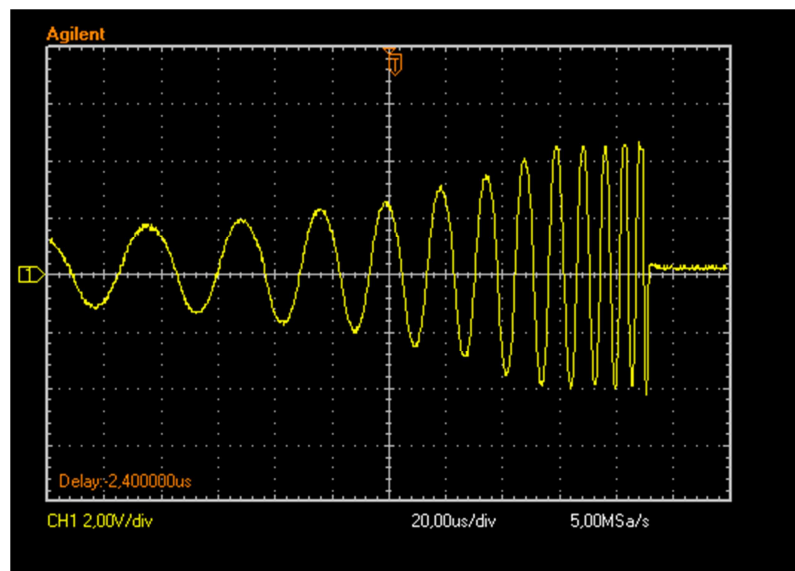
Figure 1-2 Measurement a voltage proportional to the injected current during the frequency sweep mode (FSM). The amplitude of the current is automatically scaled according to the law for medical products IEC 60601-1.

Due to the enlarged period of time being used for all 16 sweeps, this technique is not capable to deal with fast dynamics. However, the complex impedances can be analyzed regarding the fluid content of the regional pulmonal tissue. The analyses can exemplarily be analyzed according to shifts of the resulting Cole-Cole curves and thus might deliver information about arising edema or pneumonia.

3. Discussion

The proposed EIT device is capable to provide difference in time and difference in frequency modes of operation. In these modes the image acquisition is really fast due to the parallel construction and the FGA base data processing. Furthermore within the multi-frequency mode a

frequency sweep mode has been developed to perform intermediately impedance sweep measurements and thus, to recognize early fluid shifts within the pulmonal tissue. With this data arising pneumonias or edema can be recognized and the physicist is able to start the treatment before the patient evolves a severe lung disease or even a systemic sepsis.

Until now the system is tested using impedance dummies. Further studies in the near future will show how sensible the device will detect fluid shift within the pulmonal tissue.

References:

- [Brown 1985] Brown B H, Barber D C and Seagar A D, "Applied potential tomography: possible clinical applications", Clin. Phys. Physiol. Meas., Vol. 6, No. 2, 109-121, 1985
- [Trokhanova 2008] Trokhanova O V, Okhapkin M B and Korjenevsky A V. "Dual-frequency electrical impedance mammography for the diagnosis of non-malignant breast disease", Phys. Meas., Vol. 29, pp. 331-344, 2008
- [Deibele 2008] Deibele J, Luepschen H and Leonhardt S, "Dynamic separation of pulmonary and cardiac changes in electrical impedance tomography", Physiological Measurement, Vol. 29, pp. 1-14, 2008
- [Oh 2007] Oh T I, Woo E J and Holder D, "Multi-frequency EIT system with radially symmetric architecture: KHU Mark 1", Physiological Measurement, Vol. 28, pp. 183-196, 2007
- [Jun 2009] Jun S C, Kuen J, Lee J, Woo E J, Holder D and Seo J K, "Frequency-difference EIT (fdEIT) using weighted difference and equivalent homogeneous admittivity: validation by simulation and tank experiment", Phys. Meas., Vol 30, pp. 1087-1099, 2009

On a new electronic design for data acquisition and conditioning for Electrical Impedance Tomography measurements

J. Cuan-Lee[1], R. Martinez-Alonso[2],
R. G. Moreno-Alvarado[3], J. J. Gutierrez C.[4], M. P. Ramirez T.[4]

[1]HILMA S.A. de C.V., G. I. Ramirez 687, C.P. 16030, Mexico.

jcuan@asajiaudio.com

[2]CFE, Don Manuelito 32, C.P. 01780, Mexico.

ruben.martinez08@cfe.gob.mx

[3]SEPI-ESIME, Sta. Ana 1000, C.P. 04430, Mexico.

[4]ULSA, B. Franklin 47, C.P. 06140, Mexico.

marco.ramirez@lasallistas.org.mx

1   Introduction

The Electrical Impedance Tomography (EIT) is a medical imaging technique that provides information regarding the internal impedance properties of biological tissues. It is based onto voltage measurements on the boundary of the body under examination, while applying very low electrical currents. Traditionally, the data acquisition system is performed through an array of electrodes attached to the boundary of the imaged object [2],[7].

Indeed, to perform EIT measurements, currents must be injected through a set of electrodes, which will also conform the main recollection arrangement, when searching for patterns that might be used to approach images of the impedance distributions within the object. By virtue of the mathematical problem posed by A. P. Calderon [1], the internal conductivity can be inferred in unique form by using these boundary data [2],[7].

In fact, most EIT systems deal with the electronic performance of the current source for determining the accuracy. Trying to overcome this challenge, the previous proposals of EIT systems (see e.g. [3] and [5]), were based onto precision current sources, looking for the maximum accuracy available for signal generation.

Another problem in multi-frequency EIT systems, is the accuracy of the voltage generator, and the precision of the digital phase sensitive demodulator, which share a common platform, based onto a Field Programmable Gate Array, with embedded Digital Signal Processing (see e.g.[8]).

The EIT system problem is considered, from the classical mathematical point of view, very unstable, therefore a set of accurate measurements needs to be obtained. Because of that, it is necessary to emphasize that the characteristics of the data acquisition systems must be carefully selected, in order to avoid problems when processing the signals.

Beside, taking into account that a new theory for EIT is under construction (see e.g. [6]), perhaps new proposals for data-acquisition systems are in order.

In this paper, and EIT data-acquisition system design is described. The proposal consists in two parts: 1) An analog subsystem, and 2) A control module implemented onto $16F887$ Peripheral Interface Controller (PIC). Basically, we can say the $PIC16F887$ provides control signals to manage the analog subsystem, and voltage excitation signals for controlling the current source frequency.

2 System overview

The analogue subsystem comprises a $1mA$ current source, an instrument amplifier, a MAV circuit, a sinusoidal-to-squared signal converter, and an arrangement of active filters. The system can accurately measure a load impedance going from 100Ω to $10k\Omega$, on a frequency range of $10Hz$ to $10kHz$. Notice the tissue impedances are mainly resistive on these frequency ranges [7].

In order to performance measurements in several ranges of the frequencies mentioned above, a $PIC16F887$ was used for design flexibility, as well as for controlling the current sources, and the data acquisition module. The goal is to achieve a system with low noise and high speed.

3 Analogue sub-system

3.1 Constant Current Source Module.

The Constant Current Source Module is based on a modified Howland circuit, which uses the feedback technique in order to obtain a highly accurate output, low noise and drift distortions; even with the presence of common external variations such as those given by thermal conditions.

In order to obtain the desired characteristics, a circuit according to the following specifications was specifically design for EIT purposes, by the engineering team of $HILMA$ $S.A.$ de $C.V.$: 1) Offset Voltage smaller than $15\mu V$, 2) Maximum Drift of $0.8\mu V/^oC$, 3) Common Mode Rejection Ratio bigger than $135dB$, 4) Source Ripple Rejection bigger than $140dB$, 5) Slew Rate bigger than $10V/\mu s$, 6) Noise Voltage Density at $1kHz$ close to $1.2nV/\sqrt{Hz}$, and 7) Total Harmonic Distortion close to $-120dB$.

Based on the characteristics described above, an $OPAMP$-based circuit was designed. This circuit pumps the output signal in feedback for increasing the accuracy of the sample. The applied signal must be a low-distortion sinusoidal, for avoiding the presence of undesirable harmonics that may affect the measured impedance. Also, the value of the obtained current signal will be proportional to the input voltage.

3.2 Data Acquisition Module.

The analogue module in the EIT system, shown in Figure 1A, consists of a multiplexer switching network developed with $JFET$ transistors and $CMOS$ OR gates, in order to reduce noise on the voltage measurements, and to avoid current injection errors. The multiplexer switching network is controlled by

2

the $PIC16F887$, which selects the electrical current injection, and governs the voltage measurement, by enabling the output of $CMOS\ OR$ gates.
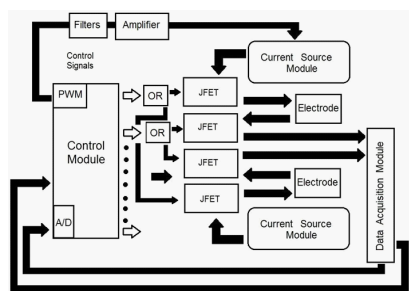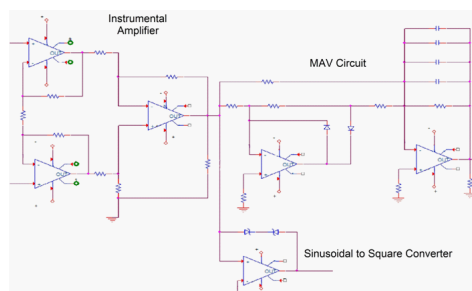

Figure 1A   Figure 1B

The results of voltage measurements are introduced into the instrumental amplifier, going latter to the MAV circuit, and to the sinusoidal-to-square signal converter shown in Figure 1B. Finally, both signals are routed to the corresponding $CMOS\ OR$ gate, which will direct the one coming out from the MAV circuit to the A/D port, and the other to some available analog input port [4].

The square signal, provided by the $PIC16F887$, is converted into a sinusoidal voltage wave of $20Vp-p$, using low-pass filters and voltage amplifiers, achieving the minimum specifications described in the previous Section. Finally, this signal is fed to the $1mA$ constant current sources for controlling their common output frequency.

Because the voltages measurements on the experimental subject are located in very low ranges, they must be introduced into the amplifier shown in Figure 1B. Also, a feedback of the common mode voltage is used to avoid errors in the impedance measurement, which might be provoked by the switching and the stray capacitance of the coaxial cable. The instrumentation amplifier output feeds the MAV circuit and the sinusoidal-to-square signal converters. The MAV circuit reaches a RMS-voltage value, and the sinusoidal-to-square signal converters provide the period reference for frequency identification.

These results will be sent, respectively, to the $PIC16F887\ A/D$ port, and to some convenient analog input port [4]. Once this process is complete, the data acquired by the $PIC16F887$ can be transferred to any CPU, using a standard USB-protocol interfaces.

4   Microcontroller control and frequency generator module

Notice the architecture of the $PIC16F887$ is capable to provide a wide variety of useful arraignments. For example, by using only one port, we can obtain until sixteen control signals for managing sixteen currents sources, while a second port can provide, through half of its terminals, the necessary signals to enable the MAV circuits, using the second half to activate the signal converters. A third port can be used to provide a PWM signal, while the fourth receives until

eight signals coming out from the sinusoidal-to-square converters. Beside, the architecture includes an A/D converter with eight available channels, that will be employed for receiving the MAV circuits outputs.

In order to enhance the quality of the EIT, the control system is developed to expand the independent measurements. The measurement and current injection electrodes are driven by $JFET$ to attach new measurement sites. The proposed measurement and injecting current scheme can provide more data to improve the quality of the reconstructed image.

More precisely, the port managing the current sources provides eight signals of $(0,1)$ outputs for the $CMOS\ OR$ gates, to govern the current injection pattern, while the second and fourth ports control the voltage and frequency sampling. This task is developed every time the current injection pattern changes, according to the variety of measurement requirements of the experimental models.

References

[1] Calderon A. P., *On an inverse boundary value problem*, Seminar on Numerical Analysis and its Applications to Continuum Physics, Sociedade Brasileira de Matematica, pp. 65-73, 1980.

[2] Holder D. S., *Electrical Impedance Tomography, Methods, History and Applications*, IOP Pub Inc, 2005.

[3] Lee J. W. et al, *Precision Constant Current Source for Electrical Impedance Tomography*, Proceedings of the 25" Annual International Conference of the IEEE EMBS,2003.

[4] Martinez R., Torres D., Madrigal M, Ugalde L. E., Guardado L., *Digital Domestic Meter for the Measurement and Billing of Electricity in Mexico*, Proceedings of the 11th WSEAS International Conference on CIRCUITS, Agios Nikolaos, Crete Island, Greece, pp. 71-76, 2007.

[5] Rafiei-Naeini M., Wright P., McCann H., *Low-Noise Measurement for Electrical Impedance Tomography*, Springer, 2007.

[6] Ramirez T. M. P., Sanchez N. V. D., Rodriguez T. O. and Gutierrez S. A., *On the General Solution for the Two-Dimensional Electrical Impedance Equation in Terms of Taylor Series in Formal Powers*, IAENG International Journal of Applied Mathematics, 39:4, 2009.

[7] Webster J.G., *Electrical Impedance Tomography*, Adam Hilger, 1990.

[8] Zarifi M. H., Frounchi J., Asgarifar S. and Baradaran Nia M., *FPGA implementation of a fully digital demodulation technique for biomedical application*, IEEE CCECE/CCGEI, 2008.

Optimization of calibration method to enable imaging acute stroke using the portable serial UCH Mk2.5 Multi-frequency Electrical Impedance Tomography (MFEIT) system

H Koo, B Packham and D Holder

Department of Medical engineering & Bioengineering, University College London, UK

INTRODUCTION

Electrical impedance tomography (EIT) may be used to image in acute stroke [1], but relatively large conductivity changes in the brain of about 100% translate into changes of about 1% on the scalp. As time difference imaging is not practicable, our approach has been to use frequency difference imaging but this requires careful calibration in order to yield accuracy across frequency capable of imaging such small changes. We have designed a MFEIT system, the UCH Mk2.5 [1] for this purpose and it is currently being used in studies in liquid filled tanks and human subjects with acute stroke. It has a single impedance measuring circuit which is multiplexed to a maximum of 32 electrodes. Individual measurements are made by serial injection of current through one pair of electrodes with voltage recording through another. The error of this across frequency after optimisation was <0.2%, measured across a resistor [1]. Published calibration methods include correction for a resistor or complex conductance phantom, with correction or optimisation of the reciprocity error [2-4]. In this study, we have set out to determine the best settings for calibration with the Mk2.5 system in MFEIT recordings in stroke, by correction against a standard load. This was conducted with recordings in a resistor, cylindrical 2D or head-shaped 3D tank and intended to address these questions; (1) what are the characteristics of the serial MFEIT system? (2) what is the best calibration method – (i) which load? (ii) one for all or individual channel calibration? Calibration data was obtained from recordings with varying resistors or varying concentrations of saline in the tanks. The efficacy of different calibration settings was assessed by calculating the total non-linearity error over frequency and electrode combinations and by image quality for a complex conductivity test object and background in the head-shaped tank.

METHOD

The UCH Mk2.5 MFEIT system is a serial EIT system with a fixed gain of 100 in the recording side. Data were recorded with 133 μA_{pp} at from 20Hz to 1.29MHz [1] : i) with one electrode combination across a single resistor from 7.6 to 55.7Ω. ii) in a cylindrical tank (19cm in diameter and 10cm high) using serial polar current drive and adjacent voltage pair recording and iii) in a 3D realistic head shaped tank with and without skull [5] with 16 electrodes and the spiral16 electrode addressing protocol [6]. The tanks were filled with saline from 0.025-0.15%, 0.05-0.2% and 0.2-0.4% in the 2D and 3D tanks without and with skull, respectively. The 3D tank was also filled with chopped carrot combined with 0.2% saline solution (σ=0.2 S/m) then a potato was inserted as a perturbation. Temporal noise was defined as the SD over time and "channel error" as the SD between channels over 10 image data sets. The "total error" was the rms temporal error across all channels and also frequencies: the error

across frequency was calculated on the basis that, for the resistive loads used, the real component of the recorded impedance should be flat across frequency. The calibration methods were; (1) 'one for all' - the same correction factor is applied to all electrode combinations in terms of magnitude and phase, calculated from a single measurement. (2) 'individual channel' - separate correction factors are applied to each electrode combination from multiple measurements. Electrode combinations in which the standing voltage was < 0.1mV or temporal error >1% were excluded. Images were reconstructed using a Weighted Frequency Difference (WFD) imaging algorithm because it has a frequency varying background [7].

RESULT

Before calibration, the temporal noise of the modulus over all resistors and tanks was less than 1%, although greater at lower loads. The modulus channel error increased with complexity of test object from 1% for the resistor to about 5% for the 3D tank (Fig. 1). The calibration method with the lower total error was with the 27.5Ω resistor, 0.075%, 0.1% and 0.35% saline and individual channel tank settings for the resistor, 2D and 3D tanks without and with the skull, respectively (Fig. 2 and 3). In reconstructed images of the desired demanding test multifrequency setting of a potato against a carrot-saline background, in the head-shaped tank without the skull, images corresponded more closely to the correct position of the test object for the above optimal calibration setting (individual correction, 0.1% saline load than for one for all calibration with a 55.7Ω single resistor) (Fig. 4).

(a) Resistor

(b) 0.025% saline in 2D cylindrical tank

(c) 0.05% saline in 3D head tank without skull
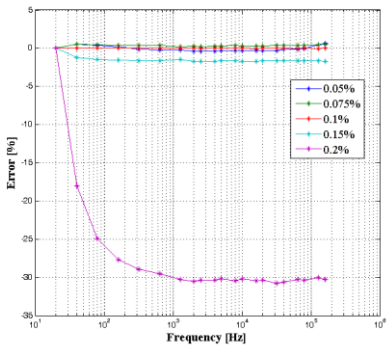
(d) 0.2% saline in 3D head tank with skull
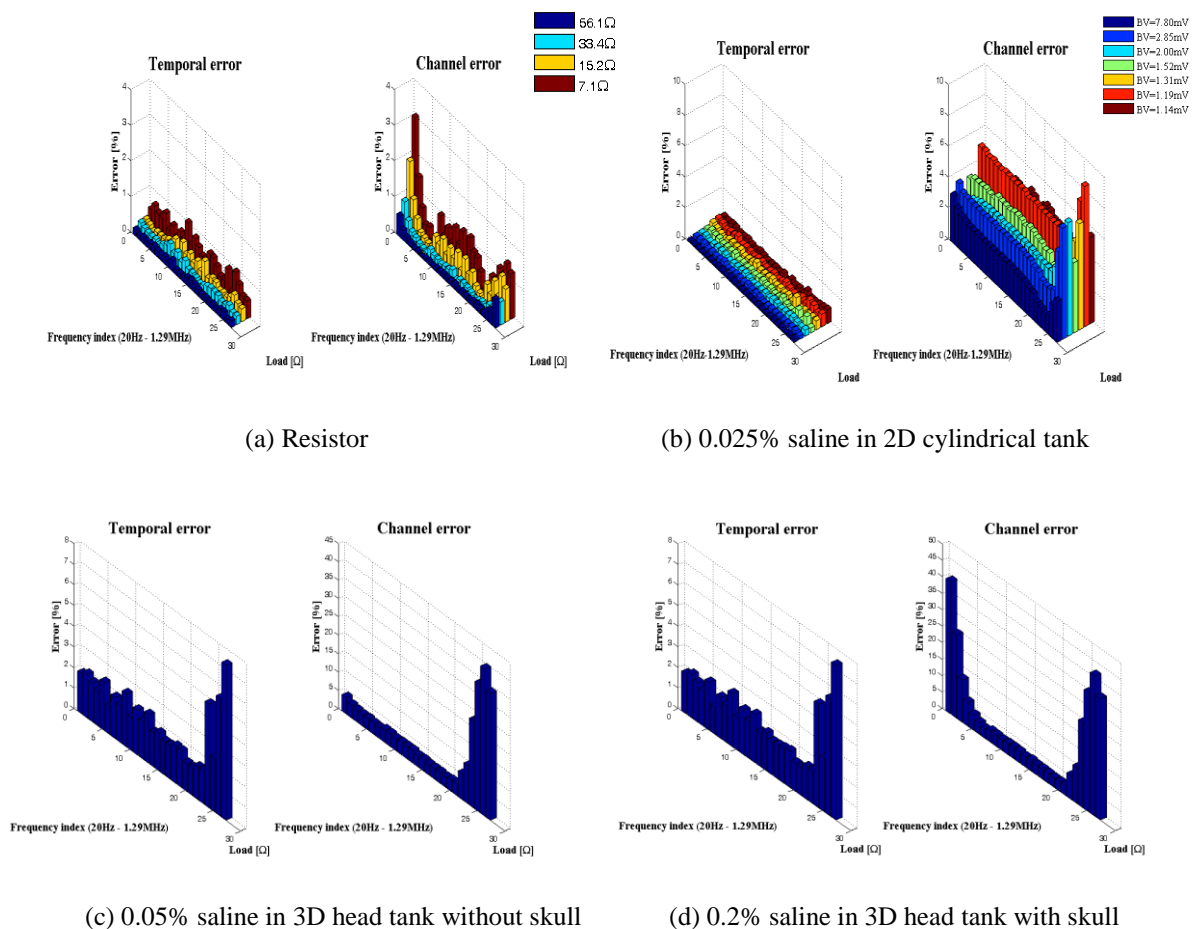
Figure 1. Characterisation of the system by temporal and channel error.
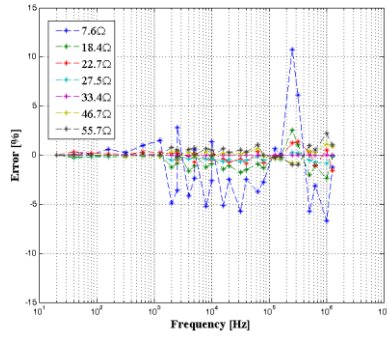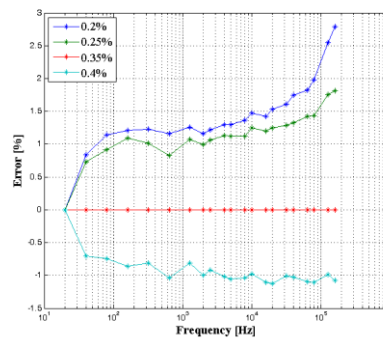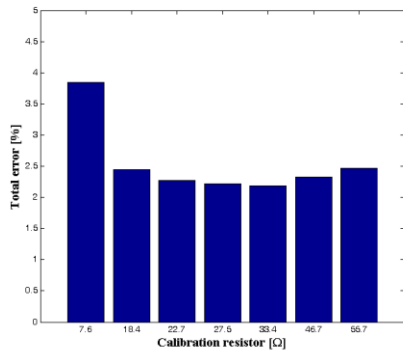
(a) Resistor
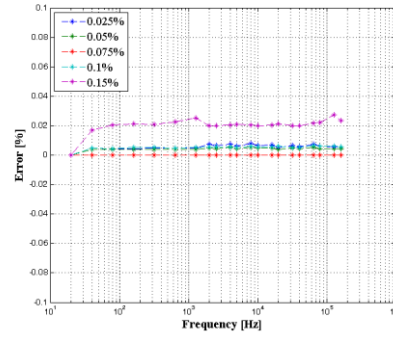
(b) 2D cylindrical tank
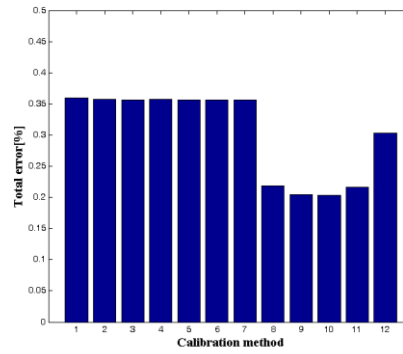

(c) 3D head tank without skull
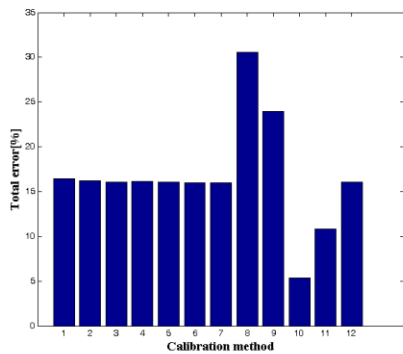
(d) 3D head tank with skull

Figure 2. Frequency spectral error after calibration by the optimal load in each object
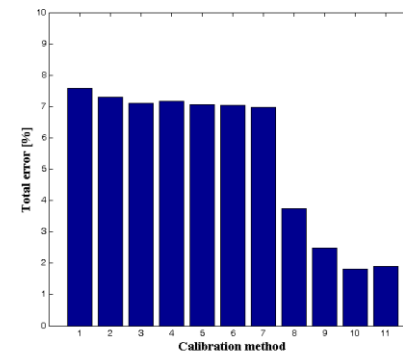

(a) Resistor

(b) 2D cylindrical tank

(c) 3D head tank without skull

(d) 3D head tank with skull

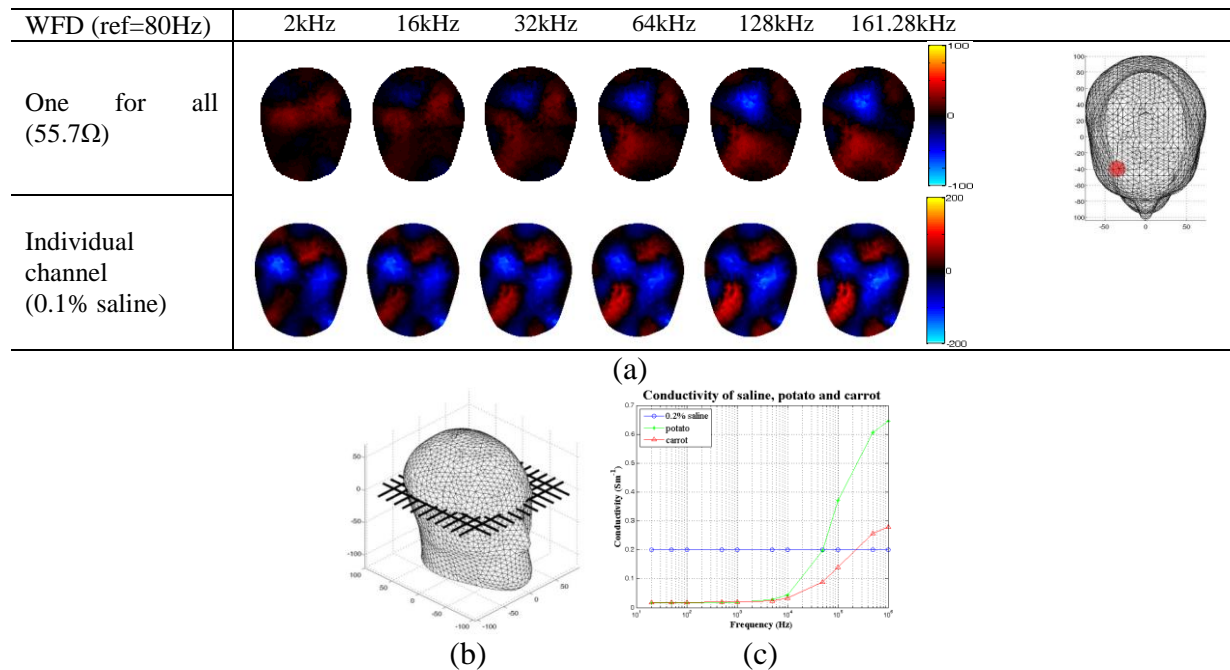Figure 3. Error comparison in test objects (1-7: Resistor, 8-12: Saline)

WFD (ref=80Hz)	2kHz	16kHz	32kHz	64kHz	128kHz	161.28kHz
One for all (55.7Ω)						
Individual channel (0.1% saline)						

(a)

(b)   (c)

Figure 4. Image comparison between 'one for all' and 'individual channel' calibration; (a) Reconstructed images (b) 0 mm slice in z-axis direction in the head mesh (c) Conductivity spectra of saline, potato and carrot

DISCUSSION

This study demonstrates that inter-channel error, across all frequencies, was greater than temporal error, presumably because of differing effects of stray capacitance between channels. It might therefore be expected that individual channel calibration would be preferable for the UCH system, especially to detect small impedance changes. In the event, the best calibration method was with 0.1% saline solution and individual correction for the 3D head shaped tank without skull. The optimal load for the 3D tank with skull was lower (0.35%) saline, probably because the skull gave greater resistivity and the optimal load gave transfer impedances in the centre of the expected load range. Our recommendation for the UCH Mk2.5 and similar systems in tank studies is therefore to use individual channel calibration for a resistive load in the middle of the expected range. Small voltage channels were found to be the primary source of errors with data from both 3D realistic head shape tank tests. Such channels needed to be removed in order to yield satisfactory results. As future work, there are several methods of improving calibration. Firstly, the small boundary voltage channels must be minimised, either through implementation of variable gain on the recording side, or improving measurement protocol to exclude these channels. To allow more accurate calibration for clinical trials, the 3D head shaped tank must be made more representative of the physiology. This first step could be the inclusion of a skin analogue, such as the vegetable skin of a marrow.

REFERENCE

[1] A. McEwan, A. Romsauerova, R. Yerworth, L. Horesh, R. Bayford, and D. Holder, *Physiol Meas.*, vol. 27, no. 5, p. S199-S210, May2006.

[2] H. Griffiths, *Physiol Meas.*, vol. 16, no. 3 Suppl A, p. A29-A38, Aug.1995.

[3] A. J. Fitzgerald, D. S. Holder, L. Eadie, C. Hare, and R. H. Bayford, *IEEE Trans. Med. Imaging*, vol. 21, no. 6, pp. 668-675, June2002.

[4] T. I. Oh, K. H. Lee, S. M. Kim, H. Koo, E. J. Woo, and D. Holder, *Physiol Meas.*, vol. 28, no. 10, pp. 1175-1188, Oct.2007.

[5] A. T. Tidswell, A. Gibson, R. H. Bayford, and D. S. Holder, *Physiol Meas.*, vol. 22, no. 1, pp. 177-185, Feb.2001.

[6] L. Fabrizi, A. McEwan, T. Oh, E. J. Woo, and D. S. Holder, *Physiol Meas.*, vol. 30, no. 6, pp. S85-101, June2009.

[7] S. C. Jun, J. Kuen, J. Lee, E. J. Woo, D. Holder, and J. K. Seo, *Physiol Meas.*, vol. 30, no. 10, pp. 1087-1099, Oct.2009.

Measurement the resistivity-temperature properties of liver tissue and applying EIT to monitor hyperthermia treatment based on phantom

Fusehng You*, Hua Cai*, Xuetao Shi, Canhua Xu, Feng Fu, Ruigang Liu, Xiuzhen Dong**

Department of Medical Electronic Engineering, School of Biomedical Engineering,

Fourth Military Medical University, Xi'an, 710032, P. R. China.

Both authors contributed equally to this work

**Correspondence author:* dongyang@fmmu.edu.cn

Abstract：In order to apply Electrical Impedance Tomography (EIT) to non-invasively monitor the temperature in during hyperthermia treatment of liver, the relationship between resistivity and temperature of liver tissue should be obtained. The impedance of fresh rabbit livers are measured *in vitro* in the processes of heating and cooling. At the frequency of 1KHz, with temperature below 58℃ the Temperature-Impedance Variation Factor (TIVF) mainly fluctuates between -1.0% ~ -2.2%. From 58℃ to 69℃, TIVF rapidly changes from -2.0% to -14.7%. At 69℃, 70℃ and 71℃, TIVF maintains around -14.7%. From 71℃ to 76℃, TIVF changes rapidly from -14.7% to - 1.0%. TIVF is mainly -1% at temperature above 76℃. A piece of pig liver was put into a phantom filled with salt solution, during heating the pig liver sample, the temperatures in different positions were measured and the impedance changes caused by heating was monitored in real-time by EIT. The images showed the resistivity of the heated liver tissue decreased gradually while its temperature raised higher. So high temperature caused nonlinear significant changes of resistivity of liver tissue, and in clinical hyperthermia therapy it is possible to monitor temperature in real time by EIT.

Keywords: hyperthermia; liver tissue; resistivity; EIT

1 Introduction

Combination of hyperthermia, radiotherapy and chemotherapy for tumor may reach a integrated effect of each method, and reduce the dose of radiation and chemical medication, thus decrease the side-effect of chemotherapy and increase the treatment effect [1,2]. For hyperthermia there are two modes for heating, one mode is warm-heating method, killing tumor cells by heating the tumor to reach the highest temperature of its endurable limitation. The other mode is high temperature coagulation method, which heating tumor to reach above 65℃ in a short time and to coagulate the proteins inside the tumor. It's important to monitor the temperature during hyperthermia so that the tumor cells were most killed and the surrounding normal tissues were less injured.

EIT is noninvasive and functional imaging modality. Many research groups have reported that EIT may be applied to monitor the impedance changes caused by hyperthermia. Griffiths [3] measured the temperature coefficients (TC) of electrical conductivity were 1.4% %/℃ for saline and 2.3%/℃ for agar in the temperature range of 15℃~25℃, also conductivity changes of agar caused by heating can be imaged by EIT. Conway[4] reported that based on agar

phantom the EIT images showed the distribution of thermal changes caused by microwave. Paulsen's[5] *in vivo* experiments showed that EIT data has qualitatively good correlations with temperature elevations during hyperthermia, but the relationship between tissue impedance and temperature (range from 20℃~70℃) is complex, the previously unheated tissue demonstrates a nonlinear conductivity increase with increasing temperature rather than the assumed and commonly used linear relationship of 2%/ ℃.

In order to estimate the temperature during hyperthermia, the more accurate relationship between resistivity and temperature should be acquired. In this study, the impedance changes of fresh rabbit liver were measured in the frequency range of 100Hz ~ 10MHz during heating and cooling processes from 30℃ to 80℃, and the temperature-impedance variation factor (TIVF) were calculated. Also the heating and cooling processes of pig liver sample were monitored by EIT based on phantom.

2 Materials and methods

All the experiments were approved by the animal ethic committee of the university.

2.1 Measurement the resistivity-temperature properties of liver tissue

The measurement system of liver impedance spectroscopy was established based on impedance analyzer (Agilent 4294A). Fig. 1 shows the tissue impedance measurement assembly in detail. A small impedance measurement box was designed, in which four silver electrodes were mounted in a straight line with a 20mm distance between the inner electrodes and a 50mm distance between the outer electrodes. In all experiments, calibration was performed with 0.9% physiological saline solution at temperature of 25℃.
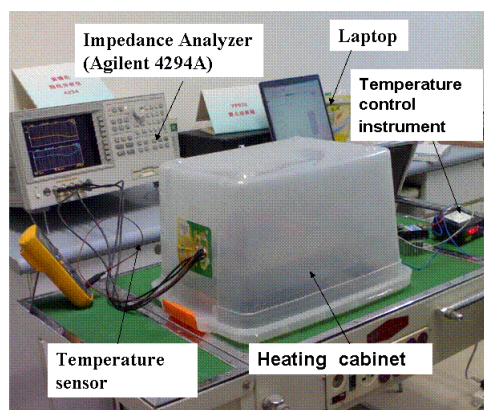

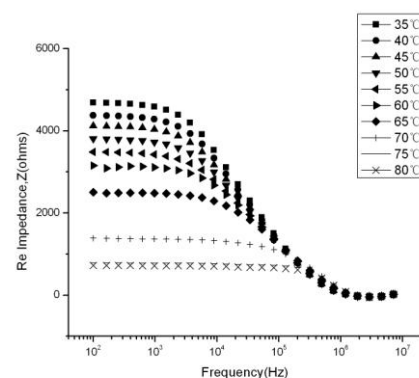| Fig. 1 The impedance measurement system of liver tissue | Fig.2 Real part Z spectra of fresh rabbit liver at 10 temperatures |

12 fresh rabbit livers (excised less than 30min) were firstly cut in shape of 50mm×6mm×6mm and placed into the measurement box. A temperature sensor (Thermocoax, fluke17B) was inserted into the tissue at a fixed distance of 10mm to the inner electrodes. The box then was put into heating cabinet which was quickly heated by two crystal heating tube (300W). The temperature in the cabinet was controlled by a temperature auto-control instrument (PID XMT81, TengHui ,China).

Agilent impedance analyzer 4294A was connected to a laptop via GBI to USB converter, its driving current was set to 0.5mA. Impedance data was recorded at each integer temperature points. At each temperature a total of 201 logarithmically spaced frequencies ranging from 100Hz~10MHz were swept and the measurement was performed for at least 6 s.

The measurements were started from 30℃, when tissue temperature reached higher than 80℃ the heating process was ended. The heated tissue was cooled in nature.

2.2 Applying EIT to monitor hyperthermia treatment based on phantom

The cylinder phantom is 284mm in diameter and 240mm in height. Sixteen electrodes were equally placed around phantom. NaCl solution with a resistivity of $480\,\Omega \cdot cm$ was injected to simulate abdominal resistivity ($500\,\Omega \cdot cm$) distribution.

Pig liver (excised less than 6h) was cut into the size of 45mm×30mm×60mm. A cartridge heater (Φ6mm×100mm, 150W) was inserted into the tissue about 30mm in depth. The temperature of the cartridge heater was monitoring by a temperature sensor which fixed in the middle of the cartridge heater and was controlled by the temperature auto-control instrument PID XMT81. Another 3 temperature sensors (T2, T3, T4) also placed in different positions to monitor the temperature distributions inside the tissue during heating and cooling. EIT system [6] (1250μA$_{p-p}$, 50KHz) applies polar driving and adjacent measurement mode and its imaging speed is 1frame/s.

3. Results

3.1 Measurement the resistivity-temperature properties of liver tissue

Table 1 shows the measured impedance of fresh rabbit liver (n=12, $\overline{\chi} \pm s$) for heating and cooling process in steps of 5℃ ranged from 30 till 80℃.

Fig.2 gives the real part of impedance spectra of fresh rabbit liver at ten temperatures. At each temperature the real part of the impedance decreases as the frequency increase. From about 100 Hz to 30 kHz the real part decreases slowly and then decrease rapidly as frequency increases. At the same frequency, the real part of impedance decrease as temperature increases.

Table 1： Impedance of the rabbit liver tissue during heating process and cooling process in steps of 5℃ （f=1KHz）

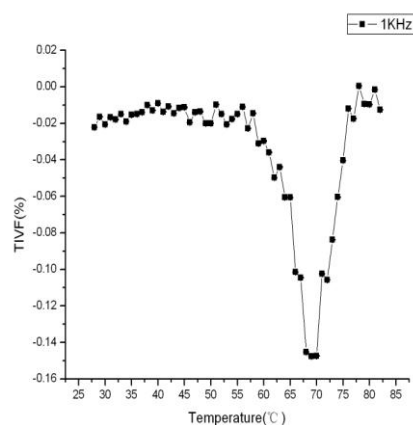| Temperature℃ (heating process)	$\overline{\chi} \pm s$	Temperature℃ (cooling process)	$\overline{\chi} \pm s$
30	5005±30.03	30	1601±28.82
35	4591±22.95	35	1454±26.17
40	4306±25.84	40	1325±25.19
45	4025±24.15	45	1210±30.25
50	3728±26.09	50	1120±30.24
55	3429±27.43	55	1032±26.84
60	3121±24.97	60	959±24.95
65	2480±32.24	65	890±26.70
70	1368±28.73	70	831±31.60
75	778±30.34	75	771±30.86
80	717±29.42	80	724±29.69

Fig.3 TIVF vs temperature at 1kHz of rabbit liver.

Fig.3 is the rabbit liver's curve of TIVF vs temperature at 1kHz. TIVF was calculated by the following equation:

$$TIVF) = \frac{\rho_{n+1} - \rho_n}{\rho_n} \times 100\% \quad \text{here } \rho_n \text{ is the resistivity at temperature n.}$$

At temperature below 58℃ the TIVF mainly fluctuates between -1.0% ~ -2.2%. From

58℃ to 69℃, TIVF rapidly changes from -2.0% to -14.7%. At 69℃, 70℃ and 71℃, TIVF maintains around -14.7%. From 71℃ to 76℃, TIVF changes sharply from -14.7% to - 1.0%. TIVF is mainly -1% at temperature above 76℃.

3.2 Applying EIT to monitor hyperthermia treatment based on phantom

Fig.4 is the reconstructed images of liver tissue during heating process. In the images the red represents a regional decrease in resistivity. The reference data was acquired before heating. From the series of images, it can be seen that the color of region of interest (ROI), corresponding to the heating tissue, becomes redder and the size of the ROI grows larger as temperatures elevation. This indicates that the changes in images are correlated with the temperature of the tissue.
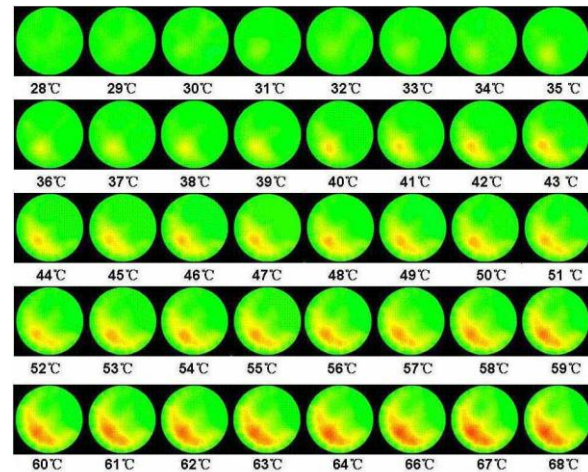
Fig. 4 EIT images of liver tissue during heating process

4 Conclusions

The measurement of rabbit liver's resistivity-temperature relation show that it's neither linear nor irreversable during heating and cooling processes. The TIVF changes rapidly from 60℃~75℃. The EIT images show significant impedance changes of liver tissue during heating in phantom, but the actual correlation between impedance changes reconstructed by EIT and temperature should be studied further.

References

[1] Wessalowski R，Van Heek-Romanowski R，lssels HT et al. Review：Estimated number of children with eligible for hyperthermia based on population and treatment-related criteria. Int J Hyperthermia.1999;15(6)：455～466.

[2] Van der Zee J，Gonzalez D，Van Rhoon GC et a1.Comparison of radiotherapy alone with radiotherapy plus hyperthermia in locally advanced pelvic tumours： prospective，randomized，multicentre trial. Lancet.2000;355(9210)：1119～ 1125．

[3] H Griffiths, A Ahmed. Applied potential tomography for non-invasive temperature mapping in hyperthermia. Clin.Phys.Physiol.Meas.1987;(8):147-153

[4] J Conway. Electrical impedance tomography for thermal monitoring of hyperthermia treatment : an assessment using in vitro and in vivo measurements. Clin. Phys.Physiol. Meas. 1987,(8):141-146

[5] Paulsen KD,Moskowitz MJ,Ryan TP,Mitchell SE,Hoopes PJ.Initial in vivo experience with EIT as a thermal estimator during hyperthermia. Int J Hyperthermia.1996, 12(5): 573-91

[6] Shuai Wanjun, You Fusheng, Zhang Wei, Zhang Hongyi, Fu Feng, Shi Xuetao, Liu Ruigang, Xu Canhua, Dong Xiuzhen,Bao Tingyi. Image monitoring for an intraperitoneal bleeding model of pigs using electrical impedance tomography Physiol. Meas.2008,29(2):(217–225)

On the electrical current trajectories when the conductivity is a polynomial function

M. P. Ramirez T., J. J. Gutierrez C.

Facultad de de Ingenieria de la Universidad La Salle,

Benjamin Franklin 47, Mexico D.F., C.P. 06140, Mexico.

marco.ramirez@lasallistas.org.mx

1 Introduction and Preliminaries

The study of the solutions for the Electrical Impedance Equation

$$\operatorname{div}\left(\sigma \operatorname{grad} u\right) = 0, \tag{1}$$

where σ is the conductivity function and u denotes the electric potential, is the base for well understanding the Electrical Impedance Tomography problem. In a variety of recent works, e.g. [4], it was shown that considering the two-dimensional case of (1), and representing σ by means of a separable-variables function

$$\sigma\left(x_1, x_2\right) = \sigma_1\left(x_1\right) \sigma_2\left(x_2\right), \tag{2}$$

the equation (1) can be rewritten into a Vekua equation [5] of the form

$$\partial_{\bar{z}} W - \frac{\partial_{\bar{z}} p}{p} \overline{W} = 0, \tag{3}$$

where $\partial_{\bar{z}} = \frac{\partial}{\partial x_2} + i \frac{\partial}{\partial x_1}$, $i^2 = -1$, $W = \sqrt{\sigma} \frac{\partial}{\partial x_2} u + i \sqrt{\sigma} \frac{\partial}{\partial x_1} u$, $\overline{W}$ is the complex conjugation of W, such that $\overline{W} = \operatorname{Re} W - i \operatorname{Im} W$, and p is an exponential function

$$p = e^{-\int \sqrt{\sigma_1}^{-1} \frac{\partial}{\partial x_1} \sqrt{\sigma_1} dx_1 + \int \sqrt{\sigma_2}^{-1} \frac{\partial}{\partial x_2} \sqrt{\sigma_2} dx_2}.$$

The biunique relation between the two-dimensional case of (1) and the Vekua equation (3) is specially relevant since, according to the Pseudoanalytic Function Theory posed by L. Bers [1], the general solution of (3) can be approached in analytic form, by means of Taylor series in formal powers:

$$W = \sum_{n=0}^{\infty} Z^{(n)}\left(a_n, z_0; z\right),$$

where every $Z^{(n)}\left(a_n, z_0; z\right)$ is called *formal power* with exponent n, complex constant coefficient a_n, center in z_0 and depending upon $z = x_2 + i x_1$. In consequence, this will allow us to approach the general solution for (1) when σ belongs to the class of functions (2).

A complete description of the mathematical procedure for approaching the formal powers can be found, e.g. [3] and [4].

We can construct the electrical current density vectors as

$$\overrightarrow{j}^{(n)} = \left(\sqrt{\sigma} \operatorname{Re} Z_0^{(n)}, \sqrt{\sigma} \operatorname{Im} Z_0^{(n)} \right).$$

From the point of view of the Applied Pseudoanalytic Function Theory, to analyze the behavior of the electrical current trajectories inside some domain, possesses great relevance, since it could reach important information about the behavior of the electric potential u at the boundary, which is one of the most important matters for Electrical Impedance Tomography. This is, if some unexpected behavior of the currents flows is observed, the mathematical methods applied for approaching u should be selected more carefully.

In this work we will focus our attention into some electrical current trajectories within the unitary circle, when the conductivity σ is a polynomial separable-variables function. This analysis rises because one of the interpolation methods posed for approaching σ in terms of a separable-variables functions, is precisely based onto polynomial expressions [4].

2 Electrical current paths when σ is a constant

For this case, the Vekua equation (3) will become the well known Cauchy-Riemann equation, for which the general solution can be approached by means of the classical Taylor series $W = \sum_{n=0}^{\infty} a_n \left(z - z_0 \right)^n$. Let us consider the term $n = 1$, with $a_1 = 1$ and $z_0 = 0$. The corresponding electrical current density vector will have the form $\overrightarrow{j}^{(1)} = (x_2, x_1)$, since $z = x_2 + ix_1$. By tracing the electrical current paths within the unitary circle, intersecting the radios at the angles $0, \frac{1}{2}\pi, \pi, \frac{3}{2}\pi$, we obtain the Figure 1.
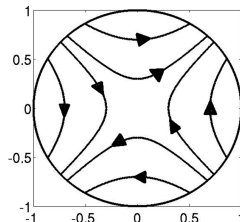

Figure 1

Notice the existence of four *groups* of electrical currents. As the reader will verify, the geometry of these groups, that we will also refer as the *dynamics* of the electrical current distributions, will preserve a pattern when considering the paths for a wide class of functions σ [4]. This pattern, of course, does not include the current intensities, but only their trajectories.

3 The case when σ depends of one spatial variable

In several previous works, e.g. [2] and [4], the case when σ has an exponential form has been deeply studied, since its corresponding Vekua equation is closely

related with a two-dimensional Yukawa equation [3], for which the general solution is known in exact form. This provides a powerful mathematical tool in order to analyze the convergence of the numerical methods that approach the solution for (1) bias Taylor series in formal powers.

Here, we consider $\sigma = (\alpha x_1 + b)^2$ because it corresponds to the class of functions used in the interpolation method posed in [4], but also because its *dynamics* posses a very particular behavior when considering the presence of zeros inside the unitary circle. It is evident we do not expect zero-valued points of the conductivity σ in medical imaging, but due to the significant difference of conductivities belonging to different kinds of tissues, at least from the numerical point of view, we can expect to deal with conductivities close to the zero value.

By applying the mathematical techniques exposed, e.g., in [3], we will have that

$$Z_0^{(1)} = (\alpha x_1 + b)\, x_2 + \frac{i}{\alpha x_1 + b}\left(\frac{\alpha^2 x_1^2}{3} + \alpha b x_1^2 + b^2 x_1\right);$$

and the corresponding current density vector will be

$$\overrightarrow{j}^{(1)} = \left(x_2\,(\alpha x_1 + b)^2,\, \frac{\alpha^2 x_1^2}{3} + \alpha b x_1^2 + b^2 x_1\right).$$

When there are no zeros within the unitary circle, let us say $\alpha = 1, b = 3$, the dynamics of the current distributions will be very similar to the homogeneous case, as it is possible to appreciate in Figure 2A. But the presence of zero-valued points, let us say $\alpha = 5, b = 3$, provokes a radical change in the dynamics of the current flows. The group corresponding to the angle π presents closed-loop trajectories. If we venture to classify the rest of trajectories as *hyperbolic* traces, the negative semiplane just after the zero-valued axe $x_1 = -\frac{3}{5}$ will possess *elliptic* traces, as it can be appreciated in Figure 2B.
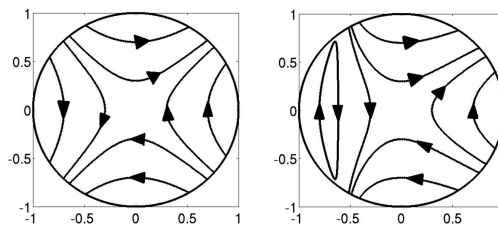

Figure 2A   Figure 2B

4   The case when σ depends upon two spatial variables

This case in closer to the medical imaging applications when employing elements of the Pseudoanalytic Function Theory [4], since all cases will depend upon two spatial variables. Let us consider then $\sigma = (\alpha x_1 + b)^2 (\beta x_2 + c)^2$. We will have that

$$Z_0^{(1)} = \frac{(\alpha x_1 + b)(\beta x_2 + c)}{\beta}\left(\frac{1}{\beta x_2 + c} - \frac{1}{c}\right) + i\frac{\alpha^2 x_1^2 + 3\alpha b x_1^2 + 3 b^2 x_1}{3\,(\alpha x_1 + b)(\beta x_2 + c)};$$

and the electrical current vector will be

$$\overrightarrow{j}^{(1)} = \left((\alpha x_1 + b)^2 (\beta x_2 + c)^2 \left(\frac{1}{\beta^2 x_2 + c} - \frac{1}{\beta c} \right), \frac{\alpha^2 x_1^2}{3} + \alpha b x_1^2 + b^2 x_1 \right).$$

Again, when no zero-valued points are located inside the unitary circle, for instance $\alpha = 1, b = 3, \beta = 1, c = 3$, the dynamics of the currents flows will keep the pattern of the homogeneous case, as Figure 3A illustrates.

But when a certain class of zero-valued points appear, for example $\alpha = 5, b = 3, \beta = 5, c = 3$, the dynamics will experiment a radical change. We can find closed-loop trajectories as shown in Figure 3B, but their location can not be explained by simple observations. Indeed, this case is located far away from the posed patterns shown previously. Its proper study could well reach useful information for the Electrical Impedance Tomography novel techniques, as well for the Mathematical Physics dedicated to the study of (1).
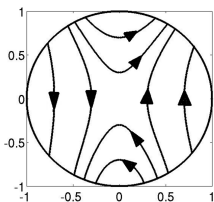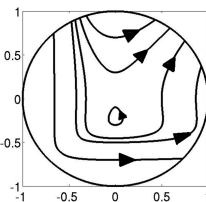

Figure 3A   Figure 3B

References

[1] L. Bers (1953), *Theory of Pseudo-Analytic Functions,* Institute of Mathematics and Mechanics, New York University, New York.

[2] R. Castillo P., V. V. Krvachenko, R. Reseniz V. (2011), *Solution of boundary and eigenvalue problems for second-order elliptic operators in the plane using pseudoanalytic formal powers*, Mathematical Methods in the Applied Sciences, Vol. 34, Issue 4, pp. 445-468.

[3] V. V. Kravchenko (2009), *Applied Pseudoanalytic Function Theory*, Series: Frontiers in Mathematics, ISBN: 978-3-0346-0003-3.

[4] M. P. Ramirez T. (2010), *On the electrical current distributions for the generalized Ohm's Law*, Submited for publication to Applied Mathematics and Computation, Elsevier, avaliable in electronic format at http://www.arxiv.com

[5] I. N. Vekua (1962), *Generalized Analytic Functions,* International Series of Monographs on Pure and Applied Mathematics, Pergamon Press.

On a numerical interpolation technique for obtaining piecewise separable-variables conductivity functions

M. P. Ramirez T., R. A. Hernandez-Becerril, C. M. Robles G.

Facultad de de Ingenieria de la Universidad La Salle,

Benjamin Franklin 47, Mexico D.F., C.P. 06140, Mexico.

marco.ramirez@lasallistas.org.mx

1 Introduction and Preliminaries

A complete new theory for the Electrical Impedance Equation has raised since K. Astala and L. Païvarïnta [1] noticed the biunique relation between the two-dimensional Electrical Impedance Equation

$$\operatorname{div}\left(\sigma \operatorname{grad} u\right) = 0, \tag{1}$$

where σ denotes the conductivity and u is the electric potential, and a Vekua equation [9] of the form

$$\partial_{\bar{z}} W - \frac{\partial_{\bar{z}} f}{f} \overline{W} = 0, \tag{2}$$

where $\partial_{\bar{z}} = \frac{\partial}{\partial x_2} + i \frac{\partial}{\partial x_1}$, $W = \sqrt{\sigma} \frac{\partial}{\partial x_2} u + i \sqrt{\sigma} \frac{\partial}{\partial x_1} u$, $\overline{W}$ is the complex conjugation of $W : \overline{W} = \operatorname{Re} W - i \operatorname{Im} W$, i is the standard imaginary unit $i^2 = -1$, f is an exponential function

$$f = e^{-\int \frac{1}{\sqrt{\sigma_1}} \frac{\partial}{\partial x_1} \sqrt{\sigma_1} dx_1 + \int \frac{1}{\sqrt{\sigma_2}} \frac{\partial}{\partial x_2} \sqrt{\sigma_2} dx_2},$$

and $z = x_2 + i x_1$.

Moreover, it was through this relation that in [1] was proved the existence and uniqueness of the solution for the Calderon Problem [3], very often named Electrical Impedance Tomography.

One of the main achievements of this discovering, was to trace a new path for applying the Theory of Pseudoanalytic Function [2] in order to approach the general solution of (2) in analytic form, bias the Taylor series in formal powers:

$$W = \sum_{n=0}^{\infty} Z^{(n)}\left(a_n, z_0; z\right),$$

originally called like that by L. Bers [2] when he showed that $Z^{(n)}\left(a_n, z_0; z\right) \to a_n \left(z - z_0\right)^n$ while $z \to z_0$. It appears that it was V. Kravchenko et al. [6], who first expressed the general solution in exact form of (1) for a certain class of σ, using new results in Pseudoanalytic Function Theory [5].

Eventually, in [4], the solution of the direct boundary value problem for (1) was approached with very high accuracy for the case when σ has an exponential form.

Indeed, many works had already remarked that when σ is a separable-variables function, it is always possible to approach the general solution of (1) by numerically constructing the formal powers $Z^{(n)}\left(a_n, z_0; z\right)$, see e.g. [4], [5], [7] and [8].

This work is dedicated to study a technique posed in [7], for obtaining a separable-variables conductivity function σ when a matrix of values is given for some bounded domain, a very natural situation in medical imaging. Specifically, we will consider the unitary circle, and by dividing it in parallel subregions, and applying cubic polynomial interpolation, we will construct a piecewise separable-variables function, showing the maximum error decreases while the number of segments and the points considered for polynomial interpolation grow.

2 The selection of subregions and points for interpolation

We will start setting the limits among the subregions of the unitary circle. For our illustrations, these subregions will be created by tracing k straight lines, parallels to the x_1-axe, having all the same distance among each other. Those lines will provoke that, when watching the circle diameter on the x_2-axe, the intersections show the diameter divided into $k + 1$ identical segments, each of them with length $\frac{2}{k+1}$, since 2 is the diameter of the unitary circle.

Consider now the subregion located on the top of the circle. Let us trace another straight line, also parallel to the x_1-axe, that will intersect the x_2-axe precisely at the high $1 - \frac{1}{k+1}$. This line crosses, from the point of view of the x_2-axe, by the *middle* of the top subregion. It is over this straight line that we should select a number m of points, being necessary that the first and the last of them are the points where the straight line intersects the circle. For our example, the distance among all the m points must be the same.

We will continue tracing straight lines at the *middle* of every subregion, and for every one of them we will locate m points, distributed in the same way that the points belonging to the top subregion.

The result will be a collection of $(k+1) \times m$ points within the unitary circle. The idea now is to relate an electrical conductivity value to every point.

Again, let us consider the m points located on the straight line crossing the *middle* of the top subregion. Knowing their electrical conductivity values, we can use standard techniques in order to obtain a continuous function g_1 that will interpolate such values. It is evident that the function g_1 will depend only of the x_1-coordinates, since the x_2-coordinates remain constant at $1 - \frac{1}{k+1}$. Let us denote this value as $y_1 = 1 - \frac{1}{k+1}$.

Finally, we define the electrical conductivity σ_1 for the top subregion of the unitary circle as

$$\sigma_1 = (x_2 + K) \frac{g_1\left(x_1\right)}{\left(y_1 + K\right)},$$

where $K > 0$ is a constant such that $x_2 + K \neq 0$ inside the unitary circle. It is evident that the conductivity function σ_1 is a separable-variables function.

2

Applying the same procedure for every remaining subregion, we will achieve our primary objective. We will have a piecewise separable-variables conductivity function of the form

$$\sigma_{pol}\left(x_1, x_2\right) = \begin{cases} (x_2 + K)\frac{g_2(x_1)}{(y_2 + K)}; 1 > x_2 \geq 1 - \frac{2}{k+1}; \\ (x_2 + K)\frac{g_2(x_1)}{(y_2 + K)}; 1 - \frac{2}{k+1} > x_2 \geq 1 - \frac{4}{k+1}; \\ (x_2 + K)\frac{g_3(x_1)}{(y_3 + K)}; 1 - \frac{4}{k+1} > x_2 \geq 1 - \frac{6}{k+1}; \\ \qquad\qquad \dots \\ (x_2 + K)\frac{g_{k+1}(x_1)}{(y_{k+1} + K)}; -1 + \frac{2}{k+1} > x_2 \geq -1. \end{cases} \qquad (3)$$

3 An example with a maximum quadratic error estimation

In order to make a first approach to the development of this interpolation method, we considered a conductivity function of the form

$$\sigma\left(x_1, x_2\right) = (B + \sin\alpha_1 x_1 + \sin\alpha_2 x_1 + \sin\alpha_3 x_1 + \sin\alpha_4 x_1) \cdot$$
$$\cdot (B + \cos\beta_1 x_2 + \cos\beta_2 x_2 + \cos\beta_3 x_2 + \cos\beta_4 x_2).$$

The numerical calculations took $B = 7, \alpha_1 = \beta_1 = 2\pi, \alpha_2 = \beta_2 = 4\pi, \alpha_3 = \beta_3 = 6\pi$ and $\alpha_4 = \beta_4 = 8\pi$. For estimating the maximum error provoked by using this technique, we considered the number of subregions from 1 to 60, and the number of points m in every straight line crossing the *middle* of the subregions, from 3 until 60. Once the piecewise conductivity function (3) was approached, we generated a matrix $(k + 1) \times m$ of values, by tracing straight lines located near the top boundary of every subregion, at 99% of the total x_2-length. Finally, we estimate the maximum quadratic error for every value of $k + 1$ and m according to the expression $e = \sqrt{\left(\sigma\left(x_1, x_2\right) - \sigma_{pol}\left(x_1, x_2\right)\right)^2}$. The smallest maximum error was found when considering 60 subregions and 60 points for interpolation at each subregion, being of this error of 0.132%.
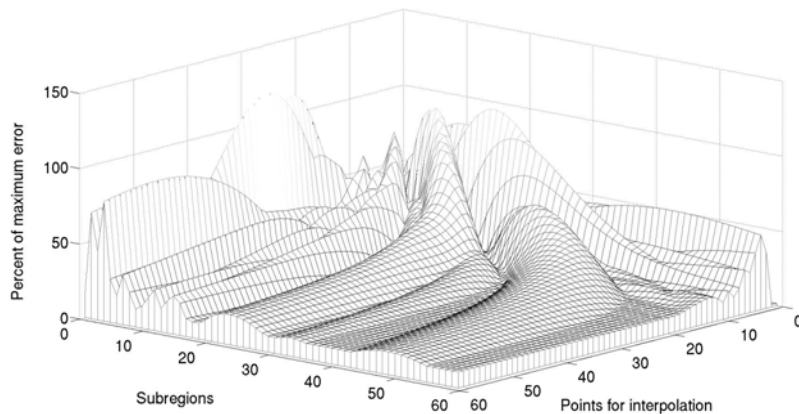
References

[1] K. Astala, L. Païvarïnta (2006), Calderon's *inverse conductivity problem in plane*, Annals of Mathematics No. 163, 265-299..

[2] L. Bers (1953), *Theory of Pseudo-Analytic Functions,* Institute of Mathematics and Mechanics, New York University, New York.

[3] A. P. Calderon (1980), *On an inverse boundary value problem*, Seminar on Numerical Analysis and its Applications to Continuum Physics, Sociedade Brasileira de Matematica, pp. 65-73.

[4] R. Castillo P., V. V. Kravchenko, R. Resendiz V. (2011), *Solution of boundary and eigenvalue problems for second-order elliptic operators in the plane using pseudoanalytic formal powers*, Mathematical Methods in the Applied Sciences, Vol. 34, Issue 4, pp. 445-468.

[5] V. V. Kravchenko (2009), *Applied Pseudoanalytic Function Theory*, Series: Frontiers in Mathematics, ISBN: 978-3-0346-0003-3.

[6] V. V. Kravchenko, H. Oviedo (2007), *On explicitly solvable Vekua equations and explicit solution of the stationary Schrödinger equation and of the equation* $\operatorname{div}(\sigma \nabla u) = 0$, Complex Variables and Elliptic Equations, Vol. 52, No. 5, pp. 353-366.

[7] M. P. Ramirez T. (2010), *On the electrical current distributions for the generalized Ohm's Law*, Submitted for publication to Applied Mathematics and Computation, Elsevier, available in electronic format at http://www.arxiv.com

[8] M. P. Ramirez T., V. D. Sanchez N., O. Rodriguez T. and A. Gutierrez S., (2009) *On the General Solution for the Two-Dimensional Electrical Impedance Equation in Terms of Taylor Series in Formal Powers,* IAENG International Journal of Applied Mathematics, 39:4.

[9] I. N. Vekua (1962), *Generalized Analytic Functions,* International Series of Monographs on Pure and Applied Mathematics, Pergamon Press.

Standardised Phantom for Electrical Impedance Tomography: A Proposal

B Tunstall and N Huber

Biomedical Engineering Research Group, Department of Engineering and Design, University of Sussex, Brighton BN1 9QT UK

Email: b.tunstall@sussex.ac.uk

Abstract: An on-going issue within Electrical Impedance Tomography is the lack of standardised test conditions that permit the comparison of system performance. This is due in part to the wide range of system designs and electrode configurations. This paper describes a phantom and nomenclature that will allow this comparison without compromising device specific information such as electrode arrangement. The phantom, potentially suitable for bi-modal imaging systems, is described showing its features and adaptability. Additionally a nomenclature for describing the phantom set-up and hence system performance is provided with examples including how spatial resolution can be communicated. This quantitative method for system performance verification and communication is offered to the research community for the comparison of systems as part of a standardised framework.

1. Introduction

It is accepted within the Electrical Impedance Tomography (EIT) research community that there is a lack of standardisation with respect to both test conditions and data exchange formats. An as example of this lack of standardisation, whilst Ultrasound has the Cardiff Test System [1], there is no equivalent, standard, phantom for EIT. This is due in part to the differences in the design and implementations of devices. Such differences include, for example, the use of planar [2] or ring-like [3] electrode arrangements. Additionally bi-modal imaging systems, such as that developed by Anderson *et al* [4], may incorporate impedance imaging due to its low-cost and non-invasive nature. This potential for bi-modality presents additional challenges to the creation of a widely accepted phantom.

This paper proposes a design for a standardised phantom that can be used to answer a number of performance related questions including:

- Spatial resolution
- Smallest detectable impedance contrast

2. Design

The proposed phantom consists of a square plane (P) and a number of interchangeable features held within a user-selected mass. The mass can be frequency independent, e.g. saline or agar, or frequency dependant, e.g. agar with additives [5]. This permits the phantom to be re-configurable to any number of specific user requirements.

The plane P has an edge length (L) that is not less than the largest dimension of a planar electrode array or electrode ring diameter, as shown in figure 1. The length L is the basis of the design allowing for the scaling of the phantom to a wide range of device sizes.

A number of holes and slots are made in P, as shown in figure 2, to allow the placement of features within any imaged region.
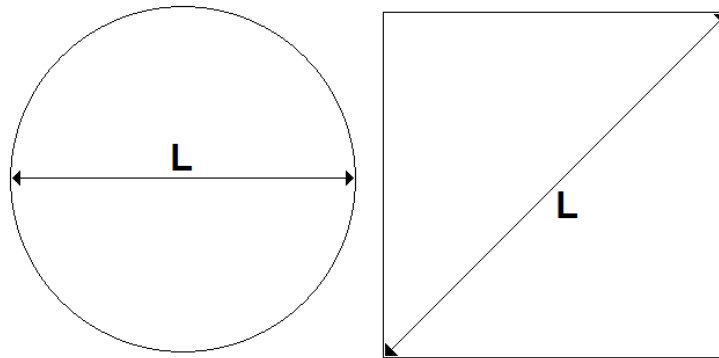
Figure 1: Definition of the distance L for ring-like and square planar electrode arrangements
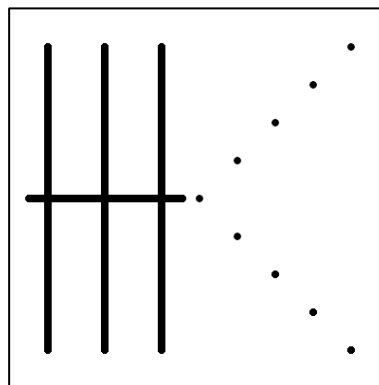

Figure 2: Layout of the plane P

The holes within P are designated and located according to the below table. The notional axes used to identify the locations are illustrated in figure 3.

Table 1: Designation and locations of holes within the plane P

Designation	Location	Designation	Location
A	0, 0	F	20, 20
B	20, -20	G	40, 40
C	40, -40	H	60, 60
D	60, -60	I	80, 80
E	80, -80		
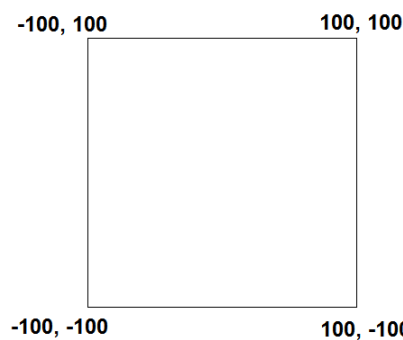
Figure 3: Designation of locations of the corners of the square plane P

In addition to these holes a number of slots are provided permitting the near infinite variation in feature locations. These slots, as seen in figure 2, allow for the determination of

resolution at both the centre and periphery of an imaged region. The designations and positions of these slots, utilising the notional axes given in figure 3, are tabulated below.

Table 2: Designation and end points of slots within the plane P

Designation	Start location	End location
1	-80, -80	-80, 80
2	-50, -80	-50, 80
3	-20, -80	-20, 80
4	-90, 0	-10, 0

The proposed sizes of the holes are given below with the threads being those of metric screws according to ISO 261. It is suggested that the slots be sized to allow for close fitting of the threads used for a given L. The preceding locations provide the centre of each hole / rounded slot end.

Table 3: Hole thread sizes for different lengths L

$\dfrac{L}{20}$ (mm)	Hole Size	$\dfrac{L}{20}$ (mm)	Hole Size
3-5	M1	18-25	M8
5-7	M2	25-30	M10
7-10	M3	30-40	M12
10-12	M4	40-55	M16
12-15	M5	55-75	M24
15-18	M6	>75	M30

The phantom design therefore permits the placement of both fixed and movable features within an imaged volume. This provides a flexible design suited to a wide-range of applications.

3. Nomenclature

Due to the flexibility of the phantom design described above it is necessary to similarly define a nomenclature to un-ambiguously provide the location, conductivity etc. of the features that have been used in every configuration. The proposed system for achieving this is given by:

<Hole | Slot> : <Designation> : [Position] : <Cross-section> : <Conductivity> : <Mass Conductivity> : <Off-plane distance>

Where:

<…>	indicates a compulsory field
[…]	indicates an optional field
|	indicates an alternative
:	is used as a separator

The designation is that given above, i.e. A-I or 1-4. Where a slot is used, e.g. 1, the location of that feature according to the plane is required. As the slots are parallel to the edges of the plane P only one position measure is required. The cross-sectional area of the feature is necessary to ensure transparency, as are the conductivities of both the feature and the

background mass. To permit the quantification of detection off-plane it is also necessary to indicate this distance.

4. Examples of Use

Let us assume that a system can detect a 5mm diameter 0.5mS/cm object within a mass of 0.7mS/cm at an off-plane distance of 10mm in the centre of the phantom, i.e. feature A. This could be simply and effectively communicated as:

Hole : A : 5mm : 0.5mS/cm : 0.7mS/cm : 10mm

Whilst a system capable of resolving two 5mm diameter objects when separated by 10% of the distance L near the centre of the imaged plane may be described as:

Hole : A : 5mm : 0.5mS/cm : 0.7mS/cm : 0
Slot : 4 : 5mm : -20 : 0.5mS/cm : 0.7mS/cm : 0

As can be seen the proposed nomenclature provides the reader with a description of the devices performance whilst obscuring any proprietary information related to its design and/or configuration.

5. Conclusions

This paper has described a generic phantom that can be used to determine the spatial resolution and impedance contrast sensitivity of any EIT system. By the use of a plane and inter-changeable features, with given designations, the phantom can be tailored to each specific application whilst providing a standardised method for the exchange of performance related information.

Through the proposed framework it will be possible to quantitatively compare EIT devices produced by different research groups and commercial organisations. Further the phantom has the potential to be used for bi-modal systems through the selection of appropriate background mass material, one that is potentially suited to a bi-modal system incorporating Ultrasound has been indicated.

It is therefore proposed that the phantom design and nomenclature described herein is adopted for the verification and communication of device performance as part of the current drive towards standardisation within EIT.

6. References

[1] K McCarty and D J Locke 1986 Test objects for the assessment of the performance of Dopplershift flowmeters *Physics in Medical Ultrasound* ed. J A Evans, Institute of Physical Sciences in Medicine Report no 47 (York: IPSM), 94-106

[2] V Cherepenin, A Karpov, A Korjenevsky *et al.* 2001 A 3D electrical impedance tomography (EIT) system for breast cancer detection *Physiol. Meas.* **22** (1), 9-18

[3] A J Wilson, P Milnes, A R Waterworth *et al.* 2001 Mk3.5: a modular, multi-frequency successor to the Mk3a EIS/EIT system *Physiol. Meas.* **22** (1), 49-54

[4] "Combined electrical impedance and ultrasound scanner", United States Patent Application 2003002809 Filing date: July 26 2002

[5] Tzu-Jen Kao, G J Saulnier, D Isaacson *et al.* 2008 A Versatile High-Permittivity Phantom for EIT *IEEE Transactions on Biomedical Engineering* **55** (11), 2601-2607

Dual scans with Combined Ultrasound and Electrical Impedance Mammography

N Béqo, B Lingham, C Lobstein-Adams, G Sze and W Wang

Biomedical Engineering Group, School of Engineering and Design, University of Sussex, Brighton, BN1 9QT, UK

E-mail: wei.wang@sussex.ac.uk

Abstract. One of the current gold standards in breast cancer detection is Sonography, also known as Ultrasound imaging. Sonography is effective for imaging soft tissues of the body and returns a high-resolution image. Its operation is highly subjective depending on the operator and the images do vary with positioning. At the University of Sussex we have successfully built an automated and repeatable Ultrasound scanner and combined and reconstructed the data in 3D. Ultrasound imaging does have its limitations when it comes to cancer detection and diagnosis. The Sussex EIM (Electrical Impedance Mammography) device is a novel imaging system developed at the University of Sussex for the detection of breast lesions *in-vivo* using quadrature detection of impedance. Combining the high-resolution images of Ultrasound with the parametric data of EIT would give a more precise diagnosis. This paper describes some of the results and 3D images we have achieved with dual modality scans.

1. Introduction

Ultrasound is a high frequency sound, above the human audible threshold, which travels freely through fluid and soft tissues but is reflected when it reaches a change in 'acoustic density'. Sonography, also referred to as Ultrasound imaging, is a widely used medical imaging and diagnostic technique [1]. Ultrasound imaging is non-invasive [2] and is effective in imaging soft body tissue. Subcutaneous body structures such as muscles, tendons, breasts etc. are normally scanned at high frequencies (7-18MHz) [3], which provide high axial and lateral resolution. Internal organs are scanned at lower frequencies (1-6MHz) [3], which results in a lower axial and lateral resolution but greater penetration. Typically the same Ultrasound machine can do both high and low frequency scans by using interchangeable transducers, which are placed directly on, and moved over, the patient by a trained professional. This introduces a subjective factor during a scan, which may have negative implications in the diagnoses. By sweeping the transducer on the patient a 2D image representation of a slice into the body is created. 3D images can be generated by acquiring and collating a series of 2D images. To eliminate operator error and introduce consistency, the 3D scanning process can be mechanized.

At the University of Sussex we have developed a dual modality, automated 3D scanner for breast cancer detection. The system combines electrical impedance measurements, [3] [4] [7] able to provide parametric imaging [7] [8] at a modest resolution, with 3-dimensional ultrasound measurements. This 3-dimensional [8] multi-modality will produce superimposed high-resolution images with tissue property information therefore complementing the two technologies and achieve a more accurate diagnostic result.

2. EIM Mk4 System

The Sussex Mk4 Electrical Impedance Mammography (EIM) system uses a quadrature method for impedance detection. The device uses a fully programmable planar array of electrodes. The control method employed is such that any two electrodes apply current to the

breast whilst any other two, similarly non-invasive, electrodes detect the developed potential difference under the direction of proprietary software. The reconstruction provides element based images based upon a tetrahedral finite element mesh, given in Figure 1, which is fundamentally based upon the location of the electrodes used within the scanner planar array plate. In addition to the geometrically corrected image data provided by the EIM images the data is also provided within the terms of "meta-information". This provides:

Vertices: Defined according to local (x,y,z) co-ordinate system
Elements: Indices into the storage of Vertex data
Local co-ordinates: The vectors (in local x,y,z definition) that describe the visually significant directions UP, LEFT and AWAY
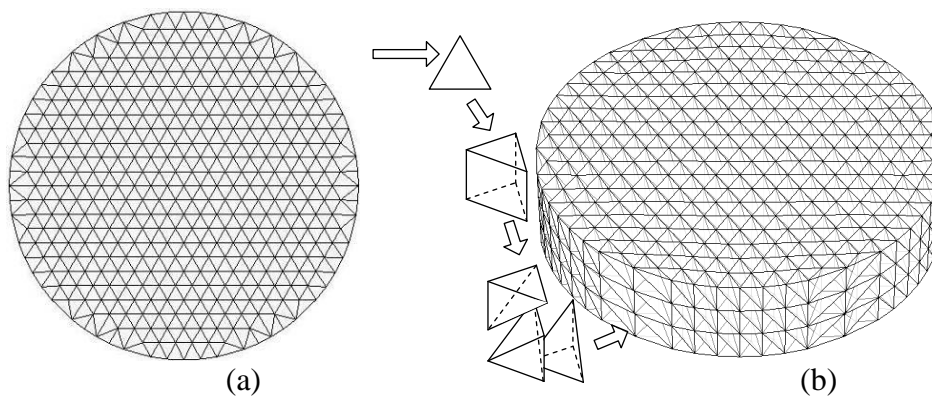
Figure 1. Triangular 2D mesh and multiple layers of tetrahedral elements as a 3D mesh.

3. Ultrasound

2D slices are captured as images via the video-out port available on standard medical ultrasound system in CCIR TV format (25Hz frame rate). The angle subtended by the U/S 'beam' is specific to the transducer used. The 3-dimensionality required by the scanner is provided by the mechanical rotation of the transducer around the circumference of the imaged cylindrical volume with individual images captured at a number of distinct angles.
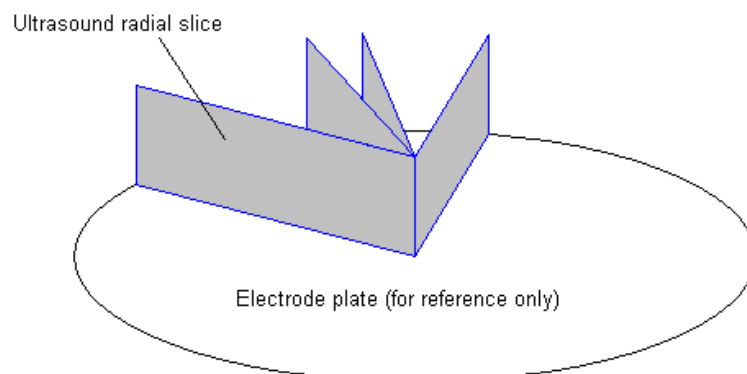
Figure 2: Ultrasound slices through the imaged volume

This image data is supported by a range of meta-information, which includes:
Angle: The angle, locally defined, at which the radial slice was taken

Range: The penetration of the beam at a given slice
Up: The angle, locally defined, of the beam angle towards the volunteers' head
Left: The angle, locally defined, at which the beam is aimed towards the volunteers' right
Away: Indicating the vector of the beam directed away from electrode plate, it is assumed that the electrode plate is perpendicular to the visually significant axis AWAY

4. Ultrasound and EIM Scans

Using the dual modality scanner, 3D reconstruction method for each modality and the image registration based on the meta-information we have produced some images from in-vivo scans of a hand. Furthermore, we have co-registered these two different modality images, resulting in a merged single 3 Dimensional image with good boundary definition and parametric Electrical Impedance information.
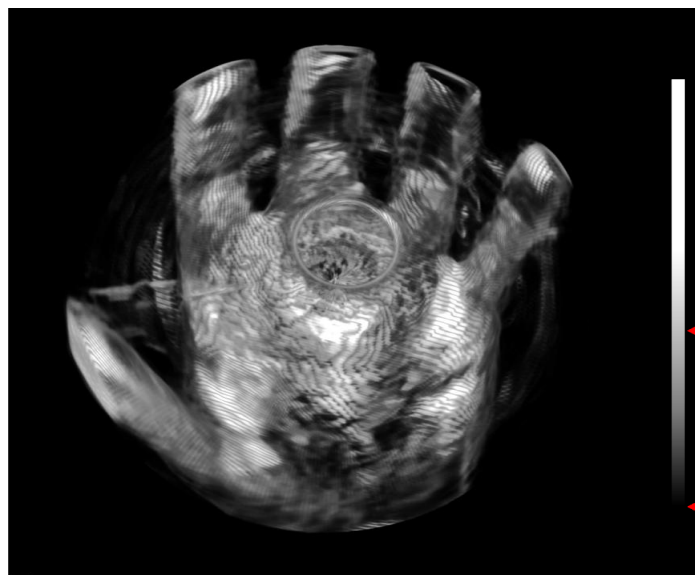
Figure 3: 3D reconstructions of a hand scanned in Ultrasound mode
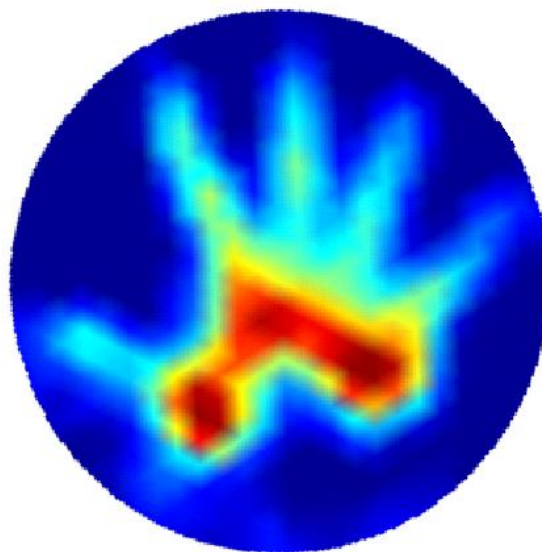
Figure 4: 3D reconstructions of a hand scanned in EIM mode
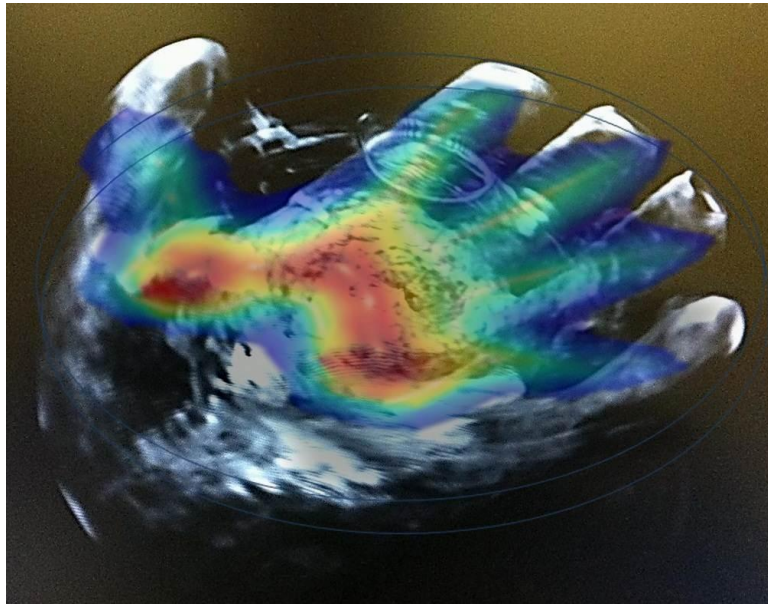
Figure 5: 3D data merger of Ultrasound and EIM scans

5. Conclusion

Based on the scan and the images we have produce we strongly advocate the supplement that the high resolution imaging of Ultrasound provides to Electrical Impedance Tomography. On its own the spatial resolution of EIT is not to the same standard as other medical imaging modalities (e.g. MRI, X-Ray). Ultrasound on the other hand has very good spatial resolution but lacks the ability to identify between tissue types. When combined these two modalities complement each other by providing the boundary information of Ultrasound to the impedance and parametric information of EIT. Further work is being carried out for more accurate and robust geometry correction and image co-registration, the authors are confident of having more results to show in the near future.

6. Acknowledgements

7. References

[1]   Udupa J K and Herman G T 2000 *3D Imaging in Medicine* 2nd edn, (Florence:CRC Press)

[2]   Herman G T 2009 *Fundamentals of computerized tomography: Image reconstruction from projection* 2nd edn (Berlin: Springer)

[3]   Henderson R P and Webster J G 1978 An Impedance Camera for Spatially Specific Measurements of the Thorax *IEEE Trans. Biomed. Eng.* **25**: 250-254

[4]   Barber D C and Brown B H 1984 Applied Potential Tomography (Review Article). *J. Phys. E.: Sci. Instrum.* **17** 723-733

[5]   Wang W, Tang M, McCormick M, Dong X 2001 Preliminary results from an EIT breast imaging simulation system *Physiological Measurement* **22** (1) 39-48

[6]   Yang Jieqiu 2006 *The Investigation and Implementation of Electrical Impedance Mammography Hardware System* PhD Thesis, De Montfort University, UK

[7]   Holder D S 2004 *Electrical Impedance Tomography: Methods, History and Applications,* (London: Institute of Physics) ISBN 0-7503-0952-0

Electrical Impedance assisted Ultrasound guided Focused Ultrasound Surgery: A comprehensive out-patient procedure?

C Lobstein-Adams, N Béqo and W Wang

Biomedical Engineering Group, School of Engineering and Design, University of Sussex, Brighton, BN1 9QT, UK

Email: wei.wang@sussex.ac.uk

Abstract

The Sussex Electrical Impedance Mammography (EIM) device is an imaging system developed at the University of Sussex for the detection of breast lesions *in-vivo* using quadrature detection of impedance. The device uses a fully programmable planar array of electrodes. Proprietary software and algorithms are used to reconstruct 3 dimensional images and extract coordinates of Regions of Interest from a scanned object.

This paper describes the novel integration of Ultrasound-guided Focused Ultrasound Surgery (USgFUS) with the current EIM system. The benefits that a system such as this could provide include the possibility of detection, diagnosis and treatment of breast cancer all within a single device. Furthermore the timescales involved will allow the process to be considered as an out-patient procedure such that a patient can be diagnosed and treated all within the same day using the same device, and in fact without the patient having to physically move. Additionally this has the potential to be performed without the use of anaesthetic, thus reducing the costs involved without compromising the patients' comfort.

1. Introduction

Electrical Impedance Tomography (EIT) entered as a medical imaging technique in the early 80s with the work of Barber and Brown [1] and has subsequently been applied to a variety of monitoring and diagnostic situations [2]. At the University of Sussex we have been investigating the use of EIT as a breast cancer imaging and diagnostic tool. With the current system, the Sussex EIM Mk4, we have achieved a high specification, flexible, software-configurable device that creates 3 Dimensional images and is adequate to be used for *in-vivo* testing and clinical trials.

The use of diagnostic ultrasound as a medical imaging device has been well established, and is a common procedure used in hospitals worldwide. High Intensity Focused Ultrasound (HIFU) utilises a similar technology, but with significantly higher power. In addition, the ultrasonic waves are focused in a small volume (in the order of millimetres). This allows the non-destructive propagation of acoustic waves through the tissue overlying the targeted volume. However, at the focal point (i.e. the cancerous region) these waves constructively superimpose, resulting in a very high local acoustic intensity, sufficient to ablate tissue by coagulative necrosis at the cellular level.

2. HIFU & FUS: The trackless scalpel

The HIFU procedure operates using the fact that when an acoustic wave travels through tissue a portion of the energy of the wave is absorbed and converted to heat. Using

focused beams this effect can be exploited deep within tissues, using a very small focus point to localize heating such that surrounding tissues are unaffected [3]. This occurs due to the energy in the individual waves being of small enough magnitude to not adversely affect the overlying tissue. When focused correctly, however, the areas of high pressure are superimposed at the focal point, thus the acoustic intensity and subsequent energy deposition is much higher in the focal region than in the surrounding tissue. The focus is adequately defined such that a target tissue volume (such as a cancerous tumour) can be rapidly heated and subsequently necrosed (given 1-2s at a temperature of 56°C or an equivalent dose [4]) without any permanent damage to the surrounding cells. By focusing consecutively at more than one location, or indeed scanning the beam, a whole portion of tissue can be ablated.

This technology is not new, and in fact has applications spanning back to investigations into the use of HIFU for non-invasive tissue ablation as early as the 1940s. Furthermore in the 1950s and 1960s Francis and William Fry, amongst others, performed work that led to treatments of neurological disorders using the combination of ultrasound and a high precision milling machine to accurately destroy tumours of the brain [5]. This type of clinical trial however has until recently been difficult to perform due to the problems and complexity associated with the targeting of the ultrasound beams. As both ultrasound technology and general medical imaging have advanced the use of HIFU for the treatment of tumours has once again become an area of interest, into which much research is being performed.

Currently, HIFU-based surgical treatment devices exist and a number have even gained FDA approved. These devices include the Sonablate 500 produced by Focus Surgery (Indianapolis, US) which has received the CE mark for prostate treatment in Europe and similar approval for use in Japan [6]. The Sonablate 500 uses ultrasound for both guidance and treatment, the combination of which can be referred to as Ultrasound-guided Focused Ultrasound Surgery (USgFUS). In contrast the company Insightec have developed the Exablate 2000 device that offers Magnetic Resonance guided Focused Ultrasound Surgery (MRgFUS) with treatment centres located worldwide [7]. These are just two of the many devices that have been developed in recent years, and this is an area that will no doubt be flooded with new devices as advances in the relevant technologies are made.

3. HIFU: Integration with EIM

One of our current research focuses at the University of Sussex (UK) is centred on the use of Electrical Impedance Mammography as a methodology for the detection and diagnosis of breast cancer. This research has culminated in the development of a device capable of performing *in-vivo* breast scans, reconstruct 3D images and extract coordinates (X,Y,Z) and Impedance Data Values from selected Region of Interests (ROI).
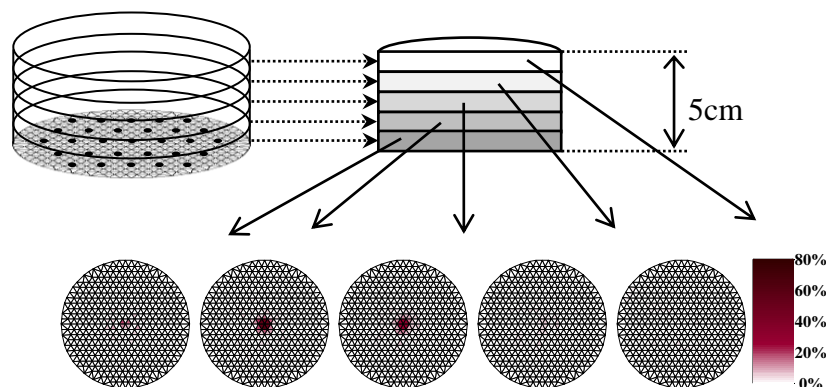

Figure 1: 3D reconstruction of layers with the Sussex EIM Mk4 with a ROI

Building on this research the possibility exists to incorporate to the EIM system a HIFU device, that would use the extracted coordinates $(X_1Y_1Z_1)$ to allow guidance of surgery for accurate ablation of cancerous tumours (see Figure 2). If the High Intensity Ultrasound already incorporates an Ultrasound Imaging module as in USgFUS, the diagnostic ultrasound device could be employed to scan again around the EIM defined Region of Interest. Using a method such as this would potentially allow a second three-dimensional image to be reconstructed from the ultrasound scan data, thus increasing the accuracy to interpret the geometry of the malignancy and the coordinates for the HIFU. Given suitably accurate image recognition software this could very well become a semi or even fully automated procedure, using a single device without the need for patient repositioning. Figure 2 (below) shows the stages of extracting a Region of Interest and its coordinates from a 3D EIM volume.
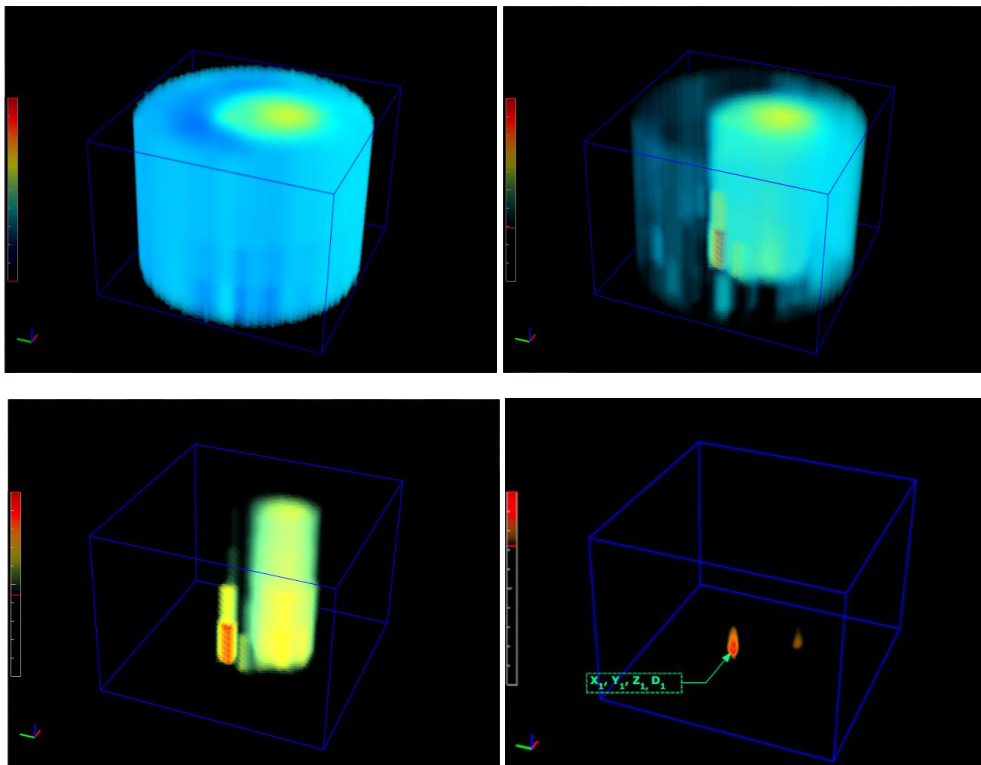

Figure 2: ROI information extraction from 3D layers in the Sussex EIM Mk4

One possible configuration to incorporate a HIFU device into the existing system would be to use a planar transducer in conjunction with a suitable acoustic lens [8] as shown in Figure 3. This would allow a number of lenses to be used with the same, planar HIFU device, thus allowing flexibility in focal depth, and therefore in the tissue that could feasibly be targeted.
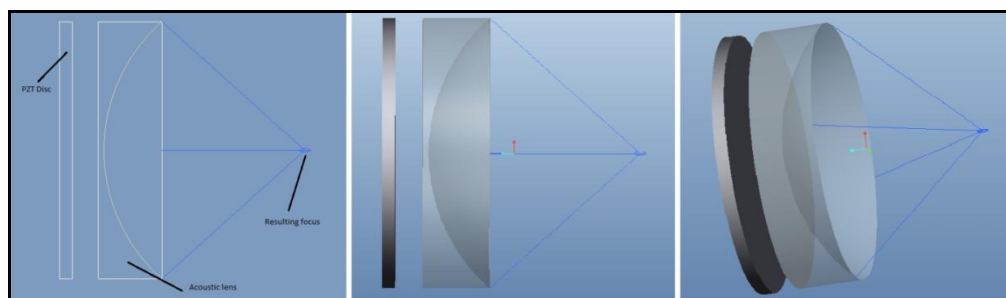
Figure 3: A planar HIFU transducer in combination with an acoustic lens

To this end a number of simulations have been carried out to determine suitable parameters for a device capable of non-invasive localised surgery. Examples of the results of such simulations are presented graphically in Figure 4.
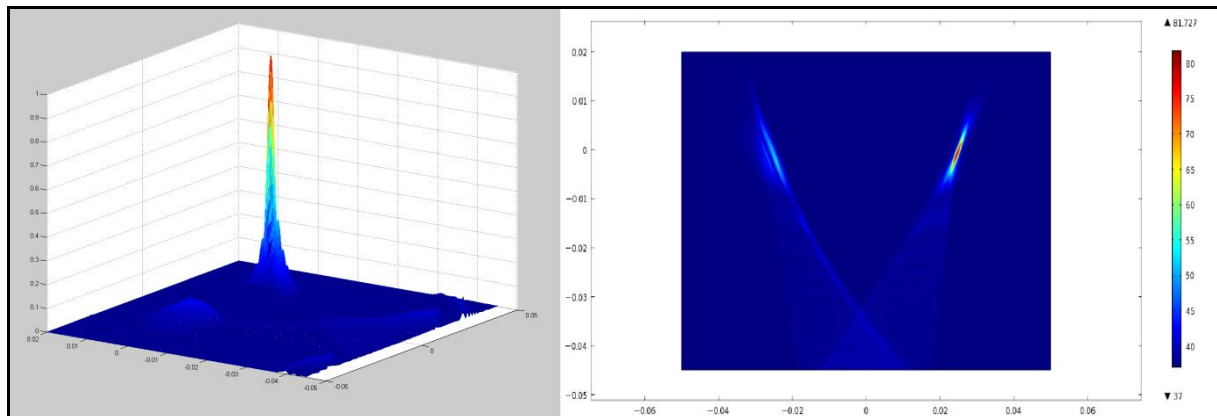
Figure 4: Example of the normalised acoustic intensity field (left) and resulting temperature rise (°C) in tissue (right) from a possible HIFU-EIM device configuration

4. Conclusion

This article has briefly outlined the plausibility of a combining HIFU as a treatment methodology with EIM for detection and diagnosis of breast cancer. Further work is currently being undertaken to develop this into a viable medical procedure. If this work is successful, the possibility of reaching a stage where breast cancer, at least in the early stages, could be detected, diagnosed and treated all within the timescale of an out-patient procedure, may become a reality. The potential therefore exists to improve the quality of life for a significant portion of the population, and to make this improvement with minimum pain or discomfort for those treated. In addition, with relevant adaptations this process could be modified to treat a larger range of cancers than that of just the breast. The potential of such research and method should not be undervalued, and the authors are confident for the future of combined detection, diagnosis and treatment of cancers using the techniques outlined in this paper.

5. References

1. Barber D C and Brown B H 1984 Applied Potential Tomography (Review Article). *J. Phys. E. : Sci. Instrum.* **17** 723-733
2. Holder D S 2004 *Electrical Impedance Tomography: Methods, History and Applications* (London: Institute of Physics) ISBN 0-7503-0952-0
3. Wu Junru Nyborg W L-M 2006 Emerging Therapeutic Ultrasound *University of Vermont, USA*
4. Haar G-t Acoustic Surgery 2001 *Physics Today* Volume 54, Issue 12, 2001
5. Wu F Wang Z B Cao Y D Zhu X Q Zhu H Chen W Z Zou J Z 2007 Wide local ablation of localised breast cancer using high intensity focused ultrasound *J Surg Oncol. 2007* Aug 1;96(2):130-6
6. Seip R Carlson R F Chen W Sanghvi N T Peenna M A Dines K A Pfile R Gardner T A Koch M Automated HIFU Treatment Planning and Execustion based on 3D Modeling of the Prostate, Urethra and Rectal Wall 2004 *Ultrasonics Symposium 2004* Volume 3 1781-1784
7. Jolesz F A MRI-Guided Focused Ultrasound Surgery 2009 *Annual Review of Medicine* Volume 60: 417-430
8. Cervera et al 2002 *Physical Review Letters* January 2002

Fast method for artefact detection and breast boundary definition

N Béqo, N Huber, R Bilal, W Zhang, G Qiao, and Wei Wang

Biomedical Engineering Group, School of Engineering and Design, University of Sussex, Brighton, BN1 9QT, UK

E-mail: wei.wang@sussex.ac.uk

Abstract. The Sussex Electrical Impedance Mammography (EIM) device is an imaging system developed at the University of Sussex for the detection of breast lesions *in-vivo* using quadrature detection of impedance. The device uses a fully programmable planar array of electrodes, utilising the 4-electrode method for tissue excitation and impedance measurement. In this paper we present a technique for fast and accurate detection of electrode-contact artefacts, and also of breast localisation on the electrode array, that has specific application in the Sussex EIM device, but can also be applied to any planar array-based system.

1. Introduction

Early breast cancer detection has been directly linked to a steady decrease in death rates from the disease for the past two decades [1]. Electrical Impedance Mammography (EIM), which images the internal impedance (or conductivity) distribution of objects from the developed voltages measured on the surface of the object, has been identified as a potential, radiation free, screening technique, as cancerous tissue is more conductive than healthy tissue [2].

The effects of the patient-electrode interface have been covered extensively in literature, as they have been shown to affect adversely the accuracy and repeatability of the image reconstruction algorithms, especially ones based on absolute imaging [4-7]. To circumvent the inherent variability of the contact impedance, the Sussex EIM system employs a 'wet' electrode system [8], which allows indirect contact between the skin and electrodes, via liquid contact medium, assisting in the reduction of artefacts and increasing the repeatability of EIM measurements. However, it was shown that this method requires very careful design to avoid unexpected artefacts due to patient positioning, such as suction vacuums, bubbles or any debris that might have been introduced in the scanner [9].

In this paper, we propose a fast method for the detection of such artefacts, which can be put to use before data capture and/or in-vivo scans, warning the operator of their presence, so that the problem can be rectified and therefore preserving the quality of the data. An extension of this method can also be applied for the better localisation of breast boundaries as it comes in contact with the electrode plate.

2. Sussex EIM Mk4

The Sussex 3D EIM Mk4 system has been designed to measure *in-vivo* impedance of breast, and to satisfy clinical operation requirements. Safety, capability in cancer detection, repeatability and durability are the main concerns.

- A circular saline tank (figure 1) with variable depth of tank to fit difference cup sizes.
- Saline is kept at body temperature during an examination.
- A planar electrode array fixed at the bottom of the tank to avoid errors caused by the geometry distortion of the electrode position.
- Electrodes are recessed into the plane to avoid contact impedance changes

During an examination, the body is laying in prone position with one side of the breasts dipping into the saline tank. The electrode plane is then raised to a position that pressed against the breast and flattened it. To satisfy our clinical requirement, a safe AC current is not exceeding 1mA for signal ranged from 10 kHz to 10 MHz.


Figure 1: Saline measurement tank embedded in the examination table.

Electrodes are arranged in a hexagonal pattern and are positioned in equal distances from each other. Around 1500 combinations have been identified as crucial and are used as measurement frames. The switching of electrodes for each frame is driven by a multiplexing device. Even though the frame number has been reduced substantially, a standard acquisition can take from 30 seconds to 5 minutes depending on the frequency range selected.

3. Artefact detection

Through the principle of reciprocity, bubbles, objects or skin contact can be mapped on individual electrodes by looking at the signal response generated at normal measurements, and when the drive-receive pairs have been swapped.

Below are three different types of combination patterns that can scan the plate quickly and identify affected pins. To increase resolution, scans can be done at +/- 120 degree angles in the same sweep method (see orange lines) and then the acquired signals can be merged.
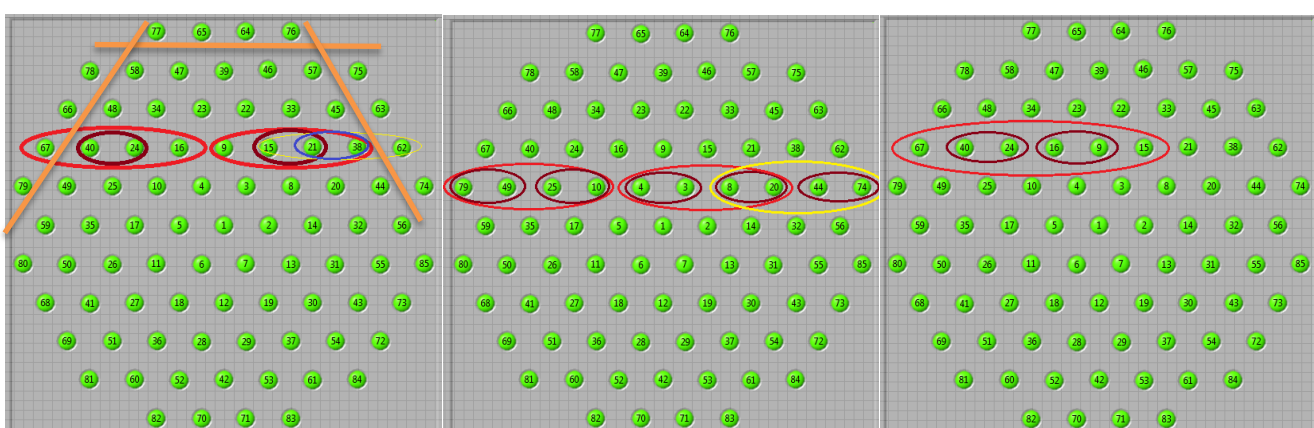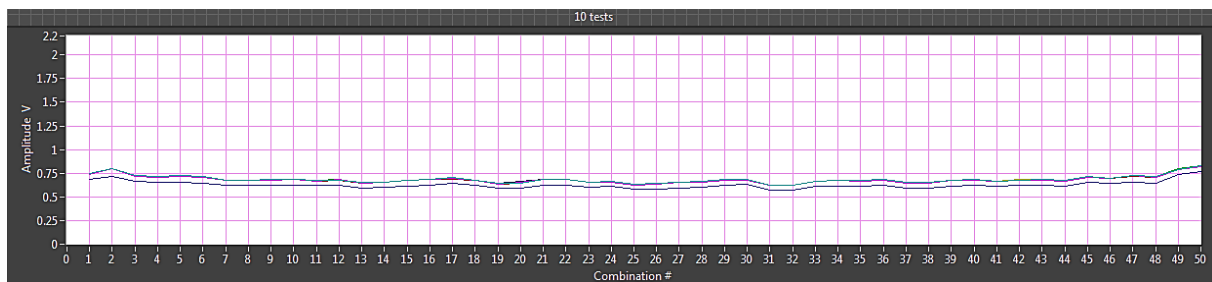

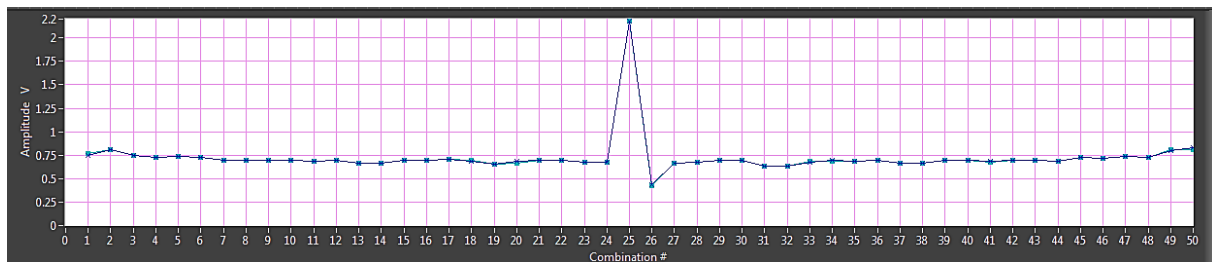**Figure 2: Electrode plate and combination patterns a), b), c)**

A flat response is expected if only saline is present in the system.

To test this hypothesis, an air bubble was artificially introduced on top of Pin1. The acquisition was done at low frequencies. Distortion can be seen on combination 25 (positive)

and 26 (negative).

**Figure 3: Flat Response in Saline**

Figure 4: Object identified on Pin1

The magnitude of the signal can be used to identify how covered the pin is (how big is the bubble) and/or map if/where the breast is laying/touching.

3. Breast Boundary Definition

In the Sussex Mk4, the scanner head plate moves up-down to accommodate different cup sizes by slightly compressing the breast and holding it steady. One of the clinical challenges here is to make sure that the plate and the breast have made good contact and there is not too much or not enough contact, also that there is no fold in the breast. A standard acquisition followed by image reconstruction can take a couple of minutes; therefore there is no fast indicative method to notify the operator that the breast is not positioned correctly before the scan.
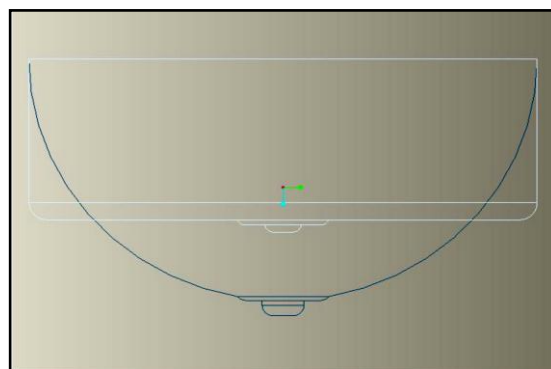
Figure 5: Comparison of breast models, normal (blue) & compressed (white)

By using the fast electrode combination above, the 1500 combinations have been reduced to 50, where all the pins alternate into Drives and Receives using the same distance in every combination. The scan is done at low frequencies.

Because there is no reconstruction involved the mapping is instant. See below a mapping example. A party balloon was filled with water and was placed inside the scanner full of

saline. The software Acquire-Map was in continuous mode, at a mapping speed of 4 seconds. The balloon was moved around the scanner to see that the map signature corresponded to the new position.

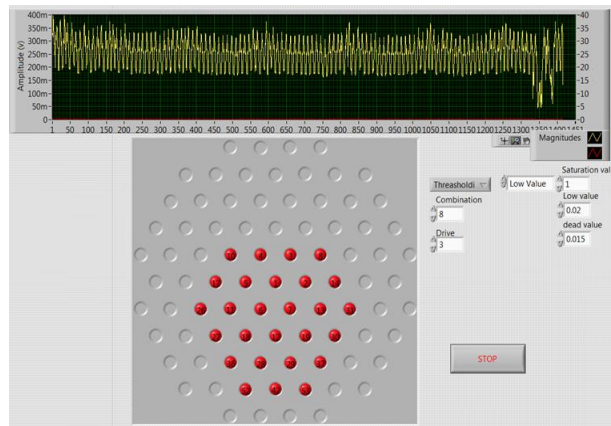Figure 6: Water filled balloon in the scanner   Figure 7: Balloon map with fast acquisition

4. Conclusion

The electrode combination patterns and the sweep method of acquisition described in this paper can be a good and fast solution to identify any artefact or foreign objects on the pins. The scan is only a couple of seconds and provides 'live' feedback from on the electrode map. Taking into consideration the amount of minutes it takes for a full acquisition and reconstruction, this dynamic scan method can help in patient positioning and reduce nipple folds that could inherently compromise the raw acquired data and the reconstruction that follows.

5. References

[1] American Cancer Society 2009 *Breast cancer facts & figures* 2009-2010

[2] Holder D S 2005 *Electrical Impedance Tomography: methods, history and applications* (London: Institute of Physics Publishing)

[3] Tunstall B, Wang W, McCormick M, Walker R and Rew D A 1997 *The Breast* 6 (4) 253

[4] Hua P, Woo E J, Webster J G, Tompkins W J 1993 *IEEE Trans. Biomedical Engineering* 40 (4) 335-343

[5] Boone K G and Holder D S 1996 *Med. and Biol. Eng. and Comput.* 34 (5) 351-354

[6] Kolehmainen V, Vaukhonen M, Karjalainen P A and Kaipio J P 1997 *Physiol. Meas.* 18 289-303

[7] Nissinen A, Heikkinen L M, Kolehmainen V and Kaipio J P 2009 *Meas. Sci. Technol.* 20 (10) 13 pages

[8] Wang W *et al* 2007 *IFMBE Proceedings, ICEBI 2007* 17 (10) 336-339

[9] Huber N *et al* 2010 *J. Phys.: Conf. Ser.* 224 (1)

Preliminary study of the sensitivity of the Sussex Mk4 Electrical Impedance Mammography planar electrode system

G Sze[1], W Wang[1], D C Barber[2] and N Huber[1]
[1]Biomedical Engineering, School of Engineering and Design, University of Sussex, East Sussex, BN1 9QT, UK
[2]Directorate of Medical Imaging & Medical Physics, Royal Hallamshire Hospital, Sheffield Teaching Hospitals, Sheffield, UK

E-mail: wei.wang@sussex.ac.uk

Abstract. The Sussex electrical impedance mammography (EIM) Mk4 system has been developed for the detection of breast cancers *in-vivo*. The system has been designed using a planar electrode array to satisfy clinical applications where it is more appropriate. This paper presents investigation of sensitivity of its planner electrode system for identifying an object.

1. Introduction

Electrical Impedance Tomography (EIT) has been researched for clinical use [1] due to its advantages of low cost, non-invasive nature and the ability to characterise human tissue types through their measured electrical properties. This characterising ability is an exclusive feature among all other screening technologies such as ultrasound, MRI and CT. However, EIT is challenging for clinical use since the image reconstruction is very sensitive to errors introduced from data collection. Since the effect of noise is higher for frames measured in weaker sensitivity areas, along with inaccurate electrode positioning and boundary shape problems, reproducibility becomes challenging, amplified by the use of inverse problem solutions for imaging. To improve on these critical problems, great effort has been made to customise its electrode interface system to be able to measure different parts of the breast effectively in clinical uses.

This paper presents an investigation based on the Sussex electrode impedance mammography (EIM) system, a planar electrode array design that overcomes the weak sensitivity problem in the central area experienced by traditional ring electrode designs, and sensitivity is now mainly depended upon distance from the electrode array. As the target is to identify abnormal tumours within mixed tissues, a system with high stability and repeatability is required.

2. System design

A saline-filled tank is used to perform breast impedance measurements, as follows:

- A circular saline tank (figure 1) with variable depth of tank to fit difference cup sizes.
- Saline is kept at body temperature during an examination.

- A planar electrode array is fixed at the bottom of the tank to avoid errors caused by the geometry distortion of the electrode position.
- Electrodes are recessed into the plane to avoid contact impedance changes.

2.1. Data acquisition method
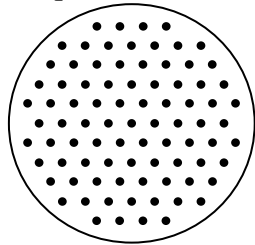
Figure 2. 85 electrodes in hexagonal arrangement.
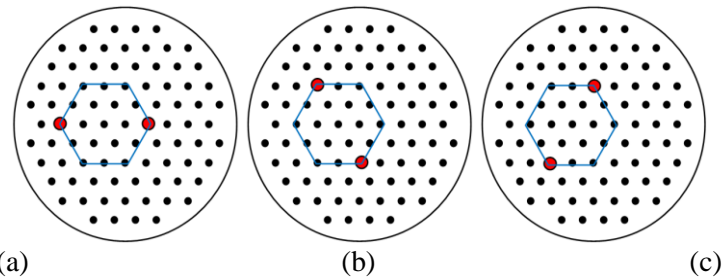
Figure 3. Three rotations of drive electrodes (in red) for a local region (blue hexagon).

A total of 85 electrodes are arranged in a hexagonal shape (figure 2) positioned equidistantly (17mm). The four electrode measurement method is used, and there is a total of 1416 frames of measurement. There are 123 different patterns of current injection, each drive gathering a maximum of 12 voltage measurements. The switching of the electrodes for each frame is driven by a multiplexing arrangement.

The hexagonal structure of the electrode positioning is designed for enhancing the accuracy in detecting multi-directional conductivity distributions of different breast tissues. A local region is defined for each pair of current injecting electrodes (figure 3). For each region, three sets of drive patterns are possible by rotating the original measurement 60° and 120° degrees. This gives essential information in reconstructing 3D conductivity images.

Multiple local measuring regions cover the entire 2D plane. Regions close to the boundary are scanned at a modified pattern. These incomplete hexagonal shape measurements are important as they can improve the resolution near the circular boundary. Besides, as abnormal tissue may not be located at the central region due to different size of stroma tissue or positional shift of the patient on the examination table, a wider sensitivity is necessary to ensure good spatial resolution throughout the 2D plane.

2.2. Sensitivity
The distance between two driving electrodes is related to the sensitivity at depth. Current penetration increases in depth with a wider distance of the drive electrodes. However the weaker electric field at depth would induce more noise. A shorter distance would produce a stronger electric field, but at the cost of depth information. Adapting to a model of a compressed breast in actual clinical use, the experimental sensitivity of the device has been simulated.

A five layer 3D mesh has been used in five simulated experiments, with the images reconstructed [2]. The thickness of each layer is 1 cm and the total thickness is 5 cm. The model has been set up with an object with size 1.4 cm diameter x 1 cm thick and + 10% conductivity difference from the background saline conductivity, which is at 0.5 mS/cm, located in the centre of the 2D plane (figure 4a position 1). The depth of the object has been set at 5 different depths as listed in table 1, which lists the vertical distance from the 2D plane to the centre of the object. At 2.5 cm depth the object has been placed at 2 different horizontal

positions: midway from the centre to the bounder (position 2), and near the boundary (position 3).
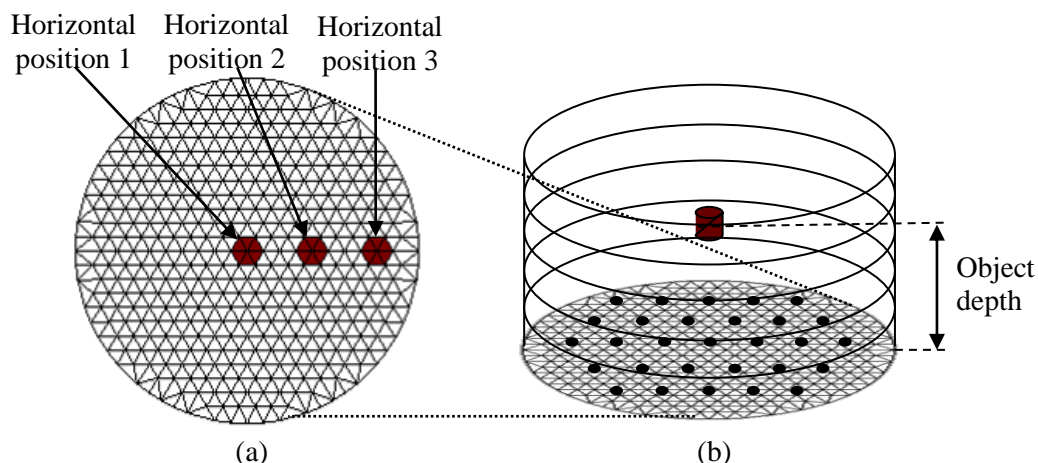
Figure 4. (a) Horizontal position of object in 2cm depth; (b) Perpendicular distance of the object (object depth) from the electrode plane.

The percentage of changes in peak conductivity, full width half maximum (FWHM), and total signal under the object have been calculated and summarised in table 1.

Table 1. Changes in peak conductivity, FWHM and total signal under object comparing.

Object depth	Horizontal position	Change in peak conductivity	Change in FWHM	Change in total signal under object
0.5 cm	1	79.0%	108.71%	112.71%
1.5 cm	1	61.8%	111.87%	115.68%
2.5 cm	1	32.0%	129.82%	92.95%
3.5 cm	1	19.7%	150.18%	98.26%
4.5 cm	1	15.4%	200.26%	109.10%
2.5 cm	2	25.2%	139.07%	104.88%
2.5 cm	3	19.3%	163.96%	114.13%

The change in peak conductivity is calculated by

$$\text{Change in peak conductivity (\%)} = \frac{\sigma_{peak} - \sigma_{background}}{\sigma_o - \sigma_{background}} \times 100 \qquad (1)$$

Where σ_{peak} is the peak conductivity value found from the reconstructed 3D image, $\sigma_{background}$ is background conductivity in the model, which is 0.5 mS/cm, and σ_o is the original object conductivity which is 0.55 mS/cm. Figure 5 plots the calculated value against depth.
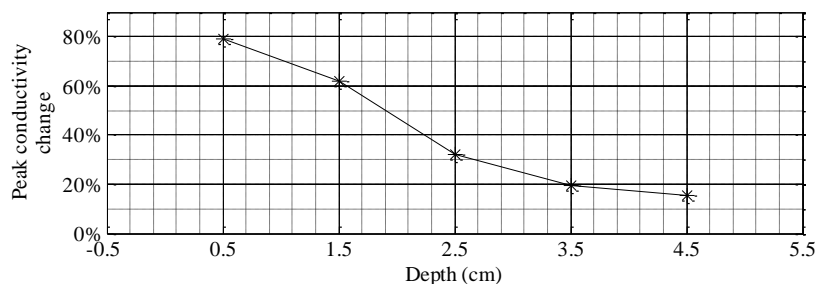
Figure 5. Sensitivity in depth.

The change in FWHM is calculated by searching half maximum value of a fitted curve. From the example plotting in figure 5, the black circular data points are taken from x axis of the reconstructed image where y = 0 (centre of the mesh) and z = the layer that original object is lying on. The black curve is the fitted curve by using the data points. The y-axis value of the black dotted line is calculated by the half maximum value of the fitted curve, which is the FWHM, and the distance between the two dotted red line is the FWHM value. This value is divided by the original object model's FWHM value and then multiplied by 100 to obtain the percentage of changes. Figure 6 shows part of reconstructed conductivity images. From left to right the five layers represent 2D planes in different depths. Layer on the left hand side (layer 1) is attaching to the electrode plane, and each layer at the right hand side is 1cm above its left hand side layer.
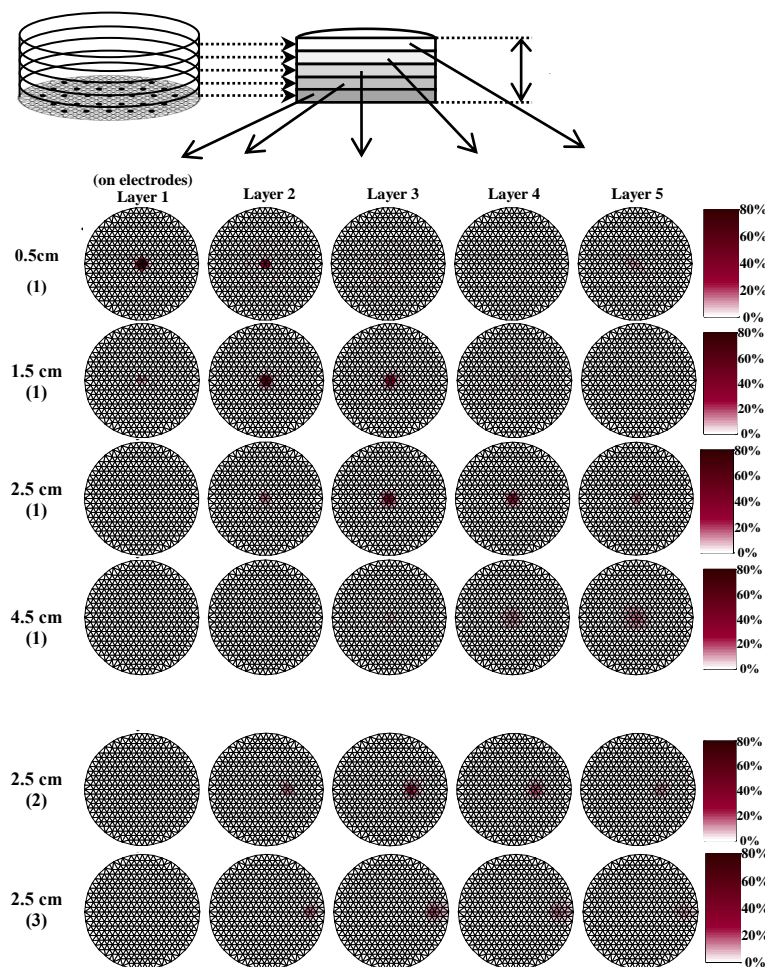
Figure 6. Static images of simulated experiments with object at different depth.

3. Conclusion

From the results shown in table 1 at 4.5 cm depth, the peak conductivity is only 15.4%, although the sensitivity of the object could still be high. The images shown in Fig 6 demonstrate the potential of the planar electrode array developed to be able to detect an abnormality.

4. References

1. Barber D C and Brown B H 1984 Applied Potential Tomography (Review Article). *J. Phys. E. : Sci. Instrum.* **17** 723-733
2. W Wang, M Tang, M McCormick, et al22 (1), 39-48, Feb 2001

Modelling Stainless Steel Electrodes in a Saline Tank System for EIT

Weida Zhang, N Huber, F Zheng, N Beqo and W Wang

Biomedical Engineering Research Group, Department of Engineering and Design,

University of Sussex, Brighton BN1 9QT UK

Abstract -- The effect of metal electrodes used in EIT systems based on saline tanks plays an important role. This paper presents a model of this effect constructed of circuit elements. First, the model is explained, and then the equations representative of the frequency response of the model are presented. Curve fitting is then used to match the model parameters to experimental measurements. The model is shown to preserve the linear relationship between R_{Saline} value and the conductivity of the saline, which is also frequency independent.

I. Introduction

A well-characterized, fully understood interface impedance leads to an optimized electrode-electrolyte interface design. Equivalent circuit models have long been used to model the interface impedance. In 1899 Warburg first proposed that the interface could be represented by a polarization resistance in series with a polarization capacitor. Electrochemical impedance spectroscopy has been used to electrically characterize the interface for various electrode materials and varying electrode sizes [1].

In EIT, the effects caused by the electrodes can be minimised when using differential reconstruction algorithms. But modelling the electrodes is still important for noise analysis [3,4], and E-Phantom design [5]. Also, at higher frequencies, the effect of the inductance and capacitance of the electrodes will come into play, especially in the case of stainless steel electrodes.

II. Theory

There are several different electrical equivalent circuit models for the electrode-electrolyte interface that can be found in the literature. The Warburg circuit equivalent and some modified Warburg models model the interface series resistor and capacitor, as in Figure 1.

The four-wire (or Kelvin) measurement set up [7] overcomes the effect of electrode impedance and lead resistance, but adds complexity to the measurement. Following this, our impedance analyser measurement setup is shown in Figure 2.
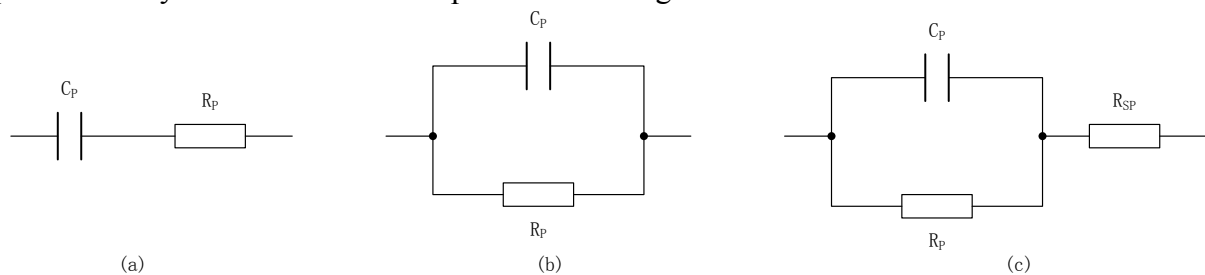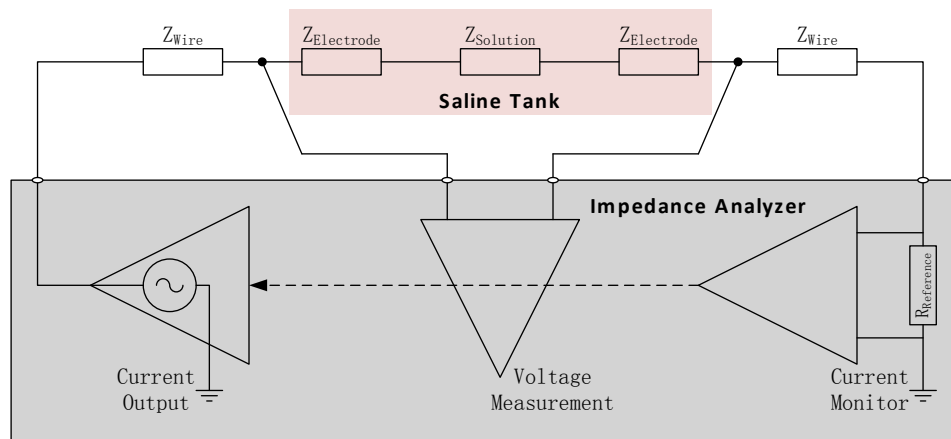

Figure 1: a) Warburg model, b) & c) Modified Warburg models

Figure 2: The four-wire impedance measurement setup.

As the measurements are given in terms of real and imaginary parts, the measurements are able to explain the impedance of the saline tank, or that of the electrodes and solution.

III. Experiment and Result Fitting

Our experiments were performed using a Solatron 1260A impedance analyser, with the measurements taken from 2 electrodes separated by 68mm on a circular tank with 45mm depth saline, with conductivity varying from 0.10~2.0mS/cm. Four of these results are shown in Figure 3 below (real component in blue, imaginary in red). Through the impedance data from the instrument, we use the modified Warburg model to find the parameters of the equivalent circuit elements. As it is difficult to fit the curve at higher frequencies than 1MHz, we are assuming it to be due to the ferromagnetic effect of the stainless steel electrodes, and make appropriate changes to the modified Warburg model, which can produce better fitting curves.

In order to establish the parameters of the circuit elements in the modified Warburg model, we tried to fit the curves using the standard model, but found it difficult to reach the minimum root mean square requirement. To match the curve shape in a more meaningful way, we put an inductor in series with the modified Warburg model (Figure 3). We then performed curve fitting on impedance curves that were obtained experimentally, which are shown in Figure 4 below.
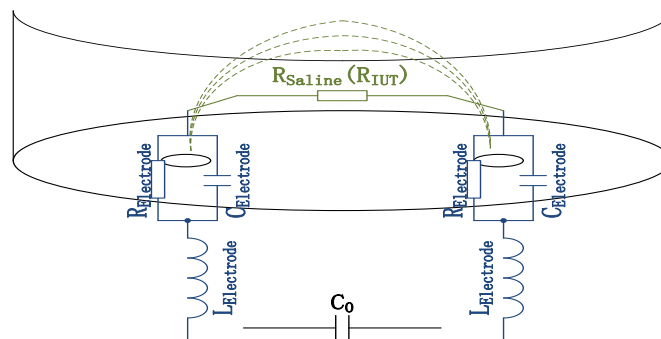
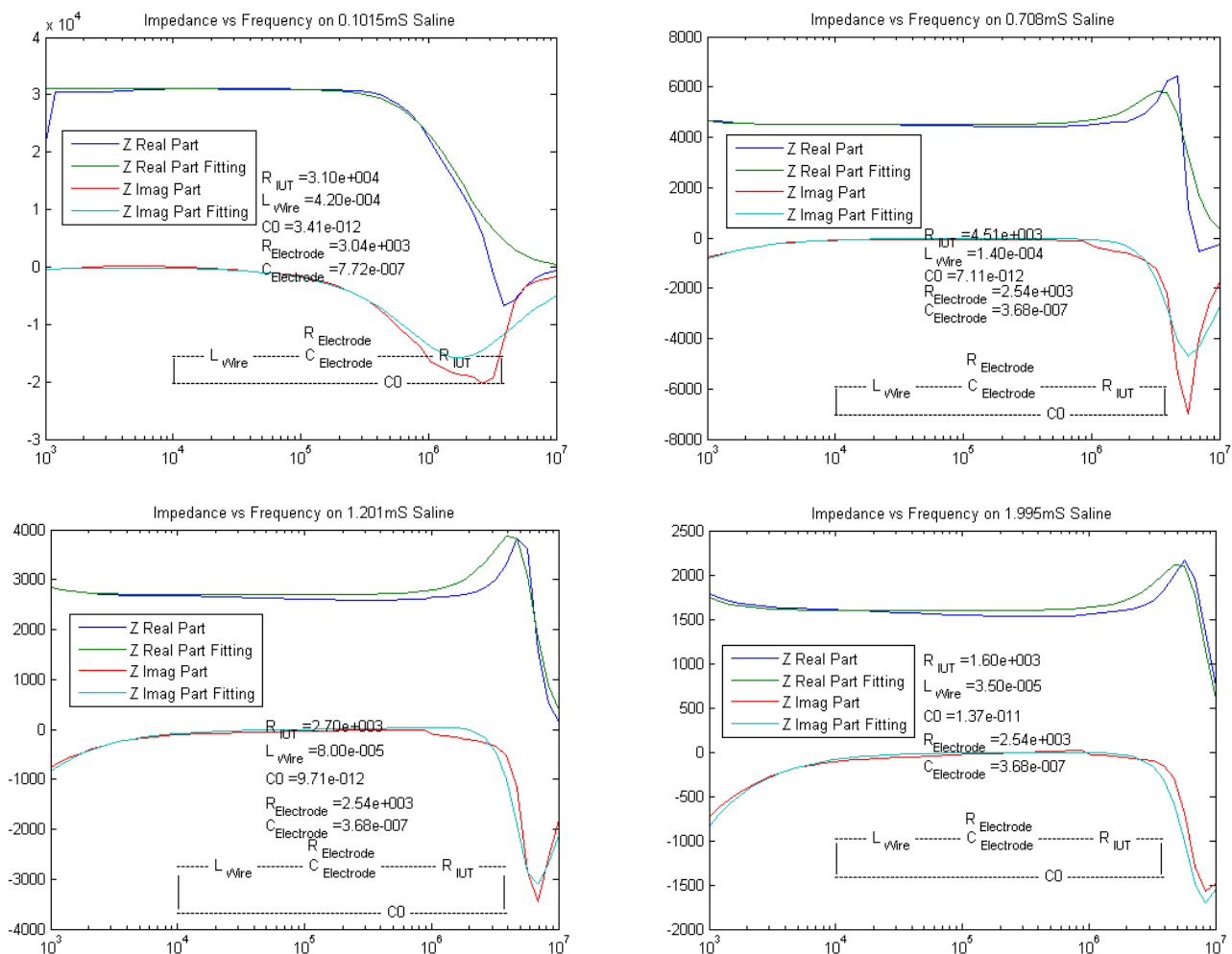**Figure 3: Developed model for stainless steel electrodes**

Figure 4: Developed model for stainless steel electrodes

Using the model shown in Figure 3, the formula of the total measured impedance can be given as follows:

$$ImpedanceModel = \left[2L_{Electrode} + \left(2R_{Electrode} \parallel \frac{C_{Electrode}}{2} \right) + R_{Saline} \right] \parallel C_0$$

$$= \frac{\left(R_{Saline} + \dfrac{2R_{Electrode}}{j\omega C_{Electrode}R_{Electrode} + 1} + 2j\omega L_{Electrode} \right)\dfrac{1}{j\omega C_0}}{R_{Saline} + \dfrac{2R_{Electrode}}{j\omega C_{Electrode}R_{Electrode} + 1} + 2j\omega L_{Electrode} + \dfrac{1}{j\omega C_0}}$$

where $R_{Electrode}$, $C_{Electrode}$ are the same as in the modified Warburg model and R_{Saline} is due to the different conductivity of the solution, $L_{Electrode}$ is the element we added, and C_0 is the distributed capacitance of the measurement.

The following table gives the parameters of the elements of the model from each measurement of different conductivity.

Conductivity	R_{IUT} (Ohm)	R_{Elec}(Ohm)	C_{Elec} (nF)	L_{Elec}(uH)	C_0 (pF)
0.1015	31k	3.04k	772	420	3.41
0.1552	19.5k	3.04k	772	420	4.41
0.1999	14.1k	2.57k	635	373	4.97
0.307	10.3k	2.54k	368	370	5.21
0.403	7.8k	2.54k	368	250	5.21
0.499	6.3k	2.54k	368	220	5.11
0.604	5.25k	2.54k	368	180	6.11
0.708	4.51k	2.54k	368	140	7.11

0.800	4k	2.52k	395	144	7.31
0.901	3.55k	2.54k	368	110	7.71
1.002	3.25k	2.54k	368	90	7.71
1.201	2.7k	2.54k	368	80	9.71
1.407	2.3k	2.54k	368	60	11.7
1.600	2.05k	2.54k	368	50	11.7
1.803	1.8k	2.54k	368	45	13.7
1.995	1.6k	2.54k	368	35	13.7

IV. Conclusion

From the table, it can be seen that the 2nd column shows the impedance of the saline, which should be inversely proportional to the conductivity, from the definition of conductivity.

$$R = \frac{l}{A \times \rho}$$

And it is inverse to the conductivity of the saline in the fitting result as shown in Figure 5 below:
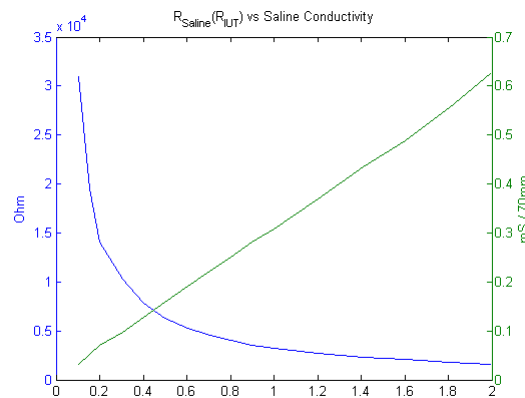
Figure 5: Curve fitting result of R_{Saline}

The parameters of the resistor and capacitor in the modified Warburg model, which are in the 3rd and 4th rows, are not changing with conductivity, due to the shape of the electrodes remaining constant. The 6th row does not vary significantly, and it is representative of the measurement error. The inductor we added to the circuit model we believe is due to the ferromagnetic stainless steel electrodes, playing a role in the electric field much as the core in a transformer would. And because the electric field distribution is dependent on the conductivity, the induction of the electrodes varies with conductivity, needing further study.

References:

[1] Wendy Franks et al, *IEEE TRANSACTIONS ON BIOMEDICAL ENGINEERING,* VOL. 52, NO. 7, JULY 2005

[2]

[3] Neil Joye et al, *IEEE EMBS Conference* pp. 559-562, 2008.

[4] Neil Joye et al, *Annual International Conference of the IEEE EMBS* pp. 3247-3250, 2009.

[5] Herv´e Gagnon et al, *IEEE TRANSACTIONS ON BIOMEDICAL ENGINEERING,* VOL. 57, NO. 9, SEPTEMBER 2010

[6] J. Riistama et al, *IEEE EMBS Annual International Conference,* pp. 6021-6024, 2006.

[7] R. Pallàs-Areny, J.G. Webster, "Sensors and Signal Conditioning,second ed.", *Wiley,* New York, 2001.

[8] John B. Troy et al, *IEEE EMBS Annual International Conference,* pp. 879-881, 2006.

Review of the Research and Development in EIT

Guizhi Xu, Shuai Zhang, Ying Li, Jianjun Zhang, Guoya Dong

The Key Laboratory of Electromagnetic Field and Electrical Apparatus Reliability of Hebei Province,
Hebei University of Technology, Tianjin 300130, China, Email: gzxu@hebut.edu.cn

Abstract — **Electrical impedance tomography (EIT) is a new imaging modality that produces images by computing electrical conductivity within the body. More and more research groups on EIT have emerged in recent years, and made a greater progress in this technique. This paper reviews EIT research in the words, introduces the progress in our group, and gives the future perspectives for biomedical EIT.**

I. INTRODUCTION

EIT is a non-invasive medical imaging technique by which images of the internal impedance distribution of the human body can be reconstructed mathematically from voltage measurements made by electrodes placed on the skin. Technical advances in EIT may allow us to obtain more accurate tissue characterization and image quality, and this will undoubtedly help to advance clinical acceptance.

The underlying relationships, which govern the interaction of electricity and magnetism, are summarized by Maxwell's equations. For the case of EIT, several simplifying assumptions can be applied to reduce the complexity of the problem. The region can therefore be considered as an ionic conductor, and thus the quasi-steady equations of Maxwell can be used.

In EIT, there are three main problems: the forward problem, the inverse problem, and the hardware system.

There are four essential ways to use EIT in the clinical environment:

Imaging the distribution of impedance with the body;

Imaging the frequency variation of impedance within the body;

Imaging the variation in impedance during a physiological change, e.g. breathing;

Imaging the variation in impedance during a pathological change, e.g. brain hemorrhage and cancer occurring.

Although EIT does not yet make the transition from an exciting medical physics discipline into widespread routine clinical use, the bright prospect has encouraged the researchers fighting their way in it.

II. PROGRESS OF EIT IN THE WORLD

Since 1980's, more and more researchers and groups have devoted to study EIT technique not only in the theory, but also in clinical applications. There has been good progress in all fields covered –algorithms, hardware theory and clinical applications. The extreme goal of the researchers is to find a best algorithm, and to build an ideal hardware that the best image reconstruction of EIT can be gotten for clinical use.

A. The Algorithms in forward and inverse problems

In the forward problem, many familiar numerical methods can be widely used in EIT researches, for example, Finite Element Method (FEM), Boundary Element Method (BEM), Finite Difference Method (FDM), Finite Volume Method (FVM), and Element-Free Method (EFM), etc.

In the inverse problem, conductivity image reconstruction can be generally classified into two distinct types: those which seek a full reconstruction of the conductivity distribution, using iterative methods to take account of the non-linearity of the inverse problem, and those which linearise the reconstruction and therefore result in a less accurate, although faster solution. A number of reconstruction algorithms have been proposed in the following:

Perturbation Method (PM) is an iterative method, in which the finite element method or other numerical methods was used to repeatedly solve the forward problem, using a linear form of the sensitivity relationship (the Perturbation matrix), to correct an estimated conductivity distribution.

Double Constraint Method (DCM) is also an iterative technique starting with an assumed uniform conductivity at each iteration. The FEM forward problem solver is used successively by applying Neumann and then mixed boundary conditions.

Modified Newton-Raphson Method (MNRM) implements a FEM solver and a modified Newton-Raphson iterative method to compute the conductivity distribution. A forward transform to describe the relationship between the boundary voltages and the conductivity, the Jacobian matrix is

recalculated at each iteration and thus an efficient FEM implementation is required to compute the forward transformation and Jacobian.

Newton One-Step Error Reconstruction Method (NOSERM) is a single step strategy based on the iterative Newton-Raphson method, in which the Jacobian matrix is calculated prior to reconstruction and stored. This results in a much faster image reconstruction but at the expense of accuracy.

Layer Stripping Method (LSM) involves finding the conductivity at the boundary of a disc or sphere and using this information to estimate the internal voltage at a radius. Using this data, the process is repeated and thus the conductivity distribution is obtained layer by layer. In this method, optimal currents are used to facilitate a direct solution to the full non-linear reconstruction problem.

Linearised Sensitivity Matrix Method (LSMM) is based on the sensitivity theorem of Geselowitz, as a means of image reconstruction. It is similar to the Newton - Raphson algorithm, in that the sensitivity matrix is the same as the Jacobian.

Back-projection Method (BPM) is reminiscent of the techniques used in X-ray Computed Tomography. It back-projects the normalized boundary measurements along the equi-potential loci, which are formed when current is injected through a dipole on the surface, instead of back projecting along straight lines. In a two dimensional plane, these form curved lines which extend from the dipole to the boundary and are orthogonal to the current path.

B. The hardware system

Since the beginning of EIT in the early 1980's, a number of research groups have produced EIT systems for laboratory use, but a few have been used for clinical investigations. The first commercially available system was the Sheffield MK1, and development of this has led to the real time MK2 system, and the multi-frequency EITS (EIT Spectroscopy) systems MK3a and MK3b.

To obtain high-quality images, we need measurements with good accuracy, precision and repeatability. The data acquisition is a very important part of EIT hardware system, which consists of waveform, current source, multiplexers, differential amplifier and demodulator, etc. Published designs for EIT systems differ in four main respects:

(1) The number of electrodes (16, 32 or 64 electrodes); (2) The overall architecture, in particular how much of the system is distributed away from a central unit; (3) The work frequency or frequency range (at a fixed frequency or multi-frequency); and (4) The way current injected (adjacent, opposite, or adaptive patterns) is distributed to the electrodes.

C. The groups of EIT research

There are more than 100 groups worldwide who are actively performing EIT research. In each group there is free to pursue clinical applications in their own sphere of interest, including recordings in medical conditions in heart and chest medicine, gastric emptying, breast imaging, and imaging of brain function. And we think it is still considered as an exciting area of engineering in medicine and biology [1]-[2].

In UK, Sheffield Group is the first group to develop a successful EIT system. They work on all aspects of EIT, particularly in relating to lung imaging. The latest EIT system from Professor Brian Brown's group at Sheffield, termed the Sheffield Mark 3, is by far the most widely used in published clinical studies and include the new development of multi-frequency recording. David Holder and Richard Bayford at University College London, and their group is also an earlier group researching EIT in the world, and has made greater progress in EIT technology.

In USA, David Rensselaer Group of the EIT Imaging Project has developed a series of non-invasive medical imaging devices, e.g. Adaptive Current Tomography (ACT), which create images of a patient based upon the conductivity varying naturally of the body.

In Canada, a model linking contrast variations in EIT difference images to lung volume changes was developed [3]. The proposed model is the first step in enabling inter individual comparisons of EIT images since: (1) it provides a framework for incorporating the effects of anthropometric variables, gender and posture, and (2) it references the images to a physical quantity (volume) verifiable by spirometry.

In Moscow, the Institute of Radio Engineering and Electronics of Russian Academy of Sciences group developed both the measurement equipment for EIT and methods of inverse problem including measurement system and reconstruction

algorithm for 3D EIT static imaging, and also developed the first experimental measuring system for MIT (Magnetic Induction Tomography) with 16 transmitting and receiving coils built and tested recently in the laboratory.

In China, there are several groups employing the research of EIT. Fourth Military Medical University Group has developed the Quasi-polar drive pattern for brain EIT, High Precision Multi-frequency EIT system and an image monitoring system for intraperitoneal bleeding, and so on [4]. Chongqing University group and Tianjin University group both have done much work in imaging algorithms, hardware system, etc.

There are also many groups devoting to study EIT technology and the application in Japan, Korea, Finland and other countries.

D. The conferences related with EIT

In UK, the Engineering and Physical Sciences Research Council (EPSRC) Engineering Network in Biomedical EIT was established in 1998. The annual international conferences of EIT has been continued to organize in London or other place, a workshop was held for interested parties. The website and discussion list will continue (www.eit.org.uk) [5].

In 2008, there was a meeting about EIT research in Xi'an, China. This conference topic was how to promote the development of EIT in China, and the cooperation between groups.

In the annual international conference of IEEE EMBS (Engineering in Medicine and Biology Society), there were some special topics or sections about EIT, and a lot of papers have been published.

III. THE PROGRESS OF OUR GROUP IN EIT

Since 1995, our group has been to study some EIT problems, and achieved more progress in the research, which are introduced separately as follows:

In forward problem, there are several models have been developed by our group. They are 2D (two dimension) circle head model, 2D realistic head model, complete electrode realistic head mode, and 3D (three dimension) sphere head model with FEM, FVM, BEM[8]-[9].

Several algorithms in inverse problem are studied in our group shown in the following [10]-[11]:

Direct back-projection of the boundary data produces unacceptable image artifacts due to the dipole approximation. In order to improve image quality, we develop a node back-projection algorithm to improve the back-projected image. The results of three experiment modes are shown in Fig. 1, (a) is a steel rod leaned in the phantom, (b) a resin rods (2*4 cm) suspended the section near the bottom in the phantom, (c) is five resin rods put in the phantom, the reconstruction images are the second to five images from bottom to top section respectively.
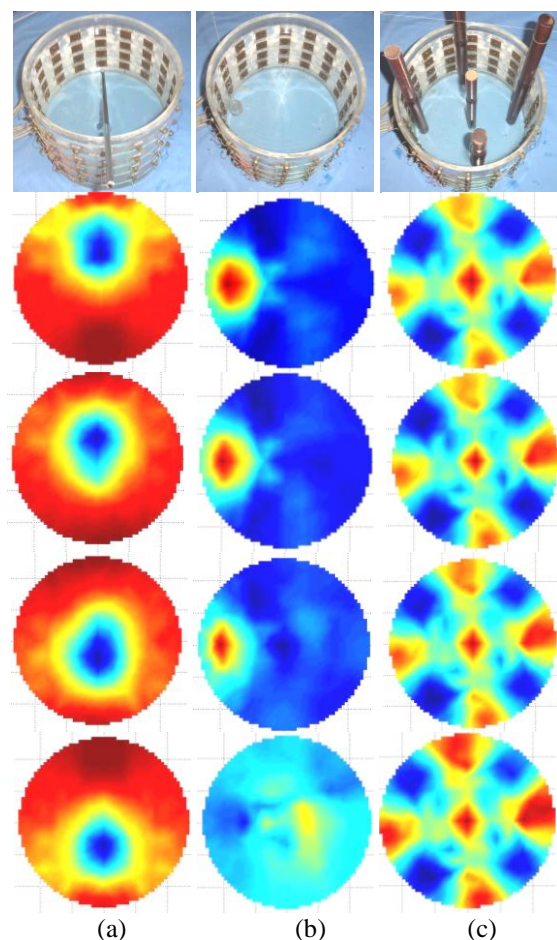

(a)   (b)   (c)

Fig. 1. The node back-projection reconstruction results

We have developed three types EIT system: basic structure system, improved EIT system with DDS, EIT system with DSP. For the purpose of improving the speed of imaging of the impedance distribution, the Digital signal processor (DSP) system is designed. The new DSP chip makes the system much more stable and quicker. Fig.2 is the DSP hardware system. It includes a computer, a

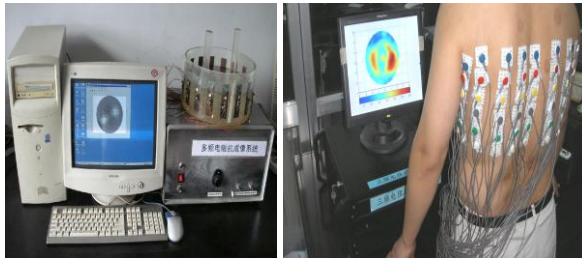saline tank and the hardware consisted of different kinds of modules[12].

Fig. 2. Hardware system with DSP

According to the data measured from this system, using the node back-projection algorithm, we can get the reconstruction images of impedance in the process of respirations, as shown in Fig.3.
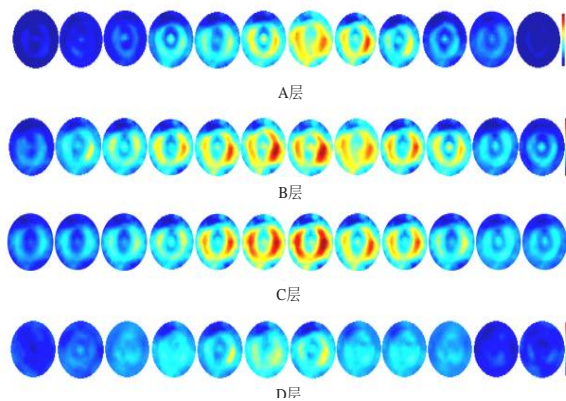

Fig. 3. The reconstruction image series of respirations

IV. FURTHER PERSPECTIVES AND WORKS FOR EIT

It is not entirely clear where the bottleneck in EIT image and data quality lies; maybe, it is principally in the errors produced by the interaction of skin impedance with instrumentation. These errors are then magnified by the ill-conditioned inverse solution in the reconstruction algorithms. The extensive researches in the field of electrical bio-impedance are resulting in the implementation of methods in clinical practice and other applications. Although the general acceptance of EIT is still limited, it is happy that various types of hardware and imaging reconstruction algorithm have been proposed recently. On the other hand, more and more novel algorithms are used in image reconstruction, for example, Magnetic Resonance EIT (MREIT), Response Surface Methodology MREIT (RSM-MREIT), Magnetic Induction Tomography (MIT), and Magneto-acoustic Tomography with Magnetic Induction (MAT-MI), etc [13]-[15].

In MREIT, currents are injected through electrodes placed on the surface of a subject and cross-sectional resistivity (or conductivity) images are reconstructed using internal magnetic flux density as well as boundary voltage measurements. The spatial resolution of MREIT is much higher than that of traditional EIT. MREIT falls into two categories: those utilizing internal current density and those utilizing only one component of measured magnetic flux density. RSM-MREIT algorithm is a new MREIT algorithm, which belongs to the latter one and solves the rotation problem in MREIT.

There is considerable interest in MIT, which avoids the skin interface problem. MIT applies a magnetic field from an excitation coil to induce eddy currents in the material to be studied, and the magnetic field from these is then detected by sensing coils. The technique has been variously named mutual inductance tomography (also MIT) and electromagnetic tomography (EMT). MIT is sensitive to all three passive electromagnetic properties: conductivity, permittivity and permeability. A number of experimental systems exist but so far no MIT system has reached routine use either industrially or medically. MIT is a low-resolution imaging modality which aims at the 3D reconstruction of the electrical conductivity in objects from alternating magnetic fields. In MIT systems the magnetic field perturbations to be detected are very small when compared to the excitation field (ppm range). The voltage, which is induced by the excitation field in the receiver coils, must be suppressed for providing sufficient dynamic range.

In MAT-MI, the sample is located in a static magnetic field and a time-varying (μs) magnetic field. The time-varying magnetic field induces an eddy current in the sample. Consequently, the sample will emit ultrasonic waves by the Lorentz force. The ultrasonic signals are collected around the object to reconstruct images related to the electrical impedance distribution in the sample. MAT-MI combines the good contrast of electrical impedance tomography with the good spatial resolution of sonography. MAT-MI has two unique features: providing an explicit or simple

quantitative reconstruction algorithm for the electrical impedance distribution; promising to eliminate the shielding effects of other imaging modalities, in which the current is applied directly with electrodes.

A new method for the monitoring of extra cellular lung water, called focused conductivity spectroscopy, is suggested, which aims at reconstructing a pulmonary edema index by measuring the electrical conductivity of the region of interest at several frequencies [16]. In contrast to EIT the minimum number of strategically placed electrodes is used.

At present, there are four topic areas in EIT: (1) Reconstruction algorithms, (2) Instrumentation, (3) Clinical applications, (4) New developments, including MR-EIT and MIT.

REFERENCES

[1] Margaret Cheney and David Issacson, "Electrical Impedance Tomography," Siam Review, vol.41, no.1, 85-101,2000

[2] David Isaacson and Jennifer Mueller, "Biomedical applications of electrical impedance tomography," 2003 Physiol. Meas. 24, 3-5.

[3] Nicolas Coulombe and Hervé Gagnon, "A parametric model of the relationship between EIT and total lung volume," Physiol. Meas. vol.26, no.4 185-192. February 2005.

[4] You Fusheng and Dong Xiuzhen, "An image monitoring system for intraperitoneal bleeding using electrical impedance tomography and its preliminary results in vivo," Proceedings of the IEEE Engineering in Medicine and Biology 27th Annual Conference Shanghai, China, September 1-4, 2005.

[5] David Holder, "biomedical applications of electrical impedance tomography", Physiol. Meas. vol.23, no.1, February 2002.

[6] David Isaacson, Jennifer Mueller, Samuli Siltanen "biomedical applications of electrical impedance tomography", Physiol. Meas. vol.24, no.2 Editorial. May 2003.

[7] Richard H Bayford, Bill R B Lionheart, "biomedical applications of electrical impedance tomography", Physiol. Meas. vol.25, no.1, February 2004.

[8] Guizhi Xu and Qingxin Yang, "Electrical Characteristics of Real Head Model Based on Electrical Impedance Tomography," IEEE Transactions on applied superconductivity, vol.14, no.2, June 2004, 1617-1620.

[9] Guizhi Xu and and Huanli Wu, "3-D Electrical Impedance Tomography Forward Problem with Finite Element Method" IEEE Transactions on Magnetics, vol. 41, no. 5, May 2005, 1832-1835.

[10] Jianjun Zhang, Weili Yan, Guizhi Xu, Quanming Zhao. A new algorithm to reconstruct EIT images: Node-back-projection algorithm. Proc. of 29th Annual International Conference of IEEE Engineering in Medicine and Biology Society,2007,4390-4393.

[11] Ying Li and Liyun Rao, Proceedings of the 26th Annual International Conference of the IEEE EMBS, San Francisco, CA, USA. September 1-5, 2004, 578-581.

[12] Shuai Zhang, Guizhi Xu, Renping Wang, Shuo Yang, Weili Yan. To detect lung ventilation with multi-frequency EIT system. Proc. of 29th Annual International Conference of IEEE Engineering in Medicine and Biology Society, 2007, p 4161-4164

[13] Nuo Gao and Shanan Zhu, "Detecting Human Head Conductivity Distribution by Means of a RSMMREIT Algorithm," Proceedings of the IEEE Engineering in Medicine and Biology 27th Annual Conference Shanghai, China, September 1-4, 2005.

[14] Y Ziya Ider and Serkan Onart, "Algebraic reconstruction for 3D magnetic resonance–electrical impedance tomography (MREIT) using one component of magnetic flux density" Physiol. Meas. vol.25, no.1 281-294, February 2004.

[15] Yuan Xu and Bin He, "Magnetoacoustic tomography with magnetic induction (MAT-MI)," Phys. Med. Biol. vol.50 5175-5187, October 2005.

[16] Michael Mayer and Patricia Brunner, "Monitoring of lung edema using focused impedance spectroscopy: a feasibility study," Physiol. Meas. vol.26, no.4 185-192. February 2005.

Development of the new Multichannel Simultaneous Magnetic Induction Measurement System (MUSIMITOS 2+)

Axel Cordes and Steffen Leonhardt

Philips Chair for Medical Information Technology, RWTH Aachen University,
Pauwelsstraße 20, 52074 Aachen, Germany
cordes@hia.rwth-aachen.de

Abstract: The old magnetic induction measurement device MUSIMITOS, built by our group, was successfully used and tested during several trials. However, during this trials some points which the first system did not fulfill were discovered. For the new design, this requirements were considered. The number of measurement channels were increased up to 12 plus 12 additional analog channels including flow- and pulse-reference. For measuring the excitation currents and voltages, a separate channel was implemented. Thus, the control module and the measurement cards have to be redesigned as well. Finally, the present system is now rack-mounted for a better protection during transports.
This article describes the new MUSIMITOS2+ and some first measurements with the system addressing vital parameter monitoring.

Keywords: Breathing, Heart Activity, Magnetic Induction, MUSIMITOS

Introduction:
A few year back, our group has built for vital parameter monitoring a magnetic induction measurement device called Simultaneous Magnetic Induction Measurement System MUSIMITOS (see [1]). During several trials with animals and and a few healthy volunteers (e.g. the creators), the system was used with success. However, during this trials, some demands were discovered which lead to a new system design. The old system was limited to 6 measurement channels which fits perfect to the needs of the used coil configurations. Since it is possible, that the patient moves in the bed or in case of the neonates was placed on a different position in the incubator, the capability for using more receiving channels for a signal enhancement was increased.
However, this was not the first system with a number of measurement channels greater then ten. Other groups (compare: [2-8]) developed measurement systems earlier, which were build mainly for oedema detection in the head. However, most of them could be used for vital parameter monitoring as well but vital parameter monitoring requires less complex technology but more system integration in the clinical environment. Thus, we could use cheaper and less complex designs for the high frequency parts and could implemented full network based data visualization for bedside monitoring as well as monitoring form an observation room. For enabling network based system control, the control board required an implementation of TCP/IP since the version in the old system was configurable through RS232 only.
Furthermore, the measurement cards have to be redesigned in the new system. Since the measurement cards of the old system were soldered with the backplane for a better SNR. The new system should follow a modular concept for better system checks and to enable

extension. Transportation and storage of the measurement device was sometimes difficult. The device was stored on a small vehicle or tied to the trial incubator. This causes risk of damage.

Description of the System:
The new rack system incorporates a a PC for signal demodulation and data storage. The power supply is now stored inside a 19 inch housing. It also includes an network Switch, cooling fan and some connections for USB and network. The measurement technique fits into a 19 inch housing as well. A picture of the new measurement system is presented in figure 1. Here, all necessary parts are stored inside a flight rack for better handling on transports and protection of the device. Front and back can be closed with separate hatches. Each functional component is located in one module which could be replaced for testing or development.
The functional block diagram of the measurement device is presented in figure 2.

Figure 1: Photo of MUSIMITOS2+
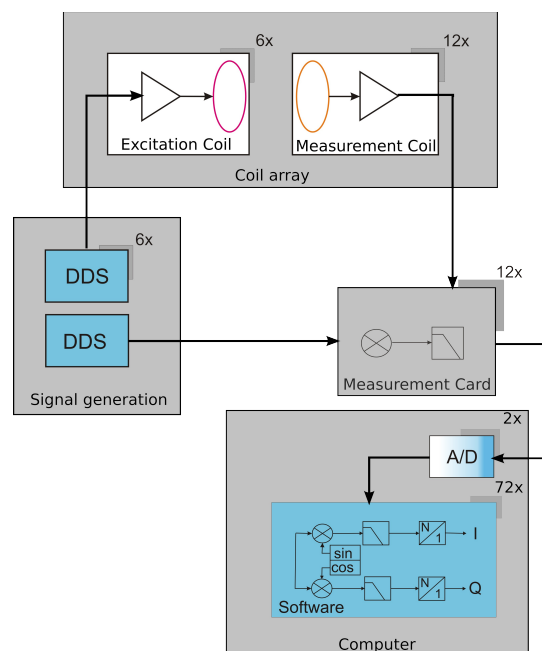
Figure 2: Block diagram MUSIMITOS2+

Power-supply, the control board for the DDS and amplifiers are not shown in the diagram.
The signal generation for the excitation signals as well as for the reference mix signal are generated through two Analog Devices DDS AD9959.
External cabling from the DDS boards to the amplifiers close to the excitation and measurement coils are realized in symmetry technology via Twisted Pair Cables. The DDS reference signal is routed to every measurement card/port and there mixed (Analog Devices AD835) with the recorded voltage from the measurement coil. A low pass filter is implemented in hardware after the mixer circuit for eliminating the higher frequency parts which will generated during the mixing process. Two NI PCI-6123 ADC-Cards sample the NF-signal of the 12 measurement cards with a samplerate of 500 kHz. In the software based IQ-demodulation, this sample rate is down sampled to 2.3 kHz. For research, the measured data streams of the I- and Q-components are directly stored on the harddisk of the computer inside the rack. The implemented IQ-demodulation enables the detection of the 6 excitation

frequencies out of every measurement coil. Therefore, the system could measure 72 HF signal paths separated in I- and Q-component. For the recording of analog reference devices, which are necessary for the validation, 12 analog channels with a samplerate of approx. 7 kHz are implemented. An additional measurement channel is reserved for measuring the currents in the excitation coils and the voltage at the end of the excitation amplifiers.

To use this device as a stand alone measurement system, the IQ data stream as well as the system configuration is realized with TCP/IP functionality. Thus, the visualization of the measured data can be presented on a separate computer or notebook which is required in clinical use.

The microcontroler for controlling the system and the measurement computer is based on a linux operation system. For performance reasons, the demodulation software was realized as a stand alone C++ application and not in a LabView or Matlab framework.

First system tests:

For a device validation we used 4 measurement coils in combination with one excitation coil under a divan bed. One adult volunteer lies on the bed face down and breath as normal as possible. Figure 3 gives an overview of the measurement. As reference we used the build in flow sensor. As presented in the figure, breathing detection is possible with the new device. The signals of the measurement coils correspond with the signal of the flow sensor. The 90° phase shift between flow reference and measurement signal comes from the measurement design. The flow reference measures the real air flow, but the magnetic induction signal corresponds more to the volume. Second test was the validation of heart activity monitoring. Here, we used 2 measurement coils and a PPG sensor. The results are presented in figure 4.
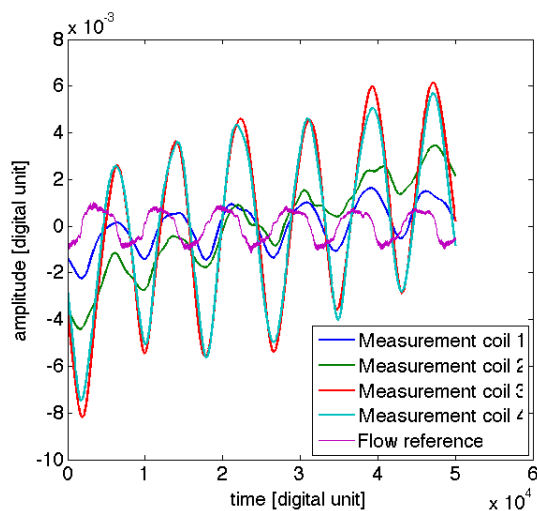

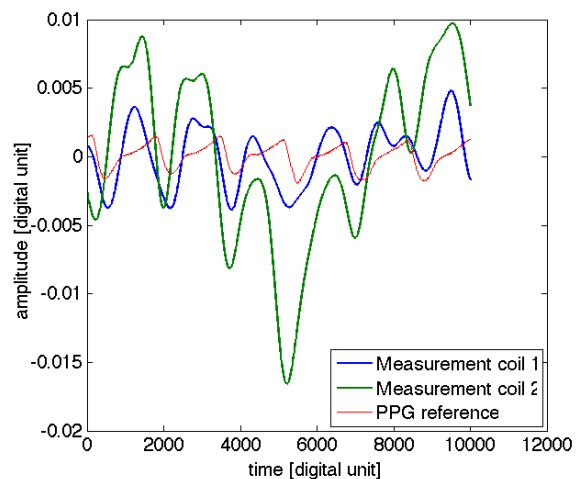*Figure 3: Detection of breathing with 4 measurement coils and flow reference sensor*

Figure 4: Detection of heart activity with 2 measurement coils and the PPG reference sensor

Note that, the new device enables also detection of heart activity. Since the volunteer did not hold his breath during the trial, the curve of measurement channel 2 is partly overlapped with breathing due to weak signal separation. However, this is addressed to the analyzes and not to the measurement system. Since all measurement data was low-pass filtered, the plots are free of noise which is present in the original signal.

Conclusion:
In this article, the new Simultaneous Magnetic Induction Measurement System MUSIMITOS2+ was presented. After the system description, we demonstrated the functionality for vital parameter monitoring with two sample trials. Until now, no performance analyzes was performed. This is planned for the future work. Furthermore, the visualization software for breathing and heart activity monitoring and separation has to be adapted to the increased number of channels and setup routines. In future animal trials, the system will be further validated and tested in combination with a new visualization software.

References:
[1] Steffen M, Heimann K , Bernstein N, Leonhardt S,"Multichannelsi- multaneous magnetic induction measurement system (MUSIMITOS)", Physiological Measurement , Vol. 29, pp. 291-306, 2008
[2] Scharfetter H, Köstinger A, Issa S, "Hardware for quasi-single-shot multifrequency magnetic induction tomography (MIT): the Graz Mk2 system", Physiological Measurement , Vol. 29, pp. 431-443, 2008
[3] Hamsch H, Igney CH, Vauhkonen M, "16 Channel Magnetic Induction Tomography System Featuring Parallel Readout", IFMBE Proceedings, Vol. 17, pp. 484-487, 2007
[4] Watson S, Williams R J, Gough G, Griffiths H, "A magnetic induction tomography system for samples with conductivities below 10 S m−1", Physiological Measurement , Vol. 11, pp. 11 pp, 2008
[5] Z Xu Z, Luo H, He W, He C, Song X, Zahng Z, "A multi-channel magnetic induction tomography measurement system for human brain model imaging", Physiological Measurement , Vol. 30, pp. 175-186, 2009
[6] Korjenevsky A V, Cherepenin V, Sapetsky S A, "Magnetic induction tomography: experimental realization", Physiological Measurement , Vol. 21, pp. 89-94, 2000
[7] Griffiths H, Zolgharni M, Ledger P D, Watson S, "The Cardiff Mk2b MIT head array: optimising the coil configuration", J Phys Conf Ser , Vol. 224, 2010
[8] Rosell-Ferrer J, Merwa R, Brunner P, Scharfetter H, "A multifrequency magnetic induction tomography system using planar gradiometers: data collection and calibration", Physiological Measurement , Vol. 27, pp. 271-280, 2006

Active Electrode Based Electrical Impedance Tomography System

Pascal O. Gaggero[1], Andy Adler[2,1], Josef X. Brunner[1], Stephan Böhm[1], Peter Seitz[1]

[1]Centre Suisse d'Electronique et de Microtechnique (CSEM), [2]Systems and Computer Engineering, Carleton University, Ottawa, Canada

Abstract: EIT can image the distribution of ventilated lung tissue, and is thus a promising technology to help monitor patient breathing to help selection of mechanical ventilation parameters. Two key difficulties in EIT instrumentation make such monitoring difficult: 1) EIT data quality depends on good electrode contact and is sensitive to changes in contact quality, and 2) EIT electrodes are difficult and time consuming to place on patients. This paper presents the design and initial tests of an active electrode based system to address these difficulties. An electrode belt is designed incorporating 32 active electrodes, each of which contains the electronic amplifiers, switches and associated logic. Tests show stable device performance with a conventient ease of use and good imaging ability in volunteer tests.

1   Introduction

Electrical Impedance Tomography (EIT) determines images of the conductivity within a body from electrical stimulation and measurement at electrodes placed on the body surface. EIT has shown significant promise as a technology to monitor the distribution of air within the lungs of mechanically ventilated patients. Such patients can have highly heterogeneous lungs, and data which EIT can provide are helpful to select lung protective ventilator settings. EIT fills a unique niche, by providing tomographic information without a bulky system or ionizing radiation.

Although EIT shows dramatic promise, it is still largely a technology in the research phase. We identify two key factors which impact the reliability and convenience of use of EIT technology. First, EIT is very sensitive to issues associated with the patient interface (electrodes and cables). The electrode contact with the body tends to have relatively high contact impedance, Z_c, which also varies with time due to body movement and drying of the contact. Such high Z_c means that all interference sources have a large effect; these include common mode gain, thermal noise, and EM interference and crosstalk between cables. Second, EIT is often inconvenient to apply since many systems require individual placement of electrodes – which can be especially difficult on the back of heavy or high-risk patients.

This paper describes design and initial testing of a system to address these factors. System design is based on an electrode belt containing active electrodes with minaturized supporting electronics mounted immediately onto the electrodes. The active electrodes system is motivated by the work of Rigaud *et al* [1], Li *et al* [2] and Guardo *et al* [3].

2   Hardware design

The design concept was to put the electronics as closely as possible to the patient to minimize problems related to the analog transmission of signal on high impedance lines.
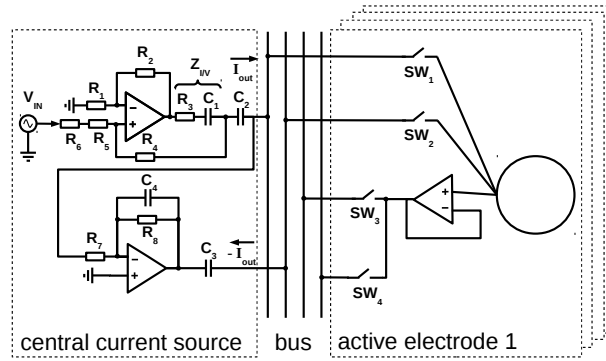
Figure 1: The central current source with the feedback circuit (on the left side of the bus) and the basic elements of an active electrode (on the right side of the bus) are depicted. Capacitance $C_{1-3} = 220\ nF$ are the DC blocking filter. Resistors $R_{3,6} = 390\ \Omega$ determine the conversion factor between voltage and current. Resitors $R_{1,2,5,4} = 10\ k\Omega$. Resistors $R_{7,8} = 5.6\ k\Omega$ are chosen equal to get a unity gain inverter. Capacitance $C_4 = 15\ pF$ avoids the oscillation of the circuit at high frequency.

The most direct way to accomplish that is to place an Analog to Digital Converter (ADC) and Digital to Analog Converter (DAC) on each electrode and communicate in the digital domain with the rest of the system. Unfortunately, it was not possible to meet the price and size requirements with multiple DACs Therefore we decided to move signal generation and measurement to a central Sensor Belt Connector (SBC). Since the analog signal should not be transmitted from the electrode to the SBC on high impedance lines using simple lead wires, the solution was to implement a voltage buffer as close as possible to the electrode.

The selected system architecture is shown in Fig. 1. Active electrodes are fabricated into a supported belt which surrounds the thorax, which allows placement of amplifiers and circuit logic as close as possible to the body. Having a voltage buffer close to the electrode has two beneficial effects: 1) it increases the input impedance of the electrode and 2) it reduces the length of high impedance paths. The input inpedance of an active electrode is determined by the stray capacitance of the buffer (2 pF) and other active elements (total about 15 pF). The input impedance of the same electrode but without active elements with 1 m bus cable was measured to be at least 200 pF (i.e. stray capacitance of the cable with adjacent ground lines). Being able to transmit the signal on low impedance line also reduces the coupling of external signal on the bus line and the cross-talk between the bus lines. The acquisition chain is shown in Fig. 2. In practice an electrode belt will tend to get dirty, for example sweat or blood could enter in contact with the belt structure or the electronic and induce damage. Thus, there is an hygiene requirement for the belt to be cleaned (sterilized) between patients. Since washable/sterilizable electronics are still experimental and their reliability not yet demonstrated, we recommend a one-time use belt strategy.

The electrodes: Each active electrode is referred to as a "node". Nodes could, in principle, drive multiple active electrodes, but our design uses one node per electrode. The tasks of an active electrode are: 1) injecting a current, 2) sinking a current, 3) buffering a voltage and multiplex the measurement on the analog lines of the bus using (SW_3 and SW_4) and 4) do nothing. Each node is managed by a embeded micro-controller (Atmel Atmega328) which contains the state table of the node. At start-up each node takes its reset value and waits for a pulse signal broadcast by the central unit on the sync line.
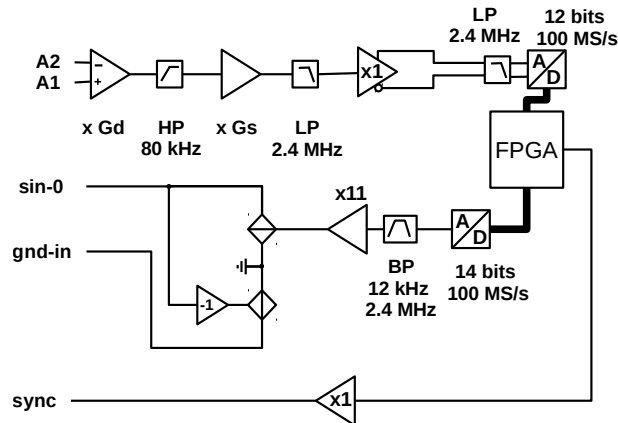
2

Figure 2: The implementation of the acquisition chain and signal generator on the SBC. The gain of the instrumentation amplifier, G_d, is set in combination with the gain, G_s, of the second amplifier stage to best fit the voltage input range of the ADC.

Each time the node measures a pulse, it triggers an interrupt, which fetches the next state in the state table and applies it to the analog switches.

The central current source: The voltage signal reference is generated using a DAC and is subsequently buffered to be supplied to a transimpedance circuit, the current source [4] itself. After flowing through the body the current needs to be sinked. The first approach consists of simply sinking the current to ground. Tests showed this approach gave high common mode voltage errors, so a third circuit, a commanded voltage source, is used to "actively" sink the current and balance the injection voltage, and significantly reduce the common mode voltage. This circuit has advantages over symmetrical current sources which injecting current with 180° phase difference. These systems face the challenge to exactly match source and sink current levels, and typically require an additional external ground electrode to absorb current differences. For electrical safety, decoupling capacitors are placed in the current source circuit to avoid the undesired injection of direct current into the body.

3   Volunteer Tests

The designed system has been tested in terms of its electronics performance and behaviour in phantom tests. We have also performed numerous tests of human volunteers. Results show that the system is quick to place onto the subject, and normally functions immediately with very few poor electrode contacts. In some cases, a few electrodes are identified that give poor signals; this is addressed by pressing on the electrodes or by applying skin preparation gel. The time to place the belt and begin data acquisition is consistently under 1 min. We present an example of images acquired on a male healthy volunteer. Data were obtained at a frame rate of 15 frames/s and images were reconstructed using a linear time difference Gauss-Newton reconstruction algorithm using EIDORS [5]. Fig. 3 illustrates an image sequence and the conductivity time curves at a sample heart and lung pixel. The "lung pixel" shows a decrease in the conductivity with the inhalation, whereas the "heart pixel" shows an increase in the conductivity. This effect is physiologically reasonable as spontaneous breathing decreases thoracic pressure resulting in increased cardiac filling. In a mechanically ventilated patient, on the other hand, "heart pixels" follow the lungs
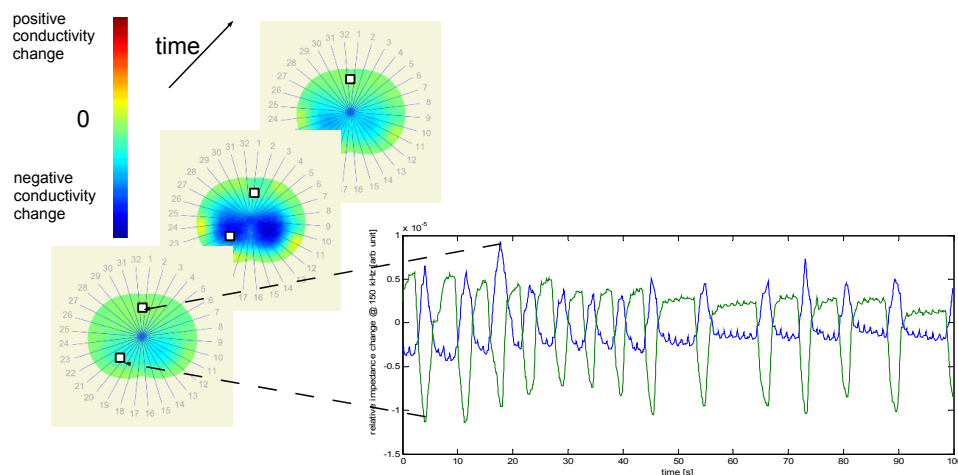
Figure 3: Temporal evolution of the EIT reconstructed impedance changes for two pixels one in the heart (blue) and one in the right lung (green) region.

because of pressure increases from the ventilator. Another effect is the movement of the heart during breathing which also affects EIT images.

4   Discussion

We present the design and initial tests of an active electrode EIT system, designed to address two key difficulties in EIT instrumentation: 1) EIT data quality depends on good electrode contact and is sensitive to changes in contact quality, and 2) EIT electrodes are difficult and time consuming to place on patients. An electrode belt was designed incorporating 32 active electrodes, each of which contains the required electronic amplifiers, switches and associated logic. Tests show stable device performance with a convenient ease of application and good imaging ability in volunteer tests.

5   Bibliography

[1] B. Rigaud, S. Y, C. N, and M. JP, "Experimental acquisition system for impedance tomography with active electrode approach.," *Medical & Biological Engineering & Computing*, vol. 31, pp. 593–599, 1993.

[2] J. H. Li, C. Joppek, and U. Faust, "Fast eit data acquisition system with active electrodes and its application to cardiac imaging.," *Physiological Measurement*, vol. 17 Suppl 4A, pp. A25–A32, 1996.

[3] R. Guardo, C. Boulay, B. Provost, D. Bohsina, and S. Mallette, "Micro-controller based active electrodes for impedance tomography," *Engineering in Medicine and Biology Society*, vol. 1, pp. 545 – 546, 1994.

[4] U. Tietze and C. Schenk, *Electronic Circuits*. Berlin, DE: Springer, 2nd, ed., 2008.

[5] A. Adler and W. R. Lionheart, "Uses and abuses of eidors: an extensible software base for eit.," *Physiol Meas*, vol. 27, no. 5, pp. S25–S42, 2006.

Towards the development of a fully integrated circuit for multi-frequency impedance measurements

Iasonas F. Triantis[1], Loucas Constantinou[1], Panagiotis Kassanos[1], Andreas Demosthenous[1] and Richard Bayford[2]

[1] Analogue and Biomedical Electronics Research Group, Dep. Electronic and Electrical Eng., University College London, WC1E 7JE, UK
[2] Biomodelling Informatics group, Dept. Natural Sciences, Middlesex University in London, NW4 4BT

email: i.triantis@ee.ucl.ac.uk

Abstract

This paper presents progress towards the development of a multi-frequency electrical impedometry system on a single chip. The system is based on synchronous detection and has been designed in CMOS technology. Preliminary measurements show its use with two frequencies simultaneously.

Introduction

A typical impedance measurement system may be separated into three main components: 1) the electrodes; 2) the current (or voltage) source; and 3) the measurement part. The majority of research in impedometric technology is carried out using discrete component electronics. This approach translates into limited component matching, increased cabling and crosstalk, reduced robustness and limited portability. Integrating the signal injection and measurement electronics on a single chip, placed very close to – or attached to the electrodes, could overcome these limitations. In this way it would increase the impedance measurement capabilities of the system and provide a portable solution, thus making it more appropriate for continuous monitoring even outside the hospital setting. The purpose of research in our group is the development of an electrical impedometry system on a single chip for a range of applications including lung imaging, bio-impedance sensors and bioassays [2,3].
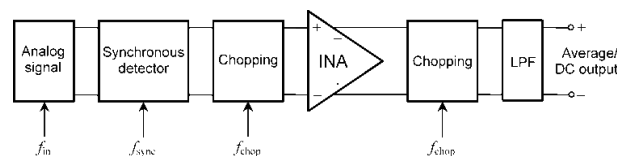

Figure 1. System-level diagram of a monitoring channel. It employs synchronous detection. Chopping is employed to eliminate DC offsets. The output is a DC value proportional to the real or imaginary value (depending on the demodulation phase) of the measured impedance.

Methods

We have integrated a 4-channel, 8-electrode impedometry system on a single chip. The on-chip current driver exhibits high output impedance and constant output current (scalable from 10μA to 1mA) within a bandwidth ranging from a few kHz up to 1MHz [4]. The four-channel integrated instrumentation on the chip (one channel shown in Fig. 1) employs synchronous detection to deliver simultaneous two-frequency measurements for real and imaginary impedance components. Chopping and a fully-differential instrumentation amplifier architecture are employed to eliminate DC offsets [5]. The amplifier is gain programmable to accommodate for different impedance ranges depending on the chosen application. A low-pass filter (LPF) provides an output DC value proportional to the measured impedance, digitized through the on-chip 10-bit ADC. The chip was fabricated in 0.6μm CMOS technology.

Results

The designed current driver exhibited a bandwidth of approximately 1MHz and the total harmonic distortion of the output was less than 60dB. The output impedance was greater than 1MΩ at 10kHz. Fig. 2 illustrates the output of the instrumentation stage with 2 frequencies applied at the input (75 kHz and 200kHz – Fig.2a). The demodulation was carried out by two channels (0° and 90°) per frequency. In order to display the operation over the whole phase range, the 200kHz signal was phase shifted at a rate of 5kHz and the corresponding real and imaginary outputs (Fig. 2b) clearly exhibited cosinusoidal relation to the input phase. Crosstalk from the bench-top testing setup cabling was evident in that first measurement, making the case for full system integration even stronger. Reducing test cables' proximity generated much cleaner outputs over the other two channels, as is evident in Fig. 2c.
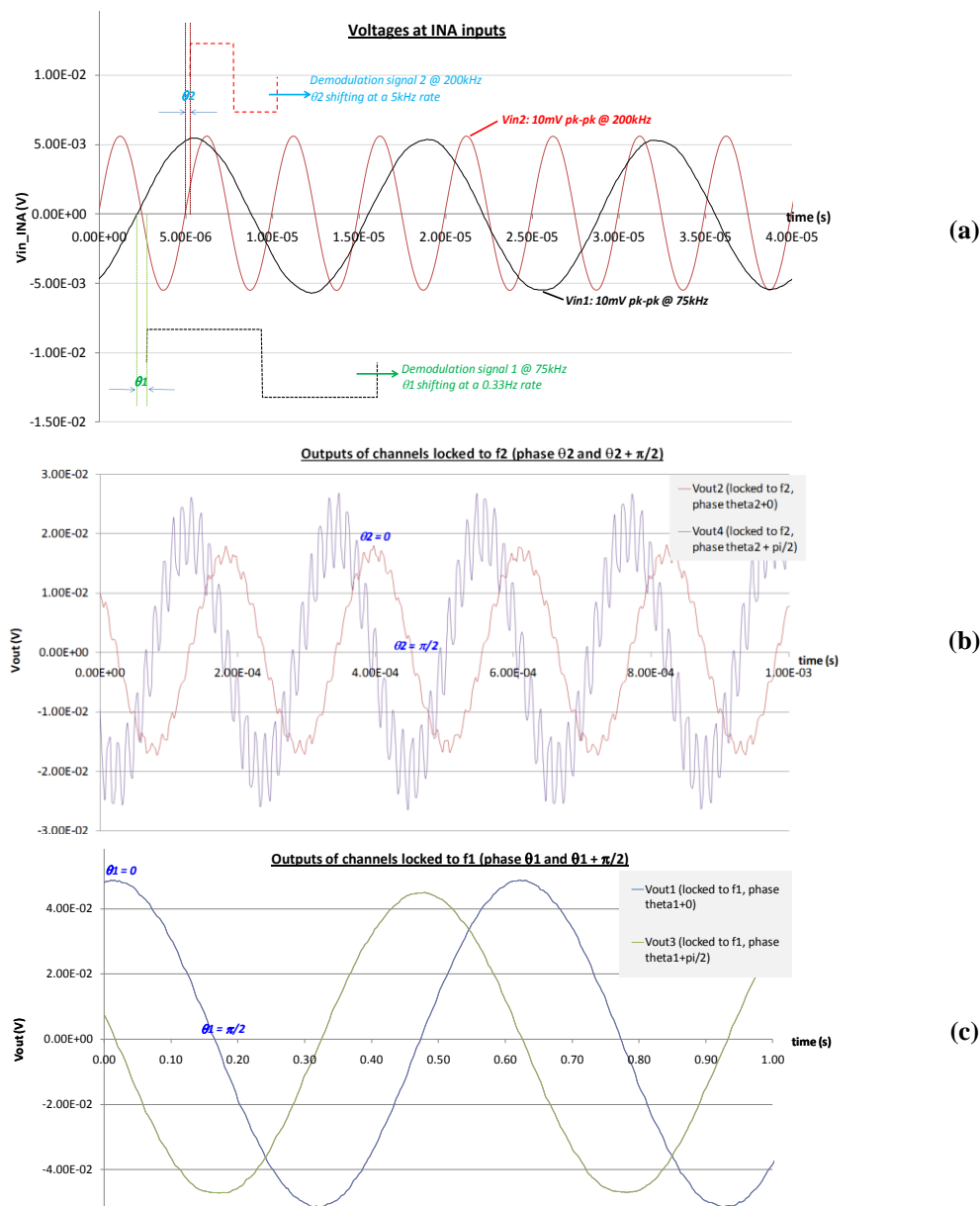
Figure 2. Simultaneous two-frequency operation of the integrated 4-channel instrumentation(make the figures larger, there to small

Conclusion

This paper describes the preliminary implementation of an integrated impedometry system. Simultaneous two-frequency signal measurements demonstrated the chip's potential for multi-frequency bioimpedance applications.

References

[1]. R. H. Bayford, "Bioimpedance Tomography (Electrical Impedance Tomography)," Ann. Rev. of Biomed. Eng., vol. 8, pp. 63-91, Aug. 2006.

[2]. P. Kassanos, R. K. Iles, R. H. Bayford and A. Demosthenous, "Towards the Development of an Electrochemical Biosensor for hCGβ Detection", Physiol. Meas., vol. 29, pp. S241-54, June 2008.

[3]. R. Bayford, P. Kantartzis, A. Tizzard, R. Yerworth, P. Liatsis, and A. Demosthenous, "Development of a Neonate Lung Reconstruction Algorithm Using a Wavelet AMG and Estimated Boundary Form," Physiological Measurement, vol. 29, no. 6, pp. 125-138, Jun. 2008.

[4]. H. Hong, A. Demosthenous, I.F. Triantis, P. Langlois, and R. Bayford, "A High Output Impedance CMOS Current Driver for Bioimpedance Measurements," Proc. 2010 IEEE Biomed. Circuits Syst. Conf. (BioCAS'10), Paphos, Cyprus, pp. 230-233, Nov. 2010.

[5]. M. Rahal and A. Demosthenous, "A Synchronous Chopping Demodulator and Implementation for High-Frequency Inductive Position Sensors," IEEE Trans Instrum Meas., vol. 58, pp. 3693-701, Oct. 2009.

Bio-impedance Measurement Method Based on Digital Auto Balancing Bridge

Nan Li[1,2], W Zhang[1], W Wang[1], N Huber[1] and H Xu[2]

[1] *Biomedical Engineering Research Group, Department of Engineering and Design, University of Sussex, Brighton BN1 9QT UK*

[2] *School of Electronic Science and Engineering, National University of Defense Technology , Changsha, 410073, China*

Email: nl74@sussex.ac.uk

Abstract: In this paper is presented the design of a novel digital auto-balancing bridge circuit for application in bio-impedance measurements. Compared to the traditional analog auto balancing bridge method, the digital method was designed to improve performance. The hardware consists of FPGA, ADC, DACs and operational amplifiers, etc. Direct Digital Synthesis, digital demodulation and modulation, digital filtering and some DSP algorithms were applied to realize the auto balancing function of the bridge at wide bandwidth. Simulation results have shown that, this method has advantages in bio-impedance measurement applications.

1. Introduction

Bio-impedance measurements are the basis of electrical impedance tomography (EIT). In the traditional current injection excitation method, conducting electrodes are attached to the surface of the observed object and small currents are injected into the object via a subset of these electrodes. The resulting electrical potentials are measured off the remaining electrodes and used to calculate the impedance distribution between electrodes. But there are many difficulties in practice; for example, a large number of precision components are required to tune the current source to achieve high output impedance; the bandwidth of the system is easily influenced by a variation of the load impedance and parasitic capacitance; the calibration of a current source is complex and time consuming, and so on.

In contrast, the voltage injection method, which applies voltage on electrodes and measures the injected current has many advantages: a precision voltage source is easier to implement and more stable under heavy capacitive loading, hence achieving higher bandwidth without complex tuning. The auto-balancing bridge is among the methods traditionally used for voltage injection. In this paper, we present an improved auto balancing bridge method, which applies advanced digital processing techniques to achieve an operational frequency range of 10Hz to 10 MHz with high accuracy and stability.

2. Analysis of Auto balancing Bridge

The general principle of the auto balancing bridge method is shown in fig. 1. When current flows through reference resistor (R_f) it is not balanced with the current flow through the measured object (Z_x), and hence an imbalance current that equals I_x-I_f flows into the null detector at the G terminal. The null detector detects the imbalance current and controls both

the magnitude and phase angle of voltage output (V_f), which can cancel the imbalance voltage on terminal G, so that the detected current reduces to zero. Once the bridge is in balance, current I_f will equal current I_x, and the impedance of Z_x can be calculated by I_f and V_o.

Generally, a negative feedback operational amplifier is suitable for null detector applications in the low frequency range. The architecture of this circuit is shown in fig.2. Due to the operation amplifier's "virtual short" effect, the negative pin of the amplifier maintains the same potential with the positive pin. When the positive pin is connected to ground, the potential at the negative pin is zero volts, so the current I_f will balance with I_x. Under this balance condition, the complex impedance of Z_X can be calculated by measuring (V_X and V_R).
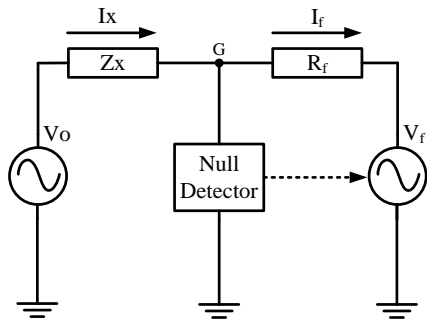
Figure 1: Auto balancing bridge principle.   **Figure 2: Analog auto balancing bridge.**
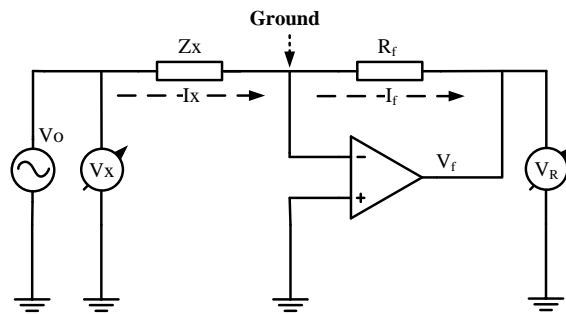
In practice, the performance of amplifiers (offset voltage, bandwidth, gain, etc.) will degrade with the increase in operational frequency. At higher frequency, the auto balancing function needs to be realized by amore complex analogue circuit including a phase detector, an integrator, a vector modulator and so on. As a rule, more analogue components in the circuit will introduce more instability factors, and the performance of the analogue circuit (linearity, bandwidth, noise, etc.) will degrade due to temperature drift and device degradation. To avoid this problem, we have implemented the null detector in a Field Programmable Gate Array (FPGA), which coined the name digital auto balancing bridge (DABB).

3. Hardware Design

A brief functional diagram of the DABB is shown in fig.3. DAC1 is used to generate the excitation signal (V_o) at the user-defined frequency. The imbalance current (I_b) is converted to voltage (V_b) which is amplified to the ADC's input range. The ADC then converts this imbalance signal and sends it to the FPGA. The FPGA will generate a balancing signal to the DAC2, in order to cancel the imbalance current. When V_b is less than a user-defined threshold, the bridge reaches a balance condition and the measurement of Z_x can be performed.
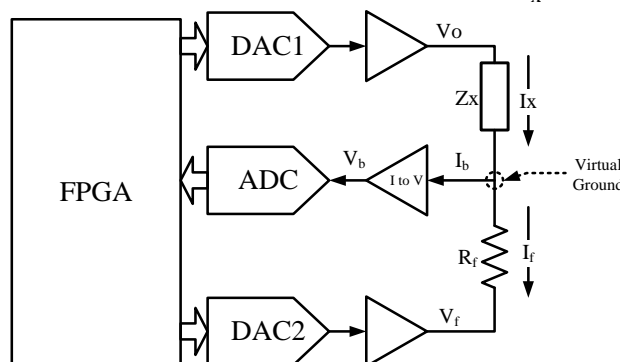

Figure 3: Hardware Architecture of Digital Auto Balancing Bridge

4. Software Design

The software will perform the detection of the imbalance current and generate a current to make the potential at the virtual ground point equal to zero volts. The functional diagram of the FPGA program is shown in fig.4. NCO1 generates the excitation signal by Direct Digital Frequency Synthesis (DDS). The output voltage is applied to the test object. The imbalance signal will be acquired by the ADC and separated into 0°/90°quadrature vector components in the FPGA. Two digital filters extract the information of the signal's real part and imaginary part respectively. The digital modulator module calculates the phase and amplitude of the imbalance signal and generates an output voltage to cancel it out. Once the bridge is in balance, the impedance will be calculated by FPGA. In the case of multi-frequency EIT, the system will switch to the next excitation frequency point for the next set of measurements, following the flowchart shown in fig. 5.
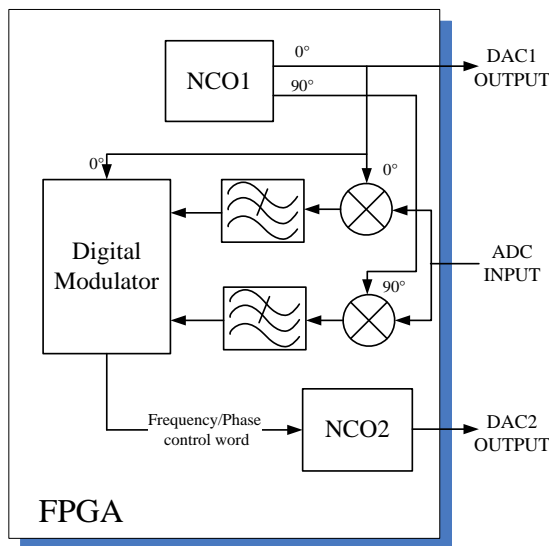
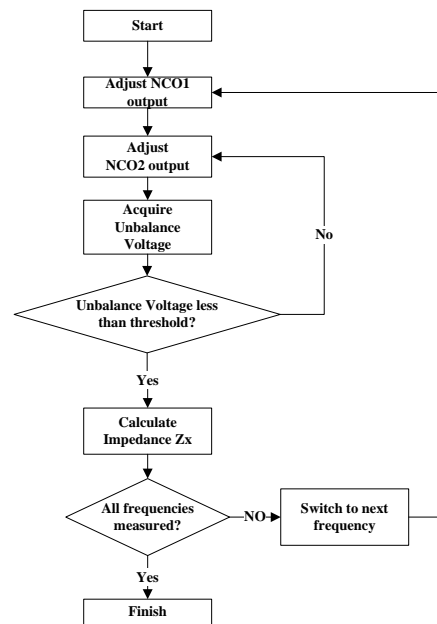**Figure 4: Software Architecture in FPGA**   **Figure 5: Flowchart of Software**

5. System Simulation

5.1 Bandwidth performance under heavy capacitive loads (versus current injection)

From the graphs shown in fig.6, we can see that the DABB is more capable of driving capacitive loads. It displays wider bandwidth (over 10MHz) than traditional current injection methods, such as the Howland current source.
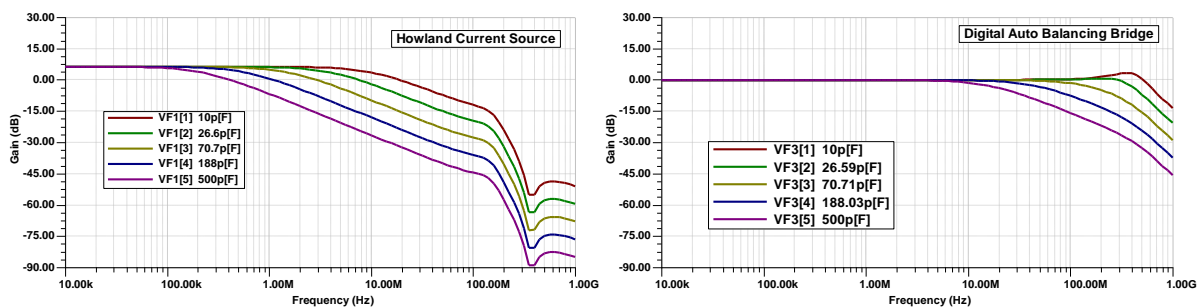
Figure 6: Simulation of bandwidth under heavy capacitive loads

5.2 Overall Bandwidth Performance (versus analog auto balancing bridge)

The overall bandwidth of an auto balancing bridge is determined by the source bandwidth and the feedback speed. We simulated the FPGA program to evaluate the feedback delay and build a circuit model of the analogue circuitry with which to interact. Fig.7 shows the simulation results. The purple line is the imbalance signal bode curve of an analog auto balancing bridge, which applies negative feedback to an operational amplifier. The blue line is for DABB. From the graph, using the DABB method, the rejection ratio of the imbalance signal is lower than -60dB up to 10MHz, which means this method can achieve high precision at a wide frequency range.
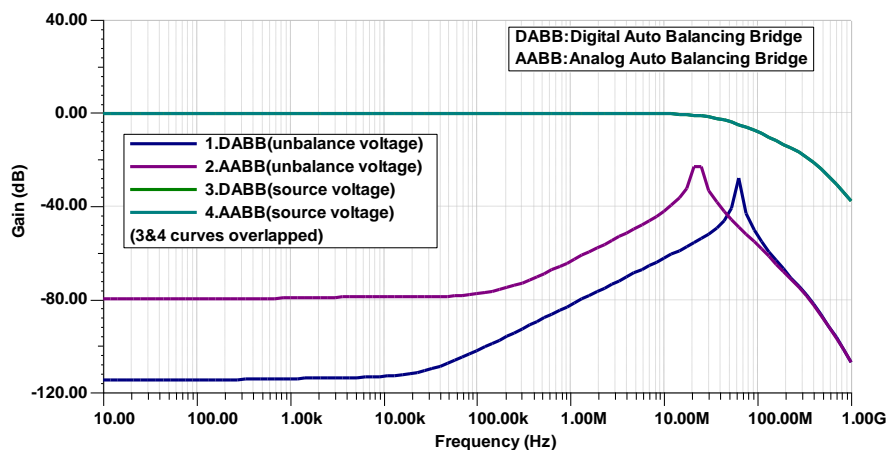

Figure 7: Simulation of overall bandwidth

6. Conclusion

For improved bio-impedance measurements at high frequencies, a digital auto balancing bridge method has been designed. Using high speed digital devices and digital algorithms, this method can effectively measure impedance over a wide frequency range (10Hz to 10MHz). The simulation result indicates that the DABB method has more advantages than the traditional current injection method and the analogue auto balancing method.

Reference
[1] Boone K G and Holder D S 1996 Current approaches to analogue instrumentation design in electrical impedance tomography *Physiol. Meas.* **17** 229–47
[2] Zhu Q, Lionheart W R B, Lidgey F J, McLeod C N, Paulson K S and Pidcock M K 1993 An adaptive current tomography using voltage sources *IEEE Trans. Biomed. Eng.* **40** 163–8
[3] Gary J Saulnier, Alexander S Ross and Ning Liu, 2006 A high-precision voltage source for EIT *Physiol. Meas.* **27** S221–S236
[4] Choi M H, Isaacson D, Saulnier G J and Newell J C, 2003 An iterative approach for applying multiple currents to a body using voltage sources in electrical impedance tomography *Proc. 25th Annual Int. Conf. of the IEEE Engineering in Medicine and Biology Society*, **4** 3114–7
[5] 《Impedance Measurement Handbook 4th Edition》 Agilent Technologies Co. Ltd., 2009

Magnetic induction tomography based on brain physical phantom

Ruigang Liu, Ye Li, Wenlei Liu, Feng Fu, Xuetao Shi, Fusheng You, Xiuzhen Dong*
Department of Medical Electronic Engineering, School of Biomedical Engineering,
Fourth Military Medical University, Xi'an, 710032, People's Republic of China.
Email: dongyang@fmmu.edu.cn; ruigang@fmmu.edu.cn

Abstract: Magnetic induction tomography (MIT) is a kind of contactless and noninvasive method to reconstruct the conductivity distribution in a human cross-section, such as brain especially. We constructed a brain physical phantom which was very close to the real conductivity distribution by setting artificial skull. Using our MIT data acquisition system on this phantom and difference algorithm, we have obtained a series of reconstructed images of conductivity perturbation objects. The minimum conductivity difference between the object and the background was 0.03 S/m. The minimum volume of the objects was 3.4 cm^3.

Keywords: Magnetic induction tomography, brain, physical phantom.

1. Introduction

Magnetic induction tomography is a kind of contactless electrical impedance tomography [1, 2]. Magnetic field is ease to penetrate the skull than electrical field. Therefore, MIT is expected to detect the diseases in skull, such as brain edema [3].

In numerical simulation, it is easy to set the lower conductivity value to denote the skull. But, most of physical phantom just push one or several conductivity perturbation objects in the water tank, not include the artificial lower conductivity skull. Therefore, there exists very big difference between the real brain and the physical phantom of simple tank.

2. Methods
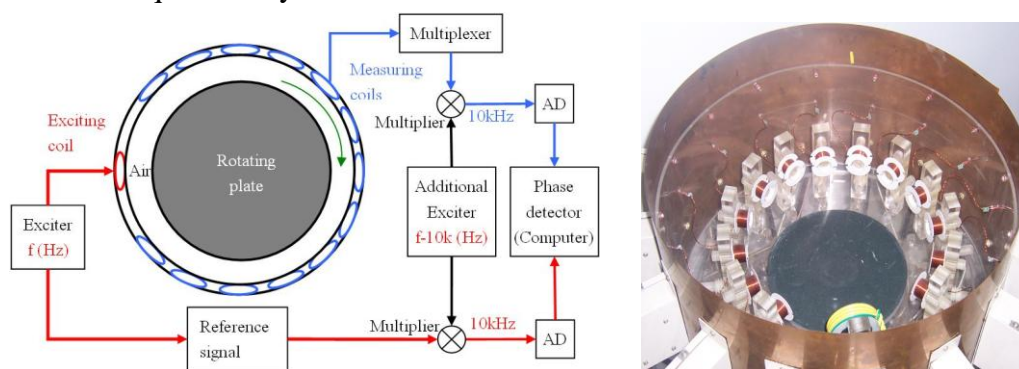
2.1. MIT data acquisition system

Fig. 1. Block diagram and photo of FMMU MIT data acquisition system

Our data acquisition system was consisted of one exciting coil and 13 measuring coils, see the Fig 1 [4, 5]. The distance of two opposite coils was 22cm. The exciting coil could be injected sine current at 1 ~ 10 MHz. The physical phantom and the conductivity perturbation objects were placed on one circle plate, which was able to be rotated by 22.5° at each time. Through 16 turns, the plate was rotated 360°. There were 16*13 data in one frame. It was about one minute to get one whole dataset.

2.2. Brain physical phantom

Our brain physical phantom was showed in Fig. 2. The tank was a half sphere vessel made

by insulted plastic, whose outside diameter was 20.5 cm and height was 10.2 cm. The artificial skull was a sphere shell made by gypsum, whose inside diameter was 18.6 cm, height was 15 cm and depth was 0.45 cm. The conductivity of gypsum was 0.012 S/m. The saturation $CaSO_4$ solution was injected into the tank and the artificial skull to denote the scalp and brain tissue, whose conductivity was 0.24 S/m. The conductivity relation of artificial scalp, skull and brain tissue was $0.24 : 0.012 : 0.24,\ 1 : 1/20 : 1$. This relation was very close to the human brain. The distance of the tank and the skull was 0.5 cm. Some insulated packing block was used to keep the artificial skull float on the tank and same distance. The conductivity perturbation objects were the agar block or NaCl solutions, which was injected into the container. The conductivity of all of materials in this paper was measured by Solatron 1260 impedance analyzer.
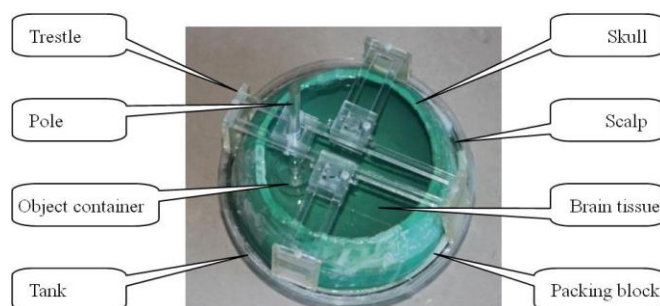

Fig. 2. Brain physical phantom

All of the conductivity perturbation object containers were made by organic glass and the shape is a cylinder. There were 5 kinds of container, whose parameters were listed in Tab 1.

Tab. 1. Parameters of Conductivity perturbation object container

No.	Total height (cm)	Outside dismeter (cm)	Total Volume (cm^3)	Inner Volume (cm^3)
OC-1	4.0	6.0	113.1	68.7
OC-2	3.0	2.0	9.4	3.4
OC-3	3.0	3.0	21.2	10.0
OC-4	3.0	4.0	37.7	20.0
OC-5	3.0	5.0	58.9	33.5

2.3. Reconstruction Algorithm

The reconstruction algorithm needed two steps. In first step, we would solve the forward problem, which could be described by $\frac{1}{\mu}\nabla^2 A - j\omega\sigma A = -J_s$ [6].

In second step, we used the regularized Newton-Raphson algorithm to solve the inverse problem, which could be described by $\Delta\sigma = -H^{-1}J^T\left[V_c(\sigma) - V_m\right]$ [7].

This inverse problem in MIT is serious ill-posed. In this paper, we used the eigenvalue threshold method (ETM) to regularize the Hessian matrix [7] [8].

We used the difference dataset of two frame to reconstruct the conductivity distribution change by $\Delta\sigma_{21} = \Delta\sigma_2 - \Delta\sigma_1 \approx -H^{-1}J^T\left[V_{m1} - V_{m2}\right]$.

3. Results

3.1. Agar block imaging
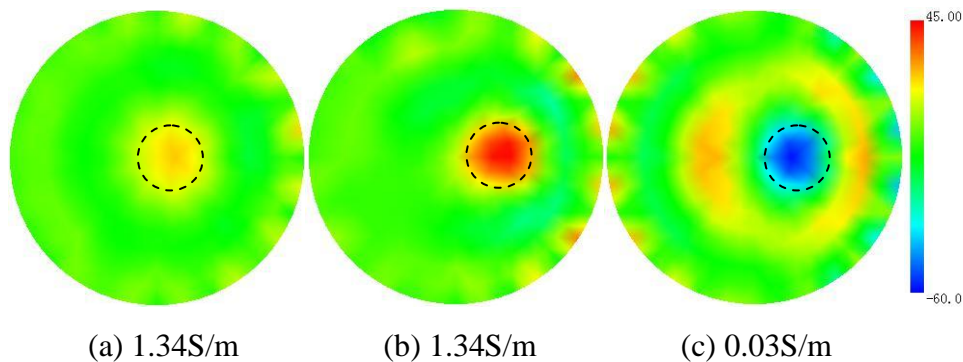

(a) 1.34S/m   (b) 1.34S/m   (c) 0.03S/m

Fig. 3. The reconstructed images of agar block

The conductivity perturbation object was an agar block, which was injected into the container OC-1. The exciting current frequency was 5.8 MHz. The regularization parameter was set as $ec = 1.0e - 10$. The difference imaging results were showed in Fig. 3. There were two kinds of agar block. In Fig. 3-a and 3-b, the conductivity was 1.34S/m. In Fig. 3-c, the conductivity was 0.03 S/m. The conductivity of background in (a), (b) and (c) was 0.24S/m. The dash circles denoted positions of the conductivity perturbation object.
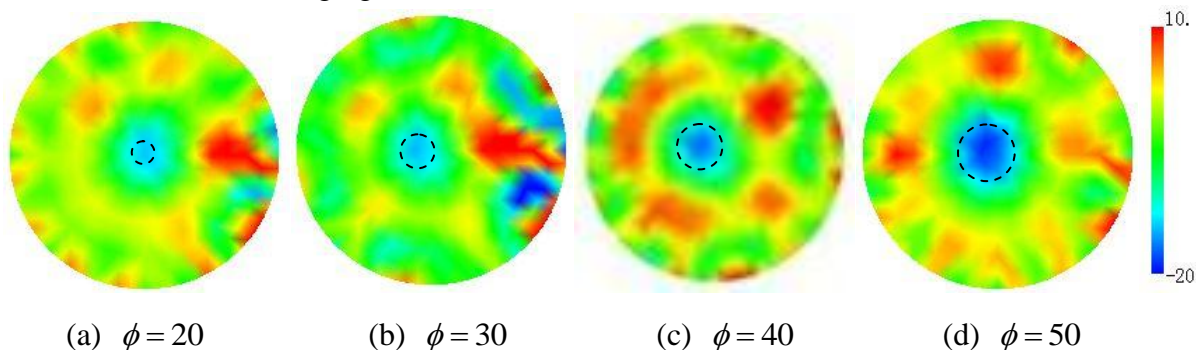
3.2. NaCl Solution imaging

(a) $\phi = 20$ (b) $\phi = 30$ (c) $\phi = 40$ (d) $\phi = 50$

Fig. 4. The reconstructed images of NaCl solution with 0.17S/m

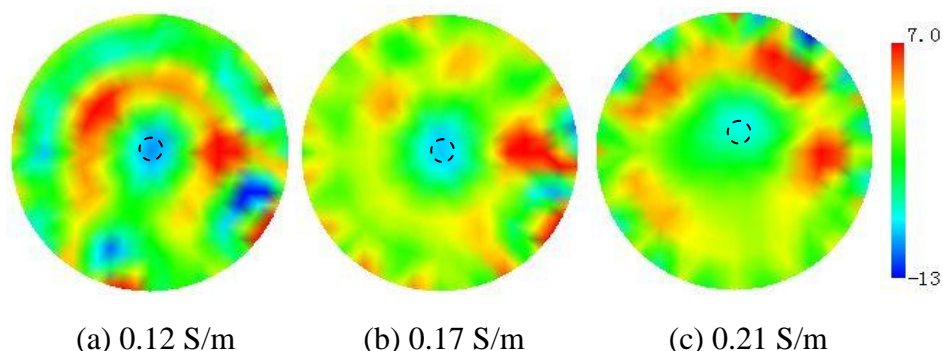(a) 0.12 S/m   (b) 0.17 S/m   (c) 0.21 S/m

Fig. 5. The reconstructed images of NaCl solution with different conductivity

First, the conductivity of NaCl solution was 0.17S/m, which was injected into the container OC-2, OC-3, OC-4 and OC-5, respectively. The exciting current frequency was 5.8 MHz. The regularization parameter was set as $ec = 1.0e - 10$. The difference imaging results were showed in Fig. 4. The conductivity of background in (a), (b) and (c) was 0.24S/m. The

dotted circles denoted positions of the conductivity perturbation object.

Second, a group of different conductivity of NaCl solution was injected into the same object container OC-2. The other conditions were same as the above. The difference imaging results were showed in Fig. 5.

4. Discussion and Conclusion

We constructed a brain physical phantom for MIT imaging. It was able to simulate the conductivity distribution of the main structures of human brain. By the trestle and poles, the conductivity perturbation objects were able to be set at any position and any height in the background solution. Compared with the water tank phantom without artificial skull, our phantom was more close to the reality.

From Fig. 3~5, conductivity perturbation objects could be distinguished in the reconstructed images. Especially in the Fig 5-c, the conductivity difference between the perturbation object and the background solution was just 0.03 S/m, about 12.5% conductivity change. Additionally, the minimum volume of the object was 3.4 cm^3. In clinical brain diagnosis, hemorrhage less than 10 ml was still in the early stage. Therefore, early brain edema and small hemorrhage would be expected. We thought these results should be owed to the single coil pattern. Certainly, more measuring time was spent for the mechanical rotating.

Acknowledgement

Referrences

[1] Korjenevsky A and Cherepenin V. 1997. Magnetic induction tomography. *Journal of Communications technology and electronics*. 42: 469-474.

[2] Griffiths H, Stewart W R and Gough W. 1999. Magnetic induction tomography. A measuring system for biological tissues. *Ann. N. Y. Acad. Sci.*, 873: 335-345.

[3] Merwa R, Hollaus K, Biro O and Scharfetter H. 2004. Detection of brain oedema using magnetic induction tomography: a feasibility study of the likely sensitivity and detectability. *Physiol Meas*, 25: 347-354.

[4] Liu R, Li Y, You F, Shi X, Fu F and Dong X. 2008. Preliminary Imaging Results of Magnetic Induction Tomography Based on Physical Phantom. *Proc. 30th Annu. Conf. IEEE EMBS,* Vancouver, Canada, 4559-4562.

[5] Li Y, Dong X, Liu R, You F, Shi X and Fu F. 2005. The influence of position to phase and magnitude detecting in medical magnetic induction imaging. *Proc. 27th Annu. Conf. IEEE-EMBS*, Shanghai, China, 1656-1658.

[6] Merwa R, Hollaus K, Brandstatter B and Scharfetter H.. 2003. Numerical solution of the general 3D eddy current problem for magnetic induction tomography (spectroscopy). *Physiol. Meas.*, 24: 545–554.

[7] Wang C, Liu R, Fu F, You F, Shi X and Dong X. 2007. Image reconstruction for Magnetic Induction Tomography and Preliminary simulations on a simple head model. *Proc. 29th Annu. Conf. IEEE EMBS,* Lyon, France, 4406-4409.

[8] Liu R, Dong X, Qin M, Tang M, You F and Shi X. 2000. A regularized method in reconstructed algorithm of electrical impedance tomography. *J. Fourth Mil. Med. Univ.*, 21: 107-109.

Parallel multi-frequency EIT system with self-calibration: KHU Mark2.5

Pil Joong Yoo, Hun Wi, Tong In Oh and Eung Je Woo

Impedance Imaging Research Center and Department of Biomedical Engineering, Kyung Hee University, Gyeonggi-do, KOREA

E-mail: ejwoo@khu.ac.kr

Abstract. Multi-channel, multi-frequency electrical impedance tomography (EIT) systems require a careful calibration to minimize systematic errors. Current source and voltmeter calibrations in a conventional EIT system are cumbersome. Since proper calibrations improve measurement accuracy and also image quality, it is desirable to implement an automatic self-calibration inside a clinical EIT system. In this paper, we describe the design of a new EIT system called the KHU Mark2.5 including automatic self-calibrations of multiple independent current sources and voltmeters.

Keyword: EIT, parallel, multi-frequency, self-calibration, KHU Mark2.5

1. Introduction

Electrical impedance tomography (EIT) has been finding clinical applications in pulmonary function monitoring, cardiac imaging, cancer detection and others [1]. This means that we need clinical EIT systems with enough performance and stability. We have lately developed a fully parallel multi-frequency EIT system called the KHU Mark2 [2]. It is based on an impedance measurement module (IMM) comprising an independent current source and a voltmeter. Using multiple IMMs, we may construct a multi-channel system to accommodate almost any electrode configuration.

In a multi-channel EIT system, proper calibrations of current sources and voltmeters are essential to maximize its performance. For each current source, we need to maximize its output impedance above 1 MΩ, for example, up to a maximum operating frequency. Since we inject currents with variable amplitudes from multiple current sources, we must carefully calibrate any small changes in their current amplitudes and phases. Within each voltmeter, all voltage gains at all measurement frequencies must be identical and this requires an intra-channel voltmeter calibration. Among multiple voltmeters, their gains must be matched and this requires an inter-channel voltmeter calibration.

To automate such calibration procedures, we developed the KHU Mark2.5 as a clinical EIT system including self-calibrations. In this paper, we describe the self-calibration methods implemented in the KHU Mark2.5 EIT system.

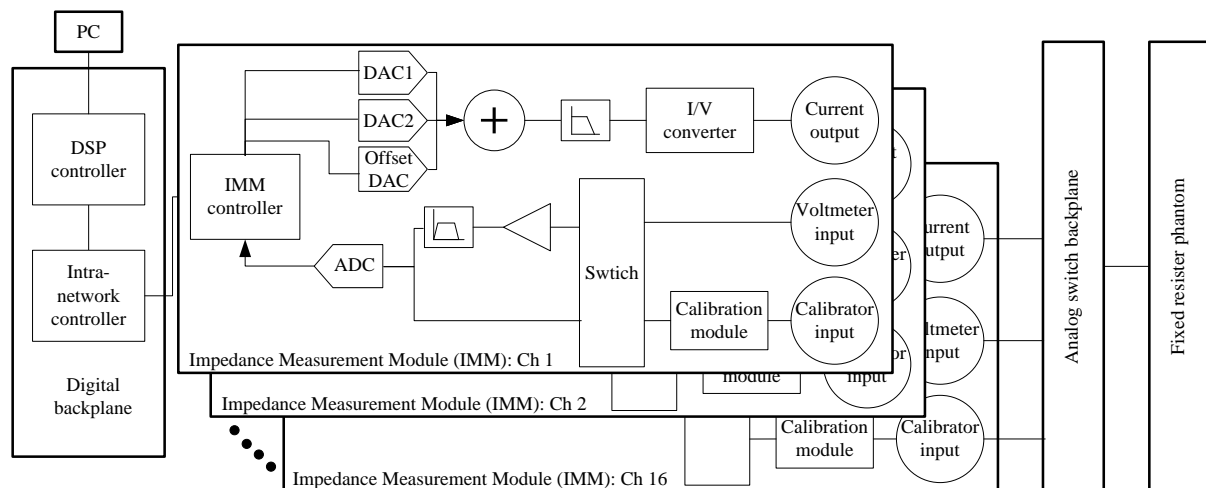## 2. Method

2.1 System structure

There are four main parts in the KHU Mark2.5 system as shown in figure 1: (i) digital

backplane including DSP as the main controller and the FPGA-based intra-network controller, (ii) IMMs including self-calibration circuits, (iii) customizable analog backplane with optional switches for electrode connections and (iv) resister phantom for intra- and inter-channel voltmeter calibrations.

2.2 Impedance measurement module (IMM) with calibration circuit

The new IMM used in the KHU Mark2.5 includes a single-ended constant current source, a voltmeter and calibration circuit. We used two 16-bit DACs to generate two different sinusoidal waveforms and one 10-bit DAC to produce a dc output. These three DAC outputs are summed to be fed to a voltage-to-current converter. This facilitates current injection of multiple sinusoidal frequencies at an exactly same time, which will be beneficial especially in frequency-difference imaging. The 10-bit DAC is used to remove any dc component at the output of the current source.

We adopted the current source calibration technique called the droop method described by Cook *et al* [3]. Inside the calibration circuit, there are switches (AQY221R2VY, Nais) and current measurement unit to find optimal settings for digital potentiometers inside the enhanced Howland circuit and four generalized impedance converters (GIC).


Figure 1. Structure of the KHU Mark2.5.

2.3 Self-calibration method

Figure 2 shows the procedure of the self-calibration in the KHU Mark2.5. First, the output of the current source in an IMM is connected to the calibrator input within the same IMM. In step A, we measure the dc offset for one sinusoidal period to adjust the 10-bit DAC output depending on its polarity and size. In step B, we null out any phase change in the measured current by the phase-sensitive demodulation due to components and analog circuits. In step C, we search for optimal values of digital potentiometers to maximize the output resistance and minimize the output capacitance of the current source at the same time. In step D, we connect two current source outputs in two IMMs to the resistor phantom. They are supposed to produce currents with the same amplitude but opposite polarity. We measure the exit current through the ground cable and minimized it by adjusting the output of one current source with the other as the reference. We repeat this for all current sources using the same reference current source. This step allows us to have multiple balanced current sources. In step E, we connect all IMMs in the same way we plan to use the KHU Mark2.5 in a chosen application. We measure voltages from all IMMs and null out phase changes in all voltmeters at all

operating frequencies. In step F, we collect intra- and inter-channel calibration factors from all voltmeters at all operating frequencies so that gains are matched for all frequencies and all channels. Figure 2 describes these steps.
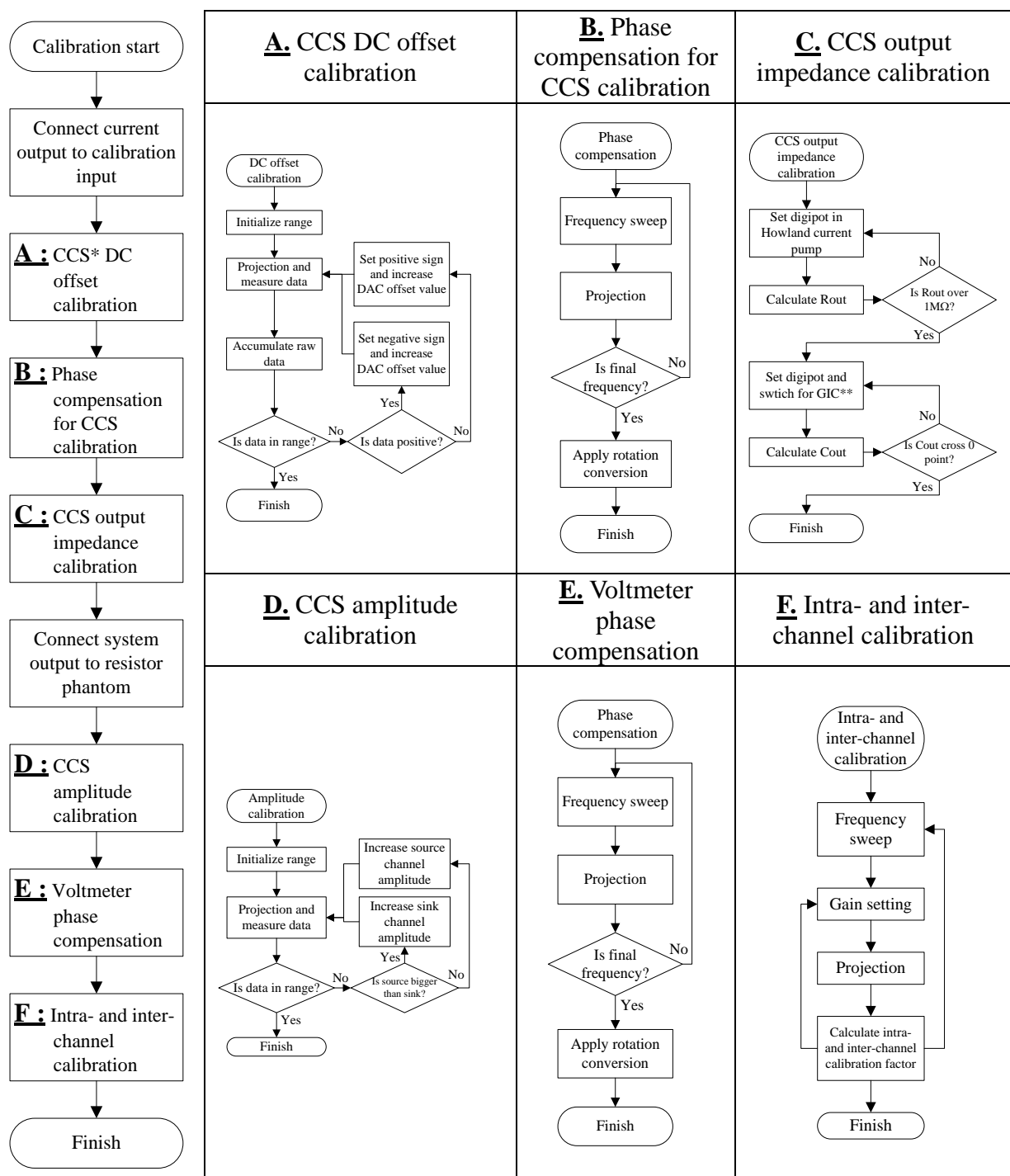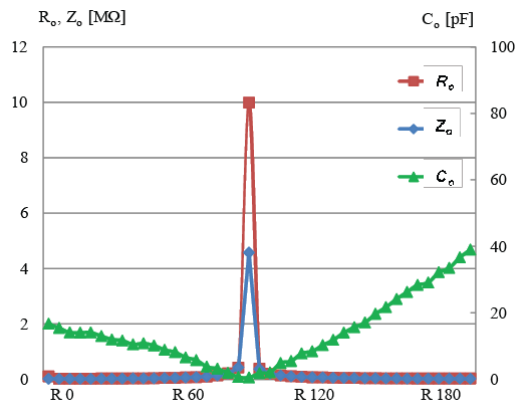

* CCS: constant current source, **GIC: generalized impedance converter
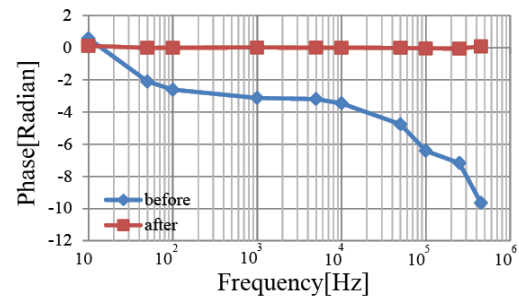
Figure 2. Flowchart of self-calibration methods.

3. Result

We measured the average dc offset current of 3.16 µA before the dc offset calibration in the current source. After calibration, it was reduced up to 0.24 µA. Figure 3 shows an example of the output impedance calibration for the first IMM at 10 kHz. The output impedance was
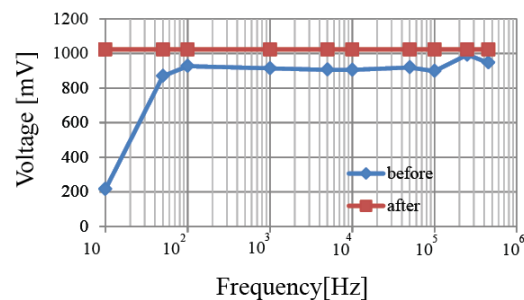
larger than 4 MΩ in this case after current source self-calibration. The current outputs between a source and a sink were balanced within 0.62%. Figure 4 and 5 present frequency responses of IMMs before and after intra- and inter-channel voltmeter calibrations.

Figure 4. Voltmeter phase compensation.

Figure 3. Current source output impedance calibration.

Figure 5. Voltmeter gain calibration.

4. Conclusion and discussion

We incorporated automatic self-calibrations of multiple independent current sources and voltmeters inside the developed clinical EIT system called the KHU Mark2.5. It significantly reduces time and efforts for system calibrations. Currently, the self-calibrations are implemented in the PC program. We plan to implement those calibration functions in the FPGA of each IMM and the FPGA of the intra-network controller. We will investigate effects of these self-calibrations in particular experimental settings for chosen clinical applications.

Reference

[1]   Holder D S 2005 *Electrical Impedance Tomography: Methods, History and Applications* (IOP: Bristol, UK)
[2]   Oh T I, Wi H, Kim D Y, Yoo P J and Woo E J 2011 Fully parallel multi-frequency EIT system with flexible electrode configuration: KHU Mark2. *Physiol. Meas.* in press
[3]   Cook R D, Saulnier G J, Gisser D G, Goble J G, Newell J C and Isaacson D 1994 ACT3: a high-speed, high-precision electrical impedance tomography *IEEE Trans. Biomed. Eng.* **41** 713–22
[4]   Oh T I, Lee K H, Kim S M, Koo H, Woo E J and Holder D 2007 Calibration methods for a multi-channel multi-frequency EIT system *Physiol. Meas.* **28** 1175–88

Cascaded multi-channel EIT system with fast data acquisition by frequency-division and space-division multiplexing

Hun Wi, Pil Joong Yoo, Tong In Oh and Eung Je Woo

Impedance Imaging Research Center and Department of Biomedical Engineering, Kyung Hee University, Gyeonggi-do, Korea

E-mail: ejwoo@khu.ac.kr

Abstract. Three-dimensional multi-frequency EIT imaging may require an EIT system with many channels, flexible electrode configurations and fast data collection protocols. We developed a multi-frequency EIT system which can be cascaded to form a system with a larger number of channels. In this paper, we show how two independent 16-channel EIT systems are cascaded to form a 32-channel system. We also demonstrate multi-channel and multi-frequency current injection methods for faster data acquisitions based on both frequency-division and space-division multiplexing.

Keyword: EIT, cascading, frequency-division multiplexing, space-division multiplexing

1. Introduction

Three-dimensional electrical impedance tomography (EIT) is needed since externally injected current spreads inside the three-dimensional human body [1]. Multi-frequency EIT imaging is desirable since admittivity values of biological tissues change with frequency [2]. Three-dimensional multi-frequency EIT imaging, however, requires a complicated hardware with many channels, flexible electrode configurations and fast data collection protocols. As the hardware complexity increases, it is more plausible that measurement accuracy degrades.

In this paper, we propose a new EIT hardware structure based on the idea of system cascading, frequency-division multiplexing and space-division multiplexing. We will explain how we developed a 16-channel fully-parallel multi-frequency system which can be cascaded to form a system with a larger number of channels. Using a cascaded EIT system based on our 16-channel KHU Mark2 EIT system, we will show how to implement frequency-division and space-division multiplexing for faster data acquisitions.

2. Method

2.1 The cascaded EIT system

Figure 1 shows an example of a cascaded EIT system. A PC controls two independent EIT systems through two USB connections. Before synchronization, they operate independently using their own timing clocks. We first choose one of them as the master and others as slaves. The master controller (DSP) sends a clock synchronization signal through its intra-network controller to other intra-network controllers in the slave systems. It resets the PLL modules

implemented in all of the intra-network controllers to synchronize all timing clocks in all EIT systems as shown in figure 2. Each intra-network controller then sends a trigger signal to all impedance measurement modules (IMMs) inside the corresponding EIT system (either master or slave) so that timings among IMMs are synchronized.

After such synchronization steps, the PC may initiate a series of scans by sending the 'start scan' command to the intra-network controller of the master EIT system. It then generates a synchronized start-timing signal to the intra-network controllers in all slave EIT systems so that each intra-network controller in each slave system transfers the signal to all IMMs.
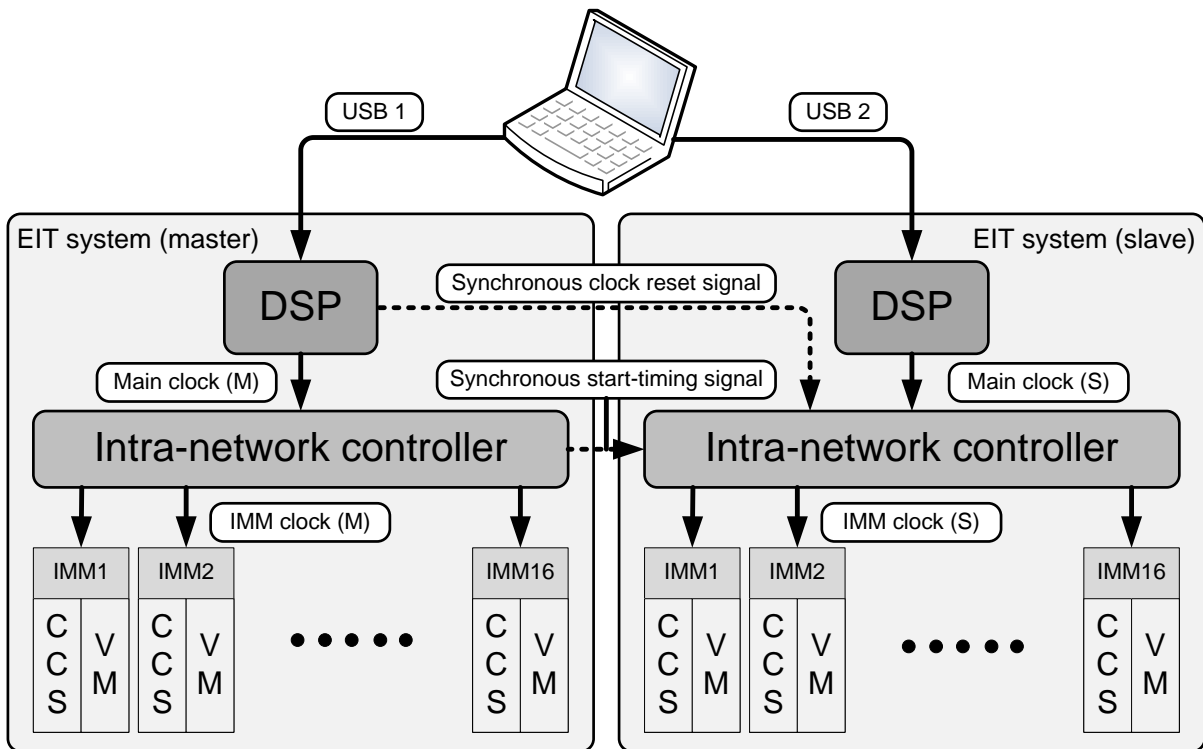
Figure 1. Example of a cascaded EIT system (IMM: impedance measurement module, CCS: constant current source, VM: voltmeter).
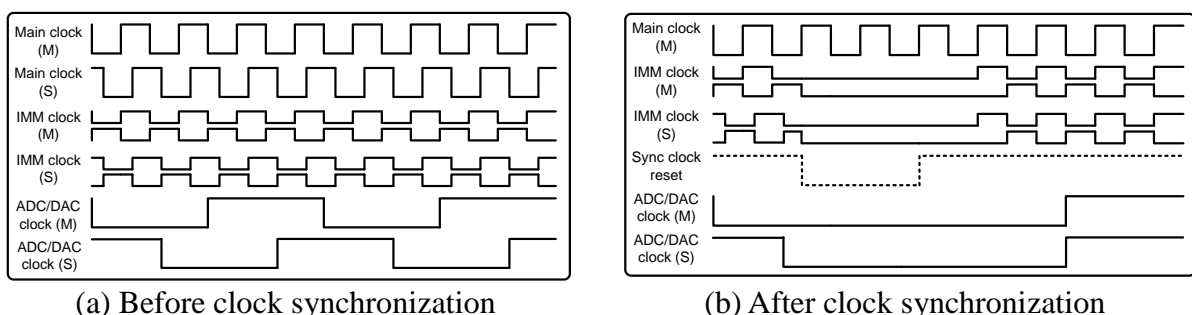
(a) Before clock synchronization   (b) After clock synchronization
Figure 2. Clock synchronization in a cascaded EIT system using clock reset signal.

2.2 Frequency-division and space-division multiplexing

In order to efficiently collect multi-frequency data using a multi-channel EIT system, we used two different strategies of frequency-division multiplexing and space-division multiplexing. Each IMM has an independent constant current source and a voltmeter. Each IMM can inject

sinusoidal current with three different frequencies at the same time. Such current injection can be done on multiple IMMs. There are numerous combinations in practice on how to assign current amplitudes and frequencies to all IMMs. As an example, the first IMM injects current at 1 kHz and the ninth IMM injects 10 kHz current at the same time. We can measure voltages of both frequencies simultaneously. Instead of injecting current with a single sinusoidal frequency, we may let a certain IMM inject current with three different frequencies mixed together as shown in figure 3(b). All of these details can be describe in a script file of which contents will downloaded to all IMMs in a cascaded multi-channel multi-frequency EIT system.

(a) Space-division multiplexing

(b) Frequency-division multiplexing
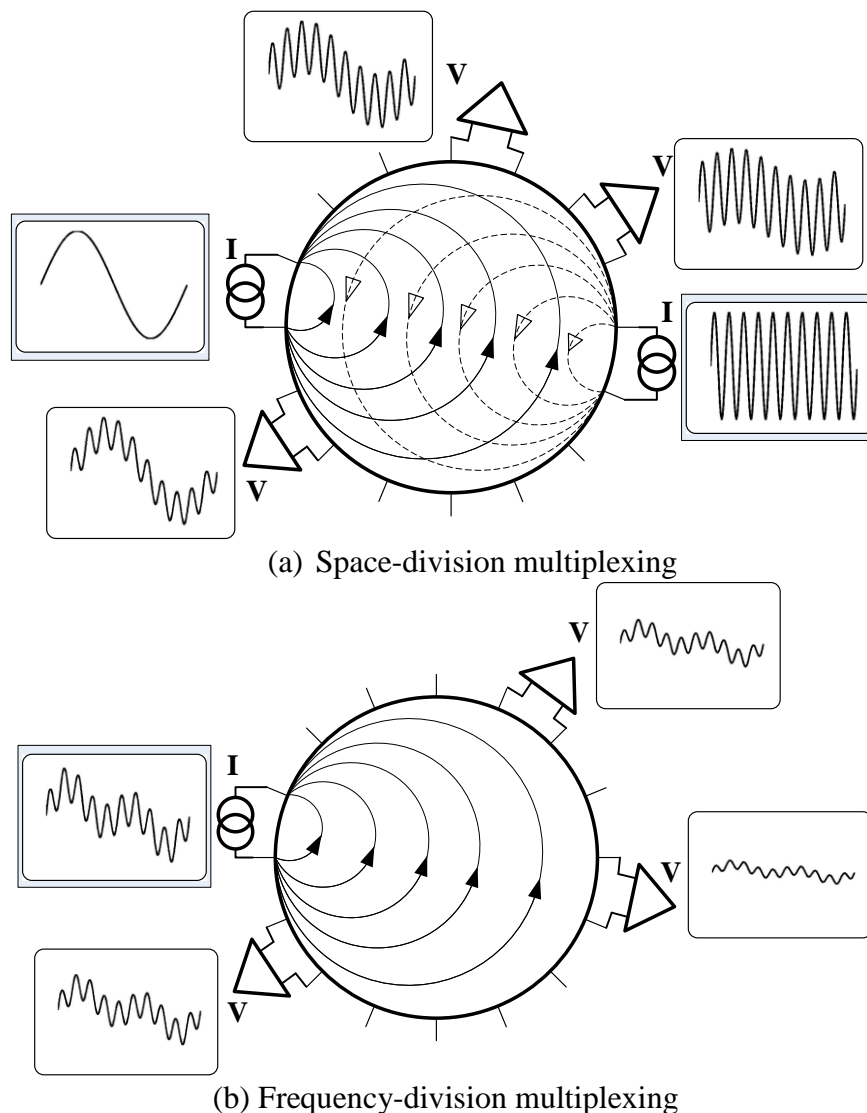
Figure 3. Examples of frequency-division and space-division multiplexing.

3. Result

We evaluated our multi-channel and multi-frequency data collection protocols using the frequency-division and space-division multiplexing. We used a phantom filled with 0.5 S/m saline. We placed a piece of carrot (0.016 S/m) as an anomaly. As shown in figure 4, we could produce the same images using different data collection protocols. The results indicate that we may choose the fastest method by fully utilizing the frequency-division and space-division multiplexing.
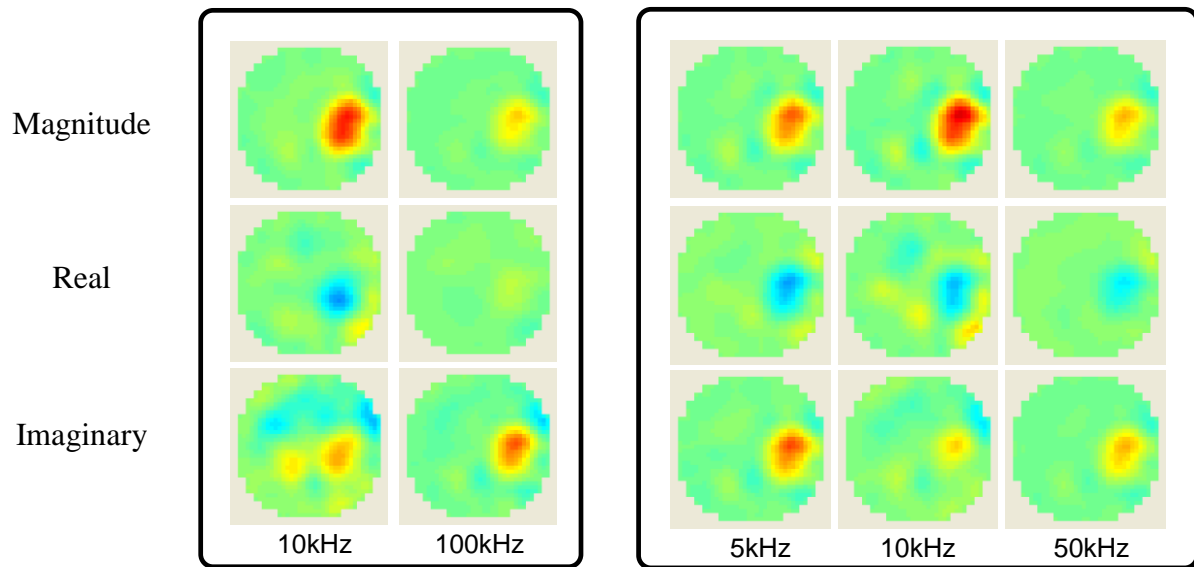
(a) Space-division multiplexing   (b) Frequency-division multiplexing

Figure 4. Images of a conductivity phantom using collected data sets with different data collection schemes.

4. Conclusion and discussion

We could successfully construct a cascaded EIT system to increase the number of channels without increasing the hardware complexity. After cascading, we could synchronize all independent IMMs belonging to different EIT systems before cascading. Faster data acquisitions are possible by incorporating both frequency-division and space-division multiplexing. We need to pay attention to the total harmonic distortion of injecting currents to minimize systematic artifacts. We should also restrict the total amount of injection currents at any time within a safe level.

Acknowledgement

Reference

[1]   Metherall P, Barber D C, Smallwood R H and Brown B H 1996 Three-dimensional electrical impedance tomography *Nature* **380** (6574) 509-12
[2]   Gabriel S, Lau R W and Gabriel C 1996 The dielectric properties of biological tissues: II. Measurements in the frequency range 10 Hz to 20 GHz *Phys. Med. Biol.* **41** 2251-69
[3]   Jun S C, Kuen J, Lee J, Woo E J, Holder D and Seo J K 2009 Frequency-difference EIT (fdEIT) using weighted difference and equivalent homogeneous admittivity: validation by simulation and tack experiment *Physiol. Meas.* **30** 1087–99
[4]   Oh T I, Wi H, Kim D Y, Yoo P J and Woo E J 2011 Fully parallel multi-frequency EIT system with flexible electrode configuration: KHU Mark2. *Physiol. Meas.* in press

An FPGA based Magnetic Induction Tomography system for prospective biomedical applications

H-Y Wei, M Soleimani

Department of Electronic and Electrical Engineering, University of Bath, Bath, UK

Abstract: This paper reports on the development of an FPGA based Magnetic Induction Tomography (MIT) system for prospective biological applications built at the University of Bath. The performance of this MIT system is characterised , including an initial test of measurement of saline solutions with a basic two channel setup (one transmitter and one receiver). A National Instrument multiplexing system has been developed for multiple channel MIT measurements. All the excitation, measurement and channel switching are controlled by LabView program.

1. Introduction

Magnetic Induction Tomography (MIT) is a contactless tomography technique able to map the passive electromagnetic properties (mainly conductive properties) within an object. Both excitation sensors and measurement sensors are constructed as coils. By establishing a sinusoidal signal in the transmitting coil, a changing magnetic flux is set up, which induces a voltage across the receiving coil. This induced voltage is proportional to the magnetic field strength, also known as the background or primary signal [1]. If an object is positioned between the two coils, an eddy current will be induced on the object. This eddy current can create a secondary magnetic field, which will induce a perturbation voltage across the receiving coil. The magnitude of this voltage is proportional to the object's conductivity.

In biomedical applications, due to its low conductivity features ($\sigma < 3$ S/m) of the measuring samples [1,4], the magnitude of signal perturbation is several orders less than the acquired signal in industrial applications, which generally monitors high conductivity of materials [2], such as metals ($\sigma > 10^6$ S/m). The signal perturbation induced by biological samples is generally <1% [1], and increases in proportion with driving frequency and tissue conductivity. For biological applications, the perturbation is mainly dominated by the phase shift, which contains the information required for image reconstruction.

For medical applications MIT systems, the sensitivity of the coils is going to be degraded significantly due to its extremely small conductivity. A very accurate measurement system is required. In this paper, the National Instrument (NI) FPGA based system developed for a prototype MIT system is described. The performance of the phase measuring capability of the system is carried out with the following parameters: phase linearity, phase noise (with different input levels) and phase drift. Two phase measurement techniques in LabView software (FFT tone measurement and Quadrature demodulation) are also compared to decide which technique will be implemented to perform the phase measurement for the latter experiments.

2. System Development

In this section, we explain the initial stage of our medical MIT design based on 'off-the-shelf' NI hardware devices. The following system requirements were considered when selecting the NI devices:

- A device to generate the transmitting signal within a wide range of frequencies (kHz to MHz), because different target measuring materials have different optimal operating frequencies.
- A high speed direct digitisation device for taking measurements from the receiving coil. Direct digitisation here is defined as analog-digital conversion of the high frequency signal without down-converting the signal into a lower frequency range. Direct digital sampling eliminates the mixing process and therefore requires less electronics components and it offers better flexibility on future modifications.
- The devices need to be capable of expanding the system into a multi-channel MIT system.

Based on the considerations above, a high speed MIT system is constructed by the following NI devices: NI 2593 (500 MHz 2x 8:1 multiplexer), NI 5781 (40 MHz baseband transceiver) and NI 7951 (Virtex-5 LX30 LabView Programmable FPGA module).

3. System Characterization Setup

The NI based measurement system setup is shown in figure 1. AO-Ch0 is connected to AI-Ch0 and AO-Ch1 is connected to AI-Ch1. AO-Ch0 generates the variable driving signal, whose amplitude and phase can be altered for system characterization. AO-Ch1 is the reference signal source, which generates a fixed amplitude of 1V p-p that is directly fed into AI-Ch1 for the phase and amplitude calculations.
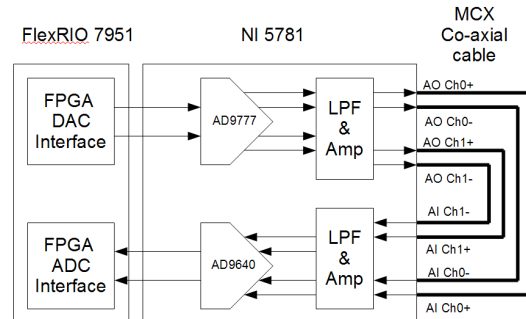

Figure 1. System block diagram

In this system setup, the driving frequency is set to 10 MHz. With the configuration shown in figure 1, the following parameters were characterized to evaluate the hardware performance: phase linearity, phase noise vs. signal input level and phase drift.

Each phase measurement was an average of fifty samples. The phase measurements were calculated by two techniques: FFT Tone measurement and I/Q demodulation. In linearity experiment, linear regression model is applied into both results to quantify the linearity between the actual and measured phase difference. The parameter R^2 is measure in the model to indicate the goodness of linearity; R^2 value will be closed to 1 if the results show a good linearity.

4. Saline Experimental Setup

A two channel measurement system was assembled to test the capability of the system for saline detection, as illustrated in figure 2. The coils were attached onto a 20 cm diameter perspex cylindrical tube. Each channel consisted a 4 turns balanced coil, wound on a 4 cm diameter plastic tube. An operation frequency of 10 MHz was chosen to avoid resonance of the coil sensors [3]. The distance between the transmitter and the receiver was 20 cm. In order to increase the magnetic flux strength and phase stability, a fully differential amplifier THS4500 was used to amplify the transmitting output signal from 1 Vp-p to 4 Vp-p. For the receiving coil, a high speed amplifier THS4275 was used to buffer and amplify the receiving signal.

In this experiment, saline solutions were prepared by dissolving different weight of NaCl into deionised water. Different concentrations of saline, 0% (σ = 0.00042 S/m), 1% (σ = 1.72 S/m), 3% (σ = 2.31 S/m) and 5% (σ = 7.26 S/m), were used to emulate the biological tissue measurement capability of the NI-system.

The saline bottles were moved along the x-axis. The output of the receiving coil buffer was connected to NI 5781 for data sampling. For each position along the axis, two hundreds phase measurements were captured. The average phase measurements then could be calculated.
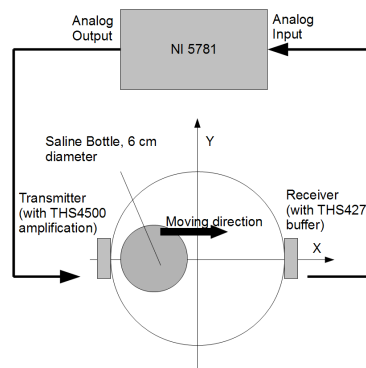
Figure 2: The system setup for the saline measurement

5. Results

Figure 3 shows test results obtained from the MIT system.
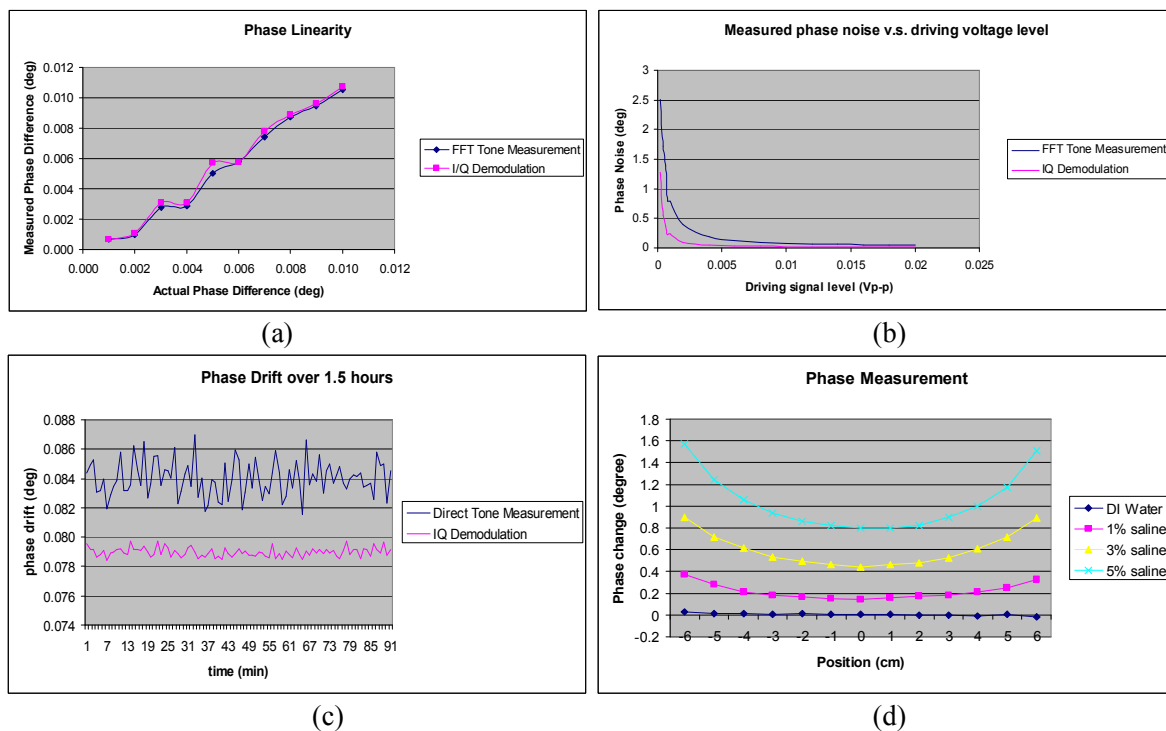

(a)

(b)

(c)

(d)

Figure 3. (a) Shows the relationship between the actual and measured phase. (b) shows measured phase noise versus the driving signal level. (c) shows phase drift measurement over a period of 90 minutes. (d) shows phase measurements versus the saline bottle position along the x-axis.

- Phase Linearity

The actual phase difference between the driving signal and the reference signal varied from 0.001 degree to 0.1 degree (by changing the LabView program settings). However, figure 3(a) only shows the phase linearity result from 0.001 degree up to 0.01 degree to find out whether our system has a capability of detecting a phase difference in milli degree ranges.

From the linear regression model, the R^2 values is calculated, which is 0.9871 and 0.9823 for FFT measurement and I/Q demodulation respectively. If all the measurements (0.001 degree to 0.1 degree) are taken into account, the R^2 value for FFT measurement becomes 0.9997 and 0.9996 for I/Q demodulation.

It is observed that FFT Tone measurement has a slightly better phase measurement linearity, since its R^2 value is closer to 1 (perfect linearity).

- Phase noise vs. driving signal level.

The phase noise was measured against the driving signal level (defined in LabView, generated through AO-Ch1). The driving voltage was varied from 0.1 mVp-p to 20 mVp-p. Figure 3(b) shows the results from the Tone measurement and I/Q demodulation.

For the same driving level, it shows that I/Q demodulation technique offer a better noise stability than FFT tone measurements. When the driving signal was decreased, large amount of phase noise was observed in the sampled signal and gave us an erroneous result (A phase noise of 2.5 degrees was detected when the signal amplitude was decreased to 1mV). This observation also suggests that, an amplifying buffer is required at the receiving coil to ensure a better phase noise performance.

- Phase drift

The phase drift was measured over 1.5 hours and the result is shown in figure 3(c). The time interval between each phase measurement was one minute.

The phase drift result also showed that the direct tone measurement had a larger fluctuation than the I/Q demodulation. The maximum difference observed for Tone measurement was 5.45 millidegree. Under the same condition, only 1.27 millidegree difference was observed.

- Saline Experiment

Figure 3(d) shows the phase change at 10 MHz on the receiver when different saline bottles were moved to different positions along the x-axis. In previously obtained results, its shows that I/Q quadrature demodulation technique have a better phase stability performance than FFT technique. Therefore I/Q demodulation was implemented for the phase measurement in this saline test. The graph shows that the measured phase shift varied very systematically as a function along the x-axis, which also indicates that the measuring area around the sensor coils was more sensitive than in other areas.

6. Conclusion

The study has shown a preliminary characterization for our NI based MIT system. From the system performance results, it is shown that the NI-device has a capability of measuring phase differences in milli-degree ranges, provided that the detected signal remains large enough (over 20 mVp-p). Furthermore, it was noticed that the quadrature (I/Q) demodulation method offered much better measurement stability than the FFT tone measurement technique, and FFT tone measurement had a better phase linearity performance. From the saline experimental results, we found that the MIT sensors were capable of detecting low conductivity objects. Different concentrations of saline solution (i.e. different conductivities) were distinguished clearly from the amount of the phase shift perturbation observed at the receiver coil. From the results obtained in the saline test, the maximum phase shift was around 1.6 degrees, which occurred when the saline bottle was closest to the transmitter or receiver. These encouraging results suggest that it will be possible to create a functional MIT multi-channel system using NI hardware for biomedical applications.

Reference

1. Griffiths H, 2001, Magnetic induction tomography, *Meas. Sci. Technol.* 12, 1126
2. X. Ma, A. J. Peyton, S. R. Higson, A. Lyons and S. J. Dickinson, "Hardware and software design for an electromagnetic induction tomography (EMT) system for high contrast metal process applications", Meas. Sci. Technol., vol. 17, pp. 111-118, 2006.
3. S. Watson, "Instrumentation for low-conductivity Magnetic Induction Tomography", PhD thesis, University of Glamorgan, United Kingdom, 2009.
4. H. Scharfetter, H. K. Lackner, and J. Rosell, "Magnetic induction tomography: Hardware for multi-frequency in biological tissue," Physiological Measurement, vol. Vol. 22, No. 1, pp. pages 131–146, Feb 2001

OpenMEEG for calibrating the conductivity of nested compartment models

Maureen Clerc[1], Jean-Michel Badier[2], Emmanuel Olivi[1],
Alexandre Gramfort[1,3], Théodore Papadopoulo[1]

[1] Athena Project Team, INRIA Sophia Antipolis France
[2] INSERM U751, La Timone, Marseille, France
[3] Parietal Project Team, INRIA Saclay, France

March 15, 2011

1 Introduction

Bioelectric phenomena at low temporal frequency can be described by the electrostatic Poisson equation

$$\text{div } \sigma \nabla V = \text{div } J^p$$

where J^p are primary current sources and $\sigma \nabla V$ the Ohmic current. Appropriate boundary conditions (b.c.) must be set on the domain boundary, typically imposing the potential (Dirichlet b.c.) or the normal current (Neumann b.c.).

Solving this electrostatics equation for the electric potential is a problem common to different fields such as electroencephalograhy (EEG), electrocardiography (ECG), functional electrical stimulation. The main difficulty of the model concerns the conductivity field, which is not homogeneous, and whose values depend on the tissue type. Although the tissue structure can be revealed by imaging methods such as CT, Magnetic Resonance Imaging, diffusion Magnetic Resonance Imaging, conductivity values must nevertheless be assigned to the different tissues. In order to calibrate conductivity, injected current Electrical Impedance Tomography (EIT) can be used: it consists of injecting current on the outer boundary, and measuring the associated electric potential.

This article presents the usage of OpenMEEG for this problem. The thrust of OpenMEEG is to propose accurate forward problems, in several instances, including electro- and magneto-encephalography (EEG-MEG) and Electrical Impedance Tomography (EIT). OpenMEEG allows to compute the electric potential and magnetic fields due to boundary current injection or to sources within the compartments.
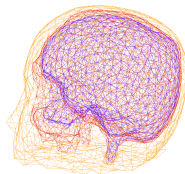
Figure 1: Nested compartment model of a head.

After presenting the injected current EIT forward model and its solution by the symmetric Boundary Element Method in section 2, we present its implementation and solution by OpenMEEG in section 3. A companion article in this conference presents a clinical study currently being conducted with this methodology.

2 Forward EIT for nested compartment model

This article considers EIT for calibrating the conductivity of nested compartment models, and focusses on a head model for electroencephalography. A current j is applied on the scalp, and the primary current sources within the head are considered negligible, hence the potential follows

$$\mathrm{d}iv\ \sigma\nabla V = 0 \text{ within the volume}$$
$$\sigma\frac{\partial V}{\partial n} = j \text{ on the outer boundary.}$$

As depicted in figure 1, the compartments are described through the interfaces between the tissues. In this paper we consider a three-layer head model. Conductivities of the brain+CSF[1], the skull, and the scalp are respectively denoted σ_1, σ_2 and σ_3. The surfaces enclosing these homogeneous conductivity regions are denoted S_1 (inner skull boundary), S_2 (skull-scalp interface) and S_3 (scalp-air interface).

In models where the conductivity is constant within each compartment, the Boundary Element Method (BEM) can be used. Among the several BEMs that have been proposed, we have selected the symmetric Boundary Element Method for its superior accuracy [3], notably in cases where there are strong conductivity ratios between neighboring compartments. The symmetric BEM considers as unknown variables both the potential and the normal current of each interface. The boundary condition $\sigma\frac{\partial V}{\partial n} = j$ on the outer boundary is thus readily handled.

Denoting V_i, resp. $p_i = (\sigma\partial_n V)_i$ the restriction to surface S_i of the potential, resp. the normal current, the

$$A_\sigma \begin{bmatrix} V_1 & V_2 & V_3 & p_1 & p_2 \end{bmatrix}^T = B_\sigma \tag{1}$$

---

[1] cerebro-spinal fluid

where A_σ is a matrix and B_σ a source term depending linearly on the injected current j. The matrix A_σ is symmetric (whence the denomination of "symmetric BEM") and has a block structure

$$A_\sigma = \begin{pmatrix} N_\sigma & D^T \\ D & S_\sigma \end{pmatrix} \tag{2}$$

with

$$N_\sigma = \begin{bmatrix} (\sigma_1 + \sigma_2)N_{11} & -\sigma_2 N_{12} & 0 \\ -\sigma_2 N_{21} & (\sigma_2 + \sigma_3)N_{22} & -\sigma_3 N_{23} \\ 0 & -\sigma_3 N_{32} & \sigma_3 N_{33} \end{bmatrix}$$

$$S_\sigma = \begin{bmatrix} (\sigma_1^{-1} + \sigma_2^{-1})S_{11} & \sigma_2^{-1}S_{12} \\ \sigma_2^{-1}S_{21} & (\sigma_2^{-1} + \sigma_3^{-1})S_{22} \end{bmatrix}$$

$$D = \begin{bmatrix} -2D_{11} & D_{12} & 0 \\ D_{21} & -2D_{22} & 0 \end{bmatrix}$$

Note that the dependency of A_σ on σ has a simple structure: the blocks N_{ij}, S_{ij} and D_{ij} only depend on the geometric structure of the meshes, and not on the conductivities. Thus A_σ is of the form:

$$A_\sigma = \tilde{D} + \sum \sigma_i^{-1}\tilde{S}_i + \sum \sigma_i \tilde{N}_i$$

The source term B_σ is equal to

$$B_\sigma = \begin{bmatrix} 0 & -D_{23}^T j & D_{33}^T j - \dfrac{j}{2} & 0 & \sigma_3^{-1}S_{23}j \end{bmatrix}^T . \tag{3}$$

The problem is discretized using mixed P1/P0 boundary elements. The unknowns $[V_1 \; V_2 \; V_3 \; p_1 \; p_2]^T$ are discretized using $P1$ (continuous, piecewise linear) elements for the potential and $P0$ (piecewise constant) elements for the normal current. The injection current j is thus represented with $P0$ boundary elements on the scalp, i.e. a constant value on the two triangles representing the injection and extraction electrodes and zero elsewhere.

3 OpenMEEG implementation

The OpenMEEG software package makes the symmetric BEM readily available and usable by bioelectrostatic researchers. We here give a brief summary its main features, but for a longer presentation of the OpenMEEG environment the interested reader may refer to the recently published article [2].

OpenMEEG is a free, opensource, C++ library, distributed under the opensource license CeCILL-B, intended to give users the freedom to modify and redistribute the software. OpenMEEG can be invoked either via a command line interface or via higher-level languages (Matlab, Python).

The matrices A_σ and B_σ are assembled by invoking the commands `om_assemble` with the options `-HeadMat` and `-EITSourceMat`, respectively. A full flowchart of OpenMEEG routines is displayed in figure 2. For EIT, only the top (green) boxes of the flowchart need to be considered.
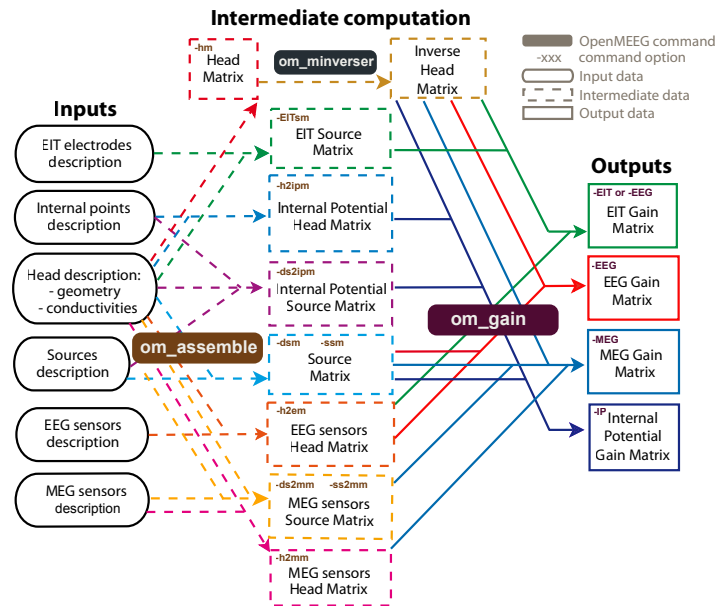
Figure 2: Flowchart of the OpenMEEG routines. For EIT, consider the top (green) boxes.

4 Conclusion

In practise, calibrating conductivities with EIT requires to compute the EIT forward problem for different conductivity values and to find the conductivity that best explains the measured data. Concerning head conductivity, it has been showed that the scalp/skull conductivity ratio may be calibrated using injected current EIT [4]. A companion paper in this conference presents an ongoing clinical study on this topic [1], using OpenMEEG.

References

[1] Maureen Clerc, Laurent Koessler, Jean-Michel Badier, and Martine Gavaret. In vivo scalp-to-skull conductivity ratio calibration: an EIT study. In *EIT conference*, 2011.

[2] Alexandre Gramfort, Théodore Papadopoulo, Emmanuel Olivi, and Maureen Clerc. Openmeeg: opensource software for quasistatic bioelectromagnetics. *BioMedical Engineering OnLine*, 9(45), September 2010.

[3] Jan Kybic, Maureen Clerc, Toufic Abboud, Olivier Faugeras, Renaud Keriven, and Théodore Papadopoulo. A common formalism for the integral formulations of the forward eeg problem. *IEEE Transactions on Medical Imaging*, 24:12–28, January 2005.

[4] S. Vallaghé and M. Clerc. A global sensitivity analysis of three and four-layer eeg conductivity models. *IEEE Transactions on Biomedical Engineering*, 56(4):988–995, April 2009.

Evaluation of the UCH Mk2.5 Multi-Frequency EIT system for imaging stroke in liquid filled anatomically realistic tanks.

B. Packham[1], H. Koo[1], S. Ahn[2], S. C. Jun[2] and D. S. Holder[1].

1. Department of Medical Physics and Bioengineering, University College London
2. Department of Information and Communications, Gwangju Institue of Science and Technology, Korea

1. Introduction

Imaging of acute stroke might be possible using Electrical Impedance Tomography (EIT), as ischaemic cortical tissue, blood and normal cortical tissue have different conductivity spectra [1]. This could be used in ambulances or remote diagnostic centres to permit early utilization of life-saving thrombolytic (clot-dissolving) agents, that can substantially improve the outcome of patients [2]. Time difference imaging is not possible in acute stroke, because patients present to medical services after the onset of symptoms. Our approach has been to apply frequency difference imaging, Multi-Frequency Electrical Impedance Tomography (MFEIT), but this is more susceptible to noise and calibration errors.

We employ a method for image reconstruction based on a sensitivity matrix generated from an anatomically realistic Finite Element Mesh of the head and an assumption of linearity. Unfortunately, images generated with this are dominated by artefacts related to substantial background changes over frequency [1]. This has led to the development of a weighted frequency difference algorithm in which there is compensation for a complex background which changes over frequency [3]. The UCH Mk2.5 employs a four electrode method in which current is serially injected through one pair of electrodes and recorded through others with a fixed gain. For empirical measurements in a human or tank, the voltages generated from differing electrode combinations are sometimes small; as noise is largely fixed, this can lead to excessively noisy channels which affect image quality unless removed by a data cleaning method [4].

The purpose of this study was to determine if acceptable MFEIT images could be obtained in an anatomically realistic tank with a linear frequency difference reconstruction algorithm. Studies were conducted in liquid filled tanks of increasing difficulty using biological test objects with complex conductivity. Secondary goals were to establish a robust method of cleaning noisy data from electrode combinations with low standing voltages and to evaluate the best reconstruction algorithm.

2. Methods.

Data was recorded with the UCH Mark 2.5 MFEIT system, a 32 channel serial injection and record system, using the four electrode method, which injected a peak current of 133 μA_{pp} at 30 frequencies between 20 Hz and 1.6 MHz [5]. Recordings were in an anatomically realistically head shaped latex tank, with 31 Ag-AgCl foil electrodes, 1cm in diameter, positioned in a modified 10-20 EEG placement system, with an additional electrode positioned at the tip of the

nose as a grounding electrode [6]. Data was collected using a spiral pattern injection protocol, "spiral_s-o", with 373 combinations and 10 data sets, taking 10 minutes overall to collect, were averaged together [7]. Images were taken of a cylinder of potato, 2.4 cm in diameter and 7cm long, in either 0.2% saline solution (conductivity of 0.2 Sm^{-1}), or a complex background prepared from cubes, 2mm in length, of carrot in 0.2% saline at 24° C $\pm$ 0.5° C. Electrode contact impedances were all < 500 Ω.

Temporal noise of the data was calculated as the standard deviation over time as a percentage of the mean over time for the real component of the voltage for each combination. Different cleaning methods were evaluated which employed elimination of real voltages from channels with a standing voltage of 0.1-1 mV and temporal noise of 0.5-10%. Data were calibrated using a single 20 frame reference recording of 0.2% saline in the 3D head shaped tank.

Implemented reconstruction algorithms assumed linearity and employed truncated singular value decomposition, using 40 singular values, of a sensitivity matrix generated using a Finite Element Mesh of the tank with 52,000 elements. 1) A time difference algorithm was used to produce the 'gold standard' images. 2) The second algorithm was a 'simple frequency difference' (FD) algorithm, which expresses boundary voltages as a percentage difference of a reference frequency, 80 Hz. 3) A weighted frequency difference (WFD) algorithm was also implemented.

3. Results

3.1 Boundary Voltage Processing

Temporal noise exponentially increased with decreasing boundary voltage (Fig. 1), showing noise to be largely fixed random noise.

Figure 1. Boundary Voltage Processing: Noise Analysis.

Shown is the temporal noise for combinations in the baseline and perturbation recordings made in the 3D head tank with a carrot background. Noise is plotted against the combinations' boundary voltage showing that the noise is inversely related to boundary voltage amplitude
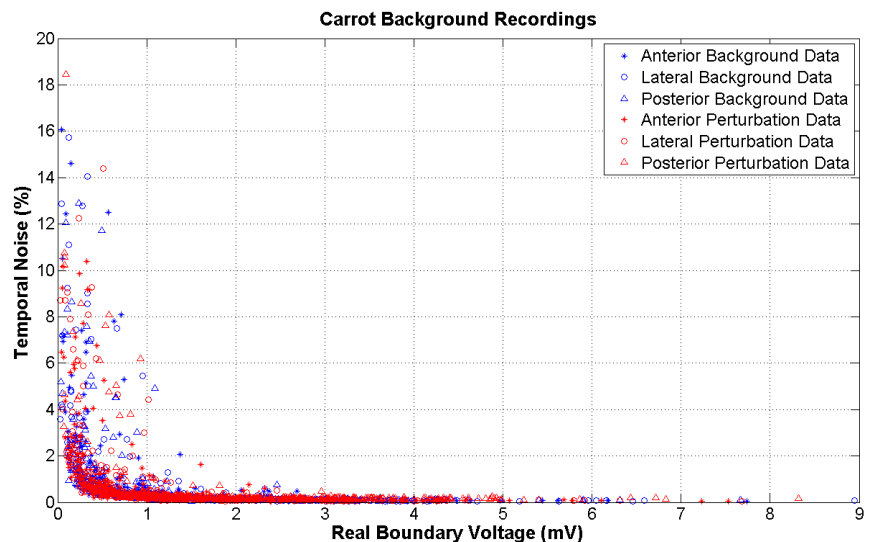
Without data cleaning, images were noisy and of poor quality. On the other hand, image quality also degraded with too strict cleaning thresholds as too much data was removed (Fig. 2). Optimal quality was obtained with the exclusion of channels with temporal noise > 1% and standing voltages < 0.1 mV, which was used for the final images.
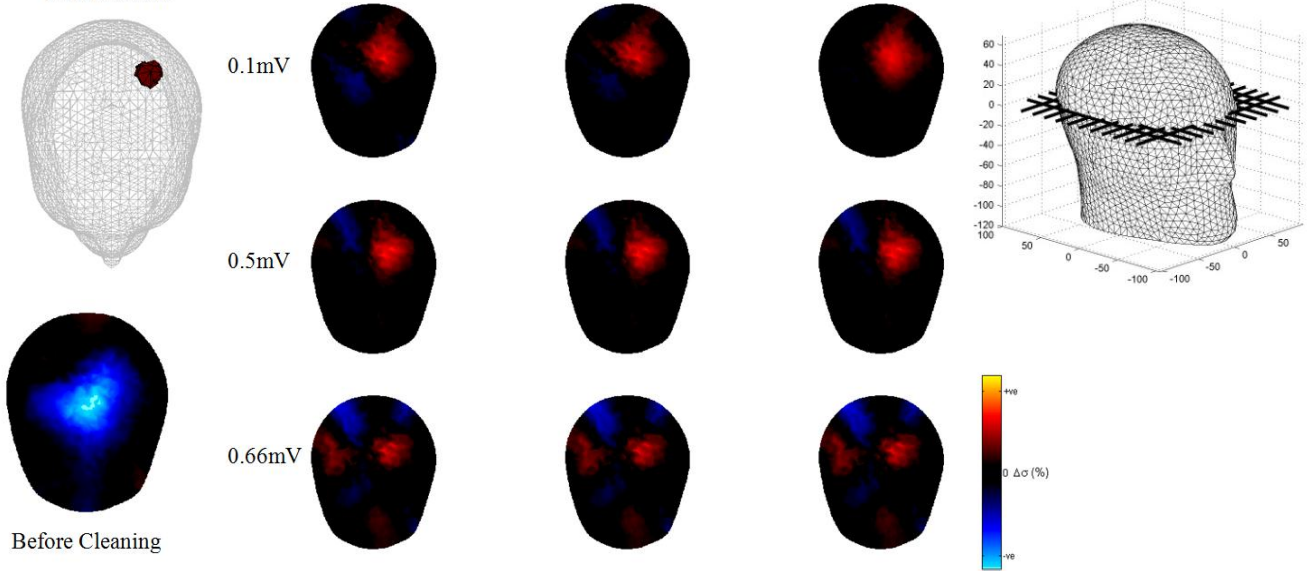
Figure 2. Boundary Voltage Processing: Image Reconstruction. Shown are the effects on image quality for combined cleaning methods at differing thresholds. Data was collected with a carrot background and the perturbation placed in the posterior of the tank. All images are rasterised to the plane shown (top right subplot), which is 0 on the z-plane, generated using the WFD algorithm and with 40 singular values

3.1 Reconstructed images

With the WFD algorithm, high quality images were obtained with both backgrounds in which the test object perturbation corresponded closely to that in time difference images. However, image quality from the anterior position, where there was less electrode coverage with the spiral protocol, was less than that for other test object positions (Fig. 3).

Images reconstructed with the simple FD algorithm and the complex background did not correspond to those obtained with the time difference method.
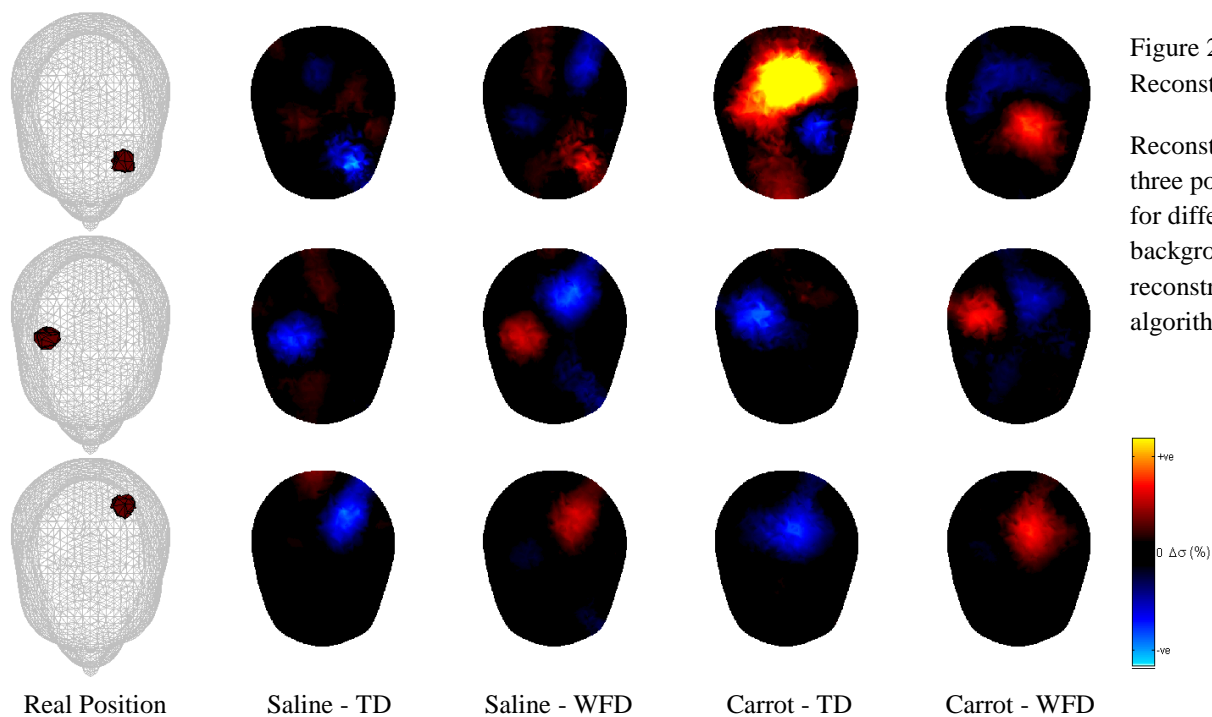

Figure 2. Image Reconstruction.

Reconstructions at all three positions (rows) for differing backgrounds and reconstruction algorithms (columns).

Real Position   Saline - TD   Saline - WFD   Carrot - TD   Carrot - WFD

4. Discussion

In terms of technical concerns, about 10-45% of electrode combinations had to be removed due to low signal to noise ratio (SNR). A future modelling study is planned to ensure that removal of these combinations does not introduce errors into the reconstruction. The removal of such a large number of combinations might be addressed through utilising a system with a variable gain, or by altering the spiral protocol to minimise the prevalence of these small boundary voltages and therefore combinations with low SNR, possibly through implementing an adaptive protocol. However, neither option is likely to be an absolute solution in human recordings, as isopotential lines will vary unpredictably in naïve subjects and so some combinations may always be of low voltage. The image quality of the anterior placed perturbation was less than for the other two positions; this is probably due to the lower electrode density in this region.

These findings are encouraging to the view that this approach could be used to produce frequency difference images in the adult head with scalp electrodes. However, no skull was employed in these studies. Work in progress is to extend this work with a skull in place and to evaluate image quality quantitatively. The cleaning criteria and choice of WFD algorithm are currently being employed in clinical studies.

References

[1] A. Romsauerova, A. McEwan, L. Horesh, R. Yerworth, R. H. Bayford, and D. S. Holder, "Multi-frequency electrical impedance tomography (EIT) of the adult human head: initial findings in brain tumours, arteriovenous malformations and chronic stroke, development of an analysis method and calibration," *Physiological Measurement*, vol. 27, no. 5, p. S147-S161, May2006.

[2] A. Stemer and P. Lyden, "Evolution of the Thrombolytic Treatment Window for Acute Ischemic Stroke," *Current Neurology and Neuroscience Reports*, vol. 10, no. 1, pp. 29-33, Jan.2010.

[3] S. C. Jun, J. Kuen, J. Lee, E. J. Woo, D. Holder, and J. K. Seo, "Frequency-difference EIT (fdEIT) using weighted difference and equivalent homogeneous admittivity: validation by simulation and tank experiment," *Physiological Measurement*, vol. 30, no. 10, pp. 1087-1099, Oct.2009.

[4] L. Fabrizi, A. McEwan, T. Oh, E. J. Woo, and D. S. Holder, "A comparison of two EIT systems suitable for imaging impedance changes in epilepsy," *Physiological Measurement*, vol. 30, no. 6, p. S103-S120, June2009.

[5] A. McEwan, A. Romsauerova, R. Yerworth, L. Horesh, R. Bayford, and D. Holder, "Design and calibration of a compact multi-frequency EIT system for acute stroke imaging," *Physiological Measurement*, vol. 27, no. 5, p. S199-S210, May2006.

[6] A. T. Tidswell, A. Gibson, R. H. Bayford, and D. S. Holder, "Validation of a 3D reconstruction algorithm for EIT of human brain function in a realistic head-shaped tank," *Physiological Measurement*, vol. 22, no. 1, pp. 177-185, Feb.2001.

[7] L. Fabrizi, A. McEwan, T. Oh, E. J. Woo, and D. S. Holder, "An electrode addressing protocol for imaging brain function with electrical impedance tomography using a 16-channel semi-parallel system," *Physiological Measurement*, vol. 30, no. 6, p. S85-S101, June2009.

In vivo scalp-to-skull conductivity ratio calibration: an EIT study

Maureen Clerc[1], Laurent Koessler[2,3], Jean-Michel Badier[2], Martine Gavaret[2]

[1] Athena Project Team, INRIA Sophia Antipolis France
[2] INSERM U751, Université de la Méditerranée, Marseille, France
[3] CRAN, Nancy Université, France

March 15, 2011

1   Introduction

This work concerns conductivity calibration in the context of high-density EEG pre-surgical epileptic exploration. High-density EEG measurements may be used to solve the inverse problem of source localization, in order to localize the foci of the epileptic activity within the brain. The solution of the inverse problem relies on a forward problem, linking sources to measurements. In turn, this forward problem is dependent on the conductivity of the head tissues.

Prior work has shown that the scalp-to-skull conductivity ratio is a sensitive parameter for source localization, because it has an influence on the depth of the estimated dipoles [6]. There have been several studies demonstrating the feasibility of injected-current Electrical Impedance Tomography to calibrate the scalp-to-skull conductivity ratio [5, 4]. This study we perform a clinical assessment of the use of injected current Electrical Impedance Tomography to calibrate the scalp-to-skull conductivity ratio.

2   Materials and Methods

EIT data were recorded on a 64-channel cap from 20 epileptic patients, who gave informed consent[1]. The time-course of the injected current consisted of one period of a sine wave, at three frequencies (15 Hz, 60 Hz and 150 Hz). Thirty electrode pairs were selected for current injection/extraction (see diagram in Figure 1).

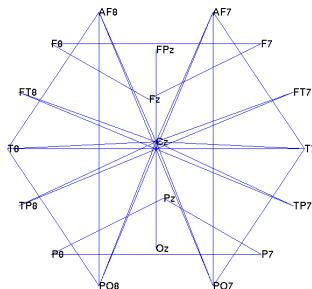[1]Ethical-committee approved study IDRCB-2008-A00434-51.

Figure 1: Thirty electrode couples used for current injection and extraction.

Magnetic Resonance images (T1) of the patients were segmented into three regions (brain+CSF, skull and scalp) and the corresponding three interfaces (inner skull, outer skull, outer scalp) were meshed. These interfaces were provided to OpenMEEG to solve the forward EIT problem (see companion paper [2] in this conference).

For each tested conductivity ratio $r = \sigma_{scalp}/\sigma_{skull}$, and for each electrode pair p the simulated potential $V_{sim}(r, p)$ and measured potential $V_m(p)$ were compared using the Relative Difference Measure (RDM) as a goodness-of-fit:

$$RDM(r, p) = \left\| \frac{V_{sim}(r,p)}{\|V_{sim}(r,p)\|} - \frac{V_m(p)}{\|V_m(p)\|} \right\| .$$

where the norm $\|V\|$ represents the discrete ℓ^2 norm over the set of 64 electrodes, excepting the pair of electrodes used for injection, at which the potential simulation and measurement are less reliable and might corrupt the study. The type of fit provided by the RDM is purely topographic: because of the amplitude normalization, the RDM is immune to the magnitudes of the potential distributions, but compares their topographic spread over the electrodes. The RDM was selected to measure goodness-of-fit because it allows to localize brain activity, and because it is tolerant to uncertainty on the injected current amplitude.

RDM curves were thus obtained, for each electrode pair p, by varying the conductivity ratio. Prior simulations and in vivo studies in this field show that if the model and the data correspond, the RDM curves should have a specific shape, with a well-defined minimum corresponding to the optimal conductivity ratio [1]. For each patient, the electrode pairs were separated in two groups: the electrode pairs whose RDM did not display a minimum within the range of conductivity ratios were set apart as pairs for which the model was ill-fitting. For the remaining curves, the optimal conductivity ratio r^* was computed, and the value of the RDM at this optimal conductivity ratio was stored.
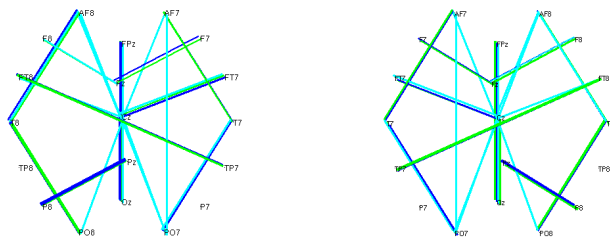
2

Figure 2: Electrode pairs separated in two groups: on the left, pairs whose RDM that display a minimum within the explored conductivity range, and on the right, ill-fitting pairs (for at least one of the stimulation frequencies considered). The colors in the left image code for the stimulation frequencies: 15 Hz in cyan, 60 Hz in green, 150 Hz in blue.

3 Results

For space limitations, we here present results on a single subject. In Figure 2 we display the electrode pairs separated in two groups as explained above. It can be noted that pairs of electrodes that are far apart are generally in the "ill-fitting" group, meaning that the homogeneous skull model is not a good model for such electrode pairs.

Figure 3 displays electrode pairs whose RDM has a minimum in the conductivity range, along with the optimal conductivity ratio on the z-axis. One can note a high variability of the optimal conductivity ratio according to electrode pair, that had not previously been reported in similar studies. A variability of conductivity according to stimulation frequency (color-coded as 15 Hz in cyan, 60 Hz in green, 150 Hz in blue) can also be observed.

According to this preliminary study, using injected-current EIT for calibrating the scalp-to-skull conductivity ratio may not be straightforward, because a unique conductivity ratio does not seem to fit the model. This can be related to recent studies on skull conductivity that stress the necessity of considering it as a composite medium with different conductivities [3].

References

[1] M. Clerc, J.-M. Badier, G. Adde, J. Kybic, and T. Papadopoulo. Boundary element formulation for electrical impedance tomography. In *ESAIM: Proceedings*, volume 14, pages 63–71. EDP Sciences, September 2005.

[2] Maureen Clerc, Jean-Michel Badier, Emmanuel Olivi, Alexandre Gramfort, and Théodore Papadopoulo. Openmeeg for calibrating the conductivity of nested compartment models. In *EIT conference*, 2011.
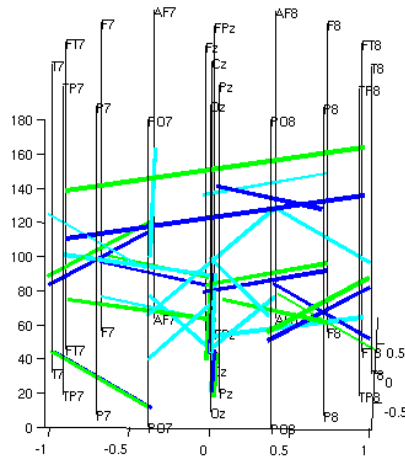
Figure 3: A 3D view of the electrode pairs represented in Figure 2, in which the optimal conductivity ratio is represented along the vertical axis.

[3] Moritz Dannhauer, Benjamin Lanfer, Carsten H. Wolters, and Thomas Knösche. Modeling of the human skull in eeg source analysis. *Human Brain Mapping*, 2010. doi: 10.1002/hbm.21114.

[4] Sonia I. Gonçalves, Jan C. de Munck, Jeroen P.A. Verbunt, Fetsje Bijma, Rob M. Heethaar, and Fernando Lopes da Silva. In vivo measurement of the brain and skull resistivities using an EIT-based method and realistic models for the head. *IEEE Transactions on Biomedical Engineering*, 50(6), 2003.

[5] T.F. Oostendorp, J. Delbeke, and D.F. Stegeman. The conductivity of the human skull: Results of *in vivo* and *in vitro* measurements. *IEEE Transactions on Biomedical Engineering*, 47(11):1487–1492, December 2000.

[6] S. Vallaghé and M. Clerc. A global sensitivity analysis of three and four-layer eeg conductivity models. *IEEE Transactions on Biomedical Engineering*, 56(4):988–995, April 2009.

FE modelling and meshing of patient-specific anatomical models

P. YOUNG[1,2], F. HERMANS[3], R.M. HEETHAAR[3], A. DATTA[4] and M. BIKSON[4]

[1] School of Engineering, Mathematics and Physical Sciences, University of Exeter, Exeter, UK
[2] Simpleware Ltd, Exeter, UK
[3] VU University Medical Center, Amsterdam, The Netherlands
[4] Department of Biomedical Engineering, The City College of the CUNY, New York, USA

1 Introduction

There has been increasing interest in the generation of models appropriate for computational modelling from imaging modalities such as MRI and CT. Although a wide range of mesh generation techniques are available, these on the whole have not been developed for meshing from 3D imaging data. The paper will focus on techniques specific to image-based meshing, and will also discuss new tools improving the interface with commercial CAD, FEA and CFD packages. A number of examples, including head and thorax models, will be presented.

2 Methods

Most meshing techniques available in commercial and research codes rely on using intermediate CAD (Computer Aided Design) representations of the surface of objects of interest provided either as higher order descriptions or surface tessellations [1]. These techniques are often non-conforming with gaps or overlaps at interfaces where two or more structures meet.

The 'image-based approach' presented by the authors [2], on the contrary, is tailored to meshing from 3D imaging data, and does not decouple the surface creation from the volume meshing stage. Modelling complex topologies with possibly hundreds of disconnected domains via a 'CAD approach' is virtually intractable. For the same problem, image-based meshing is by contrast remarkably straightforward, robust, accurate and efficient. Meshes can be generated automatically and exhibit image-based accuracy with domain boundaries of the finite element model lying exactly on the iso-surfaces, taking into account partial volume effects and providing sub-voxel accuracy. The presented technique is also topology and volume preserving, avoiding loss or gain of volume.

An example of the complexity of meshes than can be generated with minimal user interaction from the segmented data is shown in Figure 1. This head model has 15 regions of interest that have been meshed to a high quality and with conformal interfaces i.e. matching nodes and elements which eliminates the need for contact constraints.
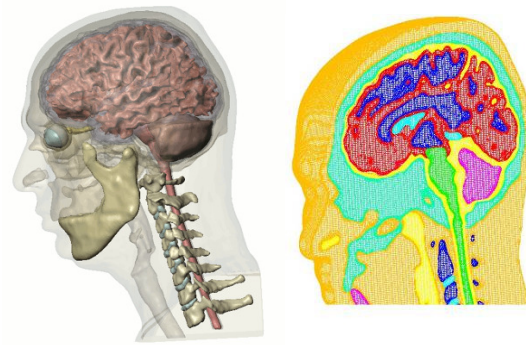

Figure 1 Multipart mesh of the head from MRI

The framework also offers the possibility to generate multipart meshes using multiple meshing algorithms. Topologically complex volumes are meshed using conservative and robust algorithms whereas simpler regions can benefit from more classic tetrahedralisation methods producing a higher level of mesh density control. The result is a set of tools with a high level of robustness that benefit from flexible meshing techniques where possible.

3 FE Simulation of EIT through the Human Thorax

This study uses MRI data from a healthy 25 year old male to build a realistic human torso model for FE simulation of EIT and IC.
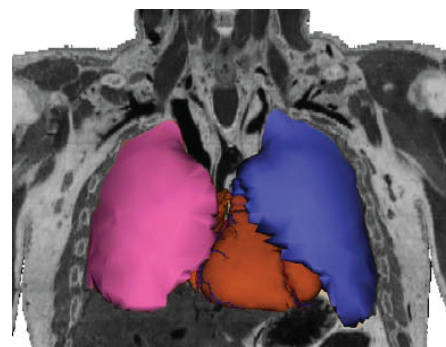

Figure 2 Segmentation of heart and lungs from MRI data

Four models were generated from high resolution MRI data recorded for both end-inspiration and end-expiration conditions. The images were segmented in Simpleware ScanIP generating

models of the torso, heart and lungs (c.f. Figure 2). In addition, patches relating to electrode placement were introduced around the surface of the torso model. Each of the generated geometries were then converted into high quality tetrahedral meshes using Simpleware ScanIP+FE, leading to models containing approximately 350,000 elements.

The models were then exported directly into COMSOL Multiphysics® with each having part-specific material properties assigned. In COMSOL the models were set up by creating boundary conditions, current injection points and sub-domain settings. The skin was defined as an 'insulating' boundary with internal conditions set to 'continuity'. Simulations were run to replicate the IC and EIT tests, and streamline plots related to local current density were produced to visualise the electrical current distribution through the thorax for different electrode setups and expiratory states. These simulations show how clinical impedance tests can be modelled, giving an insight into current distribution through the human body. Figure 3, for example, shows the streamlines flowing parallel to the aorta in a four electrode configuration.
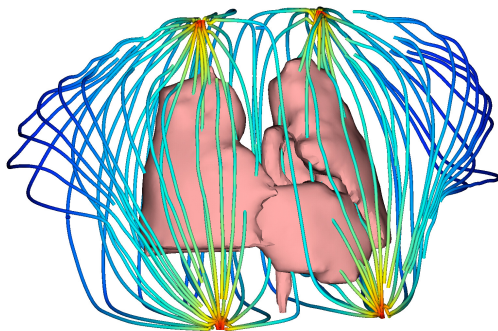

Figure 3 FEM solution of the four current electrode setup

4 FE Analysis of Transcranial Current Stimulation in the Human Head

A critical factor for Transcranial Current Stimulation efficacy and safety is the spatial focality of induced neuronal modulation. One objective of this research is to study the spatial focality of a 4 x 1 concentric-ring electrode configuration [3] by using high-resolution MRI-based finite element models of the human head.

MRI images of the head were segmented in ScanIP into compartments representing the brain tissue, CSF, skull, muscle, fatty tissue, eyes, blood vessels, and the scalp. The stimulation disks were imported as CAD models and two models were generated: one for a distant bipolar configuration, and another using a 4 x 1 concentric-ring electrode configuration which consists of four disks arranged in circular fashion around one centre electrode (c.f. Figure 4).
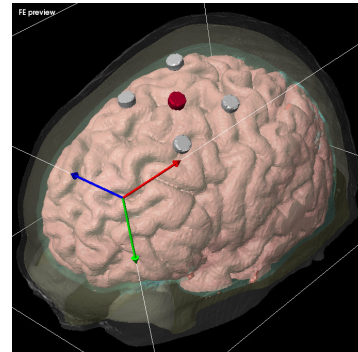

Figure 4 4 x 1 ring configuration in the segmented brain model

From the segmented data, the corresponding volumetric meshes were generated and exported to COMSOL Multiphysics® for calculation. The models comprised of around 10 million tetrahedral elements with ~14 million degrees of freedom each.
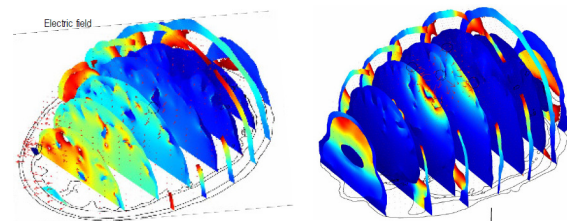

Figure 5 FEM of the Distant bipolar configuration (left) and the 4 x 1 ring configuration (right)

The results in Figure 5 show that the novel 4 x 1 ring configuration leads to significant increases in focality compared to commonly used distant bipolar configurations. Superficial cortical regions can be selectively targeted using a 4 x 1 system.

5 Conclusions

The ability to automatically convert any 3D image dataset into high quality meshes is becoming the new modus operandi for anatomical analysis. New tools for image-based modelling have been demonstrated, improving the ease of generating meshes for computational mechanics and opening up areas of research that would not be possible otherwise.

References

[1] J.R. Cebral et al., From Medical Images to Anatomically Accurate Finite Element Grids. *Int. J. Num. Meth. Eng.*, **51**, 985-1008.

[2] P.G. Young et al., An efficient approach to converting 3D image data into highly accurate computational models. *Phil Roy Soc A*, **366**, 3155-3173.

[3] A. Datta et al., Transcranial current stimulation focality using disc and ring electrode configurations: FEM analysis. *J. Neural Engg.*, **5**, 163-174.

Preliminary observations with fEITER data under auditory stimulation

H McCann[1]**, S T Ahsan**[1]**, J L Davidson**[1]**, R L Robinson**[1]**, P Wright**[1]**, A Bryan**[2]**,
B J Pollard**[2]**, T Quraishi**[2] **and C J D Pomfrett**[2,3]

[1] School of Electrical and Electronic Engineering, University of Manchester, UK
[2] Division of Clinical and Scientific Services, Department of Anaesthesia, CMFT
[3] School of Biomedicine, University of Manchester, UK

E-mail: h.mccann@manchester.ac.uk

Abstract. We discuss preliminary data taken with human subjects under auditory stimulation, using the new EIT-based system fEITER (*functional Electrical Impedance Tomography of Evoked Responses*). These data were recorded during an experimental process intended to identify optimal fEITER stimuli for clinical trials that are still underway. The dataset reported here is extremely limited in the statistical sense, with only two subjects. Extreme auditory stimulus elicits apparently large EIT voltage changes, as high as 1 mV with the configuration reported here, and containing fast components (~ 100 ms) as well as components that persist for many seconds. Examination of these single-event responses both at the level of the raw voltage changes and after image reconstruction, suggests that they may be neurophysiological in nature. With more typical auditory stimuli of a much more controlled nature, repeatable single-event EIT voltage responses are observed. In this case, maximal voltage changes observed are about 70 µV at typically 200 ms after stimulus; given that system noise is around 10 µV (rms) and that the rheoencephalographic (REG) signal is of order 50 µV (peak-to-peak), image reconstruction of these single-event signals is very challenging.

1. Introduction

We have reported the design and electronic performance of the fEITER system, and some preliminary data, at two previous conferences in this series [1, 2]. The 32-electrode (Fig. 1) fEITER instrument captures EIT data at 100 frames per second (fps), presently using a fixed-frequency sinusoidal current excitation (10 kHz, 1 mA pk-pk) [3] in 20 near-diametric current patterns (CPs). The amplitude and phase of voltage waveforms between nearest-neighbour electrodes are measured using digital phase-sensitive demodulation. With simultaneous voltage measurements during each CP, each EIT frame consists of 546 measurements. Their short-term noise level, expressed as a standard deviation, is typically 7 - 10 µV, which is to be compared with highest EIT voltage values of about 70 mV in each frame. The fEITER system includes an
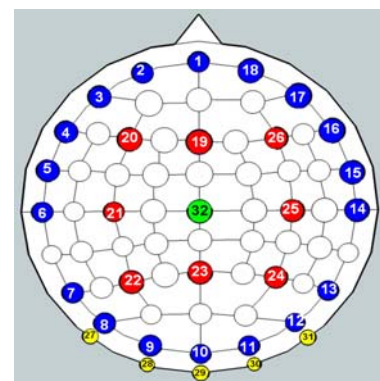
**Figure 1: Arrangement of the 32 scalp-mounted Covidien *Zipprep*™ electrodes in the tests reported here.**

integrated commercial (CED μ1401) stimulus generation and sequencing system that controls auditory and visual stimulation devices, and is currently being used in an MHRA-approved clinical trial at Manchester Royal Infirmary.

2. Methodology

EIT auditory stimulus data were captured continuously in 1-minute blocks before, during and after stimulus presentations, with the subjects blindfolded. Subject A has a profound hearing deficit in the left ear, at approximately 55 dB down over the entire audible spectrum; this is normally corrected by using a hearing aid which was not used in the tests described here. Subject B has a minor hearing deficit in the right ear due to perforation of the eardrum, for which no corrective prosthetic is used.

Two types of auditory stimulus were administered to each subject: A gross stimulus in the form of a sharp bang (release of a party-popper at 3m proximity), and controlled stimuli presented binaurally using inner-ear headphones. For the former, subject A was informed only that there would be a surprise stimulus, whereas subject B was informed about the nature of it and had heard it before the experiment; these conditions conform well to those necessary to evoke the auditory startle reflex (ASR) which is a measure of the brainstem response to an unexpected auditory stimulus [4]. The controlled-stimulus paradigm consisted of two sequences of 11 tone bursts, administered over a 1-minute period. The 2.5 kHz tone bursts were each of 50 ms duration and pseudo-randomly spaced, and they increased in intensity over the range 73 - 87 dB SPL during each sequence of 11 bursts. All controlled auditory tests were carried out with and without a "white noise" auditory background supplied by headphones that fully covered each ear. Except for the gross stimuli administered to subject A, the time of each individual stimulus was temporally encoded by an event marker in the fEITER output data.

Forward calculations were performed in EIDORS 3D [5], using a 7-tissue head model [6], with a total of 53,336 tetrahedral elements, and with the skull conductivity (σ_s) set at 0.05 S/m [7]. Image reconstruction was carried out on a sub-set region of 24,465 elements comprising of the grey and white matter and CSF using an SVD algorithm for each 10 ms frame with respect to an initial reference interval. Figure 2 shows an example frame of EIT voltage measurements under no-stimulus conditions. Despite using only a generic head model, the measurements agree well with the forward calculations. However, since the skull conductivity value mainly affects the maximum EIT values obtained by forward calculation, it can be seen clearly that there is scope to optimize σ_s further.
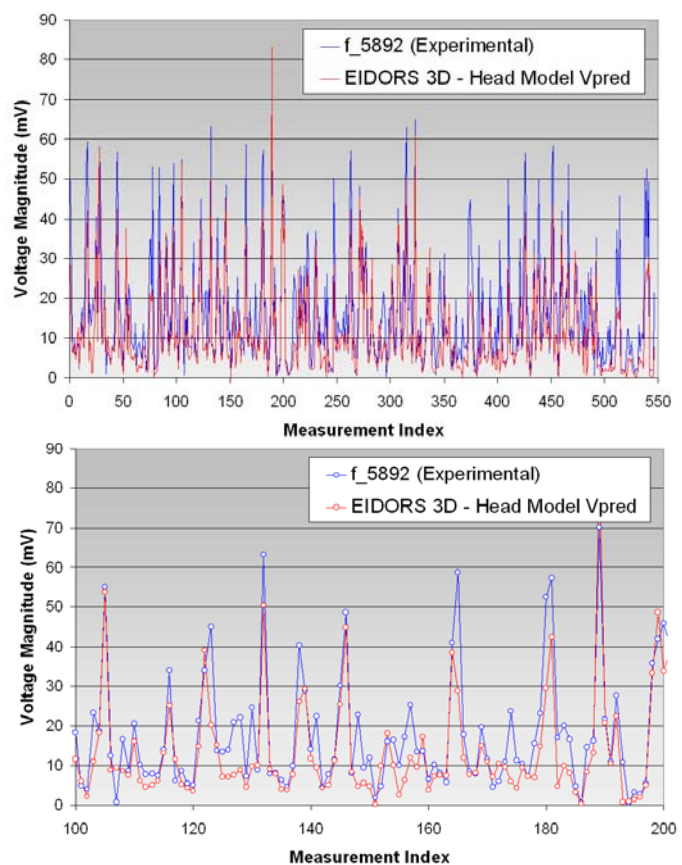

Figure 2: EIT voltages measured on the scalp, compared with forward calculations based on a generic head model, for a full frame of data (upper) and a part of the frame (lower).

3. Results

In response to gross auditory stimulus, transient EIT voltage changes for both subjects show some effects in the order of 1 mV. The fastest changes (from approx. 80 ms after onset of stimulus) are observed on the frontal regions of the head. Large changes also occur on the rear approx. 500 ms later. The earliest changes at scalp locations near those corresponding to the auditory cortices occur at approx. 100 ms after the start of stimulus. Subject B was exposed to 8 party-popper events over a period of 42 minutes, and showed voltage responses that are broadly left-right (L-R) symmetric. The measured EIT voltage responses show clear evidence of habituation. Figure 3 shows the EIT voltage for approx. 10 seconds after exposure 3, at symmetric locations near left and right auditory cortices. The observation of short-term (< 1 sec, ~ 100 μV) and long-term (several sec, ~ 200+ μV) responses in the EIT signal at these locations is characteristic of these tests.

(a)   (b)
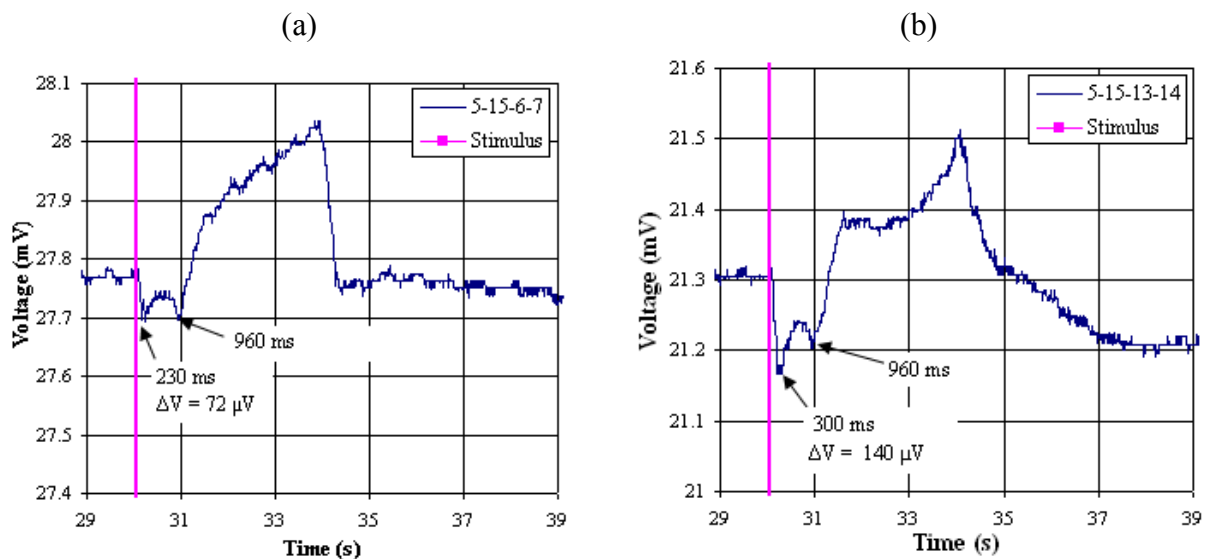
Figure 3: EIT voltage changes on gross auditory stimulus (subject B, exposure 3), measured over: (a) LHS auditory cortex, and (b) RHS auditory cortex. (Legend i-j-m-n refers to current injection between electrodes i and j, and voltage measurement between electrodes m and n.)

Subject A was exposed to three party-popper events over a period of a few minutes, but two of them were separated by only about 2 seconds. The EIT voltage response of subject A is grossly L-R asymmetrical: signals observed near the LHS auditory cortex are very large, approx. 1.2 mV for 6-14-21-22, whereas the signals at the symmetrical RHS locations are much smaller, in the case of 6-14-24-25 being barely visible above the signal variation due to the REG waveform, and in another case (21-25-14-15) being reduced by over 50% relative to its symmetric counterpart. This observation corresponds with the known asymmetry of the subject's hearing, and allowing for contralateral neural processing. EIT responses near the auditory cortices for both subjects show features resembling, in latency and in relative form, the well-established P1-N1-P2 complex observed in EEG monitoring of auditory evoked potentials [8]. For these tests, the large EIT voltage changes allow reconstruction of images of conductivity change due to stimulus. An example image is shown in Figure 4, where there appears to be substantial activation in the cerebellum, linked to brain stem activity.

In the controlled auditory tests, both subjects showed repeatable EIT responses to individual stimuli, irrespective of the presence of white noise. Again, the response of subject A was grossly L-R asymmetric, and subject B was broadly L-R symmetric. The short-term responses (< 1 sec) show maximum values of about 80 μV at approx. 200 ms after stimulus. Figure 5 shows the voltage changes observed in the maximum response case recorded from subject A.

The relationships of the measurement signatures shown are characteristic of the stimulus. The frontal signal is fastest to both rise and fall, whilst the rear shows virtually no response. It is remarkable that the three left-hand-side measurements show such large differences in the form of response from sites that are very close to each other.

(a)   (b)
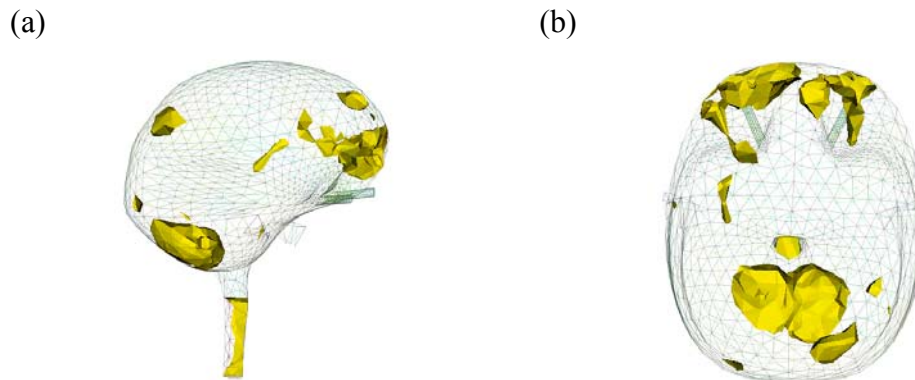
Figure 4: Isosurfaces of 3D reconstructions of conductivity change at 800 ms after gross auditory stimulus: (a) elevation view, and (b) plan view (subject A).

4. Conclusions and future work

The sub-set of fEITER auditory data presented here are extremely limited in statistical terms. It is not straightforward to establish conclusively that the fEITER responses observed here are indeed due to neural processing. Nevertheless, several aspects of the data suggest that the signals do reflect neural processing, such as the observed asymmetries with two different stimulus types, and the appearance of the well-known P1-N1-P2 complex. The images reconstructed from the gross stimulus case are also suggestive of neural functional imaging. However, image reconstruction is challenging for the smaller signals obtained from controlled auditory stimulus. The clinical trial data that is presently underway will present much better statistics.
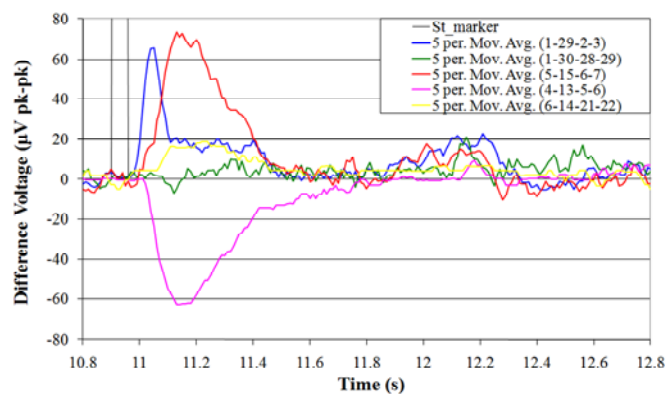
Figure 5: Maximum EIT voltage changes in response to controlled auditory stimulus, measured on subject A, with a 5-sample moving average, showing front, side and rear data.

5. References

[1]   Davidson J L *et al.*, (2009) fEITER – a new instrument for OR and ICU applications in *Proc. 10th Int. Conf. Biomedical Applications of Electrical Impedance Tomography*, Manchester,UK

[2]   Davidson J L *et al.*, (2010) fEITER: A New EIT Instrument for Functional Brain Imaging, *Proc. XIth Int. Conf. Electrical Impedance Tomography*, FL, USA, J. Phys. Conf. Series **224** (2010) 012025

[3]   Rafiei-Naeini M and McCann H (2008) Low-noise current excitation sub-system for medical EIT, *Physiol. Meas.* **29**(6) S173-S184

[4]   Bakker M J et al., (2009) Quantification of the auditory startle reflex in children, *Clin. Neurophysiology* **120**, 424-430

[5]   Polydorides N and Lionheart W R B (2002) A Matlab based toolkit for three-dimensional electrical impedance tomography: a contribution to the EIDORS project, *Meas. Sci. Technol.* **13** 1871-83

[6]   Holder D S, private communication

[7]   Hoekema R et al., (2003) Measurement of the Conductivity of Skull, Temporarily Removed During Epilepsy Surgery, *Brain Topogr.*, **16**, 29-38.

[8]   Martin B A, Tremblay K L, and Stapells D R, (2007) Principles of Cortical Auditory Evoked Potentials, 482 – 507, in *Auditory Evoked Potentials, Basic Principles and Clinical Application*, (eds. Burkard R F, Eggermont J J, and Don M), Lippincott Williams and Wilkins

Breast MREIT Phantom Experiments Using Less Than 1 mA Injection Currents

Hyung Joong Kim, Young Tae Kim, Atul S. Minhas, Zijun Meng, and Eung Je Woo

Impedance Imaging Research Center and Department of Biomedical Engineering, Kyung Hee University, Korea

E-mail: ejwoo@khu.ac.kr

Abstract. Latest MREIT experiments of *in vivo* human subjects successfully produced conductivity images using 3 mA current injections. *In vivo* human and disease model animal experiments still require further reduction of imaging currents. In this paper, we describe an MREIT breast phantom imaging experiment to show its feasibility as a new tool to diagnose breast tumor. Noting that the breast consists of soft tissues and relatively small imaging region, we performed breast phantom MREIT imaging experiments using a multi-channel breast coil. With injection currents of less than 1 mA, we could produce conductivity images of a breast phantom which distinguish two different tissues of a small conductivity contrast. We suggest future development of fast pulse sequences and optimized electrode configurations for better image quality, which will be followed by animal and human experiments.

Keyword: MREIT, conductivity image, breast

1. Introduction

Early detection and diagnosis of breast tumor will increase the survival rate of the disease. Breast MRI relies on contrast enhancement using an imaging agent to distinguish malignant from benign lesions (1). Considering the high contrast in conductivity between normal and cancerous tissues in the breast, conductivity imaging looks promising for the diagnosis of breast cancer (2-6). In this study, we conducted MREIT imaging experiments of a breast phantom to find its feasibility to detect breast tumor. Reducing the amplitude of imaging currents to a value less than 1 mA, we show the feasibility of breast MREIT.

2. Method

We built an acrylic phantom of the thorax ($30 \times 14 \times 15$ cm^3) and breast (11 cm in diameter). Figure 1(a) shows the picture of the breast phantom. After filling the phantom with saline of 0.12 S/m conductivity (0.3 g/l NaCl and 1 g/l CuSO$_4$), two different biological tissues of porcine muscle and chicken breast were positioned in the phantom. Their conductivity values were 0.64, and 0.60 S/m. We attached four carbon-hydrogel electrodes around the breast area of the phantom and chose the electrode configuration in figure 1(b) (7,8). We placed the phantom inside the bore of a 3 T clinical MRI scanner (Siemens Medical Solutions, Erlangen, Germany) with a multi-channel breast coil.

Using a custom-designed MREIT current source, we injected the first current I_1 between one pair of electrodes. We changed the injection current amplitude from 3 mA down to 500 µA with the total pulse width of 28 ms. We used the multi-echo ICNE pulse sequence (9,10) with TR/TE = 800/20 ms, FOV = 180×180 mm^2, slice thickness = 4 mm, NEX = 10, matrix size = 128×128, number of slices = 7, and total imaging time = 60 min. After acquiring the first magnetic flux density (B_z) data set for I_1, the second injection current I_2 with the same amplitude and pulse width was injected through the other pair of electrodes to obtain the second data set. We used the single-step harmonic B_z algorithm implemented in CoReHA (conductivity reconstructor using harmonic algorithms) for multi-slice conductivity image reconstructions (11).
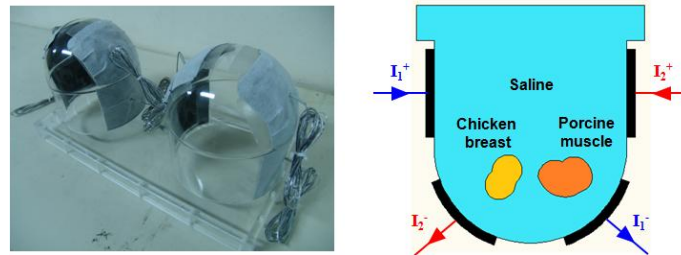

**Figure 1.** (a) Breast phantom and (b) electrode configuration.

3. Result

Figure 2(a), (b) and (c) show MR magnitude, magnetic flux density, and reconstructed conductivity images of the breast phantom with 3 mA current injection, respectively. Carbon-hydrogel electrodes with a large surface area and the multi-channel transmit/receive breast coil improved SNRs in measured magnetic flux density images. Two different tissues on the left and right sides show their conductivity contrasts in figure 2(c), whereas the MR magnitude image in figure 2(a) does not distinguish them.

Figure 3 shows an MR magnitude of a breast phantom in (a) and reconstructed conductivity images in (b-e) with 3, 1, 0.7, and 0.5 mA current injections, respectively. All the conductivity images except the case of 0.5 mA current injection show clear contrast between two different tissues. The conductivity image with 0.7 mA current injection is noisy but still distinguishes two tissues.

(a) (b) (c)
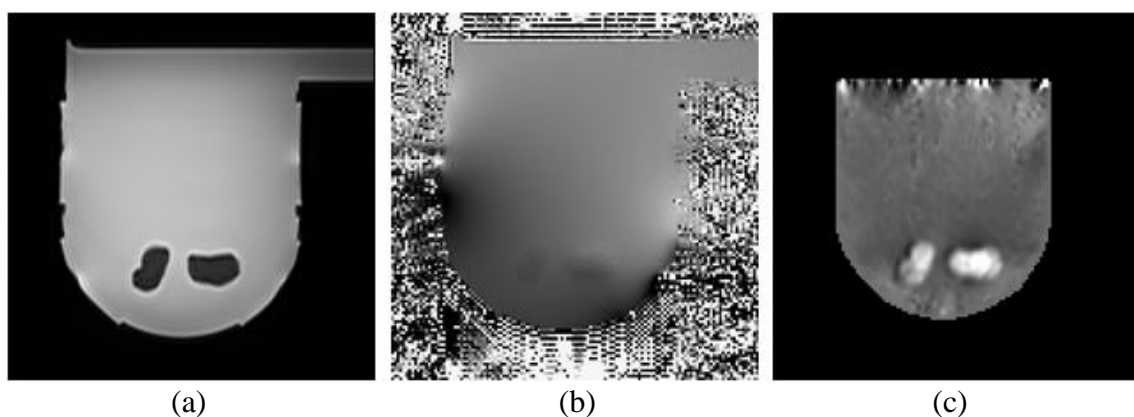
Figure 2. (a) MR magnitude image, (b) magnetic flux density image, and (c) reconstructed conductivity image of the first breast phantom with 3 mA current injection.
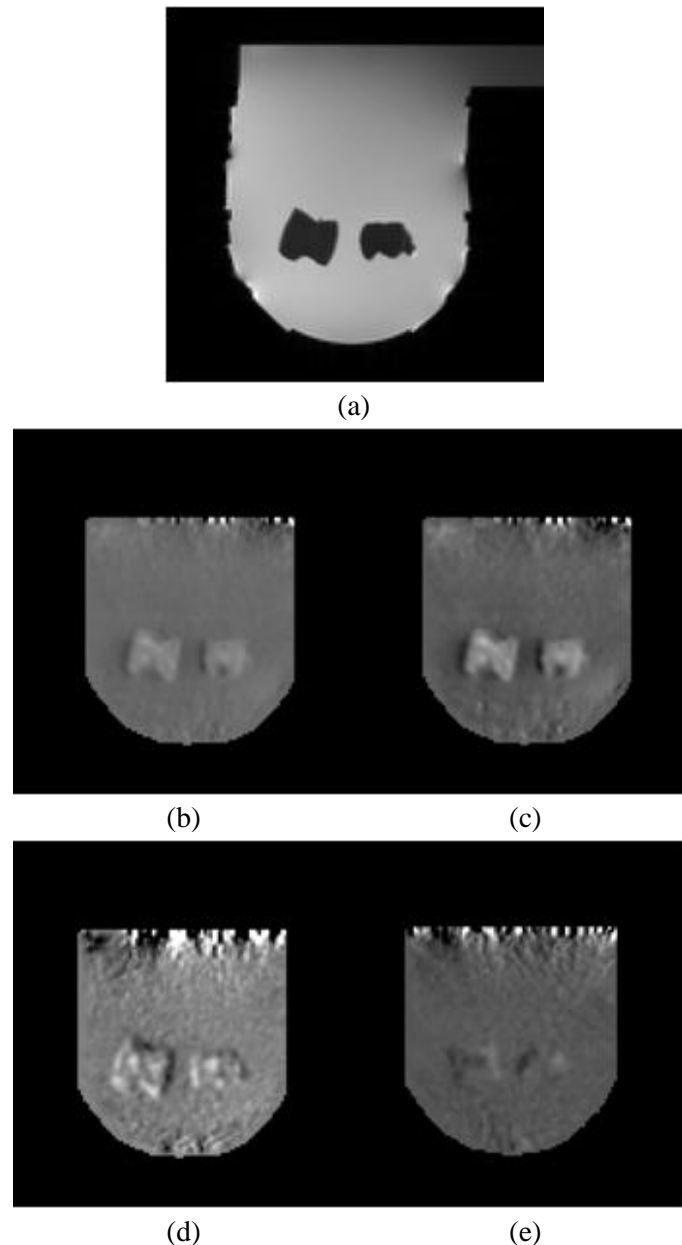
Figure 3. (a) MR magnitude image of the second breast phantom. (b)-(e) are reconstructed conductivity images with 3, 1, 0.7 and 0.5 mA current injections, respectively.

4. Conclusion and discussion

Compared with other breast imaging techniques, a conductivity imaging method may better differentiate cancerous tissues since their conductivity values are several times higher than those of normal breast tissues (12). In this study, we performed breast phantom MREIT imaging experiments using a multi-channel breast coil and current injections as small as 0.5 mA. To distinguish two tissues of 0.64, and 0.60 S/m conductivity values, we found that the injection current amplitude should be at least 0.7 mA. To distinguish cancerous breast tissues with significantly larger conductivity values compared with normal tissues, we speculate that breast MREIT using less than 1 mA injection currents is feasible. We may further reduce the amplitude of injection currents by incorporating specialized breast coils and improved pulse sequences. Based on the results in this study, we plan to optimize the electrode configuration

to produce more uniform current distributions inside the breast for better SNRs in measured magnetic flux density images.

Acknowledgement

References

[1]   Rankin S C 2000 MRI of the breast *Br. J. Radiol.* **73** 806-18

[2]   Assenheimer M, Laver-Moskovitz O, Malobek D, Manor D, Nahliel U, Nitzan R and Saad A 2001 The T-scan technology: Electrical impedance as a diagnostic tool for breast cancer detection *Physiol. Meas.* **22** 1–8

[3]   Cherepenin V A, Karpov A Y, Korjenevsky A V, Kornienko V N, Kultiasov Y S, Ochapkin M B, Trochanova O V and Meister J D 2002 Three-dimensional EIT imaging of breast tissues: system design and clinical testing *IEEE Trans. Med. Imaging* **21** 662–7

[4]   Hartov A, Soni N and Halter A 2005 Breast cancer screening with electrical impedance tomography, in Electrical Impedance Tomography: Methods, History and Applications, IOP Publishing Bristol UK 167–85

[5]   Kerner T E, Paulsen K D, Hartov A, Soho S K and Poplack S P 2002 Electrical impedance spectroscopy of the breast: clinical imaging results in 26 subjects *IEEE Trans. Med. Imaging* **21** 638–45

[6]   Kao T J, Boverman G, Kim B S, Isaacson D, Saulnier G J, Newell J C, Choi M H, Moore R H and Kopans D B 2008 Regional admittivity spectra with tomosynthesis images for breast cancer detection: preliminary patient study *IEEE Trans. Med. Imaging* **27** 1762–8

[7]   Woo E J and Seo J K 2008 Magnetic resonance electrical impedance tomography (MREIT) for high-resolution conductivity imaging *Physiol. Meas.* **29** R1–R26

[8]   Lee B I, Oh S H, Kim T S, Woo E J, Lee S Y, Kwon O, Seo J K 2006 Basic setup for breast conductivity imaging using magnetic resonance electrical impedance tomography *Phys. Med. Biol.* **51** 443–455

[9]   Feinberg D A, Mills C M, Posin J P, Ortendahl D A, Hylton N M, Crooks L E, Watts J C, Kaufman L, Arakawa M, Hoenninger J C and Brant-Zwadwaski M 1985 Multiple spin-echo magnetic resonance imaging *Radiology* **155** 437–42

[10]   Minhas A S, Jeong W C, Kim Y T, Han Y Q, Kim H J, Woo E J 2011 Experimental performance evaluation of multi-echo ICNE pulse sequence in MREIT *Magn. Reson. Med.* at press

[11]   Jeon K, Minhas A S, Kim Y T, Jeong W C, Kim H J, Kang B T, Park H M, Lee C O, Seo J K and Woo E J 2009 MREIT conductivity imaging of postmortem canine abdomen using CoReHA *Physiol. Meas.* **30** 957–66

[12]   Muftuler L T, Hamamura M J, Birgul O and Nalcioglu O 2006 In vivo MRI electrical impedance tomography (MREIT) of tumors *Technol. Cancer. Res. Treat.* **5** 381–7

Detection of Brain Electrical Impedance Change after Ionization Injury: Preliminary Results

Feng Fu , Chaoshuang Chen, Feng Xiao, Xuetao Shi, Ruigang Liu, Fusheng You, Xiuzhen Dong*

Department of Medical Electronic Engineering, School of Biomedical Engineering, Fourth Military Medical University, Xi'an, 710032, P. R. China.

Abstract—In this paper, we propose a systematic demonstration of electrical impedance imaging technique used for the detection of ionization injury of brain tissue. By comparing normal brain tissue of rabbits (control group) and ionization injured brain tissue of rabbits (experimental group) we observed that the experimental group showed a striking contrast with the control group. During a span of twelve hours the one dimension impedance of the former group has ascended remarkably and in two-dimensional images the location and area of the injury can be observed. The results of the completed experiments suggest that electrical impedance tomography (EIT) may become an effective technique to detect incipient ionization injury.

Keywords-electrical impedance, radiation injury

I. INTRODUCTION

In medicine the largest use of ionizing radiation is in medical radiography to make images of the inside of the human body using X-rays. It is also used to treat diseases in radiation therapy. However, exposure to large doses of ionizing radiation will cause acute radiation disease and even death in severe cases.[1]

In clinical practice X-rays with high energy generated by medical linear accelerator are widely used to treat non-neoplastic lesions. This so-called radiotherapy is the process in which DNA double-strand of the tumor cell breaks under X-ray irradiation, leading to the failure of division and finally apoptosis of the tumor cell.[2] Unlike the mechanism of tumor radiotherapy, the main cause of ionization injury is that ionizing radiation produced by X-rays gives rise to the abnormal distribution of charged ions within tissue, causing damage to the cell membrane-specific proteins. Then transmembrane movement of water molecules becomes abnormal, which renders slow growth of intracellular water content and change of ion concentration. In modern radiotherapy, despite the employment of three-dimensional conformal and even intensity modulated technology, ionization injury is inevitable due to pursuit of a higher therapeutic gain ratio and difference between fatal dose for certain tumor and tolerance dose for normal tissue. The possible injuries include edema, fibrosis, hemorrhage, paralysis and even death. At present, there are several ways to detect ionization injury: MRI, CT, pathophysiology, biochemistry, immunochemistry and molecular biology methods. Among these approaches, MRI and CT have a relatively late detection, which cannot be confirmed as

---

* Correspondence author: dongyang@fmmu.edu.cn

positive until three or four weeks after exposure. In addition detection of this kind is too expensive to be popularized. The pathophysiology method falls into static observation so it is unable to make dynamic detection of ionization injury. The rest of the previous mentioned approaches can achieve long-term dynamic observation, yet they all belong to invasive in vitro detection.[3，4]

The significance of early detection of ionization injury in clinical practice lies in the following aspects.[5] Firstly, tissue edema will be avoided by early drug intervention. Secondly, irreversible injuries brought by multiple radiotherapies can be averted by timely adjustments of radiotherapy schemes. Thirdly, individual differences of sensitive tissues can be detected so as to increase target tumor dose. Therefore, it is of important clinical significance to seek a real-time and inexpensive detection method that is capable of discovering ionization injury as soon as possible.

II. MATERIALS AND METHODS

A. Experimental animals

The protocols of this study, in agreement with international rules and standards, were approved by the animal ethics committee of the University. 20 rabbits of either gender were randomly divided into two groups. All the rabbits were normally fed with temperature of 25±1℃ and humidity of 55±5%.

B. Experimental system

The EIT system (FMEIT-5) used in this experiment had a working frequency of 50 kHz while the magnitude of the exciting current was set as 750 μA. Polar driving mode was adopted and the imaging rate was 1 frame per second. 16 electrodes were fixed onto the skull of the rabbit with metallic dental posts.

C. preparation of ionization damage model

Varian 23Ex Accelerator 6MVX was used to irradiate the brainstem of the anesthetized rabbit, with X-ray beam coming from the top.

D. experiment procedure

1) The rabbit was anesthetized with pentobarbital sodium through helix vein after being weighted. When the rabbit went numb it was fixed onto the animal experimental platform.

2) The hair at the top of the rabbit head was removed using a pet razor until the scalp could be seen. Then the skull was exposed by stripping the fascia with a scalpel. During the process gauze was used to stop bleeding.

3) 16 alligator clip electrodes were respectively connected to 16 metallic dental posts equally dilled into the exposed area of the skull, with sequence of Electrode 1 on the left, Electrode 5 on the anterior, electrode 9 on the right and Electrode 13 on the posterior. Alligator clips were basically clipped at the same position of each dental post, whose contact impedance, consistency, stability and signal to noise ratio (SNR) all met the experimental requirements

4) The rabbit was fed for 3 to 5 days. After recuperation it was used for the modeling of ionization injury.

5) The rabbit was monitored in the light of experiment content and pertinent experimental data was taken.

E. Indicators of analysis

The reconstructed value by EIT is the change of electrical impedance of each subdivision unit. These values would be quite inconvenient to be used if not processed by any image

display means. Therefore the reconstructed data is mapped into pseudo-color image through a particular mapping.

III. RESULTS

The boundary voltage changes(which means the impedance variation of target) of experimental and control group are shown in Figure 1. The curves consist of points that represent the average value of the 10 measurements at a given time. The control group had a mean of 982.38mv with standard error of 16.54mv in a span of 12 hours and the overall change of voltage amounted to 33.08mv. The experimental group had a mean of 1100.02mv with standard error of 99.25mv in the same time period and the change added up to 199.5mv. Paired t test was taken to come to the conclusion that the difference had statistically significance ($p<0.05$).

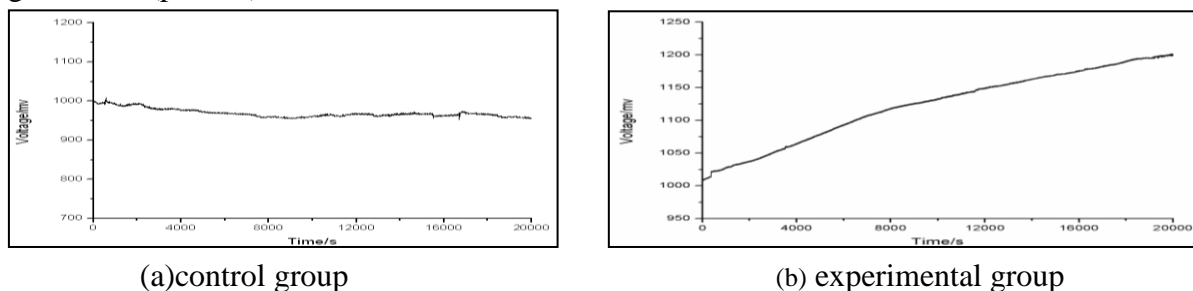(a)control group   (b) experimental group

Fig.1 Time-varying of rabbit brain tissue impedance

Figure 2 showed impedance distribution change after the ionization injury. A blue area with dramatically increasing levels at the lower part of the image can be observed, whose location is basically in consistence with that of the model. This indicated a rise of electrical impedance in the brain tissue of the rabbit.
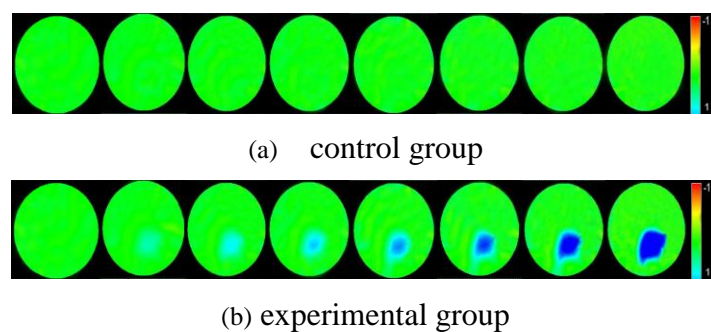

(a)   control group

(b) experimental group

Fig.2 EIT image sequences of rabbit brain

IV. DISCUSSION

The characteristic of bioelectrical impedance is one of the key features of biological tissues. The primary substances that constitute the conductance/resistance characteristic of living organisms are closely related to tissue cell activity as well as the electrochemical environment of intracellular and extracellular fluid. When ionization injury occurs the distribution of some ions in intracellular and extracellular fluid and water content inside the cell will change, which leads to a short-term irreversible change of electrical impedance. In the development of maladies and the resulting injuries, microscopic mechanisms of different injuries remain complicated or unclear while electrical impedance change of tissues exhibit some distinctness[6]. Thus it is possible to speculate microscope change and development of

diseases together with the sequent injuries by detecting electrical impedance change of biological tissues.

Although the study of this project only aims at early changes of physical properties after ionizing radiation injury, pertinent methods can be extended to the research of biological effects of electromagnetism[7,8]. Combined with research methods of cytology, further detection of electrical impedance characteristic of ionization injured tissues is able to incipiently observe the change of intracellular and extracellular environments as well as initially establish the relationship between electrical impedance change and biological effects of electromagnetism. Sequentially early quantitative basis might be provided to assess ionization injury so that new ideas and methods for the study of ionization protection could be developed.

ACKNOWLEDGMENT

REFERENCES

[1]   Yokoya A, Shikazono N ,Fujii K, Urushibara A, Akamatsu K, Watanabe R. DNA damage induced by the direct effect of radiation. Radiation Physics and Chemistry,2008,77(10): 1280-1285

[2]   Juan-Felipe P.J. Abascal, Simon R. Arridge, David Atkinson , Raya Horesh, Lorenzo Fabrizi, Marzia De Lucia , Lior Horesh, Richard H. Bayford , David S. Holder, Use of anisotropic modelling in electrical impedance tomography; Description of method and preliminary assessment of utility in imaging brain function in the adult human head, NeuroImage 43 (2008) 258–268

[3]   Wang X, Xiong D, Wang J, Chen D, Zhang L, Zhang Y, Wang S, Zhang X.Investigation on damage of DNA molecules under irradiation of low frequency ultrasound in the presence of hematoporphyrin– gallium (HP–Ga) complex. Ultrasonics Sonochemistry, 2008,15(4): 761-767

[4]   A.C. Thompsona, E.A. Blakelya, K.A. Bjornstada.A synchrotron-based X-ray exposure station for radiation biology experiments,2007: 226-228

[5]   M.A. Bennett , R.A. Williams, Monitoring the operation of an oil/water separator using impedance tomography, Minerals Engineering 17 (2004) 605–614

[6]   Demirkazık FB, Salih Emri et al. Radiation-induced liver injury and foreign body reaction secondary to the diaphragmatic Teflon patch in an operated malignant pleural mesothelioma patient: CT, MRI and PET-CT findings. Magnetic Resonance Imaging,2000,18(6): 707-714

[7]   O. Gilad, D.S. Holder, Impedance changes recorded with scalp electrodes during visual evoked responses:Implications for Electrical Impedance Tomography of fast neural activity, NeuroImage 47 (2009) 514–52

[8]   Carl Blackman. Cell phone radiation: Evidence from ELF and RF studies supporting more inclusive risk identification and assessment. Electromagnetic Fields (EMF) Special Issue,2009,205-216

A method for recording Electrical Impedance Tomography images in human acute stroke subjects.

David Holder[1], Andrea Romsauerova[1], Joshua Luis[1], Jonathan Cornell[1], Brett Packham[1], Emma Smith, Karolina Wloch, Darius Parvin, Sujin Ahn[2] and Sung Chan Jun[2].

[1]. Departments of Medical Physics and Clinical Neurophysiology, University College London and UCL Hospitals, London, UK.
[2]. Department of Information & Communications, Gwangju Institute of Science and Technology, Gwangju, Korea

1. Introduction

MFEIT (Multi-Frequency Electrical Impedance Tomography) has the potential to distinguish between haemorrhagic and ischemic brain stroke in emergency situations where CT or MRI are not available. This could provide vital urgent neuroimaging, which would allow the rapid use of "clot-busting" thrombolytic drugs [1,2]. Development of this application has recently been a major goal in our group. The UCLH Mk2.5 [3] was designed for this purpose. It comprises a single current drive and recording circuit, multiplexed to up to 64 electrodes and records at 30 frequencies from 20 Hz – 1 MHz. The purpose of this study was to collect data in acute stroke subjects and so determine whether the UCLH MK2.5 could distinguish between ischaemic and haemorrhagic stroke in human subjects.

2. Methods

EIT data were recorded in subjects admitted to the UCH specialist acute thrombolysis unit for management of acute stroke. Data were recorded with the UCLH Mk 2.5 EIT system at from 80Hz to 161.28 kHz and up to 293 µA rms using the "spiral16s-o" or EEG31 protocol [4,5]. Each image data set of 373 or 258 combinations respectively took about 1 minute to record. Up to 4 sets of 5 data sets were recorded in each subject using the greatest tolerated current pattern [6]. EEG cup electrodes were applied to the abraded scalp in a modified EEG10-20 position and were localised to within 1mm using a photogrammetric method based on 16 digital camera images (Nikon D70) and Photomodeler (EOS systems, Vancouver, Canada).

Impedance data was calibrated using single channel data from a 56 Ω resistor or by individual channels using a realistic head shaped tank with 0.35% saline. Data cleaning was accomplished first by analysis visually using a Matlab routine "Viewdata"; anomalous data points due to movement or poor electrode contact at individual time points or in electrode combinations were removed. Then electrode combinations were removed if the standing voltage <0.25mV or 2% SD noise over time.

Images were reconstructed using a linear assumption sensitivity matrix method with singular value decomposition of in the inverted matrix. Images were assessed using a simple frequency difference method of data at a given frequency referenced to that collected at a specified frequency or else using the weighted frequency difference method with which correction is made for a complex background [7].

These were either referenced to 80Hz or else images were made of adjacent frequency pairs. Reconstruction was performed using a detailed Finite Element Method mesh of about 100000 elements created from high resolution 1mm slice CTs by segmentation with a custom written algorithm based on a hierarchical expectation maximization algorithm and then meshing using CUBIT (Sandia Labs, USA).

3. Results

Data has been collected in 14 subjects with acute stroke, 7 each with 16 electrodes and the spiral16 protocol or 32 electrodes and the EEG31 protocol. In each case, it was possible to attach the electrodes with satisfactory electrode contact impedance and localize electrode positions with a tightness of <1mm. It was possible to produce Finite Element Meshes of about 100000 elements from high resolution 1mm slice CT scans obtained for clinical diagnostic purposes; in general high resolution MRI scans were not collected (Fig. 1). Impedance raw data generally monotonically decreased with frequency after correction for movement artifact. (Fig. 2).
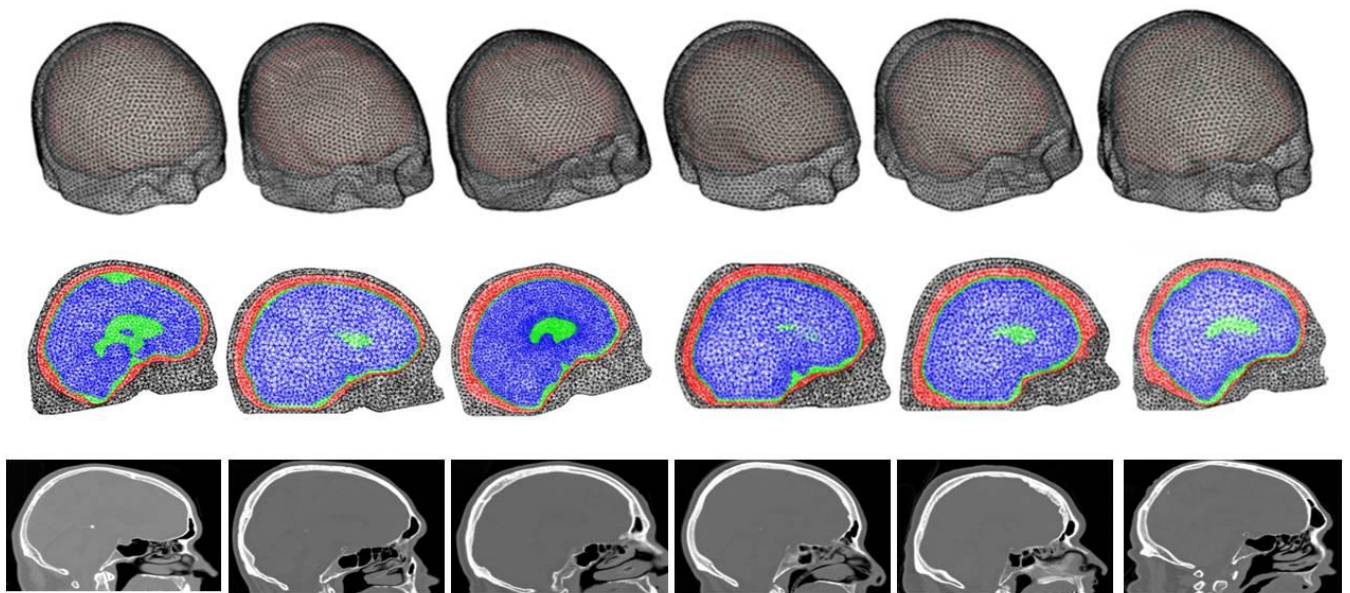

Figure 1. Examples of Finite Element meshes generated from subjects' CTs.

4. Discussion.

This study has been undertaken in an attempt to produce validated EIT images in acute stroke. Following an unsuccessful preliminary study [2], technical improvements have included improved calibration and optimisation of the EIT instrumentation, production of patient-specific Finite Element Meshes and localisation of electrodes on the mesh using a photogrammetric method convenient for use at the bedside. Initial analysis of the data indicates that it appears to be of satisfactory quality. However, the satisfactory production of images which correspond to the known pathology requires great accuracy in several fields. In addition, it is not yet clear whether the best available reconstruction algorithm, the

wieghted frequency difference approach, is robust for inhomogeneous backgrounds; it has so far only been validated in tanks with complex conductivity, but uniform, backgrounds. Work in progress is in progress to reconstruct images with the different algorithms and determine if significant changes can be seen which correspond to the known regions of pathology.
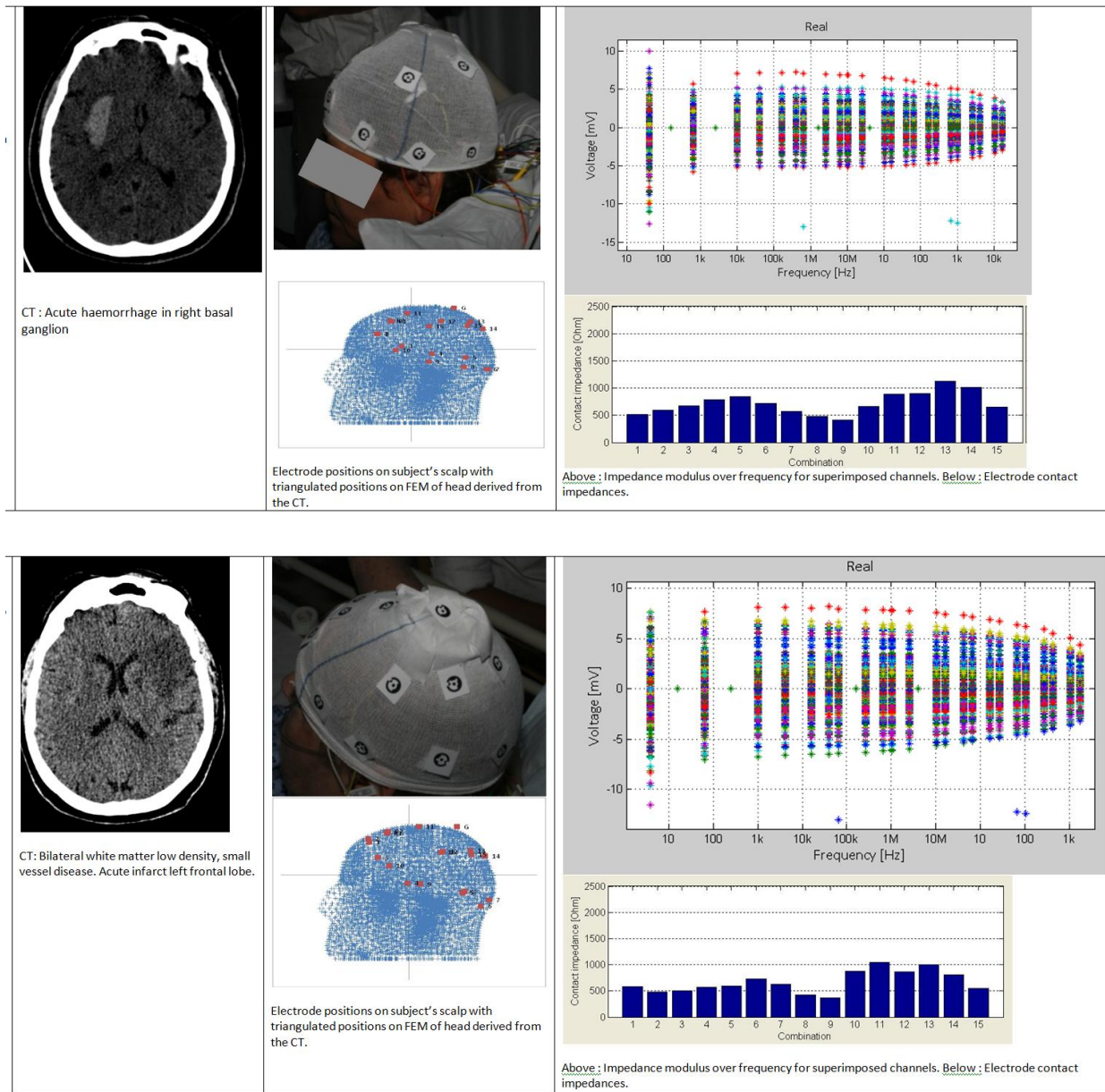

Fig. 2. Examples of reconstructed data from tow subjects. Upper – Right basal ganglion haemorrhage; lower : left frontal infarction.

Reference List

1. Horesh L, Gilad O, Romsauerova A, McEwan A, Arridge SR, Holder DS (2005) Stroke type differentiation by multi - frequency electrical impedance tomography - a feasibility study. IFMBE, Prague, Czech Republic, pp 1252-1256

2. Romsauerova A, McEwan A, Horesh L, Yerworth R, Bayford RH, Holder DS (2006) Multi-frequency electrical impedance tomography (EIT) of the adult human head: initial findings in brain tumours, arteriovenous malformations and chronic stroke, development of an analysis method and calibration. Physiol Meas 27: S147-S161

3. McEwan A, Romsauerova A, Yerworth R, Horesh L, Bayford R, Holder D (2006) Design and calibration of a compact multi-frequency EIT system for acute stroke imaging. Physiol Meas 27: S199-S210

4. Fabrizi L, McEwan A, Oh T, Woo EJ, Holder DS (2009) An electrode addressing protocol for imaging brain function with electrical impedance tomography using a 16-channel semi-parallel system. Physiol Meas 30: S85-101

5. Bagshaw AP, Liston AD, Bayford RH, Tizzard A, Gibson AP, Tidswell AT, Sparkes MK, Dehghani H, Binnie CD, Holder DS (2003) Electrical impedance tomography of human brain function using reconstruction algorithms based on the finite element method. Neuroimage 20: 752-764

6. Romsauerova A, McEwan A, Holder DS (2006) Identification of a suitable current waveform for acute stroke imaging. p S211-S219

7. Jun SC, Kuen J, Lee J, Woo EJ, Holder D, Seo JK (2009) Frequency-difference EIT (fdEIT) using weighted difference and equivalent homogeneous admittivity: validation by simulation and tank experiment. Physiol Meas 30: 1087-1099

Feasibility of high-resolution MREIT with less than 1 mm pixel size

Hyung Joong Kim, Young Tae Kim, Atul S. Minhas, Zijun Meng, and Eung Je Woo

Impedance Imaging Research Center and Department of Biomedical Engineering, Kyung Hee University, Gyeonggi-do, Korea

E-mail: ejwoo@khu.ac.kr

Abstract. Recent experimental MREIT studies demonstrated conductivity image reconstructions of postmortem and *in vivo* animal and human subjects with a few millimeter pixel size. In order to visualize a conductivity distribution within a tissue or a small animal, it is necessary to develop a high-resolution MREIT technique. In this study, we demonstrate the capability of MREIT to perform conductivity imaging at a spatial resolution with a micrometer pixel size. The experimental results using a 4.7 T research MRI scanner with a multi-echo ICNE pulse sequence and high-performance RF coils demonstrate that we can distinguish two different anomalies in reconstructed conductivity images with a spatial resolution as low as 400 μm. We plan to apply the developed experimental method to *in vivo* head imaging of small animals to investigate the feasibility of functional MREIT as a new neuro-imaging method.

Keyword: MREIT, conductivity, micrometer spatial resolution, neuro-imaging

1. Introduction

Recent experimental studies in magnetic resonance electrical impedance tomography (MREIT) have reported conductivity image reconstructions with a spatial resolution of 1.4 mm (1-5). Such a resolution could be sufficient to distinguish different human tissues for certain applications. Since fine structures are obscured in images with such a macroscopic resolution, we need to improve the spatial resolution with a less than 1 mm pixel size. However, this requires breakthroughs in experimental MREIT techniques to reduce measurement noise.

High-resolution MREIT is also needed in small animal experiments to distinguish their internal structures. To find the feasibility of MREIT as a new functional brain imaging modality, we plan to perform *in vivo* head imaging experiments using small animals. In this study, we conducted MREIT phantom experiments to reconstruct conductivity images with a micrometer pixel size. To compensate for the reduced SNR due to a small pixel size, we adopted a multi-echo ICNE pulse sequence (6,7) and high-performance small volume RF coils. After describing experimental methods, we will compare reconstructed conductivity images at various spatial resolutions.

2. Method

We used an octagon-shaped acrylic phantom shown in figure 1. Its four long edges were 15

mm and the other four short edges were 10 mm. We installed four recessed electrodes to inject currents. We placed two hollow cylindrical anomalies of thin insulating films (cellulose acetate, 0.3 mm thickness) with 5 mm diameter. On the side of one hollow cylinder, we made four equally-spaced holes along the central plane of the phantom where current-injection electrodes were located. We filled the background of the phantom including inside and outside of the two hollow cylinders with a saline of 0.12 S/m conductivity (0.3 g/l NaCl and 1 g/l $CuSO_4$).

For imaging experiments, we placed the phantom inside the bore of a 4.7 Tesla MRI scanner (BioSpec 47/40, Bruker). Using a custom-designed MREIT current source, we injected the first current I_1 between one pair of electrodes. The injection current amplitude was 3 mA with the total pulse width of 28 ms. The multi-echo ICNE pulse sequence was used with TR/TE = 800/20 ms, FOV = 55×55 mm^2, slice thickness = 2 mm, NEX = 8, matrix size = 128×128, number of slices = 7, and total imaging time = 40 min (7). After acquiring the first magnetic flux density (B_z) data set for I_1, the second injection current I_2 with the same amplitude and pulse width was injected through the other pair of electrodes to obtain the second data set. We used the single-step harmonic B_z algorithm implemented in CoReHA (conductivity reconstructor using harmonic algorithms) for multi-slice conductivity image reconstructions (8,9).

3. Result

Figure 1(a), (b) and (c) show an MR magnitude, magnetic flux density, and reconstructed conductivity images, respectively, of the phantom with two cylindrical anomalies. The pixel size of the images in figure 1 was 400 μm. The anomaly on the left (with four holes) show a different conductivity compared with the one on the right (without holes). Such a contrast was not seen in the magnitude image in figure 1(a). Note that the anomaly on the right appears to be an insulator since we are producing a conductivity image at a low frequency in MREIT.

(a)   (b)   (c)
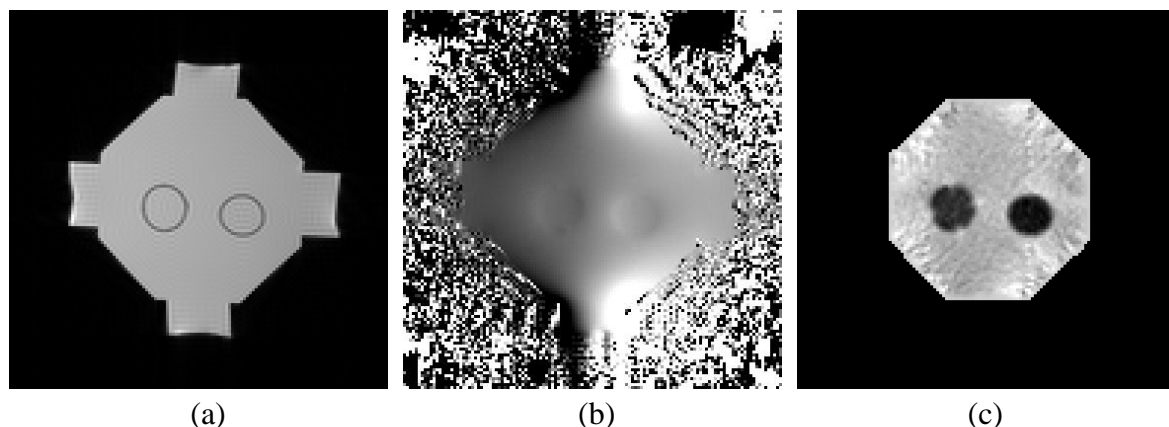
Figure 1. (a) MR magnitude, (b) magnetic flux density, and (c) reconstructed conductivity images of the phantom with a 400μm pixel size.
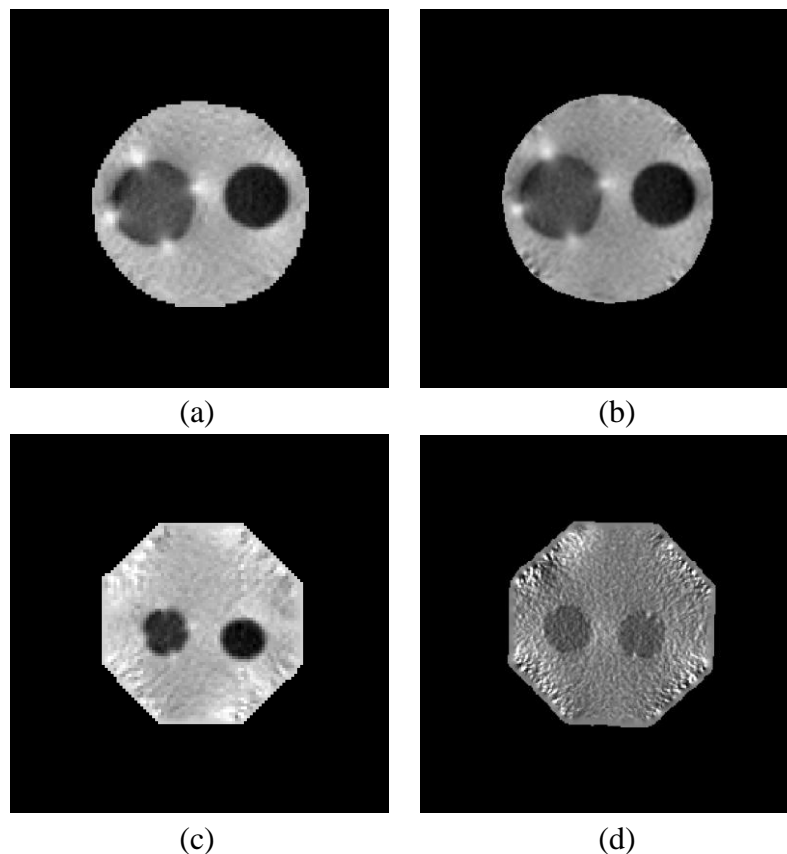
Figure 2(a) and (b) show reconstructed conductivity images at spatial resolutions of 1.4 and 1 mm, respectively. The conductivity images in (c) and (d) were reconstructed from a second octagonal phantom with two anomalies at spatial resolutions of 400 and 200 μm, respectively. All the conductivity images except the one with 200 μm pixel size showed clear contrast between two different anomalies. The conductivity image with 200 μm size was too noisy compared with other cases primarily due to a poor SNR in measured data.

4. Conclusion and discussion

The results demonstrate that the existing MREIT technique can produce conductivity images with a spatial resolution of as low as 400 μm. Using the multi-echo pulse sequence and high-performance small volume RF coil, we could do this with imaging currents of 3 mA.

Note that current can enter the hollow insulating cylinder with four holes and produced ion conduction through the hollow cylinder. This increased the apparent conductivity of the hollow cylinder with four holes to distinguish itself from the other one without any hole (10). The results clearly indicate that the reconstructed apparent conductivity is affected by ion mobility as well as ion concentration. We plan to try conductivity image reconstructions of hollow cylindrical anomalies of thin insulating film with various hole configurations to investigate contrast mechanism in MREIT. We will also adopt this kind of phantom design as a macroscopic model of conductivity change during neural activity. We will undertake *in vivo* head imaging experiments using small animals using the experimental setup developed in this paper.

Figure 2. Reconstructed conductivity images of two different anomalies at different spatial resolutions: (a) 1.4 mm, (b) 1 mm, (c) 400 μm and (d) 200 μm.

References

[1] Woo E J and Seo J K 2008 Magnetic resonance electrical impedance tomography (MREIT) for high-size conductivity imaging *Physiol. Meas.* **29** R1–R26

[2] Muftuler L T, Hamamura M J, Birgul O and Nalcioglu O 2006 In vivo MRI electrical impedance tomography (MREIT) of tumors *Technol. Cancer. Res. Treat.* **5** 381–7

[3] Kim H J, Lee B I, Cho Y, Kim Y T, Kang B T, Park H M, Lee S Y, Seo J K and Woo E J 2007 Conductivity imaging of canine brain using a 3 T MREIT system: postmortem experiments *Physiol. Meas.* **28** 1341–53

[4] Kim H J, Oh T I, Kim Y T, Lee B I, Woo E J, Seo J K, Lee S Y, Kwon O, Park C, Kang B T and Park H M 2008 In vivo electrical conductivity imaging of a canine brain using a 3 T MREIT system *Physiol. Meas.* **29** 1145–55

[5] Kim H J, Kim Y T, Minhas A S, Jeong W C, Woo E J, Seo J K and Kwon O J 2009 In vivo high-resolution conductivity imaging of the human leg using MREIT: the first human experiment *IEEE Trans. Med. Imaging* **28** 1681–7

[6] Feinberg D A, Mills C M, Posin J P, Ortendahl D A, Hylton N M, Crooks L E, Watts J C, Kaufman L, Arakawa M, Hoenninger J C and Brant-Zwadwaski M 1985 Multiple spin-echo magnetic resonance imaging *Radiology* **155** 437–42

[7] Minhas A S, Jeong W C, Kim Y T, Han Y Q, Kim H J, Woo E J 2011 Experimental performance evaluation of multi-echo ICNE pulse sequence in MREIT *Magn. Reson. Med.* at press

[8] Jeon K, Minhas A S, Kim Y T, Jeong W C, Kim H J, Kang B T, Park H M, Lee C O, Seo J K and Woo E J 2009 MREIT conductivity imaging of postmortem canine abdomen using CoReHA *Physiol. Meas.* **30** 957–66

[9] Seo J K, Kim S W, Kim S, Liu J J, Woo E J, Jeon K and Lee C O 2008 Local harmonic B_z algorithm with domain decomposition in MREIT: computer simulation study *IEEE Trans. Med. Imaging* **27** 1754–61

[10] Oh T I, Kim Y T, Minhas A S, Seo J K, Kwon O, Woo E J 2011 Ion mobility imaging and contrast mechanism of apparent conductivity in MREIT *Phys. Med. Biol.* at press

Is the 16 channel Spiral16 or 32 channel EEG31 electrode protocol better for stroke MF imaging in the head shaped tank?

Tugba Doru, Brett Packham, Hwan Koo and David Holder

Department of Medical Physics and Bioengineering, University College London, UK

1. Introduction

Multifrequency Electrical impedance tomography (MFEIT) could be used for imaging in acute stroke (10) and EIT for fast neural activity (5), or epilepsy patients (3). Electronic hardware systems suitable for this include the UCH Mk 2.5 (7) and the KHU Mk 1 (8). EIT in the adult human head poses special demands as it is in 3D and the skull presents an impedance barrier. Specially designed electrode addressing protocols are needed to yield good images. Although a full analysis has not to our knowledge been conducted, reasonable images may be obtained with an ad-hoc protocol designed for injection of current through widely spaced pairs of electrodes, the "EEG31" protocol (1). As this requires a system in which any 4 electrodes may be addressed independently, we developed a different protocol for use with the KHU Mk 1 system, "spiral_s-o" (also referred to as spiral16), as this was hard wired to address electrode pairs sequentially (4). This was evaluated empirically in a saline filled anatomically realistic 3D head shaped tank and, perhaps surprisingly, image quality appeared to be equivalent with 16 electrodes and this approach as for the EEG31. However, this was only evaluated for use in imaging epileptic seizures, and so at a single frequency and for time difference imaging (3).

We are now conducting human clinical trials of MFEIT in acute stroke. For this, we cannot undertake time difference imaging for practical reasons as the requirement is for an image at a single time as the subject presents. We have adopted the approach of frequency difference imaging with which images are reconstructed from differences in multifrequency data collected at the same time and with the use of a "weighted" frequency difference algorithm (6) to compensate for background changes over frequency.

The purpose of this study was to evaluate if the spiral16 was as effective as the EEG31 protocol in MFEIT imaging intended for acute stroke and so extending down to recording at 20 Hz. Image quality was evaluated with images recorded in an anatomically realistic head-shaped tank with a potato from 20 Hz – 160 kHz. In addition, we evaluated two methods for removing data from electrode channels which derived from those with low standing voltages and were therefore noisy.

2. Method

EIT images were collected in an anatomically realistic head shaped tank without a skull (3), filled with 0.2% saline solution and a test object of a cylinder of potato, 2.5 cm diameter and 10 cm in length with a UCH Mark 2.5 MFEIT system recording with 133 μA_{pp} from 20 Hz-160 kHz. Images were reconstructed of the difference between 40 frames of background, only saline, and another 40 with the potato placed in one of three positions in the midline, with both the spiral16 and EEG31 protocol (Table 1). Reconstructions used a sensitivity matrix linearised approach and time difference (TD) or weighted frequency difference (WFD)

algorithms, in the latter a correction is made for the background variation in conductivity over frequency (6).

Data were calibrated against a data set recorded in the same tank filled with 0.2% saline; channels in this correction factor with standing voltages < 0.1 mV were discarded (117/373 and 131/258 for spiral16 and EEG31 respectively).

Two cleaning methods were applied to the data. In the "Fabrizi" method, data were discarded with noise > 1% or a change in boundary voltage on test object introduction > 6x the SD that in all channels (3). In the "Packham" method, data from electrode combinations were excluded if the standing voltage < 0.1mV or contained > 1% noise (9).
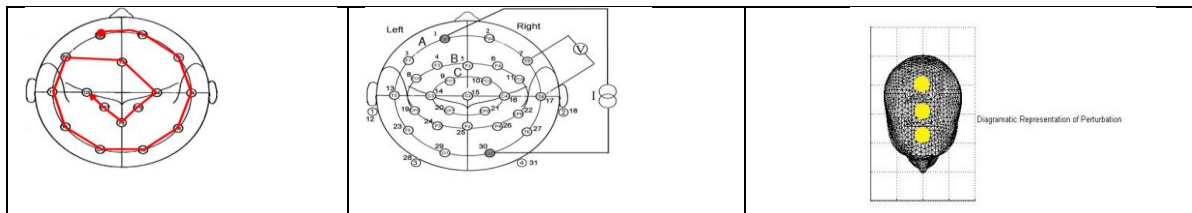

Table1: a) Spiral16 protocol, b) EEG31 protocol, c) Test object in posterior, central, anterior positions (from top to the bottom, respectively).

3. Results

For TD images, the "Fabrizi" data cleaning method was superior but the "Packham" method was superior for WFD images (Table2-3). Both removed 35-36% of electrode combinations for spiral16 protocol and 7-14% of electrode combinations for EEG31 protocol.
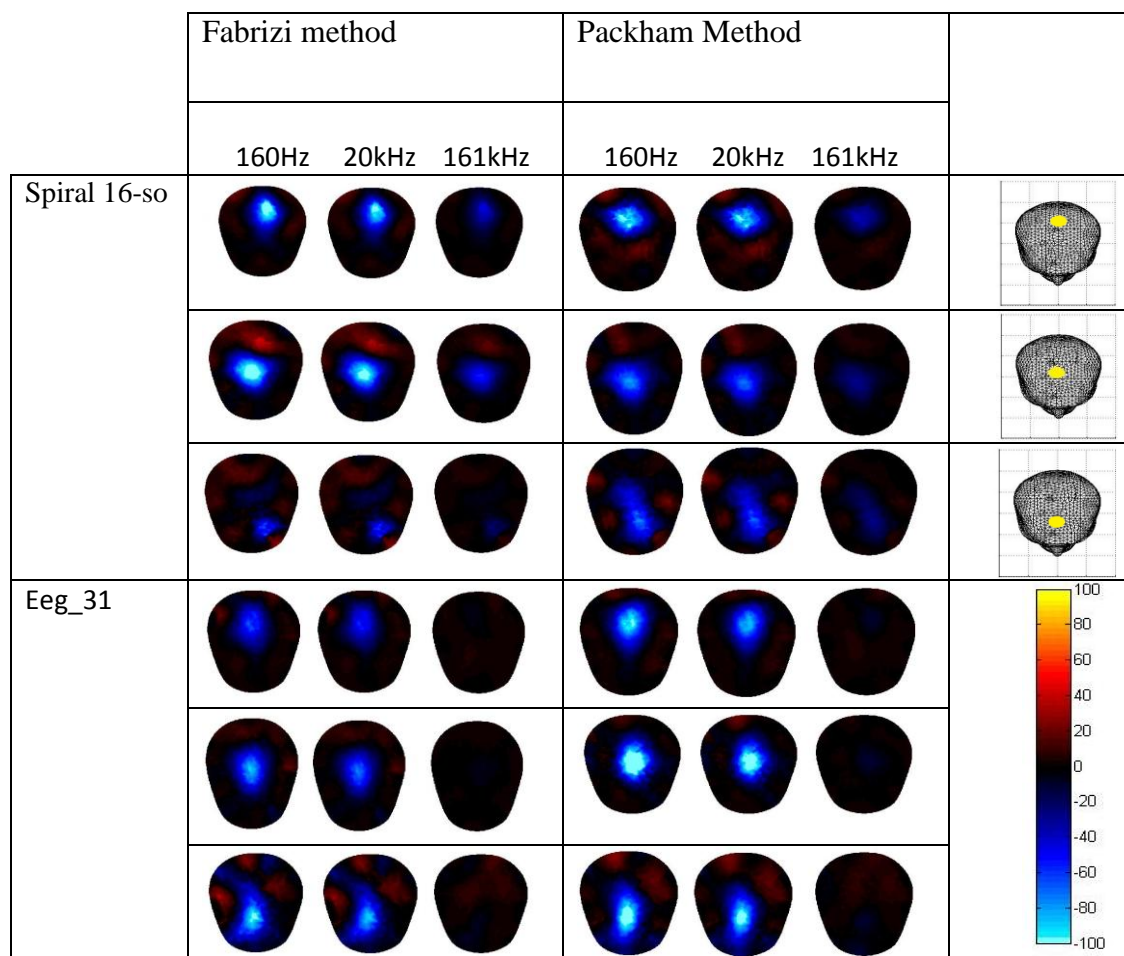

Table 2: Time difference images for Spiral_16s-o and EEG31 protocol with both cleaning method, for 40 singular value.

Overall, better image quality, obtained with the best cleaning method, was obtained with the EEG31 protocol. In general, images were less clear from the anterior positions. FWHM values and region of the interest was considered to evaluate the image quality (Table 4).
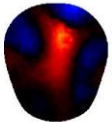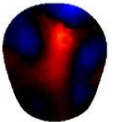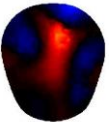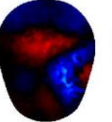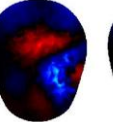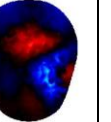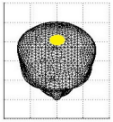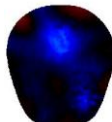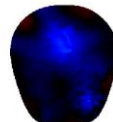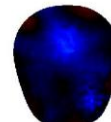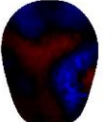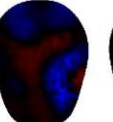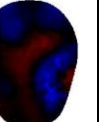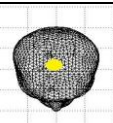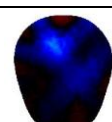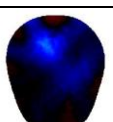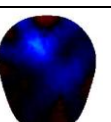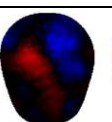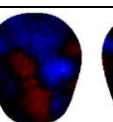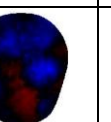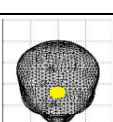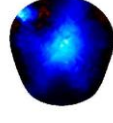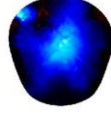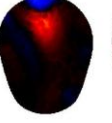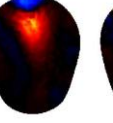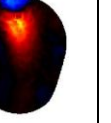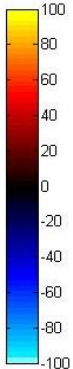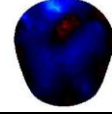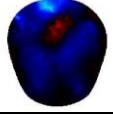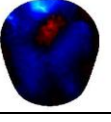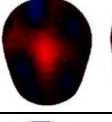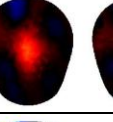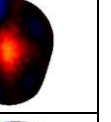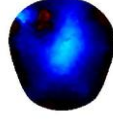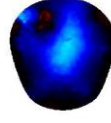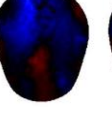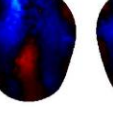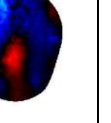
Table 3: Weighted frequency difference images for Spiral_16s-o and EEG31 protocol with after Fabrizi and Packham data removal. Reference frequency was chosen 80 Hz, and all images were reconstructed at 40 singular value.
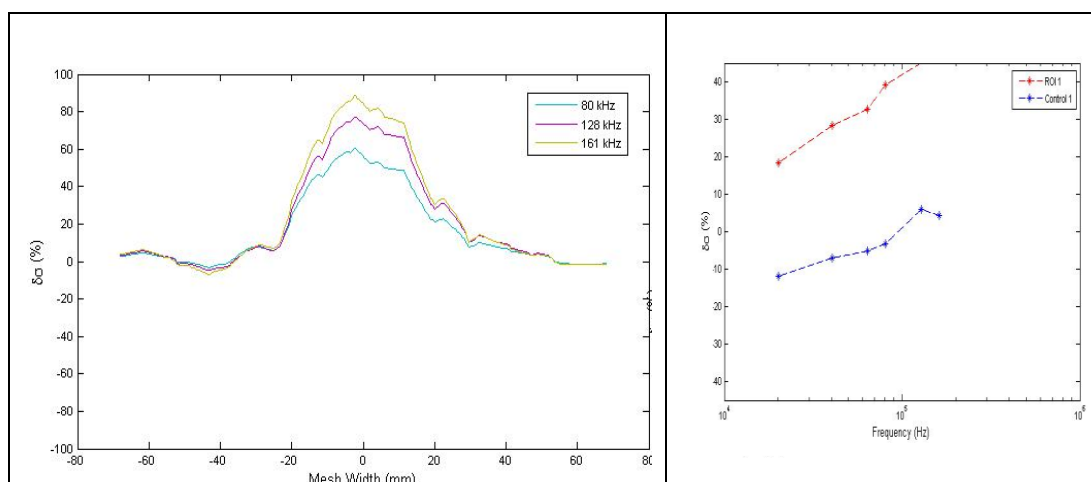
Table 4: An example of the data used to analyse the FWHM and frequency response of regions of interest. This example data is from data with a centrally positioned perturbation, recorded with EEG31 protocol, cleaned by the Packham method and reconstructed using the WFD algorithm.

4. Discussion

Overall, in contrast to the previous findings for EIT of epilepsy technical settings, it appears that the older EEG31 electrode addressing protocol gives superior images for MFEIT stroke recordings. Possible reasons for this include that anterior test object positions were collected in this study, where the spiral 16 protocol has fewer electrodes, and it may also be that the higher spatial sampling with more electrodes is more robust to poorer image quality at extremes of the frequency range; Fabrizi only collected data at 4kHz (2). This suggests that until further studies are undertaken, human clinical recordings would be best accomplished with 31 scalp electrodes in the EEG 31 configuration.

Data cleaning methods appear necessary in empirical tank studies because by chance some electrode combinations record small standing voltages which are relatively noisy because some noise is fixed. The UCH Mk2.5 is more sensitive to this because it has fixed gain but this will still be a problem for variable gain systems if some electrode combinations lie close to isopotential lines. The Fabrizi method excluded some channels simply on the basis of noise, but also excluded channels with artefactually large voltage changes related to insertion of the test object, presumably because they had a low standing voltage which was exaggerated by the movement of potential lines with the perturbation. This gave superior images with the time difference algorithm. However, this advantage did not persist with the multifrequency WFD approach where the conceptually simpler Packham method excluded channels just on the basis of noise and low standing voltage.

Work in progress includes quatiative analysis of these images and extension of the study to the head-shaped tank with a human skull in place.

Reference List

[1]   Bagshaw AP, Liston AD, Bayford RH, Tizzard A, Gibson AP, Tidswell AT, Sparkes MK, Dehghani H,   Binnie CD, and Holder DS. Electrical impedance tomography of human brain function using reconstruction algorithms based on the finite element method. Neuroimage 20: 752-764, 2003.

[2]   Fabrizi L, McEwan A, Oh D, Woo EJ, and Holder DS. Comparison of two EIT systems suitable for imaging impedance changes in epilepsy. Hanover NH, USA: 2008.

[3]   Fabrizi L, McEwan A, Oh T, Woo EJ, and Holder DS. A comparison of two EIT systems suitable for imaging impedance changes in epilepsy. Physiol Meas 30: S103-S120, 2009.

[4]   Fabrizi L, McEwan A, Oh T, Woo EJ, and Holder DS, An electrode addressing protocol for imaging brain function with electrical impedance tomography using a 16-channel semi-parallel system. Physiol Meas 30: S85-101, 2009.

[5]   Gilad O. Preliminary studies in imaging neuronal depolarization in the brain with Electrical or Magnetic   Detection Impedance Tomography (Dissertation), University College London, London, UK, 2007.

[6]   Jun SC, Kuen J, Lee J, Woo EJ, Holder D, and Seo JK. Frequency-difference EIT (fdEIT) using weighted difference and equivalent homogeneous admittivity: validation by simulation and tank experiment. Physiol Meas 30: 1087-1099, 2009.

[7]   McEwan A, Romsauerova A, Yerworth R, Horesh L, Bayford R, and Holder D. Design and calibration of a compact multi-frequency EIT system for acute stroke imaging. Physiol Meas 27: S199-S210, 2006.

[8]   Oh TI, Woo EJ, and Holder D. Multi-frequency EIT system with radially symmetric architecture: KHU Mark1. Physiol Meas 28: S183-S196, 2007.

[9]   Packham B, Koo H, Ahn S, Jun SC, Holder DS, Evaluation of the performance of a Multi-Frequency EIT system for imaging stroke in human subjects with scalp electrodes in liquid filled anatomically realistic tanks: identifying effective data pre-processing and frequency difference reconstruction algorithms. EIT Conference, Bath,UK, 2011.

[10]   Romsauerova A, McEwan A, Horesh L, Yerworth R, Bayford RH, and Holder DS. Multi-frequency electrical impedance tomography (EIT) of the adult human head: initial findings in brain tumours, arteriovenous malformations and chronic stroke, development of an analysis method and calibration. Physiol Meas 27: S147-S161, 2006.

Evaluation of Reconstructed Images of Regional Lung Changes Using a Model

Robert P, Patterson[1], Jie Zhang[2], Fei Yang[3], and Andy Adler[4]

1. University of Minnesota, Dept.of PM and R and Institute for Engineering in Medicine, Minneapolis MN USA (patte001@umn.edu)
2. University of Minnesota, Dept of Radiology, Minneapolis MN USA
3. Washington University School of Medicine, Department of Radiation Oncology, St. Louis, MO, USA
4. Carleton University, Systems and Computer Engineering, Ottawa, ON, Canada

INTRODUCTION Recent studies have shown that using EIT to monitor ventilator dependent patients appears to have much promise (Frerichs et al. 2006). Its application allows a possible view of regional ventilation that is dependant on the amount of positive end expiratory pressure (PEEP). Since EIT is a low resolution imaging modality, questions arise as to where in the image and to how large will be the area of change. Using a model, this study will attempt to answers the question of how regional lung images will change with changes in regional resistivity and also where their location and size will appear in the image. This approach presented here would be useful in evaluating various reconstruction algorithms as suggested by Adler et al (2009).

MEDHODS The model was created from human MR images that were obtained with a 1.5 T Siemens Sonata scanner. Forty-three thoracic transverse images were obtained from abdomen to neck and gated to coincide with end-diastole. The images were digitized at a spatial resolution of 1.5 mm/pixel in right-left and anterior-posterior directions. The resolution in the cranial-caudal direction was 5 mm/pixel identical to the MRI slice thickness. Upon segmentation, thirty-six tissue types and blood containing regions were obtained. Each tissue was assigned an appropriate electrical resistivity.. A 3D electrical model of the thorax at the end of diastole was thus created, with a resolution of $1.5 \times 1.5 \times 5$ mm^3 and 3.8 million control elements. The model was solved using a finite difference program developed in our laboratory (Belalcazar A and Patterson 2004, Yang and Patterson 2008, 2010).

   In order to answer questions about regional lung changes, two regions were created in the posterior portion of the right lung where the resistivity can be independently varied (Figure 1). Each region was created in all of the 43 layers in the same anterior-posterior position. Using the model the lung resistivity in each region was changed in 200 Ω-cm steps from 600 Ω-cm up to 2200 Ω-cm. The difference images were created using the reference frame with the entire right and left lung at 1400 Ohm-cm, which is assume to be a typical value at end expiration.

   The image reconstructions were created using both the Sheffield (Brown and Seagar, 1987) and NOSER (Cheney et al. 1990) algorithms. The areas of the resulting images of the regional modifications were calculated using 40% and 80% of the maximal change averaged over 10 pixels.

RESULTS An examples of the results for one case of reduced lung resistivity are shown in Figures 1 and 2. Figures 3 shows the percentage change of the resistivity as viewed in the image as a function of resistivity change using the Sheffield algorithm. Figure 4 show the image area changes for the same case as shown in Figure 3, but using NOSER algorithm.
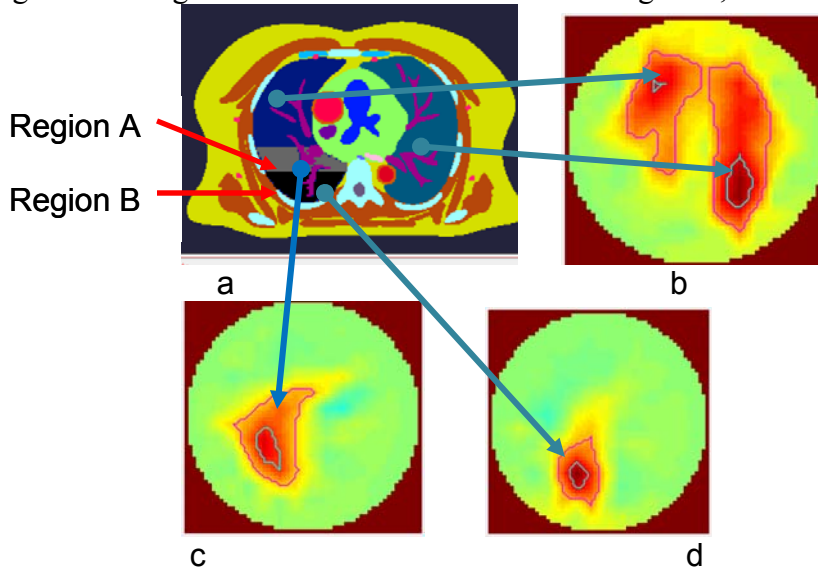
Figure 1, Reconstrction using Sheffield algorithm (a)- Modified regions of the right lung in the segmented mid-thorax of the model. (b)- Difference image when left lung and unmodified regions of the right lung were changed from 1400 to 1000 Ohm-cm. (c)- Difference image when the mid-right lung region was changed from 1400 Ohm-cm to 1000 Ohm-cm. (d)- Difference image when the lower modified of the right lung was changed from 1400 to 1000 Ohm-cm.
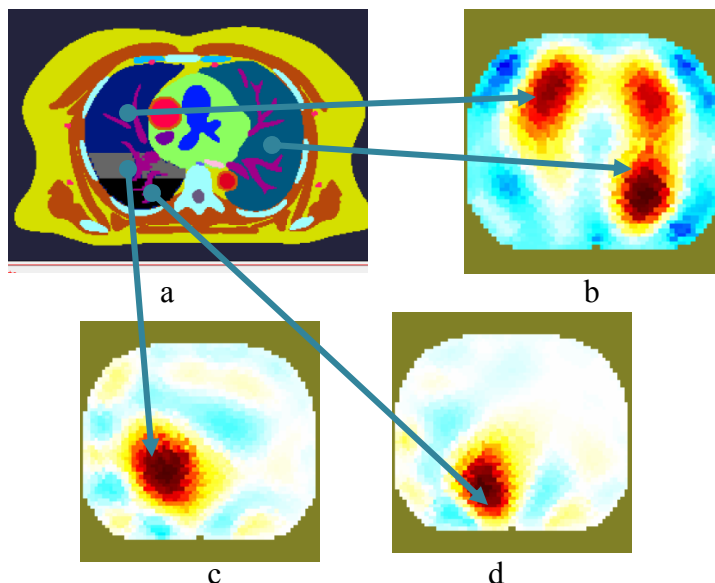
Figure 2, Reconstrction using NOSER algorithm (a)- Modified regions of the right lung in the segmented mid-thorax of the model. (b)- Difference image when left lung and unmodified regions of the right lung were changed from 1400 to 1000 Ohm-cm. (c)- Difference image when the mid-right lung region was changed from 1400 Ohm-cm to 1000 Ohm-cm. (d)- Difference image when the lower modified of the right lung was changed from 1400 to 1000 Ohm-cm.
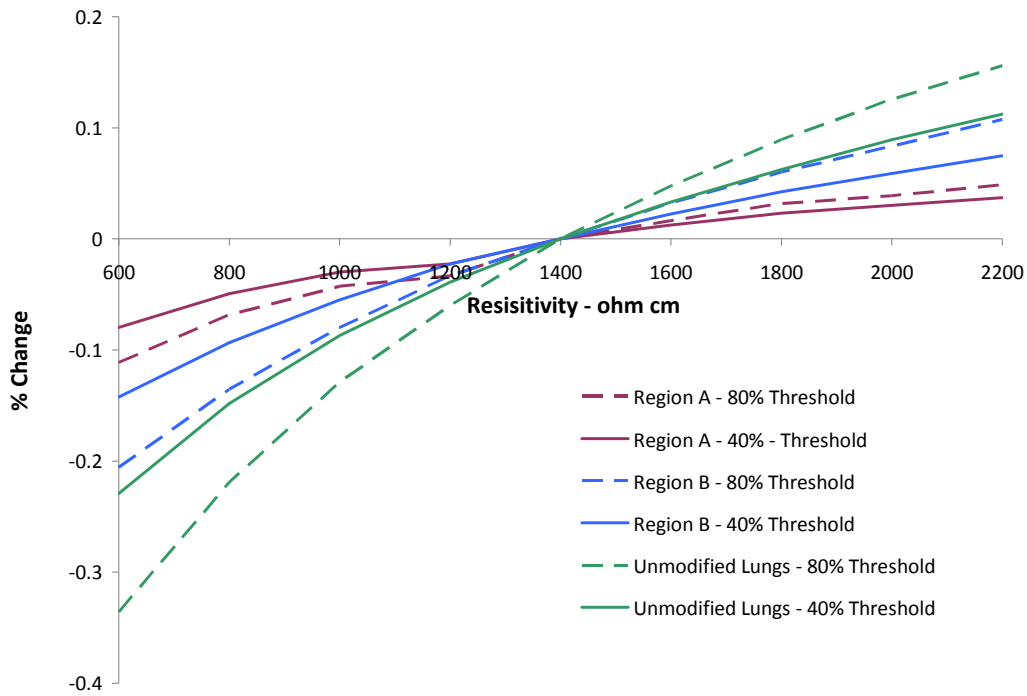
Figure 3. The percentage change in the image resisitivity as a function of lung resistivity for the reconstructed image using the Sheffield algorithm
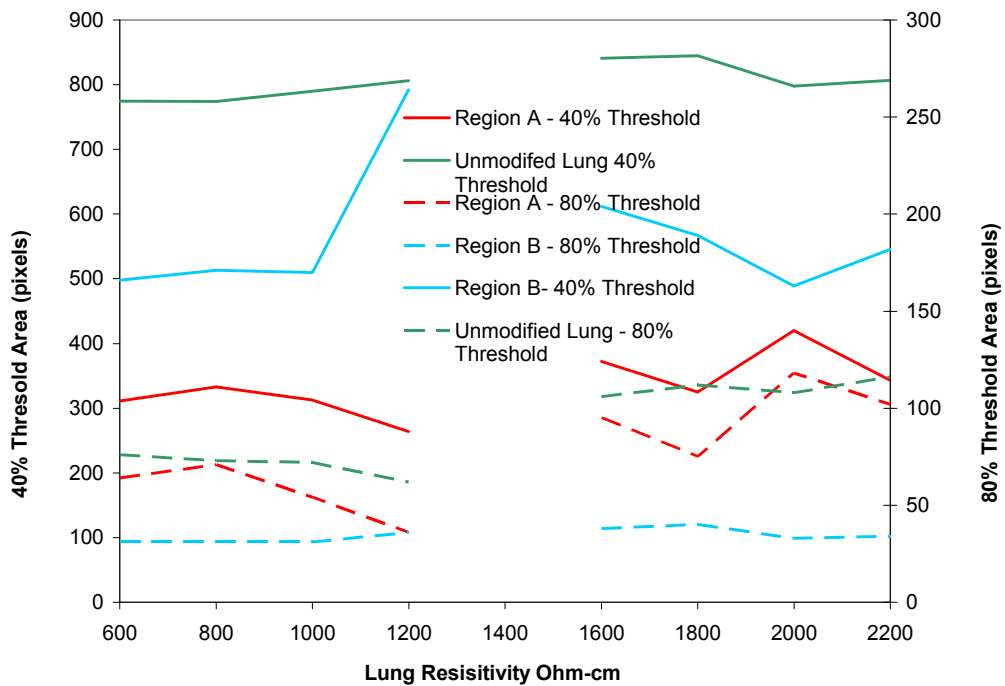
Figure 4 The change in image area as a function of lung resistivity using the Sheffield reconstruction algorithm

DISCUSION - The percentage change in the image resulting from changing lung resistivity is slightly nonlinear with the change from decreasing resistivity approximately twice that for the same about of increase. The area of the lung shows some change as a function of lung resistivity, but there is no consistent pattern. The examples shown for both reconstruction algorithm (figures 1 and 2) an overlap in modified regions A and B. Clearly, the shape of the change in the image differs from the shape of the are in the lung model. The shape, overlap and the location of the change in the image need to be studied more.

This approach, using an actual high resolution thorax model, can be useful in studying and comparing different reconstruction algorithms.

References
Adler A, Arnold J H, Bayford R, Borsic A, Brown B, Dixon P, Faes T J C, Frerichs I, Gagnon H,Gaerber Y, Grychtol B, Hahn G, Lionheart W R B, Malik A, Patterson R P, Stocks J, Tizzard A, Weiler N and Wolf G K 2009 Physiol. Meas. 30, S35-S55.

Belalcazar A and Patterson R P 2004 Physiol. Meas. 25, 475-487.

Brown B H and Seagar A D 1987 Clin. Phys. Physiol. Meas. 8, 91-97.

Cheney M, Isaacson D, Newell J C, Simske S and Goble J 1990 Int. J. Imaging Syst. Technol. 2(2), 66-75.

Frerichs I, Scholz J and Weiler N 2006 Springer Berlin Heidelberg chapter 10: Electrical Impedance Tomography and its Perspectives in Intensive Care Medicine, pp. 437-447.

Yang F and Patterson R 2010 in `Proceedings of the 32nd Annual International Conference of the IEEE Engineering in Medicine Conference' Buenos Aires, Argentina pp. 3105-3108.

Yang F and Patterson R 2008 Ann. Biomed. Eng. 36(5), 762-768.

Yang F, and Patterson R.2010 Proceedings of the 32nd Annual International Conference of the IEEE Engineering in Medicine Conference, August 31- September 4, Buenos Aires, Argentina pp. 3105-3108.

LEVEL SET BASED RECONSTRUCTION ALGORITHM FOR EIT LUNG IMAGES

Peyman Rahmati[1], Manuchehr Soleimani[2], and Andy Adler[1]

[1]Carleton University, Ottawa, Canada. {prahmati,adler}@sce.carleton.ca

[2] Bath University, UK. {m.soleimani}@bath.ac.uk

ABSTRACT

We show that electrical impedance tomography (EIT) image reconstruction algorithms based on the Level Set (LS) method are suitable for real data, which is breathing data in our application. The LS based reconstruction method (LSRM) helps track fast topologically changing interfaces, which are typically smoothed by traditional voxel based reconstruction method (VBRM), during the monitoring process. We represent lung images by applying the LSRM using difference solver and then compare the results with the VBRM. According to our results, LSRM outperforms its voxel based counterparts in producing high quality, high contrast images of lung.

Index Terms— Inverse Problem, Electrical Impedence Tomography, Image Reconstruction Algorithm

1. INTRODUCTION

Tomographic imaging systems seek to see the inside objects, by introducing energy and measuring its interaction with the medium. Electrical Impedance Tomography (EIT) measures the internal impedance distribution using surface measurements. Electrical current is applied to the medium and the voltage at the surface is measured using electrodes. The impedance distribution is then estimated based on the measured voltages and medium geometry. Some of typical applications of these techniques are for geophysical imaging [1, 2, 3], process monitoring [4, 5], and functional imaging of the body [6, 7].

In this paper, we focus on image reconstruction in EIT using the level set approach. The level set approach has become popular because of its ability to track propagating interfaces [8, 9], and more recently it has been applied in variety of applications in inverse problems and in image processing [10, 11, 12, 13]. Level set based reconstruction method (LSRM) is a nonlinear inversion scheme using an optimization approach to iteratively reduce a given cost functional, which is the norm of the difference between the simulated and measured data. In comparison to the voxel based reconstruction method (VBRM) (e.g. [14]), the LSRM has the advantage of introducing the conductivity of background and that of inclusions as known priori information into the reconstruction algorithm, enabling it to reconstruct sharp contrasts [4]. The unknown parameters to be recovered from the data are the size, number, shapes of the inclusions. These unkown parameters are given as the zero level set of a higher dimensional function, called level set function. In every iteration, the level set function (LSF) is modified according to an update formula to modify the shape of the inclusion at its zero level set (see fig. 1).

The level set method for shape based reconstruction is well studied in electrical and electromagnetic imaging for simulated data [10, 11, 12, 15, 16, 17, 18, 19]; however, it has been seldom shown to be used for human data. This study is the first implementation of LSRM for EIT breathing real data demonstrating the results of applying a difference solver.

The remainder of the paper is organized as follows: in the next section, we formulate level set approach using difference solver for EIT; in section 3, we introduce into the level set technique employed for solving the inverse problem of EIT lung images; the experimental data is represented in section 4; in section 5, we evaluate the performance of LSRM for lung monitoring data and compare LSRM to VBRM; and finally section 6 presents discussions and conclusions.

2. DIFFERENCE AND ABSOLUTE RECONSTRUCTION METHODS

There are two primary reconstruction types in EIT: "absolute (static) imaging" which attempts to recover an estimate of the absolute conductivity of the medium from the achieved data frame, and "difference imaging" which attempts to recover an estimate of the change in conductivity between two times based on the change between two data frames, v_2 and v_1. Difference EIT can compensate for measurement errors which do not change between data frames. Difference EIT is based on a difference data vector, $[y]_i = [v_2]_i - [v_1]_i$ or, in order to decrease measurement noise, the normalized difference data $[y]_i = [v_2]_i - [v_1]_i/[v_1]_i$. Using a finite element model (FEM), the medium is discretized into N elements with conductivity σ. The conductivity change vector $x = \sigma_2 - \sigma_1$ is the change between the present conductivity distribution, σ_2, and that at the reference measurement, σ_1. The linearized difference forward solution for small changes in conductivities over time is given by [20]:

$$y = J\hat{x} + n, \tag{1}$$

where J is Jacobian or sensitivity matrix around the reference conductivity distribution, defined by $\frac{\partial y}{\partial x}|_{\sigma_1}$ and n is the measurement noise, typically assumed to be an uncorrelated white Gaussian noise. In an EIT application where the conductiity of the medium ($\hat{x}$) is unknown, we need to solve an inverse problem to find an estimate of the conductivity, refered to as $\hat{x}$. The most common approach to find $\hat{x}$ is the use of the Gauss-Newton (GN) algorithm for EIT reconstruction [21, 22]. The GN method solves the EIT inverse problem by minimizing the following quadratic residue [20]:

$$\|y - J\hat{x}\|^2_{\sum_n^{-1}} + \|\hat{x} - x_0\|^2_{\sum_x^{-1}}, \tag{2}$$

where $\sum_n^{-1}$ and $\sum_{\hat{x}^{-1}}$ are the covariance matrix of measurement noise and that of conductivity vector ($\hat{x}$), respectively; and x_0 represent the expected value of element conductivity changes. By solving (2) for $\hat{x}$, the linearized EIT inverse solution is obtained as [20]:

$$\hat{x} = (J^T J + \lambda^2 R)^{-1} J^T y, \tag{3}$$
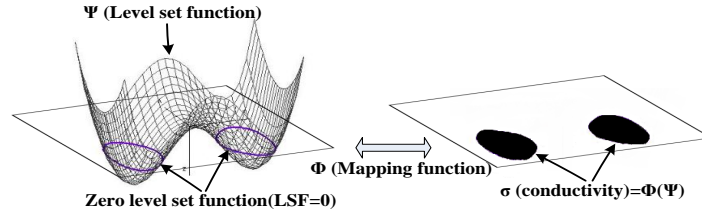
Fig. 1: LSF mapping to a 2D plane. From left to right columns, The 3D representation of an arbitarary LSF and its zero level set function crossing zero level set surface, and 2D mapping of the LSF on the zero level set surface.

where R is the regularization matrix and λ is the regularization hyperparameter to which can control the trade off between resolution and noise attenuation in the reconstructed image. In the remainder of this paper, the GN approach is considered the reference technique. GN image reconstruction is understood to result in smoothed images, since the regularization matrix is typically based on a penalty filter for non-smooth images.

3. LEVEL SET METHOD

One effective method to allow the reconstruction of sharp images is the Level Set method [12]. The classic formulation of this method assumes that the reconstructed image can take only two conductivity values: one for background with value σ_b and another one for inclusions with value σ_i. The regions which form the background and the inclusions are defined by a LSF, Ψ: a signed distance function to identify the unknown interface between the two conductivities. The value of the LSF is zero on the interface, negative inside the interface, and positive outside.

Compared to the more typical VBRMs, the LSRMs are more accurate reconstruction of objects with high step change of conductivity at the interface (high contrast objects). This is because most regularization schemes for the traditional methods, which are necessary for stabilizing the inversion, have the side-effect of artificially smoothing the reconstructed images. Therefore, these schemes are not well-suited for reconstructing high contrast objects with sharp boundaries.

In order to arrive at a robust and efficient shape-based inversion method, a powerful technique needs to be incorporated for computationally modelling the moving shapes. Level set technique [8, 9] is capable of easily modeling the topological changes of the boundaries. The LSRM has been shown the capability of being suitable for reconstructing object with fast changes at its interface over time, applicable to EIT in brain for cryosurgery monitoring [4]. Fig. 1 shows a two pahses image reconstructed using the LSRM. The LSF Ψ has separated the zero level set surface into two regions: foreground (inclusions) and background. The mapping function Φ projects the LSF to a 2D mesh to be applied for inverse solution calculation using FEM. Fig. 1, right panel, shows the conductivity of the inclusions in black where the LSF is negative and that of background in white where the LSF is positive. To begin with, we need to define an initial LSF, which may be a circle on level zero; and then deform this inital LSF using a predefined energy functional iterationally. Fig. 2 represents the steps as k represents the iteration number. After

defining the initial LSF, the mapping function Φ projects the LSF to a 2D mesh to be fed to difference solver block to calculte the system senitivity matrix, Jacobian (J_k), as well as element differential potential vectors, Δd_i. The next step is to update the energy functional which is Guass-Newton formula, ΔLSF_k. The initial LSF is then deformed by ΔLSF_k generating a new LSF. This new LSF is fed again to difference solver block for another iteration if the current iteration number (k) is not bigger than a maximum iteration number (K). In the following, we discuss about the mathematical presentation of the LSRM.
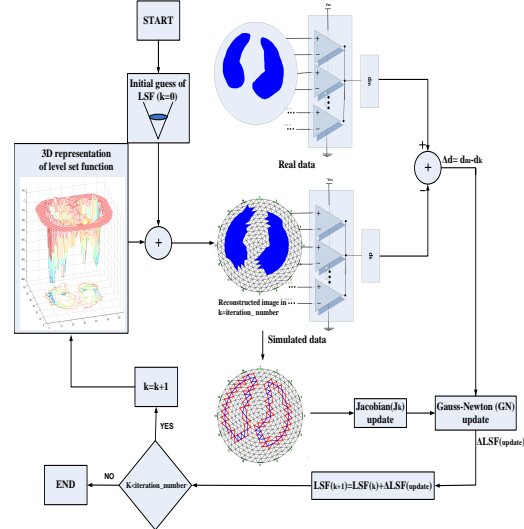
Fig. 2: The level set based reconstruction algorithm using difference solver. Steps from top to down: LSF initial guess, inverse difference solver, Guass-Newton update, LSF displacement by the given update, and iteration number increment.

In this technique, the shapes which define the boundaries, are represented by the zero level set of a LSF Ψ. If D is the inclusion with conductivity σ_i embedded in a background with conductivity σ_b, the boundary of the inclusion, which is also an interface between two materials, is given by the zero level set [17]:

$$\partial D := \{r : \Psi(r) = 0\}, \qquad (4)$$

where the image parameter at each point r is [17]

$$\sigma(r) = \begin{cases} \sigma_i & \text{for } \{r : \Psi(r) < 0\}, \\ \sigma_b & \text{for } \{r : \Psi(r) > 0\} \end{cases} \qquad (5)$$

If we change this LSF for example by adding an update, we move the shapes accordingly. This update to a given LSF causes the shapes being deformed in a way which reduces an error residue (cost functional).

The LSRM combines the general idea of GN optimization approach with a developed shape-based inversion approach. In order to mathematically derive the LSRM, we define the mapping (Φ) which assigns a given LSF Ψ_D to the corresponding parameter distribution by $\sigma = \Phi(\Psi_D)$. The parameter distribution σ has the same meaning as in the traditional GN inversion scheme. The only difference is that in the shape-based situation it is considered as having only two values, namely an "inside" value and an "outside" value. In shape-based reconstruction approach, We are looking for the LSF Ψ_D which have finally divided the image into two separate areas as foreground (inclusion) and background.

Having defined this mapping Φ, we can now replace the iterated parameter σ_n by $\sigma_n = \Phi(\Psi_D) = \Phi(\Psi_n)$. Instead of the forward mapping $F(\sigma)$, we need to consider now in the new GN type approach the combined mapping [17]:

$$d(\Psi) = G(\Phi(\Psi)), \tag{6}$$

where d is data point, G is system matrix, and $\Phi(\Psi)$ stands for conductivity, see fig. 1.

According to the chain rule, the level set (LS) sensitivity matrix can be written as below:

$$Sensitivity = J_{LS} = \frac{\partial d}{\partial \Psi} = (\frac{\partial G}{\partial \Phi(\Psi)})(\frac{\partial \Phi(\Psi)}{\partial \Psi})$$
$$= (J_{GN})(M), \tag{7}$$

where $\frac{\partial G}{\partial \Phi(\Psi)}$ stands for the traditional GN sensitivity matrix (J_{GN}), and $\frac{\partial \Phi(\Psi)}{\partial \Psi} = M$ is the matrix representing the mapping function ($\Phi(\Psi)$). Then, the new GN update is [17]:

$$\Psi_{k+1} = \Psi_k + \cdots$$
$$\lambda \left[(J_{(LS,k)}^T J_{(LS,k)} + \alpha^2 L^T L)^{-1} (J_{(LS,k)}^T (d_{real} - d(\Psi_k))) \right] \cdots$$
$$- \left[\alpha^2 L^T L (\Psi_k - \Psi_{int}) \right] = \Psi_k + GN_{update}$$
$$= LSF(k) + \Delta LSF, \tag{8}$$

where Ψ_{int} in the update term corresponds to the initial estimate of the LSF. There are two parameters λ and α to be tuned in this level set formulation.

Fig. 2 illustrates the algorithm to calculate the above update formula. The optimal choice of the two parameters, λ and α, depends on the mesh density, the conductivity contrast and the initial guess [4]. The length parameter λ determines the magnitude of the LSF displacement, changing the shape of inclusion, in a given update. The higher the λ, the higher the LSF displacement will be. The effect of the regularization parameter α depends on the choice of the regularization operator L. An identity matrix for L increases the stability of the inversion due to not smoothing out the LSF. However, a first order difference operator for L will smooth the LSF [4]. As α increases, the smoother the final LSF tends to be. A large value for α disturbs the reconstruction algorithm to separate close objects to each other properly (low distinguishibility). To have a better distinguishibility, in our experiments shown in the following section, we will choose L to be the identity operator. This allows us to better separate different objects

from each other. In our results, we have put a value of zero for our initial guess of Ψ_{int} in the above shape-reconstruction form.

4. EXPERIMENTAL DATA AND RESULTS

Human breathing data were acquired from a healthy young male subject during normal breathing while seated. Electrodes were placed around the chest at the 6th intercostal space. EIT surface potential data corresponds to end-expiratory, and end-inspiratory cycles. Images were reconstructed on a mesh roughly conforming to the anatomy of the subject.

We tested the suitablility of the LSRM for lung data using the breathing data. Fig. 3 shows the reconstructed images for one stage of breathing cycle using eithor the VBRM or the LSRM. The reconstructed image by the LSRM represents the air distribution isnide the lungs after 10 iterations (fig. 3(c)). As inspired air increases, the resistivity of the lungs increases which has been shown as blue regions in the reconstructed images in fig. 3. The reconstructed images show the superiority of the LSRM with respect to the VBRM in terms of creating sharper reconstructions with larger contrasts at the interface between the inclusion and the background, presenting step change of conductivity.
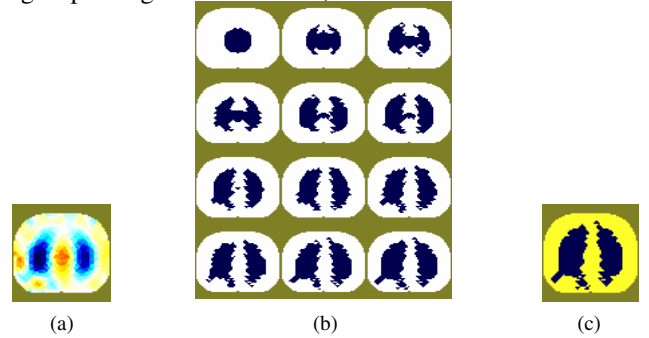
Fig. 3: level set based reconstruction algorithm using a difference solver for breathing data (scale=1). (a) The lung reconstructed image using GN approach. (b) The iterations of the LSRM for the same lung image in (a). (c) The final lung reconstructed image using the LSRM.

5. CONCLUSION AND DISCUSSION

We proposed the LSRM in difference mode for real data of breathing, which have not already been investigated for EIT. The inverse solution of Guass-Newton formula updates the sensitivity matrix and consequently the LSF with every iteration, dividing the medium into two maximally homogeneous areas; the foreground and the background. The LSRM depicts the capability of finding the big conductivity changes at the interface between lung and the background (fig. 3). Due to the update sensitivity matrix has been calculated on a narrow band region, involving the elements sharing an edge with the interface between foreground and background (see fig. 2), the LSRM is faster and less computationally expensive comparing with the VBRM.

There are many cases of inverse problems where more than two phases need to be reconstructed from given data.

For these applications, novel level set descriptions have to be developed to model these multi-phase situations in an efficient way, such as the Color level set technique [23]. In the original color level set technique, n LSFs are used in order to describe the evolution of up to $m = 2n$ different phases. This approach has also been investigated more theoretically in [24]. Irishina et al. in [25] described four different breast tissue types (skin, fatty tissue, fibroglandular tissue and a possible hidden tumor) by three different LSFs in a modified color level set representation for the application of early breast cancer detection. In this work, the theoretically possible $2^3 = 8$ different characteristic tissue values are enforced to fall into 4 different groups of characteristic tissue values.

Our results represents that the LSRM is suitable to be applied for EIT real data of breathing (fig. 3); Comparing with the VBRM, the LSRM shows high quality and high contrast lung images.

6. REFERENCES

[1] Loke M H, and Barker R D 1996a *Rapid least-squares inversion of apparent resistivity pseudo-sections using quasi-Newton method Geophysical Prospecting* vol 48 p 181

[2] Loke M H, Barker R D 1996b *Practical techniques for 3D resistivity surveys and data inversion Geophysical prospecting* vol 44 p 499

[3] Church P, McFee J E, Gagnon S and Wort P 2006 Electrical impedance tomographic imaging of buried landmines IEEE Transaction of Geoscience and Remote Sensing vol 44 p 2407

[4] Soleimani M, Dorn O and Lionheart W R B 2006a *A Narrow-Band Level Set Method Applied to EIT in Brain for Cryosurgery Monitoring IEEE Trans. Bio. Eng.* vol 53 No 11

[5] Manwaring P, Halter R, Wan Y, Borsic A, Hartov A, Paulsen K 2008 *Arbitrary geometry patient interfaces for breast cancer detection and monitoring with electrical impedance tomography Conf Proc IEEE Eng Med Biol Soc.* p 1178

[6] Gao N, Zhu S A, He B 2006 *A New Magnetic Resonance Electrical Impedance Tomography (MREIT) Algorithm: RSM-MREIT Algorithm with Applications to Estimation of Human Head Conductivity Physics in Medicine and Biology* vol 51 p 3067

[7] McCann H, Polydorides N, Murrieta-Lee JC, Ge K, Beatty P, Pomfrett CJ 2006 *Sub-second functional imaging by electrical impedance tomography Conf Proc IEEE Eng Med Biol Soc.* p 4269

[8] Osher S and Sethian J 1988 *Fronts propagation with curvature dependent speed: Algorithms based on hamilton-jacobi formulations J. Computational Phys.* vol 56 p 12

[9] Sethian J A 1999 *Level Set Methods and Fast Marching Methods* (2nd ed. Cambridge, U.K.: Cambridge Univ. Press)

[10] Santosa V 1996 *A level-set approach for inverse problems involving obstacles in ESAIM: Control, Optimization and Calculus of Variations1* p 17

[11] Litman A, Lesselier D and Santosa F 1998 *Reconstruction of a two-dimensional binary obstacle by controlled evolution of a level-set Inverse Prob.* vol 14 p 685

[12] Dorn O, Miller E L and Rappaport C M 2000 *A shape reconstruction method for electromagnetic tomography using adjoint fields and level sets Inverse Prob.* vol 16 p 1119

[13] Osher S and Paragios N 2003 *Level Set Methods in Geometric Level Set Methods in Imaging, Vision, and Graphics* (Eds. New York, NY: Springer) p 1

[14] Polydorides N, Lionheart W R B and McCann H 2002 *Krylov subspace iterative techniques: On the detection of brain activity with EIT IEEE Trans. Med. Imag.* vol 21 no 6 p 596

[15] Boverman G, Khames M and Miller E L 2003 *Recent work in shape-based methods for diffusive inverse problems Review of Scientific Instruments* p 2580

[16] Chan T F and Tai X C 2004 *Level set and total variation regularization for elliptic inverse problems with discontinuous coefficients Journal of Computational Physics* p 40

[17] Soleimani M, Lionheart W R B and Dorn O 2006b *Level set reconstruction of conductivity and permittivity from boundary electrical measurements using experimental data Inverse Problems in Science and Engineering* vol 14 No 2 p 193

[18] Soleimani M 2007 *Level-Set Method Applied to Magnetic Induction Tomography using Experimental Data Research in Nondestructive Evaluation* vol 18 p 1

[19] Banasiak R and Soleimani M 2010 *Shape based reconstruction of experimental data in 3D electrical capacitance tomography NDT&E International* vol 43 p 241

[20] Adler A, Dai T and Lionheart W R B 2007 *Temporal Image Reconstruction in Electrical Impedance Tomography Physiol. Meas.*, vol 28 p 1

[21] Cheney M, Isaacson D, Newell J C, Simske S and Goble J C 1990 *NOSER: an algorithm for solving the inverse conductivity problem Int. J. Imaging Syst. Technol.* vol 2 pp 66

[22] Adler A, Guardo R 1996 *Electrical impedance tomography: regularized imaging and contrast detection IEEE Trans. Med. Imaging* vol 15 pp 170

[23] Dorn O, Lesselier D 2009 *Level set methods for inverse scatteringsome recent developments Inverse Problem* vol 25 p 11

[24] DeCezaro A, Leito A, Tai X C 2009 *On multiple level-set regularization methods for inverse problems Inverse Problem* vol 25

[25] Irishina N, lvarez D, Dorn O, Moscoso M 2009 *Detecting and imaging dielectric objects from real data: A shape-based approach Mathematical and Computer Modelling* in press

Measurement of lung air volume during digital sport shooting using EIT

Satoru Nebuya [1], Naoaki Itakura [2], Junko Kataoka[3], Brian H. Brown[4], Makoto Noshiro[1]

[1] Graduate School of Medical Science, Kitasato University, Sagamihara, Japan
[2] Dept. of System Engineering, University of Electro-Communications, Chofu, Japan
[3] Japan Woman's College of Physical Education
[4] Dept. of Medical Physics, University of Sheffield, Sheffield, UK

nebuya@kitasato-u.ac.jp

Abstract. Lung air volume had been measured to investigate difference in respiration patterns during digital sport shooting (DSS) between one male athlete and five male beginners using electrical impedance tomography (EIT). The athlete had shown high score in DSS, periodic respiration pattern and same absolute lung air volume synchronized with timing at triggering. On the other hand, five beginners had shown lower scores in DSS, no periodic respiration pattern and any similarity with that of an athlete. When all of beginners had learned the respiration pattern of an athlete measured with EIT, their scores at DSS had shown clear increase.

1. Introduction

A breathing method has been well known as a way to give sedative effect or relaxation commonly. In addition, it has been often used in athletes to get higher score at their competition by eliciting physiological and psychological effects. However, a small number of quantitative investigations had been carried out to show a correlation between a breathing method and physiological state. Although a spirometer, a thermistor and an impedance phlethysmography have been used to verify respiration pattern during sports, they have some disadvantages to use in sports field. A spirometer can measure volume of air directly but there is restraint to do sports. Other indirect measurement methods demand strict calibration and are unable to measure absolute lung air volume.

A novel indirect measurement method had been proposed using electrical impedance tomography (EIT) [1]-[3]. As the method could measure absolute lung air volume non-invasively, it had been considered to achieve quantitative measurement of both respiration pattern and absolute lung air volume.

Shooting is one of traditional competition in an Olympic game. However, quantitative analysis of physiological and psychological behaviour has not been carried out to get a higher score. In this study, lung air volumes during digital sport shooting (DSS) had been measured to investigate relationship between respiration pattern and score of shooting for an athlete and five beginners using EIT.

1

2. Method

Absolute DSS does not need to use bullets but a laser beam. And it had been designed similar condition of bullet gun shooting. One male athlete and five male beginners had done DSS. The athlete had gotten an experience of shooting for 20 years and won some national prizes. The athlete had achieved 60 shots per target within 70 minutes at distance of 10 meters to a target (Fig.1). However, five of beginners shot at half distance of it as it were too hard to shoot a target for them. The highest score, a ten, was achieved by shooting a laser shot into the centre. A full mark of a competition was 600 points. During DSS, we had recorded EIT, score at a shot, timing at triggering, acceleration of a gun point, respiration waveform by thermistor, heart rate using optical pulse-meter and perspiration (Fig.2). A Sheffield Mk3.5 system is used for the EIT indirect measurement of absolute lung air volume [4]. Eight ECG electrodes (F-150U5, Nihon Koden Co) are placed around the chest at 5 cm above the xiphoid process.

Fig. 1 a target for DSS.
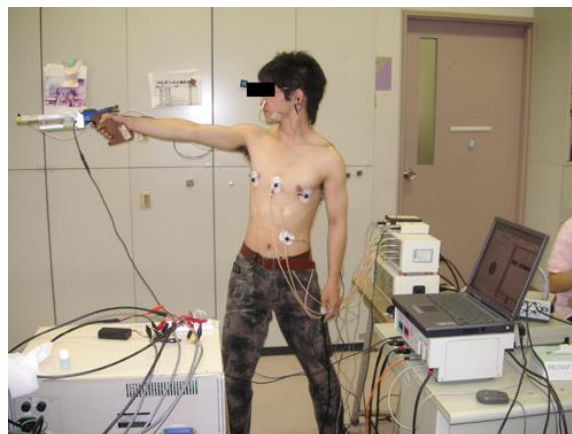
Fig. 2 Experimental scene.

3. Results and discussion

Examples of respiration waveforms estimated with EIT and timings at triggering were shown in Fig.3. Fig.3(a) and (b) show respiration waveform measured from an athlete and a beginner respectively. In the Fig.3(a), the result shows periodic pattern of shooting and respiration waveform measured with an athlete. Intervals of shooting were longer than that in a beginner (Fig.3(b)) and the athlete stop breathing at close lung air volume for approximately 15 seconds before a triggering at every shooting. On the other hands, a beginner shot about every 10 seconds and respiration pattern was not the same. In addition, lung air volumes were quite different at every shooting in Fig.3(b). Such a trend was similar in all of five beginners.

From those results, three important points were considered to get higher score in DSS as follows.

　　1) the athlete held his breathing about 10 seconds before triggering.
　　2) the athlete had rests over half minutes after every shooting.
　　3) absolute lung air volumes at triggering were same.

After first trial of DSS by beginners, they were tained to follow these points and tried DSS again on other days.
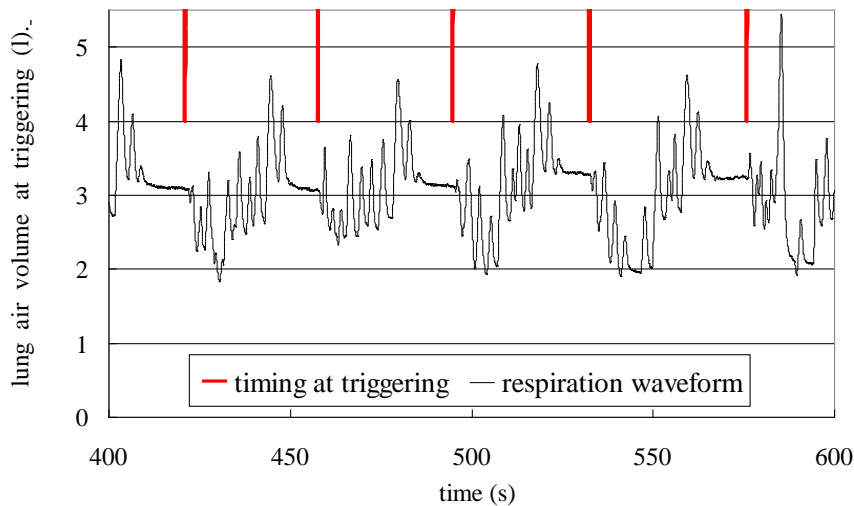
(a) an athlete
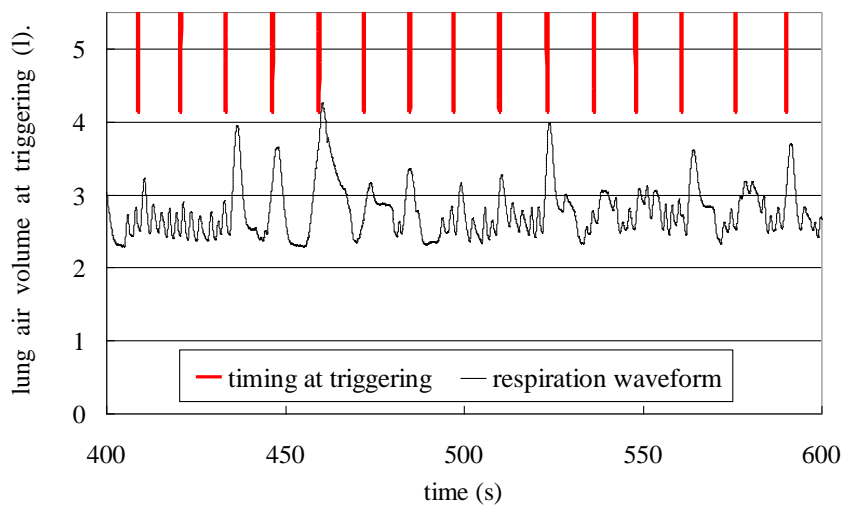
(b) a beginner

**Fig. 3 Relationships between timing at triggering and respiration waveform
in an athlete and a beginner**

Table 1 shows relationship between lung air volumes at triggering and shooting points between before and after training. All of lung air volumes at triggering during 60 shots were averaged in all of subjects. Coefficients of variations (CV) were also calculated in order to check dispersions of lung air volumes. Before training, averaged lung air volumes were different in all of the biginers and CV%s were clearly bigger than that in the athlete. On the other hands, CV%s were decreased and averaged scores were increased obviously in all of the

3

beginers after training. Then we considered that a training method by monitoring their respiration pattern was very feasible for beginners to increase their score in short term.

To decrease trembling of a hand, apnea is considered to be effective. However, oxygen deficit have to be avoided as it also occurs trembling. The reason of that the athlete had stopped breathing for same period and level of lung air volume was considered to keep constant PaO2 to decrease trembling of his hand and maintain stable muscle condition of his arm and body. In our further investigation, this assumption will be verified by analyzing other physiological parameters we had recorded.

Table 1   Relationship between lung air volumes at triggering and shooting points between before and after training.

	lung air volume (l)		SD		CV%		score per a shot (points)	
	before	after	before	after	before	after	before	after
beginner 1	3.0	2.0	0.5	0.2	17.8	9.1	7.1	7.6
beginner 2	4.9	4.1	0.6	0.1	12.6	3.1	7.2	7.9
beginner 3	3.7	2.9	0.4	0.3	12.0	10.4	7.1	8.1
beginner 4	2.5	1.7	0.7	0.4	27.0	24.8	6.3	7.8
beginner 5	1.4	1.5	0.7	0.2	52.2	13.2	7.5	9.2
athlete	3.3		0.3		9.1		9.3	

SD: standard deviation, CV: coefficient of variation,
before: before training, after: after training

References
[1]   Brown B H, Primhak R A, Smallwood R H, Milnes P, Narracott A J and Jackson M J, 2002, *Neonatal lungs –can absolute lung resistivity be determined non-invasively?*, Med. Biol. Eng. & Comp. 40, 388-394.
[2]   Brown B H, Milnes P and Mills G H, *Indirect measurement of lung density and air volume from electrical impedance tomography (EIT) data*, 2006, Proc. 7th Conf. Biomed. Appli. Electrical Impedance Tomography, Seoul, 85-89.
[3]   Nebuya S, Kitamura K, Kobayashi H, Noshiro M and Brown B H, *Measurement accuracy in pulmonary function test using electrical impedance tomography*, 2007, Proc. VIII International Conf. on Electrical Bio-Impedance, Graz, 17, 539-542.
[4]   Wilson A J, Milnes P, Waterworth A R, Smallwood R H, Brown B H, 2001, *Mk3.5: a modular, multi-frequency successor to the Mk3a EIS/EIT system*, Physiological Measurement, 22, 49-54

An integrated lung function reference laboratory for test and calibration of EIT devices

G. Hahn, A. Just, J. Dittmar, M. Quintel

Department of Anaesthesiology, Emergency and Intensive Care Medicine
University Medical Centre Göttingen

Robert-Koch-Str. 40, D-37075 Göttingen, Germany

E-mail: ghahn@gwdg.de

Introduction

It has been shown in several validation studies that the distribution of ventilation is reliably accessible by application of Electrical Impedance Tomography (EIT). Many validation studies (e.g. Hinz *et al.*, 2003) have been performed on animals since invasive reference techniques are much easier applicable for ethical reasons in animals than in humans. Application of invasive reference techniques in combination with EIT in humans is only possible if the primary disease requires an invasive examination technique which is only the case in severely ill patients (e.g. Victorino *et al.*, 2004). Since the thoracic shape, location of the lungs and other anthropometric parameters are quite different between animals (e.g. pigs) and patients, animal studies can't surrogate a validation on humans.

We believe that the application of state of the art non invasive reference techniques for lung function tests is mandatory simultaneously to EIT at any time for well controlled studies on human volunteers as well as on patients with various lung diseases. The target of the described integrated concept was to combine proven technical reference techniques in the field of EIT and physiological reference methods for lung function testing in one laboratory environment. Therefore we established an integrated concept in our laboratory consisting of the following facilities.

Methods

Two main areas are covered by the reference laboratory, a methodological one and a physiological one. In the methodological area we combined test procedures based on specific types of phantoms (Hahn *et al.*, 2000, Hahn *et al.*, 2008) to be able to quantify the performance of different types of EIT systems themselves and the reliability of their results of measurements. The purely resistive phantoms are intended to quantify the specific electrical properties of a tested EIT system. Additionally the integrity of the cable harness for the electrodes can be tested if appropriate adapters are used. Especially an extension of such resistive phantoms to multiple planes is helpful for the test of the basic function of multiple plane EIT systems. We also built electrolytic tanks of realistic human geometry for comparison of theoretical simulations and real measurements.

A major improvement that allows a quantitative comparison between non invasive global reference techniques and local EIT measurements in one plane is the extension of EIT for simultaneous measurements in multiple planes. We developed an upgrade kit for the Goe-MF II EIT system that allows a synchronisation of multiple Goe-MF II devices via the USB bus in a phase locked loop so that measurements in multiple planes can be performed completely synchronised. This approach allows a flexible extension of an existing, CE certified Goe-MF II system by simply adding an additional one to a free USB port. Thus a modular and flexible extensibility of EIT measurements to the number of planes needed is secured without affecting the existing CE certification.

The physiological part of the laboratory covers established common methods for lung function tests as described below:

Spirometry is accomplished by a MasterScreen Pneumo® pneumotachometer (Carefusion, Höchberg, Germany) in combination with a software package (JLab 5.3, Carefusion, Höchberg, Germany) for quantification of flow and lung volume changes.

Since standard spirometry is not able to quantify quasi static lung volumes (e.g. the functional residual capacity, FRC) we use a body plethysmograph for this purpose and modified a MasterScope® Body (Carefusion, Höchberg, Germany) in such a way that EIT measurements in three planes can be performed simultaneously to the plethysmographic measurements. Therefore we equipped the body box with air tight cable glands and installed three sets of EIT harnesses. Body plethysmography is the "gold standard" for lung volume quantification. Briefly described, in a bodyplethysmograph a pneumotachometer is used to measure airflow while a pressure transducer at the mouthpiece with a shutter measures the alveolar pressure. Thoracic gas volumes (TGV) as well as airway resistance (RAW) can be determined and it is possible to distinguish between restrictive and obstructive lung diseases.

Due to the demands of different physiological conditions the body box can't be used in all cases (e.g. different body positions, see below). We additionally use an IOS Impulse Oscillometry system (Carefusion, Höchberg, Germany) to be able to acquire spirometric volumes and central as well as peripheral airway resistance data under specific conditions. To put it simply, during Impulse Oscillometry short pulses are applied to the respiratory system by a loudspeaker at the mouthpiece and the mechanical respiratory input impedance (not an electrical one) is determined based on the flow and pressure measurements. This technique allows a reliable determination of central and peripheral airway resistance.

All these non-invasive reference techniques are global ones and should be applied preferably in combination with synchronous multiple plane EIT measurements. If invasive reference measurements in a single plane are ethically justified access to the facilities of Computed Tomography (CT) is guaranteed by a modern CT for scientific purposes.

The presented integrated approach comprises the facilities to perform measurements under the following physiological conditions: Of course measurements in different body positions (standing, sitting, supine, left and right lateral) are possible. In addition a tilt table allows rotating volunteers from a standing position to a complete head down position. In all positions breathing at well defined levels of positive end-expiratory pressure (PEEP) can be established. The reason for breathing in different positions is an artificial change of the gravitational forces to the chest lung system. We therefore use occasionally the additional

facilities of parabolic flights to change the magnitude of the gravitational forces from microgravity to approximately double gravity but with an unchanging direction.

Results

Due to the various measurement capabilities of the described approach we would like to present here only an exemplary result of a synchronous multiple plane EIT measurement in parallel to spirometry on a human volunteer.

After a short transient oscillation of the phase locked loop the synchronicity of the Goe-MF II systems in a multiple plane configuration was verified to be always less than 100 microseconds with a remaining phase jitter of less 10 microseconds. This guaranties a proper switching of the selected pattern of current injection and voltage measurements inside and between the EIT systems connected to the USB bus.

Figure 1 shows in the left panel the tomographic results (Goe-MF II 3D device, EIT group Göttingen, Germany) of a thoracic measurement in three planes at a frame rate per plane of 6.6 frames per second in conjunction with a spirometric measurement. The subject was in a sitting position at normal breathing. The electrode planes were located as follows: bottom plane at the level of the xiphoid process, mid plane 4.5 cm above the bottom plane and the upper plane 4.5 cm above the mid plane. The right panel shows in the upper tracing the spirometric data.
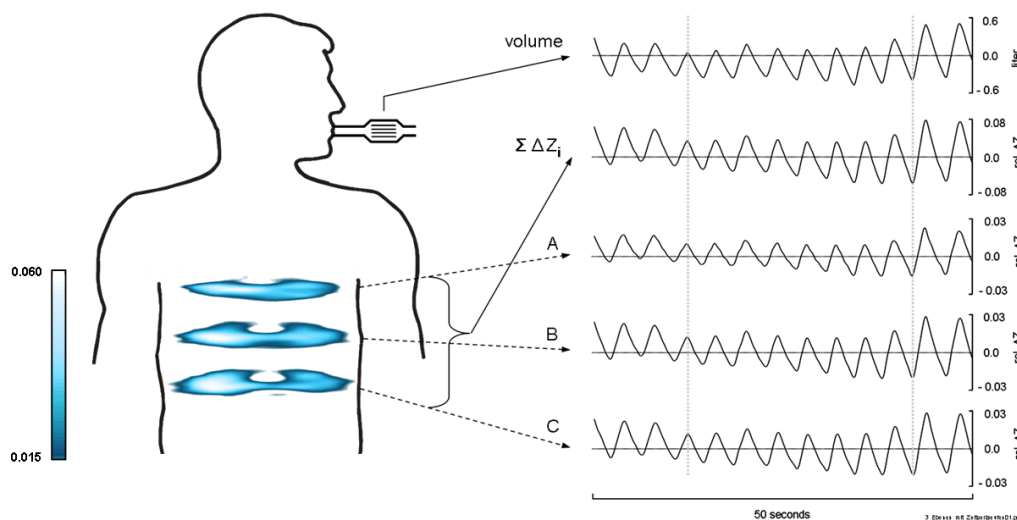
Figure 1 Simultaneous measurement of ventilation distribution in three electrode planes. Left panel: functional tomograms of ventilation distribution. Right panel: tracings of spirometry (reference measurement) and multiple plane EIT. Upper tracing: reference volume by spirometry. Tracing below: sum of the mean relative impedance changes in the three planes. Tracings A, B and C: mean relative impedance change in the upper plane, middle plane and bottom plane, respectively.

The tracing ($\Sigma \ \Delta Z_i$) below the tracing of the volume was computed from the sum of the mean relative impedance changes in each of the planes. Tracing A originates from the upper plane, tracing B from the middle plane and tracing C from the bottom plane. In all thoracic levels the original amplitude and time pattern of the spirometric reference measurement is well reflected by the EIT measurement. As expected from lung physiology (West, 1962; Milic Emili *et al.*,

1966; Milic Emili, 1986) the total amplitude of ventilation is less in the upper part of the lungs (tracing A). The two vertical grey lines indicate the proper synchronicity of the three EIT modules (Goe-MF II with upgrade kit). By this combination of a global, non invasive reference technique and a synchronous multiple plane EIT measurement that covers the lungs it is possible to quantify cranio-caudal redistributions in pathologic lungs on a breath by breath basis.

Summary

We present a framework of a laboratory environment that covers several technical facilities for tests of EIT systems as well as established facilities for physiological lung function reference measurements. It allows an efficient test and comparison of different devices and methodological approaches for lung function monitoring by using EIT. We believe in the value of this integrated concept for future work in the field of EIT development and application.

Acknowledgments

References

Hahn G, Beer M, Frerichs I, Dudykevych T, Schroder T and Hellige G 2000 A simple method to check the dynamic performance of electrical impedance tomography systems *Physiol Meas* **21** 53-60

Hahn G, Just A, Dittmar J and Hellige G 2008 Systematic errors of EIT systems determined by easily-scalable resistive phantoms *Physiol Meas* **29** S163-72

Hinz J, Neumann P, Hahn G, Dudykevych T, Maripu E, Anderssonn L G, Hellige G, Burchardi H and Hedenstierna G 2003
Electrical Impedance Tomography measures ventilation distribution - A comparison with ventilation scintigraphy *Chest* **124** 314-22

Milic-Emili J, Henderson J A, Dolovich M B, Trop D and Kaneko K 1966
Regional distribution of inspired gas in the lung *J Appl Physiol* **21** 749-59

Milic-Emili J. Static distribution of lung volumes. In*: Handbook of Physiology. The Respiratory System. Mechanics of Breathing.* Bethesda, MD. Am. Physiol. Soc., 1986, sect. 3, **vol. III**, pt. 2, chapt. 31, 561–574.

Victorino J A, Borges J B, Okamoto V N, Matos G F, Tucci M R, Caramez M P, Tanaka H, Sipmann F S, Santos D C, Barbas C S, Carvalho C R and Amato M B 2004
Imbalances in regional lung ventilation: a validation study on electrical impedance tomography *Am J Respir Crit Care Med* **169** 791-800

West J B 1962
Regional differences in gas exchange in the lung of erect man *J Appl Physiol* **17** 893-8

Effects of high-frequency oscillatory ventilation determined by EIT in patients with chronic airway obstruction

Sven Pulletz[1], Ute Achtzehn[2], Andreas Pechmann[2], Michael Quintel[3], Norbert Weiler[1], Inéz Frerichs[1]

1 Department of Anaesthesiology and Intensive Care Medicine, University Medical Centre Schleswig-Holstein, Campus Kiel, Kiel, Germany
2 Department of Internal Medicine IV, Medical Centre Chemnitz, Chemnitz, Germany
3 Department of Anaesthesiology, Emergency and Intensive Care Medicine, University Medical Centre, Göttingen, Germany

Introduction: High-frequency oscillatory ventilation (HFOV) is an alternative type of mechanical ventilation routinely used only in neonatal patients (Gerstmann *et al.*, 2001). In adults, HFOV is almost exclusively applied only in patients with acute lung injury or acute respiratory distress syndrome. It is expected that in these patients HFOV reduces the incidence of ventilator-associated lung injury (Chan *et al.*, 2007). HFOV is usually considered as contraindicated in patients with obstructive lung disease because of the theoretical risk of air trapping and hyperinflation. According to our knowledge HFOV has never been applied in patients with chronic obstructive pulmonary disease (COPD).

The aim of this study was to establish if HFOV can be safely and effectively applied in patients with exacerbation of COPD and respiratory failure. Electrical impedance tomography (EIT) was used to monitor the effects of HFOV on regional lung ventilation and aeration.

Methods: Ten patients with acutely exacerbated COPD (age: 63 to 83 years, GOLD stages II-IV) requiring intensive care treatment who failed on non-invasive ventilation were studied. Analgesia and sedation was accomplished by intravenous fentanyl and midazolam, no muscle blocking agents were administered. All patients were studied in a head-up tilted ($20°$) supine position. After initial conventional mechanical ventilation (CMV) of less than 72 hours all patients were transferred to HFOV for 24 hours and then back to conventional ventilation. During HFOV an oscillation frequency of $300 \cdot \text{min}^{-1}$ and power of 70 was used when arterial partial pressure of CO_2 ($PaCO_2$) was higher than 60 mmHg, otherwise the frequency of $360 \cdot \text{min}^{-1}$ and power of 60 were chosen. Regional lung volume changes were assessed by EIT (Goe-MF II, CareFusion, Hoechberg, Germany). EIT data were acquired at $25 \text{ scans} \cdot \text{s}^{-1}$ using a set of 16 self-adhesive ECG electrodes placed around the chest at the 5-6th intercostal space. Excitation electrical currents of 5mArms and 50 kHz were used during all EIT

examinations. EIT scans were generated using a back-projection image reconstruction algorithm which calculates the instantaneous changes in electrical impedance relative to reference electrical impedance in a total of 912 image pixels. To characterize the ventilation distribution in the chest cross-section, regional tidal volumes were determined from the series of EIT scans acquired at different examination time points. Regional tidal amplitude of relative impedance change was calculated as the difference between the inspiratory (maximum) and expiratory (minimum) values from multiple consecutive either conventional breaths or oscillations in each image pixel. During CMV, the EIT signal was band-pass filtered, the cut-off frequencies were set below the first and above the third harmonic of the breathing rate. During HFOV, the EIT signal was also band-pass filtered, the cut-off frequencies were set below the first and above the second harmonic of the oscillation rate. Arterial blood gases, spirometry and hemodynamics parameters were repeatedly obtained in all phases of CMV and HFOV at different settings.

Results: HFOV was tolerated well, no adverse effects or hemodynamic compromise were observed. The patients were transferred to HFOV after an average period of 49 hours and 44 minutes. The EIT data revealed an expected large difference between the small oscillations during HFOV and larger mechanical breaths during CMV. Ventilation was more homogeneously distributed during HFOV than during initial CMV (Figure). No signs of severe hyperinflation induced by HFOV were identified by EIT. Higher respiratory system compliance and tidal volume were found during CMV after 24 hours of HFOV than before. Effective CO_2 elimination and oxygenation were achieved.

Conclusions: Contrary to present recommendations on the use of HFOV in adult patients our pilot study indicates that the use of HFOV in patients with acute exacerbation of COPD can be safely and effectively applied in this patient group. Adequate pulmonary gas exchange with good CO_2 elimination and oxygenation was achieved and no adverse effects or hemodynamic compromise observed. The distribution of ventilation was more homogeneous during HFOV compared with CMV and the respiratory system mechanics improved after 24 hours of HFOV. Along with a the results of a recent experimental HFOV study (Wolf *et al.,* 2010), our study indicates that EIT is a suitable tool for monitoring regional lung ventilation distribution during HFOV.

References:
Chan K P, Stewart T E and Mehta S 2007 High-frequency oscillatory ventilation for adult patients with ARDS *Chest* **131** 1907-16
Gerstmann D R, Wood K, Miller A, Steffen M, Ogden B, Stoddard R A and Minton S D 2001 Childhood outcome after early high-frequency oscillatory ventilation for neonatal respiratory distress syndrome *Pediatrics* **108** 617-23

Wolf G K, Grychtol B, Frerichs I, Zurakowski D and Arnold J H 2010 Regional lung volume changes during high-frequency oscillatory ventilation *Pediatr Crit Care Med* **11** 610-5
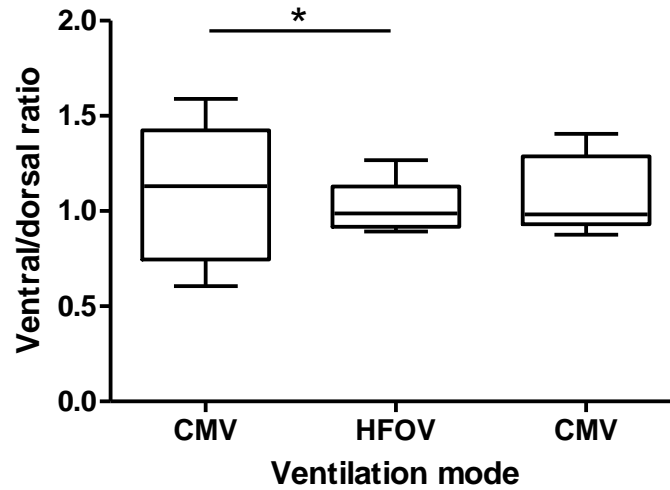
Figure: Ventilation distribution between the ventral and dorsal halves of the chest cross-section in COPD patients during conventional (CMV) and high-frequency oscillatory ventilation (HFOV). The CMV data were obtained before (left box) and after 24 h of HFOV (right box). The HFOV data (middle box) reflect the ventilation distribution after 24h of HFOV immediately before transition to CMV. A significant difference in variance is indicated.

Integration of EIT with ECG and respiration monitoring

Hyunji Kim, Tae Eui Kim, Tong In Oh and Eung Je Woo

Impedance Imaging Research Center and Department of Biomedical Engineering, Kyung Hee University, Gyeonggi-do, Korea

E-mail: ejwoo@khu.ac.kr

Abstract. Electrical impedance measurements (EIT) can produce real-time images of conductivity variations associated with respiratory and cardiac cycles. We present how we could integrate our EIT system with ECG and respiration monitoring. In addition to allowing ECG and/or respiration gated EIT imaging, such an integrated system may improve the clinical significance of the patient monitoring. We integrated a 16-channel KHU Mark2 EIT system with a custom-developed ECG and respiration monitor. The EIT system sends signals of actual EIT data collection times to the monitor. It also gets trigger signals from the monitor for gated EIT image reconstructions.

Keyword: EIT, ECG, respiration, patient monitoring

1. Introduction

Electrical impedance tomography (EIT) produces cross-sectional images of a conductivity distribution inside the human body using measured boundary current-voltage data sets. EIT can produce functional images of conductivity variations associated with physiological events such as cardiac and respiratory cycles [1,2]. To correlate such events with EIT images, we may use a biosignal-gated EIT imaging method. Incorporation of ECG and respiration monitoring signals into EIT images can improve interpretation of EIT images [3]. This may allow us to capture fast cardiac events in EIT images and also improve the signal-to-noise ratio (SNR) in EIT measurements.

Recently, we developed a fully-parallel fast EIT system called by the KHU Mark2 [4]. It has the maximum data acquisition speed of 100 frames/s. We integrated the KHU Mark2 system with a custom-developed ECG and respiration monitor using a conductive fabric electrode belt. The ECG monitor transfers an R-wave trigger signal to the EIT system for synchronized EIT measurements [5]. At the same time, the EIT system provides timing signals of its actual voltage measurement times.

2. Method

We developed an ECG and respiration monitor using a fabric electrode belt as a sensor. The fabric electrode belt includes multiple conductive fabric ECG electrodes and a piezoelectric sensor to measure respiration-related changes of the chest volume. We modified the KHU Mark2 EIT system so that it gets two trigger signals for biosignal-gated EIT imaging. At the same time, it sends its own data collection timing signals to other devices.

Getting R-wave trigger signals from the ECG monitor, for example, the KHU Mark2 initiates a series of EIT data acquisitions with a chosen frame rate. We implemented such

timing controls inside the intra-network controller of the KHU Mark2 EIT system since it controls all impedance measurement modules (IMMs). Inserting any needed time delay after the gating signal, the intra-network controller broadcasts a series of 'projection start' signals to IMMs. During normal and also gated imaging modes, the intra-network controller of the EIT system also generates timing signals of actual EIT data acquisition times. One may use this signal to correlate EIT images with separately acquired biosignals. Figure 1 shows the structure of the integrated KHU Mark2 EIT system with the ECG and respiration monitor.
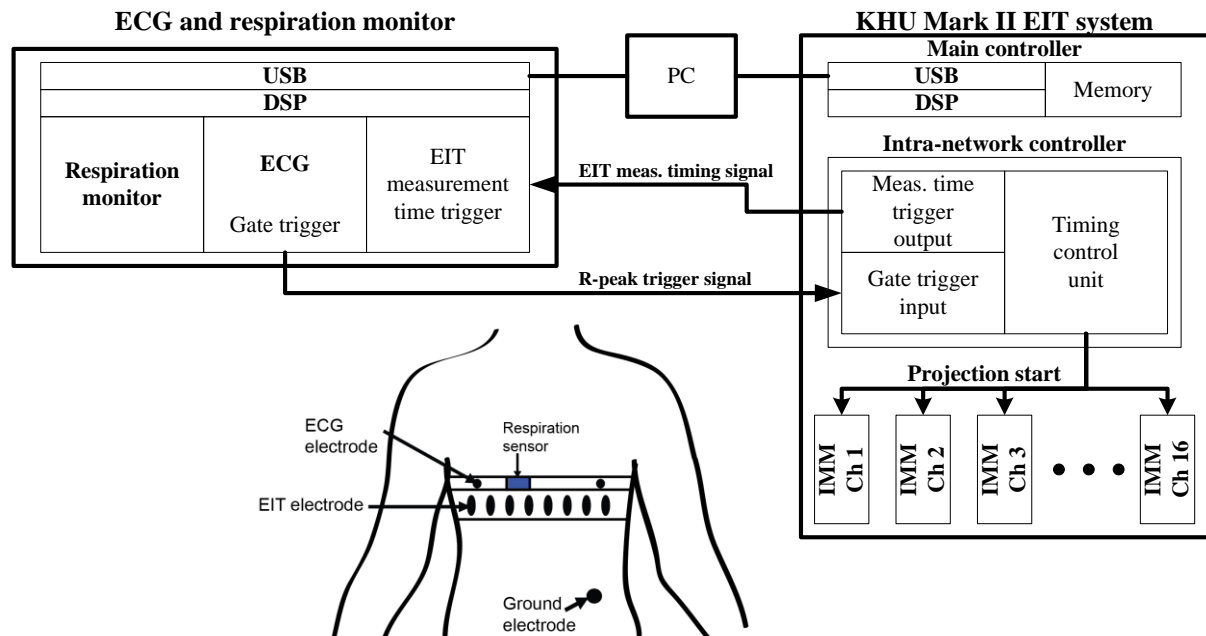
Figure 1. Integration of KHU Mark2 EIT system with ECG and respiration monitor.

3. Result

Figure 2(a) and (c) show measured ECG and respiration signals, respectively. The R-peak trigger signal in (b) can initiate a series of EIT measurements. Figure 2(d) plots the timing signal from the KHU Mark2 providing accurate timing information on EIT data acquisitions.
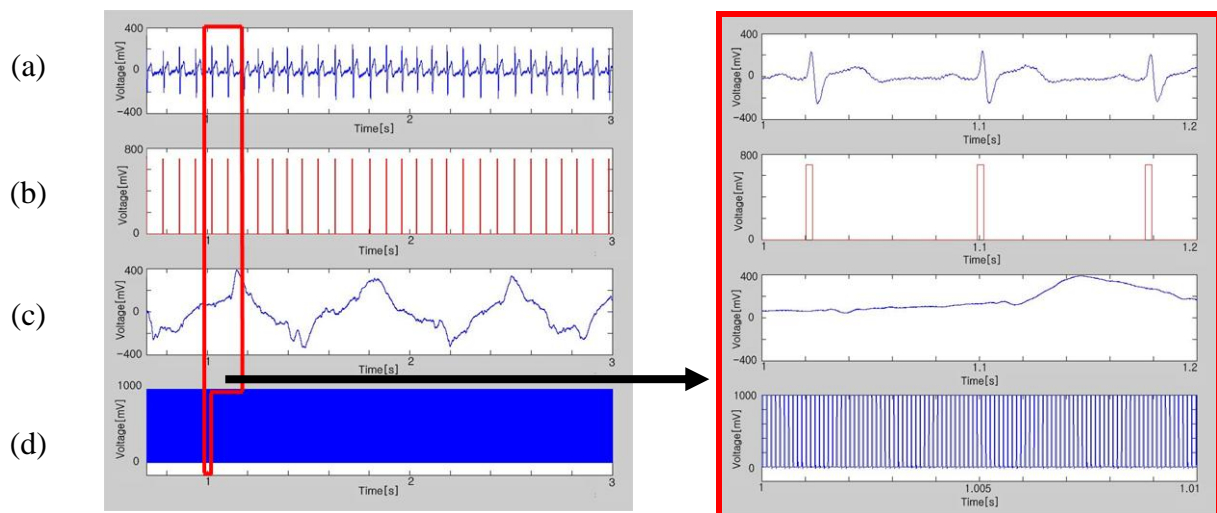
Figure 2. (a) ECG, (b) R-peak trigger signal, (c) respiration signal and (d) EIT data acquisition timing signal. We expanded the time scale in the right side.

Figure 3 shows an example of ECG-gated EIT imaging. The EIT images in figure 3 are consistent since they were captured right after R-waves. Figure 4 shows an example of respiration gating where we averaged EIT images acquired at the same respiration phase.

(a) ECG signal

(b) R-peak trigger signal

(c)   (d)   (e)   (f)   (g)
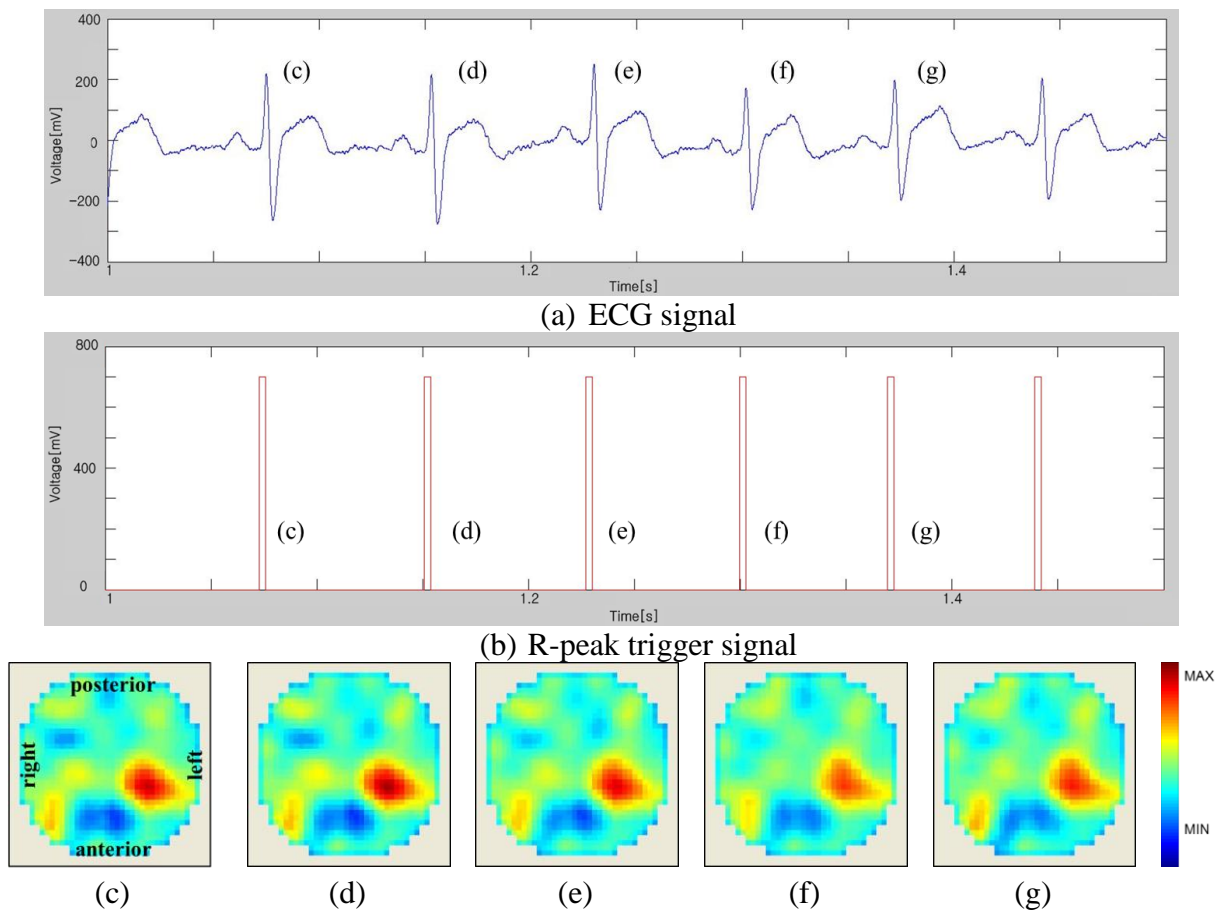
Figure 3. Example of ECG-gated EIT imaging.

(a) Respiration signal and EIT measurement time points

(b)   (c)   (d)   (e)   (f)
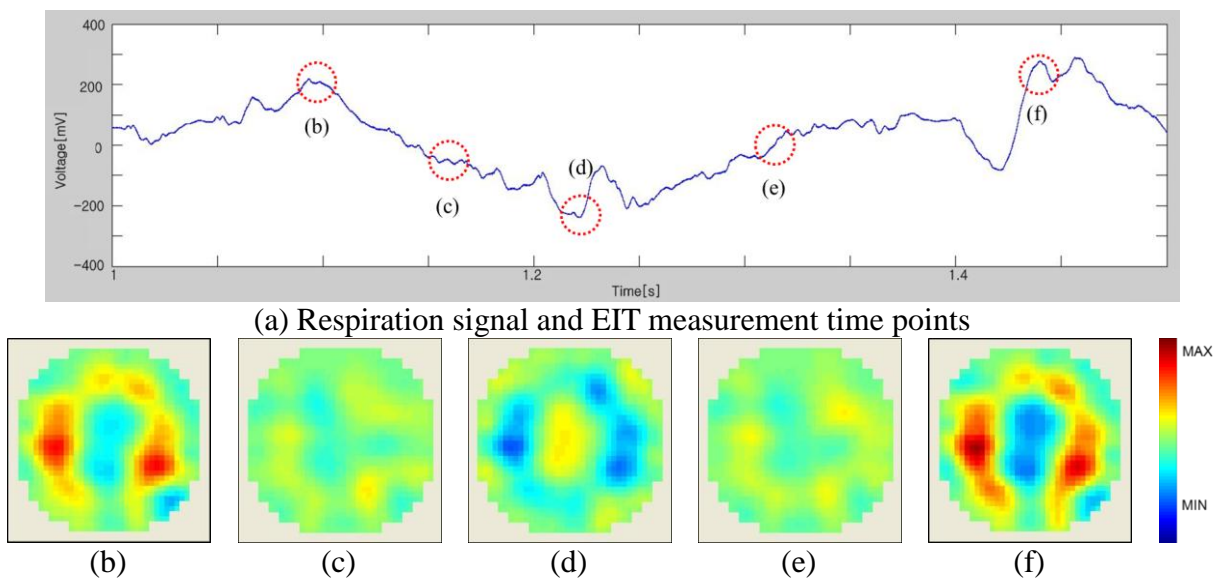
Figure 4. Example of respiration-gated EIT imaging.

4. Conclusion and discussion

We demonstrated how to integrate the KHU Mark2 EIT system with a ECG and respiration monitor. The integration will be a valuable feature of the KHU Mark2 as a clinical EIT system. Gating signals from the monitor allows us to perform biosignal-gated EIT imaging. Data acquisition timing signals from the KHU Mark2 help us to interpret EIT images together with separately acquired biosignals. With these two functions, we plan to image fast cardiac events as well as slow respiratory events with better SNRs and event synchronizations. We may also apply this integrated system to reject motion artifacts in EIT images [6]. As a part of our future studies, we plan to integrate our EIT system with EEG for multi-modal functional bead imaging.

Acknowledgement

Reference

[1]   Holder D S, 2005 *Electrical Impedance Tomography: Mehods, History and Applications* (IOP: Bristol, UK)
[2]   Li J H, Joppek C and Faust U 1996 Fast EIT data acquisition system with active electrodes and its application to cardiac imaging, Physiol. Meas. **17** A25-A32
[3]   Brown B H, Barber D C, Morice A H and Leathard A D 1994 Cardiac and respiratory related electrical impedance changes in the human thorax *IEEE Trans. Biomed. Eng*. **41** (8), 729-734
[4]   Oh T I, Wi H, Kim D Y, Yoo P J and Woo E J 2011 Fully parallel multi-frequency EIT system with flexible electrode configuration: KHU Mark2. *Physiol. Meas*. in press
[5]   Eyuboglu B M, Brown B H and Barber D C 1989 In vivo imaging of cardiac related impedance changes *IEEE Eng. Med. Biol*. **8** (1), 39-45
[6]   Zhang J and Patterson R P 2004 Analysis on the influence of tissues/organs' movements in EIT images of lung ventilation using finite difference thorax models *IEMBS'04*, *San Francisco, CA*

Regional ventilation distribution in sub-lobar acute lung injury – An experimental validation study on electrical impedance tomography

Gunnar Elke[1], Matthew K. Fuld[2,3], Ahmed F. Halaweish[2,3], Norbert Weiler[1], Eric A. Hoffman[2,3] and Inéz Frerichs[1]

1 Department of Anaesthesiology and Intensive Care Medicine, University Medical Centre Schleswig-Holstein, Campus Kiel, Kiel, Germany
2 Department of Radiology, Division of Physiologic Imaging, University of Iowa Carver College of Medicine, Iowa City, Iowa, United States
3 Department of Biomedical Engineering, University of Iowa, Iowa City, Iowa, United States

E-mail: elke@anaesthesie.uni-kiel.de

Introduction

Electrical impedance tomography (EIT) is able to trace ventilation-related changes in electrical properties of lung tissue. Previous studies using computed tomography (CT) suggested a good correlation between regional impedance and lung tissue density changes in healthy and acutely injured lungs (Frerichs *et al* 2002, Victorino *et al* 2004, Wrigge *et al* 2008). However, no validation data exist in regional acute lung injury (ALI).

The objective of this experimental study was to validate EIT measurements of regional ventilation by dynamic Xenon-multidetector-row CT (Xe-MDCT) in two animal models of regional sub-lobar ALI.

Methods

The study was approved by the University of Iowa committee for animal care and adhered to the guidelines on animal experimentation. Nine anaesthetized pigs (body weight 33 ± 2 kg) were studied in supine position during volume controlled mechanical ventilation with the following ventilatory settings: tidal volume 13 ± 2 ml/kg body weight, respiratory rate 18 ± 2 min^{-1}, PEEP 5 cmH$_2$O, fraction of inspired oxygen (F$_1$O$_2$) 0.21. Regional ALI was induced via a bronchoscope within two adjacent sub-lobar segments of the right lung by repetitive saline lavage (n=4) or endotoxin (n=5) (2.5-5mg Escherichia coli O55:H35 lipopolysaccharide, Sigma L4005, Sigma Chemical Co., St. Louis, Missouri, USA). ALI was allowed to develop for up to 90 minutes and was verified by MDCT. In the two injury models, the preinjured animals served as their own control.

60-s EIT measurements were obtained during continuous mechanical tidal ventilation with a scan rate of 25 scans/s (Goe MF II system, CareFusion, Höchberg, Germany). In order to determine accurate positioning of the EIT electrodes, an initial CT scan identified the lung region where ALI was planned to be induced. The respective intercostal space level was then tagged by the laser light of the CT scanner and 16 electrodes (Blue Sensor BR-50-K, Ambu, Ølstykke, Denmark) were accordingly placed on the thorax in one transverse plane. EIT scans were generated using a weighted back-projection reconstruction algorithm. Xe-MDCT imaging was performed using a Siemens Sensation 64 (Siemens AG, Forchheim, Germany) and correspondingly acquired in supine position without moving the animal between scans. The scanner settings were 80 KV, 150 mA, 1.2 mm slice thickness, 0.5 rotation time at the

same thoracic region. Time series images were acquired during tidal breathing with scanning at end-expiration including 7-baseline (room-air) and 50-wash-in breaths (53%Xe/47%O2). Regional ventilation was determined using the University of Iowa's Pulmonary Analysis Software Suite (PASS).

Changes in regional lung ventilation between ALI and control were determined from ventilation profiles generated as follows: Total ventilation was calculated over the whole image corresponding to 100% of ventilation in the chest cross-section. EIT and Xe-MDCT images were divided into 32 ventrodorsal regions of interest (ROI) in the right and left hemithorax. Then fractional ventilation within each ROI relative to the total ventilation was calculated. Regional ventilation difference profiles for both methods were generated by subtracting the corresponding control and ALI values.

GraphPad Prism 4.0 (GraphPad Software, San Diego, CA, USA) was used for statistical analysis. EIT and CT measurements were compared by Spearman's Rho correlation. Statistical significance was assumed at $p < 0.05$.

Results

In 4 out of 9 animals analyzed so far, regional lung ventilation difference images revealed a ventilation decrease in the injured lung with a corresponding increase in the non-injured lung compared to control, with regional ventilation changes occurring in spatially similar locations (see figure). Values of Spearman's rho ranged from 0.931-0.936 for the right and 0.943-0.979 for the left hemithorax in control. In ALI, value ranges were 0.857-0.933 (right hemithorax) and 0.948-0.981 (left hemithorax) ($p < 0.001$).

Conclusion

In this experimental study a good correlation was found between regional lung ventilation determined by EIT and Xe-MDCT in the 4 animals with sub-lobar ALI compared to date.

EIT   Xe-MDCT
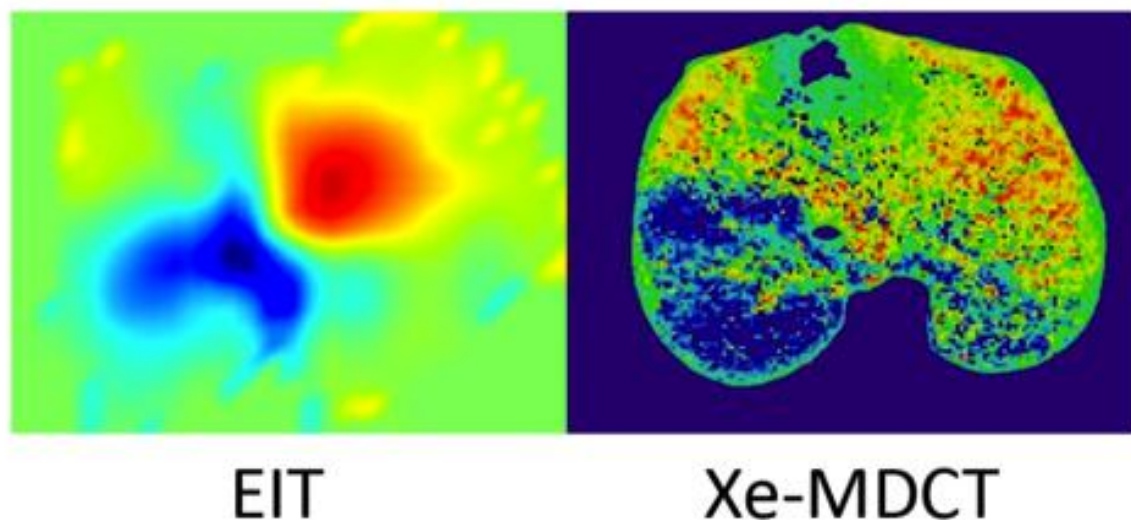
Figure. Regional lung ventilation difference after ALI induction determined by EIT (left) and Xe-MDCT (right) in one of the studied animals.

References

1. Victorino JA, Borges JB, Okamoto VN *et al* 2004 Imbalances in regional lung ventilation: a validation study on electrical impedance tomography Am. J. Respir. Crit. Care Med. **169** 791-800

2. Frerichs I, Hinz J, Herrmann P *et al* 2002 Detection of local lung air content by electrical impedance tomography compared with electron beam CT J. Appl. Physiol. **93** 660-666

3. Wrigge H, Zinserling J, Muders T *et al* 2008 Electrical impedance tomography compared with thoracic computed tomography during a slow inflation maneuver in experimental models of lung injury Crit. Care Med. **36** 903-909

Unsupervised localization of heart and lung regions in EIT images: a validation study

Damien Ferrario[1], Andy Adler[1,2], Josesp Solà[1], Stephan Böhm[1] and Marc Bodenstein[3]

[1]CSEM - Centre Suisse d'Electronique et de Microtechnique, Switzerland
[2]Systems and Computer Engineering, Carleton University, Ottawa, Canada
[3]Department of Anesthesiology, Johannes Gutenberg-University Mainz, Germany

Abstract: We describe an algorithm for automatic detection of heart and lung regions in a time series of EIT images. Candidate regions are identified in the frequency domain and image based classification techniques applied. The algorithm was validated on a set of simultaneously recorded EIT and CT data in pigs. In 20 of 21 cases, identified regions in EIT images corresponded to those manually segmented in the matched CT image. Results confirm the accuracy of anatomical features in EIT images, as long as morphologically accurate information is used in EIT reconstruction.

1. Introduction

Electrical Impedance Tomography (EIT) generates images of the conductivity distribution in the body, using electrical stimulation and measurement at surface electrodes. EIT shows promise for monitoring blood and air movement in the thorax, driven by its ability to generate an image of the regional distribution of these phenomena. In order to evaluate a sequence of EIT images, it is important to accurately identify the relevant anatomical regions: the heart and lungs (H&L). Several methods have been used to identify lungs ROI within a sequence of EIT images. Hahn *et al* (1995) used the standard deviation and Kühnel *et al* (1997) the maximum linear regression, to compute images of the ventilation distribution. Pulletz *et al*. (2006) showed that both methods give similar results. One limitation to such work is the lack of validation against gold standards.

In this paper, we propose an improved procedure to detect H&L ROIs from EIT images, and then validate our method by comparing EIT-based ROIs to manually segmented CT regions.

2. Methods

Overview: This work was performed in four stages: 2.1) the EIT image sequence was reconstructed, 2.2) the image sequence was analysed with a novel algorithm which uses temporal and spatial information to detect and localize H&L regions, 2.3) the acquisition of simultaneous EIT and CT images, and 2.4) validation of detected regions against manually segmented CT images.

2.1. EIT morphological reconstruction

We reconstruct EIT images that correspond morphologically to the matched CT image. Normalized time difference EIT images of conductivity change are reconstructed from EIT measurements using a one-step Gauss Newton algorithm based on a finite element model (FEM) of the thorax shape. FEM models were generated using Netgen based on boundary shape and electrode positions take from the CT image of the specific subject. Such anatomically accurate models are an important factor in the precision of the results; this requirement is elaborated in the

discussion section. The EIT sensitivity (Jacobian) matrix was calculated from a 3D tetrahedral FEM of 20799 vertices, in which the identified 2D body boundary in the CT slice containing the electrode positions was extruded into the vertical direction by half the body width above and below the electrode plane. Images were reconstructed onto a coarser 2D FEM model (946 vertices), also constructed from the anatomical body shape, but without electrode refinement. Parameters in this model are chosen as follows: the prior estimate of covariance between image elements is set to be the Gaussian high pass filter; noise variance is modelled to be equal on all EIT data channels; and the Tikhonov factor was chosen heuristically to give a good compromise between noise and image resolution.

2.2. Unsupervised detection of the heart and lungs activity on EIT images

The goal is to automatically identify ROIs for the H&L from a sequence of EIT images ($x(i,t)$, with pixel index, i, and time index, t). Initially, cardiac and respiratory frequencies are estimated, and the energy of each pixel at both frequencies is calculated. Cardio-respiratory images are then generated by associating to each pixel an energy value. Finally, adjacent pixels with significant activity are identified and associated to the H&L ROIs (see fig. 1).
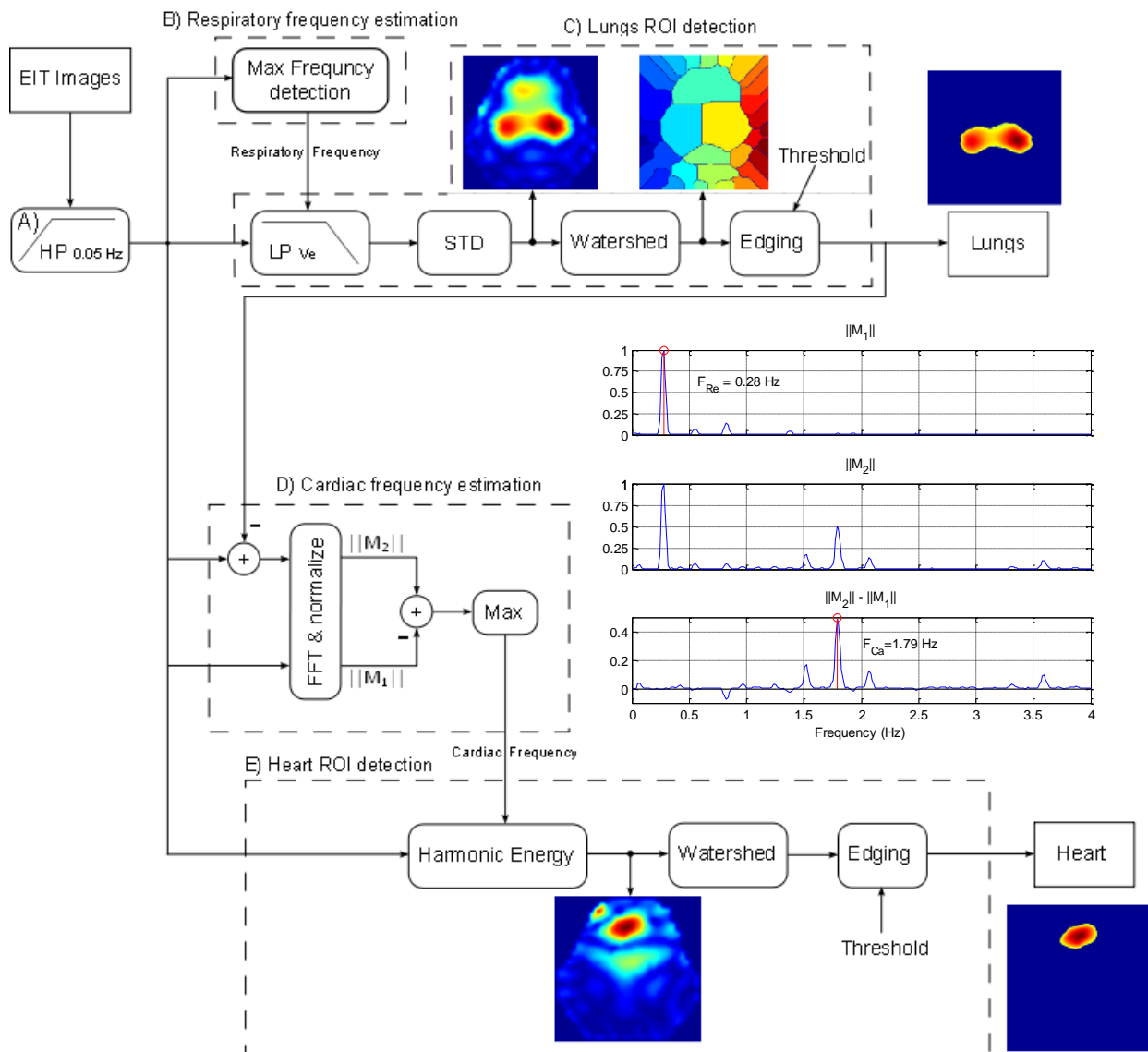
Fig. 1: Block diagram of the automatic detection of the lungs and heart activity using EIT.

Step A: a High Pass (HP) filter (cutoff frequency: 0.05 Hz, 4th order FIR filter) is applied to $x(i,t)$ to remove activity at low frequencies that is not related to heart or lungs activity.

Step B: the respiratory frequency f_{Re} is estimated. Initially, an averaged signal $m_1(t)$ is calculated. Respiratory frequency (f_{Re}), is then estimated as (example in fig. 1B):

$$M_1(f) = FFT(m_1(t)), \tag{1}$$

$$f_{Re} = \arg\max_f \|M_1(f)\|. \tag{2}$$

Step C: pixels depicting respiratory activity are detected and grouped together in a lung ROI, as suggested by Hahn *et al* 1995. $x(i,t)$ is Low Pass (LP) filtered (to get $x_{Re}(i,t)$) and the respiratory activity of each pixel is then estimated using a temporal standard deviation (std). Lungs ROI are identified via a watershed technique (Fernand 1994). The lungs ROI is assigned to the regions containing the two highest local maxima. Finally, a threshold, T is applied to respiratory activity levels, determining the ROI size.

Step D: the cardiac frequency (f_{Ca}) is estimated. The spectral content of all pixels not part of the lungs are summed ($m_2(t)$, with FFT $M_2(f)$); some respiratory component is still present but less than the image average. M_1 and M_2 are normalized and subtracted to highlight the cardiac frequencies. Cardiac frequency is estimated as:

$$f_{Ca} = \arg\max_f \|M_1(f)\| - \|M_2(f)\|. \tag{3}$$

Heart activity of each pixel is then calculated by estimating the actual energy at the cardiac frequency of pixel time series via a non-parametric periodogram approach. Finally heart ROI is detected similarly to that of ventilation detection.

2.3. EIT and CT data acquisition methods.

To evaluate the accuracy of the measures calculated in 2.2, we compare the H&L regions identified in the EIT image to those in simultaneously acquired CT images. Data were acquired on healthy piglets (weighing 23±2 kg) according to a protocol approved by the responsible animal use committee for the University of Mainz, Germany (licence no. 1.5 177-07/401-75, Landesuntersuchungsamt Rheinland-Pfalz, 56028 Koblenz, Germany). Briefly, the protocol was as follows: The animals were investigated using static thoracic computed tomography at a CPAP level of 5, 15 and 45 mbar in apnea during the 25 seconds duration of the static CT (1 mm slices, HRCT: Somatotom Plus 4, Siemens, Erlangen, Germany). Simultaneously, EIT measurements were taken (using Goe-MF II EIT device, CareFusion, San Diego, CA, USA) with a sample frequency of 13 Hz controlled by MCFEIT study software (University of Goettingen, Germany).

For each animal, the CT slice corresponding to the electrode positions was taken and manually segmented by an expert to identify H&L regions. Inclusion criteria for analysis were: 1) healthy subject, with no obvious pneumonia or lung collapse, and 2) EIT electrode level at a position caudal to the maximum heart area in the CT.

2.4. Assessment of unsupervised algorithm accuracy

Detection accuracy was determined from measures of precision (P) as a function of the algorithm threshold, T, where P is the fraction of each EIT region within the corresponding regions in the CT image. Clearly, for very low T, all regions are identified, and P is low. We consider detection to be *accurate* if P becomes 100% at high T.

3. Results

An example algorithm output is shown in fig. 2. for different values of threshold. Note that identified ROIs are reasonable at all T values, but for high T values, only very central region

pixels are identified, *i.e.* maximizing the algorithm precision. In total, data from seven animals at three different PEEP levels were analysed, resulting in 21 tests, of which 20/21 were *accurate* for heart ROI detection and 21/21 for lungs. The single unsuccessful subject showed two separate heart ROIs, possibly due to movement of the heart during the cardiac cycle.
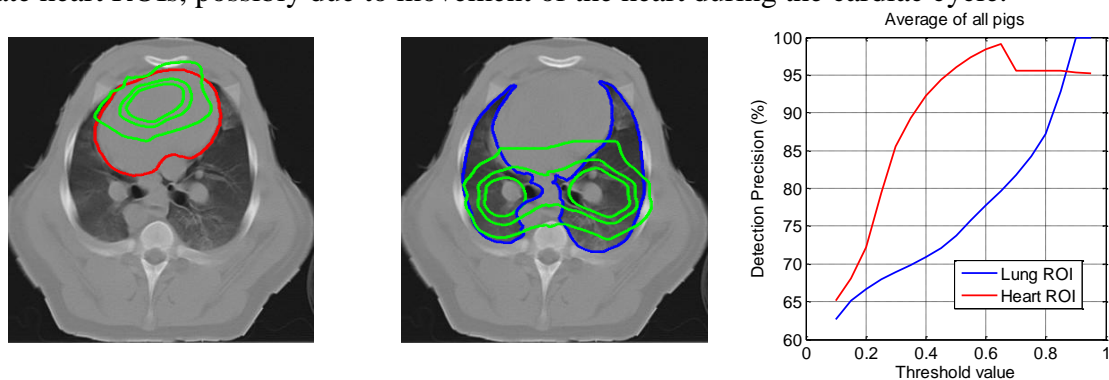
Fig. 2: Automatically identified heart and lung regions from EIT (green) with three level of *T* (0.25, 0.6 and 0.75) and the corresponding CT image (red and blue) at a PEEP of 5 mbar. Overall *P* vs threshold is shown for heart and lung regions (right).

4. Discussion

In this paper, we describe and evaluate an automatic algorithm to detect heart and lung regions in EIT images. Results show an accurate detection in almost all cases. Such results help validate EIT images as an accurate representation of physiological activity in the thorax, and provide additional support for physiological monitoring strategies based on EIT. Specifically, given accurate identification of anatomical regions in EIT images, it would be possible to specifically monitor organs or regions of interest.

Another significant finding in this project is the importance of accurate anatomical models for EIT reconstruction. While it is common to use average, or even circular models, to represent the thorax, we were able to use CT data to determine accurate thorax morphology and electrode locations. This results in much more anatomically-accurate EIT images (Fig. 3).
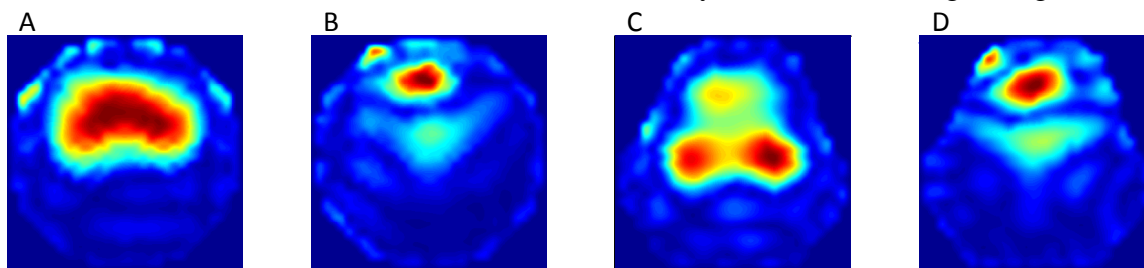
Fig. 3: Influence of morphologically accurate EIT reconstruction. Energy distribution at respiratory (A, C) and cardiac frequency (B, D). Accurate morphology images (C, D) show better correspondence to the lung anatomy and better separation of regions, compared to use of a circular model (A, B).

5. References

Fernand M, *Signal Processing* **38** 113–125, 1994

Hahn G, *et al*, *Physiol. Meas* **16** A161–73

Kerrouche N, McLeod CN, Lionheart WRB, *Physiol. Meas.* **22** 147, 2001

Kühnel G, *et al*, *Biomed. Technol. Berl.* **42** 213–4, 1997

Pikkemaat R, Leonhardt S, *J. Phys.: Conf. Ser.* **224** 012028, 2010

Pulletz S, Huibert R, *et al*, *Physiol. Meas* **27** S115-S127, 2006

Ventilation inhomogeneity in cystic fibrosis patients as measured by means of electric impedance tomography

Zhanqi Zhao[1], Rainald Fischer[2], Ullrich Müller-Lisse[3], Knut Möller[1]

[1]Department of Biomedical Engineering, Furtwangen University, Villingen-Schwenningen, Germany

[2]Department of Pneumology, University of Munich, Munich, Germany

[3]Department of Radiology, University of Munich, Munich, Germany

Abstract

Objective: The distribution of ventilation within the lung is inhomogeneous. We hypothesized that the degree of inhomogeneity in patients with cystic fibrosis (CF) differs from that in healthy subjects.

Method: Three adult patients with cystic fibrosis (CF) and two healthy subjects were recruited for this preliminary study. Subjects were asked to breathe in as deep and exhale as hard as possible three times. Electric impedance tomography (EIT) measurements were performed during spirometry tests. The global inhomogeneity index(GI) was applied to assess the degree of ventilation homogeneity at 25%, 50%, 75% and 100% of maximum inspiratory volume.

Results: Airway obstruction was detected in CF patients but not in healthy volunteers during spirometry tests. GI decreased as inspiratory volume increased in CF patients (0.59 ± 0.20 at 25% and 0.39 ± 0.09 at 100%, $p<0.01$, Mean$\pm$SD) while GI remained unchanged in healthy subjects (0.40 ± 0.05 at 25% and 0.37 ± 0.03 at 100%, $p=0.31$).

Conclusion: Degree of ventilation homogeneity appears to vary during forced respiration in CF patients, but not in healthy volunteers. EIT is a practical method to measure the inhomogeneity of ventilation distribution.

Introduction

Cystic fibrosis (CF) is an inherited, chronic disease of the body's mucus and sweat glands that mainly affects the lungs and the digestive system. The alteration of lung structure and small airways leads to flow reduction during in- and expiration [1-2]. There is still no cure for CF, and it tends to increase in severity over time [3]. Despite improved treatment, mean survival time of CF patients is only 37 years [4].

Distribution of tidal volume in lungs is often inhomogeneous. The degree of inhomogeneity reveals information about the patients' respective lung conditions. The routine diagnosis tools for CF patients such as spirometry and body plethysmography are unable to assess ventilation distribution. Other methods such as multibreath washout technique and computed tomography (CT) are inconvenient or even potentially harmful to the patient and therefore not suitable for outpatients.

Electrical Impedance Tomography (EIT) is a noninvasive, radiation-free imaging technique, which can monitor both regional lung ventilation and tidal volume distribution, by measuring the electrical potentials at the chest wall surface. The rationale is that changes in regional air content and regional blood flow modify the electrical impedance of lung tissue [5-6]. We have recently developed an EIT-based Global Inhomogeneity (GI) index to assess ventilation inhomogeneity [7]. We hypothesized that due to disease-related airway obstruction, ventilation inhomogeneity in CF patients varies during forced respiration and it can be detected with EIT.

Patients and Methods

Three patients with cystic fibrosis (CF) (1 male and 2 female; body height, 180, 165 and 156 cm; body weight, 64, 58 and 55 kg; age at examination, 32, 35 and 30 years, respectively) and two healthy volunteers (2 male; body height, 178 and 168 cm; body weight, 62 and 60 kg; age at examination, 50 and 28 years, respectively) were investigated. Written informed consent was obtained from all patients prior to the study. The study was approved by the local ethics committee.

All subjects were asked to breathe in as deep and exhale as hard as possible three times at the spirometer, according to standard ATS spirometry guidelines [8]. An EIT electrode belt, which carries 16 electrodes with a width of 40 mm, was placed around the chest in the fifth intercostal space while one reference electrode was placed on the patients' abdomen (EIT Evaluation KIT 2, Dräger Medical, Lübeck, Germany). EIT images were continuously recorded at 20 Hz and stored during spirometry tests.

GI index has been described in previous studies [7, 9]. In this preliminary study, the GI index was slightly modified to evaluate the inhomogeneity degree at 25%, 50%, 75% and 100% of maximum inspiratory volume. For every forced respiration, four difference images, which represent the respective differences of impedance between 25%, 50%, 75%, 100% of maximum inspiratory volume and inspiration begin (0%), were generated. Lung regions in EIT images were defined using the LAE method [10]. The median value of the pixels in the lung area is calculated for each difference image. The GI index is defined as the sum of the absolute differences between the median value and every pixel value, which is normalized with the sum of the impedance values within the lung area:

$$GI = \frac{\sum\limits_{x,y \in lung} \left| DI_{xy} - Median\left(DI_{lung}\right) \right|}{\sum\limits_{x,y \in lung} DI_{xy}} \qquad (1)$$

where DI is the value of the differential impedance in the difference images; DI_{xy} denotes the pixel in the identified lung area; DI_{lung} are all pixels in the lung area under observation.

Data analysis was performed using MATLAB (The MathWorks Inc., Natick, MA, USA). Lilliefors test was used to confirm the distribution of the data. In case of normal distribution, results were expressed as mean $\pm$ SD. Unpaired t-test was used to evaluate the difference of GI index between level 25% and 100%, 50% and 100%, 75% and 100%. $P < 0.05$ was considered statistically significant. The significant levels were corrected for multiple comparisons using Holm's sequential Bonferroni method.

Results

Figure 1 shows the ventilation distribution during one forced inspiration-expiration cycle and one normal spontaneous breath in a CF patient. According to the GI index, air distribution was more homogeneous during forced breathing than during spontaneous breathing.

When the forced breathing cycle was analyzed at 4 different levels, the GI index decreased as inspiratory volume increased in CF patients, while it remained unchanged in healthy subjects (Table 1).

Figure 2 shows the difference images of one CF patient at different preselected levels of the forced breathing cycle. In this particular patient, the right lung was inhomogeneously ventilated at 25% and 50% of the maximum inspiratory volume. Ventilation distribution became more homogeneous at higher inspiratory volume levels.
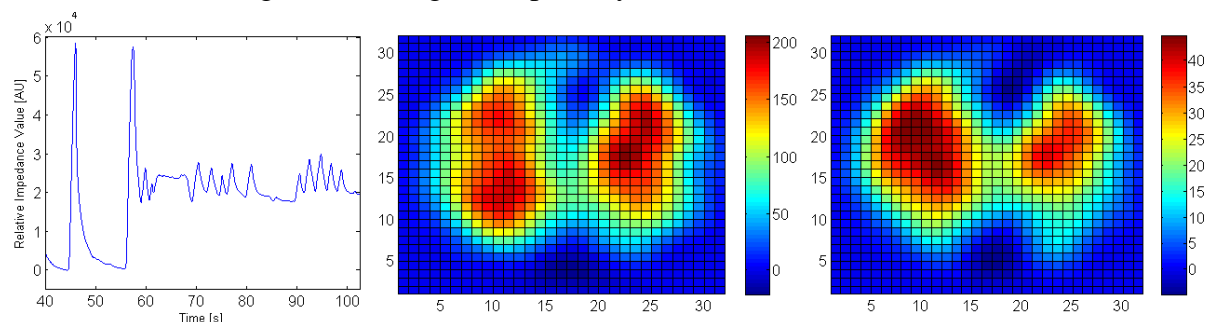
Fig. 1 Typical global impedance curve (left) and tidal images of EIT during forced breathing (middle) and normal, spontaneous breathing (right) in one CF patient. Please note the difference of scales in the EIT images. AU: arbitrary unit.

Table 1 GI index of CF patients and healthy volunteers at different levels of maximum inspiratory volume. *Significant difference between 25% and 100%.

Subjects Category	25% *	50%	75%	100% *	* p-value
CF	0.59±0.20	0.49±0.15	0.43±0.12	0.39±0.09	p<0.01
Healthy	0.40±0.05	0.36±0.03	0.35±0.02	0.37±0.03	
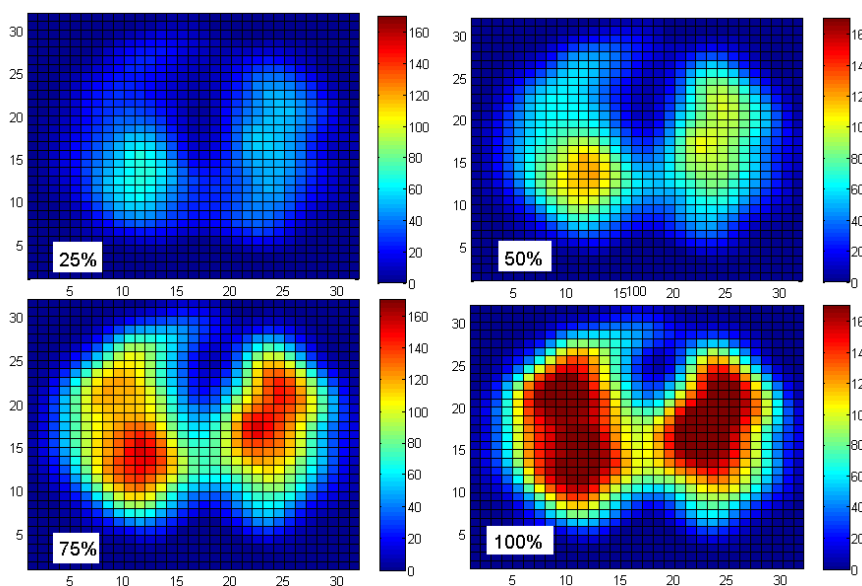
Fig. 2 Difference images of one CF patient at 25% (top left), 50% (top right), 75% (bottom left) and 100% (bottom right) of maximum inspiratory volume.

Discussion

In this preliminary study of 5 spontaneously breathing subjects, EIT, as applied during lung function tests demonstrated that ventilation homogeneity differed between CF patients and healthy subjects during forced respiration.

Since its early application in the 1980s [11], EIT analysis of the inhomogeneity of air distribution within the lungs has attracted the attention of researches all over the world [7]. However, methods were missing which could both simplify the complex information provided by EIT, and consider the contribution of every pixel in EIT images [7]. Hence, we defined the GI index to quantify tidal volume distribution within the lung. The reliability and potential use of the GI index for mechanically ventilated patients has previously been investigated [7, 9]. The GI index has also been applied for spontaneously breathing subjects in different body positions [12].

Differences in ventilation homogeneity between healthy volunteers and patients with critical lung disease have previously been reported [7]. In theory, the degree of ventilation inhomogeneity should be relatively low for CF patients when compared to patients with critical lung disease such as acute respiratory distress syndrome. Therefore, it should be more difficult to distinguish patients with CF from healthy volunteers by means of EIT. However, due to chronic airway obstruction in CF patients, it may take longer for air to distribute within their lungs. During cycles of forced inspiration and expiration, there should be more time for air distribution. Thus we assessed the ventilation distribution with EIT during lung function tests, with recording of three subsequent cycles of forced breathing. As we hypothesized, the EIT-based GI index demonstrated ventilation inhomogeneity at the onset of forced breathing in CF patients, while ventilation became more homogeneous during later phases of inspiration. No significant changes of ventilation over the breathing cycle were found in healthy volunteers.

A limitation of the present study is that only three patients with CF and two healthy subjects were included. To corroborate these early results, more subjects will be examined by means of EIT.

Conclusion

The degree of ventilation homogeneity varies during forced respiration in CF patients. The EIT-based GI index appears to be a practical method to measure the inhomogeneity of ventilation distribution.

Acknowledgment

References

[1]   H. Bitterling, "Imaging of patients with Mucoviscidosis," in *Multi slice CT*, M. Reiser, *et al.*, Eds., 2. ed Berlin: Springer Verlag, 2004, pp. 131-136.

[2]   M. Maffessanti, M. Candusso, F. Brizzi, and F. Piovesana, "Cystic fibrosis in children: HRCT findings and distribution of disease," *J Thorac Imaging,* vol. 11 (1), pp. 27-38, Winter 1996.

[3]   R. Fischer, S. Nahrig, M. Kappler, and M. Griese, "[Cystic fibrosis care in transition from adolescence to adult age]," *Internist (Berl),* vol. 50 (10), pp. 1213-4, 1216, 1218-20, Oct 2009.

[4]   J. M. Torpy, C. Lynm, and R. M. Glass, "JAMA patient page. Cystic fibrosis," *JAMA,* vol. 302 (10), p. 1130, Sep 9 2009.

[5]   P. Nopp, E. Rapp, H. Pfutzner, H. Nakesch, and C. Ruhsam, "Dielectric properties of lung tissue as a function of air content," *Phys Med Biol,* vol. 38 (6), pp. 699-716, Jun 1993.

[6]   B. H. Brown, D. C. Barber, A. H. Morice, and A. D. Leathard, "Cardiac and respiratory related electrical impedance changes in the human thorax," *IEEE Trans Biomed Eng,* vol. 41 (8), pp. 729-34, Aug 1994.

[7]   Z. Zhao, K. Moller, D. Steinmann, I. Frerichs, and J. Guttmann, "Evaluation of an electrical impedance tomography-based global inhomogeneity index for pulmonary ventilation distribution," *Intensive Care Med,* vol. 35 (11), pp. 1900-6, Nov 2009.

[8]   M. R. Miller, J. Hankinson, V. Brusasco, F. Burgos, R. Casaburi, A. Coates, R. Crapo, P. Enright, C. P. van der Grinten*, et al.*, "Standardisation of spirometry," *Eur Respir J,* vol. 26 (2), pp. 319-38, Aug 2005.

[9]   Z. Zhao, D. Steinmann, I. Frerichs, J. Guttmann, and K. Moller, "PEEP titration guided by ventilation homogeneity: a feasibility study using electrical impedance tomography," *Crit Care,* vol. 14 (1), p. R8, Jan 30 2010.

[10]   Z. Zhao, D. Steinmann, D. Muller-Zivkovic, J. Martin, I. Frerichs, J. Guttmann, and K. Moller, "A lung area estimation method for analysis of ventilation inhomogeneity based on electrical impedance tomography," *J Xray Sci Technol,* vol. 18 (2), pp. 171-82, Jan 1 2010.

[11]   D. C. Barber and B. H. Brown, "Applied potential tomography," *J. Phys. E: Sci. Instrum.,* vol. 17pp. 723-33, 1984.

[12]   Z. Zhao, N. Kiefer, M. Kulcsar, S. Lang, and K. Möller, "Ventilation inhomogeneity in upright and supine position assessed by electrical impedance tomography", in *MEDICON 2010, IFMBE Proceedings*, P. D. Bamidis and N. Pallikarakis, Eds., (Springer, Chalkidiki, Greece, 2010), vol. 29.

Characterisation of the morphological and growth patterns of colorectal tumour cell lines via electrical impedance spectroscopy

Martina F. Callaghan, Torben Lund, Ivan M. Roitt, Richard H. Bayford

Department of Natural Sciences, Middlesex University, London, U.K.

M.Callaghan@mdx.ac.uk

Abstract. Tissue characterisation based on the spectral characteristics of their electrical properties is an appealing approach to distinguishing between healthy and cancerous tissue. To maximise the contrast between different tissue types, the spectral characteristics of the target tissues must be known so as to interrogate them at the optimal frequencies. Here we use electrical impedance spectroscopy measurements to characterise the growth of three different colorectal tumour cell lines (HCT-116, HBT-39 and HT-29). We assess the correlation between the acquired impedance spectra and the distinct proliferative, morphological and adherence characteristics of the cell lines as observed by visual inspection on an inverted microscope. The results show that differences in growth behaviour in tissue culture dishes of the cell lines is mirrored by differences in their impedance spectra both at particular frequencies and in their development over time.

1. Introduction

There are different impedance-based approaches to distinguishing between different tissue types or states based on their different spectral characteristics, e.g. bioimpedance spectroscopy [1,2] and multi-frequency electrical impedance tomography (MfEIT) [3,4]. It is hoped that such approaches will lead to an effective means of cancer diagnosis. The spectral characteristics of the tissues must be well understood so as to maximise the potential contrast by examining the tissues at the optimal frequency. The spectral response of a tissue depends on the complex conductivity of the various cellular compartments: the intra-cellular space, the extra-cellular space and the capacitance of the cell membrane. These parameters are in turn affected by diverse interlinked factors such as pathological state, cell density, ionic concentration and water content.

Understanding the behaviour of cells *in vitro* can give a first indication of the spectral behaviour of such cells in bulk form but also allows one to study the effect of various experimental conditions, e.g. cell density, nanoparticle uptake and biomarker expression on the impedance parameters. Here we have used electrical impedance spectroscopy (EIS) to quantitatively characterise the differences in growth patterns and morphology between different colorectal cancer cell lines by using an electric cell substrate impedance sensing (ECIS) approach [5].

2. Methods

2.1. Cell Culture

Three human colorectal tumour cell lines were obtained from American Tissue Culture Collection: HCT-116 (ATCC-CCL-247), HTB-39 (ATCC-HTB-39) and HT-29 (ATCC-HTB-38). HCT-116 is a colorectal carcinoma of epithelial origin and is tumorigenic in nude

mice; HTB-39 is a colorectal adenocarcinoma derived from a metastatic site and is of epithelial origin; HT-29 is a colorectal adenocarcinoma of epithelial origin that is also tumorigenic in nude mice. Each cell line has a distinct genetic pattern and expresses different levels of the carcinoembryonic antigen (CEA) biomarker on the cell surface. The cultures were grown in eight well 8W10E+ ECIS arrays (Wolf Labs, UK) with Dulbecco's essential minimal medium (Glutamax) supplemented with 10% foetal calf serum and 1% penicillin-streptomycin. Cell suspensions of equal concentration were seeded in six of the wells. The remaining two wells were left blank as controls. The cultures were incubated at 37°C with 5% CO_2. To acquire impedance spectra the cultures were removed from the incubator at a series of time points after seeding: 2 hours, 7 hours and at 16 and 8 hour intervals thereafter.

2.2. Impedance Measurements

Impedance measurements were made in the frequency domain using a two-electrode approach on a Solartron 1260 impedance analyser (Advanced Measurement Technology, UK). A stimulating signal of 10mV r.m.s. was employed across a frequency range of 100Hz to 10MHz. Each well of the arrays contained a total of forty electrode elements 0.25mm in diameter. These are configured as two sets of twenty on interdigitated combs, which act as the counter and working electrodes. This configuration allows for sampling over the full base of the well. The impedance profiles were assessed using two parameters: the normalised resistance and the normalised reactance. The normalised resistance was calculated as the mean resistance of the cell-containing wells normalised to the mean resistance of the blank wells. The normalised reactance was calculated as the mean reactance of the cell-containing wells normalised to the mean reactance of the blank wells.

2.3. Lysing the Cells

After the final impedance measurement on day five the cultures were washed twice with 300μl of Mg^{2+}- and Ca^{2+}- free phosphate buffered saline (PBS) to remove traces of foetal calf serum. The cells were lysed for fifteen minutes with 200μl of 0.2% SDS heated to 98°C before the lysates were transferred to tubes containing 500μl 1M NaOH. The wells were washed twice with 300μl of PBS and the lysate solutions were left overnight at room temperature to ensure full denaturation of the DNA. After dilution to 5ml with PBS, the absorbance at 280nm was measured using a Helios Zeta spectrophotometer (Thermo Scientific, UK). These absorbance measurements give an estimate of the cell density.

3. Results

3.1. Visual Inspection

Each of the cell lines was observed to have distinct morphology and growth patterns when viewed under a microscope. The HT-29 cells grow as adherent monolayer cells until they reach confluence. The HCT-116 cell line also grows as adherent cells but appears to exhibit a lesser degree of contact inhibition. The HBT-39 cell line grows as adherent cells but the cells do not appear to form a complete monolayer but instead leave minor gaps in the cell layer. The growth is not contact-inhibited but the sister cells appear to dissociate into the medium and remain unattached. Optical density measurements indicate equivalent cell densities for each of the cell lines: HT-29 = 0.128 ± 0.004; HCT-116 = 0.137 ± 0.011; HBT-39 = 0.132 ± 0.003.

3.2. Impedance Profiles

3.2.1.   Normalised Resistance

The normalised resistance (figure 1, left) increases with time for all cell lines and plateaus at later time points. It is highest for the HCT-116 cell line. The peak value at the last time point of the experiment is approximately 20% lower for the HT-29 cell line and 50% lower for the HBT-39 cell line.

3.2.2.   Normalised Reactance

All of the cell lines show a steep increase in normalised reactance (figure 1, right) at early time points. The HT-29 and HCT-116 cell lines appear to have similar temporal profiles over the time span studied continuing to increase until plateauing from the 71-hour time point. The behaviour of the HBT-39 cell line appears to be reversed. After the initial rise in normalised reactance, it plateaus before showing signs of increasing again from the 55-hour time point. The peak values of the HT-29 and HCT-116 cell lines at the last time point differ by less than 4% whereas the corresponding normalised reactance of the HBT-39 line is 40% lower.
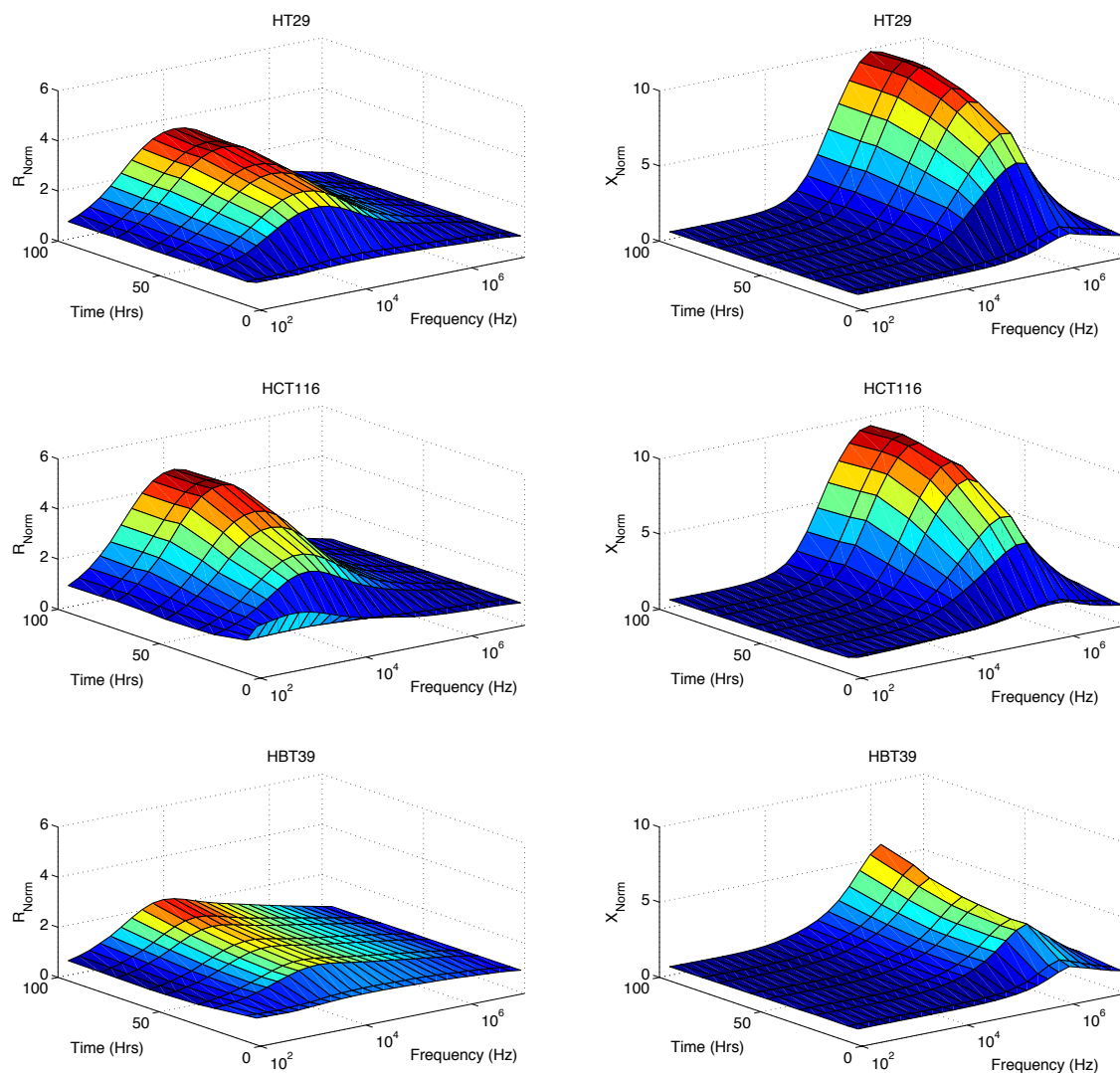
Figure 1: The normalised resistance (left column) and reactance (right column) of the HT-29, HCT-116 and HBT-39 cell lines across the frequency range 100Hz to 10MHz over 96 hours of growth.

4. Discussion

Each of the cell lines exhibit a steep rise in both the normalised resistance and the normalised reactance at the early time points as the seeded cells settle and attach to the base of the wells.

The further increase in the normalised resistance over time is due to cell proliferation since an increase in cell packing density results in an increase in the resistance of the extracellular matrix as the routes available for extracellular current flow become progressively restricted. The HCT-116 cell line had the highest normalised resistance suggesting that the cells are most densely packed for this particular line. This is in keeping with the observations that it exhibits less contact inhibition since this feature allows scattered mutli-layer regions to form. The HBT-39 cell line has the lowest normalised resistance and yet the optical density measurements indicate that this culture has approximately the same number of cells as the other lines. It appears that the lower normalised resistance is reflecting the unusual growth pattern of this line whereby it does not form a complete monolayer but instead leaves minor isolated gaps in the extracellular matrix.

The increasing normalised reactance over time is a further reflection of cell proliferation. The barrier-like nature of the cellular membranes means that their electrical behaviour is analogous to that of a capacitor. As the number of cells increases, the charge storing nature increases, which is reflected by a concomitant increase in reactance. The normalised reactance appears to be particularly sensitive to the cells directly in contact with the electrodes, which would account for the differences observed between the cell lines. The HT-29 and HCT-116 both achieve confluency and have equivalent reactance profiles whereas the HBT-39 does not achieve a fully confluent layer reflected by a much lower normalised reactance.

The spectral differences observed here reflect variances in the biophysical characteristics of the cell lines tested, which suggests that it may be possible to distinguish between tumorogenic and normal tissue *in vivo*.

5. Future

Given that we now have known impedance signatures for each of these cell lines, our next step is to examine what effect capturing or attaching small gold and iron core nanoparticles to the cells has on their impedance spectra.

References

[1] B. Blad and B. Baldetorp, "Impedance spectra of tumour tissue in comparison with normal tissue; a possible clinical application for electrical impedance tomography.," *Physiological measurement*, vol. 17 Suppl 4, Nov. 1996, pp. A105-15.

[2] B.H. Brown, J. a Tidy, K. Boston, a D. Blackett, R.H. Smallwood, and F. Sharp, "Relation between tissue structure and imposed electrical current flow in cervical neoplasia.," *Lancet*, vol. 355, Mar. 2000, pp. 892-5.

[3] R.J. Yerworth, R. Bayford, B. Brown, P. Milnes, M. Conway, and D.S. Holder, "Electrical impedance tomography spectroscopy (EITS) for human head imaging," *Physiological Measurement*, vol. 24, 2003, p. 477–489.

[4] T.I. Oh, H. Koo, K.H. Lee, S.M. Kim, J. Lee, S.W. Kim, J.K. Seo, and E.J. Woo, "Validation of a multi-frequency electrical impedance tomography (mfEIT) system KHU Mark1: impedance spectroscopy and time-difference imaging.," *Physiological measurement*, vol. 29, Mar. 2008, pp. 295-307.

[5] J. Wegener, C.R. Keese, and I. Giaever, "Electric cell-substrate impedance sensing (ECIS) as a noninvasive means to monitor the kinetics of cell spreading to artificial surfaces.," *Experimental cell research*, vol. 259, Aug. 2000, pp. 158-66.

Preliminary clinical study on prostate cancer detection using transrectal EIT

Yuqing Wan[1], Ryan Halter[1], Andrea Borsic[1] and Alex Hartov[1]
[1]Thayer School of Engineering, Dartmouth College, Hanover, NH 03755, USA

Introduction

Prostate cancer is reported to account for 25% of new cancer cases in men in the United States in 2009. Approximately 192,280 men were diagnosed with prostate cancer and 27,360 men were expected to die from it. Prostate cancer ranks as the most common cancer (excluding non-melanoma skin cancer) and is the second leading cause of cancer death (lung cancer being the most fatal cancer) [1].

Electrical impedance tomography (EIT) is a novel technology being employed in various fields including medical imaging and geological measurements. In biomedical applications, alternating current (AC) within a safety range is injected into human tissue at certain frequencies through electrodes attached to the tissue surface. Voltages are measured on some or all the electrodes simultaneously. The ultimate goal of EIT is to infer the internal conductivity (σ) and/or permittivity (ε) from the measured physical quantities (currents and voltages) on the surface.

We have developed an ultrasound coupled transrectal electrical impedance tomography (TREIT) system [2] and corresponding reconstruction algorithms [3] to detect prostate cancer. The imaging system mainly consists of an EIT data acquisition module, a transrectal ultrasound (TRUS) imaging module, a computer, a monitor and a power supply (Figure 1). Ultrasound provides *a priori* anatomical information to guide EIT reconstruction. Thirty electrodes are plated along the periphery of an opening (20 mm × 60 mm) on a flexible Kapton circuit board, which is wrapped around the ultrasound probe with the opening aligned with the acoustic window on the probe. A circular external electrode (ventral electrode) is placed on the patient's lower abdomen to collect cross-prostatic electrical signals (Figure 2).

(a) Diagram of the TREIT system.   (b) Photo of the TREIT system.
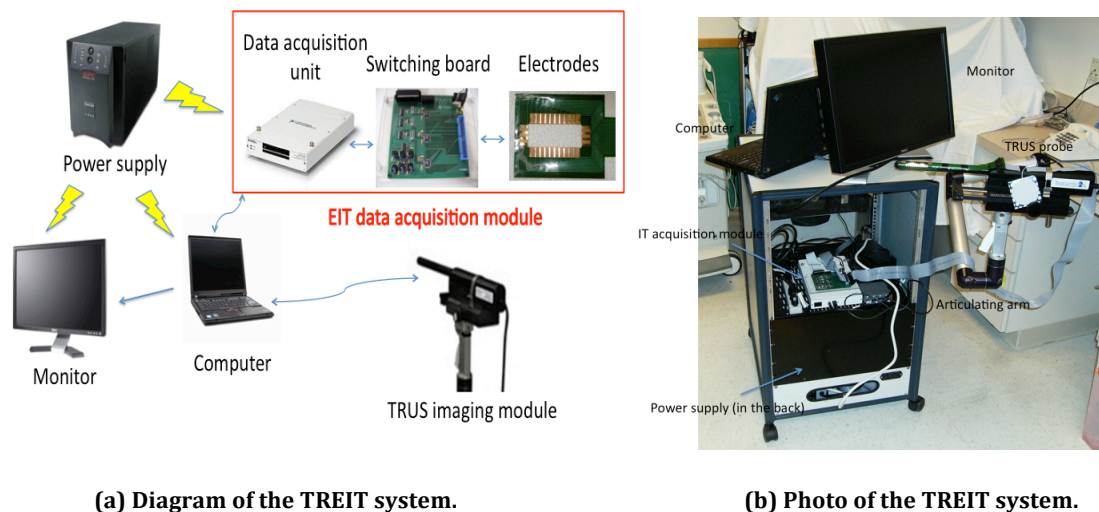
Figure 1 The diagram and photo of the TREIT system.
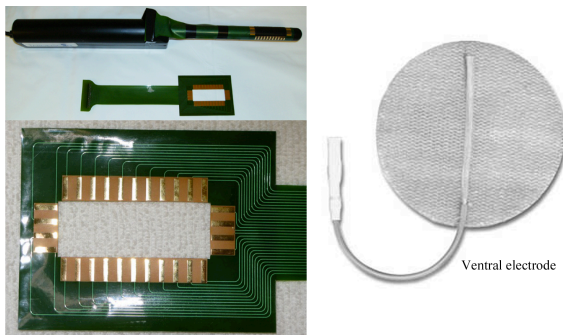
Figure 2 Electrodes on the probe and the ventral electrode.

Figure 3 Clinical data collection.

The TREIT system is able to detect high contrast inclusions of 1.0 cm in diameter, positioned 2.3 cm away from the probe surface. The system is also found to be capable of differentiating inclusions of 20% contrast to the background [2].

We have been collecting clinical data from a total of 57 patients prior to their prostatectomy operations over the past year (Figure 3). This study mainly focuses on a preliminary analysis of the clinical data and correlations between the electrical properties revealed by EIT and cancerous locations of the prostate confirmed by pathological findings.

Method

The clinical data collection takes place after the patient is anesthetized during a radical prostatectomy surgery in the operation room (OR). We adhere the ventral electrode to the lower abdomen of the patient. The sterilized TRUS probe with electrodes is covered with a conductive natural membrane sheath to keep the probe clean. Ultrasound gel filled the gap between the probe and the sheath on the acoustic window to help acquiring better ultrasound images. In addition, ultrasound gel is coated outside the sheath to provide lubrication during probe insertion into the rectum and establish an acoustic interface between the sheath and the rectal wall. With the help of the real time image displayed on the large screen monitor, the physician is able to position the probe so that the prostate is in the center of the acoustic window and electrodes. Then the articulating arm is locked at this fixed position during the 5-10 minute data acquisition process. We acquire EIT data at frequencies of 400 Hz, 3200 Hz, 25600 Hz and 102400 Hz after the 3D ultrasound scan. At the end of the data collection, both the sheath and the ventral electrode are disposed and patient resumes his surgery. Then the TREIT system is transferred to lab to image a saline solution (0.1 S/m) to obtain reference data for difference imaging. Later, the prostate specimen after dissection in the OR is pathologically analyzed by cutting the whole specimen into 7 to 15 slices depending on the size of the specimen. Pathologists will determine cancerous and benign prostatic hyperplasia (BPH) regions based on histological findings and they will draw maps with different colors in each slice indicating those regions.

EIT images of the prostate are reconstructed under the guidance of the *a priori* anatomical information from the ultrasound scan. First of all, the prostate volume is segmented from the 3D ultrasound data using commercial software Mimics 13.1. With precise co-registration, the surface mesh of the segmented prostate is then embedded into a pre-made cylindrical mesh. A

3D finite element method (FEM) volume mesh with prostate geometry is generated for the reconstruction. The generic pre-made cylindrical mesh containing models of the TRUS probe and 31 electrodes simulates lower abdomen. In the reconstruction algorithm, the nodes outside the prostate volume region are set to have one single value and the nodes inside the prostate volume are allowed to fluctuate individually and converge to optimized values satisfying the inverse problem. With all the clinically collected ultrasound and EIT data, we are able to reconstruct the conductivity and permittivity images for each patient. The difference reconstruction is based on the patient data and a saline solution data collected at the end of clinical data collection. The Tikhonov regularization used in the reconstruction is set to 500 for all the patients, which is found to work well in phantom experiments.

The pathological findings are used as gold gauge to analyze the EIT reconstruction. Under the assumption that the pathological slices are of the same thickness from the apex to the base of the prostate, we uniformly clip our reconstructed EIT 3D images in the axial direction to the same number of slices as that of pathological tissue pieces. The ellipsoidal shape of the prostate slices are morphed using thin plate spline method [4] into the true shape of the prostate at that level which is obtained from our ultrasound image. The cancerous regions can then be mapped into the reconstruction slice.

Each patient's reconstruction values are linearly normalized such that 0 represents the minimum conductivity/permittivity, and 1 represents the maximum conductivity/permittivity. A pixel-based mean value will be calculated in the cancerous region and normal region for each patient. A paired, one side Student's T-test will be performed across the patients to evaluate the TREIT system's ability to differentiate cancerous tissue from normal tissue.

It is worth noting that not all the data collected are analyzed in this study. Data that are erroneous due to hardware and/or software failure during data collection process are excluded in this analysis. Additionally, patient data with unrealizable reconstructed values (*e.g.* conductivity greater than 1 S/m) at a particular frequency will be removed from the analysis. This results in the number of patient involved in this study is smaller than the total number of patients.

Results

Figure 4(a) shows a slice of a histological map of a patient. Red regions correspond to cancerous tissue and the ellipsoid represents the prostate slice. Figure 4(b) shows the conductivity reconstruction at this particular level. Red regions correspond to higher conductivity values and blue regions correspond to lower conductivity values. The elliptical prostate shape in Figure 4(a) is warped into the shape of the real prostate shape in Figure 4(b) with the cancerous regions warped accordingly, which are depicted by the two white closed lines in Figure 4(b).

(a)   (b)
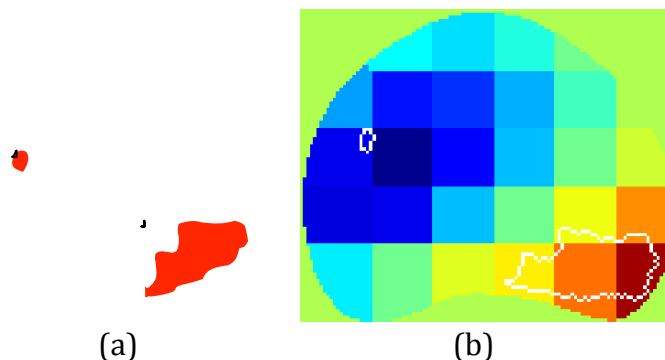
Figure 4 (a) One slice of a histological map of the dissected prostate after prostatectomy. The ellipsoid represents the prostate slice. The red regions correspond to cancerous tissues in the particular prostate slice. (b) Reconstructed conductivity image at the same level of the

Paired Student' T-test is performed to evaluate the null hypothesis that the difference of the two means is normally distributed with mean 0 against the alternative that conductivity mean of the cancerous tissue is greater than that of the normal tissue (one-tailed) at a significance level of 5%. The T-test result is shown in Table 1 and 2.

Table 1. T-test results for normalized reconstructed conductivity

Frequency (Hz)	Number of patients	Null hypothesis (accept = 0; reject = 1)	p value	Cancerous mean	Normal mean
400	15	1	0.0019	0.5672	0.4705
3200	24	1	0.0018	0.5387	0.4724
25600	26	1	0.0175	0.5592	0.5132
102400	23	0	0.9412	0.4752	0.4931

Table 2. T-test results for normalized reconstructed permittivity

Frequency (Hz)	Number of patients	Null hypothesis (accept = 0; reject = 1)	p value	Cancerous mean	Normal mean
400	15	0	0.7851	0.4484	0.4744
3200	24	0	0.6074	0.4995	0.5079
25600	26	1	0.0323	0.4821	0.4476
102400	23	0	0.7126	0.4592	0.4646

The statistical results suggest that at low frequencies from 400 Hz to 25600 Hz the conductivity means of cancerous tissue are significantly greater than those of normal tissue in the prostate gland. At 25600 Hz, the permittivity mean of cancerous tissue is greater than that of normal tissue. At other frequencies, the electrical properties are not showing significant difference.

Discussion and Conclusion

The findings that at frequencies from 400 Hz to 25600 Hz cancerous tissue is more conductive than normal tissue contradicts previous *ex vivo* findings by Halter *et al* [5] that cancerous tissue has a significantly lower conductivity than benign tissue ($p < 0.05$) at frequencies from 0.1 kHz to 100 kHz. This might be explained by the fact that in this study, all the data are collected *in vivo*. Cancerous regions might have more blood vessels, which increase local conductivity, whereas for *ex vivo* measurements, conductivities depend more on the cellular structures.

This study indicates that EIT is a promising technique to detect prostate cancer. Currently we are still continuing analyzing the clinical data in order to establish a scheme to accurately differential prostate tissue types with our TREIT system.

Bibliography

[1] Ahmedin Jemal, Rebecca Siegel, Elizabeth Ward, Yongping Hao, Jiaquan Xu, and Michael J Thun. Cancer statistics, 2009. CA Cancer J Clin, 59(4):225–49, 2009.

[2] Y Wan, R Halter, A Borsic, P Manwaring, A Hartov and K Paulsen Sensitivity study of an ultrasound coupled transrectal electrical Impedance Tomography system for prostate imaging Physiological Measurement, 31(8):S17–29, 2010.

[3] Borsic A, Halter R, Wan Y, Hartov A, and Paulsen K. Electrical impedance tomog- raphy reconstruction for three-dimensional imaging of the prostate. Physiol. Meas., 31:S1–16, 2010.

[4] Fred L. Bookstein. Principle warping: Thin-plate splines and the decomposition of deformations. IEEE Transactions on Pattern Analysis and Machine Intelligence, 11(6):567–585, 1989.

[5] Ryan J. Halter, Alan Schned, John Heaney, Alex Hartov, and Keith D. Paulsen. Elec- trical properties of prostatic tissues: I. single frequency admittivity properties. The Journal of Urology, 182(4):1600–1607, 2009.

Imaging of regional conductivity change using a planar array of voltage-sensing electrodes and two pairs of current-injection electrodes

Eun Jung Lee[1], Jin Keun Seo[1], Munkh Erdene[1], Tong In Oh[2] and Eung Je Woo[2]
[1]Department of Computational Science and Engineering, Yonsei University, Seoul, KOREA
[2]Department of Biomedical Engineering, Kyung Hee University, Gyeonggi-do, KOREA
E-mail: eunjunglee@yonsei.ac.kr

Abstract. We propose a new EIT image reconstruction algorithm using multiple boundary voltage data from a planar array of voltage-sensing electrodes. The current injection electrodes are placed so that the induced internal currents approximately flow in the direction parallel to the surface of the voltage-sensing probe. The proposed algorithm uses the interrelationship between the measured voltage differences and the computed current, which allows us to derive a PDE-based Ohm's law. Based on the derived voltage-current relation, we produce images of conductivity changes within a local region underneath the voltage-sensing probe. We describe the new image reconstruction algorithm and its numerical simulation results.

1. Introduction

In electrical impedance tomography (EIT), it is most common to attach electrodes around an imaging object such as the thorax and abdomen to provide cross-sectional images of an internal conductivity distribution. Currents are injected through some or all of the electrodes and boundary voltages are measured on some or all of the electrodes [1-4]. In some cases, however, it is not practical or desirable to attach electrodes around a chosen imaging region. There have been several previous studies to use a planar array of electrodes [5, 6]. They used some or all of the electrodes for current injections and voltage measurements and adopted conventional EIT image reconstruction methods.

Rabbani *et al.* proposed a focused impedance measurement (FIM) using two pairs of current injection electrodes and one pair of voltage-sensing electrodes [7]. By adding two voltage measurements subject to two orthogonal current injections, they could enhance the sensitivity of the tetra-polar surface impedance measurement to the conductivity of the internal local region underneath the voltage-sensing electrodes. Increasing the number of voltage-sensing electrodes between two pairs of current-injection electrodes, they suggested a pigeon hole imaging (PHI) based on a simple back-projection algorithm [8].

In this paper, we propose a new EIT image reconstruction algorithm for the electrode configuration of the PHI shown in figure 1. It consists of a probe with an array of voltage-sensing electrodes and two pairs of current-injection electrodes. Each injected current produces internal current flows approximately in the tangential directions of the voltage-sensing probe. Hence, the measured data of voltage differences on the probe enable us to apply a kind of Ohm's law inside a region underneath of the probe. We will describe a new conductivity image reconstruction algorithm based on this observation with its numerical simulation results.

2. Methods

2.1. Electrode configuration

Let a subject to be imaged occupy a three-dimensional domain Ω with its boundary $\partial\Omega$. Let Γ denote the surface of the planar array of voltage-sensing electrodes. Figure 1 and 2 show examples of such an electrode configuration on the abdomen and a simplified computation model, respectively.
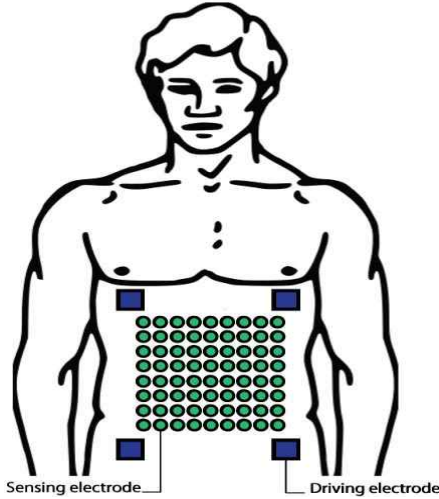
Figure 1. Electrode configuration on the abdomen as an example.
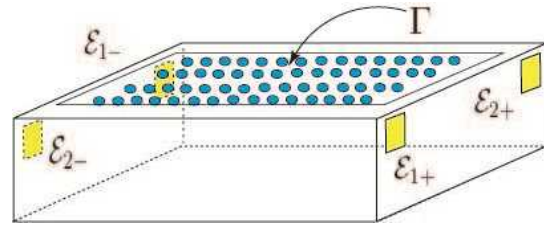
Figure 2. Simplified three-dimensional model of the electrode configuration for numerical simulations

2.2. Image reconstruction algorithm

When we inject currents into the object between two pairs of diagonal electrodes, for example, the induced voltages satisfy the following second order elliptic equation:

$$\nabla \cdot \left(\sigma \nabla u_j\right) = 0 \quad \text{in } \Omega$$
$$n \times \nabla u_j = 0 \quad \text{on } E_{\{1\pm\}} \cup E_{\{2\pm\}}$$
$$\sigma \frac{\partial u}{\partial n} = 0 \quad \text{on } \partial\Omega(E_{\{1\pm\}} \cup E_{\{2\pm\}}) \text{, for j=1,2,}$$

where u_1 is the induced voltage for the injection current I through $\mathscr{E}_{1+}$ and $\mathscr{E}_{1-}$ and u_2 is the induced voltage subject to the injection current I between $\mathscr{E}_{2+}$ and $\mathscr{E}_{2-}$. Using the voltage-sensing probe Γ shown in figure 2, we measure the induced voltage data:

$$u|_\Gamma = f.$$

We try to reconstruct an image of the regional conductivity change underneath Γ from the relationship between the measured voltage data f and computed current densities using FEM. Let v_j be the solution of the above mixed boundary value problem when the domain is filled with a homogeneous material. The proposed conductivity image reconstruction algorithm is based on the following approximation in a region underneath Γ :

$$\begin{bmatrix} \frac{\partial v_1}{\partial x} & \frac{\partial v_1}{\partial y} \\ \frac{\partial v_2}{\partial x} & \frac{\partial v_2}{\partial y} \end{bmatrix} \begin{bmatrix} \frac{\partial}{\partial x}\left(\frac{1}{\sigma}\right) \\ \frac{\partial}{\partial y}\left(\frac{1}{\sigma}\right) \end{bmatrix} \approx \begin{bmatrix} \Delta_{xy} u_1(x,y,0) \\ \Delta_{xy} u_2(x,y,0) \end{bmatrix} \qquad where \; \Delta_{xy} = \frac{\partial^2}{\partial x^2} + \frac{\partial^2}{\partial y^2}$$

3. Numerical simulation

3.1. Example 1

We set the imaging domain as $[0,1] \times [0,1] \times [0,0.4]$ and attached four square shaped driving electrodes with length 0.1 on the sides of the domain as shown in figure 2. We placed two anomalies with radius 0.02 at (0.3,0.3,0.2) and (0.7,0.7,0.2). Their conductivity values were 0.3, while the background conductivity was 0.03. In figure 3, we plotted a reconstructed conductivity image using the proposed algorithm.
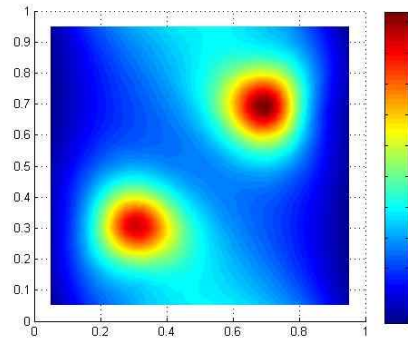
Figure 3. Reconstructed conductivity image.

3.2. Example 2

We used a well-known Shepp-Logan model shown in figure 4 to apply our reconstruction algorithm. We set the imaging domain as $[0,2] \times [0,2] \times [0,1]$. Along $x = 1$, there were three spherical and one cubic anomalies. The top sphere was centered at (1, 1.7, 0.8) with radius 0.15 and the other two spheres were located at (1, 1.3, 0.8) and (1, 1, 0.8) with radius 0.1. The cube was located at (1, 0.6, 0.8) with side lengths of 0.2 and 0.3. Two upper ellipses were located at (0.5, 1, 4, 0.8) and (1.5, 1.4, 0.8) and bottom ones were at (0.5, 0.6, 0.8) and (1.5, 0.6, 0.8). The conductivity value of these anomalies was 0.2 and the background conductivity was 0.03. Figure 5 shows a reconstructed conductivity image of the Shepp-Logan model. In figure 6, the reconstructed conductivity values below 1 were changed to 1 to show a clearer image.
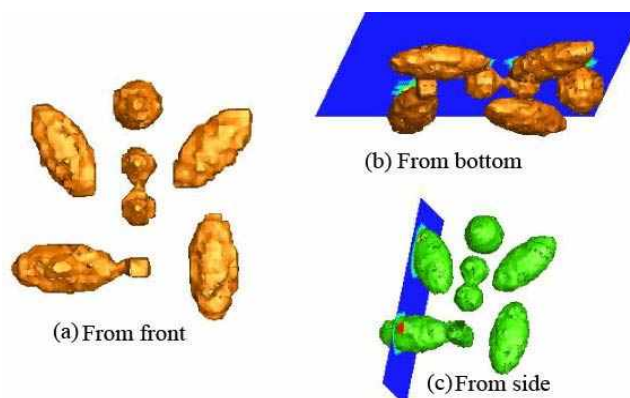
Figure 4. Shepp-Logan model : (a) front view, (b) bottom view and (c) side view.
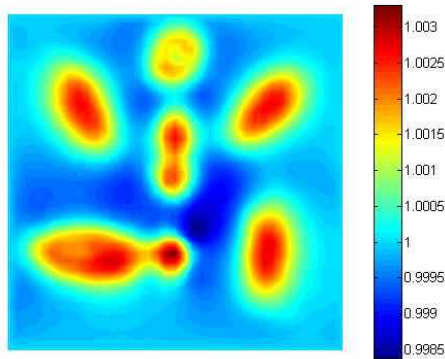
Figure 5. Reconstructed conductivity image of the Shepp-Logan model in figure 4.
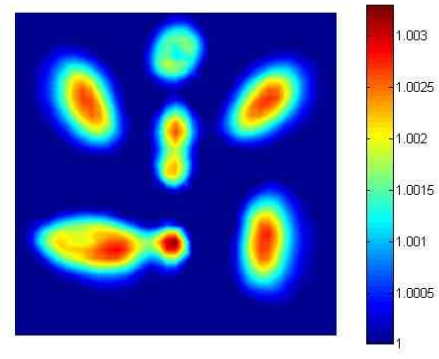
Figure 6. Reconstructed conductivity image in figure 5 after thresholding.

4. Discussion and Conclusions

We may implement the proposed electrode configuration using a probe or a belt which can be placed on the chest or abdomen. Taking advantage of the adopted electrode configuration, we could derive the relationship between measured voltage data on the probe and computed current densities in a region underneath the probe. We developed a new conductivity image reconstruction algorithm based on such a PDE-based Ohm's law along the probe. From numerical simulations, we found that it provides conductivity images with a better quality compared with that of conventional EIT methods using a sensitivity matrix. We plan to implement the proposed novel method by modifying an existing EIT system for future studies of admittivity image reconstructions of phantoms and human subjects.

Acknowledgments

References

[1] Brown B H, Barber D C and Seagar A D 1985 Applied potential tomography: possible clinical applications *Clin. Phys. Physiol. Meas.* **6** 109-21

[2] Cheney M, Isaacson D and Newell J C 1999 Electrical Impedance Tomography *SIAM Review* **41** 85-101

[3] Holder D S 2005 *Electrical Impedance Tomography: Methods, History and Applications* (IOP: Bristol, UK)

[4] Adler A, Arnold J H, Bayford R, Borsic A, Brown B, Dixon P, Faes T J C, Frerichs I, Gagnon H, Garber Y, Grechtol B, Hahn G, Lionheart W R B, Malik A, Patterson R P, Stocks J, Tizzard A, Weiler N and Wolf G K 2009 GREIT: a unified approach to 2D linear EIT reconstruction of lung images *Physiol.Meas*. **30** S35-55

[5] Boverman G, Kao T, Isaacson D and Saulnier G J 2009 An implementation of Calderon's method for 3-D limited-view EIT, *IEEE Trans. Med. Imaging* **28** 1073-82

[6] Sadleir R J, Tang T, Tucker A S, Borum P and Weiss M 2009 Detection of intraventricular blood using EIT in a neonatal piglet model, *Conf Proc IEEE EMBS* Minnesota, USA

[7] Rabbani K S, Sarkar M, Akond M H R and Akter T 1999 Focussed impedance measurement (FIM): a new technique with improved zone localization *Ann. New York Acad. Sci*. **873** 408–20

[8] Rabbani K S 2010 Focused Impedance Method (FIM) and Pigeon Hole Imaging (PHI) for localized measurements – a review *J. Phys.: Conf. Ser*. **224** 012003

Using Ultrasound Information in EIT Reconstruction of the Electrical Properties of the Prostate

A. Borsic, H. Syed, R. J. Halter, A. Hartov

Thayer School Of Engineering, Dartmouth College, 8000 Cummings Hall Hanover, NH 03755, US

E-mail: `Andrea.Borsic@Dartmouth.edu`

1. Abstract

In the present paper we present a novel method for using prior structural information from Ultrasound (US) imaging to improve the reconstruction of the electrical properties of the prostate by EIT. In an ongoing clinical project we have equipped a US transrectal probe for image-guided biopsy of the prostate with an array of 30 printed electrodes, which adhere to the surface and are placed around the US imaging window, not to interfere with the collection of US images. These electrodes allow acquiring tetrapolar impedance measurements that can be used for reconstructing conductivity and permittivity distributions in a volume in front of the probe encompassing the prostate. This electrical mapping is valuable, as US imaging in this context is not indicative of the presence of cancer; US information is used only for delineating the boundaries of the prostate and for guiding a biopsy needle within the volume of the gland. Providing a map of the electrical properties of tissues can indicate regions of the prostate where cancer is present, and where it might be optimal to take more biopsy samples. The reconstruction of the electrical properties is though very challenging in this physical setup, as the injected current density decays very rapidly with distance from the probe, and so sensitivity. In the present work we show a method based on exploiting US information which enhances EIT image reconstruction. As EIT electrodes and the US sensing element are mounted on the same probe imaging information between the two modalities is automatically co-registered. In the method we propose US images are segmented, producing a surface of the prostate. This surface is embedded in a FEM used for forward modeling in EIT, and the volume is subdivided in a small number of elements (e.g. 40) in which the conductivity is estimated. In simulations and in phantom experiments this arrangement resulted in significant improvements.

2. Ultrasound Image Collection and Processing

The imaging probe developed for this project (show in Figure 1(a)) is based on a TargetScan 3D US system (Envisioneering Medical Technologies, St Louis, MO) which consists of a probe with a single US element that is mechanically rotated and translated to construct a full 3D volumetric view of the prostate without moving the probe, itself. A set of 30 electrodes, printed of a flexible and adhesive substrate is applied to the probe. This arrangement limits movement artifacts (the probe can scan a 3D volume with no need for repositioning) and allows for the precise coregistration of the EIT image with the US data because the EIT sensing array is fixed with respect to the probe and therefore with the imaging field-of-view. Geometrically the TRUS probe is approximately 20 cm in length and 2 cm in diameter. In Figure 2(a) we show a typical

(a) US + EIT probe.

(b) FEM model of the probe.
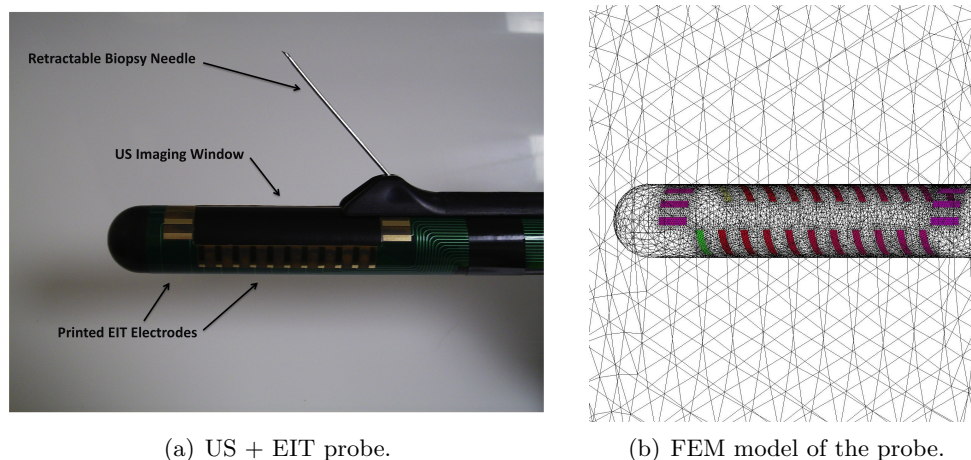
Figure 1. On the left, photograph of the transrectal ultrasound-guided prostate biopsy probe equipped with 30 printed electrodes. On the right, FEM model of the probe, used for EIT image reconstruction.

(a) US image of an agar phantom.

(b) Segmented image.
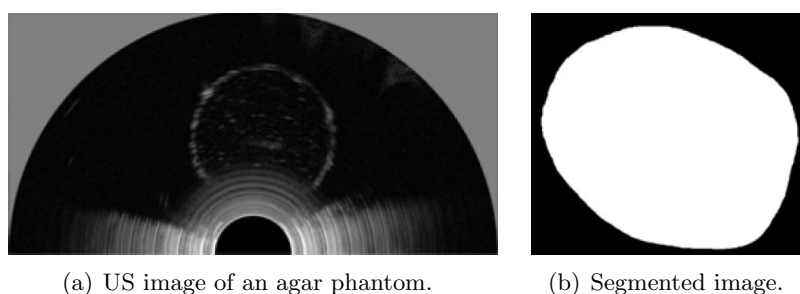
Figure 2. On the left, ultrasound image of an agar phantom resembling the shape of a prostate. The phantom is submerged in a water bucket, and the probe is placed at approximately 5mm from it. The imaged volume is three-dimensional and the image shows a cross section of the imaging volume. On the right, binary segmented image of a 2D section of the phantom.

US image collected on a agar phantom resembling the shape of the prostate. The phantom is immersed in a bucket of water (allowing US and EIT imaging) and the probe has been placed in its proximity, at a distance of 5mm. From the US image it is possible to delineate the boundaries of the phantom/prostate and to produce a segmented binary image as in Figure 2(b).

The TargetScan 3D US volume is formed by stacking 2D axial images at a distance of 1mm from each other. We typically use one image every 5mm, to reduce the manual segmentation work, and by using a total of approximately 8 to 12 images, we can produce from the set of binary images a surface mesh as illustrated in Figure 3(a). The surface mesh so obtained is subsequently smoothed with a function from the VTK toolbox (http://www.vtk.org) called vtkSmoothPolyDataFilter and the resulting surface is embedded in a volume mesh representing the US+EIT probe, as illustrated in Figure 3(c). The whole volume is re-meshed using the public domain program TetGen (http://tetgen.berlios.de), allowing to perform EIT reconstructions.

3. Using Ultrasound Information In Image Reconstruction

The use of US imaging allows us, with the process described in the preceding section, to build a forward model where the exact boundary of the prostate, as extracted by US information, is embedded in a volume mesh. This information can be used as a hard prior to enhance EIT

(a) Segmented surface.   (b) Smoothed surface.   (c) Smoothed surface embedded in a volume mesh simulating the probe.
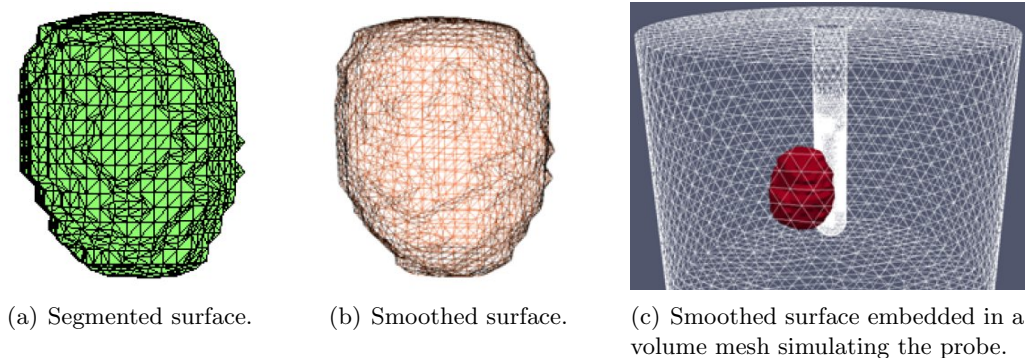
Figure 3. On the left, surface of the phantom/prostate obtained by segmenting a stack of 2D US cross sections. Center, smoothed surface mesh of the phantom/prostate. Right, smoothed surface of the phantom/prostate embedded in a volume mesh which models the imaging probe.

reconstruction. Similar approaches have been developed for example by Vahukonen [1] [2], where in medical imaging applications ad-hoc basis functions were used to reconstruct the conductivity of lungs in thoracic meshes where the profile of the lungs was supposed to be known a priori. Soleimani [3] considered combining US information with EIT imaging in cryosurgery, proposing to use Level Set methods where the initial level set is formed on the basis of the boundary captured by ultrasound. Steiner [4] considered a data fusion approach in imaging breast tumors with ET and US. In our specific application US is indicative only of the boundary of the prostate, and does not indicate malignant masses. The only information we incorporate therefore in image reconstruction is relative to the surface of the prostate. As we discuss in the following, this ability constitutes a significant improvement with respect to a simple EIT approach, with no prior information. Prostate normal tissues are more conductive than surrounding tissues [5]. The actual conductivity value depends on the measurement frequency, but in general the prostate gland itself represents an electrical contrast with respect to the surrounding tissues. Prostate cancer is instead less conductive [5] than normal prostate tissues. Imaging cancer requires therefore the ability of distinguishing a smaller contrast (cancer) in a spatially larger source of contrast (prostate). This is generally challenging for EIT. Being the boundary separating the prostate and surrounding tissues available, we use this information for automatically building an ad-hoc basis function for describing the conductivity distribution. The interior of the prostate volume is subdivided in a small number of sub-volumes (e.g. 40), where the conductivity is estimated, the exterior of the prostate is treated as a uniform region, whose value is fitted to the data. By this approach imaging of contrasts within the prostate can be significantly enhanced.

4. Numerical Experiment Results

In Figure 4 we show results from numerical experiments, indicating that significant enhancements can be obtained by using ultrasound information as priors in image reconstruction. Figures 4(a) and 4(d) show respectively the vertical and horizontal cross sections of a simulated prostate (red volume) with an inclusion (white volume). The prostate is in proximity of the imaging probe (dark gray). A conductivity of 0.25 S/m was assumed for the prostate, a conductivity of 0.06 S/m was assumed for the inclusion, and a conductivity of 0.1 S/m for the background. The images in Figures 4(b) and 4(e) show EIT reconstructions using prior information from ultrasound imaging. In these reconstructions the inclusion within the prostate is clearly visible. Figures 4(c) and 4(f) show instead EIT reconstructions where no US prior information was used (an approach presented in [6]), but instead a conical region in front of the probe and encompassing the prostate was imaged. As the prostate itself is a contrast with respect to the background,

(a) Vertical cross section simulated conductivity profile.

(b) Corresponding reconstructed EIT+US image.

(c) Corresponding reconstructed EIT image, no US information.

(d) Horizontal cross section simulated conductivity profile.

(e) Corresponding reconstructed EIT+US image.

(f) Corresponding reconstructed EIT image, no US information.
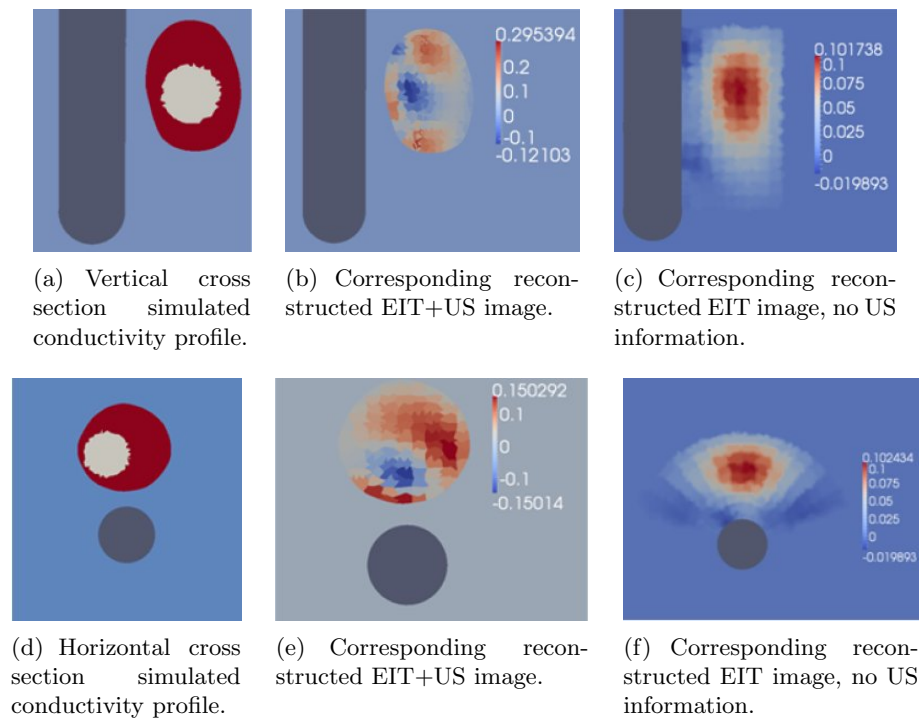
Figure 4. The first column of images shows a simulated prostate with an higher conductivity than the background, and an inclusion within the prostate with a lower conductivity. The second column of images shows EIT reconstructions using US prior information: the inclusion within the prostate can be correctly identified. The third column of images shows EIT reconstructions with no prior US information: the prostate itself results a dominating contrast and the inclusion within the prostate is lost.

the prostate becomes dominant in determining the reconstructed conductivity, which shows now increased values, and the contrast within the prostate is completely lost.

5. Concluions

A difficulty in imaging the electrical properties of the prostate is presented by the fact that the glad itself has electrical properties that differ from the background. The contrast presented by the prostate with respect to surrounding tissues can easily mask therefore the presence of smaller contrasts, indicative of cancer, within the glad. Delineating the boundaries of the prostate from US information, and incorporating this information in EIT image reconstruction algorithms significantly improves the ability of detecting anomalies within this organ.

References

[1] Vauhkonen M, Kaipio J P, Somersalo E and Karjalainen P A 1997 *Inverse Problems* **13** 523–530
[2] Vauhkonen M 1997 *Electrical Impedance Tomography and Prior Information* Ph.D. thesis Department of Applied Physics, Kuopio University
[3] Soleimani M 2006 *Biomedical engineering online* **5** 8 ISSN 1475-925X
[4] Steiner G, Soleimani M and Watzenig D 2008 *Physiological Measurement* **29** S63
[5] Halter R, Schned A, Heaney J, Hartov A and Paulsen K 2009 *The Journal of Urology* **182** 1600–1607
[6] Borsic A, Halter R, Wan Y, Hartov A and Paulsen K 2010 *Physiological Measurement* **31** S1

DEVELOPMENT OF AN EIT SYSTEM WITH A TINY ELECTRODE MATRIX

Tuykin T.S., Cherepenin V.A., Gulyaev Yu.V., Korjenevsky A.V. and Sapetsky S.A.
Kotel'nikov Institute of Radioengineering and Electronics of RAS

Abstact

The paper describes development of an EIT system with a tiny electrode matrix. The development includes three different stages - solutions: wires from measuring electronics to electrodes, wires with active shields (repeater from signal to shield), integration of measuring electronics with electrodes matrix. Advantages, disadvantages and aspects of the solutions are highlighted. The development was carried out on EIT system for gynecological application (30 mm diameter probes and 48 electrodes on it). Also method for 2D electrode placement in a tiny matrix is presented.

Introduction

Measurement of changes of electrical impedance in cervix can be used for early detection of cervical neoplasia [1]. The best way for this is using electrical impedance tomography. The first version of prototype 3D Gynecological Impedance Tomograph (GIT) was proposed in our previous publication [2]. The GIT is intended for uterus cervix diagnostics, so its probe should be less then 33 mm in external diameter. Also the system should have sufficient quantity of electrodes in matrix for detailed object imaging, dense and even electrodes placement for maximal area covering and uniform imaging, noticeable electrode size to avoid patient injuring and high contact impedance.

The main objective of the paper is not to describe GIT systems, but to discuss different constructions of system with tiny electrodes matrix (i.e. connection of measuring electronics and electrodes) and electrodes placement in a tiny matrix.

Connecting electrodes matrix and measuring electronics

Wires. Use of wires to connect electrodes matrix with measuring electronics is the most evident and trivial solution. It is easy to implement using industrial cable and soldering (see fig.1).
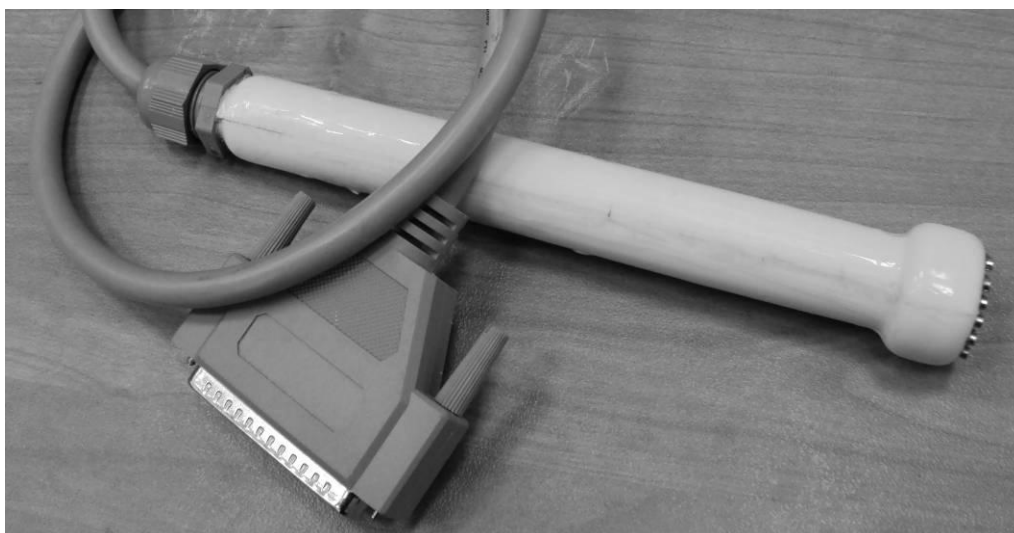
Fig. 1. GIT probe with wires

This solution does not work well for skin-electrode application with wires length about 1 m in urban environment (because of noises), but suitable for mucous membrane measuring according to the clinical tests [3].

Wires with active shields: putting signal from the line through operational amplifier repeater on a shield of each signal line (see fig. 2 GIT with repeater: typical scheme of active shield). The shielding compensates parasitic capacitance of cables and help to minimize external noises.
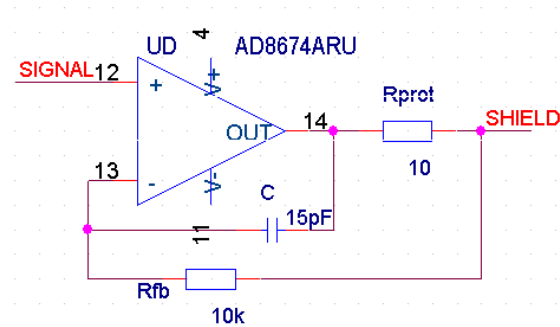
Fig. 2. Typical scheme of repeater for active shield: GIT with active shielded wires

But it is quite painstaking and exhausting work to connect a lot of signal and shield lines without shortages on a tiny electrodes matrix and on a connector (see fig. 3). Also thin cable and shield is vulnerable to breaks during measuring which are hard to repairing. Using of separate amplifiers, thin cables with shield, hand mounting on each channel increase complexity and cost of EIT system and decrease its reliability significantly. The total number of electrodes in the probe is limited by the diameter of probe channel because coaxial cable cannot be very thin.
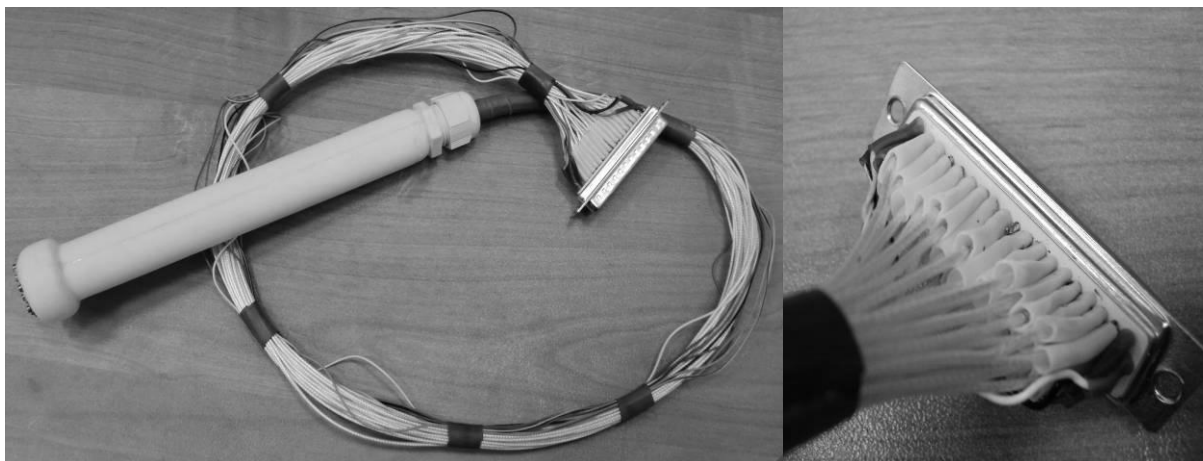
Fig. 3. GIT probe with actively shielded wires

Integration. It is difficult to start thinking about placement of all measuring electronics in available volume near electrodes matrix with such a small diameter like 30 mm. Nevertheless, thank to progress of modern microcontrollers and board interconnectors, it is not so difficult task actually. Using modern microcontroller with a lot of embedded modules (like Atmel XMEGA) helps to reduce bill of material, remove external ADC, DAC, amplifiers and to save space on board. Moreover, low price modern mixed-signal microcontrollers decrease system cost.

All interface parts like galvanic isolation, power supply and so on can be placed outside probe. In this way we need to put only microcontroller, multiplexers, ESD-protection diodes, some resistors and capacitors and electrodes inside probe. Also it is possible to use stack of several boards connected by interconnectors. In a new GIT prototype functional separation by boards was used (see fig. 4): interface board (A), board for microcontroller (B), board with multiplexers (C), measuring electrodes board (D).

Disadvantages of integration are:

it is hard to mount the boards in a laboratory conditions (with solders only), industrial oven and stencil are necessary;

it is difficult to change electrodes matrix arrangement or number of electrodes.
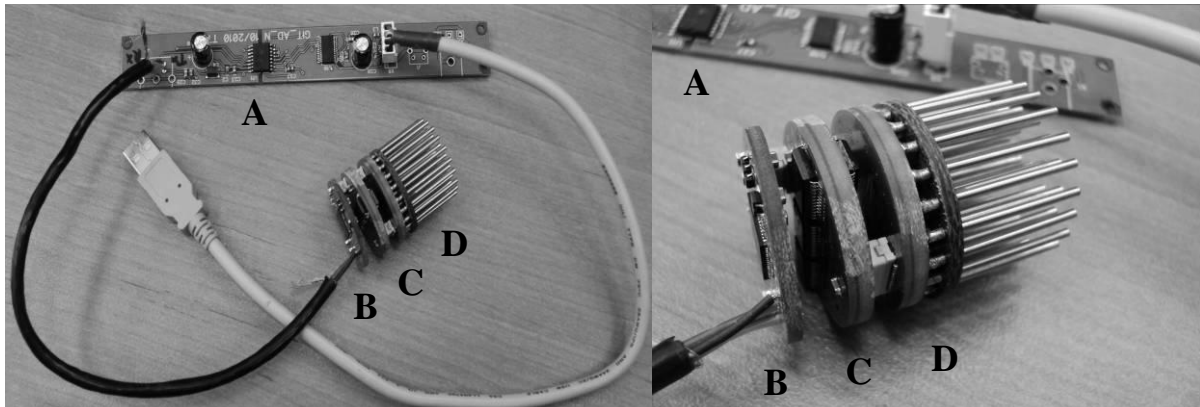
Fig. 4. GIT with electronics integrated with electrodes matrix (30 mm diameter): A -interface board (outside the probe), B - board for microcontroller, C - board with multiplexers, D - measuring electrodes board. Stack of B, C and D board is located inside probe.

Placement of electrodes in tiny matrix

The most common arrangement of electrodes for 2D electrodes matrix is orthogonal. And the first version of prototype GIT has orthogonal matrix of 32 electrodes (see fig. 5a).

(a)   (b)
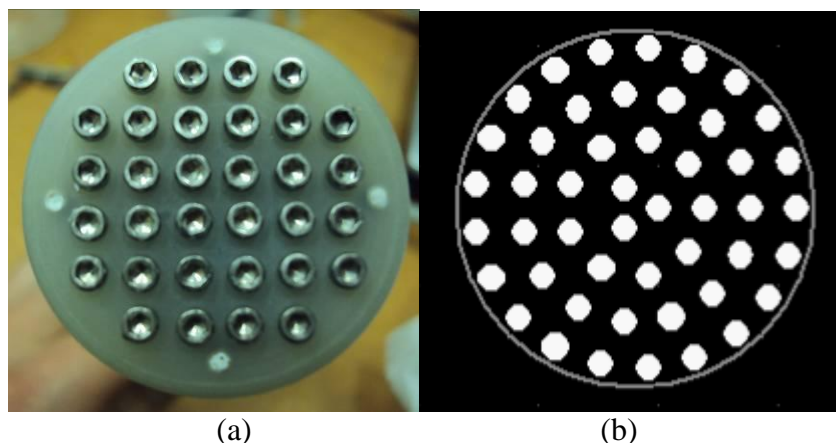
Fig. 5. Electrodes configuration: GIT with wires and 32 electrodes (a), GIT with integrated electronics on electrodes matrix and 48 electrodes (b)

After decision to integrate all measuring electronics on matrix, we have redesigned organization of electrodes also according following requirements (see fig. 5):

-for the fullest imaging of investigated region, the electrodes should cover all "corners" of the region along the edge;

-it is necessary to arrange as much electrodes as possible in the given area;

-density of electrodes should be close to uniform for even visualization, in orthogonal matrix it is provided by fixed electrodes step.

From the first requirement the edge of matrix should be covered by ring of electrodes with fixed step. If the edge is ring it is simple to cover the rest of matrix by electrodes rings too.

To create the matrix we chose desired step between electrodes. Then we fill the external ring with the electrodes, using the step measured along arc. After that we create next rings of electrodes with radius step close to the electrodes step. It is possible to rotate electrodes ring for better distribution of electrodes.

Also attention should be paid to the space limitation (i.e. possible quantity of multiplexers and total number of channels) before designing of a tiny matrix. For prototype GIT with integrated electronics we have started design from 64 channels (4 multiplexers with 16 channels for receiving and 4 multiplexers for transmitting), but finished with 48 channels due to lack of space on board for tracing.

Conclusion

Probably the best solution for commercially produced EIT system with a tiny electrodes matrix is integration of measuring electronics with the matrix, in spite of the problems arising from the very limited space. Meanwhile modern progress of mixed-signal microcontrollers, PCB-technology and board interconnectors makes this way possible and decreases significantly complicity and cost of the system in production.

Non-orthogonal circular placement of electrodes in a tiny electrode matrix for 3D EIT is more suitable for the covering of full area and uniform imaging.

References

1. B.H. Brown, P. Milnes, S. Abdul, J.A. Tidy "Detection of cervical intraepithelial neoplasia using impedance spectroscopy: a prospective study", BJOG, v. 112, pp. 802– 806, 2005

1. A. Korjenevsky, V. Cherepenin, O. Trokhanova, T. Tuykin "Gynecologic electrical impedance tomograph", J. Phys.: Conf. Ser., v. 224, 012070, 2010.

2. O.V. Trokhanova, Y.A. Chijova, M.B. Okhapkin, A.V. Korjenevsky, T.S. Tuykin "Using of electrical impedance tomography for diagnostics of the cervix uteri diseases", J. Phys.: Conf. Ser., v. 224, 012068, 2010.

Conductivity image reconstruction method for a new microscopic electrical impedance tomography (micro-EIT) system

Tong In Oh[1], Eunjung Lee[2], Jin Keun Seo[2], Eung Je Woo[1] and Tingting Zhang[2]
[1]Department of Biomedical Engineering, Kyung Hee University, Gyeonggi-do, KOREA
[2]Department of Computational Science and Engineering, Yonsei University, Seoul, KOREA
E-mail: tioh@khu.ac.kr

Abstract. A new microscopic electrical impedance tomography (micro-EIT) system which aims to produce cross-sectional conductivity images of a biological tissue sample or cells inside a small hexahedral container is proposed. The proposed micro-EIT system has a unique electrode configuration and associated data collection method. The first pair of driving electrodes is located at the left and right sides of the container facing each other. They fully cover the sides so that the induced current density is uniform and parallel when the container contains no anomaly. The second pair of driving electrodes is thin and long and located at the middle of the front and back sides. There are many miniature electrodes on the front, bottom and back sides for voltage measurements. The top of the container is open for sample manipulations. In terms of the image quality, the new micro-EIT system is advantageous over a conventional EIT method adopting multiple current injection patterns.

1. Introduction

Electrical impedance tomography (EIT) has been developed to image an admittivity distribution inside the human body [1]. A conventional EIT system injects current into the human body and measures induced boundary voltages using surface electrodes. Though the spatial resolution is low, it has numerous biomedical applications as a non-invasive, portable and low-cost medical imaging modality with a high temporal resolution [2].

A microscopic electrical impedance tomography (micro-EIT) has been also suggested to provide admittivity images of small tissue samples or cells [3-5]. The traditional micro-EIT approach inherits technical difficulties of the biomedical EIT originated from the ill-posedness of the corresponding inverse problem, the nonlinearity between the admittivity and boundary measurements and the weak sensitivity of voltage data to a local admittivity change [6-8]. Considering unavoidable measurement errors in practice, these conventional approaches should result in admittivity images with relatively low spatial resolution and accuracy.

In this paper, we suggest a container design with a significantly different electrode configuration to produce high-quality conductivity images using a new image reconstruction algorithm. Understanding the drawbacks of the conventional approach in EIT, we propose a new micro-EIT system with a small hexahedral container of a fixed dimension. The left and right sides of the container facing each other are fully covered by driving electrodes of solid metal plates. Injecting a primary current into the container through this driving electrode pair, we can create a uniform parallel current density distribution inside the container when it is filled with a homogeneous saline. We add a pair of thin driving electrodes on the middle of the front and back sides to inject a subsidiary current. This secondary current injection will produce a non-uniform internal current density distribution whose dominant direction is perpendicular to the primary uniform parallel current density. As shown in figure 1, two pairs

of driving electrodes are employed to adopt two independent injection current patterns. First, we apply a current from $\mathcal{E}_{1+}$ to $\mathcal{E}_{1-}$. Then we inject current from $\mathcal{E}_{2+}$ to $\mathcal{E}_{2-}$.

To measure resulting voltages on the surface of the container, we install arrays of small voltage-sensing electrodes on the remaining boundary except the top which is open for sample manipulations. This configuration provides a large number of voltage measurements from the three surfaces subject to two current injections. A reference data set from a homogeneous container is always available so that we can subtract it from a measured voltage data set from the same container with anomalies.

Separation of driving and sensing electrodes simplifies the hardware design and enhances the measurement accuracy. However, we are limited to two excitation patterns which result in just two sets of Dirichlet data for image reconstructions. We intend to augment this limitation by increasing the number of voltage measurements. Since conventional EIT methods adopt multiple current injections to increase the total number of measured voltage data, those EIT image reconstruction algorithms are not suitable for this new micro-EIT model. Thus, we will provide a mathematical framework of this novel micro-EIT system for the development of its image reconstruction algorithms.
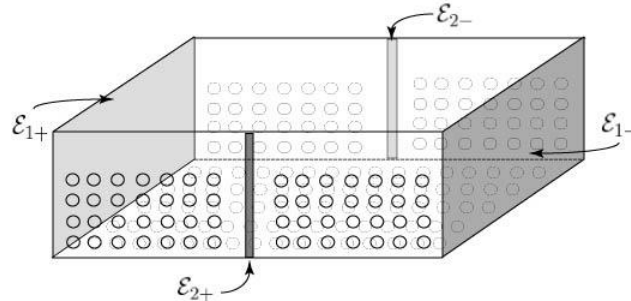
Figure 1. Sample container for micro-EIT system.

2. Image reconstruction algorithm

Let u_j (j=1, 2) satisfy the following mixed boundary value problem:

$$\nabla \cdot \left(\sigma \nabla u_j \right) = 0 \ \text{ in } \Omega$$

$$\mathbf{n} \times \nabla u_j = 0 \ \text{ on } \ \mathcal{E}_{\{1\pm\}} \cup \mathcal{E}_{\{2\pm\}}$$

$$\sigma \frac{\partial u}{\partial \mathbf{n}} = 0 \ \text{ on } \ \partial\Omega(\mathcal{E}_{\{1\pm\}} \cup \mathcal{E}_{\{2\pm\}}),$$

where the total current corresponding to u_1 through $\mathcal{E}_{1+}$ and $\mathcal{E}_{1-}$ is $\pm I$, respectively, while the total current through $\mathcal{E}_{2+}$ and $\mathcal{E}_{2-}$ is 0. Also, the total current corresponding to u_2 through $\mathcal{E}_{2+}$ and $\mathcal{E}_{2-}$ is $\pm I$, respectively, while the total current through $\mathcal{E}_{1+}$ and $\mathcal{E}_{1-}$ is 0. Here σ is the conductivity of the sample and $\mathbf{n}$ is the outward unit normal vector to the boundary. Let v_j be the solution of the above mixed boundary value problem when the domain is filled with a homogeneous material. Then we can show that $\sigma \nabla u_j$ is very close to ∇v_j. By using this, we have

$$\frac{\partial}{\partial x} \frac{1}{\sigma} \cdot \frac{\partial v_j}{\partial x} + \frac{\partial}{\partial y} \frac{1}{\sigma} \cdot \frac{\partial v_j}{\partial y} \approx \nabla^2 u_j \ \text{ near the bottom of } \Omega$$

The above approximation leads us to a projected value of σ such as

$$\tilde{\sigma}^{-1} = \int_{\text{bottom}} G(x, y; x', y') F(x', y') dx' dy' + \frac{1}{\sigma_0}$$

for some known information F, where G is a Green function of Laplace equation and σ_0 is a background conductivity.

3. Numerical simulation

Based on the proposed algorithm in section 2, we performed numerical simulations when objects were placed in a rectangular container. Figure 2(a) shows a three-dimensional conductivity distribution of a Shepp-Logan model in a 2×2×0.6 container. All anomalies within the container are aligned at z=0.2. Its reconstructed image using the proposed algorithm is shown in figure 2(b). Figure 2(c) is the reconstructed image when 5% of Gaussian noise was added to u_j-v_j in the numerical model.

(a)   (b)   (c)
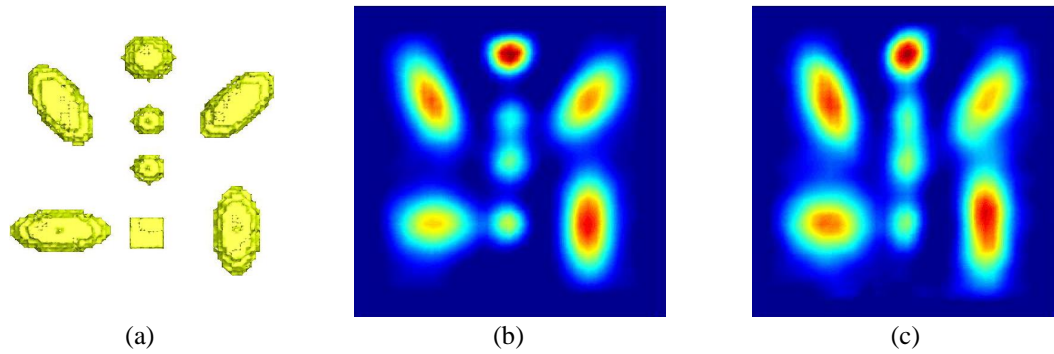
Figure 2. (a) Shepp-Logan model, (b) reconstructed conductivity image on z=0 and (c) reconstructed conductivity image with 5% of Gaussian noise to u_j-v_j.

Using the projected data to both sides and bottom plane, we can reconstruct a three-dimensional image by using back-projection and threshold techniques. In figure 3(a), two anomalies are located at (0.6, 0.7, 0.3) and (1.3, 0.3, 0.3) with radius 0.2. Figure 3(b) is a corresponding three-dimensional reconstructed image. When several anomalies are located closely as in figure 4(a), three close anomalies appears as a merged one in a reconstructed image shown in figure 4(b). In figure 4(a), four anomalies are located at (0.4, 0.35, 0.3), (0.4, 0.55, 0.3), (0.7, 0.5, 0.3), and (1.6, 0.5, 0.3) with radius 0.2.

(a)   (b)
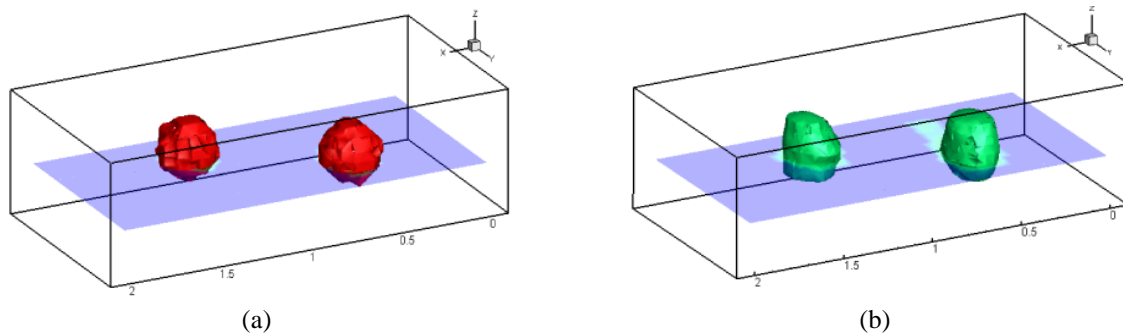
Figure 3. (a) Conductivity distribution with two anomalies and (b) reconstructed image.

(a)   (b)
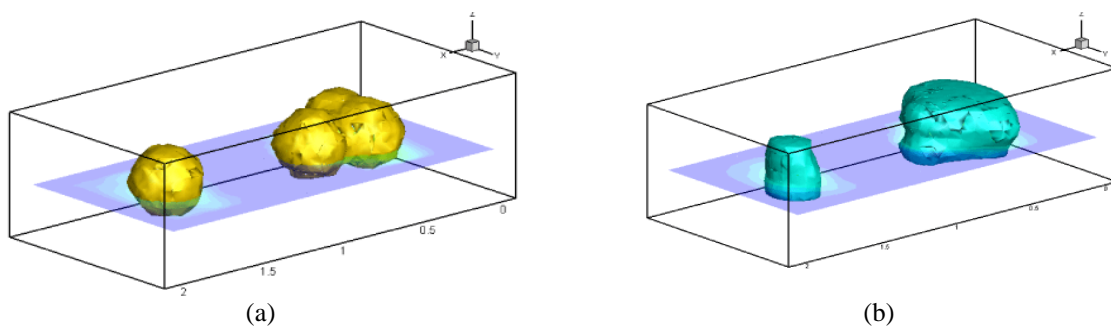
Figure 4. (a) Conductivity distribution with four anomalies and (b) reconstructed image.

4. Discussion and conclusion

We proposed a new micro-EIT system where we took advantage of the flexibility in designing the sample container and electrode configuration. We suggested inducing most desirable current densities inside the container, which can maximize voltage changes caused by anomalies. This requires an electrode configuration where only a limited number of independent current injections are possible. In order to circumvent the limitation in the total number of independent injection currents, we suggested using a large number of voltage-sensing electrodes not to decrease the total amount of measurements. The reconstructed projected images are blurred but reliable approximations of a true conductivity distribution with much better image quality compared with conventional EIT images. Numerical simulations show an excellent performance for general discontinuous conductivity distributions although the formula requires a smoothness assumption of σ. Adopting a standard back-projection method, we could also produce three-dimensional conductivity images inside the sample container from its projected images on three sides.

Acknowledgments

References

[1] Holder D 1992 Electrical impedance tomography with cortical or scalp electrodes during global cerebral ischaemia in the anaesthetised rat, *Clin. Phys. Physiol. Meas*. **13** 87-98

[2] Holder D 2005 *Electrical Impedance Tomography: Methods, History and Applications* (IOP Publishing: Bristol, UK)

[3] Griffiths H, Tucker M G, Sage J and Herrenden-harker W G 1996 An electrical impedance tomography microscope, *Physiol.Meas*. **17** A15-A24

[4] Wegener J, Keese C R and Giaever I 2000 Electric cell-substrate impedance sensing as a noninvasive means to follow the kinetics of cell spreading on artificial surfaces, *Exp. Cell Res*. **259** 158-166

[5] McCoy M H and Wang E 2008 Use of electric cell-substrate impedance sensing as a tool for quantifying cytopathic effect in influenza A virus infected MDCK cells in real-time, *J Virol Methods* **130**(1-2) 157-161

[6] Linderholm P, Vannod J, Barrandon Y and Renaud P 2007 Bipolar resistivity profiling of 3D tissue culture, Biosens. Bioelectron. 22 789-796

[7] Rahman A R A, Register J, Vuppala G and Bhansali S 2008 Cell culture monitoring by impedance mapping using a multielectrode scanning impedance spectroscopy system(CellMap), *Physiol.Meas*. **29** 227-239

[8] York T, Sun L, Gregory C and Hatfield J 2004 Silicon-based miniature sensor for electrical tomography, *Sensors and Actuators A: Physical* **110** 213-218

Microscopic electrical impedance tomography system with hexagonal sample container: experimental feasibility study

Qin Liu[1], Tong In Oh[1], Eun Jung Lee[2], Eung Je Woo[1] and Jin Keun Seo[2]

[1]Impedance Imaging Research Center and Department of Biomedical Engineering, Kyung Hee University, Gyeonggi-do, Korea
[2]Department of Computational Science and Engineering, Yonsei University, Seoul, Korea

E-mail: ejwoo@khu.ac.kr

Abstract. We describe a novel design of a microscopic electrical impedance tomography (micro-EIT) system for noninvasive monitoring of cell or tissue cultures. The core of the micro-EIT system is a sample container including two pairs of current injection electrodes and 360 voltage-sensing electrodes. In designing the container, we took advantage of a hexagonal structure with a fixed dimension and electrode configuration. This eliminated technical difficulties related with unknown irregular boundary geometry of an imaging object in conventional medical EIT. Attaching a pair of large current-injection electrodes fully covering the left and right sides of the hexagonal container, we can generate a uniform parallel current density inside the container when it is homogeneous. The 360 voltage-sensing electrodes are placed on the front, bottom and back sides of the hexagonal container in three sets of 8×15 arrays with an equal gap among all of them. We measure voltage differences between all neighboring pairs along the direction of the parallel current pathway. For the homogeneous container, all measured voltages must be same since the voltage changes linearly along that direction. Any anomaly in the container will perturb the current pathways and therefore equipotential lines to produce different voltage data. In this paper, we describe the design and construction of such a micro-EIT system with preliminary experimental results. Proposing the novel micro-EIT system design, we suggest future studies of miniaturizing the sample container for a true microscopic conductivity imaging of cell or tissue cultures.

Keyword: Micro-EIT, conductivity, cell culture

1. Introduction

Three-dimensional cell or tissue cultures become increasingly important in biological and pharmaceutical research, replacing traditional monolayer cell cultures [1]. Though numerous techniques were suggested to monitor their behavior or functionality, there still exists a need for new noninvasive methods to monitor three-dimensional cell or tissue cultures. Electrical cell-substrate impedance sensing (ECIS) or scanning impedance imaging showed a potential for providing information about the morphology and motion of cultured cells [2, 3]. ECIS does not present images but quantitative data related with cell attachment and motion. Most micro-EIT imaging systems proposed so far have much in common with a standard medical EIT system [4, 5]. This conventional approach inherits technical difficulties of EIT originated

from the ill-posedness of the corresponding inverse problem, the nonlinearity between conductivity and boundary measurements and the insensitivity of voltage data to a local conductivity change. Recently, we have proposed a new micro-EIT system design using a miniaturized hexahedral sample container [6, 7]. It has a unique electrode configuration and associated data collection method. In this study, we describe the developed micro-EIT system with a goal to noninvasively visualize conductivity distributions of biological objects placed inside the sample container.

2. Method

We designed the micro-EIT system in figure 1(a) based on a lately developed parallel EIT system called the KHU Mark2 [8]. It contains 15 impedance measurement modules (IMMs) and each IMM includes a constant current source and a differential voltmeter. To measure voltage from 360 voltage-sensing electrodes, it is equipped with a switch controller. We installed 360 gold-coated voltage-sensing electrodes on the front, bottom and back sides of the hexahedral sample container in figure 1(b). On each side, we installed a planar array of 8×15 electrodes as in figure 1(c). We sequentially injected the primary and secondary currents and measured induced voltages between all neighboring voltage-sensing electrode pairs. For each current injection, we measured 360 voltage data using 15 voltmeters in 24 switch settings as shown in figure 2.
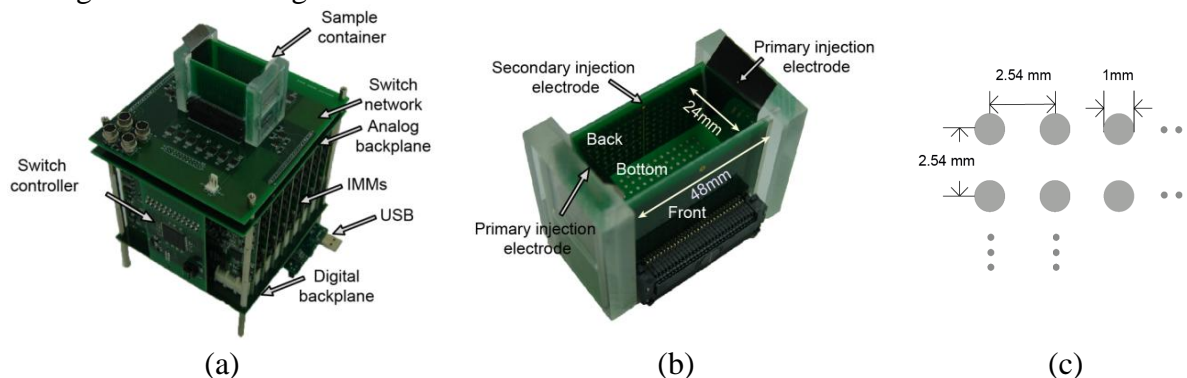
Figure 1. (a) Developed micro-EIT system, (b) sample container and (c) layout of voltage-sensing electrode.
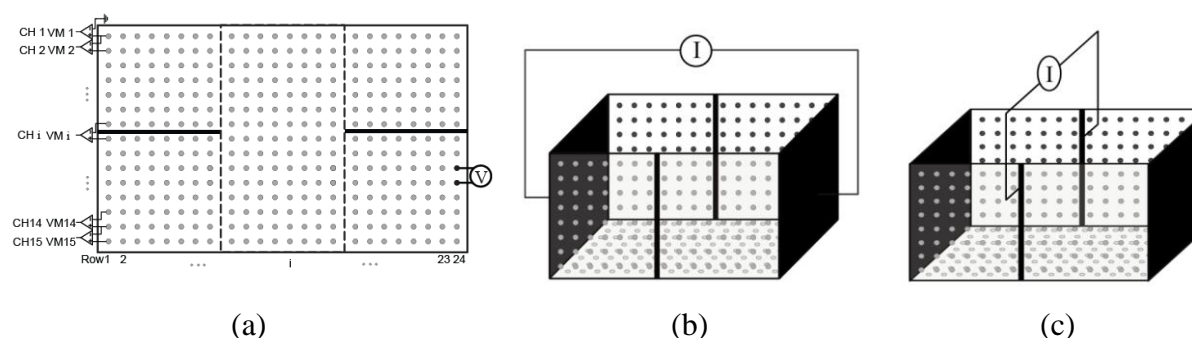
Figure 2. (a) Voltage measurement scheme, (b) primary and (c) secondary current injection method.

3. Result

3.1. Numerical simulation

We built a computational model of the sample container using COMSOL (COMSOL Inc. USA). The background was a saline of 0.2 S/m. We placed an anomaly of 0.02 S/m on the left side as shown in figure 3(a). Figure 3(b) and (c) show calculated boundary voltage maps for the primary and secondary injection currents, respectively.

Radius of anomaly: 7 mm

Conductivity of background: 0.2S/m
Conductivity of anomaly: 0.02S/m
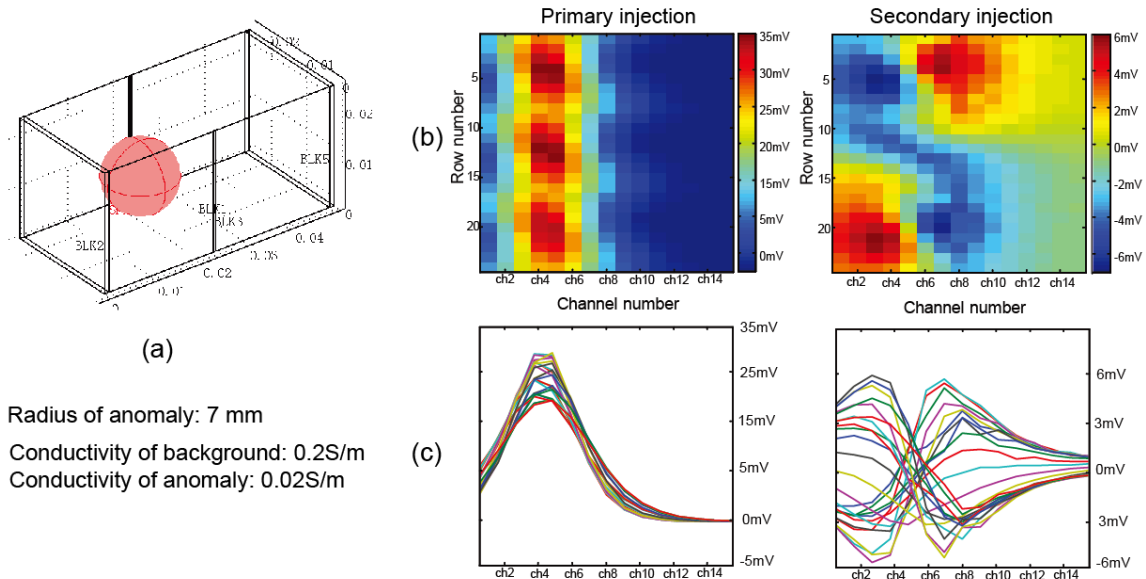
Figure 3. (a) Computational model of the sample container with an anomaly. (b) Calculated boundary voltage maps subject to the primary and secondary current injections, respectively. (c) Profiles of the boundary voltages.

3.2. *Experimental results*

Carrot: 10x10x10 mm^3

Conductivity of saline: 0.4S/m
Conductivity of carrot: 0.02S/m

< Front side >   < Bottom side >   < Back side >
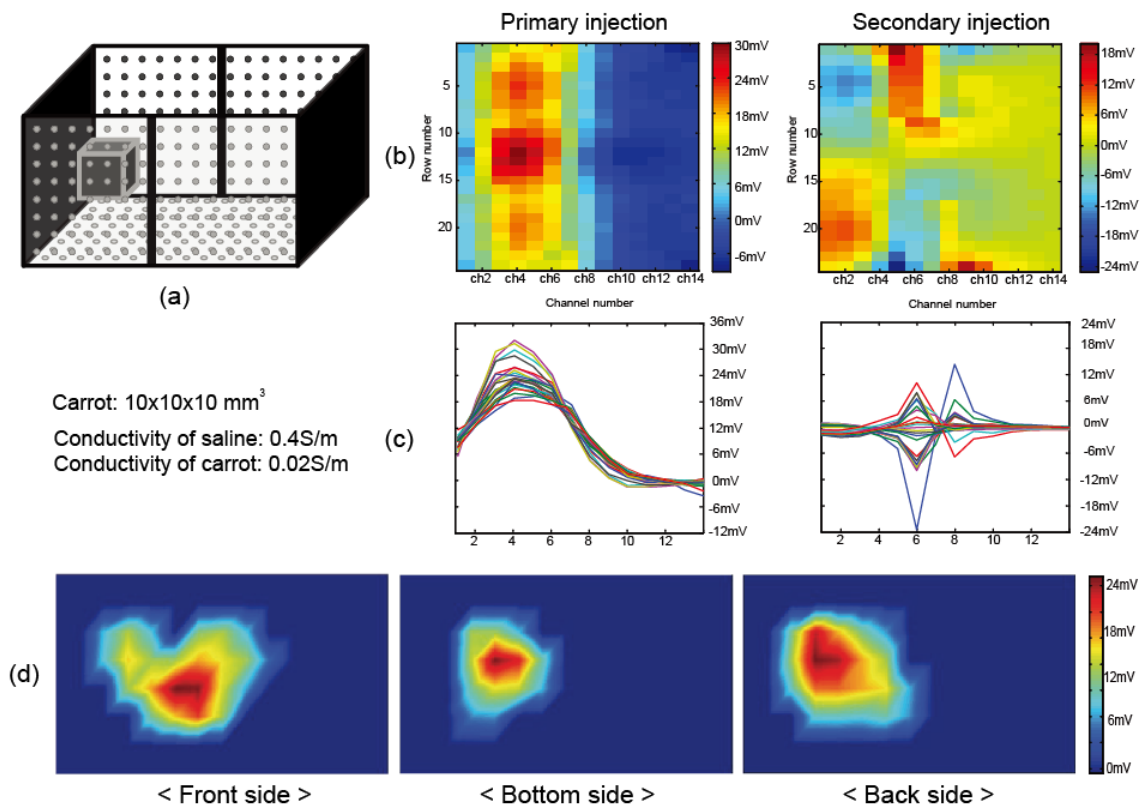
Figure 4. (a) Experimental setting with an anomaly in the container. (b) Measured boundary voltage maps subject to the primary and secondary current injections, respectively. (c) Profiles of the boundary voltages. (d) Projected images on the front, bottom and back sides using a conductivity image reconstruction algorithm.

We filled the container in figure 4(a) with a saline of 0.4 S/m. The anomaly was a piece of carrot ($10\times10\times10$mm^3). We injected sinusoidal currents at 1 kHz and measured boundary

voltage data. Figure 4(b) and (c) plot measured boundary voltage maps and their profiles. We produced projection images in figure 4(d) on the front, bottom and back sides using a conductivity image reconstruction algorithm.

4. Conclusion and discussion

Carefully observing measured boundary voltage data subject to the secondary injection current, we found that voltages at the upper part of the container are higher than those at the lower part. We could attribute these systematic artifacts to the existence of highly conductive voltage-sensing electrodes on the bottom side whereas the top of the container is open. We suggest decreasing the electrode size as small as possible.

The idea of the uniform parallel current density by using the primary current injection turns out to be very effective in improving the quality of conductivity images. In principle, measuring (possibly many) voltages following directions of current flows subject to (possibly small number of) externally injected currents is advantageous since equipotential lines are perpendicular to current streamlines. In designing a sample container for a micro-EIT system, we suggest injecting one or a few currents, which would produce uniform and parallel current density distributions inside a homogeneous container, and measuring many voltages at the sides, which are parallel to the internal current flows. We may increase the number of voltage-sensing electrodes until the measured voltages between neighboring voltage-sensing electrode pairs become smaller than a noise level of the system.

We plan to reduce the size of the sample container as small as possible by using a conventional printed circuit board technology. Since we also plan to increase the number of voltage-sensing electrodes as large as possible, we should reduce the noise level in voltage measurement at the same time.

Reference

[1]   Kim J B, Stein R and O'hare M J 2004 Three-dimensional in vitro tissue culture models of breast cancer - a review *Breast Cancer Res. Treat*. **85**, 281-91

[2]   Giaever I and Keese C R 1993 A morphological biosensor for mammalian cells *Nature* **366**, 591-592

[3]   Oliphant T E, Liu H, Hawkins A R and Schultz S M 2006 Simple linear models of scanning impedance imaging for fast reconstruction of relative conductivity of biological samples, *IEEE Trans. Biomed. Eng*. **53**(11), 2323-2332

[4]   Griffiths H, Tucker M G, Sage J and Herrenden-Harker W G 1996 An electrical impedance tomography microscope, *Physiol. Meas*., **17** A15-A24

[5]   Rahman A R A, Register J, Vuppala G and Bhansali S 2008 Cell culture monitoring by impedance mapping using a multielectrode scanning impedance spectroscopy system (CellMap) *Physiol. Meas*., **29**, 227-39

[6]   Liu Q, Wi H, Oh T I, Woo E J and Seo J K 2010 Development of a prototype micro-EIT system using three sets of 15×8 array electrodes *J. Phys.: Conf. Ser*., **224**, 012161

[7]   Lee E J, Seo J K, Woo E J and Zhang T 2011 Mathematical framework for a new microscopic electrical impedance tomography system *submitted to Inv. Prob*

[8]   Oh T I, Wi H, Kim D Y, Yoo P J and Woo E J 2011 Fully parallel multi-frequency EIT system with flexible electrode configuration: KHU Mark2. *Physiol. Meas*. in press

Using of electrical impedance mammography for monitoring of the efficiency of dyshormonal breast diseases treatment

O V Trokhanova[1], M B Okhapkin[1], L A Musaeva[1] and A V Korjenevsky[2]

[1]Yaroslavl State Medical Academy, Yaroslavl, Russia

[2]Kotel'nikov Institute of Radioengineering and Electronics of the RAS, Moscow, Russia

I. Introduction

Evaluation of efficiency of surgical treatment of focal benign and malignant mammary gland diseases is carried out through the comparison of the results of ultrasonic examination, X-ray mammography and biopsy before and after the operation. Using abovementioned methods is difficult for efficiency evaluation of conservative treatment of diffusion dyshormonal mammary glands diseases. The cause of mastopathy development has not been fully determined yet, that is why the pathogenetic therapy is not worked out. The existing methods of treatment allow to influence the main symptoms and essentially reduce social discomfort caused by this disease. Absence of pathogenetic treatment and predicting positive changes in mammary glands, which may happen while using such treatment, makes the evaluation of efficiency of treatment very difficult using ultrasonic and X-ray examinations. The method of electrical impedance mammography occupies a special place here, because the created method of revealing and differential diagnostic of dyshormonal mammary glands diseases essentially increases the exactness of diagnostics, widens and qualitatively improves screening of these diseases at women of all age groups and also gives the possibility to evaluate condition of mammary gland in progress.

The aim of our report is to reveal peculiarities of electrical conductivity of mammary glands in women with mastopathy, who take hormonal contraception preparations, and to make clear the possibility and necessity of using of electrical impedance mammography for reliable monitoring of the results of treatment using these preparations.

II. Material and methods

The report presents main results of a comprehensive examination of mammary glands of 355 women aged from 20 to 50, which formed following clinical groups:

- The 1st clinical group composed of 216 women with mastopathy without cystic component.

- The 2nd clinical group composed of 139 women with mastopathy without cystic component, who take hormonal contraception preparations.

In both groups there were formed subgroups according to the degree of age change of mammary glands (20-34 years, 35-40 years, 41-44 years, 45-50 years).

The comprehensive examination of mammary glands of women of both groups made before and after 1, 6, and 12 months from the beginning of using the preparations of hormonal contraception. The following diagnostic methods were applied: visual examination; palpation; cytological method of examination of secrete from nipples; ultrasonic examination; X-ray mammography; electrical impedance mammography with the help of multifrequency 256-electrode electrical impedance mammograph [1], the frequencies used were 10 kHz and 50 kHz. All examination results were statistically processed by alternative variation method with obtaining a mean value and standard deviation.

There are many different ways of treatment of dyshormonal mammary gland diseases. But one of the important methods is using of preparations of hormonal contraception. That is why we choose for our examination women, who take the following preparations for treatment of mastopathy: "Yarina" (0.030 mg of etinilestradiol; 3 mg of drospirenon), "Marvelon" (0.030 mg of etinilestradiol; 0.15 vg of dezogestrel), "Janin" (0.030 mg of etinilestradiol; 2 mg of dienogest), "Logest" (0.020 mg of etinilestradiol; 0.075 of gestogen).

There is no consensus of opinion about influence of hormonal preparations on mammary glands in up-to-date literature. Therefore contraceptives were prescribed only to women with mastopathy without cystic component, that is without focal lumps in mammary glands [2, 3].

III. Results

There are no visual changes of mammary glands and atypical cells by cytological method of examination of secrete from nipples in women of both clinical groups using the primary observation and dynamic observation in 12 months.

All women have pains concentrated in zones without clear contours. So the comparison estimation of palpable changes using dynamic observation is not reasonable. But

questioning has revealed that the pains stopped after 2-3 months of using the preparations at 87.8% of women.

The signs, which are typical for mastopathy, were detected at the ultrasonic investigation and X-ray mammography at all women before and after 12 months of taking the preparations. But it is difficult to reveal a degree of changes in structure of mammary glands during treatment at the ultrasonic investigation. The analysis of results of the ultrasonic investigation after 12 months of taking the hormonal preparations allowed to reveal singular cysts sized up to 7 mm at 3 women (2,2%) and multiple cysts sized up to 5 mm at 2 women (1,4 %) aged below 34 years from the 2nd group. The analysis of results of the X-ray mammography after 12 months allowed to reveal the decrease of density of the structure of mammary glands, increasing of clearness of structure due to decrease of oedema, decrease of volume of glandular tissue at 40% of women from the 2nd group. The changes were not revealed at the X-ray mammography at 40% women.

The visual estimation of electrical impedance mammograms during the dynamic observation in 1, 6 and 12 months from the beginning of using of the hormonal preparations has revealed electrical impedance image corresponded to mastopathy without cystic component (well-defined undistorted contour of the mammary gland, abnormalities of the image architectonics due to the change of ratio of the mammary gland tissues, increase of hyperimpedance areas on the images due to fibrous changes, increase of the mean electroconductivity zones due to hyperplasia of glandular tissue at adenosis, appearance of hypoimpedance inclusions with well-defined contours, which correspond to the evident pocket-shaped dilatation of ducts). Hypoimpedance inclusions on the mammograms with electrical conductivity corresponding to the mammary gland cysts have appeared at 5 women before 34 years from the 2nd group after 12 months.

A quantitative estimation of electrical impedance images at women of both clinical groups were made after 1, 6 and 12 months from the beginning of taking the preparations. We used the mean values from the second level of scanning at the frequencies 50 and 10 kHz. The values of mean conductivity of mammary glands at women with mastopathy without cystic component, who take hormonal contraceptives, increase statistically significant with age at both frequencies as well as in the control group. Comparison of average electroconductivity after 1 and 6 months of using of hormonal contraceptives with primary data shows the absence of changes in the corresponding age groups and statistically significant increase of the indices of average electroconductivity appears after 12 months of taking the preparations at the frequency 50 kHz. The comparison of the indices at the frequency 10 kHz shows

statistically significant decrease of electroconductivity in all age groups after 1 and 6 months of using the preparations and practically in all groups after 12 months of taking hormonal contraceptives. The indices of average electroconductivity are higher at the frequency 50 kHz than at 10 kHz at women with mastopathy without cystic component, who take hormonal contraceptives. It is not typical for the 1st clinical group, where there is not statistically significant difference between various frequencies.

The increase of indices of electroconductivity at the frequency 50 kHz after 12 months of preparations using prove their favourable influence on the mammary glands, because they confirm the slowdown and decrease of proliferative processes which are always followed by the reduction of electrical conductivity indices. Besides, the decrease of indices of electrical conductivity at 10 kHz proves the reduction of oedema.

IV. Conclusions

1. Changes in the mammary glands on the background of taking oral hormonal contraceptives are not visible by the traditional methods of mammary glands investigation. The possibility to reveal the minimal changes in mammary glands using the method of electrical impedance mammography and the possibility to give both visual and quantitative estimations of electrical impedance mammograms makes this method superior to the traditional methods (ultrasonic examination, X-ray mammography) in this application.

2. Hormonal oral contraceptives, which are taken for treatment of diffuse mastopathy, influence mammary glands during the prolonged using. The decrease of average electrical conductivity is observed only after 12 months of taking of the preparations.

3. The electrical impedance mammography is a new, accessible, safe and highly informative method, which the doctors can use without restriction of number of examinations as a method of reliable monitoring of the condition of mammary glands at women, who use the combined oral contraceptives.

References

1. Trokhanova O.V., Okhapkin M.B. and Korjenevsky A.V. "Dual-frequency electrical impedance mammography for the diagnosis of non-malignant breast disease", *Physiol. Meas.*, v. 29, pp S331-S344, 2008.

2. Saveleva I.S. The peculiarities of hormonal contraception and mammary glands, *Gedeon Richter* N 2, pp 27-31, 2000.

3. Speroff L, Darney PD. *A clinical guide for contraception*, Philadelphia: Lippincott Williams & Wilkins, 2001.

Electrical Impedance Tomography in geophysics, application of EIDORS

Lesparre N., Adler A., Gibert D., Nicollin F.

Introduction

The open-source collaborative software suite EIDORS (Adler and Lionheart, 2006), has been written primarily with a focus on medical imaging. This paper describes our work to adapt EIDORS for applications in geophysics. In geophysics, we apply EIT in order to image inner structures of geological objects since the rock resistivity can vary by several orders of magnitude depending on the rock nature, porosity and water content. The geometry of the electrode array consists most often in profiles of regularly spaced electrodes. And the geometrical factor is usually calculated to represent quickly the apparent conductivities, this allows to control the data quality in the aftermath of their acquisition. The distance between the electrodes defines the spatial resolution and the penetration depth. The spatial resolution of the method in geophysics is of the order of meters and the penetration depth can reach 500m.

We adapted the software EIDORS to inverse two sets of geophysical data. The first data set correspond to a study of the impact of excavations on clay properties in the Mont Terri underground rock laboratory. The second data set has been acquired on la Soufrière de Guadeloupe volcano to constrain the geometry of the hydrothermal system. EIDORS allows us to take into account the geometry of the electrode arrays and to make joint inversion of huge data sets in order to achieve a 3D tomography of the geological object. Moreover, the possibility of interaction with the EIDORS community allowed rapid development and answering of questions. This leads to a collaboration which aims at developing the geophysical applications of this free and open access software.

Applications

The Mont Terri project

The Mont Terri project (Switzerland), started with the observation of low humidity in the opalinus clay layer during the excavation. This rock presents useful properties of permeability suitable for nuclear waste storage. An underground rock laboratory has been constructed which welcomes experiments to characterise the mechanical behaviour of opalinus clay and follow the variations of its properties induced by the excavation or by a heating of the formation.

Three arrays of electrodes have been placed on rings around a gallery to follow the excavation damaged zone, Fig. 1. The gallery finite element model is computed from the positions of the electrodes to fix the gallery geometry, Fig. 2 . Low conductivity area are determined and interpreted as more damaged zones, Fig. 3 and 4. Repeated measurements on rings allow to perform a time monitoring which shows a reduction of the damaged zone. This confirms the auto-healing properties of the opalinus clay (Gibert *et al.*, 2006). The inversion of these data sets requires to take into account the circular geometry of the array and with parameters that can be different from those of the direct problem. We adapted EIDORS to fulfill these requirements since this software offers the possibility to choose the algorithm of the direct and inverse problems.

The study of la Soufrière de Guadeloupe volcano

The study of volcanoes with this method is also particularly interesting since hydrothermal

conduits can be characterized by high conductivities, regions with low densities can be interpreted as non altered rock and the regions with the lower densities may correspond to fractured areas. An array of electrodes has been set up on profile around and across the volcano, Fig. 5. The apparent resistivity shows a high conductivity zone under the volcano which may be interpreted as an area altered by the hydrothermal system. The data set reveals also that the volcano is highly heterogeneous and could be made of andesite blocks of cubic meter size whom interstices are filled with altered material and ashes, Fig. 6 (Nicollin *et al.*,2006).

Contributions to EIDORS

The scale of a geological object is huge compared to a human body, however the mesh of the direct problem has to be fine in order to insure its precision. Moreover the resolution of the inverse problem requires a high number of iteration of the direct problem (hundreds of times). The direct problem must then be computed quickly. To decrease this time of computation we introduced an electrode "pivot" to make an artificial protocol of acquisition.

To reduce the number of inverse parameters, we defined a mapping in order to gather the direct problem elements into larger composite elements. The gathering of elements was defined following the resolution of the method : elements of the inversion further from the electrodes were made coarser than the nearer one. This proceeding accelerates the inversion and improve its robustness.

Developments required for geophysical tomography

Geological rocks present a high anisotropy in conductivity and it would be very interesting to develop models taking into account this particularity since its influence on the EIT reconstruction in three dimensions is significant (Nicollin *et al.*, 2010). It would be also valuable to introduce finite elements to EIDORS to better represent geophysical objects and eliminate eventual edge effects.

References

Adler, A. & Lionheart, W.R.B., 2006. Uses and abuses of EIDORS: An extensible software base for EIT, *Physiol. Meas*, **27,** S25-S42.

Gibert, D., Nicollin, F., Kergosien, B., Bossart, P., Nussbaum, C., Grislin-Mouëzy, A., Conil, F. & Hoteit, N., 2006. Electrical tomography monitoring of the excavation damaged zone of the Gallery 04 in the Mont Terri rock laboratory: Field experiments, modelling, and relationship with structural geology, *Applied clay science* , **33** , 21-34.

Nicollin, F., Gibert, D., Beauducel, F., Boudon, G. & Komorowski, J.-C., 2006. Electrical tomography of La Soufri\`ere of Guadeloupe Volcano: Field experiments, 1D inversion and qualitative interpretation, *Earth Planet. Sci. Lett.* , **244** , 709-724.

Nicollin, F., Gibert D., Lesparre N. & Nussbaum C., 2010. Anisotropy of Electrical Conductivity of the Excavation Damaged Zone in the Mont Terri Underground Rock Laboratory, *Geophys. J. Int.* , **181** , 303320, doi: 10.1111/j.1365 246X.2010.04517.x.
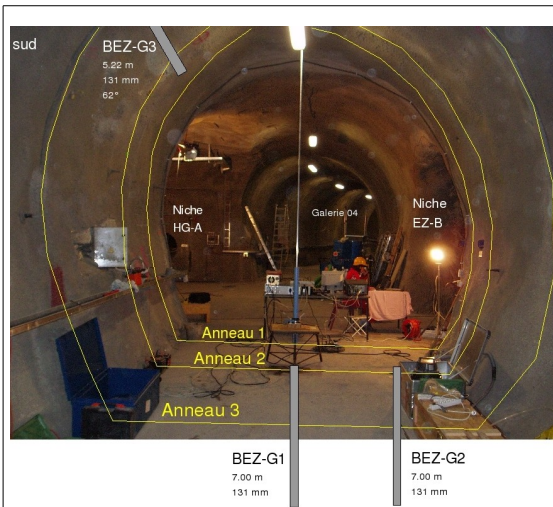
Figure 1 : Installations in the zone EZG-04 of the Mont Terri underground rock laboratory. The yellow rings represent the three rings of electrodes covered by concrete. Drills allow also
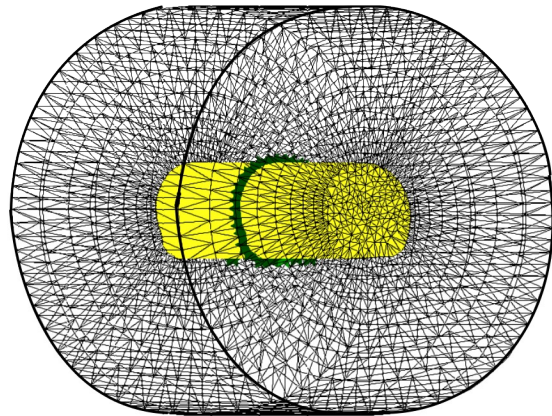
Figure 2 : Finite element model of the gallery. The green points represent the electrodes, the yellow zone corresponds to the gallery.
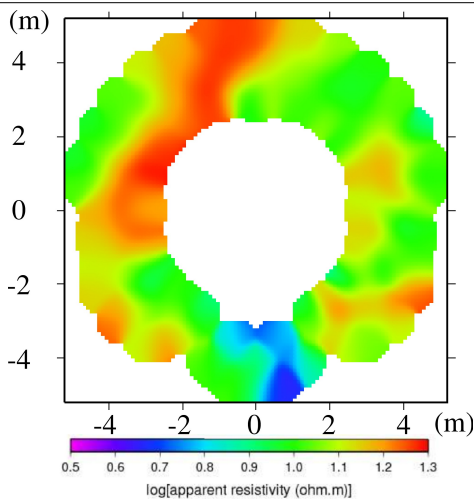
Figure 3 : Apparent resistivity measured on the second ring in March 2005. High resistivity areas enlighten the damaged areas.
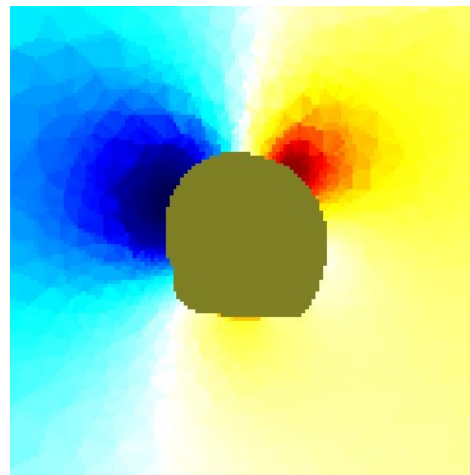
Figure 4 : Resolution of the inverse problem with EIDORS, the blue area correspond to a low conductivity zone.
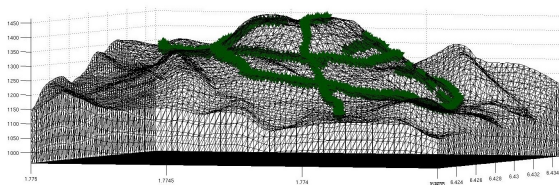
Figure 5 : Finite element model of la Soufrière de Guadeloupe volcano. The green points represent the electrodes.
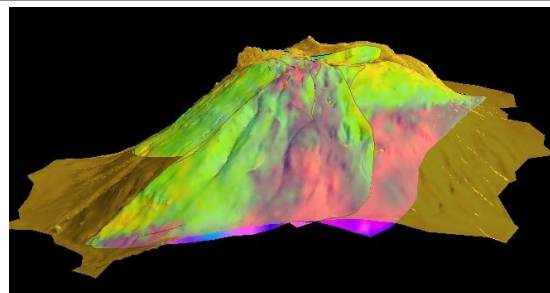
Figure 6 : Apparent resistivity of la Soufrière de Guadeloupe volcano. The pink area correspond to a high conductivity

	zone.

The importance of shape: thorax models for GREIT

Bartłomiej Grychtol[1] William R B Lionheart[2] Gerhard K Wolf[3] Marc Bodenstein[4] and Andy Adler[5]
[1]University of Strathclyde, Glasgow, UK [2]School of Mathematics, University of Manchester, UK [3]Children's Hospital Boston, Harvard Medical School, USA [4]Department of Anaesthesiology, University Mainz, Germany [5]Carleton University, Ottawa, Canada

Abstract: Time difference EIT is useful if the positions of the electrodes are poorly known, as it allows image reconstruction of reasonable quality even when, as is often the case, EIT data from the thorax is reconstructed onto a 2D circular model. However, even though inaccurate models may (and often are) used, there is a significant penalty in terms of reconstructed image accuracy. We focus on developments of the GREIT EIT image reconstruction algorithm. This algorithm represents a novel, optimization based approach to linear EIT reconstruction. So far, results have only been shown for circular thorax geometries, which precludes meaningful definition of conductivity contrast in the models. In this paper, we develop and validate an implementation of the GREIT algorithm for arbitrary thorax shapes. The results are validated on EIT data with simultaneous CT reference data. Results show significant improvements in the anatomical accuracy of reconstructed EIT images, in particular when physiological lung conductivity contrast is taken into account.

1 Introduction

Electrical Impedance Tomography (EIT) is an attractive method for monitoring patients during mechanical ventilation, because it can provide a non-invasive continuous image of pulmonary impedance which indicates the distribution of ventilation. Based on these advantages, there is significant interest in EIT to monitor patients with respiratory compromise.

One limitation is that much clinical and physiological research in lung EIT is done using older and proprietary algorithms; this is an obstacle to interpretation of EIT images because the reconstructed images are not well characterized. Many of these EIT imaging algorithms are based on circular and 2D models of the medium sensitivity and assume homogenous conductivity distribution. Since thoracic EIT data are typically reconstructed with time difference (TD-EIT) algorithms the effect of these limitations are less evident, since TD-EIT is less sensitive to the exact configuration and geometry of the electrodes. However, models with incorrect shape information do result in significant inaccuracies and artefacts in images.

A recent systematic approach to choice of EIT reconstruction for thoracic TD-EIT is a reconstruction algorithm called GREIT (Graz consensus Reconstruction algorithm for EIT)[1]. One limitation of [1] is that it did not clarify the details of how to implement GREIT for arbitrary geometry body shapes. Instead, results were shown for a circular model in order to allow better comparison to the Sheffield backprojection. In this paper we: 1) develop the formulation of GREIT for arbitrary model geometry, and 2) evaluate the effect of using accurate thorax geometries and lung conductivity contrasts using EIT data from pigs with simultaneous CT.

GREIT Framework

The framework for the GREIT algorithm consists of: 1) detailed finite element models of a representative adult and neonatal thorax; 2) consensus on the performance figures of merit for EIT image reconstruction; and 3) a systematic approach to optimize a linear reconstruction

matrix to desired performance measures. Consensus figures of merit, in order of importance, are: a) uniform amplitude response, b) small and uniform position error, c) small ringing artefacts, d) uniform resolution, e) limited shape deformation, and f) high resolution. GREIT is designed to calculate a linear reconstruction matrix, $\mathbf{R}$ which performs well against the figures of merit, while maintaining small noise amplification and small sensitivity to electrode and boundary movement.

We represent linear EIT image reconstruction as a matrix, $\mathbf{R} \in \mathbb{R}^{N \times M}$ which maps measurements $\mathbf{y}$ to a reconstructed image $\mathbf{x}$:

$$\mathbf{x} = \mathbf{R}\mathbf{y} \tag{1}$$

where a frame of TD (or normalized TD) EIT data, $\mathbf{y} = \mathbf{v} - \mathbf{v}_r \in \mathbb{R}^M$ is used to reconstruct an image $\mathbf{x} \in \mathbb{R}^N$. The current EIT data frame is $\mathbf{v}$ which is compared to a reference data frame $\mathbf{v}_r$ which is typically averaged over times when the conductivity is stable. Images are represented on N pixel image elements.

The GREIT framework from which the reconstruction matrix, $\mathbf{R}$ is calculated, definition of a forward model, a noise model, and desired performance metrics are illustrated in fig. 1. The *forward* model allows calculation of EIT measurement data $\mathbf{y}_k$ from a conductivity change distribution $\mathbf{x}_k$. The model represents the details of the body geometry, the electrode size and contact impedance, and the reference conductivity around which conductivity changes occur. The *noise* model allows calculation of representative noise (electronic measurement noise and electrode movement artefacts) samples in EIT measurements. Based on the performance metrics defined above, we create a training set of desired images, $\tilde{\mathbf{x}}_k$, centred on each target, but with a blurring corresponding to figures of merit, as illustrated in fig. 1.

Type of Signal	Training Inputs (measurements)	Desired Output (reconstructed images)
Conductivity targets	$\boldsymbol{y}_t^{(k)}$	$\tilde{\boldsymbol{x}}_t^{(k)}$
Noise - noise, movement	$\boldsymbol{y}_n^{(k)}$	$\tilde{\boldsymbol{x}}_n^{(k)} = 0$
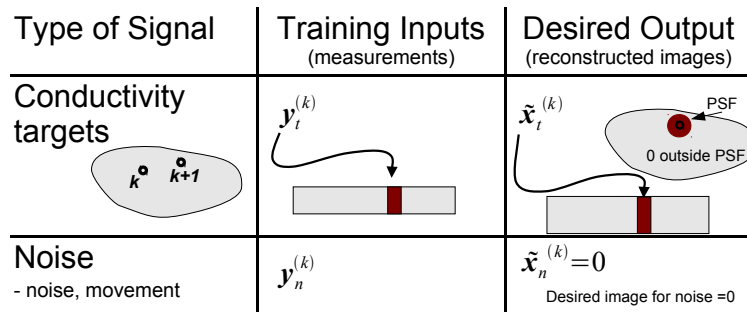
Figure 1: Illustration of signals and training data. Rectangles represents a matrix where column (k) represents a training sample, and the circle represents the corresponding desired image pattern.

Based on the *forward model*, *noise model*, and *desired performance metrics*, the GREIT reconstruction matrix $\mathbf{R}$ which best fits the requirements may be expressed as minimization of the norm

$$\epsilon^2 = \sum_k \|\tilde{\mathbf{x}}_k - \mathbf{R}\mathbf{y}_k\|_{\mathbf{W}_k}^2 \tag{2}$$

where $\mathbf{W}_k$ is a diagonal weighting matrix for each sample.

2   GREIT for arbitrary models

In this section, we elaborate on how GREIT is adapted to work with arbitrary models of thorax geometry. 1) The boundary shape, lung tissue outline and electrode positions (if available) are extracted from a CT, CBCT or MRI transverse slice of the thorax (c.f. fig. 2). 2) A 3D FEM for the forward model is built using Netgen [2] by extruding the extracted 2D outlines of the boundary and (optionally) the lungs. The mesh is refined around the electrodes. 3) The forward model is built using either homogenous conductivity or a contrast in the lung region (and others, if available). 4) To calculate the GREIT reconstruction matrix **R**, the desired solutions for a set of small (less than 5% diameter of the model) contrasting targets are calculated using the forward model and taking into account the desired figures of merit. In contrast to the original formulation in [1], we use uniform, rather than random, distribution of targets covering the entire image (a minimum of 500 are recommended). 5) The GREIT reconstruction matrix is calculated according to eq. 2 with an initial estimate of the noise weighting **W**. 6) The final value of **W** (and the reconstruction matrix **R**) that results in the desired noise figure (currently 0.5, after [1]) is found iteratively using the simplex search method [3].

   This procedure can be used with arbitrary stimulation pattern and number of electrodes, and can produce images beyond the 32-by-32 pixel resolution.
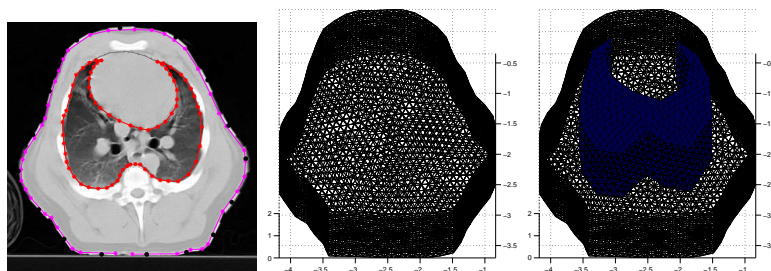
Figure 2:   Thorax CT (manually segmented) and the Finite Element Models used.

3   Results

The proposed algorithm was applied to a dataset of EIT and CT data acquired in a 23 kg anaesthesized swine during conventional mechanical ventilation at the University of Mainz under local ethical approval. The boundary shape, lung outline and positions of the electrodes were extracted from a CT slice in the electrode plane and used to build two conforming forward models with a) homogenous conductivity and b) conductivity contrast in the lung region (fig. 2). A 30 s period of ventilation was taken as reference for the reconstruction of two single frames of EIT data corresponding to inspiration and expiration in one breathing cycle with a) the Sheffield backprojection algorithm, b) the original GREIT algorithm using homogeneous circular model [1] and the new algorithm with c) homogenous conductivity distribution as well as lung-to-background conductivity ratios of d) 0.75, e) 0.50 and f) 0.25 (roughly physiological for soft tissue and lung at expiration [4]). The results are presented in fig. 3 as the difference between inspiration and expiration.

   Comparing the three reconstructions on homogenous models, the results show that using the correct geometry greatly reduces both the streak and the centre artefacts present in
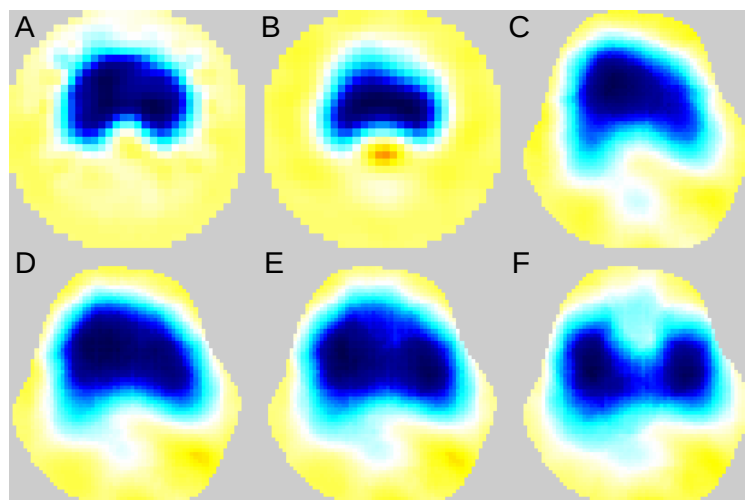
Figure 3: Reconstructed TD-EIT images of ventilation (inspiration minus expiration). *A:* Sheffield backprojection (circular model); *B:* GREIT using circular homogeneous model[1]; *C:* GREIT using conforming FEM model from CT (fig. 2) with homogeneous conductivity; and *D–F:* GREIT using conforming FEM model with lung-to-background conductivity ratio of 0.75, 0.50 and 0.25, respectively. All images represent the same measurement data and are normalised to the same range.

backprojection and GREIT, respectively, and leads to more anatomical shape and position of the lungs (c.f. fig. $3A–C$). Images in fig. $3D–F$ further demonstrate the increasing ability of the GREIT framework to separate the lungs when provided with more realistic conductivity distribution.

4   Discussion

Our motivation is to develop reconstruction algorithms that provide anatomically correct, and thus more readily interpretable, EIT images. The preliminary results presented here suggest that correct boundary shape and realistic conductivity distribution greatly improve the image quality and are major steps towards achieving this goal. Further research is necessary to establish just how well the boundary shape must be matched to obtain good results and what the effects of changing conductivity distribution are.

References

[1] A. Adler *et al* "GREIT: a unified approach to 2D linear EIT reconstruction of lung images" Physiol. Meas., 30:S35–S55, 2009
[2] Schöberl, J. "NETGEN An advancing front 2D/3D-mesh generator based on abstract rules" Computing and Visualization in Science, 1(1):41-52,1997
[3] Lagarias, J.C., J. A. Reeds, M. H. Wright, and P. E. Wright "Convergence Properties of the Nelder-Mead Simplex Method in Low Dimensions" SIAM Journal of Optimization, 9(1):112–147, 1998
[4] C. Gabriel, S. Gabriel and E. Corthout "The dielectric properties of biological tissues: I. Literature survey" Phys. Med. Bio., 41(11):2231-49, 1996

Augmenting information content through multimodal impedance imaging

D. Gürsoy,[*] Y. Mamatjan[†] and H. Scharfetter[*]

Abstract

We investigated every possible combination of electrical and magnetic measurements to improve impedance imaging. Combining those modalities opens a new possibility to increase the limited number of usable independent measurements. We performed a simulation for those modalities to make better use of both electrical and magnetic measurements gathered by an array of both electrodes and coils around a body. The normalized sensitivity matrices for each technique were computed based on finite element method and the singular value decomposition was performed on the resultant matrices. Based on the singular value spectrum, the information content of measurements in the Shannon's sense were calculated assuming 60 dB noise in measurements. The results were shown that the combined multi-modality approaches are promising and can greatly improve the information content of the data.

1 Introduction

Several noninvasive modalities have been developed for imaging the electrical conductivity distribution of a human body. Figure 1 demonstrates the basic principles of these modalities. The main idea is based on generating a current density distribution inside a body and recording the resultant electromagnetic fields by means of the sensors positioned around the body. Electrical impedance tomography (EIT) [1] uses an array of body surface electrodes both to inject currents to the body and measure the surface potentials. Induced-current EIT (ICEIT) [2] uses coils to induce currents, and electrodes to record the surface potentials, partly like in EIT. Magnetic induction tomography (MIT) [3], on the other hand, offers a completely contactless data acquisition by using coils instead of electrodes for both excitation and detection. As it is seen that these techniques differ by how the excitation and detection are implemented, yet the same principle underlies all techniques. The measured data are then used to reconstruct the cross-sectional impedance images of the body by means of Newton-type methods.

Typical impedance imaging systems usually have 8 to 16 sensors. In principle, half of the square of the number of sensors gives the maximum independent number of measurements available from sensor data (e.g. $8^2/2 = 32$ considering 8 electrodes). Increasing measurements beyond a certain number normally does not contribute to an improvement in imaging performance because of the high correlation between data. This also degrades the

---

[*]Institute of Medical Engineering, Graz Univeristy of Technology, Graz, Austria. E-mail: guersoy@tugraz.at

[†]Department of Systems and Computer Engineering, Carleton University, Ottawa, Canada.
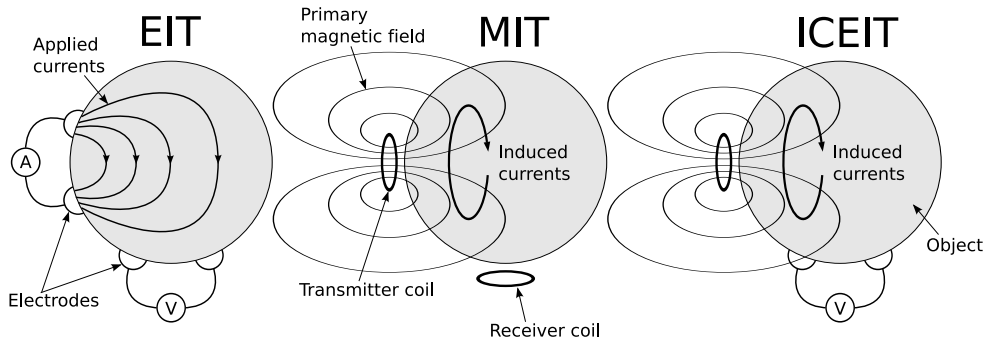
Figure 1: A comparative demonstration of different modalities: EIT, MIT and ICEIT.

spatial resolution significantly (i.e. about 10% percent of the medium diameter). A previously proposed option to increase the number of independent measurements is to locate the sources and sensors so that the overall orthogonality between the data is maximized [4]. However, another new possibility, which we proposed in this paper, is to augment the data acquired from different imaging techniques to increase the number of independent measurements. Therefore, we performed a simulation study considering a homogenous cylindrical phantom as a conducting body. The normalized sensitivity matrices for each technique were computed based on finite element method and the singular value decomposition was performed on the resultant matrices. Based on the singular value spectrum, the information content of measurements in the Shannon's sense [5] was calculated assuming 60 dB noise in measurements.

2   Methods

These modalities are illustrated in figure 1 to show how the measurements in EIT, MIT and ICEIT are acquired. However, once both the coils and the electrodes are usable for measurements, one can augment EIT data with MIT data or vice versa to double the amount of available measurements. Hereafter, we will refer to the multi-modal measurements as EIT-MIT, EIT-ICEIT, ICEIT-MIT and EIT-MIT-ICEIT. For instance EIT-MIT represents the data augmented from EIT and MIT modalities. Similarly, EIT-MIT-ICEIT refers to the all possible measurements that these techniques can offer. The numerical evaluation was performed on a cylindrical phantom with a radius of 10 cm and a height of 25 cm. 8 circular electrodes of 1 cm radii are uniformly located at the surface of the phantom on the central plane. Likewise, 8 coils of 2.5 cm radii are radially positioned on a ring of 12 cm radius, i.e, located 2 cm away from the surface. The meshes were created in 3-D using Netgen software. The electrical conductivity of the phantom was selected to be uniform and 1 Sm^{-1}. The sensitivity matrices for each technique were computed based on finite element method and the singular value decomposition was performed on the resultant matrices. For the details of the formulation one can refer to [6].

The information content of the measured data about the conductivity of a medium was used to evaluate the amount of independent measurements. The term *information in measurements* (IM) is used to describe the decrease in uncertainty about the contents of a medium, due to a set of measurements (for details, refer to [5]). Mathematically speaking, IM is defined as:

$$IM = \frac{1}{2} \sum_{i=1}^{t} \log_2 \left(SNR_k + 1 \right), \tag{1}$$
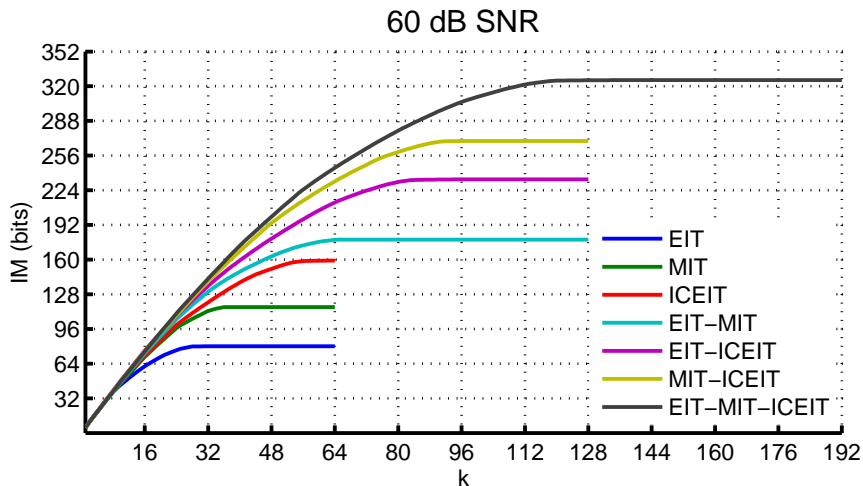
Figure 2: Information in measurements at 60 dB SNR.

where SNR_k is the signal to noise ratio of the kth measurement. In this paper, it is defined as $SNR_k = \rho_k/\rho_t$ where ρ_k represent the ith singular value of the sensitivity matrix which relates the voltage perturbations to the conductivity perturbations. The unit of IM as provided in equation (2) is *bits*. A large IM means that the measurements are more informative about the contents of a medium which indicates an improved spatial resolution.

3   Results

IM for each imaging modality was computed assuming a 60 dB SNR level in measurements. The required number of truncation (i.e. the truncation index t) for 60 dB SNR level was found as explained in [7]. The corresponding curves were plotted in figure 2. Each curve ascends with increasing measurements and reaches a plateau. The total maximum IM is found to be 80, 116, 160, 179, 235, 270 and 326 bits for the measurements acquired from EIT, MIT, ICEIT, EIT-MIT, EIT-ICEIT, MIT-ICEIT and EIT-MIT-ICEIT systems, respectively. Note that the saturation is achieved at small k values for EIT and MIT which clearly indicates the large number of redundant or nearly dependent information in measurements for MIT and EIT. On the other hand, the IM content of ICEIT approximately doubles the contents of EIT and MIT and shows promising results for imaging.

4   Conclusions

In this paper, we investigated the merits of augmenting data acquired from the combination of different imaging modalities and compared the systems based on the information content of the measurements about the medium. The results show that the number of independent measurements can easily be increased by means of augmenting data which in turn could increase the limits of spatial resolution. Although the combined multimodality tomography could provide many opportunities, unifying them in practice could bring in persisting problems related to the existing electrode and coil based systems, i.e., electrode contact problems [8] and motion artifacts [9].

References

[1] D. S. Holder, editor. *Electrical impedance tomography: Methods, history and applications*. Institute of Physics Publishing, Bristol, 1995.

[2] W. R. Purvis, R. C. Tozer, D. K. Anderson, and I. L. Freeston. Induced current impedance imaging. *Science, Measurement and Technology, IEE Proceedings A*, 140(2):135–141, 1993.

[3] H. Griffiths. Magnetic induction tomography. *Measurement Science and Technology*, 12(8):1126–1131, 2001.

[4] D. Gürsoy and H. Scharfetter. Optimum receiver array design for magnetic induction tomography. *Biomedical Engineering, IEEE Transactions on*, 56(5):1435–1441, 2009.

[5] A. Adler, R. Youmaran, and W. R. B. Lionheart. A measure of the information content of EIT data. *Physiological Measurement*, 29(6):101–109, 2008.

[6] M. Soleimani. Computational aspects of low frequency electrical and electromagnetic tomography: A review study. *International Journal of Numerical Analysis and Modeling*, 5(3):407–440, 2008.

[7] D. Gürsoy and H. Scharfetter. The effect of receiver coil orientations on the imaging performance of magnetic induction tomography. *Measurement Science and Technology*, 20(10):105505 (9pp), 2009.

[8] K. G. Boone and D. S. Holder. Effect of skin impedance on image quality and variability in electrical impedance tomography: a model study. *Medical and Biological Engineering and Computing*, 34(5):351–354, 1996.

[9] D. Gürsoy and H. Scharfetter. Reconstruction artefacts in magnetic induction tomography due to patient's movement during data acquisition. *Physiological Measurement*, 30(6):165–174, 2009.

Electrode positions and current patterns for 3D EIT

Maimaitijiang Yasheng and Andy Adler

Carleton University, Ottawa, Canada

Abstract: For a 3D electrical impedance tomography (EIT) system, it is necessary to optimize electrodes geometries placed around a body surface, and correspondingly apply stimulation and measurement patterns to produce maximum distinguishability. Optimising EIT image reconstruction requires designing systems electrode geometry and current injection such that the full ensemble of measurements provides as high SNR as possible over all of the volume under investigation and be localized for a certain region of interest. A 3D simulation study is undertaken using 8 electrode geometries and 16 different stimulation and measurement patterns (Δ_{sm}) for each electrode geometry. The electrode geometries studied were Planar, Planar-offset, Planar-interleaved, Zigzag, Zigzag-offset, Zigzag-interleaved and Square proposed by [5] for an adjacent pattern. The simulation results show that the Planar-interleaved geometry with Δ_{88} produced the highest distinguishability in comparison to all other electrode geometries and current patterns.

1 Introduction

In Electrical Impedance Tomography (EIT), several publications [1, 2] reported that the linear relationship between global tidal impedance variation and tidal volume cannot be used to calculate end-expiratory lung volume (EELV), since EELV is a global parameter of the whole lung while impedance is measured only at one thoracic level that reflects the impedance variations only in one cross-section of the thorax. Thus, it becomes necessary to develop 3D multiplane EIT to provide more information not only about the regional volume redistribution but also about aeration and ventilation of the whole lung.

An optimized EIT system have large distinguishability [8], which is determined by current stimulation amplitude, the accuracy of voltage measurement, stimulation and measurement patterns, and the number and placement of electrodes. This paper investigates combined electrode positions and current patterns, and minimum distinguishability for the separation of two electrode planes. Regarding current patterns, the early consideration on optimizing the drive patterns for EIT was done by [3] using a pair of point drive electrodes approach. A typical system based on the adjacent voltage measurement is the Sheffield Mark I described by [4], where they applied currents through neighbouring electrodes and measured the voltages from all remaining adjacent electrode pairs. Since then most of the EIT systems have been designed Sheffield prototype with only single plane of electrodes. Various electrode placement strategies within two-electrode plane were investigated by [5] using only adjacent stimulation and measurement patterns. Recently, various stimulation and measurement patterns were studied by [8] and proposed a new distinguishability criteria as a complementary to the previous studies done by [6, 7]; [8] suggested that the measurement patterns separated by one electrode less than 180 as an optimal current pattern in one electrode plane. This new result motivated us to further investigate electrode placement strategies in multiple planes with optimized current patterns to maximize the distinguishability.

In this paper, a 3D simulation was conducted to investigate 7 electrode geometries: Planar, Planar-offset, Planar-opposite, Zigzag, Zigzag-offset, Zigzag-opposite and Square proposed by [5] and applied 16 current patterns (from adjacent to opposite patterns) for each electrode geometry. We simulated each scenario for (i) a single cubic object for in-plane and off-plane, and (ii) two full-height cylindrical objects using a 3D circular Finite

Element Model (FEM). We used the formulation for the distinguishability of conductivity targets [8] and applied it for designing electrode positions and finding optimal stimulation and measurement patterns for each electrode position.

2 Methodology

2.1 Distinguishability

We briefly describe the distinguishability formulation in this section but more details can be found in[8]. EIT system depends on making a set of transfer impedance measurements from an array of electrodes placed around a body. Most EIT systems apply a set of current patterns k at electrodes to make a set of voltage measurements $\mathbf{v}^k = \mathbf{T}(\boldsymbol{\sigma}_0)\mathbf{c}^k$, where $\mathbf{T}(\boldsymbol{\sigma}_0)$ is the *transfer impedance* matrix of the medium with impedance distribution $\boldsymbol{\sigma}_0$ (in units of Ω). We can define a transfer impedance change $\mathbf{T}_\triangle = \mathbf{T}(\boldsymbol{\sigma}_0) - \mathbf{T}(\boldsymbol{\sigma}_1)$ for a small perturbation $\boldsymbol{\sigma}_1$. Difference imaging was used to produce images of conductivity changes , $\Delta\boldsymbol{\sigma} = \boldsymbol{\sigma}_1 - \boldsymbol{\sigma}_0$ between two states by taking the reference data set ($\mathbf{d_0}$) and further measurements ($\mathbf{d}$) after a certain time interval to provide time-differential measurements $\Delta\mathbf{d} = \mathbf{d} - \mathbf{d_0}$. This method can be applied to image conductivity changes that occur in the human body as a result of physiological functions *i.e* breathing.

Since we generally want to distinguish small changes in conductivity, we linearize around $\boldsymbol{\sigma}_0$ to obtain a conductivity change with a linear function of measurements as $\Delta\mathbf{d} = \mathbf{J}\Delta\boldsymbol{\sigma} + \mathbf{n}$, where $\mathbf{J}$ is Jacobian and $\mathbf{n}$ is zero-mean white Gaussian noise with covariance $\boldsymbol{\Sigma}_n$.

From measurements $\Delta\mathbf{d}$, an impedance change image estimate $\Delta\hat{\boldsymbol{\sigma}}$ is reconstructed from a linearized difference EIT reconstruction algorithm as defined from the norm

$$\Delta\hat{\boldsymbol{\sigma}} = \arg\min_{\boldsymbol{\sigma}} \|\Delta\mathbf{d} - \mathbf{J}\Delta\boldsymbol{\sigma}\|_{\boldsymbol{\Sigma}_n^{-1}} + P(\boldsymbol{\sigma}), \tag{1}$$

where $P(\cdot)$ represents a penalty or regularization term.

We are interested in the image output $m = A_R \Delta\bar{\sigma}_R$ within a ROI of area A_R with an average impedance change in ROI ($\Delta\bar{\sigma}_R$). In order to *distinguish* $\boldsymbol{\sigma}_1$ from $\boldsymbol{\sigma}_0$, we must reject the null hypothesis H_0: $m = 0$. The probability of H_0 is based on the z-score, which may be further extend as

$$z = \frac{\bar{m}}{\sigma_m} = \frac{A_R \Delta\bar{\sigma}_R}{\left(\mathbf{R}_R^t \boldsymbol{\Sigma}_n \mathbf{R}_R\right)^{\frac{1}{2}}} = A_R \Delta\bar{\sigma}_R \sqrt{\mathbf{J}_R^t \boldsymbol{\Sigma}_n^{-1} \mathbf{J}_R} = \sqrt{\Delta\mathbf{d}\boldsymbol{\Sigma}_n^{-1}\Delta\mathbf{d}} = \|\Delta\mathbf{d}\|_{\boldsymbol{\Sigma}_n^{-1}}$$

where $\mathbf{J}_R = \frac{1}{A_R}\mathbf{J}$, since we require $\Delta\mathbf{d} = \mathbf{J}_R m$ for changes in the ROI.

The proposed formulation for the distinguishability [8] in terms of a hypothesis test shows that distinguishability is a product of impedance change amplitude, measurement strategies and the inverse of noise amplitude. In this paper we aim to maximize the distinguishability by optimizing electrode placement strategies and the current injection patterns.

2.2 Simulation

EIDORS [9] was employed for simulating electrode geometries and current patterns. A tank phantom in Fig. 1 was modelled for all the simulations. The EIT model has been reconfigured to calculate the jacobian using Netgen by simulating current patterns and measuring signals from corresponding electrodes.

Electrode geometries and current patterns: A cylinder (30 cm height and 28 cm of diameter) is encircled by 2-plane 8 electrodes which are positioned with the equal distance to middle of the cylinder with the distance of 4 cm between two electrode layers as shown

in Fig. 1. All distances are normalized to the height of the cylinder and doubled it. We investigated 7 electrode placement (EP) strategies: Planar, Planar-offset, Planar-opposite, Zigzag, Zigzag-offset, Zigzag-opposite and Square proposed by [5] for an adjacent pattern and we extended them with 16 different injection and measurement patterns for each EP.

Figure 1: A diagram of *left*: Planar electrode configuration with two-layer 16 electrodes, *middle*: a single cubic object moving horizontally in two vertical planes, *right*: two cylindrical targets with the same volume spaning the full height of the cylindrical volume (2.5 D).

The objective is to select a combination of such an electrode geometry with current patterns that the full ensemble of measurements provides high z value not only in a limited region of interest but also overall areas in and out of electrode plane for impedance measurement. A diagram of electrode placement configuration for Planar electrode configuration is shown in Fig. 1:*left*. For the offset arrangement, the lower plane electrodes were rotated to be positioned at the half inter-electrode distance. For each EP and simulation protocol, a sequence of current patterns is injected and voltages are measured to form a data set, where separate electrodes are used for stimulation and measurement.

For the two-layer electrode plane, the adjacent or opposite stimulation is depend on the electrode geometry and current injection patterns unlike a single plane in [8], so it should be noted that current pattern Δ_{11} is an adjacent stimulation and measurement pattern for Planar, Planar-offset, Zigzag, Zigzag-offset, and Square geometries, while Δ_{11} is an opposite pattern for Planar-opposite and Zigzag-opposite geometries. Δ_{44} is an opposite pattern for Planar, Planar-offset, Zigzag, Zigzag-offset, and Square geometries.

Simulation models: Two different simulation models were used based on (i) a single cubic object and (ii) two cylindrical objects with full-height perturbation. The background conductivity is 1 S/m. For (i), the simulation was performed by moving a target of 50 ml with conductivity of 1.01 S/m in two different vertical planes for 14 horizontal positions in the tank (Fig. 1:*middle*) with 3 cm steps. First vertical plane for the object is set in between two electrode planes, which we call the *central-plane* and the second vertical plane is 6 cm above the *central-plane* (Fig. 1:*middle*).

For (ii), two cylindrical objects of the same volume in 2.5 D span the full height of the tank. A central object is fixed in the center and the other outer object, wrapped around the central object, is expanded with 2.5 cm steps to 4 different sizes of radius without changing total volume in Fig. 1:*right*. The central object has the conductivity of 1.01 S/m and the outer object has the conductivity of 0.99 S/m.

For the distinguishability of two objects, distinguishability values for simulation were

3

calculated directly using the distinguishability criteria formulated in section 2.1 taking into account the average distinguishability values. It is a measure of the ability of EIT to reliably distinguish structural details of targets, and specifically whether the same volume target is present as two objects or one.

3   Results and discussions

The results of distinguishability for 7 electrode geometries and 16 current patterns are shown in Fig. 2. We calculated the average values of detectability for different target positions in each case. Although we simulated all the combinations of stimulation and measurement patterns, we present representative results with equal number of stimulation and measurement patterns Δ_{sm}. The stimulation and measurement patterns for Planar-opposite and Zigzag-opposite geometries were rearranged to make their z values easy to compare with other configurations, and were renamed to Planar-interleaved and Zigzag-interleaved geometries.

Figure 2: Average distinguishability values for 7 electrode geometries and 16 current patterns. *left*: a cubic object moved horizontally in the *central plane*, *middle*: a cubic object moved horizontally in *off-plane*, *right*: two full-height cylindrical objects (2.5 D). Each distinguishability value is the average value at 7 target positions.

Fig. 2 shows that different Δ_{sm} produced significantly different z values for all electrode geometries. It was observed that Planar-interleaved and Zigzag-interleaved geometries produced the similar results and highest distinguishability values for Δ_{11} and Δ_{88}. Zigzag, Zigzag-offset and Square geometries provided similar characteristics with increasing z value from Δ_{11} to Δ_{88}. Planar and Planar-offset geometries have similar patterns with maximum z value for Δ_{44}. Thus, Planar-interleaved configuration with Δ_{88} is considered to offer the best potential performance for EIT systems with a two-ring electrode phantom system.

In the future work, we will investigate varying distances between the 2 electrode layers and evaluate selected electrode configurations with a real measurement system.

4   References

[1] Bikker IG, Leonhardt S, Bakker J, *et al. Intensive Care Med* 2009; 35: 13621367.
[2] Hinz J, Hahn G, Neumann P, *et al. Intensive Care Med* 2003; 29: 3743.
[3] Seagar A D 1983 *PhD Thesis University of Canterbury, Christchurch.*
[4] Brown B H and Seagar A D 1987 *Clin. Phys. Physiol. Meas.* 8, Suppl. A, 91-97.
[5] Graham B and Adler A, *Physiol. Meas.* 28 (2007) S29S44.
[6] Isaacson D 1986 *IEEE T Med Imaging* 5:91-95.
[7] Lionheart WR, Kaipio J, McLeod CN 2001, *Physiol. Meas.* 22 85-90.
[8] Adler A and Maimaitijiang Y, 2011, accepted for publication in *Physiol. Meas. SPE*
[9] Adler A and Lionheart WR, *Physiol. Meas.* 27:S25-S42, 2006.

The Statistics of Normalized Data in Electrical Impedance Tomography.

[1] P. Hashemzadeh, [2] A. Adler and [1]R. Bayford

[1] Department of Natural Science, Middlesex University, NW4 4BT, London, UK. [2] Department of Systems and Computer Engineering, Carleton University.

E-mail: `hashemzadeh1354@gmail.com`

Abstract. This study focuses on the noise statistics of the normalized data, in time-difference imaging. The commonly practiced normalization procedure, represents the normalized data as the ratio of two random variables. We provide closed form expressions for computing estimates of the first, second order moments, and the covariance matrix of normalized data. The expressions are derived using Taylor series expansion method for the function of random variables (propagation of uncertainty, delta method), and accurate provided that the signal to noise ratio of the reference measurement is larger than 16 dB. The analysis presented here, provides an explanation as well as insight, into the potential cause and presence of spikes in normalized data. Furthermore, we demonstrate that the statistics of normalized data, is significantly different to that of the raw measurements. We validate the closed form expressions using a Monte-Carlo method. We also conclude, that a minimum SNR of 13 dB is required for the reference measurement, in order to guarantee the existence of moments, and to ensure the accuracy of reconstructed images.

1. Introduction

Electrical impedance tomography is a low frequency imaging modality [1, 2]. It involves estimating the unknown electromagnetic properties, namely the permittivity and conductivity in a given domain from a finite number of voltage measurements made on it's boundary [3]. It is therefore a parameter estimation problem, and is the subject of much interest in inverse problems and signal processing [4, 5].

This paper focuses on the noise statistics of normalized data in time-difference imaging. The normalization procedure implemented in the freely distributed software package (EIDORS) [6], represents the normalized data as the ratio of two random variables. Moreover, at times, large unexpected spikes are observed in the normalized data. If the measurement noise is an additive Gaussian random process, then the normalized data will have a Cauchy distribution [7]. It is well known that the Cauchy distribution is an example of a distribution which has no mean, variance or higher order moments defined [7, 8]. However if the signal to noise ratio (SNR) of the reference measurement is above 13 dB, then estimates of the mean and variance may be obtained numerically [7, 9, 8].

Under the stated condition, one can then obtain an estimate of the covariance matrix of the normalized data. This matrix features explicitly in the Gauss-Newton solver, Kalman filter, and the Cramér Rao Bound analysis [10, 3, 5, 11].

The outline of the paper is follows : In section 2, we formulate the problem and describe the normalization procedure in time-difference imaging. In section 3, we provide closed form expressions for approximating the first, and second order moments of normalized data. Moreover, we outline a method for computing the non-diagonal elements of the covariance matrix. In section 4, we validate the closed form expressions using a Monte-Carlo method. Finally, the conclusion of this study is discussed in section 5.

2. Formulation of the Problem

Time-difference imaging is a linearized solution to the nonlinear estimation problem [12, 13, 10, 3]. We consider, an underlying probability space $(\Omega, \mathcal{F}, \mathbb{P})$[8]. Where, Ω denotes the sample space, $\mathcal{F}$ is a sigma field on Ω, and $\mathbb{P} : \mathcal{F} \to [0, 1]$ is the probability measure. The voltage measurements represent a discrete time stochastic process. This can be expressed succintly by $\mathbf{v} : \Omega \times \mathbb{N}^+ \to \mathbb{R}^M$ ($\forall k \in \mathbb{N}^+, \mathbf{v}[k] : \Omega \to \mathbb{R}^M$). Where, M denotes the dimension of the measurement vector. In practice, only a finite number of samples can be recorded. We denote the total number of discrete observations by N_s. The normalization procedure involves selecting a reference time index, denoted by $k_0 \leq N_s$. The voltages measured at time index k_0 are used to form difference voltages. The *normalized* difference voltages are computed using the expression below

$$\delta v_i[k] = \frac{v_i[k]}{v_i[k_0]} - 1; \qquad 1 \leq i \leq M \tag{1}$$

It is clear from equation (1), that the normalization procedure results in the ratio of two random variables. As a result, $\delta\mathbf{v}[k]$ may not have first and second order moments (i.e $\mathbb{E}(\delta v_i) = \pm\infty$, and $\mathrm{VAR}(\delta v_i) = \infty$). It is by this, that we mean that the first and second order moments do not exist. If they exist, then the objective is to compute the covariance matrix of the normalized voltages denoted here, by $C_{\delta\mathbf{v}}$.

3. Covariance Matrix

The covariance matrix of normalized data features explicitly in the expressions for image reconstruction and lower bound analysis [14, 15, 10, 3, 5, 11]. One must therefore, ensure that is it is computed accurately. The elements of this matrix at time index k, can be computed below by

$$[C_{\delta\mathbf{v}}[k]]_{i,j} = \mathbb{E}\left[\left(\frac{v_i[k]}{v_i[k_0]}\frac{v_j[k]}{v_j[k_0]}\right)\right] - \mathbb{E}\left[\frac{v_i[k]}{v_i[k_0]}\right]\mathbb{E}\left[\frac{v_j[k]}{v_j[k_0]}\right]; \tag{2}$$

The closed form expressions presented here, are based on a Taylor series expansion method (propagation of uncertainty, delta method) [9], and accurate provided that the SNR of the reference measurements is $\frac{S_R}{N_R} > 16$ dB. We introduce the following notation

for convenient $Z = v_i[k]$, $W = v_i[k_0]$. The mean (first order moment) reads as

$$\mathbb{E}(\delta v_i) = \mathbb{E}\left[\frac{Z}{W}\right] - 1 \simeq \frac{\mu_z}{\mu_w} - \frac{\sigma_z \sigma_w \rho_{z,w}}{\mu_w^2} + \frac{\mu_z}{\mu_w^3}\sigma_w^2 - 1 \tag{3}$$

The variance (second order moment) of the difference voltage is given by

$$\mathrm{VAR}(\delta v_i) = \mathrm{VAR}\left(\frac{Z}{W} - 1\right) \simeq \frac{\sigma_z^2}{\mu_w^2} - 2\left(\frac{\mu_z \sigma_z \sigma_w \rho_{z,w}}{\mu_w^3}\right) + \frac{\mu_z^2 \sigma_w^2}{\mu_w^4} \tag{4}$$

Where μ_z, and σ_z, respectively denote the mean and variance of Z, and μ_w, σ_w respectively denote the mean and variance of W. Here, $\rho_{z,w}$ is the correlation coefficient of the pair (Z, W). It is clear from the expressions (3), and (4), that if $\mu_w \to 0$, then $\mathbb{E}(\delta v_i) \to \pm\infty$, and $\mathrm{VAR}(\delta v_i) \to \infty$. This is the potential explanation behind the presence of spikes in normalized data. The spikes will occur, if $\mu_w \simeq 0$, or $\mu_w < 4\sigma_w$. However, If $\mu_w > 6\sigma_w$ ($\frac{S_R}{N_R} > 16$ dB), then $\mathrm{VAR}(\delta v_i) < \infty$, and we have obtained an an accurate estimate for diagonals of the covariance matrix $\mathrm{C}_{\delta v}$. It should be noted that expressions (3), and (4) do not require the assumption that the measurement noise is additive Gaussian.

We now focus on computing, the non-diagonal elements of the covariance matrix $\mathrm{C}_{\delta v}$. In order to simplify the analytical expressions, for the non-diagonal elements, we make the assumption, that the raw measurements are corrupted by a Gaussian random process. It can be seen from expression (2), that $(v_i[k]v_j[k], v_i[k_0]v_j[k_0])$ form a product pair. We must, first compute the mean, variance and the correlation coefficient of this product pair. Once, these values are obtained, we can simply use expression (3) to compute the expected value of this ratio. The remaining terms $\mathbb{E}\left[\frac{v_i[k]}{v_i[k_0]}\right]\mathbb{E}\left[\frac{v_j[k]}{v_j[k_0]}\right]$, can be computed directly using expression (3).

We introduce the following set of notations for convenience: $X_1 = v_i[k]$, $X_2 = v_j[k]$, $X_3 = v_i[k_0]$, $X_4 = v_j[k_0]$, $\sigma_{i,j} = \mathrm{Cov}(X_i, X_j)$, $\sigma_i^2 = \mathrm{Var}(X_i)$, $Z = X_1 X_2$, and $W = X_3 X_4$. It is trivial to show that $\mu_z = \mathbb{E}Z = \sigma_{1,2} + \mu_1\mu_2$, and $\mu_w = \mathbb{E}W = \sigma_{3,4} + \mu_3\mu_4$. The expression for $\mathrm{Var}(Z)$, is given below by

$$\sigma_z^2 = (\mu_1\sigma_2)^2 + 2\mu_1\mu_2\sigma_{1,2} + (\mu_2\sigma_1)^2 + (\sigma_1\sigma_2)^2 + \sigma_{1,2}^2 \tag{5}$$

By inspection, $\mathrm{Var}(W)$ reads as

$$\sigma_w^2 = (\mu_3\sigma_4)^2 + 2\mu_3\mu_4\sigma_{3,4} + (\mu_4\sigma_3)^2 + (\sigma_3\sigma_4)^2 + \sigma_{3,4}^2 \tag{6}$$

The expression for $\mathrm{Cov}(Z, W)$, is given below by

$$\sigma_{z,w} = \mu_1\mu_3\sigma_{2,4} + \mu_1\mu_4\sigma_{2,3} + \mu_2\mu_3\sigma_{1,4} + \mu_2\mu_4\sigma_{1,3} + \sigma_{1,3}\sigma_{2,4} + \sigma_{1,4}\sigma_{2,3} \tag{7}$$

We obtain the correlation coefficient, using the simple relation $\rho_{z,w} = \frac{\sigma_{z,w}}{\sigma_z \sigma_w}$. At this stage, we have all the terms required, to compute $\mathbb{E}\left[\left(\frac{v_i[k]}{v_i[k_0]}\frac{v_j[k]}{v_j[k_0]}\right)\right]$ using expression (3).

4. Results and Discussions

Here, we compare the analytical expressions presented in section 3, against a Monte-Carlo simulation. It is worth noting that $(\mathrm{VAR}(\frac{Z}{W}) < \infty) \Rightarrow (\mathbb{E}[\frac{Z}{W}] < \infty)$. The
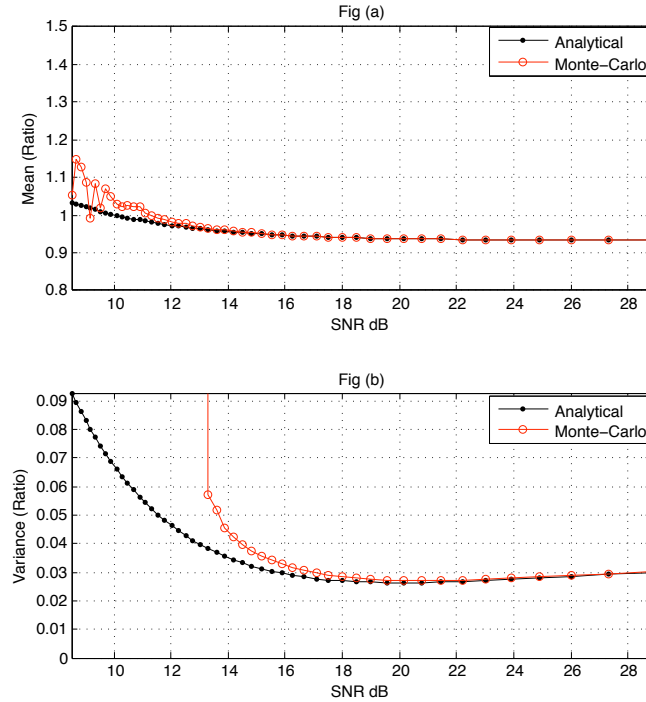
Figure 1. This figure shows the first and second order moments of the ratio Z/W as a function of $20 \log \frac{\mu_w}{\sigma_w}$ on the x-axis. Black solid dotted line corresponds to the Taylor expansion method, and red solid line with circle is the Monte-Carlo method. The parameter are $\mu_z = 0.75, \mu_w = 0.8, \rho_{z,w} = 0.5, \sigma_z = 0.15$, and $\sigma_w \in [0.029, 0.24]$. Fig (a) is the plot of $\mathbb{E}[\frac{Z}{W}]$ (first order moment), Fig (b) is the plot of $\text{VAR}(\frac{Z}{W})$ (second order moment).

results are show in Fig. 1. The numerical results, are as expected, and agree well with the theory. In Fig 1 (b), the Monte-Carlo simulations show, that when $|\mu_w| < 4\sigma_w$ $(20 \log(\frac{\mu_w}{\sigma_w}) < 13$ dB$)$, then $\text{VAR}(\frac{Z}{W}) \to \infty$. This is a fundamental result in statistics, and under such condition, it becomes difficult to compute an accurate mean and variance. It is also clear that when, $|\mu_w| < 4\sigma_w$ $(20 \log 10(\frac{|\mu_w|}{\sigma_w}) < 13$ dB$)$, the mean and variance computed using the Taylor method is no longer accurate. However, when $|\mu_w| > 4\sigma_w$ $(20 \log 10(\frac{|\mu_w|}{\sigma_w}) > 13$ dB$)$, then the analytical approach begins to agree well with the Monte-Carlo simulation, and this is particularly true for $|\mu_w| > 6\sigma_w$ $(20 \log 10(\frac{|\mu_w|}{\sigma_w}) > 16$ dB$)$.

5. Conclusions

In this study, we have presented closed form expressions for computing the first and second order statistics of the normalized data, in time-difference imaging. These expressions are accurate provided that the signal to noise ratio of the reference measurement is above 16 dB. Moreover, they provide an explanation and insight, into the potential cause and presence of spikes in normalized data. We validate the closed form expressions using a Monte-Carlo procedure. It is also concluded that in order to

guarantee accuracy in time-difference imaging, one must ensure that the minimum SNR of the reference measurement is above 13 dB.

[1] R. Bayford. Bioimpedance (electrical impedance tomography). *Annu. Rev. Biomed. Eng.*, 8:63–91, 2006.

[2] D. Holder. *Techniques In Electrical Impedance Tomography.* Taylor Francis Ltd, 1 edition, December 2004.

[3] Jari Kaipio Erkki Somersalo. *Statistical and Computational Inverse Problems.* Springer; 1 edition, 2004.

[4] A. Tarantola. *Inverse Problem Theory and Methods for Model Parameter Estimation.* SIAM, 2005.

[5] Steven M. Kay. *Fundamentals of Statistical Signal Processing - Estimation Theory.* Prentice Hall PTR, 1993.

[6] N. Polydorides and William R B Lionheart. A matlab toolkit for the three-dimensional electrical impedance tomography: a contribution to the electrical impedance and diffuse optical reconstruction software project. *Meas. Sci. Technol*, 13:1871–1883, 2002.

[7] George Marsaglia. Ratios of normal variables. *Journal of Statistical Software*, 16(4):1–10, May 2006.

[8] G. Grimmett and D. Stirzaker. *Probability and Random Processes.* OXFORD University Press, 2001.

[9] Gary W. Oehlert. A note on the delta method. *The American Statistician*, 46(1):27–29, Feb 1992.

[10] A. Adler T. Dai and W. R. B. Lionheart. Temporal image reconstruction in electrical impedance tomography. *Physiol. Meas.*, 28:S1–S11, 2007.

[11] P Hashemzadeh P Kantaritzis P Liatsis S Nordebo and R Bayford. A Cramér Rao Bound approach for evaluating the quality of experimental setups in electrical impedance tomography. In *The Eigth IASTED International Conference On Biomedical Engineering.*, Innsbruck, Austria, Feb 2011. ACTA Press.

[12] E. Somersalo M. Cheney and D. Isaacson. Existence and uniqueness for electrode models for electric current computed tomography. *SIAM J. Appl. Math*, 52:1023–1040, 1992.

[13] M. Cheney D. Isaacson JC. Newell S. Simske and J. Globe. Noser: Algorithm for solving the inverse conductivity problem. *Int J. of Imaging. Sys.*, 2:66–75, 1990.

[14] A. Adler T. Dai, M. Soleimani. Four-dimensional regularization for electrical impedance tomography imaging. In *13- International Conference On Electrical BioImpedance and the 8th Conference on Electrial Impedance Tomography*, volume 17, pages 408–411. Springer, 2007.

[15] M. Soleimani C. G-Laberge A. Adler. Imaging of conductivity changes and electrode movement in EIT. *Physiol. Meas.*, 27(5), 2006.

A residual minimizing solver for the inverse problem of EIT

Bart Truyen, Luca Dimiccoli, Jan Cornelis

Dept. Electronics & Informatics (ETRO) and CAMP Research Group, Vrije Universiteit Brussel, Brussels, Belgium, and Interdisciplinary Institute for Broadband Technology (IBBT), Ghent, Belgium.

Abstract

Despite their theoretical limitations and numerically often disappointing performance, Output-Least-Squares (OLS) algorithms retain a dominant role in solving the inverse problem of Electrical Impedance Tomography. We present a new approach based on a double-constrained variational formulation of the problem. The method relies on a nonlinear integral transform, which relates the conductivity in the interior of a closed domain to the dissipated power as computed from the Cauchy data on the boundary. The kernel of this transform involves the unknown electric potential field at the target conductivity function, which on the boundary is constrained by the Dirichlet conditions. A first-order Taylor series approximation, centred at a known prior, leads to a bilinear residual expression, which is then used to define a Tikhonov regularized misfit measure on the discrete L_p norm, where $p = 1, 2, \infty$. Unlike for the error measure in OLS, the misfit function is defined over the entire domain, and not restricted to the boundary. What emerges is an iterative algorithm requiring the solution of a sequence of sparse matrix problems, the structure of which is retained during the entire calculation. For $p = 2$ the iteration essentially reduces to a Gauss-Newton method. To the expense of computing the misfit measure also over the interior of the domain, the algorithm lends itself particularly well for accelerated implementations, exploiting the sparse structure demonstrated by the constitutive matrix problems.

The forward model

Consider the set of all the admissible isotropic conductivity functions σ defined on a closed, simply connected domain $\Omega \in \mathbb{R}^d$, $d = 2, 3$ such that

$$\mathcal{Q} = \{\sigma(\mathbf{r}) \mid 0 < \sigma(\mathbf{r}) < \infty\},$$

and $\mathbf{r} \in \Omega$ specifying the position. The forward model in electric impedance tomography (EIT) is derived from Maxwell's time-harmonic equations at the quasi-static limit and describes the potential field in the closure of Ω, with known electrical properties and imposed boundary conditions. This problem has been extensively analyzed and reviewed in many publications. Assuming no charges or current sources in the interior of Ω, when a current is impressed at the boundary, the scalar electric potential u satisfies the elliptic partial differential equation

$$\nabla \cdot \big(\sigma(\mathbf{r})\nabla u(\mathbf{r})\big) = 0, \qquad \mathbf{r} \in \Omega. \tag{1}$$

The applied current pattern $\{I_l\}_{l=1}^L$, inducing u, is expressed by the Neumann boundary conditions

$$\int_{e_l} \sigma(\mathbf{r})\nabla u(\mathbf{r}) \cdot \mathbf{n}\, ds = I_l, \quad \mathbf{r} \in \Gamma_E,\ l = 1, \ldots, L$$

$$\sigma(\mathbf{r})\nabla u(\mathbf{r}) \cdot \mathbf{n} = 0, \quad \mathbf{r} \in \partial\Omega \setminus \Gamma_E, \tag{2}$$

where $\mathbf{n}$ is the outer normal to $\partial\Omega$, and $\Gamma_E = \cup_{l=1}^{L} e_l$, with e_l the surface of the l'th electrode. The voltage measurement recorded at the l'th electrode is given by

$$U_l = u(\mathbf{r}), \quad \mathbf{r} \in e_l, \; l = 1, \ldots, L. \tag{3}$$

Upon enforcing the charge conservation principle on the applied currents and making a choice of ground

$$\sum_{l=1}^{L} I_l = 0, \quad \exists\, \mathbf{r}_g \in \partial\Omega \text{ s.t. } u(\mathbf{r}_g) = 0,$$

the model admits a unique solution $(u, U) \in H^1(\Omega) \oplus \mathbb{R}^L$. For a fixed model conductivity σ, the impressed current pattern I and the induced electrode potentials U are linearly related by the Neumann-to-Dirichlet map $\Lambda_\sigma : I \to U$.

The inverse problem

The inverse problem of EIT consists in estimating σ given the simultaneous knowledge of the measured boundary potentials $U = U^{(i)}$, and the injected current patterns $I = I^{(i)}$, for a series of experiments $i = 1, \ldots, d$.
For this purpose we consider the variational form of the governing equations (1)

$$\int_{\Omega} \sigma \nabla u \cdot \nabla u \; dw = \int_{\partial\Omega} u\, \sigma \nabla u \cdot \mathbf{n} \; ds. \tag{4}$$

Then from (2) and with $\partial\Omega$ restricted to Γ_E the surface integral simplifies to yield

$$\int_{\partial\Omega} u\, \sigma \nabla u \cdot \mathbf{n} \; ds = \sum_{l=1}^{L} U_l \int_{e_l} \sigma \nabla u \cdot \mathbf{n} \; ds = \sum_{l=1}^{L} U_l I_l = P,$$

with P the dissipated power within Ω.
Suppose $G : \mathcal{Q} \to \mathbb{R}$ is a convex function, the inverse problem can be expressed as a nonlinear constrained minimisation norm problem

$$\sigma^* = \operatorname*{argmin}_{\sigma} \zeta(\sigma) \tag{5}$$

where

$$\zeta(\sigma) = \left\{ \begin{array}{l} \displaystyle\sum_{i=1}^{d} \min_{u} \left\{ \left| \int_{\partial\Omega} \sigma \nabla u\big(I^{(i)}\big) \cdot \nabla u\big(I^{(i)}\big) \; ds - P^{(i)} \right| + \alpha G(\sigma) \right\} \\[2mm] \text{subject to } u(\mathbf{r}, I^{(i)}) = U^{(i)}, \quad \mathbf{r} \in e_l, \; l = 1, \ldots, L \end{array} \right.$$

with α a positive regularization parameter.

The numerical problem

In order to cast the continuous EIT problem into a finite dimensional setting, a numerical approximation method like finite elements can be applied, where the governing equations are discretized on a finite dimensional model of the domain, say $\Omega_h(m, n)$ comprising n nodes

connected in m elements. In particular we will assume here a 'point electrode' model where the uniform potential on each of the L electrodes is modelled by a single node in the model. For reasons of mathematical convenience, linear Lagrangian finite elements are assumed, with element-wise linear and constant basis functions for the support of electric potential u and conductivity σ, respectively

$$u(\mathbf{r}) = \sum_{i=1}^{n-L} v_i \phi_i(\mathbf{r}) + \sum_{i=n-L+1}^{n} U_{i-n+L} \phi_i(\mathbf{r}), \qquad \sigma(\mathbf{r}) = \sum_{i=1}^{m} \sigma_i \psi_i(\mathbf{r})$$

where $\{\phi_i\}_{i=1}^{n}$ and $\{\psi_i\}_{i=1}^{m}$ are the respective basis in Ω_h, and $v \in \mathbb{R}^{n-L}$ is the vector of nodal potentials away from the electrodes.

On the discrete domain the weak form of the Neumann problem (1)-(2) is approximated by means of the Galerkin formulation. To this end, $\{\phi_1, \ldots, \phi_n\}$ are chosen as test basis for the potentials. Substituting these into the variational form of the forward model (1)-(2), and imposing the Dirichlet boundary conditions (3), while assuming the 'point electrode' model, one arrives at

$$\sum_{j=1}^{n-L} v_j \int_{\Omega} \sigma \nabla \phi_i \cdot \nabla \phi_j dw + \sum_{j=n-L+1}^{n} U_{j-n+L} \int_{\Omega} \sigma \nabla \phi_i \cdot \nabla \phi_j dw = \sum_{l=1}^{L} \int_{e_l} \phi_i I_l ds.$$

In matrix form the vector of nodal potentials $v \in \mathbb{R}^{n-L}$ satisfies the $n \times n$ system of equations

$$\begin{pmatrix} \mathbf{A}_{11} & \mathbf{A}_{12} \\ \mathbf{A}_{12}^T & \mathbf{A}_{22} \end{pmatrix} \begin{pmatrix} v \\ U \end{pmatrix} = \begin{pmatrix} 0 \\ I \end{pmatrix} \qquad (6)$$

for $I = I^{(i)}, U = U^{(i)}, v = v^{(i)}$, and $\mathbf{A}_{11}, \mathbf{A}_{12}, \mathbf{A}_{22}$ being block partitions of $\mathbf{A}(\sigma)$, with

$$\mathbf{A}(\sigma)_{ij} = \sum_{s=1}^{m} \sigma_s \int_{\Omega_s} \nabla \phi_i \cdot \nabla \phi_j \, dw, \quad 1 \le i, j \le n. \qquad (7)$$

This is an important result, as it summarizes the crux of the proposed approach for solving the inverse problem of EIT. In order to see this, remark that only for σ, with $U = \Lambda_\sigma I$ there exists a vector v of nodal potentials such that the overdetermined system of equations (6) is satisfied exactly for given U and I. For any other admissible conductivity, no such solution can be found. This result follows immediately from the positive definiteness of Λ_σ.

From (6), let the i'th residual equation be

$$r^{(i)}(\sigma, v^{(i)}) = \begin{pmatrix} 0 \\ I^{(i)} \end{pmatrix} - \mathbf{A}(\sigma) \begin{pmatrix} v^{(i)} \\ U^{(i)} \end{pmatrix}, \qquad i = 1, \ldots, d$$

so that the residual evaluated over each of the applied current patterns $I^{(i)}$ is defined in vector concatenated form

$$r(\sigma, v) = \text{vec}([r^{(1)}(\sigma, v^{(1)}) | r^{(2)}(\sigma, v^{(2)})| \ldots |r^{(d)}(\sigma, v^{(d)})]) \qquad (8)$$

and the regularized misfit measure in (5) becomes

$$\zeta(\sigma) = \min_{v} \left\| \begin{pmatrix} r(\sigma, v) \\ \alpha \mathbf{D}_q \sigma \end{pmatrix} \right\|_p$$

where $\mathbf{D}_q \in \mathbb{R}^{m-q,m}$ is a discrete approximation to the q'th derivative operator, and $||\cdot||_p$ is the vector p-norm, for $p = 1, 2, \infty$.

Clearly $r(\sigma, v)$ is a nonlinear function of σ due to the presence in (8) of the electric potential field v, which itself depends on the unknown conductivity function σ. At a feasible point σ_0, the residual $r(\sigma, v)$ admits a Taylor series approximation. Assuming that $\Delta\sigma = \sigma - \sigma_0$ and $\Delta v = v - v_0$ are sufficiently small such that higher order terms can be neglected, a bilinear approximation is obtained

$$r(\sigma, v) \simeq r(\sigma_0, v_0) + \partial_\sigma r(\sigma_0, v_0)(\sigma - \sigma_0) + \partial_v r(\sigma_0, v_0)(v - v_0).$$

The Jacobian of $r(\sigma_0, v_0)$ can be expressed straightforwardly in terms of the partial derivatives $\partial_\sigma r^{(i)}(\sigma_0, v_0^{(i)})$ and $\partial_{v^{(i)}} r^{(i)}(\sigma_0, v_0^{(i)})$ computed for each of the excitations $I^{(i)}$.

Taking into account the affine structure manifested by $\mathbf{A}(\sigma)$, which can be made more explicit by rephrasing (7) as

$$\mathbf{A}(\sigma) = \sum_{i=1}^{m} \sigma_i \mathbf{S}^{(i)},$$

where $\mathbf{S}^{(i)} \in \mathbb{R}^{n,n}$ is defined as

$$\mathbf{S}_{ij}^{(k)} = \int_{\Omega_k} \nabla\phi_i \cdot \nabla\phi_j \, dw.$$

The partial derivatives $\partial_\sigma r^{(i)}(\sigma_0, v_0^{(i)}) \in \mathbb{R}^{n,m}$ are then formed by concatenating the vectors

$$\partial_{\sigma_j} r^{(i)}(\sigma, v) = \mathbf{S}^{(j)} v^{(i)}$$

evaluated over all the elements of the model, for $v^{(i)} = v_0^{(i)}$

$$\partial_\sigma r^{(i)}(\sigma_0, v_0^{(i)}) \equiv \mathbf{X}_\sigma^{(i)} = [\mathbf{S}^{(1)} v_0^{(i)} | \mathbf{S}^{(2)} v_0^{(i)} | \dots | \mathbf{S}^{(m)} v_0^{(i)}].$$

Evaluating $\mathbf{X}_\sigma^{(i)}$ for each of the current patterns $I^{(i)}$, then yields $\partial_\sigma r(\sigma_0, v_0) \in \mathbb{R}^{dn,m}$ in block concatenated form

$$\partial_\sigma r(\sigma_0, v_0) \equiv \mathbf{X}_\sigma = [\mathbf{X}_\sigma^{(1)T} | \mathbf{X}_\sigma^{(2)T} | \dots | \mathbf{X}_\sigma^{(d)T}]^T.$$

The partial derivative $\partial_{v^{(i)}} r^{(i)}(\sigma_0, v_0^{(i)}) \in \mathbb{R}^{n,n-L}$ instead are identical for all $I^{(i)}$, and are obtained from the block partitioned form of $\mathbf{A}(\sigma_0)$

$$\partial_{v^{(i)}} r^{(i)}(\sigma_0, v_0^{(i)}) \equiv \mathbf{A}_1(\sigma) = \begin{pmatrix} \mathbf{A}_{11}(\sigma_0) \\ \mathbf{A}_{12}^T(\sigma_0) \end{pmatrix}.$$

A solution $\sigma^* = \operatorname{argmin}_\sigma \zeta(\sigma)$ can then be computed iteratively

$$\sigma_{k+1} = \sigma_k + \Delta\sigma$$

with the update $\Delta\sigma$ computed as the solution of

$$\min_{\Delta\sigma, \Delta v} \left\| \mathbf{M} \begin{pmatrix} \Delta v \\ \Delta\sigma \end{pmatrix} + \begin{pmatrix} -r \\ \alpha\mathbf{D}_q\sigma \end{pmatrix} \right\|_p, \qquad \mathbf{M} = \begin{pmatrix} \mathbf{I}_d \otimes \mathbf{A}_1 & \mathbf{X} \\ \mathbf{O} & \alpha\mathbf{D}_q \end{pmatrix} \tag{9}$$

where $\otimes$ denotes the Kronecker product.

After each iterate, the matrices $\mathbf{A}_1(\sigma)$ and $\mathbf{X}(\sigma)$ are updated from $\Delta\sigma$ and Δv. The vector concatenated form of v implies that also the updates $\Delta v^{(i)}$ will be found in vectorized form $\Delta v = \operatorname{vec}([\Delta v^{(1)} | \Delta v^{(2)} | \dots | \Delta v^{(d)}])$. For $p = 2$, the least-squares update step in (9) is essentially defining a Gauss-Newton method, which can be solved efficiently by means of a sparse QR factorization of the matrix $\mathbf{M}$, since the matrices $\mathbf{A}_1$ and $\mathbf{X}$ have full-column rank.

Co-registration and fusion of EIT images with MRI scan data

J.L. Davidson[1,2], R.A. Little[2,3], P. Wright[1,2], J. Naish[2,3], R. Kikinis[4], G.J.M. Parker[2,3] and H. McCann[1,2]

[1]School of Electrical and Electronic Engineering, University of Manchester, UK
[2]Biomedical Imaging Institute, University of Manchester, UK
[3]Imaging Sciences, Manchester Academic Health Sciences Centre, University of Manchester, UK
[4]Surgical Planning Laboratory, Brigham and Women's Hospital, Harvard Medical School, Boston, MA, USA

Abstract **In this paper we describe our adopted methodology of combining EIT with MRI data and present fused image results for an example laboratory phantom based on the polysaccharide gel TX151. Bespoke software was used to convert an EIT dataset into a form consistent with *3D-Slicer*, a powerful software package used for visualization and image analysis. The data fusion provides a highly effective method of directly comparing EIT with MRI data.**

Introduction

Clinicians are frequently faced with patient care challenges that require knowledge of both detailed anatomical information and the performance of an organ's key functionality. Examples include critical treatment of brain trauma, cardiac disease, tumours in many locations (e.g. brain, liver, kidney, lungs) and pulmonary conditions. In each of these cases, it may be necessary or desirable to assess organ functions in both the spatial and temporal domains. Imaging modalities capable of rapid scanning (e.g. EIT) typically lack good spatial resolution (e.g. compared with MRI), which is often crucial in understanding organ functionality and/or the progression of a disease. The inescapable conclusion is that the optimum combination of anatomical and functional imaging requires characterisation with more than one imaging modality. Initially, our target application is functional EIT of the lung but the data fusion process could be exploited in other areas such as multi-modal neurophysiology. Our overall aim is to develop a robust methodology of fusing two separate data streams together to give temporally and anatomically resolved functional imaging of the lung. This will enable an accurate and quantitative comparison of the structural and functional information provided by EIT with the complementary structural and functional information provided by MRI. Presently, we are progressing the fusion of EIT and MRI data from inanimate gel-based phantoms using *Confeitir* (CONverter of Functional Electrical Impedance Tomography Images for Registration) software [1] and *3D-Slicer* software [2].

A Tissue Realistic Phantom and Data Acquisition

A phantom of diameter 170 mm and height 85 mm was constructed using TX151 polysaccharide gel (Oil Center Research, La Fayette, LA). This is a tissue realistic material which has previously been used in the context of both EIT and MRI [3]. To every 1 litre of deionised water, 120 g TX151 was added and the result was thoroughly mixed in a blender before being poured into a cylindrical Perspex mould and allowed to set. Apertures at 25 mm and 65 mm heights on the cylinder wall were located in the mould so that Ag/AgCl EEG electrodes could be affixed to the phantom for EIT measurements. The electrodes were arranged in two rings of sixteen with an additional reference electrode placed top-centre of the phantom. EIT data were captured using the EIT sub-system of fEITER (*functional Electrical Impedance Tomography of Evoked Responses*)[4]; a biomedical EIT instrument developed for use in the operating room which complies with medical standard BS EN 60601-1:2006. The instrument operated at 100 fps and used an opposite strategy involving eight current projections per electrode ring. Measurements were acquired for (i) a homogeneous reference

condition and (ii) following the creation of an air-hole inhomogeneity within the phantom. The arrangement is shown in figure 1(a-b).

Following the EIT acquisitions, the electrodes were removed and a 3D T_1-weighted FFE/SPGR (fast field echo / spoiled gradient echo) acquisition was conducted on a 1.5 T Philips Intera scanner (Philips Healthcare, Best, Netherlands) [5]. This provided a ground truth representation of the phantom structure. The reconstructed MRI image matrix had $144 \times 144 \times 57$ cubic elements of dimensions 1.74 mm $\times$ 1.74 mm $\times$ 2.06 mm. Additionally, the phantom was modelled using *NetGen* [6] to give a tetrahedral mesh of 12966 elements for EIT image reconstruction. EIT reconstruction used a difference imaging technique based on 420 adjacent horizontal voltage measurements. The reconstruction used *EIDORS 3D* [7] and a linear conjugate gradients method described in detail by Polydorides [8]. Figure 1(c-d) shows the resulting EIT image reconstruction rendered using *MayaVi* software.
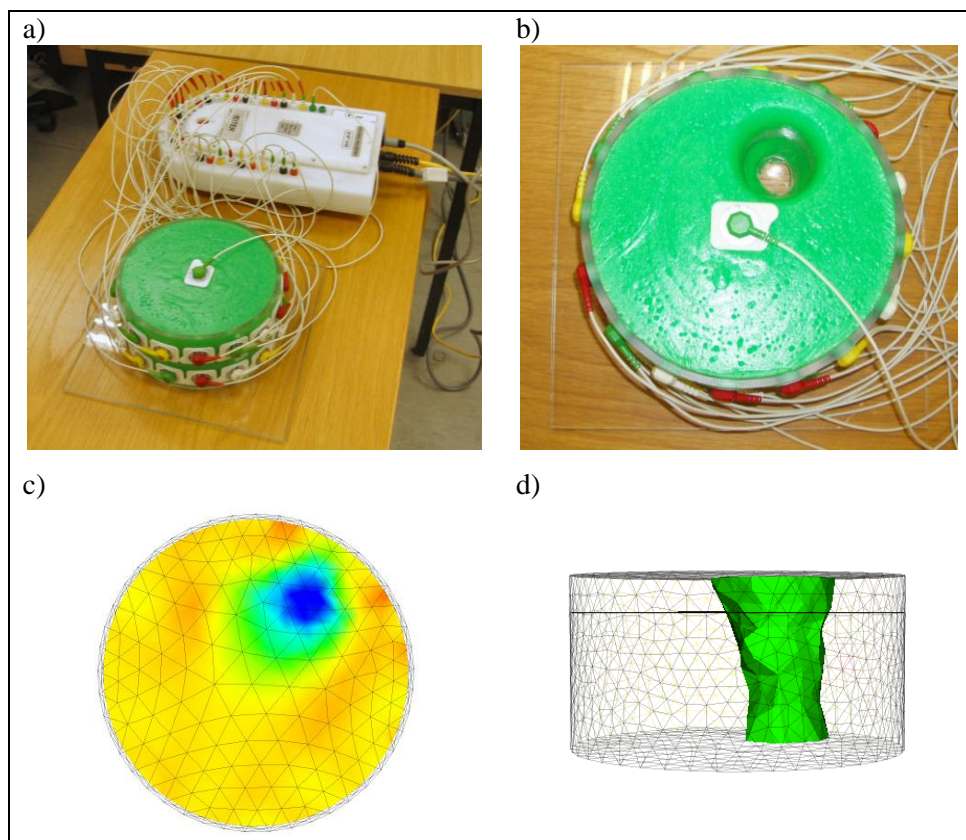
Figure 1. TX151 gel phantom and associated EIT image reconstruction used as example data for co-registration and fusion with MRI scan data; (a) general view of phantom connected to headbox of fEITER system prior to creation of inhomogeneity, (b) plan view of phantom with air-hole inhomogeneity, (c) and (d) two views of the EIT reconstruction rendered in *MayaVi* software.

Conversion of EIT Solution to Voxel Space

The Manchester *Confeitir* [1] software package was used to convert the reconstructed EIT data from the irregular tetrahedral mesh into a regular matrix with 2 mm isotropic voxels. The *Confeitir* algorithm iterates over a large number of (arbitrarily defined and irregular) simplexes and identifies voxels which have their centres within its boundary. This is more computationally challenging than finding the nearest-neighbour centroid for each voxel, but produces a more realistic result as the simpler method may populate voxels with the solutions of neighbouring tetrahedra (e.g. where a short and fat simplex is located next to a long and thin simplex).
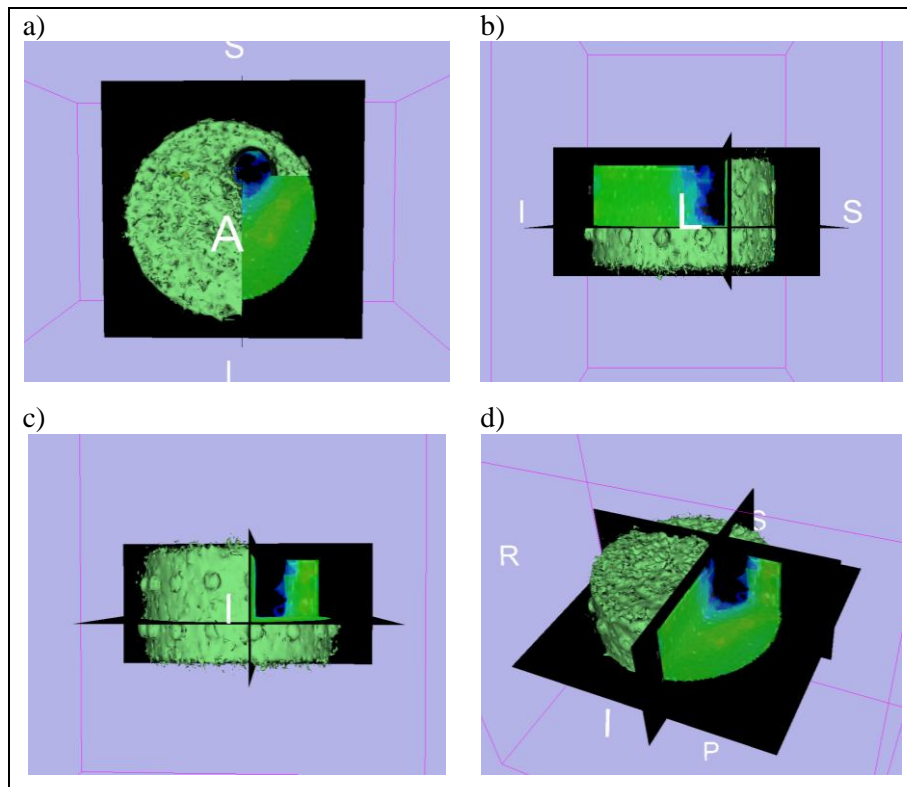
Figure 2. *3D-Slicer* images of the fused EIT and MRI data acquisitions of the TX151 phantom with heavy EIT weighting; (a) anterior view, (b) left view, (c) inferior view and (d) a doubly-oblique view.
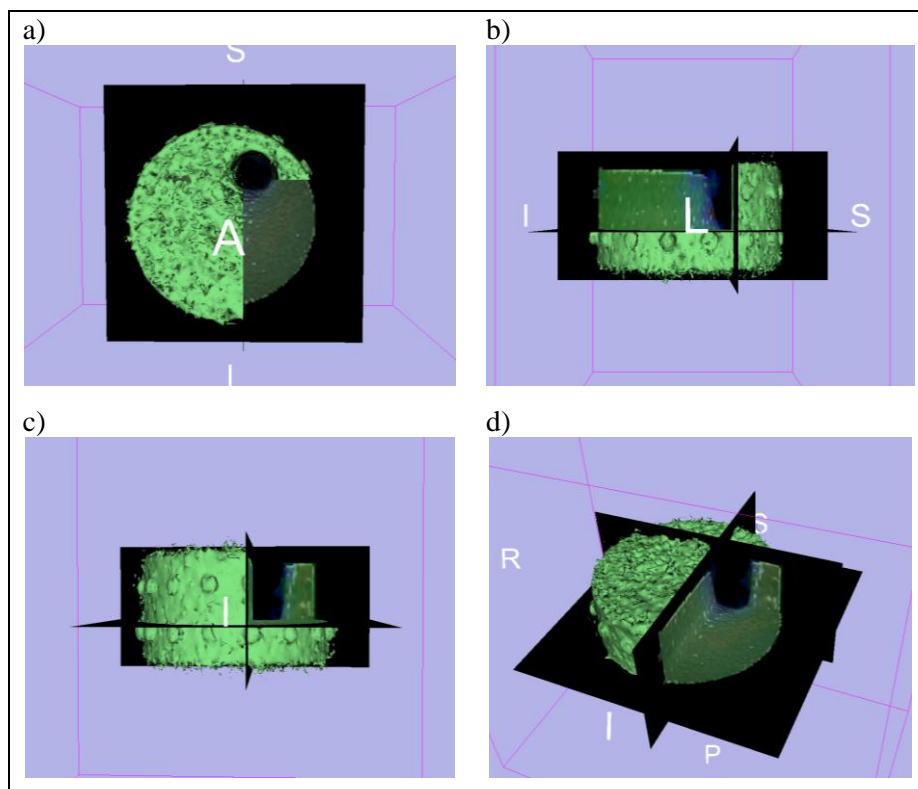
Figure 3. *3D-Slicer* images of the fused EIT and MRI data acquisitions of the TX151 phantom with MRI weighting; (a) anterior view, (b) left view, (c) inferior view and (d) a doubly-oblique view.

3D Data Fusion and Visualization

The fusion of images requires a sophisticated and robust software platform. In this study, the open source software package *3D-Slicer* was used to manipulate and visualize the resulting data. The software provides a flexible platform from which to analyse and view medical image datasets and is ideally suited to tailoring for specific research questions. For the presented TX151 phantom example, only the built-in functions of *3D-Slicer* were required.

The MRI-derived dataset was in the form of DICOM files, whilst the EIT-derived conductivity change measurements, after conversion to a regular matrix, were represented as Mayo Clinic Analyze 7.5 format files. These were imported into *3D-Slicer* and manual translation and rotation were applied until they were aligned. The MRI data were viewed in greyscale whilst the EIT data had a custom blue to red colour map applied. The built-in semi-automatic grow-cut algorithm was used to create a model of the phantom from the MR imaging volume to aid visualization of the 3D structure of the phantom.

The background and foreground fader function of *3D-Slicer* provides a convenient method to allow rapid and interactive movement between the MRI and EIT modalities of the fused dataset. Figures 2 and 3 show some of the resulting fused images of the two datasets with different viewing weightings using the fader function. Figure 2 is weighted towards the EIT data but shows some of the MRI greyscale, whilst figure 3 is weighted towards the MRI dataset but allows some of the EIT colour to be seen. For each figure, views from (a) the anterior, (b) the left, (c) the inferior, and (d) a doubly-oblique angle are shown. The EIT electrode positions can be clearly seen as circular surface features within the MRI data due to the TX151 gel setting within the apertures of the Perspex mould. More importantly, by comparing both figures, the size and positioning of the air void shows excellent correspondence between the two modalities, even showing a slight top-to-bottom tapering which was physically present in the original phantom.

Summary and Future Work

The concept of EIT and MRI data fusion using *Confeitir* and *3D-Slicer* has been successfully demonstrated. Further analysis and phantom tests will enable quantitative measurement of EIT spatial fidelity. The fusion of EIT and MRI data is an essential step in the development of combined dynamic lung function imaging with human EIT and MRI data.

Acknowledgements

References
[1]   McCormick D, Davidson J L and McCann H (2007) Conversion of EIT brain images for co-registration in Proc. *13th International Conference on Electrical Bioimpedance and the 8th Conference on Electrical Impedance Tomography* (Graz, Austria) pp 384-387

[2]   Pieper S, Halle M and Kikinis R (2004) 3D SLICER in Proc. *1st IEEE International Symposium on Biomedical Imaging: From Nano to Macro* **1** 632-635 (see http://www.slicer.org)

[3]   Mazzara G P, Briggs R W, Wu Z and Steinbach B G (1996) Use of a modified polysaccharide gel in developing a realistic breast phantom for MRI *Magnetic Resonance Imaging* **14** 639–648

[4]   Davidson J L, Wright P, Ahsan S T, Robinson R L, Pomfrett C J D P and McCann H (2010) fEITER – a new EIT instrument for functional brain imaging in Proc. *11th Int. Conference on Biomedical Applications of EIT* (Florida, USA)

[5]   Bernstein M A, King K F and Zhou X J (2004) *Handbook of MRI Pulse Sequences* (first ed.) Elsevier Academic Press

[6]   Schöberl J (1997) NETGEN – An advancing front 2D/3D-mesh generator based on abstract rules *Comput. Visual Sci.* **1** 41-52 (http://www.hpfem.jku.at)

[7]   Polydorides N and Lionheart W R B (2002) A Matlab based toolkit for three-dimensional electrical impedance tomography: a contribution to the EIDORS project *Meas. Sci. Technol.* **13** 1871-83

[8]   Polydorides N (2002) Image reconstruction algorithms for soft field tomography, PhD Thesis, UMIST, UK

Constructing resistive mesh phantoms by an equivalent 2D resistance distribution of a 3D cylindrical object

A. Just, J. Dittmar, M. Quintel, G. Hahn

Department of Anaesthesiology, Emergency and Intensive Care Medicine
University Medical Centre Göttingen

Von-Siebold-Str. 3, D-37075 Göttingen, Germany

E-mail: ajust@rz.uni-leipzig.de

Introduction

The development of Electrical Impedance Tomography (EIT) devices requires practical tools to test and calibrate them. Beneath physical tank phantoms, resistive mesh phantoms are suitable for this task. They provide predictable, stable and reproducible voltage values. To investigate systematic errors of EIT devices phantoms with constant voltages are preferable as described in Hahn et al. (2008). If assessing the performance of EIT systems under realistic conditions is requested, phantoms which yield to realistic potential distributions concerning voltage amplitude and dynamic ranges are desirable. Such phantoms were developed by Griffiths (1988), Hahn *et al.* (2000) and Gagnon *et al.* (2010). The phantoms of Griffiths (1988) and Gagnon *et al.* (2010) were constructed by using a Finite Element (FE) modelling technique and represent the voltage distribution of a 2D circular object. While they both consist of a large number of resistors (Griffiths: 624 resistors, Gagnon *et al.*: 340 resistors), the phantom of Hahn *et al.* (2000) is built of only 65 resistors.

The dynamic range of voltage amplitudes of a 2D circular object, however, is significantly smaller than that of a 3D cylindric object. So, phantoms based on 2D distributions are not optimal to assess the performance of EIT systems under realistic clinical conditions.

We present a method to construct resistor phantoms which provide a realistic potential distribution corresponding to a 3D object and which are reduced to a relative low number of resistors. In this way it becomes possible to construct efficiently phantoms for arbitrarily shaped 3D objects.

Methods

In the first step, a 3D simulation of current injection and potential measurements e.g. in adjacent pattern (16 electrodes) on a cylindrical object is performed using COMSOL Multiphysics (Comsol Multiphysics, Comsol AB, Stockholm, Sweden). The simulation provides the potential distribution for the 3D object under consideration. Afterwards, an equivalent 2D resistivity distribution is estimated by inversion applying a 2D reconstruction algorithm using a modified Simultaneous Iterative Reconstruction Technique (SIRT, Just *et al.* (2007) with 2D geometrical factors.

The resulting model is averaged in order to contain only a small number of resistivity regions (e.g. 3 rings) and a 2D simulation using COMSOL Multiphysics is performed with this model. The model is optimised in an iterative process until the deviation of the resulting distribution of potential differences from that one of the 3D object becomes minimal.

The 2D resistivity distribution is then discretized into a circular grid consisting of a certain number of circular segments. The borders of the circular segments can be allocated to resistors whose values can be calculated from the resistivities and the border lengths of the cells surrounding the resistors. This procedure is in principle consistent to network modelling techniques.

In order to check the quality of the resistor network the resulting resistor distribution is inserted into a simulation using LTSpice (Linear Technology Corporation).

Results

Figure 1 shows a 3D homogeneous cylindrical object with 16 adjacent electrodes for current injection and voltage measurement and the corresponding equivalent 2D model yielding to the same voltage distribution. The voltage distribution for an injection of 5mA at two adjacent electrodes is shown on the right panel of figure 1. The differences are in the range of 1 - 4 %.
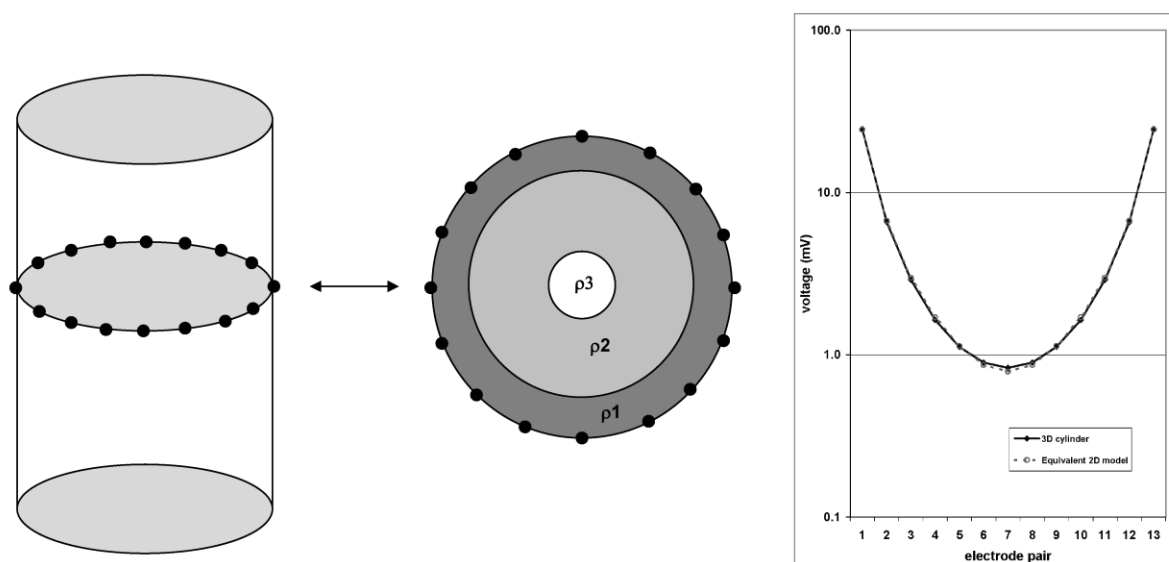
Figure 1 3D cylindrical object and equivalent 2D model. Left: homogeneous cylindrical object with resistivity 5 Ωm and 16 electrodes. Current is injected at two adjacent electrodes and potential differences are measured in adjacent pattern. Middle: Equivalent 2D circular object ($\rho1=70$ Ωm, $\rho2=20$ Ωm, $\rho3=5$ Ωm) which shows the same potential differences at current injection at two adjacent electrodes as the homogeneous cylindrical object. Right: potential differences at adjacent electrode pairs for the 3D and the 2D object.

The discretisation in circular segments of the 2D model is pictured in figure 2 along with the resulting distribution of resistors. The right panel shows the simulated voltages at a current injection of 5mA.

The differences between the simulated 2D distribution and the simulated resistor network range between 0.7 and 4.8 %.
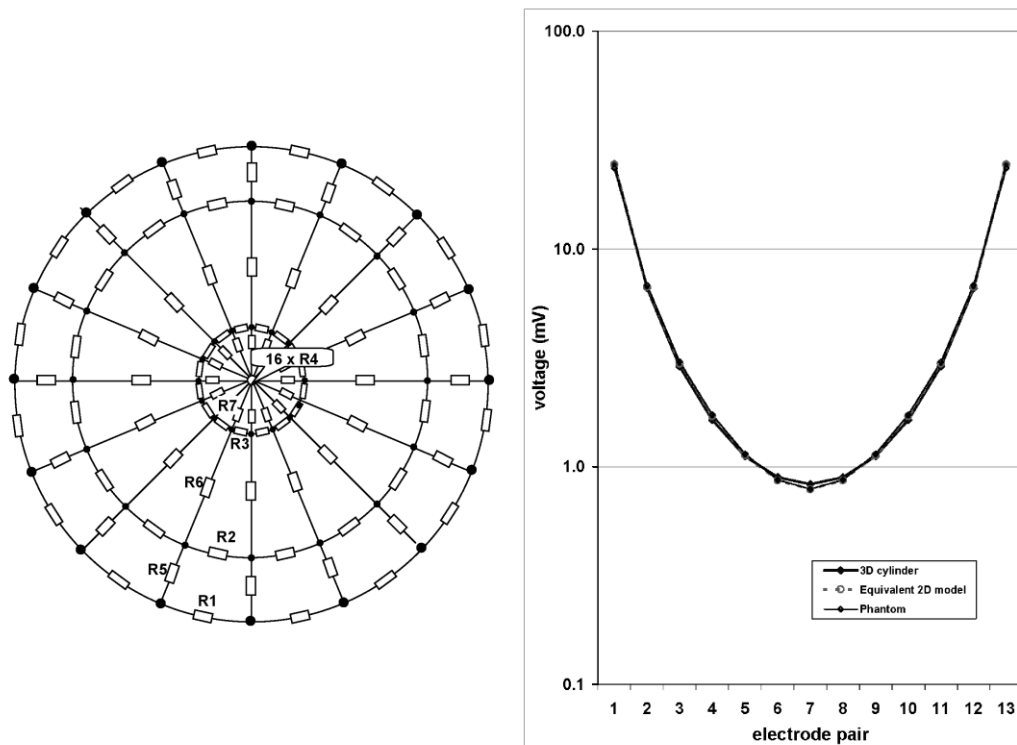
Figure 2 Resistive mesh phantom with 112 resistors which result in the same potential differences as the models in figure 1. Left: discretisation of the 2D model from figure 1 and resulting resistor network consisting of 4 rings of 16 equal resistors and 16 spokes with 3 resistors (R1=208Ω, R2=15Ω, R3=1Ω, R4=1 Ω, R5=47 Ω, R6=49 Ω and R7=50 Ω). Right: potential differences at adjacent electrode pairs for the 3D and the 2D object as well as for the resistor phantom.

Conclusion

We applied a method to construct resistor phantoms which yield to a realistic potential distribution equivalent to 3D objects and are reduced to a low number of resistors. The method can be easily extended to arbitrarily shaped 3D objects and is therefore well suited to be used as an effective construction tool for building phantoms which reflect the dynamic range of voltage amplitudes in real EIT measurements under in vivo conditions.

Acknowledgments

References

Gagnon, H., M. Cousineau, A. Adler, and A. E. Hartinger (2010), A Resistive Mesh Phantom for Assessing the Performance of EIT Systems, *Biomedical Engineering, IEEE Transactions on*, **57**(9), 2257-2266.

Griffiths, H. (1988), A phantom for electrical impedance tomography, *Clin Phys Physiol Meas*, **9** *Suppl A*, 15-20.

Hahn G, Beer M, Frerichs I, Dudykevych T, Schroder T and Hellige G 2000 A simple method to check the dynamic performance of electrical impedance tomography systems *Physiol Meas* **21** 53-60.

Hahn G, Just A, Dittmar J and Hellige G 2008 Systematic errors of EIT systems determined by easily-scalable resistive phantoms *Physiol Meas* **29** S163-72.

Just, A., C. Ruecker, G. Hahn, and G. Hellige (2007), Sensitivity of two different reconstruction algorithms to body shape and electrode position errors in absolute EIT, IFMBE Proceedings 17, Graz, ed H Scharfetter and R Merwa pp 404-7.

EIT 2011, Dept. Electronic & Electrical Engineering, University of Bath

1

Optical Shape Capture and Meshing of the Breast

J. Forsyth, A. Borsic, R. Halter, A. Hartov, K.D. Paulsen

Introduction

Electrical Impedance Tomography (EIT) is a possible alternative or complementary breast imaging modality to mammography and MRI. It is a non-ionizing technique for determining tissue conductivity and permittivity – parameters which show contrast in malignant and benign lesions [6,7]. EIT is also a low cost imaging solution [4]. Quality of images produced in EIT research has improved significantly since its introduction due to the advancement of hardware, modeling, and reconstruction algorithms [2]. One area that EIT can improve considerably is in accurately modeling the anatomic geometry and electrode locations, because errors in the model can cause significant artifacts in reconstructed images [1,3,8,10]. This has been insufficiently explored in in-vivo studies because obtaining shape and electrode information is often challenging. However, reconstructing with models that accurately represent the imaging domain is desirable because it may greatly improve the clinical value of EIT. In this manuscript we discuss a method for obtaining accurate models with an optical scanner for use in breast cancer detection.

Device

Optical shape capture is performed with the Creaform VIUscan 3D handheld scanner (Figure 1). The user "sweeps" the scanner around the focal object while the scanner continuously acquires images and stitches them together. The scanner tracks its position in space using markers visible in the scene which allows accurate image stitching. The surface it produces is viewable on a computer screen during the capture session. Once

Figure 1. Creaform VIUscan device for optical shape capture (www.creaform3d.com). It acquires a surface mesh with positional accuracies up to 50 μm.

the session is complete, the scanner provides a surface mesh and the color texture of this surface. The color allows setup of the boundary conditions (see Algorithms – Electrode Localization).

Patient Physical Setup

In an EIT exam with optical capture, the procedure will involve application of electrodes, optical capture of the breast, and EIT data collection.

An exam table was built allowing a patient to lie prone with one breast pendant through an opening (Figure 2 left). Circular electrodes are embedded in thin, flexible strips which are

EIT 2011, Dept. Electronic & Electrical Engineering, University of Bath

2

applied to the breast surface. Electrodes are color coded which makes them distinguishable in the color texture file. Once electrodes have been placed, the breast is scanned from underneath the exam table (approx. 5 minutes). After capturing the shape, EIT data is collected. The patient should remain virtually still during the procedure to minimize movement artifacts and provide the most accurate optical data.

Algorithms – Surface Processing

The surface mesh obtained requires pre-processing to prepare it for volume meshing. The first step is to remove extra elements that result from a scan (Figure 2 center). These unwanted elements are removed by finding the largest connected region. The resulting breast surface mesh will have a large opening at the base and may have some small holes (Figure 2 center). The gaps are filled with a surface reconstruction filter which was developed by Hoppe et al [5]. These steps produce a watertight surface mesh (Figure 2 right).
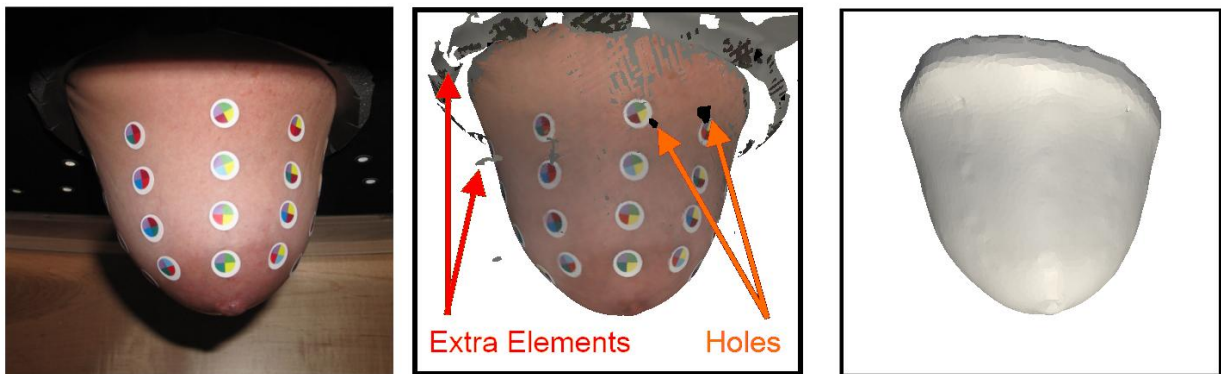
Figure 2. Photograph of a patient's breast in an IRB approved study to acquire the shape (left).

Computer rendering of the surface with color shown. Extra elements and holes may be present (center).

Rendering of the surface after finding the largest connected region and filling holes (right).

Algorithms - Electrode Localization

Surface meshes acquired with the VIUscan device have associated color information which is used to determine electrode locations. We implemented image processing techniques including the watershed algorithm and color segmentation to automatically locate and identify the electrodes. The electrode centroids are input to the volume meshing algorithm to locally refine the mesh.

Algorithms - Volume Mesh Generation

We have demonstrated the techniques for acquiring the breast shape into a surface mesh and processing the color data to locate the electrodes. To setup the boundary conditions, we represent the circular contours of the electrodes on the surface of the mesh. This is accomplished by inserting nodes along the boundaries of electrodes to represent their contours. A method for

EIT 2011, Dept. Electronic & Electrical Engineering, University of Bath

3

volume meshing with these additional nodes involves performing a triangulation around the electrodes ("stitching"). However, this produces some poor quality elements near the electrodes. As an alternative, we preserve the quality of elements and electrode contours by applying an iterative remeshing algorithm. The result for one electrode is shown in Figure 3 (right). The algorithm from which this result is derived produces high quality meshes with approximately equal element edges (Distmesh [9]). We modified the open source version which is capable of meshing simple 2D surfaces to generate 3D shapes such as a breast. In addition, we added the capability to refine the mesh in the locations of the electrodes, which optimizes reconstruction time and image quality.

Results on Patients

An example volume mesh is shown which has 45,874 nodes and 257,116 tetrahedral elements (Figure 3 center). The shape of this volume mesh accurately represents the shape of the breast it is generated from (Figure 3 left). In addition, the placement of electrodes in the volume mesh surface is consistent with their locations on the breast. Density of elements in the electrodes is about 1/3 of the density in the remainder of the mesh. The mesh element qualities are displayed in a histogram using the quality metric of inner radius ratio (Figure 4). The mean element quality is 0.81 and the standard deviation is 0.16.
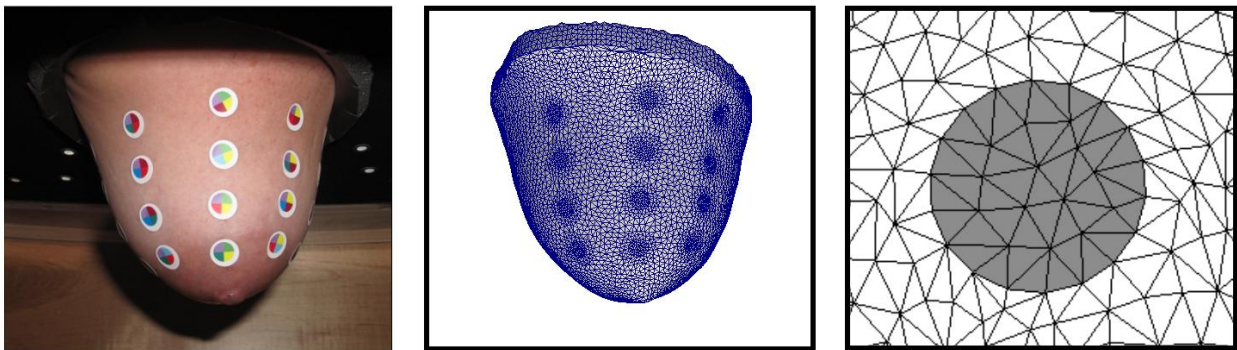
Figure 3. Photo of breast with electrode markers applied (left). Rendering of breast mesh (center). Mesh of one electrode (right).
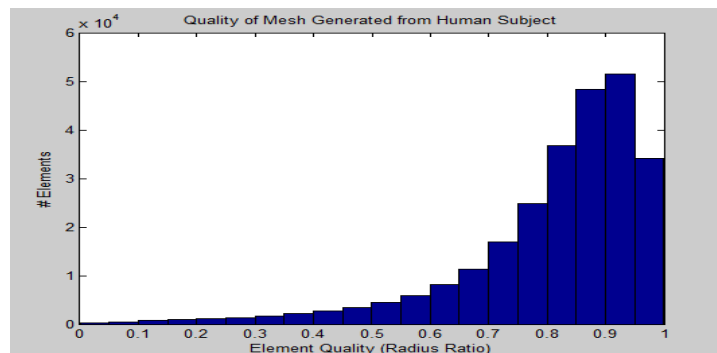
Figure 4. Histogram of tetrahedral element qualities for the volume mesh of the human volunteer's breast after the optimization algorithm was applied. Average element quality (radius ratio of insphere to circumsphere) is 0.81 ± 0.16.

EIT 2011, Dept. Electronic & Electrical Engineering, University of Bath

4

This manuscript describes a procedure and series of algorithms for accurately capturing the breast shape and electrode contours in a volume mesh for reconstruction. A successful example is shown for a human volunteer. We expect that this meshing technique will provide improvements in the quality of EIT images. Image reconstruction with phantoms and human subjects is the future work for our group.

Acknowledgements

References

[1] Adler, A.; Guardo, R.; Berthiaume, Y. , "Impedance imaging of lung ventilation: do we need to account for chest expansion?," *Biomedical Engineering, IEEE Transactions on* , vol.43, no.4, pp.414-420, April 1996

[2] Barber D C and Brown B H 1984 "Applied potential tomography" J. Phys. E: Sci. Instrum. 17 723–33

[3] W. R. Breckon and K. M. Pidcock, "Data errors and reconstruction algorithms in electrical impedance tomography," Clin. Phys. Physiol. Meas., vol. 9, no. A, pp. 105-109, 1988.

[4] Brown, B.H.; Barber, D.C. , "Low-cost functional imaging-Electrical Impedance Tomography," *Engineering in Medicine and Biology Society, 1995 and 14th Conference of the Biomedical Engineering Society of India. An International Meeting, Proceedings of the First Regional Conference., IEEE* , vol., no., pp.1/7-1/8, 15-18 Feb 1995

[5] H. Hoppe, T. Derose, T. Duchamp, J. Mcdonald, W. Stuetzle, "Surface recon-struction from unorganized points", Computer Graphics, Vol. 26, No. 2. (1992), pp. 71-78.

[6] J. Jossinet, "Variability of impedivity in normal and pathological breast tissue," Med. Biol. Eng. Comput., vol. 34, pp. 346-350, 1996.

[7] J. Jossinet, "The impedivity of freshly excised human breast tissue," Physiol. Meas., vol. 19, pp. 61-75, 1998.

[8] W.R.B Lionhart, "Boundary Shape and Electrical Impedance Tomography", In-verse Problems, Vol 14, No 1, 139-147, 1998.

[9] P.-O. Persson and G. Strang, "A simple mesh generator in Matlab," SIAM Rev., vol.46, no. 2, 2004.

[10] Soleimani M, Gomez-Laberge C and Adler A, "Imaging of conductivity changes and electrode movement in EIT", Physiol. Meas. 27 S103–13

Jacobian Optimization for 3D Electric Impedance Tomography via GPU acceleration

E A Attardo [1]**, A Borsic**[1]**, R Halter**[1]

[1]Thayer School Of Engineering, Dartmouth College, 8000 Cummings Hall Hanover, NH 03755, US

E-mail: Elia.A.Attardo@Dartmouth.edu

1. Introduction

In recent years Graphic Processing Units (GPUs) have reached very high computing capabilities. Since their introduction by NVIDIA in 2001 with the GeForce3 series, these devices are able to perform vector operations at much higher rates with respect to Central Processing Units (CPUs). The rationale for this discrepancy lies in the specialization of GPUs for compute-intensive highly parallel computation. In fact, the main objective, since the first release of these devices, was to transition part of the computational effort from CPU to GPU. In this vein, NVIDIA unveiled in 2006 the GeForce8800 GTX built with a parallel architecture named "Compute Unified Device Architecture" (CUDA) [1]. For the first time, developers have direct control over the exact computations to perform on a GPU. Also, CUDA allows developers to program GPUs for general-purpose computations. In this framework, significant speed-ups can be obtained in 3D reconstruction for Electric Impedance Tomography (EIT) with highly dense FEM meshes. In EIT, computing time is spent mostly in solving the forward problem and in computing the Jacobian matrix from the forward solutions; these can be efficiently parallelized by means of a GPU-based approach.

In this paper we present a framework for GPU-acceleration of the Jacobian computation in 3D Electric Impedance Tomography. We assess this development through numerical experiments and compare computation times required to assemble the Jacobian matrix when implemented on a CPU-based multiple computational cores server and a GPU computing server.

2. Background and Jacobian Computation

Commonly, EIT image reconstruction is formulated as a non-linear least squares Tikhonov regularized inverse problem:

$$\sigma_{\mathbf{rec}} = \arg\min_{\sigma} \frac{\mathbf{1}}{\mathbf{2}} \|\mathbf{V}(\sigma) - \mathbf{V}_{\text{meas}}\|^{\mathbf{2}} + \alpha \frac{\mathbf{1}}{\mathbf{2}} \|\mathbf{L}\,(\sigma - \sigma^*)\|^{\mathbf{2}} \tag{1}$$

where $\sigma_{\mathbf{rec}}$ is the vector of conductivities to be estimated σ is the vector of model conductivities, $\mathbf{V}(\sigma)$ is the vector of electrode voltages resulting from the forward solver, $\mathbf{V}_{\text{meas}}$ is the vector of measured electrode voltages, α is the Tikhonov factor, L is a regularization matrix, and σ^* is a reference conductivity distribution. Equation (1) is usually solved in a iterative fashion, by application of the Gauss Newton method:

$$\delta\sigma_{\mathbf{n}} = -(\mathbf{J_n^T J_n} + \alpha\,\mathbf{L^T L})^{-\mathbf{1}}[\mathbf{J_n^T}(\mathbf{V}(\sigma_n) - \mathbf{V}_{\text{meas}}) - \alpha\mathbf{L^T L}(\sigma_{\mathbf{n}} - \sigma^*)] \tag{2}$$

(a) Fine mesh used in the tests.

(b) Cross-section of fine mesh.

(c) FEM model of the probe and electrodes.
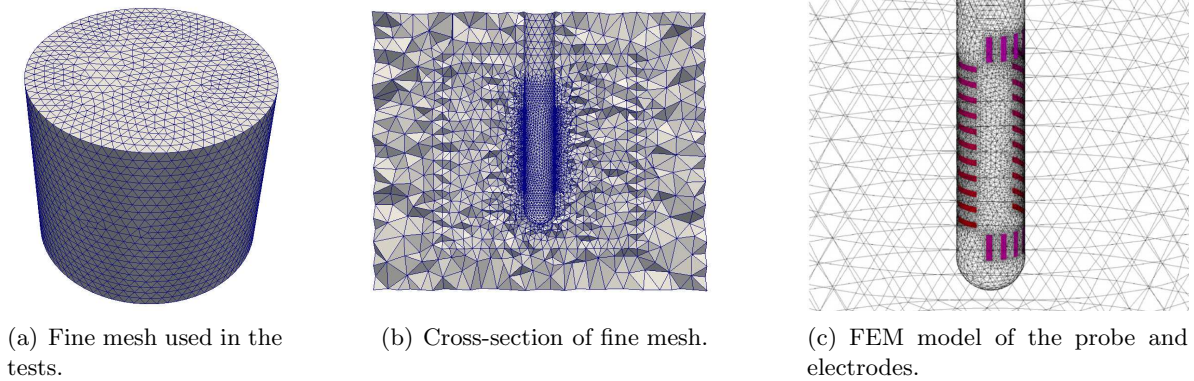
Figure 1. Three views of the used mesh in TREI with 97,973 nodes and 541,604 elements.

where n is the iteration number, $\delta\sigma_{\mathbf{n}}$ is the conductivity update for iteration n and J_n is the Jacobian of the forward operator $\mathbf{V}(\sigma)$ calculated for $\sigma = \sigma_{\mathbf{n}}$.

The conductivity is represented on a coarse mesh to limit the number of parameters being solved and improve the conditioning of the inverse problem, while a much finer mesh is used for the forward problem in order to ensure sufficient accuracy in computing the potential distribution. We use an interpolation scheme to automatically manipulate these two representations [2]. In this manuscript we explicitly address the Jacobian computation for 3D Transerectal Electric Impedance (TREIT). To this aim, we show the employed geometry and mesh in Figure 1; this mesh consists of 541,604 tetrahedral elements and 97,973 nodes.

As outlined in [3] the computation of the Jacobian is the most time-consuming operation in our reconstruction algorithm, making up almost 70% of each iteration of the reconstruction algorithm. At the first glance, one can easily recognize the number of computational operations required:

$$
\begin{aligned}
J(i,k) = \frac{\partial \mathbf{V}(i)}{\partial \sigma(k)} &= -\int_\Omega \mathbf{E}_{applied}(p) \cdot \mathbf{E}_{lead}(l) d\Omega = \\
&= -[E^x_{applied}(p) \cdot E^x_{lead}(l) + E^y_{applied}(p) \cdot E^y_{lead}(l) + E^z_{applied}(p) \cdot E^z_{lead}(l)]V(k)
\end{aligned}
\tag{3}
$$

where $\mathbf{V}(i)$ is the ith voltage measurement, σ the kth conductivity value, $\mathbf{E}_{applied}(p)$ and $\mathbf{E}_{lead}$ the applied and lead electric fields, respectively [4],and $V(k)$ is the volume of the kth element.

For the TREIT test problem employed here (mesh with 541,604 elements - see Figure 1), a typical voltage patterns we use produces a Jacobian matrix with 2430 rows. The total number of computations required for a single element is 31.6 Gflops and 8 Gflops for complex and real valued problem respectively.

3. Results

The numerical tests we present show results in computing the Jacobian matrix on a CPU-based multiple core server and a GPU computing server. The CPU-based system is a Dell Power Edge 1955 Blade Server. The server is based on two quad-core Xeon 5355 "Clovertown" CPUs, with an internal clock frequency of 2.66GHz and front-side bus speed of 1.33GHz. Due to the internal nature of the quad-core Xeon 5355 the total number of computational cores is 8; each core operates at 64-bit. The GPU-based system is a NVIDIA Tesla S1070 server [5] which consists of four Tesla GPUs [6]. Each GPU has 240 cores (960 in total) with an internal clock frequency

Table 1. Timing of Jacobian computation (Real)

Nr. of meas. patterns	MATLAB (sec)	CPU-Optim. (sec)	GPU (sec)
2430	351.39	297.5	14.19
1215	177.19	150.56	8.28
405	61.88	54	4.4

Table 2. Timing of Jacobian computation (Complex)

Nr. of meas. patterns	MATLAB (sec)	CPU-Optim. (sec)	GPU (sec)
2430	1136.85	745.42	33
1215	586.98	374	17
405	195.77	131	7.7

Table 3. Speed-up factors (Real)

	MATLAB (sec)	CPU-Optim. (sec)
CPU-Optim.	1.52	-
GPU	34.45	22.58

Table 4. Speed-up factors (Complex)

	MATLAB (sec)	CPU-Optim. (sec)
CPU-Optim.	1.17	-
GPU	24.76	21

of 1.5GHz. The memory bandwidth is 408GB/sec while the total dedicated memory is 16 GB DDR3 with a 512-bit memory interface bus operating at 1.6GHz. The Tesla GPU allows us to perform operations on double precision floating point with a peak of 345 GFlops. The interface between GPU (device) and CPU (host) is based on Peripheral Component Interconnect Express (PCI-E). Windows 7 64-bit Enterprise edition is installed on the host CPU.

We compare results of the three different Jacobian implementations. First, a straight-forward MATLAB based Jacobian computation is tested using MATLAB Release 2010b 64-bit Windows edition. Second, several C language mex (MATLAB EXecutable) files optimized for computing the Jacobian on a multi-core processor were employed [3](CPU-Optim.). In this implementation, an optimized library for a multi-core Xeon processor is used (Intel's MKL). Finally, a framework for GPU implementation of Jacobian matrix computation was developed. Specifically, several CUDA *kernels* running in parallel on each of the 240 cores are instantiated (only for one GPU). The main operations involve in each instantiation include element-wise summation, subtraction, multiplication, and computation of sparse matrix-vector products. Although four GPUs are available on the NVIDIA S1070, for the time being we are performing all computations on a single GPU.

Table 1 and 2 show the timing of Jacobian computation for real and complex quantities respectively when the number of measurement patterns is varying. Actually, the number of measurements represents the number of rows to compute in the Jacobian.

Table 3 and 4 list the speed-up factors achieved for the different computational methods. With

respect to the unoptimized MATLAB implementation, CPU-Optim and GPU implementations achieved speed-up factors of 1.52 and 34.45 for computing the real-valued Jacobian, respectively (Table 3). Further, the GPU implementation provides a speed-up of 23 when compared to the CPU implementation. Significant speed-up was also achieved for complex valued problem. In this implementation, the GPU-based Jacobian computation runs 21 times faster than CPU and roughly 25 times faster with respect to the unoptimized MATLAB version.

4. Conclusions

The numerical tests that we have conducted suggest a significant speed-up in Jacobian computation with respect to an unoptimized MATLAB and CPU-optimized implementation. For the test mesh with 541,604 elements and 97,973 nodes we have obtained a relative speed of 21 times for complex valued problem, reducing the Jacobian computation from 1136.85 sec (unoptimized MATLAB) and 745.42 sec (CPU-Optim) to 33 sec for GPU-based implementations. A remarkable gain is achieved by GPU optimization with respect to MATLAB implementation as reported in Table 4. Moreover, building the Jacobian matrix by using all computational capabilities of the NVIDIA S1070 (eg. all four GPUs) will allow us to further increase the speed-up factor and to obtain 'near' real-time reconstruction.

5. References

[1] NVIDIA 2010 *NVIDIA CUDA C Programming Guide* Version 3.2
[2] A Borsic, R Halter, Y Wan, A Hartov and K D Paulsen 2010 Electrical impedance tomography reconstruction for three-dimensional imaging of the prostate *Physiol. Meas*, **31** pp S1 - S16
[3] A Borsic, A Hartov, K D Paulsen, P Manwaring 2008 3D Electric Impedance Tomography Reconstruction on Multi-Core Computing Platforms, *Proceedings IEEE EMBC*, Vancouver
[4] Polydorides N, Lionheart W R B 2002 A MATLAB based toolkit for three dimensional electric impedance tomography: A contribution to EIDORS project *Meas. Sci, technol.* **13** pp 1871-1883
[5] `http://www.nvidia.com/docs/IO/43395/NV_DS_Tesla_S1070_US_Jun08_NV_LR_Final.pdf`
[6] `http://origin-www.nvidia.com/object/tesla_computing_solutions.html`

Robustness of GREIT reconstruction algorithm with respect to reciprocity errors in the data.

Rebecca J Yerworth[1,2], Richard Bayford[1]

[1]Department of Natural Sciences, Middlesex University, London, UK
2 City of Westminster College, London, UK

Introduction: The GREIT reconstruction algorithm (Graz consensus Reconstruction algorithm for EIT) (Adler, *et al.* 2009) set a new standard for clinical electrical impedance tomography (EIT), replacing the older back projection algorithms. Since then limited testing, and use of the algorithm has been published (Grychtol, *et al.* 2010), further characterisation is essential for the GEIT algorithm to be adopted for clinical use.

A common method of calibrating and characterising the errors in EIT measurement systems is know as reciprocity. Theoretically the voltage measured using electrodes a&b to inject, and x&y to sense (voltage measurement) should be identical to that using x&y to inject and a&b to sense. Unfortunately, this only holds true in an idea case. The reciprocity errors will, affect the quality of the reconstructed images.

Work on characterising reciprocity, and other electrode errors, has previously been published, with respect to individual EIT systems (Oh, Woo and Holder 2007) and more generically (Hartinger, *et al.* 2009), however the robustness of the GREIT algorithm, with respect to reciprocity, has not been documented. We present an investigation into how reciprocity errors degrade images produced with GREIT, and compare this to the degradation seen when the original gold standard filtered Back-projection algorithm (Brown & Seagar 1987) is used.

 the reduction of images quality produced with GREIT, and compare this to the

Method: Previously collected data from the Middlesex University (MU)/Great Ormond Street Hospital (GOSH) group, and data sets published on the GREIT web site (eidors.org/GREIT) were used. All data was for a single ring of 16 electrodes, using adjacent drive and sense electrode combinations, and had been collected with a commercial EIT system. For each data set the reciprocity errors were calculated. Impedance data from one, low reciprocity study, on a neonate, was used as the base data set which consisted of a period of regular tidal breathing. Additional data sets were created by multiplying this with the reciprocity errors occurring within the other data sets. In each case all the reciprocity error was applied to the first occurrence of each 4 electrode combination (e.g. ab,xy but not xy,ab). The original and corrupted data sets were then individually reconstructed using the GREIT and Back projection algorithms, as per Adler *et al.* (2009), using an average of the whole data set as the baseline. The quality of the resultant images was assessed visually In the first instance.

Results: The original data set had a median reciprocity error of 1.23% and 16(8%) electrode combinations had reciprocity errors of >5% of the measured voltage, a description of the corrupting data sets is given in Table 1.

Data set	Median reciprocity error	No. (%) electrode combinations with error >5%	Description
i)	0.614	0 (0)	Tank data (MU)
ii)	1.70	22 (11)	Pig (Frerichs, et al. 2003)
iii)	5.16	106 (51)	Adult human (GOSH)

Table 1. Properties of data sets used.
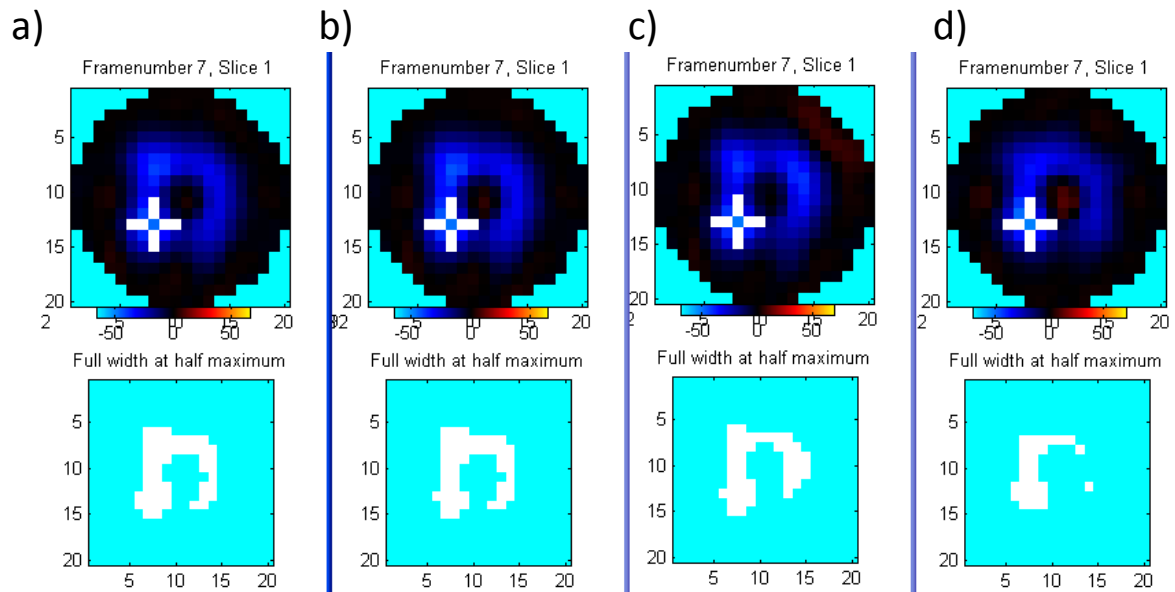
Figure 1 1st row: Neonate data reconstructed with GREIT a) normally and b-d) with added reciprocity errors. The cross indicates the peak impedance change. 2nd row: Region of pixels with intensity >= half the peak impedance change.

a)   b)   c)   d)
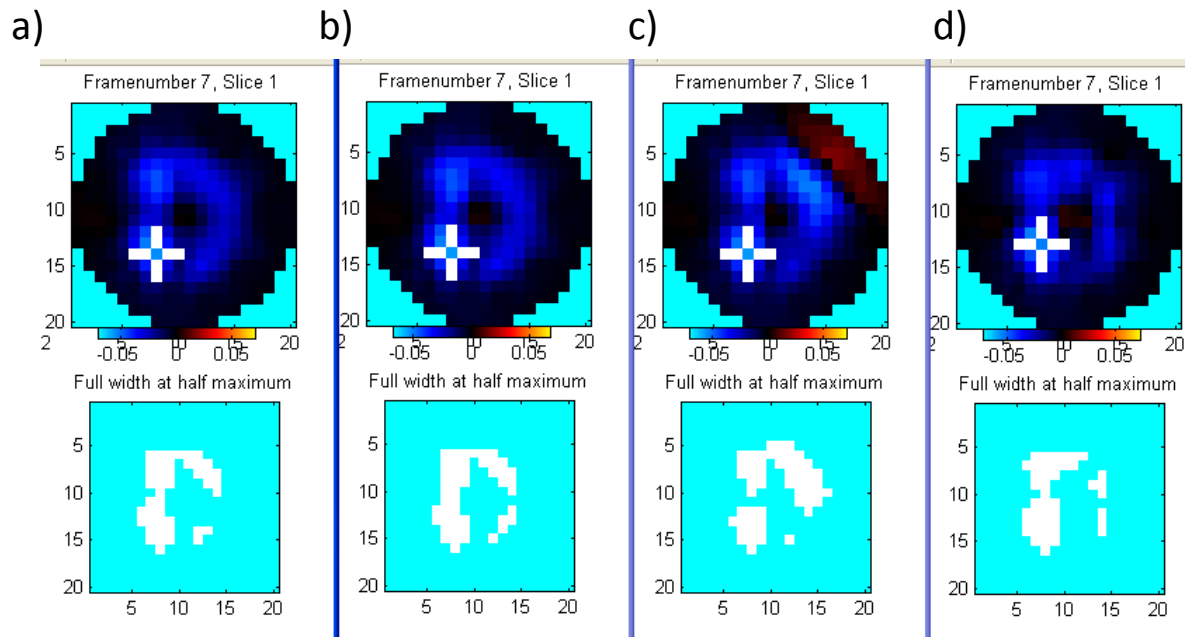
Figure 2 1ˢᵗ row: Neonate data reconstructed using Backprojection a) normally and b-d) with added reciprocity errors. The cross indicates the peak impedance change. 2ⁿᵈ row: Region of pixels with intensity >= half the peak impedance change.

Discussion and Conclusions: It can be seen that, with both algorithms, as the reciprocity error increases, the images exhibit a reduction in resolution and the segmented region shrinks. It should be noted that for images b-d the corrupting reciprocity has been added to the intrinsic reciprocity. The initial findings demonstrate the importance of minimising the reciprocity error and that both the GREIT and back projection algorithms are susceptible to these errors.

Reference list

Adler, A, JH Arnold, B Bayford, and A Borsic, B Brown, P Dixon, T J C Faes, I Frerichs, H Gagnon, Y Gärber, B Grychtol, G Hahn, W R B Lionheart, A Malik, R P Patterson, J Stocks, A Tizzard, N Weiler and G K Wolf. "GREIT: a unified approach to 2D linear EIT." Physiol. Meas. 30 (2009): S35-S55.

Brown B H and Seagar A D 1987 The Sheffield data collection system Clin. Phys. Physiol. Meas. 8 91–7

Frerichs, I, P A Dargavillle, T Dudykevych, and P M Rimensberger. "Electrical Impedance Tomography − a method for monitoring regional lung aeration and tidal volume distribution?" Intensive Care Med. 29 (2003): 2312-2316.

Grychtol, B, G K Wolf, A Adler, and J H Arnold. "Towards lung EIT image segmentation: automatic." PHYSIOLOGICAL MEASUREMENT, 2010: S31–S43.

Hartinger, A E, R Guardo, A Adler, and H Gagnon. "Real-Time Management of Faulty Electrodes." IEEE TRANSACTIONS ON BIOMEDICAL ENGINEERING 56, no. 2 (2009): 369-377.

Oh, Tong In, Eung Je Woo, and David Holder. "Multi-frequency EIT system with radially symmetric." Physiological Measurement, 2007: s183-s196.

Electrical Impedance Tomography Inverse Solutions using High Order Finite Elements and LSQR

P.D. Ledger

Civil and Computational Engineering Research Centre, College of Engineering,
Swansea University

This presentation is concerned with the solution of the electrical impedance tomography (EIT) inverse problem when the forward problem is discretised by high order finite elements and is based on the recent technical report [1] by the author. The use of LSQR for the solution of the least square problem resulting from the linearisation of the inverse problem is discussed as a novel alternative to standard Tikhanov and TSVD alternatives.

Forward Problem

As standard in EIT, the Maxwell equations can be shown to a Poisson problem for an electric potential, u. We distinguish between two classes of forward problem, the pure Dirichlet and pure Neumann cases. In the case of pure Dirichlet data $u = f_D$ on $\partial\Omega = \Gamma_D$ the forward problem expressed can be the weak form: Find $u \in X_D(f_D)$ such that

$$(\kappa(\boldsymbol{x}, \omega)\nabla u, \nabla v)_\Omega = 0 \qquad \forall v \in X_D(0), \tag{1}$$

and has a unique solution for all $f_D \in H^{1/2}(\partial\Omega)$ and $\kappa(\boldsymbol{x}, \omega) \in L^\infty(\overline{\Omega})$ (eg [2]), where $X_D(f) := \{u \in H^1(\Omega) : u = f \text{ on } \partial\Omega\}$. The corresponding pure Neumann forward problem, with Neumann data $\boldsymbol{n} \cdot \kappa\nabla u = f_N$ on $\partial\Omega = \Gamma_N$, can be expressed in the weak form: Find $u \in X_N$ such that

$$(\kappa(\boldsymbol{x}, \omega)\nabla u, \nabla v)_\Omega = \int_{\partial\Omega} \overline{v} f_N \mathrm{d}s \qquad \forall v \in X_N, \tag{2}$$

with $X_N := H^1(\Omega)$, and has a unique solution up to an additive constant for all $f_N \in H^{-1/2}(\partial\Omega)$ satisfying $\int_{\partial\Omega} f_N \mathrm{d}s = 0$ and $\kappa(\boldsymbol{x}, \omega) \in L^\infty(\overline{\Omega})$ (eg [2]). To fix the value of the additive constant the condition $\int_{\partial\Omega} u \mathrm{d}s = 0$ is added.

These weak forms are well suited to discretisation by finite element methods. In particular, a discretisation which allows for non-local mesh (h-)refinement and polynomial (p-) enrichment, known as the hp-finite element method, has become popular due to the high levels of accuracy it offers for practical problems. For problems with smooth solutions and for problems with piecewise analytic solutions with singularities due to reenterent corners and edges it can be demonstrated that combined h and p refinements lead to exponential convergence of the solution [3, 4]. By introducing a triangulation of Ω denoted by $\mathcal{T}_h$ and a corresponding discrete approximation to the continuous space $H^1(\Omega)$ as $X_{hp} \subset H^1(\Omega)$, the approximate weak solution of the pure Dirichlet and Neumann problems corresponds to: find $u_{hp} \in X_{hp} \cap X_D(f_D)$ such that

$$(\kappa(\boldsymbol{x}, \omega)\nabla u, \nabla v)_\Omega = 0 \qquad \forall v \in X_{hp} \cap X_D(0), \tag{3}$$

for the pure Dirichlet case and find $u_{hp} \in X_{hp} \cap X_N$ such that

$$(\kappa(\boldsymbol{x}, \omega)\nabla u, \nabla v)_\Omega = \int_{\partial\Omega} \overline{v} f_N \mathrm{d}s \qquad \forall v \in X_{hp} \cap X_N, \tag{4}$$

for the pure Neumann case. For practical implementation details we refer to [3, 4, 1] and references there in.

Inverse Problem

The measurement of voltages for applied currents corresponds to instances of the Neumann to

Dirichlet (NtD) map for this problem. Specifically, in the case of absolute imaging, the inverse problem corresponds to determining the unknown admittivity function $\kappa_C(\boldsymbol{x})$ from M complete sets of the NtD map: $(\Lambda_\kappa)^{-1} : Y \to H^{1/2}(\partial\Omega)$:

$$(\Lambda_\kappa)^{-1}(f_N^{(i)}) = u^{(i)}|_{\partial\Omega} \qquad i = 1, \cdots, M, \tag{5}$$

where $Y := \left\{ f \in H^{-1/2}(\partial\Omega) : \int_{\partial\Omega} f \mathrm{d}s = 0 \right\}$ and $u^{(i)}|_{\partial\Omega}, i = 1, \cdots, M$, are the solutions of (2), evaluated on $\partial\Omega$, with Neumann boundary conditions $f_N^{(i)} \in Y$, $i = 1, \cdots, M$, and $\kappa(\boldsymbol{x}) = \kappa_C(\boldsymbol{x})$. In practical applications (5) will be provided by the measurement system, however, for the purpose of numerical testing, the finite element method is employed to create the approximate initial data. This requires solving (4) with Neumann boundary conditions $\boldsymbol{n} \cdot \kappa \nabla u|_{\partial\Omega} = f_N^{(i)}$, $i = 1, \cdots, M$, and using $\kappa(\boldsymbol{x}) = \kappa_C(\boldsymbol{x})$ that should be determined from the inverse solution procedure.

A second conforming regular simplicial triangulation of Ω, denoted by $\mathcal{T}_H$, should be employed to avoid committing an inverse crime. The approximate representation

$$\kappa^{[k]}(\boldsymbol{x}) = \sum_{i=1}^{N} \kappa_i^{[k]} S_i(\boldsymbol{x}), \tag{6}$$

is introduced and an initial set of coefficients $\kappa_i^{[0]}, i = 1, \cdots, N$, are prescribed. Let $u_{HP}^{(i)}(\kappa^{[0]}(\boldsymbol{x}))$ denote the solution of (4) with Neumann boundary conditions $f_N^{(i)}$, $i = 1, \cdots, M$, the initial assumed distribution of $\kappa(\boldsymbol{x}) = \kappa^{[0]}(\boldsymbol{x})$ and the discretisation consisting of a mesh with spacing H and elements of order P. This then enables the computation of $\delta^{[0]}u_{HP}^{(i)} = \mathbb{M}_{hp}^{HP}(u_{hp}^{(i)}(\kappa_C(\boldsymbol{x}))) - u_{HP}(\kappa^{[0]}(\boldsymbol{x}))$, $i = 1, 2, \cdots, M$, where $\mathbb{M}_{hp}^{HP} : X_{hp} \to X_{HP}$ denotes a mapping from the discretisation used for the simulation of the data to that used in the inverse problem. Thus, the discrete version of changes in the DtN map: $\delta^{[0]}(\Lambda_\kappa^{hp})^{-1} : Y \to H^{1/2}(\partial\Omega)$

$$\delta^{[k]}((\Lambda_\kappa^{hp})^{-1}(f_N^{(i)})) = \delta^{[k]}u_{HP}^{(i)}|_{\partial\Omega} \qquad i = 1, 2, \cdots, M, \tag{7}$$

is available for $k = 0$. In general, at the kth iteration, $\delta^{[k]}u_{HP}^{(i)} = \mathbb{M}_{hp}^{HP}(u_{hp}^{(i)}(\kappa_C(\boldsymbol{x}))) - u_{HP}^{(i)}(\kappa^{[k]}(\boldsymbol{x}))$, $i = 1, \cdots, M$ is computed. As before, the choice of $\boldsymbol{n} \cdot \kappa \nabla w$ reflects the way in which $\delta^{[k]}u_{HP}^{(i)}|_{\partial\Omega}$ is measured in the practical system. In particular, the solution for the approximate adjoint fields $w_{HP}^{(j)}$ requires the solution of (4) with Neumann boundary conditions $\boldsymbol{n} \cdot \kappa \nabla w = g_N^{(j)}$, $j = 1, \cdots, O, g_N^{(j)} \in Y$. As standard (eg [6, 1] the linearisation of the weak form of the NtD map corresponds to performing iterations of the form

$$x^{[k+1]} = x^{[k]} + \delta x^{[k]} \qquad \text{with} \qquad A^{[k]} \delta x^{[k]} \approx b^{[k]}, \tag{8}$$

where $k = 0, 1, \cdots, x_l^{[k]} = \kappa_l^{[k]}$ and

$$b_{i+M(j-1)}^{[k]} = -\int_{\partial\Omega} \delta^{[k]}u_{HP}^{(i)} g_N^{(j)} \mathrm{d}s, \; A_{i+M(j-1),l}^{[k]} = \int_{\Omega} S_l(\boldsymbol{x}) \nabla w_{HP}^{(j)}(\kappa^{[k]}(\boldsymbol{x})) \cdot \nabla u_{HP}^{(i)}(\kappa^{[k]}(\boldsymbol{x})) \mathrm{d}\Omega \tag{9}$$

with $1 \le i \le M, 1 \le j \le O, 1 \le l \le N$.

Application of LSQR to the inverse problem

Absolute imaging requires the repeated least square solution

$$\text{minimise } \|By - c\|_2 \tag{10}$$

for ill conditioned over determined linear systems of the form $By = c$, where $B = A^{[k]}$, $y = \delta^{[k]}$ and $c = b^{k]}$. Due to the ill conditioned nature of B, the solution of the normal system is not recommended and standard techniques in the electrical impedance community involve either the application of Tikhanov regularisation or a truncated singular value decomposition (eg [6] and references therein). The application of Tikhanov regularisation suffers from the difficulty in choosing an appropriate regularisation parameter, although procedures such as the L-curve can be used to automate this procedure but they do not always give reliable results. The truncated singular value decomposition suffers similarly from the choice of an appropriate level of truncation.

It is well known that the product D^*D, where $*$ denotes the complex conjugate transpose, will be positive definite and symmetric for a general matrix D. The well known conjugate gradient (CG) method converges in n iteration when applied to the solution of a linear system $Cz = d$ when the $n \times n$ matrix C is a symmetric positive definite matrix. However, as noted by [7], a naive application of CG to the solution of the normal equations $B^*By = B^*c$ is doomed to failure as the square matrix B^*B will be more ill conditioned than the already ill conditioned B. Instead, a variant of CG specifically designed for the least square problem (10) should be employed. The CGLS algorithm, although mathematically equivalent to applying the standard CG algorithm to the normal equations, behaves differently for practical computations as it does not require the explicit calculation of B^*B. A further variant called LSQR has been found to offer further benefits when B is ill conditioned. For a more in depth discussion we refer to [7].

By iterating the LSQR variant of CG the iterations $y^{[l]}$ converge to the least square solution described by (10) as $l \to \infty$. But, depending on the maximum number of iterations N_{LSQR}, the resulting approximate solution $x^{[k],[N_{LSQR}]} = y^{[N_{LSQR}]}$ to $By = c$ can be viewed as being either under or over regularised. The maximum iterations should therefore be chosen with care as they will have a direct result on the achievable accuracy for $\|x^{[k],[N_{LSQR}]} - \mathbb{N}_H(\kappa_C)\|$ for $k = 1, 2, \cdots$, where $\mathbb{N}_H(\kappa_C)$ denotes the projection of κ_C on to the basis $S_i(\boldsymbol{x})$, $i = 1, \cdots, N$.

Numerical Example

The research report [1] describes an idealised EIT system consisting of $M = 16$ pairs of electrodes placed around a cylinder of radius $r = 1.5$ so that $\Omega = \{\sqrt{x_1^2 + x_2^2} \leq r\}$. The boundary of the cylinder is made up of the non overlapping electrodes $\Gamma_E = \Gamma_{E,1}^1 \cup \Gamma_{E,2}^1 \cup \Gamma_{E,1}^2 \cup \Gamma_{E,2}^2 \cup \cdots \Gamma_{E,1}^M \cup \Gamma_{E,2}^M$, where $\Gamma_{E,1}^i$ and $\Gamma_{E,2}^i$ denote the first and second electrode for the ith pair, and the non overlapping air-gaps $\Gamma_A = \Gamma_{A,1}^1 \cup \Gamma_{A,2}^1 \cup \Gamma_{A,1}^2 \cup \Gamma_{A,2}^2 \cdots \Gamma_{A,1}^M \cup \Gamma_{A,2}^M$, so that $\partial\Omega = \Gamma_E \cup \Gamma_A$ with $\Gamma_E \cap \Gamma_A = \emptyset$. The selection of the Neumann boundary conditions $f_N^{(i)}$, $i = 1, \cdots, M$, corresponds to the injection of currents at each of the electrode pairs. For injection at the ith electrode pair $I = \int_{\Gamma_{E,1}^i} \boldsymbol{n} \cdot \kappa\nabla u \mathrm{d}s = -\int_{\Gamma_{E,2}^i} \boldsymbol{n} \cdot \kappa\nabla u \mathrm{d}s$ and $\boldsymbol{n} \cdot \nabla u = 0$ on $\Gamma_{E,1}^j, \Gamma_{E,2}^j$, $j = 1, \cdots, M$ with $i \neq j$ and $\Gamma_{A,1}^k, \Gamma_{A,2}^k$, $k = 1, \cdots, M$. In this way the condition $\int_{\partial\Omega} f_N^{(i)} \mathrm{d}s = 0$ is satisfied in each case. Through a suitable choice of $g_N^{(j)}$ the entries in b become the perturbations in voltage differences for different electrode combinations.

The recovery of $\kappa_C = \kappa_{r,c} + \mathrm{i}\kappa_{\mathrm{i},C}$ where

$$\kappa_{r,C} = \begin{cases} (x_1^2 - 1)(x_2^2 - 1) + 1 & (x_1^2 - 1)(x_2^2 - 1) \geq 0 \\ 1 & \text{otherwise} \end{cases}$$

$$\kappa_{\mathrm{i},C} = \begin{cases} 2\omega & -0.25 < x_1 < -0.75 \quad -0.25 < x_2 < -0.75 \\ 1.25\omega & 0.25 < x_1 < 0.75 \quad\quad 0.25 < x_2 < 0.75 \\ \omega & \text{otherwise} \end{cases}$$

and $\omega = 1$, is considered when the voltages are simulated using a discretisation consisting of a unstructured mesh of triangles with maximum size $h = 0.1$ and order $p = 5$ elements. To ensure

No Noise   1% Noise

3% Noise   5% Noise
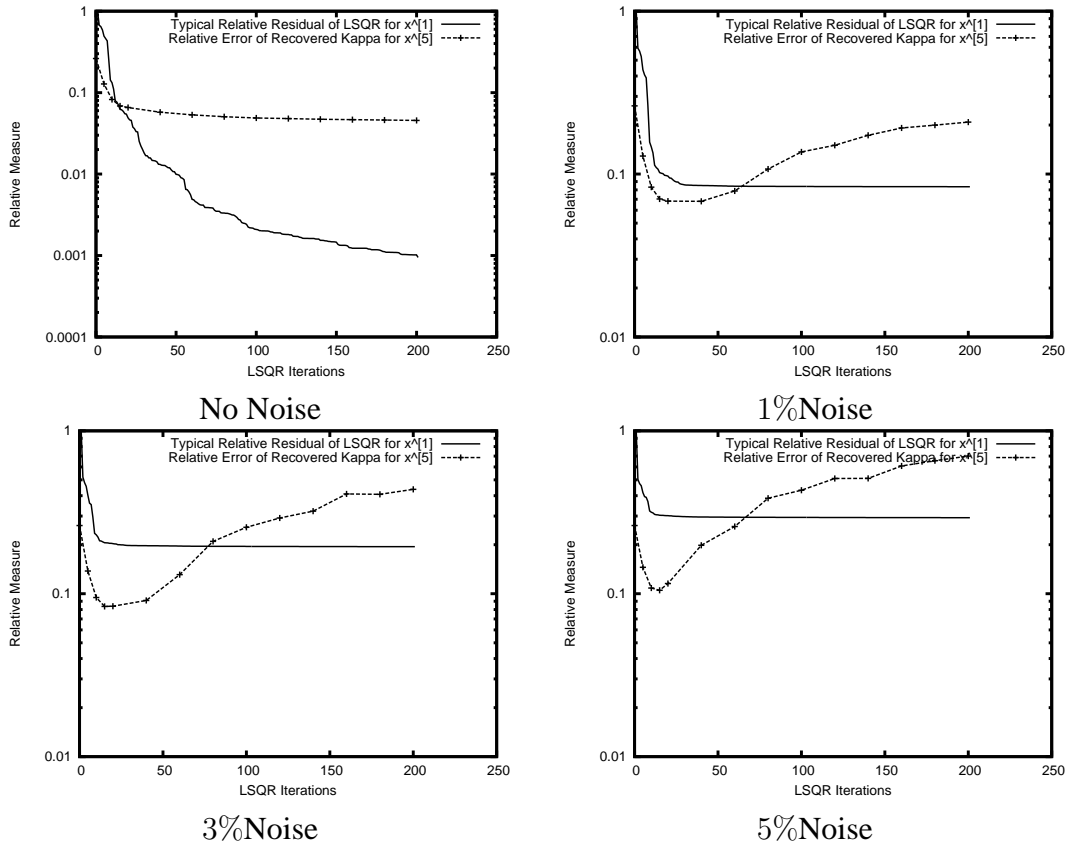
that an inverse crime is not committed the inverse problem is solved using a coarser discretisation consisting of an unstructured mesh of maximum size $H = 0.2$ and order $P = 5$ elements.

The relative residual $r^{[l]} = \|By^{[l]} - c\|/\|c\|$ is computable at each iteration l of the LSQR algorithm. By stopping the LSQR algorithm at different values of N_{LSQR}, and thereby obtaining $x^{[k][N_{LSQR}]}$, $k = 0, \cdots, 5$, the error measure $\|x^{[5][N_{LSQR}]} - \mathbb{N}_H(\kappa_C)\|/\|\mathbb{N}_H(\kappa_C)\|$ is computed for different levels of noise in the simulated voltages. The figure above shows that the choice of N_{LSQR} has a significant effect on the accuracy of the recovered κ distribution in the noisy cases, choosing too few or too many iterations result in accurate recoveries. The figure also suggests that N_{LSQR} should be chosen such that $r^{[l]} = \|By^{[l]} - c\|/\|c\|$ is not substantial reduced for $l > N_{LSQR}$ in order to achieve the minimum value of $\|x^{[5][N_{LSQR}]} - \mathbb{N}_H(\kappa_C)\|/\|\mathbb{N}_H(\kappa_C)\|$.

References

[1] P.D. Ledger, *hp finite element discretisation of the electrical impedance tomography problem* (Submitted). Research Report, Swansea University (2011) http://www.swansea.ac.uk/staff/academic/Engineering/ledgerpaul/

[2] S.C. Brenner and L.R. Scott, *The Mathematical Theory of Finite Element Methods*, Springer 1994.

[3] C. Schwab *p- and hp- Finite Element Methods: Theory and Applications in Solid and Fluid Mechanics*, Oxford University Press, Oxford,1998.

[4] L. Demkowicz, *Computing with hp-Adaptive Finite Elements: Volume 1: One and Two Dimensional Elliptic and Maxwell Problems*, Chapman and Hall, Boca Raton FL, USA, 2007.

[5] A.P. Calderón, *On an inverse boundary value problem*, Seminar on Numerical Analysis and its Applications to Continuum Physics, Rio de Janeiro (1980).

[6] W. Lionheart and N. Polydordes and A Borsic, *The reconstruction problem. Part 1 - Electrical Impedance Tomography: Methods, History and Applications*, 3-64pp, Editor D S Holder, Institute of Physics 2004.

[7] A. Björck, *Numerical Methods for Least Squares Problems*, SIAM (1996).

4

EIT 2011, Dept. Electronic & Electrical Engineering, University of Bath

12TH INTL. CONFERENCE IN ELECTRICAL IMPEDANCE TOMOGRAPHY (EIT 2011), 4-6 MAY 2011, UNIV. OF BATH   1

Scaling the EIT Problem

Alistair Boyle, Andy Adler, Andrea Borsic

Abstract

There are a number of interesting problems that could be tackled if the computing capacity of current EIT systems can be improved. We examined the performance of two such systems and found that a noticeable portion of the compute time is spent in finding the solution of sparse matrices. We developed and used a new sparse matrix testbench, Meagre-Crowd, to evaluate a selection of these sparse matrix solvers and found that there are definite performance gains available.

I. Introduction

THE procedure used to solve inverse problems in areas such as Electrical Impedance Tomography (EIT) involves numerous steps to determine a solution. Software such as EIDORS [1] implement these algorithms using the numerical linear algebra tools in MatLab to manipulate sparse matrices that result from a Finite Element Method (FEM) formulation.

Computing power has increased according to Moore's law for 40 years, approximately doubling every 18 months [2]. Until recently, this has been achieved by increasing processor clock frequencies and a corresponding improvement in instructions-per-second throughput and memory bandwidth. Taking advantage of these improvements has involved little software cost. Purchasing a new processor gains one the advantages of the new hardware when the software is recompiled. In recent years, the benefits of increasing clock frequency have been limited by power consumption. Manufacturers have turned to System-on-Chip (SoC) with multiple processor cores to maintain Moore's Law for commodity processors. Simultaneously, the cost of computing power has dropped appreciably.

This change has fundamentally altered the computing landscape. To take advantage of the continuing growth in computing power, and thus, the ability to solve ever more complicated problems, software developers are now being forced to deal with issues previously limited to those developing High Performance Computing (HPC) applications. They are venturing into the world of symmetric multiprocessing (SMP) and distributed memory computing with the widely used OpenMP and MPI standards.

For EIT, increases in problem size, in terms of required computing power, come from a number of sources: the number of nodes and elements in a discretization of the domain, the dimensionality (handling of two- versus three-dimensional domains), processing of time series data, and correlating other modalities such as CT with EIT, amongst others.

There are many ways to increase the capacity of the EIT data processing system by taking advantage of SMP and distributed resources. A quick analysis of EIDORS's use of compute time for a sample problem (Figure 1a, Section II) showed that a significant amount of time was spent in the determination of the Jacobian matrix. This step primarily employed the MatLab numerical linear algebra solver. (Where the complexities are tucked away behind the backslash $A \backslash b$ operator.) This is a relatively easy component to swap out since the solver is treated as a black box and there are a number of alternatives available.

In this work, we examine the performance of EIDORS as the size of EIT problem scales and show preliminary performance results for a selection of alternative sparse matrix solvers using an independent testbench we have developed, Meagre-Crowd.

A. Boyle and A. Adler are with the Department of Systems and Computer Engineering, Carleton University, Ottawa, ON
e-mail: boyle@sce.carleton.ca
A. Borsic is with the Thayer School of Engineering at Dartmouth, Hanover, NH

EIT 2011, Dept. Electronic & Electrical Engineering, University of Bath

12TH INTL. CONFERENCE IN ELECTRICAL IMPEDANCE TOMOGRAPHY (EIT 2011), 4-6 MAY 2011, UNIV. OF BATH   2
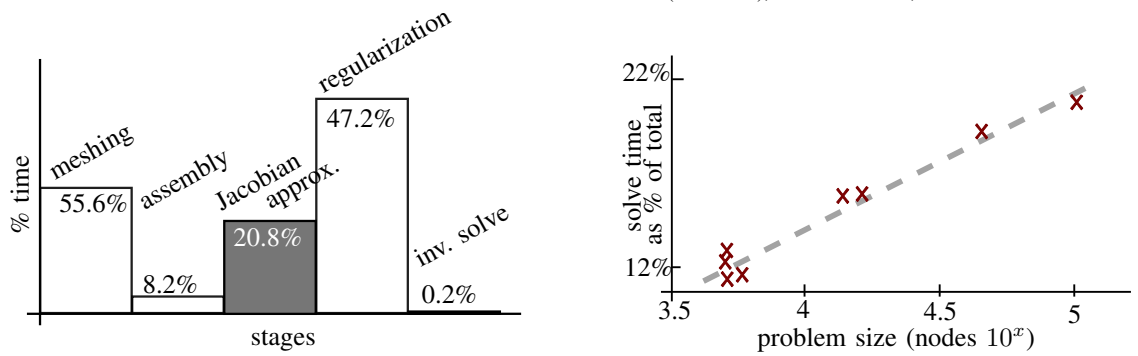
(a) Profiling EIDORS; a 101421 node 3D difference EIT problem

(b) Ratio of Jacobian approximation to total time as node density increased

Fig. 1.   Performance of EIDORS for a 3D difference EIT problem; 8 core, 64GB, 2.66GHz Intel Xeon X5550
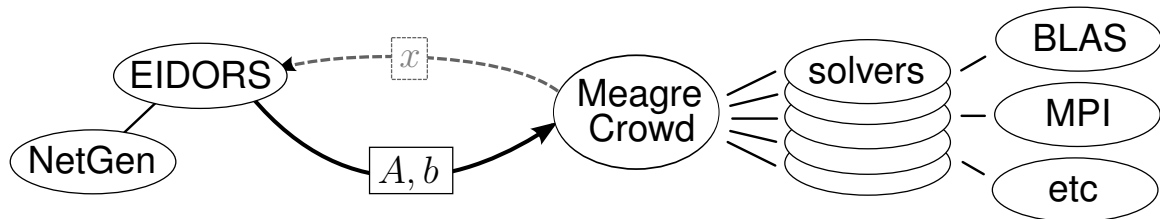

Fig. 2.   Test bench dependencies: EIDORS, NetGen, Meagre-Crowd and assorted solvers and their dependencies (BLAS, MPI, etc.)

II. Performance Profiling EIDORS

EIDORS is a testbed for algorithm development running in MatLab, so it is certainly not optimized for maximum performance. None the less, it is representative of the computational requirements of the EIT inverse problem. The procedure for finding a linearized solution can be roughly divided into five stages: mesh generation, system matrix assembly, Jacobian approximation, inverse regularization, and finding the inverse solution. In the mesh generation phase, a domain is divided into, for example, triangles or tetrahedra, for use in the FEM formulation. This mesh is then assembled into a forward system matrix that contains a system of equations describing both the properties of the domain and the boundary conditions. A Jacobian is approximated using this forward problem by adjusting conductivities and estimating their effect on the measurements. The Jacobian is regularized (including calculating a dense matrix inverse) to form an inverse problem that is tractable. Finally, the inverse problem is solved by multiplying with difference measurement data to determine a conductivity distribution that could have resulted in the measurements. Finding the Jacobian involves numerous solutions using the sparse forward system matrices and therefore, requires an efficient sparse solver to achieve reasonable performance as the problem size scales.

A difference EIT problem was selected for profiling. (3D, 3 planes of 15 electrodes, 101421 nodes, 548299 elements, single-step difference EIT, EIDORS 3.4, NetGen 4.9.11, MatLab 7.11.0.584 (R2010b containing UMFPACK 5.4.0), 8 core Intel Xeon X5550 @ 2.67GHz SMP system, 64GB memory.) It was found that meshing took 169.12 seconds, model assembly took 24.95 seconds, the Jacobian approximation took 126.324 seconds, regularization took 287.272 seconds, and the final solution was determined in 0.82 seconds (Figure 1a). The ratio of time spent in the Jacobian approximation stage compared to the total working time to obtain a solution was found to grow logarithmically with the node density (Figure 1b).

Similar initial profiling results were obtained using the New Dartmouth Reconstructor Mat-lab (NDRM) EIT code [3], solving absolute EIT reconstructions with a non-linear Tikhonov regularized Gauss-Newton solver.

III. Alternative Solvers

The requirement for a sparse solver used in general EIT problems is that for real-valued system matrices, the solver can handle symmetric matrices, while for complex-valued system

EIT 2011, Dept. Electronic & Electrical Engineering, University of Bath

12TH INTL. CONFERENCE IN ELECTRICAL IMPEDANCE TOMOGRAPHY (EIT 2011), 4-6 MAY 2011, UNIV. OF BATH   3

matrices (generally, not symmetric or Hermitian), the solver must be able to handle an unsymmetric system. Since the EIT problem can be structured as a square system matrix, solvers capable of QR decomposition are not required. In general, symmetric solvers perform in nearly the same manner as unsymmetric solvers (using similar algorithms) but must handle twice as many values. Therefore, symmetric solvers can be expected to perform twice as fast as unsymmetric solvers. For this reason, we chose to focus on unsymmetric solvers as a more general case. Similarly, we focused on real valued solvers though, in principle, these results can be extended to complex systems because the algorithms are the same with twice the numeric throughput.

Meagre-Crowd 0.4.5 [4] was used to test the performance of the sparse matrix solvers: UMFPACK 5.5.0 [5], MUMPS 4.9.2 [6], WSMP 11.01.19 [7], Pardiso 4.1.1 [8], TAUCS 2.2 [9] and CHOLMOD 1.7.1 [10]. We developed Meagre-Crowd as a new open source project that integrates sparse solvers in a common framework to benchmark sparse linear algebra performance. Code was released under the GPL. The benchmark used a shared set of dependencies so that various versions of MPI, BLAS and LAPACK (optimized to varying degrees) did not affect the results. It should be emphasized that choosing an implementation of MPI and BLAS optimized for the current platform does have a significant effect on the run-time but does not affect inter-solver comparisons within the Meagre-Crowd testbench.

A set of test matrices were generated using EIDORS 3.4 as described in the previous section. These matrices were 5041 to 101465 on a side containing 35301 to 769590 non-zero entries so that there were 5041 to 101465 unknowns solved 45 times (45 orthogonol stimulation patterns). The maximum size of the generated matrices was limited by MatLab's memory usage (64GB). Matching right-hand sides were generated to give 45 orthogonal solutions for use in the Jacobian approximation. In addition, the expected solution was stored and compared at the conclusion of each testbench run as a check of solution validity. All problems were real-valued and consequently symmetric, but the (full) unsymmetric sparse matrices were used in these tests. (CHOLMOD was a symmetric-only solver used as a comparison versus the unsymmetric solvers.) These matrices were loaded into the Meagre-Crowd testbench running on an Intel Core2 Duo T9550 at 2.66GHz with 3GB of memory. Memory usage for most solvers remained below 1GB with the exception of UMFPACK on the largest problem at 2.1GB, indicating that memory capacity was not a factor in the sparse solvers' ability to find a solution.

Solution time was defined as the time to proceed through the sparse solver phases: re-ordering, symbolic and numeric factorization, substitution and iterative refinement. The two solvers capable of multicore operation on unsymmetric matrices (WSMP and MUMPS) were compared against the field of solvers in Figure 3. The figure shows solver performance benchmarked against UMFPACK's so that, for example, at 100,000 nodes CHOLMOD was nearly seven times faster than UMFPACK.

IV. OBSERVATIONS

Absolute solver performance in terms of time-to-solution is directly related to the volume of data that is being handled. Matrices found in typical FEM formulations are stored in a sparse format that does not record the zero entries in the matrix. The number of non-zeros in the sparse matrix structure directly determine the quantity of data that must be moved over the network, in memory, and through caches. During the solution process, the sparsity and specific structure of the matrix determines the degree of fill-in, the expansion in quantity of data to be stored as a solution is derived. Solution times for UMFPACK ranged from 563ms to 7 minutes and 41 seconds; though, solution times on the smallest problems varied by a factor of two or more.

In Figure 3, we observed a noticeable performance benefit for large matrices with both MUMPS and WSMP when compared to UMFPACK, particularly when multicore capabilities

EIT 2011, Dept. Electronic & Electrical Engineering, University of Bath

12TH INTL. CONFERENCE IN ELECTRICAL IMPEDANCE TOMOGRAPHY (EIT 2011), 4-6 MAY 2011, UNIV. OF BATH   4
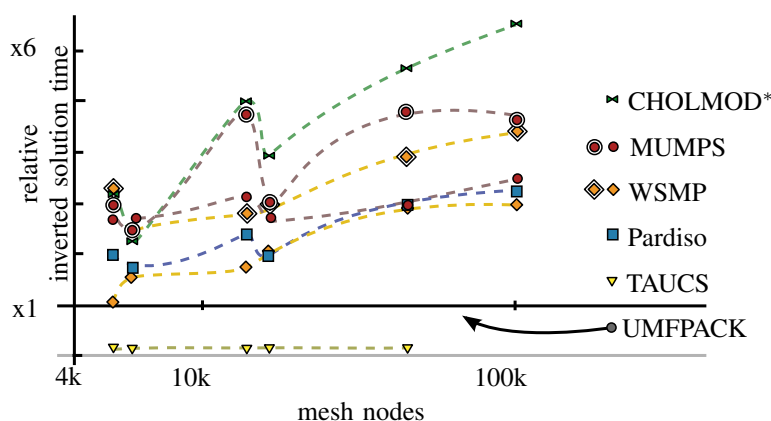

Fig. 3.   Solver Scaling: Mesh Size and Compute Nodes, solver performance for a range of mesh sizes. (Inverted solution time was measured relative to UMFPACK, where $N = t_{\text{UMFPACK}}/t_{\text{solver}}$ so that a faster solver was plotted as N times faster than UMFPACK. For WSMP and MUMPS, results for two-cores have a double-symbol. *Note that CHOLMOD is a symmetric sparse matrix solver while the others are handling unsymmetric matrices.) [Preliminary results.]

were used. CHOLMOD, the symmetric solver, showed the benefits of a reduced quantity of data. As problem size was increased, CHOLMOD increased its performance over the other solvers. The solver TAUCS, an Out-of-core (OOC) solver, was very slow due to the overhead of disk access but never exceeded more than 100MB of memory for the largest problem size. Presumably, the largest problems could be handled by a solver such as TAUCS that's performance will not be limited by memory capacity.

V. DISCUSSION

Observations regarding the performance of EIDORS (and consequently, MatLab) as the size of EIT problem scales show the limitations of the system as memory consumption and solution time grow to the capacity of the available resources. Using an independent testbench, Meagre-Crowd, we show preliminary performance results for a selection of alternative sparse matrix solvers. Solvers examined in the testbench were not optimized, but with preliminary default settings, respectable improvements are possible. Performance that grows with problem size is possible in the sparse solver portion of the EIT solution process.

Other opportunities for higher-level parallelism have not been explored here: pipe-lining of tasks and splitting of tasks such as the Jacobian calculations. Combining these higher-level algorithmic changes with the latest in sparse solvers could lead to appreciable improvements in the capacity of current EIT systems.

ACKNOWLEDGEMENTS

REFERENCES

[1] A. Adler and W. R. B. Lionheart, "Uses and abuses of EIDORS: An extensible software base for EIT," *Physiol. Meas.*, vol. 27, no. 5, pp. S25–S42, May 2006.
[2] R. Schaller, "Moore's law: past, present and future," *IEEE Spectrum*, vol. 34, no. 6, pp. 52–59, Jun. 1997.
[3] A. Borsic, A. Hartov, K. Paulsen, and P. Manwaring, "3d electric impedance tomography reconstruction on multi-core computing platforms," *Proceedings IEEE EMBC'08, Vancouver*, Aug. 2008.
[4] A. Boyle, "Meagre-crowd: A sparse solver testbench," Mar. 2011. [Online]. Available: https://github.com/boyle/meagre-crowd
[5] T. Davis, "Algorithm 832: Umfpack, an unsymmetric-pattern multifrontal method," *ACM Transactions on Mathematical Software*, vol. 30, no. 2, pp. 196–199, 2004.
[6] P. Amestoy, A. Guermouche, J.-Y. L'Excellent, and S. Pralet, "Hybrid scheduling for the parallel solution of linear systems," *Parallel Computing*, vol. 32, no. 2, pp. 136–156, 2006.
[7] A. Gupta, G. Karypis, and V. Kumar, "A highly scalable parallel algorithm for sparse matrix factorization," *IEEE Transactions on Parallel and Distributed Systems*, vol. 8, no. 5, pp. 502–520, May 1997.
[8] O. Schenk and K. G "Solving unsymmetric sparse systems of linear equations with pardiso."
[9] S. Toledo, D. Chen, and V. Rotkin, "Taucs: A library of sparse linear solvers," vol. 2.2, 2003. [Online]. Available: http://www.tau.ac.il/~stoledo/taucs/
[10] Y. Chen, T. Davis, W. Hager, and S. Rajamanickam, "Algorithm 887: Cholmod, supernodal sparse cholesky factorization and update/downdate," *ACM Trans. Math. Software*, vol. 35, no. 3, Oct. 2008.

Breast EIT using a new projected image reconstruction method with multi-frequency measurements

Eun Jung Lee[1], Jin Keun Seo[1], Munkh Erdene[1], Tong In Oh[2] and Eung Je Woo[2]
[1]Department of Computational Science and Engineering, Yonsei University, Seoul, KOREA
[2]Department of Biomedical Engineering, Kyung Hee University, Gyeonggi-do, KOREA
E-mail: seoj@yonsei.ac.kr

Abstract. We propose a new projected image reconstruction method for breast EIT imaging. We separate voltage-sensing electrodes and current-injection electrodes in such a way that internal currents induced by a pair of current-injection electrodes flow approximately along the tangential direction of the array of the voltage-sensing electrodes. This kind of tangential current flows allow us to measure voltages between equipotential lines in the normal direction to the voltage-sensing electrode array. With this electrode configuration, we apply a new projected image reconstruction algorithm using multiple boundary voltage data. We should note that the data-acquisition method is different from that of X-ray projection, T-scan and frontal plane techniques because we do not get any data along a plane that is perpendicular to the current flow. We present numerical simulation results to accurately detect and localize small anomalies.

1. Introduction

Breast imaging using electrical impedance tomography (EIT) has been actively studied since there cancerous breast tissues have significantly different admittivity values compared with surrounding normal tissues. In terms of electrode configuration and reconstruction method, there are several approaches; EIT image reconstruction using a probe with a compact array of electrodes placed over the breast [1], EIT image reconstruction using two plates of planar arrays of electrodes with the breast between them [2-4], T-scan method using a probe with an array current-sensing electrodes to measure exit currents induced by an applied voltage [5], linearized EIT reconstruction with a hemisphere geometry [6] and so on. For previous researches on breast EIT, please refer [7] and references therein.

In this paper, we propose a new image reconstruction method for breast EIT. We use an array of voltage-sensing electrodes placed on a curved probe and two pairs of current-injection electrodes. We try to locate the voltage-sensing electrodes and current-injection electrodes in such a way that induced internal currents flow approximately along the tangential direction of the voltage-sensing electrodes. This kind of planar current flows will allow us to measure voltages between induced equipotential lines in the normal direction to the voltage-sensing electrode array. The new conductivity reconstruction algorithm produces a projected conductivity image using multi-frequency boundary voltage data.

We should note that the proposed method utilizes changes in measured voltage data with respect to frequency along current flow directions, unlike the conventional projection techniques such as T-scan which uses a planner probe (like X-ray) that is perpendicular to current flow directions. We present numerical simulation results of the new method to detect and localize small anomalies.

2. Methods

2.1. Electrode configuration

Figure 1 shows the proposed electrode configuration for breast EIT. The probe is curved so that the tangential direction of the probe surface with voltage-sensing electrodes is approximately parallel to the directions of internal current flows.
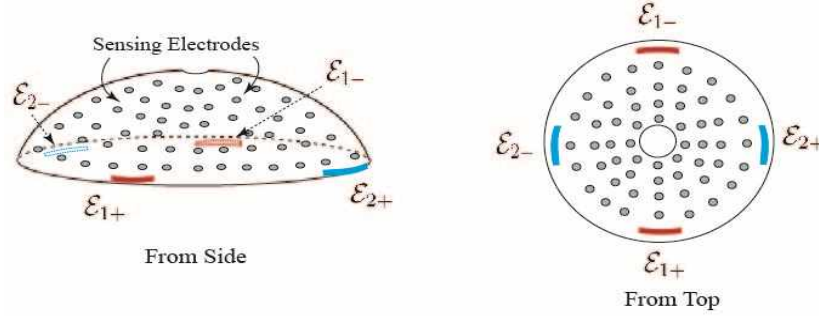
Figure 1. Proposed electrode configuration for breast EIT.

2.2. Frequency-difference method and choise of frequencies

For breast imaging, we should adopt a frequency-difference EIT method [8,9] since a time-referenced measurement data without any anomaly is not available. We let $\sigma+i\omega\varepsilon$ be the admittivity and both σ and $\omega\varepsilon$ have a unit of S/m. Note that $\sigma+i\omega\varepsilon=\sigma+i2\pi f\varepsilon_0\varepsilon_r$ where $\varepsilon_0=8.854\times10^{-12}$ F/m is the permittivity of the free space and ε_r is the relative permittivity. We assume that $\omega\varepsilon_n/\sigma_n\leq1/50$ for a frequency $f=\omega/2\pi \geq 50$kHz where the subscript n stands for a normal tissue. We assumed admittivity values of normal and cancerous breast tissues as in table 1 where the subscript c stands for a cancerous tissue. For a successful anomaly detection, we should carefully choose two frequencies ω_1 and ω_2. We chose $f_1=\omega_1/2\pi$ and $f_2=\omega_2/2\pi$ such that $50 \leq f_1 \leq 500$ Hz and $50 \leq f_2 \leq 500$ kHz.

Table 1. Assumed admittivity values of normal (n) and cancerous (c) breast tissues.

$f=\omega/2\pi$ [Hz]	σ_n [S/m]	σ_c [S/m]	$\omega\varepsilon_n$ [S/m]	$\omega\varepsilon_c$ [S/m]
≤500	0.03	0.2	$\ll \sigma_n$	$\ll \sigma_c$
50×10^3	0.03	0.2	5.6×10^{-4}	1.7×10^{-2}
100×10^3	0.03	0.2	2.8×10^{-4}	2.2×10^{-2}
500×10^3	0.03	0.2	1.1×10^{-3}	5.6×10^{-2}

2.3. Image reconstruction algorithm

For chosen f_1 and f_2, γ_1^ω and γ_2^ω denote corresponding admittivity values. Then, the governing equation implies the following relation:
$$\nabla \ln \gamma_i^\omega \cdot \nabla u_j^\omega = -\nabla^2 u_j^\omega, \ \ i,j = 1,2.$$
Applying a linear approximation by using measured boundary voltage data F_j^ω corresponding to γ_j^ω, we get the following expression for a frequency difference of $\delta(\ln(\gamma^\omega)) = \ln(\gamma_2^\omega) - \ln(\gamma_1^\omega)$:
$$\nabla^2(\delta\ln(\gamma^\omega)) \approx -(F_2^\omega - F_1^\omega) \ \ \text{in } \Gamma$$
$$\delta\ln\gamma^\omega = 0 \ \ \text{on } \partial\Gamma.$$
We reconstruct a frequency-difference admittivity image by solving the above equation.

3. Results

Figure 2 shows a finite element model of the thorax including two breast regions. We placed the curved probe on the left breast. Figure 3 plots reconstructed conductivity images of the model in figure 2 using the proposed image reconstruction algorithm.
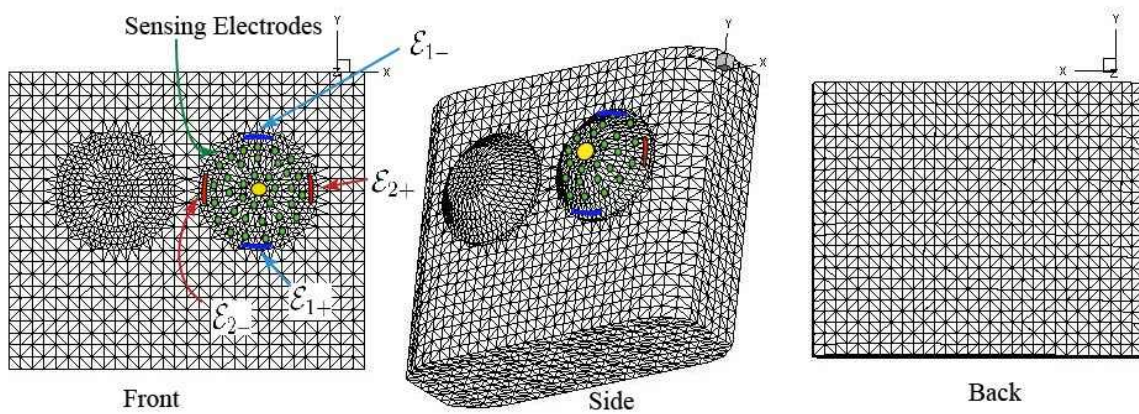
Figure 2. Numerical model of the thorax for breast EIT.
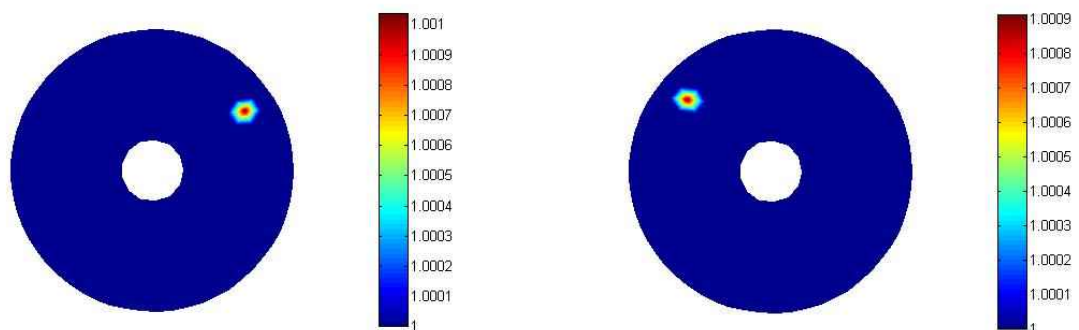
(a) One anomaly at (1.7,0.6,2.4).   (b) One anomaly at (0.5,0.3,2.4).

(c) Three anomalies at (1.7, 0.6, 2.4), (0.5, 0.3, 2.4) and (1.5, -0.6, 2.55).

Figure 3. Reconstructed conductivity images of the left breast.

4. Discussion and Conclusions

We developed a new direct image reconstruction method for locating breast tumor using multi-frequency boundary voltage data sets. Using the proposed algorithm, we can produce conductivity images clearly 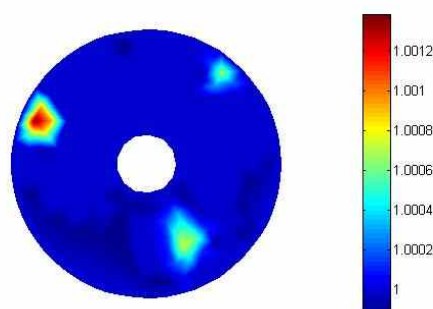distinguishing small anomalies. Simulation results show that the method is promising with a good image quality. We may implement the proposed electrode configurations using a breast cup or belt with electrodes or individual electrodes. We suggest future studies of admittivity imaging experiments on phantoms and human subjects.

Acknowledgments

References

[1] Cherepenin V A, Karpov A Y, Korjenevsky A V, Kornienko V N, Kultiasov Y S, Ochapkin M B, Trochanova O V and Meister J D 2002 Three-dimensional EIT imaging of breast tissues: system design and clinical testing *IEEE Trans. Med. Imaging* **21** 662–7

[2] Mueller J L, Isaacson D and Newell J C 1999 A reconstruction algorithm for electrical impedance tomography data collected on rectangular electrode arrays *IEEE Trans. Biomed. Eng.* **46** 1379-86

[3] Mueller J L, Siltanen S and Isaacson D 2002 A direct reconstruction algorithm for electrical impedance tomography *IEEE Trans. Med. Imaging* **21** 555–9

[4] Choi M H, Kao T J, Issacson D, Saulnier G J and Newell J C 2007 A reconstruction algorithm for breast cancer imaging with electrical impedance tomography in mammography geometry *IEEE Trans. Biomed. Eng.* **54** 700-10

[5] Assenheimer M, Laver-Moskovitz O, Malobek D, Manor D, Nahliel U, Nitzan R and Saad A 2001 The T-scan technology: electrical impedance as a diagnostic tool for breast cancer detection *Physiol. Meas.* **22** 1–8

[6] Soni N K, Hartov A, Kogel C, Poplack S P and Paulsen K D 2004 Multi-frequency electrical impedance tomography of the breast: new clinical results *Physiol. Meas.* **25** 301-14

[7] Hartov A, Soni N and Halter A 2005 Breast cancer screening with electrical impedance tomography, in Electrical Impedance Tomography: Methods, History and Applications, IOP Publishing Bristol UK 167–85

[8] Seo J K, Lee J, Kim S W, Zribi H and Woo E J 2008 Frequency-difference electrical impedance tomography (fdEIT): algorithm development and feasibility study *Physiol. Meas.* **29** 929-44

[9] Jun S C, Kuen J, Lee J, Woo E J, Holder D and Seo J K 2009 Frequency-difference EIT (fdEIT) using weighted difference and equivalent homogeneous admittivity: validation by simulation and tank experiment *Physiol. Meas.* **30** 1087-99

Electrode positions and current patterns for 3D EIT

Y. Mamatjan[1], D. Gürsoy[2] and A. Adler[1]
[1]Carleton University, Ottawa, Canada
[2]Institute of Medical Engineering, Graz University of Technology, Austria

Abstract: For a 3D electrical impedance tomography (EIT) system, it is necessary to improve electrode geometries placed around a body surface, and correspondingly apply stimulation and measurement patterns to produce maximum distinguishability. Advanced EIT image reconstruction requires designing systems with the electrode geometry and current injection such that the full ensemble of measurements provides as high SNR as possible over all of the volume under investigation not only for over a certain region of interest. A 3D two-electrode plane simulation study is undertaken using 7 electrode geometries and 16 different stimulation and measurement patterns for each electrode geometry. The simulation results show that several electrode geometries and current patterns produced promising results with the high distinguishability which can subsequently lead to improved image reconstruction.

1 Introduction

In Electrical Impedance Tomography (EIT), several publications [1, 2] reported that the linear relationship between global tidal impedance variation and tidal volume cannot be used to calculate end-expiratory lung volume (EELV), since EELV is a global parameter of the whole lung while impedance is measured only at one thoracic level that reflects the impedance variations only in one cross-section of the thorax. Thus, it becomes necessary to develop 3D multiplane EIT to provide more information not only about the regional volume redistribution but also about aeration and ventilation of the whole lung.

The distinguishability of EIT systems is determined by several factors such as current stimulation amplitude, the accuracy of voltage measurement, stimulation and measurement patterns, and the number and placement of electrodes [3]. This paper investigates various electrode geometies combined with different stimulation and measurement patterns. Regarding current patterns, the early consideration on optimizing the drive patterns for EIT was done by [4] using a pair of point drive electrodes approach. Many EIT systems are based on the adjacent voltage measurement as the Sheffield Mark I described by [5] that currents are applied through neighbouring electrodes and the voltages are measured from all remaining adjacent electrode pairs. Various electrode placement strategies within a two-electrode plane were investigated by [6] using only adjacent drive patterns. Recently in [3], we investigated various stimulation and measurement patterns by applying a new distinguishability criterion as a complementary to the previous studies done by [7, 8]. We suggested that the stimulation and measurement patterns separated radially by one electrode less than 180 as the optimal current pattern in a single electrode plane. This new result motivated us to further investigate electrode placement strategies in multiple planes with optimized current patterns to maximize the distinguishability.

In this paper, a 3D simulation was conducted to investigate 7 different electrode geometries with16 different stimulation and measurement patterns (from adjacent to opposite patterns) for each electrode geometry. We simulated each scenario for (i) a single cubic object for in-plane and off-plane, and (ii) two full-height cylindrical objects using a 3D circular Finite Element Model (FEM). We used the formulation for the distinguishability of conductivity targets [3] and applied it for designing electrode positions and finding stimulation and measurement patterns with maximum distinguishability for each electrode position.

2 Methodology

2.1 Distinguishability

We briefly describe the distinguishability formulation in this section but more details can be found in[3]. An EIT system makes a set of transfer impedance measurements from an array of electrodes placed around a body. Most EIT systems apply a set of current patterns k at electrodes to make a set of voltage measurements $\mathbf{v}^k = \mathbf{T}(\boldsymbol{\sigma}_0)\mathbf{c}^k$, where $\mathbf{T}(\boldsymbol{\sigma}_0)$ is the *transfer impedance* matrix of the medium with impedance distribution $\boldsymbol{\sigma}_0$ (in units of Ω). We can define a transfer impedance change $\mathbf{T}_{\triangle} = \mathbf{T}(\boldsymbol{\sigma}_0) - \mathbf{T}(\boldsymbol{\sigma}_1)$ for a small perturbation $\boldsymbol{\sigma}_1$. Difference imaging was used to produce images of conductivity changes , $\Delta\boldsymbol{\sigma} = \boldsymbol{\sigma}_1 - \boldsymbol{\sigma}_0$ between two states by taking the reference data set ($\mathbf{d_0}$) and further measurements ($\mathbf{d}$) after a certain time interval to provide time-difference measurements $\Delta\mathbf{d} = \mathbf{d} - \mathbf{d_0}$. This method can be applied to image conductivity changes that occur in the human body as a result of physiological functions *i.e* breathing.

Since we generally want to distinguish small changes in conductivity, we linearize around $\boldsymbol{\sigma}_0$ to obtain a conductivity change with a linear function of measurements as $\Delta\mathbf{d} = \mathbf{J}\Delta\boldsymbol{\sigma} + \mathbf{n}$, where $\mathbf{J}$ is Jacobian and $\mathbf{n}$ is zero-mean white Gaussian noise with covariance $\boldsymbol{\Sigma}_n$.

From measurements $\Delta\mathbf{d}$, an impedance change image estimate $\Delta\hat{\boldsymbol{\sigma}}$ is reconstructed from a linearized difference EIT reconstruction algorithm as defined from the norm

$$\Delta\hat{\boldsymbol{\sigma}} = arg\ \min_{\boldsymbol{\sigma}} \|\Delta\mathbf{d} - \mathbf{J}\Delta\boldsymbol{\sigma}\|_{\boldsymbol{\Sigma}_n^{-1}} + P(\boldsymbol{\sigma}), \tag{1}$$

where $P(\cdot)$ represents a penalty or regularization term.

We are interested in the image output $m = A_R\Delta\bar{\sigma}_R$ within a ROI of area A_R with an average impedance change in ROI ($\Delta\bar{\sigma}_R$). In order to *distinguish* $\boldsymbol{\sigma}_1$ from $\boldsymbol{\sigma}_0$, we must reject the null hypothesis H_0: $m = 0$. The probability of H_0 is based on the z-score, which may be further calculated as

$$z = \frac{\bar{m}}{\sigma_m} = \frac{A_R\Delta\bar{\sigma}_R}{\left(\mathbf{R}_R^t\boldsymbol{\Sigma}_n\mathbf{R}_R\right)^{\frac{1}{2}}} = A_R\Delta\bar{\sigma}_R\sqrt{\mathbf{J}_R^t\boldsymbol{\Sigma}_n^{-1}\mathbf{J}_R} = \sqrt{\Delta\mathbf{d}\boldsymbol{\Sigma}_n^{-1}\Delta\mathbf{d}} = \|\Delta\mathbf{d}\|_{\boldsymbol{\Sigma}_n^{-1}}$$

where $\mathbf{J}_R = \frac{1}{A_R}\mathbf{J}$, since we require $\Delta\mathbf{d} = \mathbf{J}_R m$ for changes in the ROI.

The proposed formulation for the distinguishability [3] in terms of a hypothesis test shows that distinguishability is a product of impedance change amplitude, measurement strategies and the inverse of noise amplitude. In this paper we aim to maximize the distinguishability by investigating various combinations of electrode placement strategies, and stimulation and measurement patterns.

2.2 Simulation

EIDORS [9] was employed for simulating electrode geometries and current patterns. A tank phantom in Fig. 1 was modelled for all the simulations. The EIT model has been reconfigured to calculate the Jacobian using Netgen by simulating current patterns and measuring signals from corresponding electrodes.

Electrode geometries and current patterns: A cylinder (30 cm height and 28 cm of diameter) is encircled by 2-plane 8 electrodes which are positioned with the equal distance to middle of the cylinder with the distance of 4 cm between two electrode layers as shown in Fig. 1. All distances are normalized to the height of the cylinder. We investigated 7 electrode placement (EP) strategies: Planar, Planar-offset, Planar-opposite, Zigzag, Zigzag-offset, Zigzag-opposite and Square proposed by [6] for an adjacent pattern and we extended them with 16 different injection and measurement patterns for each EP.
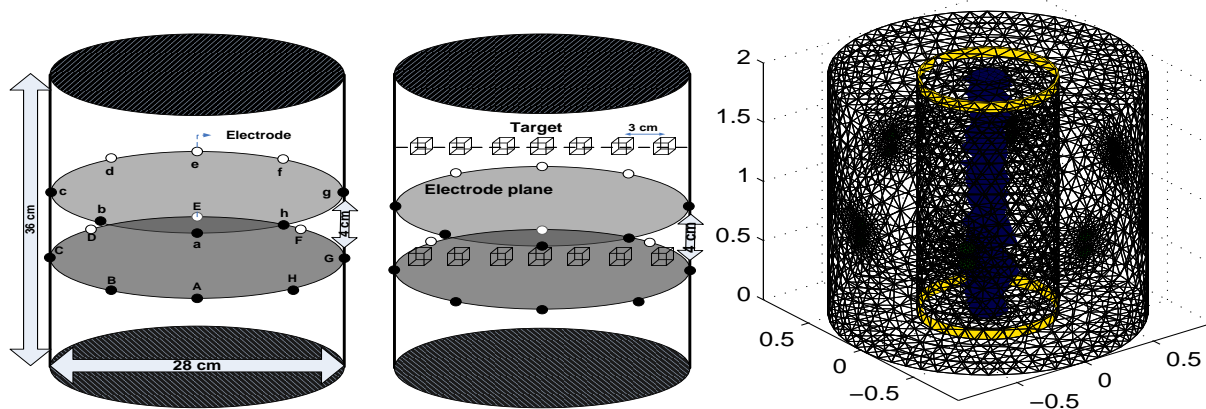
Figure 1: A diagram of *left*: Planar electrode configuration with two-layer 16 electrodes, *middle*: a single cubic object moving horizontally in two vertical planes, *right*: two cylindrical targets with the same volume spaning the full height of the cylindrical volume (2.5 D).

The objective is to select a combination of such an electrode geometry with current patterns that the full ensemble of measurements provides high z value not only in a limited region of interest but also near areas in and out of electrode plane for impedance measurement. A diagram of electrode placement configuration for Planar electrode configuration is shown in Fig. 1:*left*. For the offset arrangement, the lower plane electrodes were rotated to be positioned at the half inter-electrode distance. For each EP and simulation protocol, a sequence of current patterns is injected and voltages are measured to form a data set, where separate electrodes are used for stimulation and measurement.

Stimulation ($\Delta_s = 1, ..., 8$) and measurement ($\Delta_m = 1, ..., 8$)patterns are defined by the distance between the two active electrodes for the stimulation or measurement function and labled as Δ_{sm}. In this study we considered equal stimulation and measurement patterns ($\Delta_s = \Delta_m$). For the two-layer electrodes, the adjacent or opposite stimulation is depend on the electrode geometry and current injection patterns unlike a single-layer electrodes in [3], so it should be noted that current pattern Δ_{11} is an adjacent stimulation and measurement pattern for Planar, Planar-offset, Zigzag, Zigzag-offset, and Square geometries, while Δ_{11} is an opposite pattern for Planar-opposite and Zigzag-opposite geometries. Δ_{44} is an opposite pattern for Planar, Planar-offset, Zigzag, Zigzag-offset, and Square geometries.

Simulation models: Two different simulation models were used based on (i) a single cubic object and (ii) two cylindrical objects with full-height perturbation. The background conductivity is 1 S/m and the target conductivity is 0.005 S/m. For (i), the simulation was performed by moving a target of 50 ml in two different vertical planes for 14 horizontal positions in the tank (Fig. 1:*middle*) with 3 cm steps. First vertical plane for the object is set in between two electrode planes, which we call the *central-plane* and the second vertical plane is 6 cm above the *central-plane* (Fig. 1:*middle*).

For (ii), two cylindrical objects of the same volume in 2.5 D span the full height of the tank. A central object is fixed in the center and the other outer object, wrapped around the central object, is expanded with 2 cm steps to 5 different sizes of radius without changing total volume in Fig. 1:*right*. For the distinguishability of two objects, distinguishability values for simulation were calculated directly using the distinguishability criteria formulated in section 2.1 taking into account the average distinguishability values. It is a measure of the

3

ability of EIT to reliably distinguish structural details of targets, and specifically whether the same volume target is present as two objects or one.

3 Results and discussions

The results of distinguishability for 7 electrode geometries and 16 current patterns are shown in Fig. 2. We calculated the average values of detectability for different target positions in each case. Although we simulated all the combinations of stimulation and measurement patterns, we present representative results with equal number of stimulation and measurement patterns Δ_{sm}. The stimulation and measurement patterns for Planar-opposite and Zigzag-opposite geometries were rearranged to make their z values easy to compare with other configurations, and were renamed to Planar-interleaved and Zigzag-interleaved geometries.
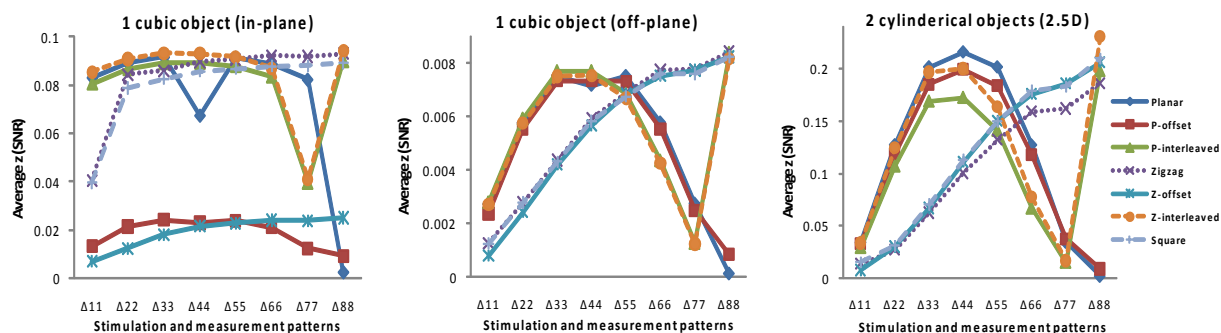

Figure 2: Average distinguishability values for 7 electrode geometries and 16 current patterns. *left*: a cubic object moved horizontally in the *central plane*, *middle*: a cubic object moved horizontally in *off-plane*, *right*: two full-height cylindrical objects (2.5 D). Each distinguishability value is the average value at 7 target positions.

Fig. 2 shows that different Δ_{sm} produced significantly different z values for all electrode geometries. It was observed that Zigzag and Square, Planar-interleaved and Zigzag-interleaved geometries produced the similar results and high distinguishability values for Δ_{88}. Zigzag, Zigzag-offset and Square geometries provided similar characteristics with increasing z value from Δ_{11} to Δ_{88} for off-plane effect with 1 and 2 objects. Planar and Planar-offset geometries have large off-plane effect. Thus, Zigzag, Square and Planar-interleaved configurations with Δ_{88} are considered to offer good performance while Zigzag-interleaved provides the best overall performance for EIT systems with a two-ring electrode phantom system.

In the future work, we will investigate varying distances between the 2 electrode layers and evaluate selected electrode configurations with a real measurement system.

4 References

[1] Bikker IG, Leonhardt S, Bakker J, *et al. Intensive Care Med* 2009; 35: 13621367.
[2] Hinz J, Hahn G, Neumann P, *et al. Intensive Care Med* 2003; 29: 3743.
[3] Adler A, Gaggero PO and Maimaitijiang Y, 2011, *Physiol. Meas.*, In press.
[4] Seagar A D 1983 *PhD Thesis University of Canterbury, Christchurch.*
[5] Brown B H and Seagar A D 1987 *Clin. Phys. Physiol. Meas.* 8, Suppl. A, 91-97.
[6] Graham B and Adler A, *Physiol. Meas.* 28 (2007) S29S44.
[7] Isaacson D 1986 *IEEE T Med Imaging* 5:91-95.
[8] Lionheart WR, Kaipio J, McLeod CN 2001, *Physiol. Meas.* 22 85-90.
[9] Adler A and Lionheart WRB, *Physiol. Meas.* 27:S25-S42, 2006.

Multi-scale interior potential approximation for EIT[3]

P. Kantartzis[1], A. Kunoth[2], R. Pabel[2], P. Liatsis[1]

[1]Information Engineering and Medical Imaging Group, City University London, Northampton square, EC1V 0HB, London, UK
[2] Institut für Mathematik, Universität Paderborn, Warburger Str. 100, 33098 Paderborn, Germany

E-mail: `p.kantartzis@city.ac.uk`

Abstract. We perform the forward EIT computations using biorthogonal B-Spline wavelet approximations. The proposed framework admits multiresolution which can be coupled with optimal preconditioning for linear-time forward operations and 'built-in adaptivity'. The multi-scale setting due to wavelets enables multi-scale approximation of the interior potential distribution with an immediate impact on the inverse problem computations. We report on sparse approximations of the interior potential distribution.

1. Introduction

In this paper, we propose a conceptually different approach for the numerical approximation of the forward operations, by means of the Domain Embedding Method (DEM) and Lagrange multipliers. Given that in the particular DEM setting the original domain or arbitrary shape can be registered to a square one, uniform grids can be employed. This is a significant reduction in the domain discretisation burden. Practically, only boundary surface discretisation is required. In the next section, the variational formulation of the problem, based on DEM, is set out. Discretisation of functions is performed by means of biorthogonal B-Spline wavelets. Numerical results of the multiscale potential distributions are provided. Concluding remarks are also drawn.

2. The DEM configuration

The forward problem is fundamental to the EIT problem as all information is encapsulated therein. In brief, forward computations account for the solution of a generalised Laplacian of the form

$$\nabla \cdot (\sigma \nabla u) = 0 \tag{1}$$

subject to the 'Complete Electrode Model (CEM) boundary conditions' in order to ensure existence and uniqueness of the solution [1]. $\Omega \subset \mathbb{R}^2$ is a bounded domain with L electrodes attached on its Lipschitz boundary surface $\partial\Omega$. $\Gamma \subset \partial\Omega$ is the union of areas under each electrode, assumed to be open connected subsets $\bigcup_{\ell=1}^{L} \Gamma_\ell = \Gamma$, whose closures are disjoint, $\bigcap_{\ell=1}^{L} \overline{\Gamma}_\ell = \emptyset$, and $\daleth := \partial\Omega \setminus \Gamma$ is the union of the remaining areas. Boundary conditions on Γ are defined as

$$u + z_\ell \sigma \nabla u \cdot \nu - U_\ell = 0 \quad \text{on} \quad \Gamma_\ell$$
$$\sigma \nabla u \cdot \nu = \imath \quad \text{on} \quad \Gamma,$$

where $\sigma, u, U_\ell, \nu, \imath, z_\ell$ are the admittivity, the interior potential distribution, the surface potential on the $\ell-$th electrode, the outward unit normal vector, the current density and the surface impedance, respectively. According to the CEM, on the interelectrode gaps we require that

$$\sigma \nabla u \cdot \nu = 0 \quad \text{on} \quad \daleth. \tag{2}$$

The weak formulation of the EIT problem on the original domain Ω can be stated as follows: Given the excitation currents $I = (I_1, \ldots, I_L)^T \in \mathbb{R}^L$, find $(u, U) \in \mathcal{H}_\Omega^1$ such that

$$a((u, U), (v, V)) = I^T \overline{V} \qquad \text{for all } (v, V) \in \mathcal{H}_\Omega^1. \tag{3}$$

with sesquilinear form is defined as

$$a_\Omega((v, V), (w, W)) := \int_\Omega \sigma \nabla v \cdot \nabla \overline{w} \, d\Omega + \sum_{\ell=1}^{L} \int_{\Gamma_\ell} \frac{1}{z_\ell}(v - V_\ell)(\overline{w} - \overline{W}_\ell) \, ds_{\Gamma_\ell} \tag{4}$$

and $\mathcal{H}_\Omega^1 := \{\mathcal{H}^1(\Omega) \oplus \mathbb{C}^L\}/\mathbb{C}$ is the (quotient) solution space.

2.1. Saddle point formulation on a fictitious domain $\square$

Assuming suitable extensions for all functions from Ω to a square domain $\square$ such that $\Omega \subset \square \subset \mathbb{R}^2$, the extension of $a_\Omega(\cdot, \cdot)$ to $\square$ is defined as

$$a_\square((v, V), (w, W)) := \int_\square \sigma \nabla v \cdot \nabla \overline{w} \, d\square + \sum_{\ell=1}^{L} \int_{\Gamma_\ell} \frac{1}{z_\ell}(v - V_\ell)(\overline{w} - \overline{W}_\ell) \, ds_{\Gamma_\ell}. \tag{5}$$

Amongst other advantages, this extension of the domain enables a flexible treatment of boundaries. For mathematical equivalence between the formulations on $a_\Omega(\cdot, \cdot)$ and $a_\square(\cdot, \cdot)$ one needs to append condition (2) to the enlarged domain $\square$. Using Lagrange multipliers as in [2], the equivalent EIT formulation is set out by minimizing the functional

$$\inf_{(v, V) \in \mathcal{H}_\square^1} \sup_{q \in \left(\mathcal{H}^{1/2}(\daleth)\right)'} \frac{1}{2} a_\square((v, V), (v, V)) - I^T \overline{V} + b(v, q), \tag{6}$$

where $b(v, q) := \int_\daleth q \sigma \nabla v \cdot \nu \, ds$ and $\mathcal{H}_\square^1$ is the appropriately defined solution space. The standard first order optimality conditions result in

$$\begin{aligned} a_\square((u, U), (v, V)) + b(v, p) &= I^T \overline{V} \\ b(u, q) &= 0. \end{aligned} \tag{7}$$

2.2. Discretisation of the continuous problem using wavelets

The wavelets we consider here are biorthogonal Riesz basis functions for the involved function spaces on $\square$ and $\daleth$. This means that they allow for a representation of the continuous saddle point problem without having to specify a certain finest resolution level. Thus, the system is discretised but not yet made finite-dimensional. Our choice of wavelets are tensor products of the biorthogonal spline-wavelets from [3], adapted to the interval as in [4]. They are defined in terms of scaling functions $\phi_{j,k}$ and corresponding wavelet basis functions $\psi_{j,k}$ (for resolution levels j and translations k). For notational convenience, we rewrite the fundamental two-scale relation $\phi(2^0 x) = \sum_m c_m \phi(2^1 x - m)$ in a compact matrix-vector form for resolution pitch 2^{-j} as $\mathbf{\Phi}_j = \mathbf{M}_{j,0}^T \mathbf{\Phi}_{j+1}$, and correspondingly the representation of the wavelets as $\mathbf{\Psi}_j = \mathbf{M}_{j,1}^T \mathbf{\Phi}_{j+1}$

where the matrices $\mathbf{M}_{j,0}, \mathbf{M}_{j,1}$ contain appropriately scaled coefficients c_m and identifying coefficients d_n for the wavelets [4]. Let $\boldsymbol{\Psi} = \{\boldsymbol{\Psi}_j\}_{j=j_0}^{\infty}$, $\tilde{\boldsymbol{\Psi}} = \{\tilde{\boldsymbol{\Psi}}_j\}_{j=j_0}^{\infty}$ be the collection of all wavelet functions from all levels, called a multiresolution basis, starting from a coarsest (minimum) level j_0. Now every function $v \in \mathcal{H}_{\square}^1$ can be expanded as

$$v = \mathbf{d}^T \boldsymbol{\Psi} =: \sum_{j=j_0-1}^{\infty} \mathbf{d}_j^T \boldsymbol{\Psi}_j := \mathbf{c}_{j_0}^T \boldsymbol{\Phi}_{j_0} + \sum_{j=j_0}^{\infty} \mathbf{d}_j^T \boldsymbol{\Psi}_j \qquad (8)$$

whose coefficients $\mathbf{c}_{j_0}, \mathbf{d}_j$ correspond to inner products defined with respect to the duals $\tilde{\boldsymbol{\Phi}}_{j_0}$, $\tilde{\boldsymbol{\Psi}}_j$. For iteratively solving the saddle point system (7), optimal preconditioning together with nested iteration yields an optimal $O(N)$ algorithm, N being the total amount of unknowns [2, 5]. Details can be found in [6].

2.3. Numerical results
For the numerical solution, we consider a homogeneous material of circular circumference embedded into the square domain. The circle is centered at $(.5,.5)$ and is of radius 0.25, and 8 equispaced electrodes are attached on its surface. The resolution is set to $j = 6$, whilst for functions defined on the boundary the resolution was set to $\zeta = 3$. The so-called 'LBB-condition' [2, 5, 7] is a stability condition which requires, in the setting considered herein, that the discretisation level on the boundary is not too high when compared to the discretisation level on $\square$. A first LBB investigation for the EIT case is reported in [5].
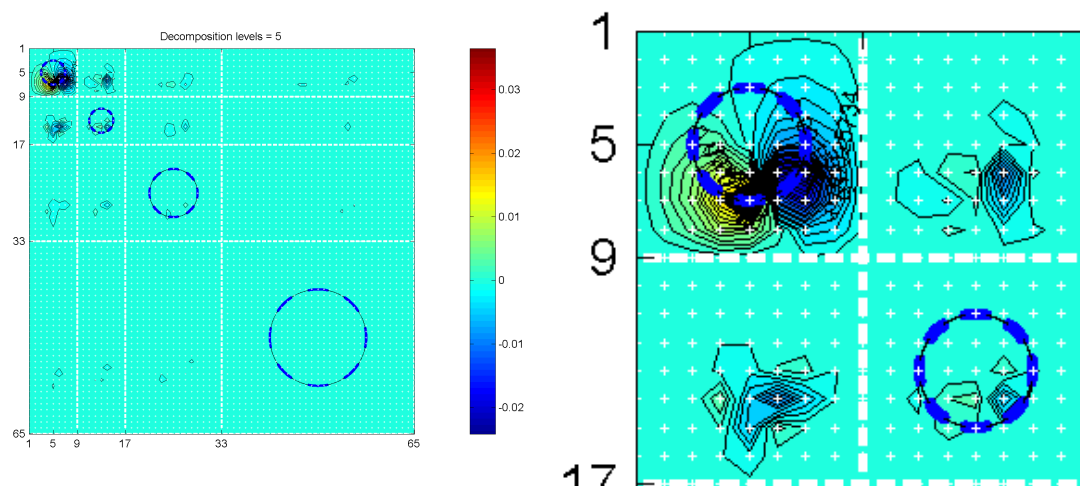
In Figure 1 (left) the wavelet coefficients of the interior potential approximation are provided. As can be seen from the zoomed-version of Figure 1 (right), notably, most coefficients are zero resulting in a sparse approximation of the potential distribution. For large-scale forward computations this is of great importance as only a few coefficients need to be stored. Further, the distribution of the wavelet coefficients serves as a prelude to adaptivity. The non-zero entries is where only local refinement is required.

Of importance is, moreover, the impact of the multiscale forward computations to the inverse problem. In fact, the multiscale forward computations give rise to multiscale sensitivity maps or simply the multiscale Jacobian. Notably, a multilevel Jacobian gives rise to multilevel material reconstructions.

3. Discussion
The forward formulation in EIT is typically approximated using the Finite Element Method due to domains of arbitrary shape. Further, piece-wise linear FEs enable many computational shortcuts and result in efficient EIT routines. This not necessarily the case for higher order, e.g., piece-wise quadratic, polynomials. While piece-wise linear FEs suffice for the interior and surface potential estimation (forward computations), it may not be sufficient for the inverse computations (gradients). This is due to the constant gradients (of piece-wise linears) over elements, required in the assembly of the Jacobian matrix. Therefore, higher order basis functions are necessitated but expected to reduce the computational shortcuts of the forward computations. This is not the case with wavelets as the forward problem can be tuned to yield uniformly bounded condition number, irrespectively of the order of the basis functions employed. In addition, computations based on wavelets are anticipated to encapsulate an additional element to the Jacobian; multiresolution. Recall that, currently, inverse computations are based on a Jacobian, assembled from insufficient information (collection of constants). Therefore, multiresolution is expected to substantially improve the inverse computations. More on this subject can be found in [6].

Figure 1. Multilevel potential distribution (contour plots) for excitation pair 1. Left: Distribution of wavelet coefficients. Right: Zoomed-in version of the coarsest level (upper left block) along with horizontal (upper right), diagonal (bottom right) and vertical (bottom left) decomposition.

4. Conclusions

In this paper, a saddle point formulation based on DEM was proposed for the solution of the forward EIT problem. A multiresolution discretization based on wavelets enabled asymptotically optimal preconditioning of the system matrix and, thus, together with nested iteration an iterative scheme of optimal complexity $\mathcal{O}(N)$. Multiscale numerical results of the interior potential distribution were presented. The suggested framework has an immediate impact on the inverse computations.

References

[1] Somersalo E, Cheney M and Isaacson D 1992 *SIAM J. App. Math.* **52** 1023–1040
[2] Kunoth A 1994 *Multilevel preconditioning* (Aachen: Shaker)
[3] Cohen A, Daubechies I and Feauveau J C 1992 *Comm. Appl. Math.* **45** 485–560
[4] Dahmen W, Kunoth A and Urban K 1999 *Appl. Comp. Harm. Anal.* **6** 132–196
[5] Kantartzis P, Kunoth A, Pabel A and Liatsis P 2010 *J. Phys: Conf. Ser.* **224** 012023
[6] Kantartzis P 2010 *Multilevel soft-field tomography* Ph.D. thesis City University London
[7] Brezzi F and Fortin M 1991 *Mixed and Hybrid Finite Element Methods* vol 15 (New York: Springer)

Single-scale interior potential approximation for EIT[3]

P. Kantartzis[1], A. Kunoth[2], R. Pabel[2], P. Liatsis[1]

[1]Information Engineering and Medical Imaging Group, City University London, Northampton square, EC1V 0HB, London, UK
[2] Institut für Mathematik, Universität Paderborn, Warburger Str. 100, 33098 Paderborn, Germany

E-mail: `p.kantartzis@city.ac.uk`

Abstract. We report numerical results of interior potential distributions based on the Domain Embedding Method (DEM) coupled with Lagrange multipliers. In the DEM, the original arbitrary domain is registered to a simpler one, herein a square. In this configuration, uniform grid discretisation engaged with single-scale linear B-Spline basis functions can be assumed in order to simplify domain integral computations and allow for flexible-boundary treatment. We emphasize on the use of the square geometry and its impact on the inverse problem setting.

1. Introduction

In a typical forward problem setting, currents are injected to (a subset of) electrodes attached to the body under consideration and the resulting voltages (on a disjoint subset of the same electrodes) are estimated up to instrumentation accuracy (or anticipated noise level). The resulting interior potential distribution is of great importance as it is extensively and repeatedly utilised for the numerical assembly of the linearised forward operator J (using the adjoint fields method [1]). Therefore, the interior potential distribution plays a central yet indirect role in the inverse problem computations, as, amongst others, it encapsulates the domain approximation. Given the arbitrary (and possibly non-stationary) domains encountered in EIT, one needs efficient means of evaluating domain integrals. In response, in the next section, we introduce the Domain Embedding Method (DEM). In the DEM setting considered herein the essential boundary conditions are appended by means of a Lagrange multiplier. Next, we provide the equivalent mathematical setting between the original and the DEM formulation. Finally, we present numerical results of the interior potential distribution and we finalise this paper with discussion and conclusions.

2. The DEM for the forward problem in EIT

According to the adjoint fields method [1], the process of assembling the forward operator in EIT requires repeated solutions of a generalised Laplacian PDE, subject to boundary conditions [2], of the form

$$
\begin{aligned}
\nabla \cdot (\sigma \nabla u) &= 0 & &\text{in } \Omega \\
\sigma \nabla u \cdot \nu &= \imath & &\text{on } \Gamma \\
u + z_\ell \sigma \nabla u \cdot \nu - U_\ell &= 0 & &\text{on } \Gamma_\ell
\end{aligned}
\tag{1}
$$

where $\sigma, u, U_\ell, \nu, \imath, z_\ell$ are the admittivity, the interior potential distribution, the surface potential on the $\ell-$th electrode, the outward unit normal vector, the current density and the surface impedance, respectively. Additional boundary conditions on the interelectrode gaps $\daleth$ require that

$$\sigma \nabla u \cdot \nu = 0 \quad \text{on } \daleth. \tag{2}$$

$\Omega \subset \mathbb{R}^2$ is a bounded domain equipped with L electrodes attached on its Lipschitz boundary surface $\partial\Omega$. $\Gamma \subset \partial\Omega$ is the union of areas under each electrode, assumed to be open connected subsets $\bigcup_{\ell=1}^{L} \Gamma_\ell = \Gamma$, whose closures are disjoint, $\bigcap_{\ell=1}^{L} \overline{\Gamma}_\ell = \emptyset$. $\daleth := \partial\Omega \setminus \Gamma$ is the union of the remaining boundary areas. Defining a sesquilinear form as

$$a_\Omega((v,V),(w,W)) := \int_\Omega \sigma \nabla v \cdot \nabla \overline{w} \, d\Omega + \sum_{\ell=1}^{L} \int_{\Gamma_\ell} \frac{1}{z_\ell} (v - V_\ell)(\overline{w} - \overline{W}_\ell) \, ds_{\Gamma_\ell}, \tag{3}$$

the weak formulation of the EIT problem on the original domain Ω can be stated as follows: Given the stimulation patterns (currents) $I = (I_1, \ldots, I_L)^T \in \mathbb{R}^L$, find $(u,U) \in \mathcal{H}^1_\Omega$ such that

$$a((u,U),(v,V)) = \sum_{\ell=1}^{L} I_\ell \overline{V}_\ell \qquad \text{for all } (v,V) \in \mathcal{H}^1_\Omega \tag{4}$$

where I_ℓ denotes the current applied to the ℓ-th electrode. In order to simplify numerically-intense domain computations whilst allowing for boundary perturbations, we embed the original domain Ω into a fictitious, square one, denoted as $\square$, i.e., $\Omega \subset \square \subset \mathbb{R}^2$. The extension of $a_\Omega(\cdot, \cdot)$ to $\square$ is defined as

$$a_\square((v,V),(w,W)) := \int_\square \sigma \nabla v \cdot \nabla \overline{w} \, d\square + \sum_{\ell=1}^{L} \int_{\Gamma_\ell} \frac{1}{z_\ell} (v - V_\ell)(\overline{w} - \overline{W}_\ell) \, ds_{\Gamma_\ell}. \tag{5}$$

where all functions were extended from Ω to $\square$. For a sound formulation we need to ensure that the resulting weak problem formulations, using either $a_\Omega(\cdot, \cdot)$ or $a_\square(\cdot, \cdot)$, are equivalent. To accomplish this, the 'natural' boundary condition (2) needs to be explicitly satisfied. Using Lagrange multipliers q as in [3], an equivalent EIT formulation for (4) in $\square$ can be recasted as a functional minimisation problem

$$\inf_{(v,V)\in\mathcal{H}^1_\square} \sup_{q\in\mathcal{Q}_\daleth} \frac{1}{2} a_\square((v,V),(v,V)) - \sum_{\ell=1}^{L} I_\ell \overline{V}_\ell + b(v,q) \tag{6}$$

with $b(v,q) := \int_\daleth q\sigma \nabla v \cdot \nu \, ds$ and $\mathcal{Q}_\daleth$ the dual of the conormal trace space. The standard first order optimality conditions read in operator form

$$\begin{bmatrix} A & B' \\ B & 0 \end{bmatrix} \begin{bmatrix} [u,U]^T \\ p \end{bmatrix} = \begin{bmatrix} I^T \overline{V} \\ 0 \end{bmatrix} \tag{7}$$

where $A : \mathcal{H}^1_\square \to (\mathcal{H}^1_\square)'$ is self-adjoint, $B : \mathcal{U}_\square \to \mathcal{U}_\daleth$ is the 'conormal trace' operator and B' its adjoint. The augmented Sobolev space for the solution vector is defined as $\mathcal{H}^1_\square := \mathcal{H}^1(\square) \oplus \mathbb{C}^L$ with dual space $(\mathcal{H}^1_\square)'$. In order to ensure well-posedness of the system (7), it is required that the so called inf sup-condition for the B-operator

$$\inf_{q\in\mathcal{Q}_\daleth} \sup_{v\in\mathcal{H}^1_\square} \frac{|\langle Bv, q\rangle|}{\|v\|_{\mathcal{H}^1_\square} \|q\|_{\mathcal{Q}_\daleth}} \geq \beta \tag{8}$$

holds for some constant $\beta > 0$. This is the case on the full boundary where $\mathcal{U}_\daleth = \mathcal{Q}_\daleth$ since standard trace theorems hold. The non-trivial and mathematically involved situation for part(s) of the boundary as required for the EIT case together with the precise definition of spaces $\mathcal{U}_\daleth$, $\mathcal{Q}_\daleth$ will be published elsewhere.

3. Discretisation

For numerical simulations operators A and B have to be made finite-dimensional. However, condition (8) does not automatically hold for any finite-dimensional subspaces of $\mathcal{H}^1_\square$ and $\mathcal{Q}_\urcorner$. The corresponding, so-called 'LBB-condition' [3, 4] is a stability condition which requires, in the setting considered here, that the discretisation level ζ on the boundary is not too high when compared to the discretisation level j on $\square$. We have tested the behaviour of the operator B in [5] for various values of j and ζ. Numerical evidence suggests that the LBB condition numerically holds as long as $\zeta + 2 < j$ and thereby confirms theoretical estimates [6].

3.1. Basis functions

Our choice of basis functions for the involved function spaces are tensor products of the linear B-Splines from [7], where zero boundary conditions were attained for $\square$. Such basis functions are also denoted als scaling functions $\phi_{j,k}$ in the wavelet literature [8] for resolution level j and translations k. For notational convenience, we rewrite the fundamental two-scale relation $\phi(2^0 x) = \sum_m c_m \phi(2^1 x - m)$ in a compact matrix-vector form for resolution pitch 2^{-j} as $\mathbf{\Phi}_j = \mathbf{M}^T_{j,0} \mathbf{\Phi}_{j+1}$ where the matrix $\mathbf{M}_{j,0}$ contains appropriately scaled coefficients c_m. Now every function $v \in \mathcal{H}^1_\square$ can be expanded as $v := \mathbf{c}^T_j \mathbf{\Phi}_j$ whose coefficients $\mathbf{c}_j$ can be interpreted as inner products defined with respect to functions $\tilde{\mathbf{\Phi}}_{j_0}$ dual to $\mathbf{\Phi}_j$ [8].

4. Numerical Results

For the numerical results, we set a homogeneous resistivity (real admittivity) experiment, consisting of four electrodes (blue line) and adjacent electrode stimulation. The original circular domain Ω of radius .25, centred at (.5,.5), is registered to a square one $\square := (0, 1)^2$. Resolution for functions on the boundary is set to $\zeta = 3$. The resulting potential distributions are shown in Figure 1 for progressively increasing resolution levels j. It can be observed that the equipotential distribution matches the expected one for a homogeneous body. However, the low resolution boundary discretisation ζ is evident in the coarser numerical results for j=4, 5. Near the interelectrode gaps boundary (black line) some contours appear to be slightly distorted. For instance, one may consider the contours near the point $(.7, .35)$ in Figure 1. However, as discretisation gets finer the potential distribution becomes smoother, waiving undesired boundary effects. It is anticipated that for relatively higher combinations of both ζ, j, boundary effects will be completely eliminated. Therefore, finer discretisation levels are desired.

5. Discussion

Apart from the flexible boundary treatment, the key advantage of the proposed formulation is the convenient square domain. The square grid configuration significantly simplifies domain integral computations. In standard FEM settings on arbitrary geometries such integral evaluations are computed over each domain element, thus are element (and domain) dependent. In the proposed DEM setting, where uniform grids are assumed, such computations can be rapidly evaluated. Furthermore, the current configuration enables standard multigrid-type iterations [9] at no additional effort, i.e., an optimal $O(N)$ algorithm for the forward computations, N being the total amount of unknowns. A second such asymptotically optimal (and for the saddle point problem simpler to implement) preconditioner is provided by the Fast Wavelet Transform, see [6, 10] in the context of EIT. Hereby, one switches to multiscale basis functions which additionaly allows for adaptivity. Details of the material in this paper can be found in [11].

In view of the inverse problem, the DEM setting gives rise to substantial computational savings for the assembly and evaluation of the sensitivity maps and eventually the linearised forward operator J, see [11]. Further, since computations take place on a square domain, the resulting reconstructions will, naturally, take place on a square domain avoiding the need for
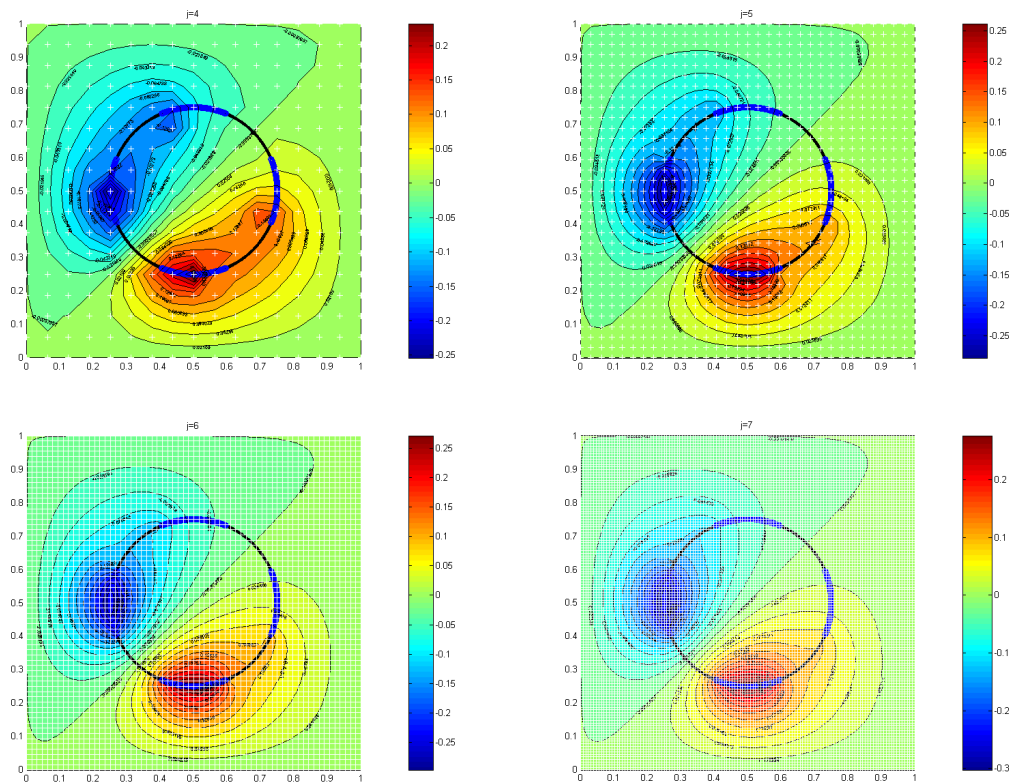
Figure 1. Forward computations (from top to bottom and left to right). The figures show the interior potential distribution for domain discretisation levels j=4,5,6 and 7.

artificial post-processing techniques, e.g., rasterisation, to make the images suitable for, e.g., clinical use. Thus, the resulting approximations are naturally 'pixelised'.

6. Conclusions

In this paper, a saddle point formulation was proposed for the solution of the forward EIT problem. The original arbitrary domain was embedded into a square geometry using DEM and Lagrange multipliers. This gave rise to computations on a standard pixelised domain whilst allowing for forward solvers of optimal computational complexity.

References

[1] Polydorides N and Lionheart W R B 2003 *Proc. 3rd Cong. Indust. Proc. Tomog.*
[2] Somersalo E, Cheney M and Isaacson D 1992 *SIAM J. App. Math.* **52** 1023–1040
[3] Kunoth A 1994 *Multilevel preconditioning* (Aachen: Shaker)
[4] Brezzi F and Fortin M 1991 *Mixed and Hybrid Finite Element Methods* vol 15 (New York: Springer)
[5] Kantartzis P, Kunoth A, Pabel R and Liatsis P 2010 *IEEE EMBC* 4991–4995
[6] Kunoth A 2001 *Wavelet Methods — Elliptic boundary value problems and control problems* (B.G. Teubner)
[7] de Boor C 2001 *A Practical Guide to Splines* revised ed (New York-Berlin: Springer)
[8] Cohen A, Daubechies I and Feauveau J C 1992 *Comm. Appl. Math.* **45** 485–560
[9] Hackbusch W 1985 *Multi-Grid Methods And Applications* 2nd ed (Germany: Springer)
[10] Kantartzis P, Kunoth A, Pabel A and Liatsis P 2010 *J. Phys: Conf. Ser.* **224** 012023
[11] Kantartzis P 2010 Ph.D. thesis City University London

A Newton Iterative Method with Initial Conductivity Estimation from Dynamic Algorithm

Hongbin Wang[1], Guizhi Xu[1], Guoya Dong[1], Ying Li[1], Shuai Zhang[1], Weili Yan[1]

[1] Province-Ministry Joint Key Laboratory of Electromagnetic Field and Electrical Apparatus Reliability, Hebei University of Technology, Tianjin 300130, P.R. China

E-mail: wanghongbin369@163.com

Abstract

The initial conductivity estimation accounts for a very important role in a Newton iterative algorithm for EIT reconstruction. A combination method is proposed that the initial conductivity is estimated from dynamic algorithm. After normalized, the pseudo conductivity estimation approximately describes the absolute conductivity distribution rather than a uniform initial distribution. Based on this method, we select generalized back projection algorithm (GBPA) to estimate initial distribution. Compared with uniform initial distribution, the images reconstructed with initial conductivity from GBPA are more accurate in terms of several metrics.

Keywords: Electrical impedance tomography, Image reconstruction, Initial estimation, Generalized Back Projection Algorithm, Image evaluation

1. Introduction

Electrical impedance tomography (EIT) seeks to reconstruct the conductivity distribution of an object using measurement data at its periphery. This technology attracts significant research interests for clinically monitoring patients, because EIT can provide a non-invasive continuous image of organs and tissue within human body [1]-[2].

Newton-type method is the standard approach of numerous ad hoc reconstruction methods which have been tried for EIT. The algorithm is to some extent the obvious feature: the inverse problem is non-linear, ill-posed and with large contrasts or complex geometries. So the computation needs processes of linearization, regularization and iteration [3]. The initial value determines the approximate direction of computation. The mismatch initial estimation probably risks guiding the iteration into local minimum intervals.

In this paper we propose a method that the initial conductivity is estimated from dynamic algorithm such as generalized back projection algorithm (GBPA). Although the result computed by dynamic algorithm is difference image, the pseudo conductivity distribution contains approximate information within the object. In section 2, we describe the method in detail, and introduce GBPA briefly for the article in which we proposed this algorithm completely has been accepted by CEFC2010 and will be published in IEEE Transactions on Magnetics soon. In section 3, we show simulation results and compare the method with the uniform initial value selection strategy.

2. Method

Based on Maxwell equations the EIT problem can be described as an elliptic equation.

$$\nabla \cdot (\sigma \nabla u) = 0 \quad \text{in} \, \Omega \tag{1}$$

where σ denotes the conductivity in the object Ω, u denotes the potential distribution.

The physical relationship between the conductivity σ and the potential perturbation u_p

is governed by an integral equation [4].

$$u_p = -\int_\Omega \sigma_p \nabla \psi_u \cdot \nabla \varphi_u dV \tag{2}$$

where ψ and φ are defined to be solution of equation (1), subscripts u and p are the uniform and perturbed equivalents respectively.

We assume that imaginary elements are substituted for previous subdivision elements. The potential of any inner node can be calculated through potential function ϕ of Finite Element Method (FEM), and represented by boundary voltage fitting curve along the equi-potential line. Then we have a novel equation from the sensitivity relationship (2)

$$\phi^{-1}\left(f_{v_u^i}\right) = \frac{-\int_\Omega \tilde{\sigma}_n \nabla \psi_u \cdot \nabla \varphi_u dV}{\int_\Omega \nabla \varphi_u^i \cdot \nabla \psi_u^i dV} \tag{3}$$

where $\tilde{\sigma}_n$ is normalized conductivity, $\tilde{\sigma}_n = \tilde{\sigma}_p / \sigma_u$; superscripts i and j corresponds to

the ith drive pair – receive pair combination and the jth imaginary element separately.

Through solving (3), we can reconstruct the normalized conductivity. When the result rewrite to resistivity form $\tilde{\rho}_n$, the calculation processes to pursue absolute values by Newton iterative method.

In terms of uniform distribution, (1) can be written as

$$\nabla \cdot \left(\frac{1}{c}\sigma\right)\nabla\varphi = \frac{1}{c}\nabla \cdot \sigma\nabla\varphi = 0 \tag{4}$$

where c is a scalar.

(4) indicates the linear relationship of boundary voltage $v(\rho)$ in terms of uniform resistivity ρ

$$v(\rho) = v(cI) = cv(I) \tag{5}$$

where I is unit resistivity vector.

Solving the coefficient c by least square method

$$c = \left[[v(I)]^T [v(I)]\right]^{-1}[v(I)]^T [v(\rho)] \tag{6}$$

If the uniform resistivity is selected to initial value, the first step of Modified Newton-Raphson Algorithm (MNR) [5] starts from uniform distribution. The resistivity variation of first step can be regarded as the pseudo result calculated by the dynamic algorithm. For the principle, GBPA solution contains distribution information. Instead of the uniform initial value, GBPA result approximates real distribution, therefore make the iteration efficient. Since the coefficient c describes from unit resistivity, the initial estimation can select $c\tilde{\rho}_n$.

3. Numerical Simulation and Evaluation

A circular model, as shown in Fig. 1., is established to assess the method. This model has 504 elements and 301 nodes. The target represents organ in human body setting resistivity $3\,\Omega\cdot m$ and that of other tissue $2\,\Omega\cdot m$.
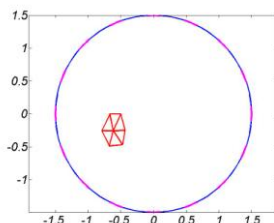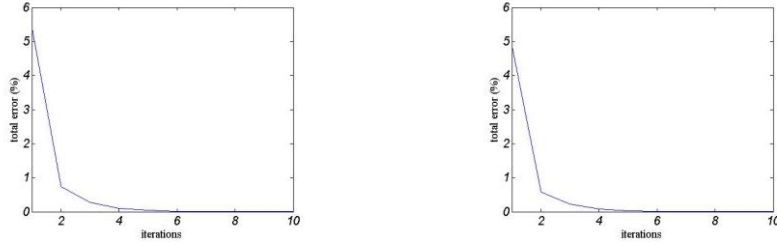

Fig. 1. The circular model with the target

In order to compare the two method of initial estimation, total error is defined as follow

$$err\_total = \sqrt{\sum_{i=1}^{m} [\rho_{\text{calculation}}(i) - \rho_{\text{true}}(i)]^2 \Big/ \sum_{i=1}^{m} [\rho_{\text{true}}(i)]^2} \qquad (7)$$

where $\rho_{\text{calculation}}(i)$ is calculated resistivity, $\rho_{\text{true}}(i)$ is real resistivity, m is the rank of resistivity vector. The iterative processions are shown in Fig. 2.
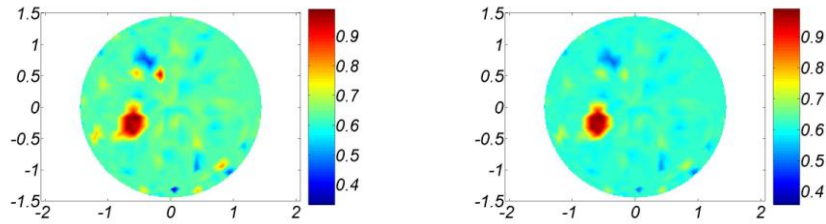

(a) Based on uniform distribution   (b) Based on solution of GBPA

Fig. 2. Error curves of the two initial estimation methods

The curves indicate that the initial error of the method based on GBPA is lower than that of uniform condition, and the same as each step error. The error decay rate of initial estimated by GBPA is higher than that of uniform condition, so that the initial value from GBPA can guide the iterative procession approximate real contribution faster.

Because the total errors almost equate to zero at 5th step from Fig. 2., the reconstruction images are selected at this step as shown in Fig. 3.

(a) Based on uniform distribution   (b) Based on solution of GBPA

Fig. 3. Reconstructed results at 5th step

To quantitatively interpret the reconstruction results, we use four metrics from [6]. We calculate a target object set $\hat{x}_s$, which contains all image pixels $[\hat{x}]_i$ greater than 75% of the maximum amplitude p. The centre of gravity (CoG) of $\hat{x}$ and $\hat{x}_s$ are calculated, and the distance from the CoG of reconstructed targets to the default targets centre is then calculated. Based on images of point targets, we use the following parameters:

(1) Position error (PE) measures the extent to which the position of target is faithfully reconstructed.

$$PE = \frac{1}{k} \sum_{s=1}^{k} p_s (r_t - r_s) \qquad (8)$$

where r_t is the CoG of default targets, r_s is the pixel position of the reconstructed target object set s, and k is the pixel number in this set. PE should be small and show small variability for targets at different radial positions.

(2) Resolution (RES) measures the size of reconstructed targets as a fraction of the medium.

$$RES = \sqrt{\sum_{k} p[\hat{x}_s]_k \Big/ \sum_{i \in \Omega} p[\hat{x}]_i} \qquad (9)$$

RES should be small in order to more accurately represent the shape of the target conductivity distribution. Low value of RES serves primarily to distinguish nearby targets.

(3) Shape deformation (SD) measures the fraction of the reconstructed pixel set which does not fit within a circle specified for targets.

$$SD = \sum_{k \notin T} p[\hat{x}_s]_k \Big/ \sum_{k} p[\hat{x}_s]_k \qquad (10)$$

where T is a circle which is centred at the CoG of $\hat{x}_s$ with an area equivalent to p_s. Large SD may result in incorrect interpretation of images.

(4) Information Entropy (IE) measures the information amount of the reconstructed images.

$$IE = \sum_i \left(\left(p[\hat{x}]_i / \sum p[\hat{x}] \right) \ln \left(p[\hat{x}]_i / \sum p[\hat{x}] \right) \right) \tag{11}$$

where we choose the ratio of any pixel amplitude and the sum of pixels amplitude. Large IE means more reconstructed information contained to provide more help to diagnosis.

In order to compare the two initial selection strategies, the four parameters are computed and showed in TABEL I.

TABLE I COMPARISON OF INITIAL DISTRIBUTION BASED ON UNIFORM AND GBPA

	PE	RES	SD	IE
Based on uniform	0.00090614	0.0068698	0.00092289	10.289
Based on GBPA	0.00082105	0.0063729	0	10.301

The results indicate that reconstructed target with initial value from GBPA have smaller position error in the comparison of the method with uniform initial. In terms of resolution, the target show by the method based on GBPA is easier to distinguish than that reconstructed based on uniform. Also, the pixels of target reconstructed by GBPA initial estimation are more densely clustered in the specified target circular range. The reconstructed image of GBPA initial selection strategy contains more image information of conductivity distribution.

4. Conclusion

In this paper the combination method is proposed for EIT image reconstruction, which determines MNR initial value with GBPA computation result. The initial estimation decreases initial error and iterative error at every step compared with uniform choice. This initial selection strategy provides theoretical ways to select initial value, therefore prevents the iteration procession falling to local minimum intervals. Compared with uniform initial estimation, the combination method performs better in the simulations at the same iterative step. For future work, efforts will be on attempting to implement the method in 3D.

Acknowledgements

References

[1] Frerichs I, Dargaville P A, Dudykevych T and Rimensberger P C 2003 Electrical Impedance Tomography: A Method for Monitoring Regional Lung Aeration and Tidal Volume Distribution? *Intensive Care Med.* 29 2312-6

[2] Luepschen H, Meier T, Grossherr M, Leibecke T, Karsten J and Leonhardt S 2007 Protective ventilation using electrical impedance tomography *Physiol. Meas.* 29 S247–60

[3] Lionheart W R 2004 EIT Reconstruction Algorithms: Pitfalls, Challenges and Recent Developments *Physiol. Meas.* 25 125-142

[4] Barber D C 1990 Image Reconstruction in Applied Potential Tomography – Electrical Impedance Tomography *Internal Report* Department of Medical Physics and Clinical Engineering, University of Sheffield, UK

[5] Peter Metherall 1998 Three Dimensional Electrical Impedance Tomography of the Human Thorax *PhD Thesis* Department of Medical Physics and Clinical Engineering, University of Sheffield, UK

[6] Adler A, Arnold J H, Bayford R, et al 2009 GREIT: a unified approach to 2D linear EIT reconstruction of lung images *Physiol. Meas.* 30 S35-S55

A Novel Forward Problem Solver Based on Meshfree Method for Electrical Impedance Tomography

Gang HU, Min-you CHEN, Wei HE, Jin-qian ZHAI

State Key Laboratory of Power Transmission Equipment & System Security and New Technology, Chongqing University, Chongqing 400044, China

gang.hu.cq@gmail.com

Abstract. In this paper the meshfree method is developed to solve the forward problem for electrical impedance tomography. Differ from finite element method and finite volume method, there is no mesh generation in meshfree method. It is easier to realize and more propitious to be developed as an adaptive procedures for image reconstruction. Numerical results are presented and compared with the results of analytical solution. It is observed that the obtained results are consistent with the results of analytical solution.

Keywords. Electrical Impedance Tomography, Forward Problem, Meshfree Method

1 Introduction

The Electrical Impedance Tomography (EIT) is the process of estimating internal conductivity (changes) through low frequency currents injected into an object and voltages measured at the surface. It was widely applied in fields of biomedicine, geophysics and industry. The methods proposed to solve the forward problem include analytical methods, finite difference methods (FDM), boundary element methods (BEM), finite element methods (FEM) and finite volume methods (FVM). While analytical methods are restricted to very simple domains and FDM typically require grids that are topologically regular in some sense, BEM, FEM and FVM are fairly easy to handle arbitrary geometries and boundary shapes. However, BEM alone can only be used on homogeneous regions, and is useful for fitting impedance values to known regions [1]. To non-homogeneous conductivity distributions on irregular domains problem, the FEM and FVM is more suitable. The comparison between FEM and FVM for EIT forward problem was described in [2]. These methods require an efficient mesh of an object with smooth but irregular surfaces, which respects interior boundaries and electrodes on the surface. The mesh density needs to be determined as a function of position so that high field strengths (for example near electrodes and where conductivity has sharp contrasts) can be accurately represented without excessive density in areas where the field varies slowly [3]. The use of adaptive meshing in both forward and inverse problems was explored in [4], but in practice, it is very time consuming for just trying to develop specific procedures to define the mesh or to properly refine it.

Recently, meshfree methods have become attractive alternatives for problems in computational electromagnetics [5]-[8]. These methods do not require a mesh to discretize the problem domain. The approximation functions are constructed entirely using a set of scattered

nodes, and no element or connectivity of the nodes is needed. Meshfree techniques include two classes: those based on collocations and those based on weak forms. The former is a truly meshfree method and does not require a mesh structure or a numerical integration procedure, but it is less stable and less accurate. Selection of nodes based on the type of a physical problem is still important for obtaining stable and accurate results [9]. The latter includes two categories: those require background cells for the integration over the entire problem domain and those require background cells locally for the integration. The methods belonging to the second category are essentially mesh free because creating a local mesh is a simpler task that can be performed automatically without any predefinition for the local mesh [9]. The meshless local Petrov-Galerkin (MLPG) methods belong to this category.

In [10], an approach combined FEM with meshfree method was proposed to solve the forward problem of EIT. The approach used element-free Galerkin (EFG) method based on moving least square (MLS) approximation function to discretize the mesh free region. The EFG method needs background cells for the integration over the entire problem domain. In this paper, a novel MLPG method based on the Radial basis functions (RBF) was developed for the numerical solution of the forward problem for EIT.

2 The Solution of Meshfree Method
2.1 The Weak Form of Forward Problem for EIT

In EIT, the potential distribution function φ and conductivity distribution function σ in the region Ω are governed by the Laplace equation (1) which subject to the boundary condition (2).

$$\nabla[\sigma(x) \cdot \nabla\varphi(x)] = 0 \quad x \in \Omega \tag{1}$$

$$\sigma(x)\frac{\partial\varphi(x)}{\partial n} = j(x) \quad x \in \partial\Omega \tag{2}$$

where x is a point in the problem domain, j is the current density applied on the boundary, $\partial\Omega$ is the boundaries of Ω and n is the unit outward normal vector to the boundary surface. The major idea in MLPG is that the implementation of the integral form of the weighted residual method is confined to a very small local sub-domain of a node. That is

$$\int_{\Omega} \psi_i \cdot \nabla(\sigma \cdot \nabla\varphi^h)d\Omega = \int_{\Omega_i} \psi_i \cdot \nabla(\sigma \cdot \nabla\varphi^h)d\Omega = 0 \tag{3}$$

where φ^h is the approximated solution of φ obtained by RBF and ψ_i is the weighted function which define on the sub-domain Ω_i. Integration by parts and application of the Gaussian integration formula lead to

$$\int_{\Omega_i} \psi_i \cdot \nabla(\sigma \cdot \nabla\varphi^h)d\Omega = \int_{\Gamma_i} \psi_i \cdot \sigma \cdot \nabla\varphi^h \cdot n d\Gamma - \int_{\Omega_i} \nabla\psi_i \cdot \nabla(\sigma \cdot \nabla\varphi^h)d\Omega \tag{4}$$

where Γ_i is the boundary of the sub-domain Ω_i and n is the unit outward normal vector to the boundary Γ_i. If the weighted function was selected in such a way that it vanishes on Γ_i (the cubic or quartic spline can be chosen), then in the case of sub-domain Ω_i is located entirely within the global domain Ω, the expression of (4) was changed to

$$\int_{\Omega_i} \nabla\psi_i \cdot \nabla(\sigma \cdot \nabla\varphi^h)d\Omega = 0 \tag{5}$$

and in the case of sub-domain Ω_i intersects with the problem boundary $\partial\Omega$, the expression of

(4) was changed to

$$\int_{\Omega_i} \nabla \psi_i \cdot \nabla(\sigma \cdot \nabla \varphi^h) d\Omega = \int_{\Gamma_{it}} \psi_i \cdot jd\Gamma \tag{6}$$

where Γ_{it} is the part of the natural boundary that intersects with the sub-domain Γ_i.

2.2 Calculation with RBF-MLPG

Using Equation (5) or (6) and integrating over the sub-domain, leads to discretized system equations for each node in the problem domain. This gives a set of algebraic equations for each node. By assembling all these sets of equations, a set of discretized system equations for the entire problem domain can then be obtained. In this paper, the RBF approximation procedure was used, the approximation of φ in sub-domain is given by:

$$\varphi^h(r) = \sum_{i=1}^{n} \Phi_i(r)\varphi_i \tag{7}$$

where n is the node number in sub-domain, $\Phi_i(r)$ is the shape function and φ_i is the potential value for node i. Substitution of equation (7) into equation (5) or (6) for all nodes leads to the following discretized system of linear equations:

$$[K][\varphi] = [f] \tag{8}$$

where [K] and [f] are "stiffness" matrix and the "load" vector respectively defined as:

$$K_{ij} = \int_{\Omega_i} \nabla \psi_i \cdot \sigma \cdot \nabla^2 \Phi_j(r) d\Omega \quad , \quad f_i = 0 \ or \int_{\Gamma_{it}} \psi_i \cdot jd\Gamma \tag{9}$$

3 Simulation Results

The model of a 2-D homogeneous circular was adopted to observe the accuracy of the RBF-MLPG method. For simplicity, we let $\sigma = 1$. To test the robust of the proposed method, two cases of EIT forward problem were simulated. The first one is a 200-node scattered point model and the second one is a uniform 217 nodes model, as shown in Fig.1.
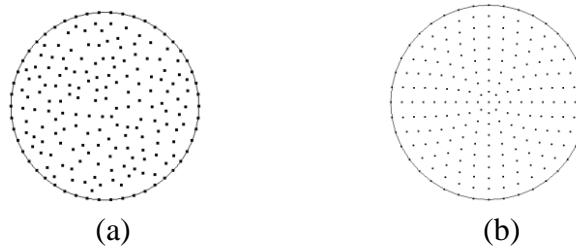

(a)   (b)

Fig.1 (a) scattered point model and (b) uniform nodes model

For precise investigation, the following error indicator was used:

$$e = \sqrt{\frac{\sum_{i=1}^{N}(\varphi_i^{exact} - \varphi_i^{num})^2}{\sum_{i=1}^{N}(\varphi_i^{exact})^2}} \tag{10}$$

where N is the node number in problem domain, φ_i^{exact} is the potential value for node i calculated by the analytical method and φ_i^{num} is the potential value for node i calculated by the numerical methods.

The errors for scattered point model and uniform nodes model were 0.49% and 0.62%, respectively. It means that stable estimates of the potential distribution can be obtained with the RBF_MLPG solution.

A FE model with the same uniform 217 nodes, shown in Fg.1 (b), was also used to carry out the FEM procedure, the corresponding error was 1.30%. Thus, more accurate estimates of the potential distribution can be obtained with the RBF_MLPG solution.

4 Conclusions

The RBF-MLPG method was developed to solve the forward problem for EIT. A local interpolation technique using RBF was used to construct the trial function entirely in terms of a set of scattered nodes. Compared to finite element method in transient procedure, MLPG does not need mesh generation which leads to more efficient computations. The results show that RBF-MLPG is highly accurate and robust.

References

1. de Munck, JC, Faes, TJC, Heethaar, RM, The boundary element method in the forward and inverse problem of electrical impedance tomography, IEEE Trans Bio-Med Eng, 47, 792-800(2000)

2. Guoya Dong, J. Zou, Richard H. Bayford, Xinshan Ma, Shangkai Gao, Weili Yan, and Manling Ge, The Comparison Between FVM and FEM for EIT Forward Problem, IEEE TRANSACTIONS ON MAGNETICS, VOL. 41, NO. 5, 1468-1471(2005)

3. William R B Lionheart, EIT reconstruction algorithms: pitfalls, challenges and recent developments. Physiol. Meas. 25, 125--142(2004)

4. Molinari M, High Fidelity Imaging in Electrical Impedance Tomography, PhD thesis, University of Southampton(2003)

5. Simone Aparecida Viana and Renato Cardoso Mesquita, Moving Least Square Reproducing Kernel Method for Electromagnetic Field Computation, IEEE TRANSACTIONS ON MAGNETICS, VOL. 35, NO. 3, 1372-1375(1999)

6. S.A. Viana, D. Rodger and H.C. Lai, Meshless local Petrov–Galerkin method with radial basis functions applied to electromagnetics, IEE Proc.-Sci. Meas. Technol., Vol. 151, No. 6, 449-451(2004)

7. Frederico G. Guimarães, Rodney R. Saldanha, Renato C. Mesquita, David A. Lowther, and Jaime A. Ramírez, A Meshless Method for Electromagnetic Field Computation Based on the Multiquadric Technique, IEEE TRANSACTIONS ON MAGNETICS, VOL. 43, NO. 4, 1281-1284(2007)

8. Yong Zhang, K. R. Shao, Youguang Guo, Jianguo Zhu, D. X. Xie, and J. D. Lavers, An Improved Multiquadric Collocation Method for 3-D Electromagnetic Problems, IEEE TRANSACTIONS ON MAGNETICS, VOL. 43, NO. 4, 1509-1512(2007)

9. G. R. Liu, Meshfree Methods: Moving Beyond the Finite Element Method, CRC Press(2003)

10. V. Cutrupi, F. Ferraioli, A. Formisano, and R. Martone, An Approach to the Electrical Resistance Tomography Based on Meshless Methods, IEEE TRANSACTIONS ON MAGNETICS, VOL. 43, NO. 4, 1717-1720(2007)